Transactions of the ASME®

Transactions of the ASME, Journal of Applied Mechanics (ISSN 0021-8936) is published bimonthly (Jan., Mar., May, July, Sept., Nov.) The American Society of Mechanical Engineers, Three Park Avenue, New York, NY 10016. Periodicals postage paid at New York, NY and additional mailing office. POSTMASTER: Send address changes to Transactions of the ASME, Journal of Applied Mechanics, c/o THE AMERICAN SOCIETY OF MECHANICAL ENGINEERS, 22 Law Drive, Box 2300, Fairfield, NJ 07007-2300. **CHANGES OF ADDRESS** must be received at Society headquarters seven weeks before they are to be effective. Please send old label and new address. **STATEMENT from By-Laws.** The Society shall not be responsible for statements or opinions advanced in papers or . . . printed in its publications (B7.1, Para. 3).

INDEXED by Applied Mechanics Reviews and Engineering Information, Inc. Canadian Goods & Services Tax Registration #126148048.

Journal of Applied Mechanics

Published Bimonthly by The American Society of Mechanical Engineers

VOLUME 70 • NUMBER 1 • JANUARY 2003

Special Section on Flow Simulation and Modeling

TECHNICAL PAPERS

ADDITIONAL TECHNICAL PAPERS

(**Contents continued on inside back cover**)

This journal is printed on acid-free paper, which exceeds the ANSI Z39.48-1992 specification for permanence of paper and library materials. ∞™
♲ 85% recycled content, including 10% post-consumer fibers.

(**Contents continued**)

Journal of Applied Mechanics **Volume 70, Number 1** **JANUARY 2003**

BRIEF NOTES

ANNOUNCEMENTS AND SPECIAL NOTES

The ASME Journal of Applied Mechanics is abstracted and indexed in the following:

Alloys Index, Aluminum Industry Abstracts, Applied Science & Technology Index, AMR Journal Article Abstracts Database, Ceramic Abstracts, Chemical Abstracts, Civil Engineering Abstracts, Compendex (The electronic equivalent of Engineering Index), Computer & Information Systems Abstracts, Corrosion Abstracts, Current Contents, EEA (Earthquake Engineering Abstracts Database), Electronics & Communications Abstracts Journal, Engineered Materials Abstracts, Engineering Index, Environmental Engineering Abstracts, Environmental Science and Pollution Management, Fluidex, Fuel & Energy Abstracts, GeoRef, Geotechnical Abstracts, INSPEC, International Aerospace Abstracts, Journal of Ferrocement, Materials Science Citation Index, Mechanical Engineering Abstracts, METADEX (The electronic equivalent of Metals Abstracts and Alloys Index), Metals Abstracts, Nonferrous Metals Alert, Polymers Ceramics Composites Alert, Referativnyi Zhurnal, Science Citation Index, SciSearch (Electronic equivalent of Science Citation Index), Shock and Vibration Digest, Solid State and Superconductivity Abstracts, Steels Alert, Zentralblatt MATH

Journal of Applied Mechanics

Preface

This special collection of papers is based on some of the invited presentations at the Fifth U.S.-Japan Symposium on Flow Simulation and Modeling that was held on March 29–31, 2000 at Rice University in Houston, TX. A large number of the other invited papers will be published in a special issue of the *International Journal of Computational Fluid Dynamics*.

The Symposium was sponsored by the Rice University George R. Brown School of Engineering and the Department of Mechanical Engineering and Materials Science. The Organizing Committee consisted of Mutsuto Kawahara (Chuo University), Tayfun Tezduyar (Rice University), and Thomas Hughes (Stanford University).

The topics covered in this special collection of papers include determination of finite element stabilization parameters and length scales; extended finite element techniques based on level set functions applied to two-fluid flows; finite element flow solvers for ship hydrodynamics applications; numerical solutions of Cauchy-Riemann equations; hierarchical divergence-free bases applied to particulate flows; aerodynamic interactions between parachutes; mesh moving techniques; and fluid-particle interactions.

We would like to thank the authors for the effort in preparing their contribution and for meeting the deadline. We also would like to thank those whom we asked for help in reviewing these papers.

Tayfun E. Tezduyar
Rice University
Associate Editor

Thomas J. R. Hughes
Stanford University
Guest Editor
May 2002

J. E. Akin

T. Tezduyar

M. Ungor

Mechanical Engineering,
Rice University,
MS 321,
Houston, TX 77005

S. Mittal

Aerospace Engineering,
IIT Kanpur,
Kanpur 208016, India

Stabilization Parameters and Smagorinsky Turbulence Model

For the streamline-upwind/Petrov-Galerkin and pressure-stabilizing/Petrov-Galerkin formulations for flow problems, we present in this paper a comparative study of the stabilization parameters defined in different ways. The stabilization parameters are closely related to the local length scales ("element length"), and our comparisons include parameters defined based on the element-level matrices and vectors, some earlier definitions of element lengths, and extensions of these to higher-order elements. We also compare the numerical viscosities generated by these stabilized formulations with the eddy viscosity associated with a Smagorinsky turbulence model that is based on element length scales.

[DOI: 10.1115/1.1526569]

1 Introduction

In recent decades, we have seen a substantial interest in and emphasis on using stabilized formulations in flow simulation and modeling with the finite element method. Streamline-upwind/Petrov-Galerkin (SUPG) formulation for incompressible flows, [1], SUPG formulation for compressible flows, [2], Galerkin/least-squares (GLS) formulation, [3], and pressure-stabilizing/Petrov-Galerkin (PSPG) formulation for incompressible flows, [4] are some of the most significant stabilized formulations that found usage in a wide range of applications. Many real-world flow problems are included among the applications that were addressed. These stabilized formulations became so attractive primarily because they stabilize the method without introducing excessive numerical dissipation. It is in this mindful way that they prevent numerical oscillations and other instabilities in solving problems with high Reynolds and/or Mach numbers and shocks and strong boundary layers, as well as when using equal-order interpolation functions for velocity and pressure and other unknowns. It was pointed out in [5] that these stabilized formulations also substantially improve the convergence rate in iterative solution of the large, matrix systems. Such matrix systems are solved at every Newton-Raphson step in iterative solution of the coupled nonlinear equation systems generated at every time level of a simulation.

The SUPG, GLS and PSPG formulations all include a stabilization parameter that is mostly referred to in the literature as "τ." In general, this parameter might involve a measure of the local length scale (i.e., the "element length") and other factors such as the local Reynolds and Courant numbers. Various element lengths and τs were proposed for the SUPG formulation, starting with those proposed in [6] and [2], and followed by the one introduced in [7]. More element lengths and τs were prescribed for the SUPG, GLS, and PSPG methods reported later. Some other τs, dependent upon spatial and temporal discretizations, were introduced and tested in [8]. Later, τs which are applicable to higher-order elements were proposed in [9].

Recently, new ways of computing the τs based on the element-level matrices and vectors were introduced in [10]. These new definitions are expressed in terms of the ratios of the norms of the relevant matrices or vectors. They automatically take into account the local length scales, advection field, and the element-level Reynolds number. Based on these definitions, a τ can be calculated for each element, or even for each element node or degree-of-freedom or element equation. It was also shown in [10] that these τs, when calculated for each element, yield values quite comparable to those calculated based on the definition introduced in [7]. In conjunction with these stabilization parameters, in [11], a discontinuity-capturing directional dissipation stabilization was introduced as a potential alternative or complement to the LSIC (least-squares on incompressibility constraint) stabilization. A second element length scale based on the solution gradient was also introduced in [11]. This new element length scale would be used together with the element length scales already defined (directly or indirectly) in [10]. New stabilization parameters for the diffusive limit were introduced in [12]. These new parameters are closely related to the second element length scale that was introduced in [11]. That second element length scale can be recognized in [12] as a diffusion length scale.

In this paper we carry out a comparative investigation of the stabilization parameters and element length scales defined in the above references, as well as the element length scales defined in other work (see [6,13]). These comparisons include extensions of all these stabilization parameters and element length scales to higher-order elements. Furthermore, we compare the numerical viscosities generated by the SUPG stabilization with the eddy viscosity introduced by a Smagorinsky turbulence model, [14], specifically one that is based on element length scales, [15].

2 Formulations and Stabilization Parameters

2.1 Advection-Diffusion Equation. Consider over a domain Ω with boundary Γ the following time-dependent advection-diffusion equation, written on Ω and $\forall t \in (0,T)$ as

$$\frac{\partial \phi}{\partial t} + \mathbf{u} \cdot \nabla \phi - \nabla \cdot (\nu \nabla \phi) = 0, \tag{1}$$

where ϕ represents the transported quantity, $\mathbf{u}$ is a divergence-free advection field, and ν is the diffusivity. The essential and natural boundary conditions associated with Eq. (1) are

$$\phi = g \quad \text{on } \Gamma_g, \mathbf{n} \cdot \nu \nabla \phi = h \quad \text{on } \Gamma_h, \tag{2}$$

where Γ_g and Γ_h are complementary subsets of the boundary Γ, $\mathbf{n}$ is the unit normal vector, and g and h are given functions. A function $\phi_0(\mathbf{x})$ is specified as the initial condition.

Given suitably defined finite-dimensional trial solution and test function spaces $\mathcal{S}_\phi^h$ and $\mathcal{V}_\phi^h$, the stabilized finite element formulation of Eq. (1) can be written as follows: find $\phi^h \in \mathcal{S}_\phi^h$ such that $\forall w^h \in \mathcal{V}_\phi^h$:

Contributed by the Applied Mechanics Division of the THE AMERICAN SOCIETY OF MECHANICAL ENGINEERS for publication in the ASME JOURNAL OF APPLIED MECHANICS. Manuscript received by the ASME Applied Mechanics Division, Jan. 18, 2002; final revision, June 11, 2002. Associate Editor: L. T. Wheeler. Discussion on the paper should be addressed to the Editor, Prof. Robert M. McMeeking, Department of Mechanical and Environmental Engineering University of California—Santa Barbara, Santa Barbara, CA 93106-5070, and will be accepted until four months after final publication of the paper itself in the ASME JOURNAL OF APPLIED MECHANICS.

$$\int_{\Omega} w^h\left(\frac{\partial \phi^h}{\partial t}+\mathbf{u}^h\cdot\boldsymbol{\nabla}\phi^h\right)d\Omega+\int_{\Omega}\boldsymbol{\nabla}w^h\cdot\nu\boldsymbol{\nabla}\phi^h d\Omega-\int_{\Gamma_h} w^h h d\Gamma$$

$$+\sum_{e=1}^{n_{el}}\int_{\Omega^e}\tau_{\mathrm{SUPG}}\mathbf{u}^h\cdot\boldsymbol{\nabla}w^h\left(\frac{\partial\phi^h}{\partial t}+\mathbf{u}^h\cdot\boldsymbol{\nabla}\phi^h-\boldsymbol{\nabla}\cdot(\nu\boldsymbol{\nabla}\phi^h)\right)d\Omega$$

$$=0. \tag{3}$$

Here n_{el} is the number of elements, Ω^e is the domain for element e, and τ_{SUPG} is the SUPG stabilization parameter.

With the notation $\mathbf{b}{:}\int_{\Omega^e}(\ldots)d\Omega{:}\mathbf{b}_{\mathrm{V}}$ denoting the element-level matrix $\mathbf{b}$ and element-level vector $\mathbf{b}_{\mathrm{V}}$ corresponding to the element-level integral $\int_{\Omega^e}(\ldots)d\Omega$. The element-level matrices and vectors are defined as follows:

$$\mathbf{m}{:}\qquad \int_{\Omega^e} w^h\frac{\partial\phi^h}{\partial t}d\Omega \qquad :\mathbf{m}_{\mathrm{V}}, \tag{4}$$

$$\mathbf{c}{:}\qquad \int_{\Omega^e} w^h\mathbf{u}^h\cdot\boldsymbol{\nabla}\phi^h d\Omega \qquad :\mathbf{c}_{\mathrm{V}}, \tag{5}$$

$$\mathbf{k}{:}\qquad \int_{\Omega^e}\boldsymbol{\nabla}w^h\cdot\nu\boldsymbol{\nabla}\phi^h d\Omega \qquad :\mathbf{k}_{\mathrm{V}}, \tag{6}$$

$$\tilde{\mathbf{k}}{:}\qquad \int_{\Omega^e}\mathbf{u}^h\cdot\boldsymbol{\nabla}w^h\mathbf{u}^h\cdot\boldsymbol{\nabla}\phi^h d\Omega \qquad :\tilde{\mathbf{k}}_{\mathrm{V}}, \tag{7}$$

$$\tilde{\mathbf{c}}{:}\qquad \int_{\Omega^e}\mathbf{u}^h\cdot\boldsymbol{\nabla}w^h\frac{\partial\phi^h}{\partial t}d\Omega \qquad :\tilde{\mathbf{c}}_{\mathrm{V}}. \tag{8}$$

From [10], the element-level Reynolds and Courant numbers can be written as

$$\mathrm{Re}=\frac{\|\mathbf{u}^h\|^2}{\nu}\frac{\|\mathbf{c}\|}{\|\tilde{\mathbf{k}}\|}, \tag{9}$$

$$\mathrm{Cr}_u=\frac{\Delta t}{2}\frac{\|\mathbf{c}\|}{\|\mathbf{m}\|}, \tag{10}$$

$$\mathrm{Cr}_\nu=\frac{\Delta t}{2}\frac{\|\mathbf{k}\|}{\|\mathbf{m}\|}, \tag{11}$$

$$\mathrm{Cr}_{\tilde{\nu}}=\frac{\Delta t}{2}\tau_{\mathrm{SUPG}}\frac{\|\tilde{\mathbf{k}}\|}{\|\mathbf{m}\|}, \tag{12}$$

where $\|\mathbf{b}\|$ is the norm of matrix $\mathbf{b}$. Also from [10], we write the components of the element-matrix-based τ_{SUPG}:

$$\tau_{\mathrm{S1}}=\frac{\|\mathbf{c}\|}{\|\tilde{\mathbf{k}}\|}, \tag{13}$$

$$\tau_{\mathrm{S2}}=\frac{\Delta t}{2}\frac{\|\mathbf{c}\|}{\|\tilde{\mathbf{c}}\|}, \tag{14}$$

$$\tau_{\mathrm{S3}}=\tau_{\mathrm{S1}}\mathrm{Re}=\left(\frac{\|\mathbf{c}\|}{\|\tilde{\mathbf{k}}\|}\right)\mathrm{Re}, \tag{15}$$

and the construction of τ_{SUPG}:

$$\tau_{\mathrm{SUPG}}=\left(\frac{1}{\tau_{\mathrm{S1}}^r}+\frac{1}{\tau_{\mathrm{S2}}^r}+\frac{1}{\tau_{\mathrm{S3}}^r}\right)^{-\frac{1}{r}}. \tag{16}$$

We note that τ_{S1}, τ_{S2}, and τ_{S3} are the limiting values for, respectively, the advection-dominated, transient-dominated, and diffusion-dominated cases. We should also note that Eqs. (9)–(15) involve the ratios of matrix norms. Our experience has shown that these ratios are relatively insensitive to the definition of the norm. Examples herein employ the Frobenius norm.

In [10], the element-vector-based τ_{SUPG} is defined as

$$(\tau_{\mathrm{SUPG}})_{\mathrm{V}}=\left(\frac{1}{\tau_{\mathrm{SV1}}^r}+\frac{1}{\tau_{\mathrm{SV2}}^r}+\frac{1}{\tau_{\mathrm{SV3}}^r}\right)^{-\frac{1}{r}}, \tag{17}$$

where

$$\tau_{\mathrm{SV1}}=\frac{\|\mathbf{c}_{\mathrm{V}}\|}{\|\tilde{\mathbf{k}}_{\mathrm{V}}\|}, \tag{18}$$

$$\tau_{\mathrm{SV2}}=\frac{\|\mathbf{c}_{\mathrm{V}}\|}{\|\tilde{\mathbf{c}}_{\mathrm{V}}\|}, \tag{19}$$

$$\tau_{\mathrm{SV3}}=\tau_{\mathrm{SV1}}\mathrm{Re}=\left(\frac{\|\mathbf{c}_{\mathrm{V}}\|}{\|\tilde{\mathbf{k}}_{\mathrm{V}}\|}\right)\mathrm{Re}. \tag{20}$$

2.2 Navier-Stokes Equations of Incompressible Flows. The Navier-Stokes equations for incompressible flows can be written as

$$\rho\left(\frac{\partial\mathbf{u}}{\partial t}+\mathbf{u}\cdot\boldsymbol{\nabla}\mathbf{u}-\mathbf{f}\right)-\boldsymbol{\nabla}\cdot\boldsymbol{\sigma}=0\quad\text{on }\ \Omega, \tag{21}$$

$$\boldsymbol{\nabla}\cdot\mathbf{u}=0\quad\text{on }\Omega, \tag{22}$$

where ρ, $\mathbf{u}$ and $\mathbf{f}$ are the density, velocity, and the external force, respectively. The stress tensor $\boldsymbol{\sigma}$ is defined as

$$\boldsymbol{\sigma}(p,\mathbf{u})=-p\mathbf{I}+2\mu\boldsymbol{\varepsilon}(\mathbf{u}). \tag{23}$$

Here p is the pressure, $\mathbf{I}$ is the identity tensor, $\mu=\rho\nu$ is the viscosity, ν is the kinematic viscosity, and $\boldsymbol{\varepsilon}(\mathbf{u})$ is the strain-rate tensor:

$$\boldsymbol{\varepsilon}(\mathbf{u})=\frac{1}{2}((\boldsymbol{\nabla}\mathbf{u})+(\boldsymbol{\nabla}\mathbf{u})^T). \tag{24}$$

The essential and natural boundary conditions associated with Eq. (21) are

$$\mathbf{u}=\mathbf{g}\ \text{ on }\ \Gamma_g,\mathbf{n}\cdot\boldsymbol{\sigma}=\mathbf{h}\ \text{ on }\ \Gamma_h, \tag{25}$$

where $\mathbf{g}$ and $\mathbf{h}$ are given functions. A divergence-free velocity field $\mathbf{u}_0(\mathbf{x})$ is specified as the initial condition.

Given suitably defined finite-dimensional trial solution and test function spaces for velocity and pressure, $\mathcal{S}_{\mathbf{u}}^h$, $\mathcal{V}_{\mathbf{u}}^h$, $\mathcal{S}_p^h$ and $\mathcal{V}_p^h=\mathcal{S}_p^h$, the stabilized finite element formulation of Eqs. (21)–(22) can be written as follows: Find $\mathbf{u}^h\in\mathcal{S}_{\mathbf{u}}^h$ and $p^h\in\mathcal{S}_p^h$ such that $\forall\mathbf{w}^h\in\mathcal{V}_{\mathbf{u}}^h$ and $q^h\in\mathcal{V}_p^h$:

$$\int_{\Omega}\mathbf{w}^h\cdot\rho\left(\frac{\partial\mathbf{u}^h}{\partial t}+\mathbf{u}^h\cdot\boldsymbol{\nabla}\mathbf{u}^h-\mathbf{f}\right)d\Omega$$

$$+\int_{\Omega}\boldsymbol{\varepsilon}(\mathbf{w}^h){:}\boldsymbol{\sigma}(p^h,\mathbf{u}^h)d\Omega-\int_{\Gamma_h}\mathbf{w}^h\cdot\mathbf{h}^h d\Gamma$$

$$+\int_{\Omega}q^h\boldsymbol{\nabla}\cdot\mathbf{u}^h d\Omega$$

$$+\sum_{e=1}^{n_{el}}\int_{\Omega^e}\frac{1}{\rho}[\tau_{\mathrm{SUPG}}\rho\mathbf{u}^h\cdot\nabla\mathbf{w}^h+\tau_{\mathrm{PSPG}}\nabla q^h]$$

$$\times\left[\rho\left(\frac{\partial\mathbf{u}^h}{\partial t}+\mathbf{u}^h\cdot\boldsymbol{\nabla}\mathbf{u}^h\right)-\boldsymbol{\nabla}\cdot\boldsymbol{\sigma}(p^h,\mathbf{u}^h)-\rho\mathbf{f}\right]d\Omega$$

$$+\sum_{e=1}^{n_{el}}\int_{\Omega^e}\tau_{\mathrm{LSIC}}\boldsymbol{\nabla}\cdot\mathbf{w}^h\rho\boldsymbol{\nabla}\cdot\mathbf{u}^h d\Omega=0. \tag{26}$$

Here τ_{PSPG} and τ_{LSIC} are the PSPG and LSIC (least-squares on incompressibility constraint) stabilization parameters.

We now define the following element-level matrices and vectors:

$$\mathbf{m}: \quad \int_{\Omega^e} \mathbf{w}^h \cdot \rho \frac{\partial \mathbf{u}^h}{\partial t} d\Omega \quad :\mathbf{m}_{\mathrm{V}}, \tag{27}$$

$$\mathbf{c}: \quad \int_{\Omega^e} \mathbf{w}^h \cdot \rho (\mathbf{u}^h \cdot \boldsymbol{\nabla} \mathbf{u}^h) d\Omega \quad :\mathbf{c}_{\mathrm{V}}, \tag{28}$$

$$\mathbf{k}: \quad \int_{\Omega^e} \boldsymbol{\varepsilon}(\mathbf{w}^h) : 2\mu \boldsymbol{\varepsilon}(\mathbf{u}^h) d\Omega \quad :\mathbf{k}_{\mathrm{V}}, \tag{29}$$

$$\mathbf{g}: \quad \int_{\Omega^e} (\boldsymbol{\nabla} \cdot \mathbf{w}^h) p^h d\Omega \quad :\mathbf{g}_{\mathrm{V}}, \tag{30}$$

$$\mathbf{g}^{\mathrm{T}}: \quad \int_{\Omega^e} q^h (\boldsymbol{\nabla} \cdot \mathbf{u}^h) d\Omega \quad :\mathbf{g}_{\mathrm{V}}^{\mathrm{T}}, \tag{31}$$

$$\tilde{\mathbf{k}}: \quad \int_{\Omega^e} (\mathbf{u}^h \cdot \boldsymbol{\nabla} \mathbf{w}^h) \cdot \rho (\mathbf{u}^h \cdot \boldsymbol{\nabla} \mathbf{u}^h) d\Omega \quad :\tilde{\mathbf{k}}_{\mathrm{V}}, \tag{32}$$

$$\tilde{\mathbf{c}}: \quad \int_{\Omega^e} (\mathbf{u}^h \cdot \boldsymbol{\nabla} \mathbf{w}^h) \cdot \rho \frac{\partial \mathbf{u}^h}{\partial t} d\Omega \quad :\tilde{\mathbf{c}}_{\mathrm{V}}, \tag{33}$$

$$\tilde{\gamma}: \quad \int_{\Omega^e} (\mathbf{u}^h \cdot \boldsymbol{\nabla} \mathbf{w}^h) \cdot \boldsymbol{\nabla} p^h d\Omega \quad :\tilde{\gamma}_{\mathrm{V}}, \tag{34}$$

$$\beta: \quad \int_{\Omega^e} \boldsymbol{\nabla} q^h \cdot \frac{\partial \mathbf{u}^h}{\partial t} d\Omega \quad :\beta_{\mathrm{V}}, \tag{35}$$

$$\gamma: \quad \int_{\Omega^e} \boldsymbol{\nabla} q^h \cdot (\mathbf{u}^h \cdot \boldsymbol{\nabla} \mathbf{u}^h) d\Omega \quad :\gamma_{\mathrm{V}}, \tag{36}$$

$$\theta: \quad \int_{\Omega^e} \boldsymbol{\nabla} q^h \cdot \boldsymbol{\nabla} p^h d\Omega \quad :\theta_{\mathrm{V}}, \tag{37}$$

$$\mathbf{e}: \quad \int_{\Omega^e} (\boldsymbol{\nabla} \cdot \mathbf{w}^h) \rho (\boldsymbol{\nabla} \cdot \mathbf{u}^h) d\Omega \quad :\mathbf{e}_{\mathrm{V}}. \tag{38}$$

The element-level Reynolds and Courant numbers are defined in the same way as they were defined before, given by Eqs. (9)–(12). The components of the element-matrix-based τ_{SUPG} are defined in the same way as they were defined before, given by Eqs. (13)–(15). τ_{SUPG} is constructed from its components in the same way as it was constructed before, given by Eq. (16). The components of the element-vector-based τ_{SUPG} are defined in the same way as they were defined before, given by Eqs. (18)–(20). The construction of $(\tau_{\mathrm{SUPG}})_{\mathrm{V}}$ is also the same as it was before, given by Eq. (17).

From [10], we write the element-matrix-based τ_{PSPG} as

$$\tau_{\mathrm{PSPG}} = \left(\frac{1}{\tau_{\mathrm{P1}}^r} + \frac{1}{\tau_{\mathrm{P2}}^r} + \frac{1}{\tau_{\mathrm{P3}}^r} \right)^{-\frac{1}{r}}, \tag{39}$$

where

$$\tau_{\mathrm{P1}} = \frac{\|\mathbf{g}^{\mathrm{T}}\|}{\|\gamma\|}, \tag{40}$$

$$\tau_{\mathrm{P2}} = \frac{\Delta t}{2} \frac{\|\mathbf{g}^{\mathrm{T}}\|}{\|\beta\|}, \tag{41}$$

$$\tau_{\mathrm{P3}} = \tau_{\mathrm{P1}} \mathrm{Re} = \left(\frac{\|\mathbf{g}^{\mathrm{T}}\|}{\|\gamma\|} \right) \mathrm{Re}. \tag{42}$$

Also from [10], the element-vector-based τ_{PSPG} is written as

$$(\tau_{\mathrm{PSPG}})_{\mathrm{V}} = \left(\frac{1}{\tau_{\mathrm{PV1}}^r} + \frac{1}{\tau_{\mathrm{PV2}}^r} + \frac{1}{\tau_{\mathrm{PV3}}^r} \right)^{-\frac{1}{r}}, \tag{43}$$

where

$$\tau_{\mathrm{PV1}} = \tau_{\mathrm{P1}}, \tag{44}$$

$$\tau_{\mathrm{PV2}} = \tau_{\mathrm{PV1}} \frac{\|\gamma_{\mathrm{V}}\|}{\|\beta_{\mathrm{V}}\|}, \tag{45}$$

$$\tau_{\mathrm{PV3}} = \tau_{\mathrm{PV1}} \mathrm{Re}. \tag{46}$$

Lastly from [10], the element-matrix-based τ_{LSIC} and the element-vector-based τ_{LSIC} are given as

$$\tau_{\mathrm{LSIC}} = \frac{\|\mathbf{c}\|}{\|\mathbf{e}\|}, \tag{47}$$

$$(\tau_{\mathrm{LSIC}})_{\mathrm{V}} = \tau_{\mathrm{LSIC}}. \tag{48}$$

For the purpose of comparison, we also define here stabilization parameters that are based on an earlier definition of the length scale h first introduced in [7]:

$$h_{\mathrm{UGN}} = 2\|\mathbf{u}^h\| \left(\sum_{a=1}^{n_{en}} |\mathbf{u}^h \cdot \boldsymbol{\nabla} N_a| \right)^{-1}, \tag{49}$$

where N_a is the interpolation function associated with node a. The stabilization parameters are defined as

$$\tau_{\mathrm{SUGN1}} = \frac{h_{\mathrm{UGN}}}{2\|\mathbf{u}^h\|}, \tag{50}$$

$$\tau_{\mathrm{SUGN2}} = \frac{\Delta t}{2}, \tag{51}$$

$$\tau_{\mathrm{SUGN3}} = \frac{h_{\mathrm{UGN}}^2}{4\nu}, \tag{52}$$

$$(\tau_{\mathrm{SUPG}})_{\mathrm{UGN}} = \left(\frac{1}{\tau_{\mathrm{SUGN1}}^2} + \frac{1}{\tau_{\mathrm{SUGN2}}^2} + \frac{1}{\tau_{\mathrm{SUGN3}}^2} \right)^{-\frac{1}{2}} \tag{53}$$

$$(\tau_{\mathrm{PSPG}})_{\mathrm{UGN}} = (\tau_{\mathrm{SUPG}})_{\mathrm{UGN}}, \tag{54}$$

$$(\tau_{\mathrm{LSIC}})_{\mathrm{UGN}} = \frac{h_{\mathrm{UGN}}}{2} \|\mathbf{u}^h\| z. \tag{55}$$

Here z is given as follows:

$$z = \begin{cases} \left(\dfrac{\mathrm{Re}_{\mathrm{UGN}}}{3} \right) & \mathrm{Re}_{\mathrm{UGN}} \leq 3, \\ 1 & \mathrm{Re}_{\mathrm{UGN}} > 3, \end{cases} \tag{56}$$

where $\mathrm{Re}_{\mathrm{UGN}} = \dfrac{\|\mathbf{u}^h\| h_{\mathrm{UGN}}}{2\nu}$.

Remark 1 *The discontinuity-capturing directional dissipation (DCDD) stabilization was introduced in* [11] *as a potential alternative or complement to the LSIC stabilization. As part of the DCDD stabilization, a second element length scale that is based on the solution gradient was also introduced in* [11].

Remark 2 *New definitions for the diffusion-dominated limits of the SUPG and PSPG stabilization parameters were introduced in* [12]. *These new definitions are closely related to the second element length scale that was first introduced in* [11] *and later employed in* [12] *as a diffusion length scale.*

Remark 3 *For the advection-dominated limits of the SUPG and PSPG stabilization parameters, equivalent length scales can be defined by simply multiplying the stabilization parameter with* $2\|\mathbf{u}^h\|$.

For the comparative investigation we would like to carry out, we also provide here element length scales defined in other studies, based on the element shapes and advection field. For notational convenience, we first define the following unit vector:

$$\mathbf{s}=\frac{\mathbf{u}^h}{\|\mathbf{u}^h\|}. \tag{57}$$

The element length given in [6] for a quadrilateral element can be written as

$$h_{\mathrm{SA1}}=\left|\left(\frac{\mathbf{x}_2+\mathbf{x}_3}{2}-\frac{\mathbf{x}_4+\mathbf{x}_1}{2}\right)\cdot\mathbf{s}\right|+\left|\left(\frac{\mathbf{x}_3+\mathbf{x}_4}{2}-\frac{\mathbf{x}_1+\mathbf{x}_2}{2}\right)\cdot\mathbf{s}\right|, \tag{58}$$

where $\mathbf{x}_a$ is the nodal coordinate vector associated with node a. For triangular elements, we use the following expression from [13]:

$$h_{\mathrm{SA1}}=\frac{1}{4}\left[|(\mathbf{x}_2-\mathbf{x}_1)\cdot\mathbf{s}|+|(\mathbf{x}_3-\mathbf{x}_2)\cdot\mathbf{s}|+|(\mathbf{x}_1-\mathbf{x}_3)\cdot\mathbf{s}|\right]. \tag{59}$$

To write some of the other element lengths given in [13], we first define a special sign function:

$$S\mathrm{Sgn}(y)=\begin{Bmatrix}-1 & y\leqslant 0\\ +1 & y>0\end{Bmatrix}, \tag{60}$$

and the streamwise components of the nodal "radial" position vectors:

$$\delta_a=(\mathbf{x}_a-\mathbf{x}_o)\cdot\mathbf{s}, \tag{61}$$

where

$$\mathbf{x}_o=\left(\sum_{a=1}^{n_{en}}\mathbf{x}_a\right)/n_{en}. \tag{62}$$

The number of upstream and downstream element nodes can be expressed as

$$n_{uen}=\sum_{a=1}^{n_{en}}\frac{1}{2}(1-S\mathrm{Sgn}(\delta_a)), \tag{63}$$

$$n_{den}=\sum_{a=1}^{n_{en}}\frac{1}{2}(1+S\mathrm{Sgn}(\delta_a)). \tag{64}$$

Then one of the element lengths given in [13] can be written as

$$h_{\mathrm{SA2}}=\left(\sum_{a=1}^{n_{en}}\frac{1}{2}(1+S\mathrm{Sgn}(\delta_a))\,\delta_a\right)\Bigg/\ n_{den}-\left(\sum_{a=1}^{n_{en}}\frac{1}{2}(1-S\mathrm{Sgn}(\delta_a))\,\delta_a\right)\Bigg/\ n_{uen}. \tag{65}$$

Another one of the element lengths given in [13] can be written as

$$h_{\mathrm{SA3}}=max(\delta_1,\delta_2,\ldots\delta_{n_{en}})-min(\delta_1,\delta_2,\ldots\delta_{n_{en}}). \tag{66}$$

A third element length given in [13] is the node-based version of the one given by Eq. (65):

$$(h_{\mathrm{SA4}})_a=\left|\delta_a-\left(\sum_{a=1}^{n_{en}}\frac{1}{2}(1-S\mathrm{Sgn}(\delta_a))\,\delta_a\right)\Bigg/\ n_{uen}\right|. \tag{67}$$

2.3 Streamline-Upwind/Petrov-Galerkin (SUPG) Stabilization and Smagorinsky Turbulence Viscosities. To compare the numerical viscosities generated by the SUPG stabilization with the eddy viscosity introduced by a Smagorinsky turbulence model, we first write an equivalent "viscosity" based on the SUPG stabilization parameter:

$$\nu_{\mathrm{SUPG}}=\tau_{\mathrm{SUPG}}\|\mathbf{u}^h\|^2. \tag{68}$$

The eddy viscosity introduced by a Smagorinsky turbulence model that is based on the element length scales [15] is written as

$$\nu_{\mathrm{SMAG}}=(0.1h_{\mathrm{SMAG}})^2(2\boldsymbol{\varepsilon}(\mathbf{u}^h):\boldsymbol{\varepsilon}(\mathbf{u}^h))^{1/2}, \tag{69}$$

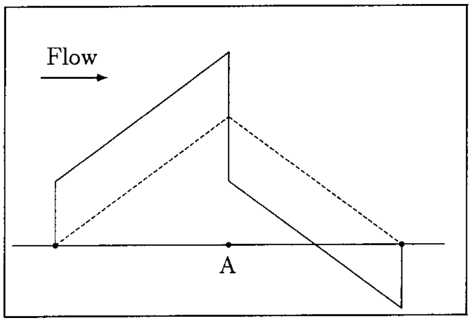

Fig. 1 For linear elements, Galerkin (broken line) and SUPG (solid line) functions, assembled for a global node *A*

where h_{SMAG} is the square-root (or cube-root) of the area (or volume) of the element.

4 Comparisons

3.1 Element Length Comparisons. We first inspect in one dimension the functions (N_a) and $(N_a+\tau_{\mathrm{SUGN1}}\mathbf{u}^h\cdot\boldsymbol{\nabla}N_a)$, which we will call, respectively, "Galerkin function" and "SUPG function." Figs. 1–3 show, for linear, quadratic, and cubic elements, these functions after they are assembled for a global node. While the Galerkin functions are continuous across element boundaries, the SUPG perturbations to them are not. For a linear element the perturbation is constant over an element, but for quadratic and cubic elements it is not. The same thing can be said for the element length h_{UGN} (see Fig. 4). When averaged over an element, and normalized by the element length for a linear element, the normalized average values of h_{UGN} for quadratic and cubic elements are approximately 0.52 and 0.30. The normalized average values of the equivalent length scale computed from τ_{S1} (with the 1-norm of the element level matrices) for quadratic and cubic elements are approximately 1/4 and 1/6.

Stabilization parameters and element lengths based on different definitions, including those based on element-level matrices and vectors and $(\tau_{\mathrm{SUPG}})_{\mathrm{UGN}}$ and $(\tau_{\mathrm{PSPG}})_{\mathrm{UGN}}$, were calculated and tested in [10]. The matrix norm used in [10] was the 1-norm. The tests were carried out for several shapes of bilinear quadrilateral

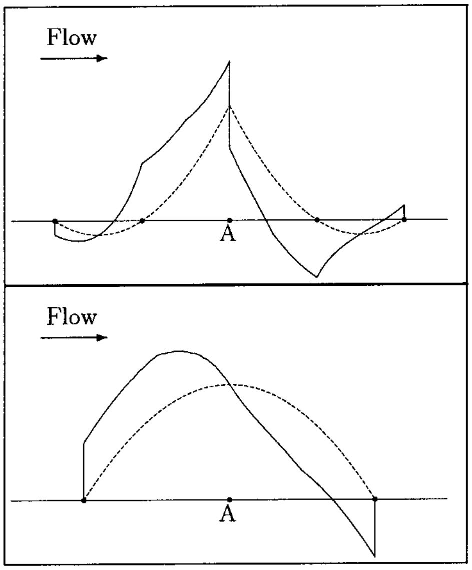

Fig. 2 For quadratic elements, Galerkin (broken line) and SUPG (solid line) functions, assembled for a global node *A*. For nodes at element boundaries (top) and interiors (bottom).

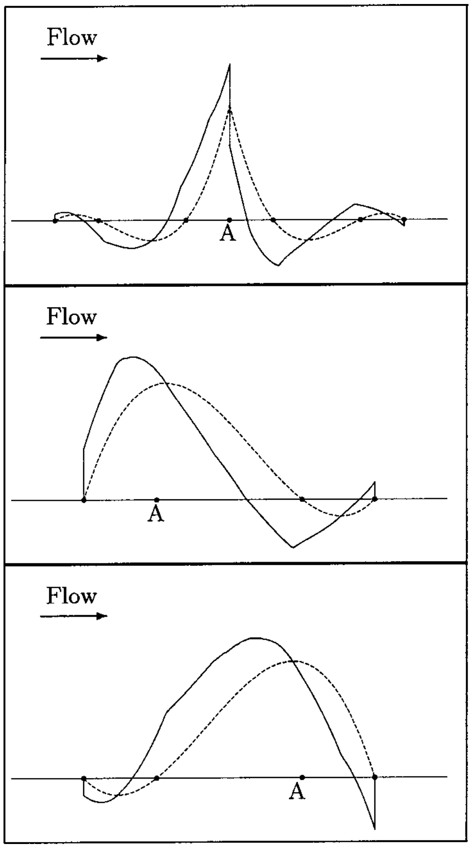

Fig. 3 For cubic elements, Galerkin (broken line) and SUPG (solid line) functions, assembled for a global node *A*. For nodes at element boundaries (top), upstream interiors (middle), and downstream interiors (bottom).

and linear triangular elements, with $\|\mathbf{u}\|=1.0$ and $\Delta t=1.0$, and as function of the advection direction. The test flow computations reported in [10] show that the definitions based on the element-level matrices and vectors perform well.

Here, element lengths are calculated and compared for linear, quadratic and cubic elements in two-dimensions, based on four of the definitions given in this paper: the equivalent length scale computed from τ_{S1} (with the Frobenius norm of the element level matrices), h_{UGN}, h_{SA1}, and h_{SA2}. Definitions that depend on the location within an element are evaluated at the origin of the natural coordinate system for quadrilateral elements and at the centroid for triangular elements. Both Lagrangian and serendipity quadrilaterals have been evaluated. The element lengths calculated based on the definitions listed above are shown in Figs. 5–7. The element shape is indicated by a dashed line and the nodes are indicated by a circled cross. Each closed curve represents a different element length definition. For each advection direction, the element length is that of a line through the element center, parallel to the advection, bounded by its intersections with the closed curve. In other words, let us imagine a line passing through the center and find its two intersection points with the closed curve. Then the distance between those two points is the element length in that advection direction. Although the results displayed here for τ_{S1} are based on the Frobenius norm of the element level matrices, we see little difference between the τ_{S1}s calculated with different matrix norms. From Figs. 5–7, we note that the difference between different element length definitions is more pronounced for higher-order elements. In general, the element length decreases with the increase in the order of the element. This observation is consistent with what we see for h_{UGN} in one dimension (see Fig. 4).

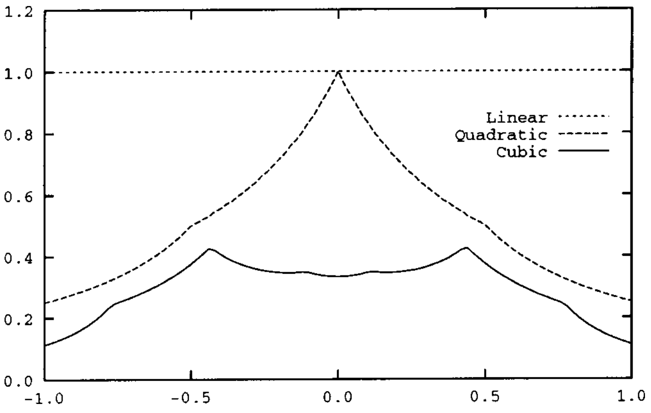

Fig. 4 Variation of h_{UGN} within linear and higher-order one-dimensional elements

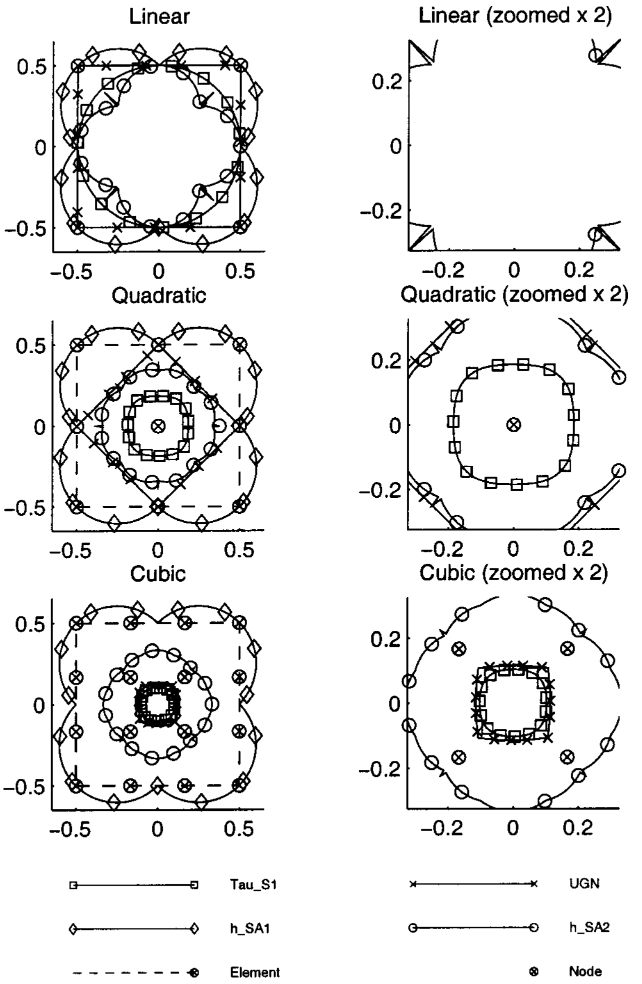

Fig. 5 For a square Lagrangian element, the element length calculated with different definitions and as function of advection direction

3.2 Comparison of Streamline-Upwind/Petrov-Galerkin (SUPG) Stabilization and Smagorinsky Turbulence Viscosities. Flow past a cylinder at Re=3,000 and Re=50,000 are used as test problems to compare the numerical viscosities generated by the SUPG stabilization with the numerical viscosity introduced by a Smagorinsky turbulence model. The stabilization parameters

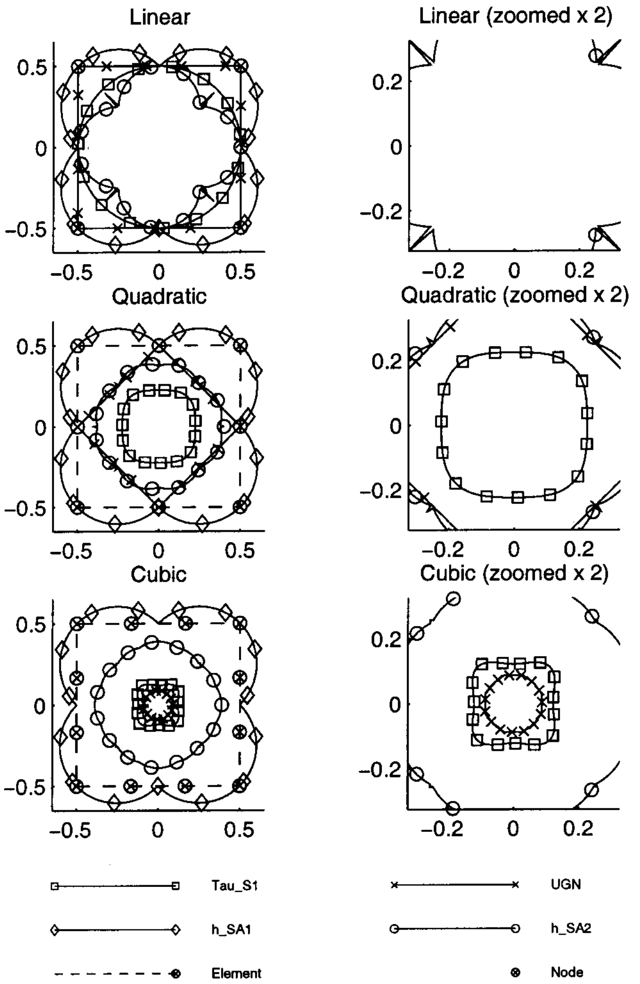

Fig. 6 For a square serendipity element, the element length calculated with different definitions and as function of advection direction

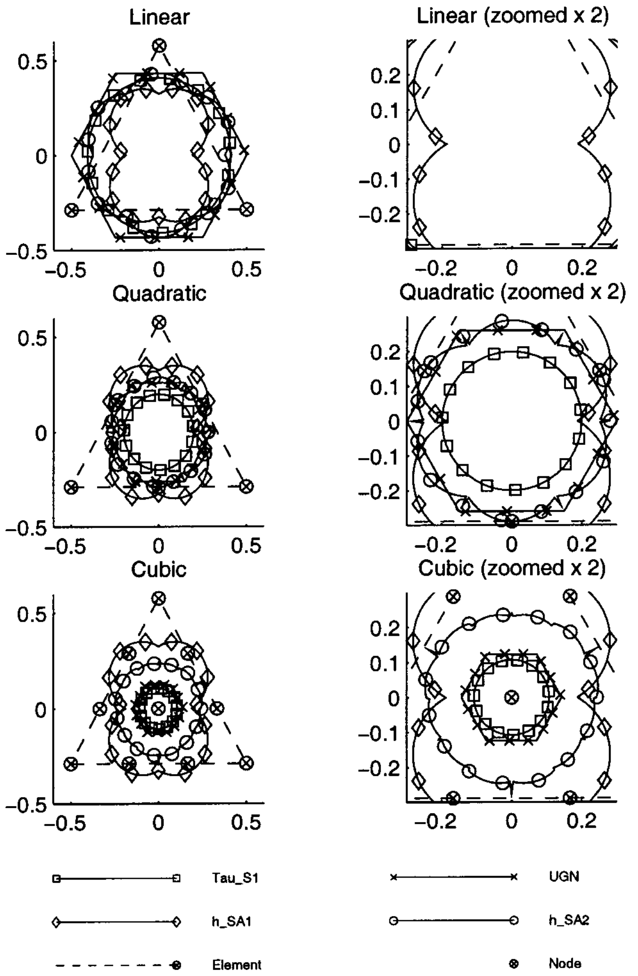

Fig. 7 For an equilateral triangular element, the element length calculated with different definitions and as function of advection direction

are computed as given by Eqs. (49)–(56), but with the τ_{SUGN2} component dropped. When calculating $\mathrm{Re}_{\mathrm{UGN}}$ used in Eq. (56), the kinematic viscosity ν is augmented with ν_{SMAG}. Velocity and pressure are both interpolated with bilinear functions. A mesh with 14,960 nodes and 14,700 quadrilateral elements is employed. Close to the cylinder surface, the radial distance between the mesh points (normalized by the cylinder diameter) is 2.5×10^{-4} at Re $=3{,}000$ and 5×10^{-5} at $\mathrm{Re}=50{,}000$. A close-up view of the mesh for the latter case is shown in Fig. 8. In each case, the computations are carried out until a developed unsteady solution is obtained. Then, based on the velocity field at a given instant, $\nu_{\mathrm{SMAG}}/\nu_{\mathrm{SUPG}}$ is calculated.

Figure 9 shows the vorticity and $\nu_{\mathrm{SMAG}}/\nu_{\mathrm{SUPG}}$ for $\mathrm{Re}=3{,}000$. Shades of gray represent values of $\nu_{\mathrm{SMAG}}/\nu_{\mathrm{SUPG}}$ ranging from 0.00 (white) to 0.05, with black indicating 0.05 and higher values. Except for the regions in black, $\nu_{\mathrm{SMAG}}/\nu_{\mathrm{SUPG}}$ is less than 5%. Because Fig. 9 shows pictures zoomed into a small part of the full domain, one can also infer that most of the full domain is marked in white, and therefore for those regions the ratio is essentially 0%. As additional information, we would like to note that when we inspect the overall data for $\nu_{\mathrm{SMAG}}/\nu_{\mathrm{SUPG}}$, we see that in most of the domain it is less than 1%. The turbulence model is active only in regions with significant vorticity. Except for a very few points in the near wake, ν_{SUPG} dominates ν_{SMAG}. When a wall damping function is used with the turbulence model, ν_{SMAG} becomes even smaller. Similar observations can be made for Re $=50{,}000$ (see Fig. 10). It is important to remember that while ν_{SMAG} is an isotropic viscosity, ν_{SUPG} is the maximum value of a directional viscosity, with the maximum value attained in the advection direction. However, in most of the domain $\nu_{\mathrm{SMAG}}/\nu_{\mathrm{SUPG}}$ is so small that, except for directions nearly perpendicular to the advection direction, ν_{SMAG} will still be substantially less than the direction-adjusted value of ν_{SUPG}. It is also important to remember that ν_{SUPG} is generated by a residual-based formulation, while ν_{SMAG} is not.

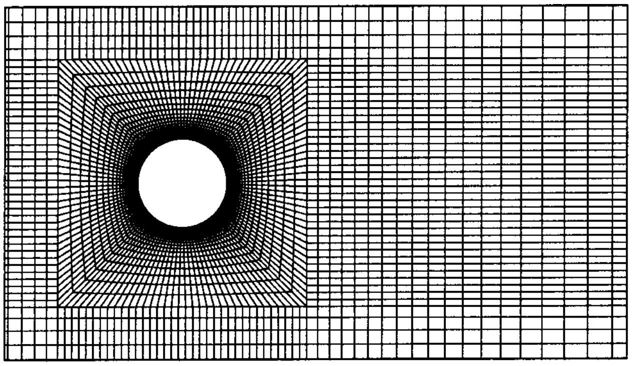

Fig. 8 Flow past a cylinder. A close-up view of the finite element mesh with 14,960 nodes and 14,700 elements.

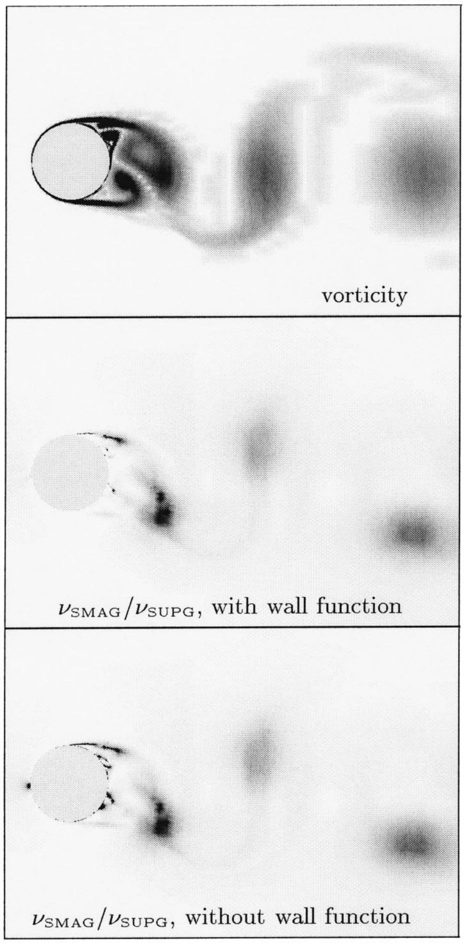

Fig. 9 Flow past a cylinder at Re=3,000. Vorticity (top) and $\nu_{\mathrm{SMAG}}/\nu_{\mathrm{SUPG}}$ with (middle) and without (bottom) the wall function in computation of ν_{SMAG}. In displaying $\nu_{\mathrm{SMAG}}/\nu_{\mathrm{SUPG}}$, shades of gray represent the values ranging from 0.00 (white) to 0.05, with 0.05 and higher values indicated by black.

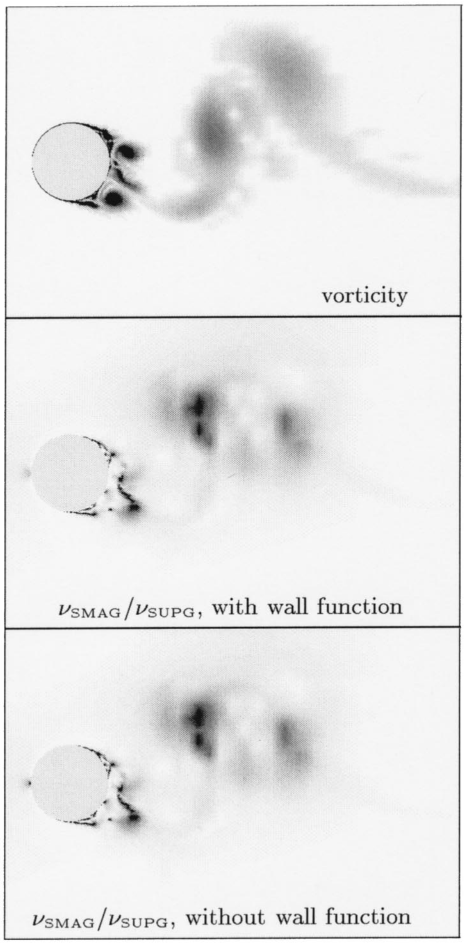

Fig. 10 Flow past a cylinder at Re=50,000. Vorticity (top) and $\nu_{\mathrm{SMAG}}/\nu_{\mathrm{SUPG}}$ with (middle) and without (bottom) the wall function in computation of ν_{SMAG}. In displaying $\nu_{\mathrm{SMAG}}/\nu_{\mathrm{SUPG}}$, shades of gray represent the values ranging from 0.00 (white) to 0.05, with 0.05 and higher values indicated by black.

4 Concluding Remarks

For the SUPG and PSPG formulations for flow problems, we presented a comparative study of the element lengths (i.e., local length scales) defined in different ways. These element lengths are closely related to the stabilization parameters used in the SUPG and PSPG formulations. Our comparisons included parameters defined based on the element-level matrices and vectors, some earlier definitions of element lengths, and extensions of these to higher-order elements. This comparative study shows that the difference between different element length definitions is more pronounced for higher-order elements, and the element length decreases with the increase in the order of the element. We believe that the parameter definitions based on the element-level matrices and vectors provide a good, general framework that automatically takes into account the local length scales and the advection field. Therefore these stabilization parameter definitions and the corresponding element length definitions are what we favor. We also compared, based on some test flow computations, the numerical viscosities generated by the SUPG stabilization with the eddy viscosity associated with a Smagorinsky turbulence model. These test computations show that, in most of the flow domain, the SUPG viscosity is much larger the Smagorinsky viscosity. It is clear that better understanding is needed for the performance of the stabilized formulations with higher-order element and also for the interaction between the stabilized formulations and the Smagorinsky turbulence model.

Acknowledgment

The work reported in this paper was partially sponsored by NASA JSC and by the Natick Solder Center.

References

[1] Hughes, T. J. R., and Brooks, A. N., 1979, "A Multi-dimensional Upwind Scheme With no Crosswind Diffusion," *Finite Element Methods for Convection Dominated Flows*, T. J. R. Hughes, ed., ASME, New York, AMD-Vol. 34, pp. 19–35.

[2] Tezduyar, T. E., and Hughes, T. J. R., 1983, "Finite Element Formulations for Convection Dominated Flows With Particular Emphasis on the Compressible Euler Equations," AIAA Paper No. 83-0125.

[3] Hughes, T. J. R., Franca, L. P., and Hulbert, G. M., 1989, "A New Finite Element Formulation for Computational Fluid Dynamics: VIII. The Galerkin/Least-Squares Method for Advective-Diffusive Equations," Comput. Methods Appl. Mech. Eng., **73**, pp. 173–189.

[4] Tezduyar, T. E., 1991, "Stabilized Finite Element Formulations for Incompressible Flow Computations," Adv. Appl. Mech., **28**, pp. 1–44.

[5] Tezduyar, T., Aliabadi, S., Behr, M., Johnson, A., and Mittal, S., 1993, "Parallel Finite-Element Computation of 3D Flows," IEEE Computer, **26**, pp. 27–36.

[6] Brooks, A. N., and Hughes, T. J. R., 1982, "Streamline Upwind/Petrov-Galerkin Formulations for Convection Dominated Flows With Particular Emphasis on the Incompressible Navier-Stokes Equations," Comput. Methods Appl. Mech. Eng., **32**, pp. 199–259.

[7] Tezduyar, T. E., and Park, Y. J., 1986, "Discontinuity Capturing Finite Element Formulations for Nonlinear Convection-Diffusion-Reaction Problems," Comput. Methods Appl. Mech. Eng., **59**, pp. 307–325.

[8] Tezduyar, T. E., and Ganjoo, D. K., 1986, "Petrov-Galerkin Formulations With Weighting Functions Dependent Upon Spatial and Temporal Discretization:

Applications to Transient Convection-Diffusion Problems,'' Comput. Methods Appl. Mech. Eng., **59**, pp. 49–71.

[9] Franca, L. P., Frey, S. L., and Hughes, T. J. R., 1992, ''Stabilized Finite Element Methods: I. Application to the Advective-Diffusive Model,'' Comput. Methods Appl. Mech. Eng., **95**, pp. 253–276.

[10] Tezduyar, T. E., and Osawa, Y., 2000, ''Finite Element Stabilization Parameters Computed From Element Matrices and Vectors,'' Comput. Methods Appl. Mech. Eng., **190**, pp. 411–430.

[11] Tezduyar, T. E., 2001, ''Adaptive Determination of the Finite Element Stabilization Parameters,'' *Proceedings of the ECCOMAS Computational Fluid Dynamics Conference 2001* (CD-ROM), University of Wales, Swansea, Wales.

[12] Tezduyar, T. E., 2001, ''Stabilized Finite Element Formulations and Interface-Tracking and Interface-Capturing Techniques for Incompressible Flows,'' *Proceedings of the Workshop on Numerical Simulations of Incompressible Flows*, Half Moon Bay, CA, to appear.

[13] Akin, J. E, 2001, *Finite Element Analysis With Error Estimates*, Academic Press, San Diego, CA, submitted for publication.

[14] Smagorinsky, J., 1963, ''General Circulation Experiments With the Primitive Equations,'' Mon. Weather Rev., **91**, pp. 99–165.

[15] Kato, C., and Ikegawa, M., 1991, ''Large Eddy Simulation of Unsteady Turbulent Wake of a Circular Cylinder Using the Finite Element Method,'' *Advances in Numerical Simulation of Turbulent Flows*, I. Celik, T. Kobayashi, K. N. Ghia, and J. Kurokawa, eds., ASME, New York, FED-Vol. 117, pp. 49–56.

J. Chessa
Graduate Research Assistant,
e-mail: j-chessa@northwestern.edu

T. Belytschko
Walter P. Murphy Professor
of Mechanical Engineering,
e-mail: t-belytschko@northwestern.edu

Department of Mechanical Engineering,
Northwestern University,
Evanston, IL 60208

An Extended Finite Element Method for Two-Phase Fluids

An extended finite element method with arbitrary interior discontinuous gradients is applied to two-phase immiscible flow problems. The discontinuity in the derivative of the velocity field is introduced by an enrichment with an extended basis whose gradient is discontinuous across the interface. Therefore, the finite element approximation can capture the discontinuities at the interface without requiring the mesh to conform to the interface, eliminating the need for remeshing. The equations for incompressible flow are solved by a fractional step method where the advection terms are stabilized by a characteristic Galerkin method. The phase interfaces are tracked by level set functions which are discretized by the same finite element mesh and are updated via a stabilized conservation law. The method is demonstrated in several examples. [DOI: 10.1115/1.1526599]

1 Introduction

Two-phase flow problems are generally solved by two types of methods, interface-tracking algorithms or interface-capturing algorithms. Interface tracking methods use a deforming mesh or grid which conforms to the interface or tracks the interface in some other explicit manner. Examples are arbitrary Eulerian-Lagrangian methods, [1], and deforming space-time finite element formulations, [2,3]. In interface-capturing methods, an auxiliary function is defined on a fixed grid that describes the interface. Some examples of interface-capturing methods are volume of fluid methods [4,5], level set methods [6,7], and marker and cell methods, [8].

The method described in this paper is an interface tracking method that shares many of the advantages of interface capturing methods: A fixed mesh is used, but we employ an enriched basis that includes the discontinuities at the interface. By embedding the interface jump conditions in the finite element basis, the accuracy of typical interface tracking methods is retained while remeshing is avoided. Remeshing can be quite expensive and can fail when the interface topology is significantly altered, as when phases join together or separate.

The methodology is called the extended finite element method. The extended finite element method was first introduced by Belytschko and Black [9] and Moës et al. [10]. A general description of the method for modeling arbitrary discontinuities in a function and/or its derivatives is given by Belytschko et al. [11]. The idea for modeling discontinuities in derivatives used here originates from Krongauz and Belytschko [12], who developed it in the context of meshless methods. The extended finite element method was originally developed for crack problems but the methodology has been extended to several other problem classes. Sukumar et al. [13] introduced a combined level set and discontinuous extended finite element method to solve elastic problems involving holes and inclusions. Wagner et al. [14] solve problems involving particulate Stokes flow. Chessa et al. [15], Dolbow and Merle [16], and Renaud and Dolbow [17] applied extended finite element method to solidification problems.

We employ the level set method to track the interface, Osher and Sethian [6,7]. The level set method is similar to pseudo-concentration methods, [18,19]; it describes the location of the interface by a signed scalar distance function, generally denoted as $\phi(\mathbf{x},t)$ on the computational domain. The interface position is the set of points at which the level set field vanishes.

The extended finite element method couples naturally with the level set method. In the method proposed in this paper the enriched basis is constructed directly in terms of the level set $\phi(\mathbf{x},t)$. Since $\phi(\mathbf{x},t)$ is approximated by the same finite element mesh, the location of the discontinuity is expressed entirely in terms of nodal values of ϕ. Thus, as will be seen, the structure of the discontinuity and its approximation of the discontinuous field are expressed entirely in terms of nodal values of the velocity and level set function.

We extend the level set methods presented by Peng et al. [20] to finite element meshes to track the phase interface. The formulation by finite elements enhances the versatility of the method; it is applicable to problems that would be difficult to solve on a structured grid, i.e., problems that require local mesh refinement or problems involving complicated geometries and/or boundaries.

Finite element formulations of level set methods were first discussed by Barth and Sethian [21] with respect to triangulated domains. Since then several papers have used the level set method in a finite element context; Rao et al. [22], Chessa et al. [15], and Quecedo and Pastor [23]. However, level set methods are more commonly seen in finite difference schemes. This is probably due to the fact that finite difference methods are more widely used in solving the conservation law equations that are used to update the level set. Furthermore, some level set techniques rely on structured grids, i.e., fast marching methods. However, level set techniques are also very robust in finite element schemes. For example, Peng et al. [20] present an efficient PDE-based method for updating the level set field in a region about the interface. They use finite difference schemes that are directly applicable to unstructured grids with no significant increase in cost or complexity.

The level set method has been used by Sussman et al. [24–27] to solve two-phase incompressible flow problems with finite difference methods. Fedkiw et al. [28,29] have used level sets in conjunction with ghost fluid methods to solve compressible-compressible and compressible-incompressible two-phase flows using finite difference schemes.

The outline of this paper is as follows; in Section 2 the governing equations are presented. In Section 3 we present the discontinuous finite element approximation for the velocity field. The finite element formulations for the level set update and the Navier-Stokes equations are presented in Sections 4 and 5, respectively. Section 6 presents examples illustrating the accuracy and application of these methods.

Contributed by the Applied Mechanics Division of THE AMERICAN SOCIETY OF MECHANICAL ENGINEERS for publication in the ASME JOURNAL OF APPLIED MECHANICS. Manuscript received by the Applied Mechanics Division, Dec. 4, 2001; final revision, Mar. 12, 2002. Associate Editor: T. E. Tezduyar. Discussion on the paper should be addressed to the Editor, Prof. Robert M. McMeeking, Chair, Department of Mechanics and Environmental Engineering, University of California–Santa Barbara, Santa Barbara, CA 93106-5070, and will be accepted until four months after final publication in the paper itself in the ASME JOURNAL OF APPLIED MECHANICS.

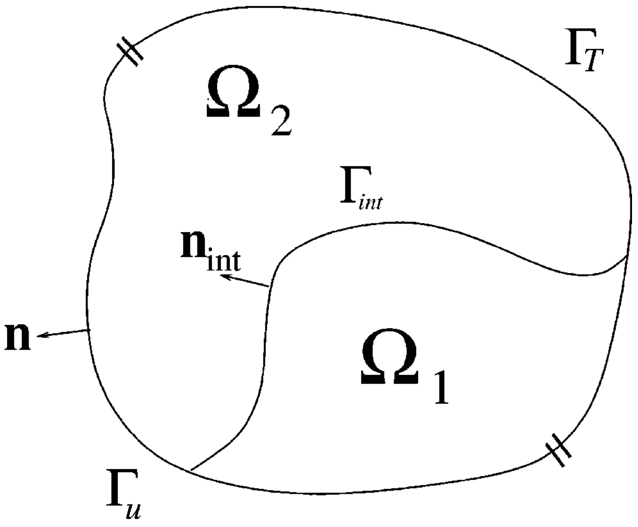

Fig. 1 Problem domain

2 Governing Equations

In this paper we consider isothermal incompressible two-phase flow which is described by the following equations for both phases:

$$\rho\left(\frac{\partial \mathbf{u}}{\partial t}+\boldsymbol{\nabla}\cdot(\mathbf{u}\otimes\mathbf{u})-\mathbf{f}\right)-\boldsymbol{\nabla}\cdot\boldsymbol{\sigma}=\mathbf{0} \tag{1}$$

$$\boldsymbol{\nabla}\cdot\mathbf{u}=\mathbf{0} \tag{2}$$

where $\mathbf{u}$ is the velocity field, ρ is the fluid density, p is the hydrostatic pressure, $\mathbf{f}$ is an applied body force, and $\boldsymbol{\sigma}$ is the Cauchy stress, which is decomposed into the deviatoric stress $\boldsymbol{\tau}$, and the hydrostatic pressure as follows:

$$\boldsymbol{\sigma}=\boldsymbol{\tau}-p\mathbf{I}. \tag{3}$$

For a Newtonian fluid the deviatoric stress τ is given by

$$\boldsymbol{\tau}=2\mu\mathbf{D} \tag{4}$$

with the rate of deformation tensor $\mathbf{D}$ defined as

$$\mathbf{D}=\frac{1}{2}(\boldsymbol{\nabla}\mathbf{u}+\mathbf{u}\boldsymbol{\nabla}) \tag{5}$$

Substituting (2-2) into (1), we obtain

$$\rho\left(\frac{\partial \mathbf{u}}{\partial t}+\boldsymbol{\nabla}\cdot(\mathbf{u}\otimes\mathbf{u})\right)+\boldsymbol{\nabla}p=\boldsymbol{\nabla}\cdot(\mu\boldsymbol{\nabla}\mathbf{u})+\mathbf{f} \tag{6}$$

These equations hold over a domain Ω which is shown in Fig. 1. The domain Ω is partitioned into Ω_1, Ω_2 where Ω_1 and Ω_2 are regions composed of fluids 1 and 2, respectively, and Γ_{int} is the interface between the two fluids. We assume that both phases are homogeneous and therefore the material properties are constant in Ω_1 and Ω_2 but since we solve (6) and (2) on Ω we consider ρ and μ to be functions of position and time due to the motion of the interface. The closure of Ω, $\partial\Omega$ is partitioned into Γ_u and Γ_T which are the boundaries where velocity and traction conditions are specified as follows:

$$\mathbf{u}(\mathbf{x},t)=\overline{\mathbf{u}}\quad\forall\mathbf{x}\in\Gamma_u \tag{7}$$

$$\mathbf{n}\cdot\boldsymbol{\sigma}(\mathbf{x},t)=\overline{\mathbf{t}}\quad\forall\mathbf{x}\in\Gamma_t. \tag{8}$$

We split the traction boundary condition into its normal and deviatoric components

$$p(\mathbf{x},t)=\overline{p}\quad\forall\mathbf{x}\in\Gamma_t \tag{9}$$

$$\mathbf{n}\cdot\boldsymbol{\tau}(\mathbf{x},t)=\overline{\mathbf{t}_s}\quad\forall\mathbf{x}\in\Gamma_t. \tag{10}$$

The vector $\mathbf{n}$ is an outward unit normal to Ω. Assuming negligible surface tension, no-slip and immiscible flow, the stress and velocity fields must satisfy the following conditions across the interface:

$$[\![\mathbf{n}_{\text{int}}\cdot\boldsymbol{\sigma}]\!]=0 \tag{11}$$

$$[\![\mathbf{u}]\!]=0 \tag{12}$$

where $\mathbf{n}_{\text{int}}$ is an outward unit normal from Ω_1. To track the fluid interface we define a level set field $\phi(\mathbf{x},t)$ on Ω such that it conforms to the following sign convention:

$$\phi(\mathbf{x},t)\begin{cases}>0 & \forall\mathbf{x}\in\Omega_1\\ =0 & \forall\mathbf{x}\in\Gamma_{\text{int}}\\ <0 & \forall\mathbf{x}\in\Omega_2.\end{cases} \tag{13}$$

Using this convention we can define the material properties on the entire domain as a function of ϕ

$$\rho(\phi)=\begin{cases}\rho_1 & \phi\geqslant 0\\ \rho_2 & \phi<0\end{cases}\quad\forall\mathbf{x}\in\Omega \tag{14}$$

$$\mu(\phi)=\begin{cases}\mu_1 & \phi\geqslant 0\\ \mu_2 & \phi<0\end{cases}\quad\forall\mathbf{x}\in\Omega \tag{15}$$

or

$$\rho(\phi)=\rho_2+\mathcal{H}(\phi)(\rho_1-\rho_2)\quad\forall\mathbf{x}\in\Omega \tag{16}$$

$$\mu(\phi)=\mu_2+\mathcal{H}(\phi)(\mu_1-\mu_2)\quad\forall\mathbf{x}\in\Omega \tag{17}$$

where $\mathcal{H}(\cdot)$ is the Heaviside function. Furthermore, we define a signed distance function $d(\mathbf{x},t)$ as

$$d(\mathbf{x},t)=\min_{\overline{\mathbf{x}}\in\Gamma_{\text{int}}}\|\mathbf{x}-\overline{\mathbf{x}}\|\operatorname{sign}(\mathbf{n}_{\text{int}}\cdot(\mathbf{x}-\overline{\mathbf{x}})) \tag{18}$$

and we require that initially

$$\phi(\mathbf{x},t=0)=d(\mathbf{x},t=0). \tag{19}$$

Since the fluids are immiscible we prohibit flow across the interface i.e.,

$$\frac{\partial}{\partial t}\phi(\mathbf{X},t)=0\quad\forall\mathbf{X}\in\Gamma_{\text{int}} \tag{20}$$

where $\mathbf{X}$ denotes the position of a point that remains on the interface. Expressing this condition in terms of spacial coordinates, we arrive at the standard level set evolution equation

$$\frac{\partial\phi}{\partial t}+\mathbf{u}\cdot\boldsymbol{\nabla}\phi=0. \tag{21}$$

This equation is used to update the level set and consequently update the interface location.

3 Enriched Finite Element With Interior Discontinuous Gradient

The domain of the problem, Ω is subdivided into elements Ω_e associated with a set of nodes $\mathbf{x}_I$, $I=1$ to n. The interpolation function (shape function) associated with node I is denoted by $N_I(\mathbf{x})$ and the set of all nodes by $\mathcal{N}$. Recall that the support of $N_I(\mathbf{x})$, which is the area over which it is nonzero, is limited to the elements connected to the node I, i.e., the support is compact. The support of a typical node I is shown in Fig. 2. Since we are dealing with a second-order partial differential equations (6), we choose the shape functions to be piecewise continuously differentiable, i.e., $C^0(\Omega)$.

The extended finite element approximation is constructed in terms of the level set function defined by (19) and the shape functions N_I. In constructing the approximation, we distinguish

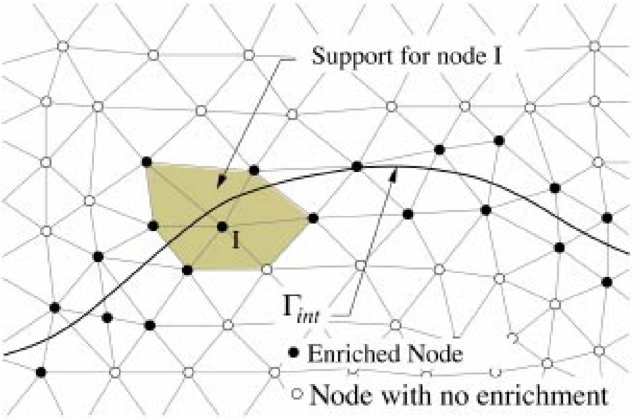

Fig. 2 A typical finite element mesh with interface Γ_{int} showing the support of a generic node I and the enriched notes

the nodes whose support is intersected by the interface Γ_{int} from all others; this set of nodes is denoted by $\mathcal{N}_{\text{enrich}}$.

Figure 2 illustrates which nodes are enriched for a typical example. The enriched approximation is given by

$$\mathbf{u}^h(\mathbf{x},t)=\sum_{I\in\mathcal{N}} N_I(\mathbf{x})\mathbf{U}_I(t)+\sum_{J\in\mathcal{N}_{\text{enrich}}} N_J(\mathbf{x})(|\phi^h(\mathbf{x},t)| - |\phi^h(\mathbf{x}_J,t)|)\mathbf{A}_J(t) \tag{22}$$

where $\mathbf{U}_I(t)$ are the nodal parameters for the standard finite element approximation and $\mathbf{A}_J(t)$ are additional nodal parameters at the enriched node J. For convenience, we also write the above as

$$\mathbf{u}^h(\mathbf{x},t)=\sum_{I\in\mathcal{N}} N_I(\mathbf{x})\mathbf{U}_I(t)+\sum_{J\in\mathcal{N}_{\text{enrich}}} N_J^{\text{enrich}}(\mathbf{x},t)\mathbf{A}_J(t) \tag{23}$$

where

$$N_J^{\text{enrich}}(\mathbf{x},t)=N_J(\mathbf{x})\Psi_J(\mathbf{x},t) \tag{24}$$

$$\Psi_J(\mathbf{x},t)=|\phi^h(\mathbf{x},t)|-|\phi^h(\mathbf{x}_J,t)|. \tag{25}$$

The second term in (25) is not essential but yields the desirable property that $\mathbf{u}^h(\mathbf{x}_I,t)=\mathbf{U}_I(t)$.

We next examine the character of this approximation around the interface Γ_{int}. Taking the gradient of (22) we obtain

$$\nabla\mathbf{u}^h=\sum_{I\in\mathcal{N}}\mathbf{U}_I(t)\otimes\nabla N_I+\sum_{J\in\mathcal{N}_{\text{enrich}}}\mathbf{A}_J(t)\otimes(\nabla N_J\Psi_J+N_J\nabla\Psi_J). \tag{26}$$

We next note that

$$\nabla\Psi_J=\text{sign}(\phi)\quad\nabla\phi=\text{sign}(\phi)\mathbf{n}_{\text{int}} \tag{27}$$

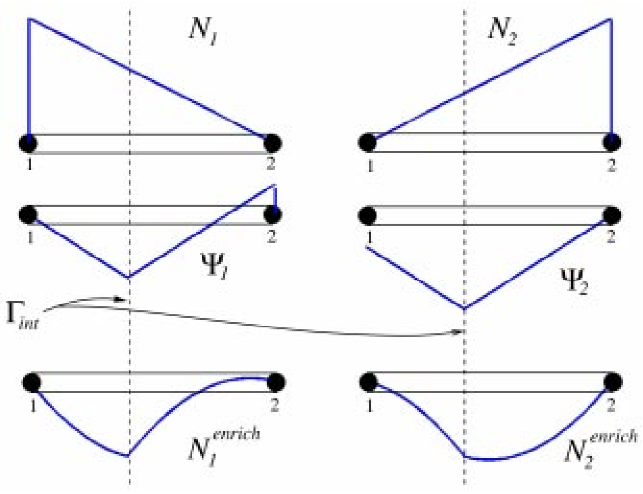

Fig. 3 Example of an enriched finite element shape function in R^1

where sign$(\cdot)$ is the sign of the number function and second equality follows from the fact that ϕ is distance function and therefore $|\nabla\phi|=1$, see (18)–(19). Substituting (27) into (26) gives

$$\nabla\mathbf{u}^h=\sum_{I\in\mathcal{N}}\mathbf{U}_I(t)\otimes\nabla N_I+\sum_{J\in\mathcal{N}_{\text{enrich}}}\mathbf{A}_J(t)\otimes(\nabla N_J\Psi_J+N_J\text{sign}(\phi)\mathbf{n}_{\text{int}}). \tag{28}$$

Therefore the jump in $\mathbf{u}^h(\mathbf{x},t)$ across the interface is given by

$$[\![\nabla\mathbf{u}^h]\!]=2\sum_{J\in\mathcal{N}_{\text{enrich}}}N_J\mathbf{A}_J\otimes\mathbf{n}_{\text{int}}\quad\text{on}\quad\Gamma_{\text{int}} \tag{29}$$

and

$$[\![\nabla\mathbf{u}^h\cdot\mathbf{n}_{\text{int}}]\!]=2\sum_{J\in\mathcal{N}_{\text{enrich}}}N_J\mathbf{A}_J\quad\text{on}\quad\Gamma_{\text{int}}. \tag{30}$$

The magnitude of the jump depends on $\mathbf{A}_I(t)$ and varies smoothly along the interface as can be seen from (30) since its spacial character results from the projection of the C^0 shape functions onto the interface. Note, that as with all piecewise continuous finite element approximations, $[\![\nabla\mathbf{u}]\!]\neq 0$ on the element edges, see [30].

The enrichment functions for a linear two-node element in one dimension are illustrated in Fig. 3. Each enrichment function is a product of the shape function N_I, and the corresponding enrichment function $\Psi(\mathbf{x},t)$. Note that the enriched shape functions vanish at the nodes. The enrichment functions for a three-node linear triangle are shown in Fig. 4. As can be seen, each enrich-

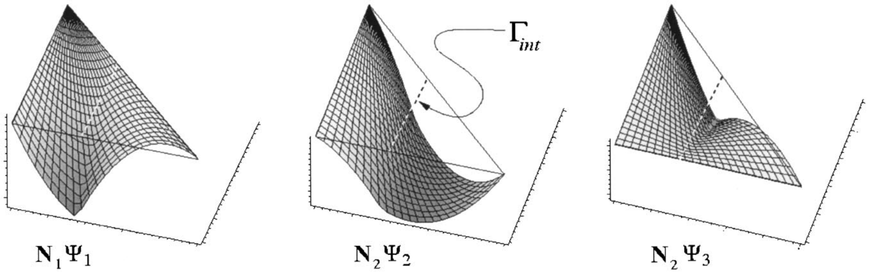

Fig. 4 Enriched finite element shape function for a three-node linear triangular element

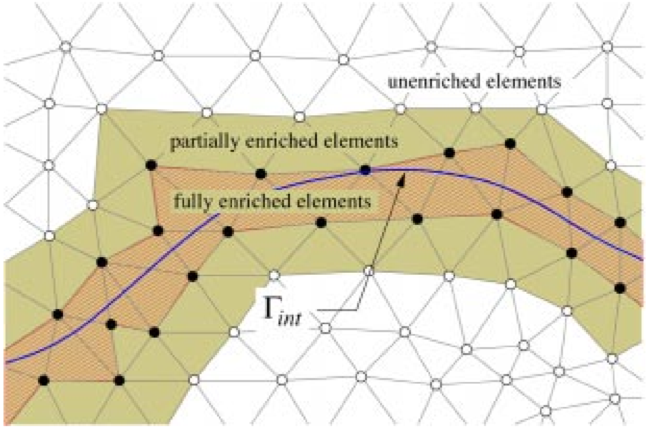

Fig. 5 Enrichment for a typical finite element mesh, showing elements that are fully enriched, partially enriched, and unenriched. Also illustrated is the boundary where the enrichment vanishes.

ment function vanishes along two of the edges. On the third edge a kink, similar to that what appears in the one-dimensional element, can be seen.

The character of this enrichment is of two types. The first type is within the elements cut by the interface; here all nodes are enriched and the enrichment is a partition of unity [31], so the enrichment function $\Psi(\mathbf{x},t)$ is reproduced exactly. The second type is within the elements adjacent to the fully enriched elements; here not all of the elements nodes are enriched. In these *partially* enriched elements the enrichment provides a *blending* so that the enrichment vanishes at the edge of the support of the bisected nodes. Figure 5 illustrates which elements are of the first and second types as well as those that are not enriched. The enrichment is local and the resulting system matrices are sparse.

The enrichment modifies the velocity field only in the elements crossed by the interface and in the adjacent elements that share the enriched nodes, see Fig. 5. In other words, only the elements that lie entirely within the supports of shape functions cut by the interface are affected by the enrichment.

The additional degrees-of-freedom $\mathbf{A}_J$ can be handled by adding nodes to the element or increasing the number of degrees-of-freedom for the enriched nodes. In either case, the modifications required in a standard finite element code are minimal.

4 Level Set Formulation

The level set function that tracks the interface is approximated by the same mesh and shape functions that are used for the velocity and pressure fields. However, no enrichment is needed for the level set function since it is continuously differentiable across the interface. Thus the level set approximation is given by

$$\phi^{h}(\mathbf{x},t)=\sum_{I\in\mathcal{N}}N_{I}(\mathbf{x})\phi_{I}(t) \tag{31}$$

where $\phi_I(t)=\phi(\mathbf{x}_I,t)$ are the nodal values of the level set. We follow the level set update method outlined in Peng et al. [20]. In this form Eq. (21) is modified as follows:

$$\frac{\partial\phi}{\partial t}+c(\phi)\mathbf{u}\cdot\nabla\phi=0 \tag{32}$$

where $c(\phi)$ is a cutoff function that is defined by

$$c(\phi)=\begin{cases}1 & \text{if } |\phi|\leqslant\delta\\ (|\phi|-\gamma)^{2}(2|\phi|+\gamma-3\delta)/(\gamma-\delta) & \text{if } \delta<|\phi|\leqslant\gamma\\ 0 & \text{if } |\phi|>\gamma\end{cases} \tag{33}$$

where δ is the cutoff distance from the interface and γ is transition distance. A characteristic method is used to stabilize the non-self-adjoint term, [32]. This, in conjunction with a forward Euler temporal discretization, yields the following update equation:

$$\phi^{n+1}-\phi^{n}=-\Delta t\left[c(\phi)\mathbf{u}\cdot\nabla\phi-\frac{\Delta t}{2}\nabla\cdot(c^{2}(\phi)(\mathbf{u}\otimes\mathbf{u})\cdot\nabla\phi)\right]\Bigg|_{t=t^{n}} \tag{34}$$

where the superscript indicates the time-step number and Δt is the time-step. Using the standard Galerkin procedure, i.e., the test and trial functions, $\phi^h(\mathbf{x},t)$ and $\psi^h(\mathbf{x})$ are in the same finite element function space $\mathcal{V}^h_\phi$, we get the following variational form of the update equation:

$$\int_{\Omega}\psi(\phi^{n+1}-\phi^{n})dV=-\Delta t\int_{\Omega}\psi c(\phi)\mathbf{u}\cdot\nabla\phi dV+\frac{\Delta t^{2}}{2}\int_{\Omega}\nabla\psi\cdot(c^{2}(\phi)\mathbf{u}\otimes\mathbf{u})\cdot\nabla\phi dV. \tag{35}$$

Because the hyperbolic nature of (21), a nonlinear viscous shock capturing operator $B_{sc}(\phi)$ is added, see Hansbo [33]. This minimizes the oscillations that may occur at discontinuities in curvature on the front. This operator is given by

$$B_{sc}(\phi)=\int_{\Omega}\nu_{sc}(\phi)(\nabla\psi\cdot\nabla\phi)dV. \tag{36}$$

where ν_{sc} is a nonlinear viscosity defined as

$$\nu_{sc}(\phi)=h^{e}\sigma_{sc}\frac{\left|\dfrac{\partial\phi}{\partial t}+\mathbf{u}\cdot\nabla\phi\right|}{|\mathbf{u}\cdot\nabla\phi|+h^{e}}. \tag{37}$$

σ_{sc} is a parameter used to control the degree of added viscosity (typically $\sigma_{sc}\approx0.1$) and h^e is a measure of element e. The following variational formulation is used to update the level set field:

$$\int_{\Omega}\psi(\phi^{n+1}-\phi^{n})dV=-\Delta t\int_{\Omega}\psi c(\phi)\mathbf{u}\cdot\nabla\phi^{n}dV+\frac{\Delta t^{2}}{2}\int_{\Omega}\nabla\psi\cdot(c^{2}(\phi)\mathbf{u}\otimes\mathbf{u})\cdot\nabla\phi^{n}dV+\int_{\Omega}\nu_{sc}\nabla\psi\cdot\nabla\phi^{n}dV. \tag{38}$$

Because of the cutoff function, only the level set in the region $|\phi|\leqslant\delta$ needs to be updated in time. This significantly minimizes the computational overhead.

For some velocity fields ϕ may deviate significantly from a signed distance function after even a few time-steps. This may cause high gradients in ϕ near the interface and introduce significant error in the interface position. These errors cause a loss of conservation of the phase volumes. This has often been cited as a shortcoming of the level set method and many interface-capturing methods, [34,35]. Extensional velocity fields and reinitialization are used to circumvent these difficulties, [7,25,26,36].

5 Navier-Stokes Formulation

We solve the Navier-Stokes equations by a characteristic based split CBS algorithm based on the projection method of Chorin [37] as described in Zienkiewicz and Codina [38] and Zienkiewicz and Taylor [32]. In this method an auxiliary velocity field $\mathbf{u}^*$ is introduced to uncouple the momentum and continuity equations; a characteristic method is used to stabilize the non-self-adjoint operators in (6). The characteristic based split formulation of (6) can be written as

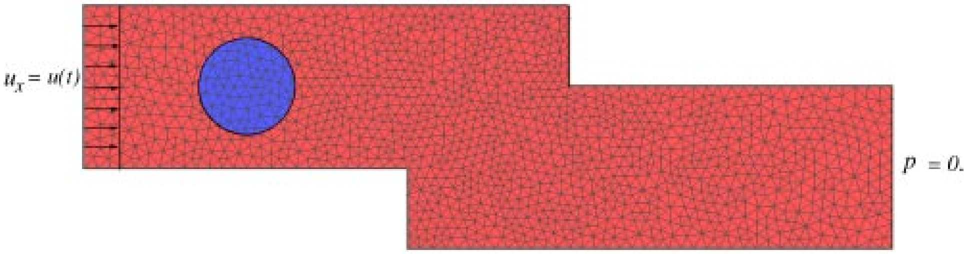

Fig. 6 Initial configuration of interstitial fluid problem

$$\mathbf{u}^* - \mathbf{u}^n = \frac{\Delta t}{\rho}\left[-\nabla\cdot(\rho\mathbf{u}\otimes\mathbf{u}) + \nabla\cdot\boldsymbol{\tau} - \rho\mathbf{f} + \frac{\Delta t}{2}(\mathbf{u}\cdot\nabla) \times(\nabla\cdot(\rho\mathbf{u}\otimes\mathbf{u})+\rho\mathbf{f})\right]\Bigg|_{t=t^n}. \tag{39}$$

The final velocity field is "*corrected*" by the pressure increment so that is divergence free

$$\mathbf{u}^{n+1} - \mathbf{u}^* = \frac{\Delta t}{\rho}\nabla p^{n+1}. \tag{40}$$

By taking the divergence of (40) and recalling that the velocity at time t^{n+1} must be divergence free (i.e., Eq. (2)) we arrive at the following Poisson equation for the pressure:

$$\Delta t \nabla^2 p^{n+1} = \nabla\cdot(\rho\mathbf{u}^*). \tag{41}$$

Applying the standard Galerkin procedure on (39) for the fractional velocity field $\mathbf{u}^*$ we get the following:

$$\int_\Omega \mathbf{W}\cdot(\mathbf{u}^*-\mathbf{u}^n)dV = \frac{\Delta t}{\rho}\left[-\int_\Omega \mathbf{W}\cdot\nabla\cdot(\rho\mathbf{u}\otimes\mathbf{u})dV - \int_\Omega (\nabla\mathbf{W}):\boldsymbol{\tau}dV + \int_{\Gamma_t}\mathbf{W}\cdot(\mathbf{n}\cdot\boldsymbol{\tau})dS - \int_\Omega \mathbf{W}\cdot(\rho\mathbf{f})dV - \frac{\Delta t}{2}\int_\Omega (\nabla\cdot(\mathbf{u}\otimes\mathbf{W}))\cdot(\nabla\cdot(\rho\mathbf{u}\otimes\mathbf{u})+\rho\mathbf{f})dV\right]\Bigg|_{t=t^n} \tag{42}$$

where $\mathbf{W}$ is a test function. Similarly, the weak form for (41) is obtained by multiplying by the pressure test function V.

$$\int_\Omega \nabla V\cdot\nabla p^{n+1}dV = \frac{1}{\Delta t}\left(\int_{\Gamma_u} V\nabla(p^{n+1}-p^n)\cdot\mathbf{n}dS + \int_\Omega \nabla V\cdot(\rho\mathbf{u}^*)dV - \int_{\Gamma_u} V(\rho\mathbf{u}^*)\cdot\mathbf{n}dS\right). \tag{43}$$

To eliminate the boundary pressure terms we use (40) and require that $\mathbf{u}^*=\mathbf{u}$ on Γ_u yielding

$$\int_\Omega \nabla V\cdot\nabla p^{n+1}dV = \frac{1}{\Delta t}\left(\int_\Omega \nabla V\cdot(\rho\mathbf{u}^*)dV - \int_{\Gamma_u} V(\rho\mathbf{u}^*)\cdot\mathbf{n}dS\right) \tag{44}$$

and for the velocity correction Eq. (41)

$$\int_\Omega \mathbf{W}\cdot(\rho\mathbf{u}^{n+1})dV = \int_\Omega \mathbf{W}\cdot(\rho\mathbf{u}^*)dV + \Delta t\int_\Omega \mathbf{W}\cdot\nabla p^{n+1}dV. \tag{45}$$

For the derivation of the finite element equations it is convenient to write the enriched approximation as

$$\mathbf{u}^h(\mathbf{x},t) = \overline{\mathbf{N}}(\mathbf{x},\phi)\overline{\mathbf{U}}(t) \tag{46}$$

where

$$\overline{\mathbf{N}}(\mathbf{x},\phi) = [N_1,\ N_2\ \ \ldots\ \ N_n,\ N_1\psi_1,\ N_2\psi_2\ \ \ldots\ \ N_{n_e}\psi_{n_e}] \tag{47}$$

$$\overline{\mathbf{U}}(t) = [\mathbf{U}_1,\ \mathbf{U}_2\ \ \ldots\ \ \mathbf{U}_n,\ \mathbf{A}_1,\ \mathbf{A}_2\ \ \ldots\ \ \mathbf{A}_{n_e}]^T. \tag{48}$$

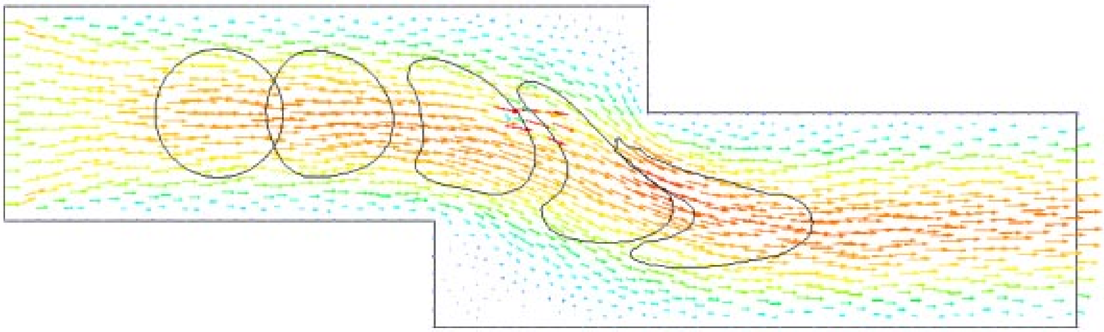

Fig. 7 Phase interface at several time-steps for interstitial fluid problem

The finite element approximations are

$$\mathbf{W}=\overline{\mathbf{N}}^{n+1}\mathbf{W} \tag{49}$$

$$\mathbf{u}^n=\overline{\mathbf{N}}^n\overline{\mathbf{U}}^n \tag{50}$$

$$\mathbf{u}^*=\overline{\mathbf{N}}^{n+1}\overline{\mathbf{U}}^* \tag{51}$$

$$V=\mathbf{NV} \tag{52}$$

$$p^n=\mathbf{Np}^n \tag{53}$$

where the superscript n on $\overline{\mathbf{N}}^n$ indicates that enriched shape functions are a function of $\phi^n(\mathbf{x},t)$ (due to the moving enrichment). Substituting (50)–(53) into Eq. (42)–(45) we obtain the following finite element equations:

$$\mathbf{M}^*\overline{\mathbf{U}}^*=\mathbf{M}\overline{\mathbf{U}}^n-\Delta t\left[\mathbf{C}\overline{\mathbf{U}}^n+\mathbf{K}\overline{\mathbf{U}}^n-\mathbf{f}^n-\frac{\Delta t}{2}(\mathbf{K}_u\overline{\mathbf{U}}^n+\mathbf{f}_s^n)\right] \tag{54}$$

$$\Delta t\mathbf{K}_p\mathbf{p}^{n+1}=\mathbf{G}_u\overline{\mathbf{U}}^*-\mathbf{f}_p \tag{55}$$

$$\overline{\mathbf{U}}^{n+1}=\overline{\mathbf{U}}^*-\Delta t\mathbf{M}^{-1}\mathbf{G}^T\mathbf{p}^{n+1} \tag{56}$$

where

$$\mathbf{M}^*=\int_\Omega(\overline{\mathbf{N}}^{n+1})^T\rho^n\overline{\mathbf{N}}^n dV \tag{57}$$

$$\mathbf{M}=\int_\Omega(\overline{\mathbf{N}}^{n+1})^T\rho^n\overline{\mathbf{N}}^{n+1} dV \tag{58}$$

$$\mathbf{C}=\int_\Omega(\overline{\mathbf{N}}^{n+1})^T(\boldsymbol{\nabla}(\rho^n\mathbf{u}^n\overline{\mathbf{N}}^n))dV \tag{59}$$

$$\mathbf{K}=\int_\Omega(\mathbf{B}^{n+1})^T\mu^n\left(\mathbf{I}_0-\frac{2}{3}\mathbf{mm}^T\right)\mathbf{B}^n dV \tag{60}$$

$$\mathbf{K}_u=-\frac{1}{2}\int_\Omega(\boldsymbol{\nabla}^T(\mathbf{u}^n\overline{\mathbf{N}}^{n+1}))^T\rho^n(\boldsymbol{\nabla}^T(\mathbf{u}^n\overline{\mathbf{N}}^n))dV \tag{61}$$

$$\mathbf{f}=\int_\Omega\overline{\mathbf{N}}^{n+1}\rho\mathbf{g}dV+\int_{\Gamma_t}\overline{\mathbf{N}}^{n+1}\mathbf{t}_s dS \tag{62}$$

$$\mathbf{K}_p=\int_\Omega(\boldsymbol{\nabla}\mathbf{N})^T\boldsymbol{\nabla}\mathbf{N}dV \tag{63}$$

$$\mathbf{G}_u=\int_\Omega(\boldsymbol{\nabla}\overline{\mathbf{N}}^n)^T\rho^n\mathbf{N}^n dV \tag{64}$$

$$\mathbf{f}_p=\int_{\Gamma_t}\mathbf{N}^T\mathbf{n}\cdot\mathbf{u}^{n+1}dS \tag{65}$$

$$\mathbf{G}=\int_\Omega(\boldsymbol{\nabla}\overline{\mathbf{N}}^{n+1})^T\overline{\mathbf{N}}dV. \tag{66}$$

In the above $\mathbf{B}$ is the gradient matrix defined as

$$\mathbf{B}^n=[\mathbf{B}_1^n\ \ \mathbf{B}_2^n\ \ \cdots\ \ \mathbf{B}_n^n]^T \tag{67}$$

$$\mathbf{B}_I^n=\begin{bmatrix}\dfrac{\partial\overline{N}_I^n}{\partial x_1} & 0\\ 0 & \dfrac{\partial\overline{N}_I^n}{\partial x_2}\\ \dfrac{\partial\overline{N}_I^n}{\partial x_2} & \dfrac{\partial\overline{N}_I^n}{\partial x_1}\end{bmatrix} \tag{68}$$

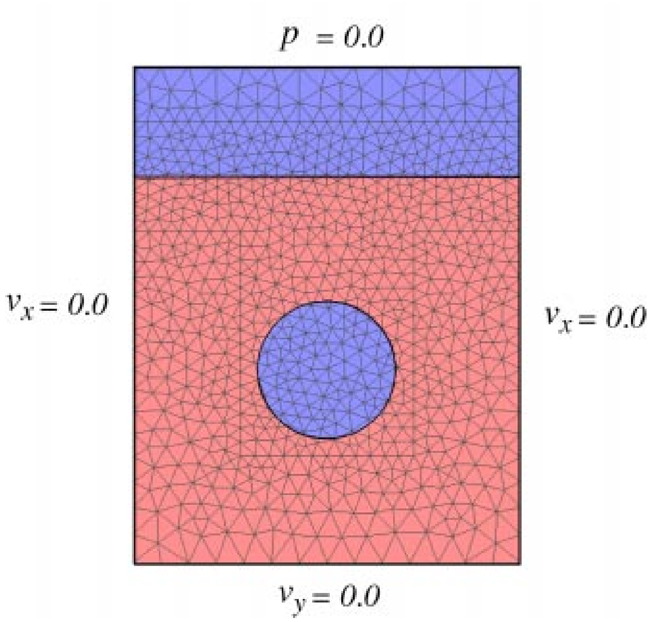

Fig. 8 Rising bubble problem

$$\mathbf{I}_0=\begin{bmatrix}2 & & \\ & 2 & \\ & & 1\end{bmatrix} \tag{69}$$

$$\mathbf{m}=[1\ \ 1\ \ 0]^T. \tag{70}$$

It should be noted that when evaluating the gradient of the enriched shape functions $\overline{\mathbf{N}}$ the chain rule must be employed due to the spacial dependence of the level set field ϕ, so

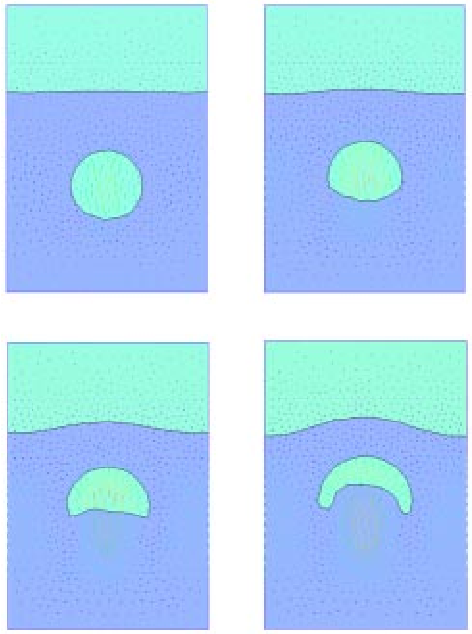

Fig. 9 Phase interface for several time-steps for rising bubble problem

$$\nabla \overline{N_I} = \nabla N_I \psi_I + N_I \nabla \psi_I . \tag{71}$$

The update of the fluid/level set system is as follows; given $\mathbf{u}^n$, p^n, and ϕ^n we first explicitly update the level set as described in Section 4 to obtain $\phi(\mathbf{x},t^{n+1})$ then solve (54) for $\mathbf{u}^*$ then (55) for p^{n+1} and finally (5) for $\mathbf{u}^{n+1}$.

It should be noted that when evaluating these discontinuous finite element matrices and vectors a quadrature rule must be used that will correctly integrate over elements where the discontinuity exists. Quadrature rules for these enriched methods are described in Chessa et al. [15] Moës et al. [10], and Sukumar et al. [13].

6 Example Problems

6.1 Interstitial Fluid in a "Jogged" Channel. Consider the problem of a interstitial fluid flowing through a "*jogged*" channel as shown in Fig. 6 at the initial time $t=0$. The mesh is completely unstructured, as can be seen from Fig. 6. An inlet velocity is prescribed at the left-hand side, no slip boundary conditions are prescribed on the channel walls and a constant pressure condition is set on the right edge. The fluid is initially at rest and is slowly ramped up to a steady-state value of 1.0. The steady-state velocity field and interfaces are shown at several time-steps in Fig. 7. Note that the interface remains quite smooth, except for some kinking in the upper-left hand corner in the final time-step.

6.2 Bubble Rising to a Free Surface. Next we consider the problem of an immersed droplet of a secondary phase rising in a denser primary phase toward a free surface as shown in Fig. 8. Slip boundary conditions are given on the sides and the bottom edges and a constant pressure is prescribed at the top edge of the computational domain. The Reynolds number inside the bubble is 320 and for the surrounding fluid is 465. The results are qualitatively similar to the exact solution for a spherical droplet in an infinite media as given by Hadamard [39]. The interface is shown for several time-steps in Fig. 9.

It should be noted that the level set method has no difficulty handling the large deformation of the interface and drastic topological changes associated with evolution of the bubble.

7 Conclusions

A method has been presented for modeling the evolution of discontinuous gradients in finite element methods. This method has been applied to two-phase flow problems in conjunction with the level set method to track phase interfaces. The method we employ to introduce the discontinuity in the gradient of the element basis thru a partition of unity. It can accurately resolve discontinuities in the velocity gradient at the interface without remeshing, even for materials with significantly differing viscosities. It is capable of handling highly deformed interfaces and interfaces where the topology significantly changes in a consistent and straightforward manner.

The evolution of the interface in time is tracked by a level set method. A finite element formulation has been developed for the level set method. The finite element formulation allows the level set method to easily be applied to problems where mesh refinement is needed and problems with complex geometries and/or boundaries where a structured grid would be difficult. In contrast to methods such as the volume of fluids methods, the level set method has an explicit representation of the interface, and in contrast to methods involving indicator functions the level set method varies smoothly over the interface.

Both the strength of the discontinuity and its location are described by nodal values. The location is described by the nodal values of the level set ϕ_I, the strength of the discontinuity by the magnitude of the enrichment $\mathbf{A}_I$. This eliminates a need for geometric construction of the interface, so the extension to three dimensions can be readily accomplished.

Acknowledgments

The authors are grateful for the research support of the Office of Naval Research and the Department of Energy.

References

[1] Huerta, A., and Liu, W. K., 1988, "Viscous Flow With Large Free-Surface Motion," Comput. Methods Appl. Mech. Eng., **69**(3), pp. 277–324,
[2] Tezduyar, T. E., Behr, M., and Liou, J., 1992, "A New Strategy for Finite Element Flow Computations Involving Moving Boundaries and Interfaces—The Deforming-Spatial-Domain/Space-Time Procedures: I. The Concept and Preliminary Tests," Comput. Methods Appl. Mech. Eng., **94**(3), pp. 339–353.
[3] Tezduyar, T. E., Behr, M., Mittal, S., and Liou, J., 1992, "A New Strategy for Finite Element Flow Computations Involving Moving Boundaries and Interfaces—The Deforming-Spatial-Domain/Space-Time Procedures: II. Computation of Free-Surface Flows, Two-Liquid Flows and Flows With Drifting Cylinders," Comput. Methods Appl. Mech. Eng., **94**(3), pp. 359–371.
[4] Noh, W., and Woodward, P., 1976, "A Simple Line Interface Calculation," *Proceedings, Fifth International Conference on Fluid Dynamics*, A. I. van de Vooran and P. J. Zandberger eds., Springer-Verlag, New York.
[5] Hirt, C. W., and Nichols, B. D., 1981, "Volume of Fluid (VOF) Method for the Dynamics of Free Boundaries," J. Comput. Phys., **39**(1), pp. 201–225.
[6] Osher, S., and Sethian, J. A., 1988, "Propagation of Fronts With Curvature Based Speed: Algorithms Based on Hamilton-Jacobi Formulations," J. Comput. Phys., **79**, p. 12.
[7] Sethian, J. A., 1999, *Level Set Methods and Fast Marching Methods*, Cambridge University Press, Cambridge, UK.
[8] Harlow, J. H., and Welch, J. E., 1996, "Numerical Study of Large Amplitude Free Surface Motion," Phys. Fluids, **9**, pp. 842–851.
[9] Belytschko, T., and Black, T., 1999, "Elastic Crack Growth in Finite Elements With Minimal Remeshing," Int. J. Numer. Methods Eng., **45**(5), pp. 601–620.
[10] Moës, N., Dolbow, J., and Belytschko, T., 1999, "A Finite Element Method for Crack Growth Without Remeshing," Int. J. Numer. Methods Eng., **46**, pp. 131–150.
[11] Belytschko, T., Moës, N., Usui, S., and Parimi, C., 2001, "Arbitrary Discontinuities in Finite Element," Int. J. Numer. Methods Eng., **50**(4), pp. 993–1013.
[12] Krongauz, Y., and Belytschko, T., 1997, "EFG Approximation With Discontinuous Derivatives," Int. J. Numer. Methods Eng., accepted for publication.
[13] Sukumar, N., Chopp, D. L., Moës, N., and Belytschko, T., 2000, "Modeling Holes and Inclusions by Level Sets in the Extended Finite Element Method," Comput. Methods Appl. Mech. Eng., submitted for publication.
[14] Wagner, G. J., Moës, N., Liu, W. K., and Belytschko, T., 2001, "The Extended Finite Element Method for Rigid Particles in Stokes Flow," Int. J. Numer. Methods Eng., **51**(3), pp. 293–313.
[15] Chessa, J., Smolinski, P., and Belytschko, T., 2002, "The Extended Finite Element Method for Stefan Problems," Int. J. Numer. Methods Eng., accepted for publication.
[16] Dolbow, J., and Merle, R., 2001, "Modeling Dendritic Solidification With the Extended Finite Element Method," *Proceedings of the First MIT Conference on Computational Fluid and Solid Mechanics*, K. J. Bathe, ed., Boston, Elsevier, New York, pp. 1135–1138.
[17] Renaud, M., and Dolbow, J., 2003, "Solving Thermal and Phase Change Problems With the Extended Finite Element Method," Computational Mechanics., accepted for publication.
[18] Dhatt, G., Gao, D. M., and Cheikh, A. B., 1990, "A Finite Element Simulation of Metal Flow in Moulds," Int. J. Numer. Methods Eng., **30**, pp. 821–831.
[19] Usmani, A. S., Cross, J. T., and Lewis, R. W., 1992, "A Finite Element Model for the Simulations of Mould Filling in Metal Casting and Associated Heat Transfer," Int. J. Numer. Methods Eng., **35**, pp. 787–806.
[20] Peng, D., Merriman, B., Osher, S., Zhao, H., and Kang, M., 1999, "A PDE-Based Fast Local Level Set Method," J. Comput. Phys., **155**, pp. 410–438.
[21] Barth, T., and Sethian, J. A., 1998, "Numerical Schemes for the Hamilton-Jacobi and Level Set Equations on Triangulated Domains," J. Comput. Phys., **145**, pp. 1–40.
[22] Rao, V. S., Hughes, T. J. R., and Garikipati, K., 2000, "On Modeling Thermal Oxidation of Silicon II: Numerical Aspects," Int. J. Numer. Methods Eng., **47**, pp. 359–377.
[23] Quecedo, M., and Pastor, M., 2001, "Application of the Level Set Method to the Finite Element Solution of Two-Phase Flows," Int. J. Numer. Methods Eng., **50**, pp. 645–663.
[24] Sussman, M., Almgren, A., Bell, J. B., Colella, P., Howell, L. H., and Welcome, M. L., 1999, "An Adaptive Level Set Approach for Incompressible Two-Phase Flows," Comput. Phys., **148**, pp. 81–124.
[25] Sussman, M., and Fatemi, E., 1999, "An Efficient Interface Preserving Level Set Re-distancing Algorithm and Its Applications to Interfacial Incompressible Fluid Flow," J. Sci. Comput., **20**(4), pp. 1165–1191.
[26] Sussman, M., Fatemi, E., Smereka, P., and Osher, S. 1997, "An Improved Level Set method for Incompressible Two-Phase Flows," Comput. Fluids, **27**(5), pp. 663–680.
[27] Sussman, M., Smereka, P., and Osher, S., 1994, "A Level Set Approach for Computing Solutions to Incompressible Two-Phase Flows," J. Comput. Phys., **114**, pp. 146–159.

[28] Caide, R., Fedkiw, R. P., and Anderson, C., 2001, ''A Numerical Method for Two-Phase Flow Consisting of Separate Compressible and Incompressible Regions,'' J. Comput. Phys., **166**(1), pp. 1–27.

[29] Merriman, T. B., Fedkiw, R. P., Aslam, P., and Osher, S., 2003, ''A Non-Oscillatory Eulerian Approach to Interfaces in Multi-Material Flows,'' J. Comput. Phys., to appear.

[30] Belytschko, T., Liu, W. K., and Moran, B., 2000, *Nonlinear Finite Elements for Continua and Structures*, John Wiley and Sons, New York.

[31] Melenk, J. M., and Babuška, I., 1996, ''The Partition of Unity Method: Basic Theory and Applications,'' Comput. Methods Appl. Mech. Eng., **139**, pp. 289–314.

[32] Zienkiewicz, O. C., and Taylor, R. L., 2000, *The Finite Element Method, Volume 3: Fluid dynamics*, Butterworth and Hienemann, Stoneham, MA.

[33] Hansbo, P., 1993, ''Explicit Streamline Diffusion Finite Element Methods for the Compressible Euler Equations in Conservation Variables,'' J. Comput. Phys., **109**, pp. 274–288.

[34] Rider, W. J., and Kothe, D. B., 1998, ''Reconstructing Volume Tracking,'' J. Comput. Phys., **141**, pp. 112–152.

[35] Rider, W. J., and Kothe, D. B., 1995, ''Streaching and Tearing Interface Tracking Methods,'' AIAA Paper 95-1717 (LANL Report LA-UR-95-1145).

[36] Sethian, J. A., and Adalstienson, D., 1999, ''The Fast Construction of Extension Velocities in Level Set Methods,'' J. Comput. Phys., **148**, pp. 2–22.

[37] Chorin, A. J., 1968, ''Numerical Solution of the Navier-Stokes Equation,'' Math. Comput., **23**, pp. 745–762.

[38] Zienkiewicz, O. C., and Codina, R., 1995, ''A General Algorithm for Compressible and Incompressible Flow, Part I. The Split Characteristic Based Scheme,'' Int. J. Numer. Methods Fluids, **20**, pp. 869–885.

[39] Hadamard, J. S., 1911, C. R. Acad. Sci., **152**, p. 1735.

J. García
e-mail: Julio@cimne.upc.es

E. Oñate

International Centre for Numerical Methods
in Engineering,
Universidad Politécnica de Cataluna,
Gran Capitán s/n,
08034 Barcelona, Spain

An Unstructured Finite Element Solver for Ship Hydrodynamics Problems

A stabilized semi-implicit fractional step algorithm based on the finite element method for solving ship wave problems using unstructured meshes is presented. The stabilized governing equations for the viscous incompressible fluid and the free surface are derived at a differential level via a finite calculus procedure. This allows us to obtain a stabilized numerical solution scheme. Some particular aspects of the problem solution, such as the mesh updating procedure and the transom stern treatment, are presented. Examples of the efficiency of the semi-implicit algorithm for the analysis of ship hydrodynamics problems are presented. [DOI: 10.1115/1.1530631]

Introduction

The prediction of the wave pattern and resistance joint to the study of the flow around a ship are topics of major relevance in naval architecture. The analytical and numerical solutions of this problem have challenged mathematicians and hydrodynamicists for over a century.

Despite recent advances in computational fluid dynamics (CFD) methods and computer hardware, the numerical solutions of ship wave problems is still a challenge. This is mainly due to the difficulties in solving the incompressible flow equations coupled to the free boundary constraint stating that at this boundary the fluid particles must remain on the water surface, whose position is in turn unknown.

This paper presents advances in recent work of the authors, [1–10], to derive a stabilized finite element method which allows us to overcome the above mentioned problems. The starting points are the modified governing differential equations for the incompressible flow and the free surface condition incorporating the necessary stabilization terms via a *finite calculus* (FIC) procedure developed by the authors, [8–10]. The FIC technique is based on writing the different balance equations over a domain of finite size and retaining higher order terms. These terms incorporate the ingredients for the necessary stabilization of any transient and steady-state numerical solution *already at the differential equations level*. In addition, the modified differential equations can be used to derive a numerical scheme for computing the stabilization parameters, [5,6,7,9].

The stabilized differential equations are first solved in time using a semi-implicit fractional step approach. Application of the standard Galerkin finite element formulation to the fractional steps equations leads to a stabilized system of discretized equations which overcomes the above-mentioned problems, allowing for equal order linear interpolations of the velocity and pressure variables over the elements. Unstructured grids of linear tetrahedra have been used in this work. The approach is similar to semi-implicit fractional methods proposed in [11–13]. The particular features of the algorithm here proposed are the additional stabilization terms introduced by the FIC formulation. These terms ensure the stabilization of the algorithm for small time-step sizes and enhance the convergence towards the steady-state solution. Free surface wave boundary effects are accounted for in the flow solution either by moving the free surface nodes in a Lagrangean manner, or else for via the introduction of a prescribed pressure at the free surface computed from the wave height.

The content of the paper is structured as follows. First the stabilized semi-implicit fractional step approach using the finite element method is then described. Details of the computation of the stabilization parameters are also given. Finally some examples of applications of the unstructured-grid solver for ship hydrodynamics problems are presented.

Finite Calculus (FIC) Formulation of Viscous Turbulent Flow and Free Surface Equations

We consider the motion around a body of a viscous incompressible fluid including a free surface.

The finite calculus form of the governing differential equations for the three-dimensional problem can be written as, [8–10] follows:

Momentum

$$r_{m_i} - \underline{\frac{1}{2}h_j\frac{\partial r_{m_i}}{\partial x_j}} = 0 \quad \text{on} \quad \Omega \quad i,j = 1,2,3 \tag{1}$$

Mass Balance

$$r_d - \underline{\frac{1}{2}h_j\frac{\partial r_d}{\partial x_j}} = 0 \quad \text{on} \quad \Omega \quad j = 1,2,3 \tag{2}$$

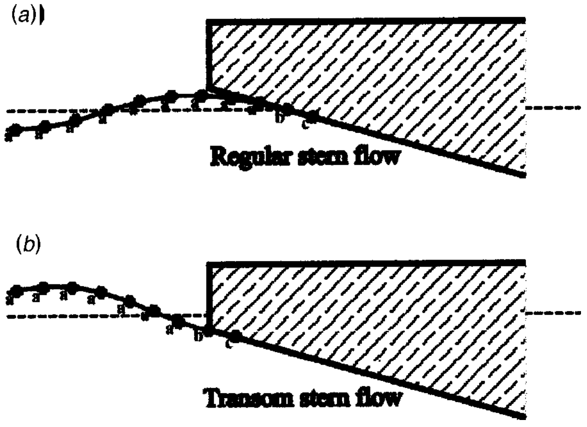

Fig. 1 Transom stern model. (*a*) Regular stern flow, (*b*) transom stern flow.

Contributed by the Applied Mechanics Division of THE AMERICAN SOCIETY OF MECHANICAL ENGINEERS for publication in the ASME JOURNAL OF APPLIED MECHANICS. Manuscript received by the Applied Mechanics Division, July 26, 2001; final revision, Mar. 12, 2002. Associate Editor: T. E. Tezduyar. Discussion on the paper should be addressed to the Editor, Prof. Robert M. McMeeking, Chair, Department of Mechanics and Environmental Engineering, University of California—Santa Barbara, Santa Barbara, CA 93106-5070, and will be accepted until four months after final publication in the paper itself in the ASME JOURNAL OF APPLIED MECHANICS.

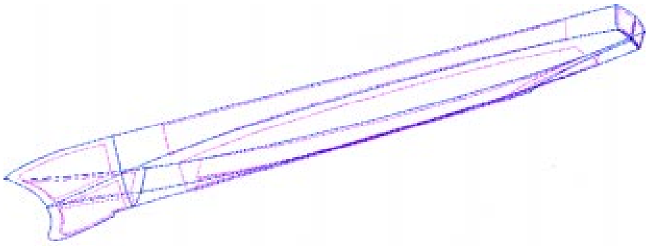

Fig. 2 DTMB 5415 model. Geometrical definition based on NURBS surfaces.

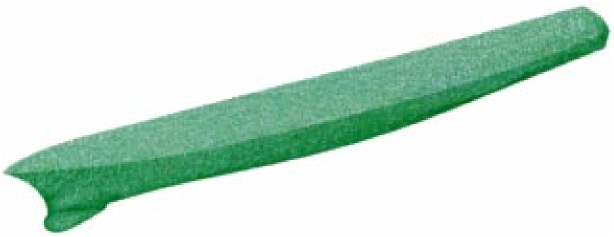

Fig. 3 DTMB 5415 model. Surface mesh used in the analysis.

Free Surface

$$r_\beta - \underline{\frac{1}{2}h_{\beta_j}\frac{\partial r_\beta}{\partial x_j}} = 0 \quad \text{on} \quad \Gamma_\beta \quad j=1,2 \tag{3}$$

where

$$r_{m_i} = \frac{\partial u_i}{\partial t} + \frac{\partial}{\partial x_j}(u_i u_j) + \frac{\partial p}{\partial x_i} - \frac{\partial \tau_{ij}}{\partial x_j}$$

$$r_d = \frac{\partial u_i}{\partial x_i}, \quad i=1,2,3$$

$$r_\beta = \frac{\partial \beta}{\partial t} + u_i \frac{\partial \beta}{\partial x_i} - u_3, \quad i=1,2.$$

In the above, u_i is the velocity along the ith global reference axis, p is the dynamic pressure ($\overline{p} = \rho(p - gz)$ where $\overline{p}$ is the total pressure, ρ is the density and g is the gravity acceleration, β is the wave elevation, and τ_{ij} are the deviatoric viscous stresses related to the kinematic viscosity μ by the standard expression

$$\tau_{ij} = \mu\left(\frac{\partial u_i}{\partial x_j} + \frac{\partial u_j}{\partial x_i} - \delta_{ij}\frac{2}{3}\frac{\partial u_k}{\partial x_k}\right). \tag{4}$$

The boundary conditions for the stabilized problem are written as

$$n_j \tau_{ij} - t_i + \underline{\frac{1}{2}h_j n_j r_{m_i}} = 0 \quad \text{on} \quad \Gamma_t \tag{5}$$

$$u_j - u_j^p = 0 \quad \text{on} \quad \Gamma_u \tag{6}$$

where n_j are the components of the unit normal vector to the boundary and t_i and u_j^p are prescribed tractions and displacements on the boundaries Γ_t and Γ_u, respectively.

The underlined terms in Eqs. (1)–(3) introduce the necessary stabilization for the numerical solution. Additional time stabilization terms can be accounted for in Eqs. (1)–(3), [4,5,9], although they have been found unnecessary for the type of problems solved here.

The *characteristic length* distances h_j represent the dimensions of the finite domain where balance of momentum and mass is enforced, [4,8]. The characteristic distances h_{β_j} in Eq. (3) represent the dimensions of a finite domain surrounding a point where the velocity is constrained to be tangent to the free surface, [2,9].

Equations (1)–(6) are the starting point for deriving a variety of stabilized numerical methods for solving the incompressible Navier-Stokes equations with a free surface using equal-order interpolations for the velocities, the pressure, and the wave height, [1–4,8,9].

Fractional Step Approach

Let us discretize in time the stabilized momentum Eq. ($1a$) as

$$\frac{u_i^{n+1} - u_i^n}{\Delta t} + \frac{\partial}{\partial x_j}(u_i u_j)^n + \frac{\partial p^n}{\partial x_i} - \frac{\partial \tau_{ij}^n}{\partial x_j} - \frac{1}{2}h_j \frac{\partial r_{m_i}^n}{\partial x_j} = 0. \tag{7}$$

A fractional step method can be simply derived by splitting Eq. (7) as follows:

$$u_i^* = u_i^n - \Delta t\left[\frac{\partial}{\partial x_j}(u_i u_j) - \frac{\partial \tau_{ij}}{\partial x_j} - \frac{1}{2}h_j \frac{\partial r_{m_i}^n}{\partial x_j}\right]^n \tag{8}$$

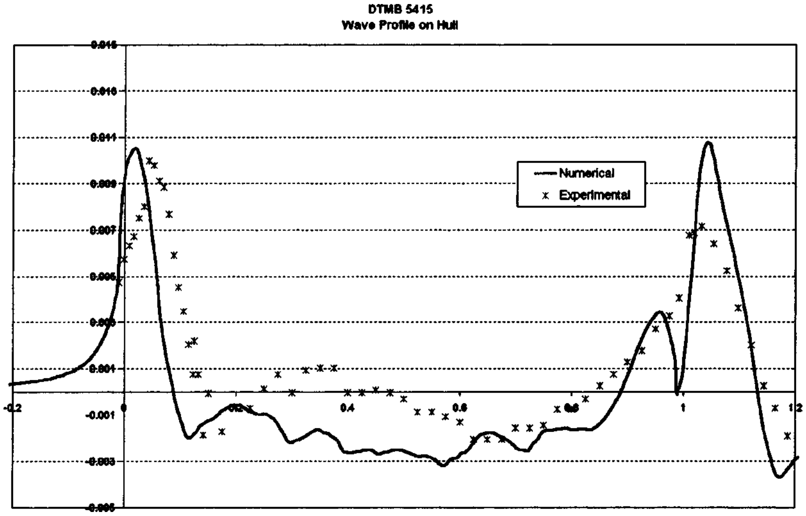

Fig. 4 DTMB 5415 model. Wave profile on the hull.

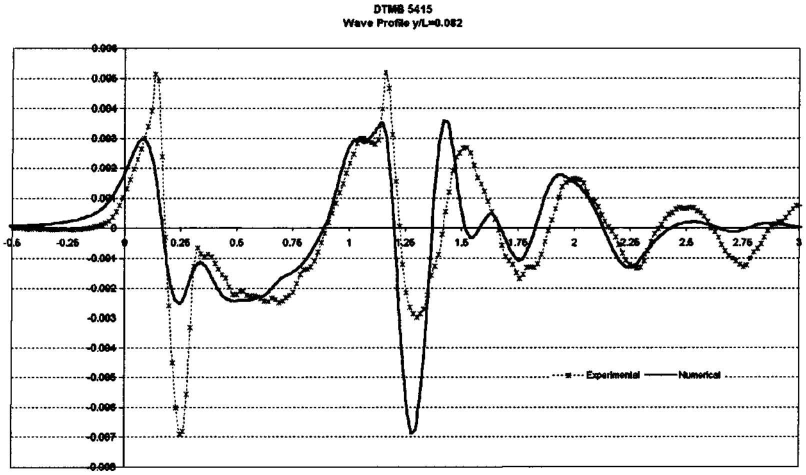

Fig. 5 DTMB 5415 model. Wave profile at $y/L=0.082$. -*- experimental values, [24]. –numerical results.

$$u_i^{n+1}=u_i^{*}-\Delta t\frac{\partial p^n}{\partial x_i}. \tag{9}$$

Note that addition of Eqs. (8) and (9) gives the original stabilized momentum Eq. (7).

Substitution of Eq. (9) into Eq. (2) gives

$$\Delta t\frac{\partial^2 p^n}{\partial x_i \partial x_i}=\frac{\partial u_i^{*}}{\partial x_i}-\tau_i u_i\frac{\partial r_d^n}{\partial x_i} \tag{10}$$

where τ_i are intrinsic time parameters defined as $\tau_i=h_i/2u_i$.

The free surface wave Eq. (3) can be also discretized in time to give, [2,7,9],

$$\beta^{n+1}=\beta^n-\Delta t\left[u_i^n\frac{\partial\beta^n}{\partial x_i}-u_3^n-\frac{1}{2}h_{\beta j}\frac{\partial r_\beta^n}{\partial x_j}\right]\quad i,j=1,2. \tag{11}$$

Pressure Stabilization

Using Eq. (1) and neglecting high-order terms it can be obtained:

$$u_i\frac{\partial}{\partial x_i}\left(\frac{\partial u_j}{\partial x_j}\right)=\frac{\partial r_{m_i}}{\partial x_i}. \tag{12}$$

Substituting Eq. (12) into Eq. (10) gives

$$(\Delta t+\tau_i)\frac{\partial^2 p^n}{\partial x_i \partial x_i}=\frac{\partial u_i^{*}}{\partial x_i}-\tau_i\left[\frac{\partial r_i'}{\partial x_i}\right]^n \tag{13}$$

with

$$r_i'=\frac{\partial u_i}{\partial t}+\frac{\partial(u_i u_j)}{\partial x_j}-\frac{\partial\tau_{ij}}{\partial x_j}\quad i,j=1,2,3. \tag{14}$$

Equation (13) is used to compute the pressure. The left-hand side is a Laplacian equation for the pressure values at time n, whereas the right-hand side includes known values of the fractional velocities, the velocities and the viscous stresses at time n.

Remark 1. Standard fractional step procedures neglect the contribution from the terms involving τ_i in Eq. (13). These terms improve the stabilization properties of the algorithm as they ensure the solution of Eq. (13) when the values of Δt are small. Also the influence of the τ_i terms has proven to be essential for obtaining improved and fully converged solutions in steady-state problems.

The finite calculus procedure can be also applied to derive a stabilized pressure increment split scheme. This can be simply derived by splitting Eq. (7) only for the pressure increment similarly as described in [14].

Remark 2. In Eq. (13) the cross derivative terms of the pressure have been neglected. These terms can be accounted for if a proper definition of the τ_i parameters is used. For details see [8].

Remark 3. The residual r_i' can be discretized using the finite elements method, [15] as

$$r_i'=\mathbf{N}\overline{\mathbf{r}_i'} \tag{15}$$

where $\mathbf{N}=[N_1,N_2,\cdots,N_n]$ contains the shape functions N_j and $\overline{(\cdot)}$ denotes nodal values.

Application of the Galerkin method to Eq. (13) gives after integration by parts

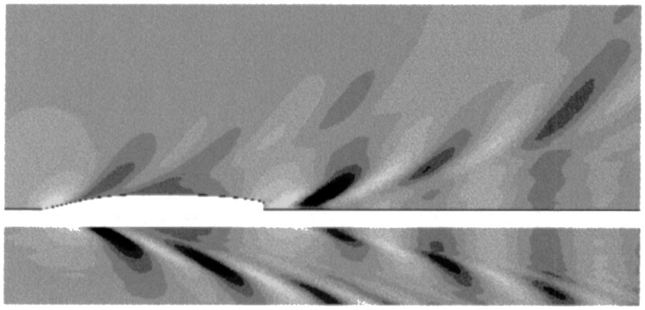

Fig. 6 Wave map of the DTMB 5415 model obtained in the simulation (above) compared to the experimental data (below)

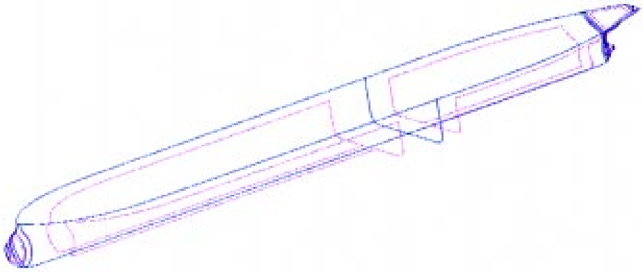

Fig. 7 KVLCC2 model. Geometrical definition based on NURBS surfaces.

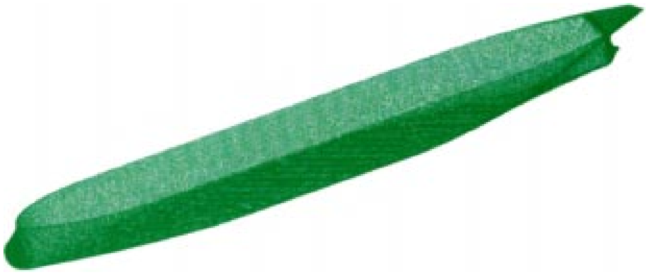

Fig. 8 KVLCC2 model. Surface mesh used in the analysis.

$$H_{kl}\overline{p}_l^n = \int_\Omega \frac{\partial N_k}{\partial x_i} u_i^* d\Omega - \int_\Omega \frac{\partial N_k}{\partial x_i} \mathbf{N}\overline{\mathbf{r}}_i'^n d\Omega \tag{16}$$

where $H_{kl} = \int_\Omega (\Delta t + \tau_i) \partial N_k / \partial x_i (\partial N_l / \partial x_i) d\Omega$ is the standard Laplacian matrix.

The values of r_i' can now be computed by projecting the pressure gradients. Neglecting the stabilization terms in Eq. (1) we can write

$$r_i' = -\frac{\partial p}{\partial x_i}. \tag{17}$$

Application of the Galerkin method to Eq. (17) gives using Eq. (15)

$$\mathbf{M}\overline{\mathbf{r}}_i'^n = \mathbf{q}^n \tag{18a}$$

with

$$M_{kl} = \int_\Omega N_k N_l d\Omega \quad \text{and} \quad q_k^n = -\int_\Omega N_k \frac{\partial p^n}{\partial x_i} d\Omega. \tag{18b}$$

Equation $(18a)$ can be solved for the values of $\overline{\mathbf{r}}_i'^n$ using an iterative Jacobian scheme.

Remark 4. The above formulation can also be aplied to the Reynolds (RANSE) equations. In this case the value of r_{m_i} in the stabilized momentum equations is given by, [7]:

$$r_{m_i} = \frac{\partial u_i}{\partial t} + \frac{\partial}{\partial x_j}(u_i u_j) + \frac{\partial p}{\partial x_i} - \frac{\partial(\tau_{ij}^n + \tau_{R_{ij}}^n)}{\partial x_j} \tag{19}$$

where τ_R^n is the Reynolds stress tensor. In this work τ_R^n has been modeled using the standard Boussinesq's approximation.

Remark 5. The value of the intrinsic time parameters τ_i have been taken as, [8,9],

$$\tau_i = \left(\frac{4\mu}{3h_i^2} + \frac{2u_i}{h_i}\right)^{-1}. \tag{20}$$

Equation (20) provides the standard values of the intrinsic time parameter for the convective limit $(u_i \rightarrow 0)$ and the viscous limit $(\mu \rightarrow 0)$.

The characteristic length distances h_i are defined here using the SUPG assumptions giving, [4,8,16],

$$\mathbf{h} = \begin{Bmatrix} h_1 \\ h_2 \\ h_3 \end{Bmatrix} = h\frac{\mathbf{u}}{|\mathbf{u}|} \tag{21}$$

where $h = [V^{(e)}]^{1/3}$, where $V^{(e)}$ is the volume of the tetrahedral element.

The characteristic lenght distances $h_{\beta i}$ in the free-surface Eqs. (3) are defined by an identical expression to Eq. (21) with $h = [A^{(e)}]^{1/2}$, $A^{(e)}$ being the area of the triangular element over the sea surface.

More details on the computation of the stabilization parameters can be found in [4–10].

Finite Element Discretization

Space discretization is carried out using the finite element method, [15]. A linear interpolation over four-node tetrahedra for both u_i and p is chosen in the examples shown in next section. Similarly, linear triangles are chosen to interpolate β on the free-surface mesh.

The discretized integral form in space is obtained by applying the standard Galerkin procedure to Eqs. (8), (13), (9), and (11) and the boundary conditions (5) and (6). Solution of the discretized problem follows the pattern given below.

Step 1. Solve Eq. (8) for the nodal fractional velocities. The Dirichlet boundary conditions on the nodal velocities are imposed when solving Eq. (8). Note that the fractional step method can be interpreted as an incomplete block LU factorization of the monolithic problem, [14,17].

Step 2. Solve Eq. (13) for the nodal pressures at time n+1. The pressures computed from Step 4 are used as a boundary condition

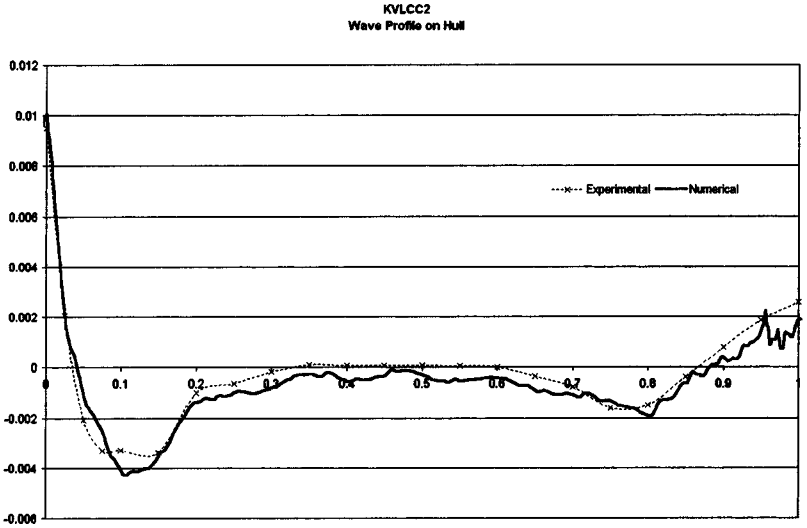

Fig. 9 KVLCC2 model. Wave profile on the hull compared to experimental data, [25]. Thick line shows numerical results.

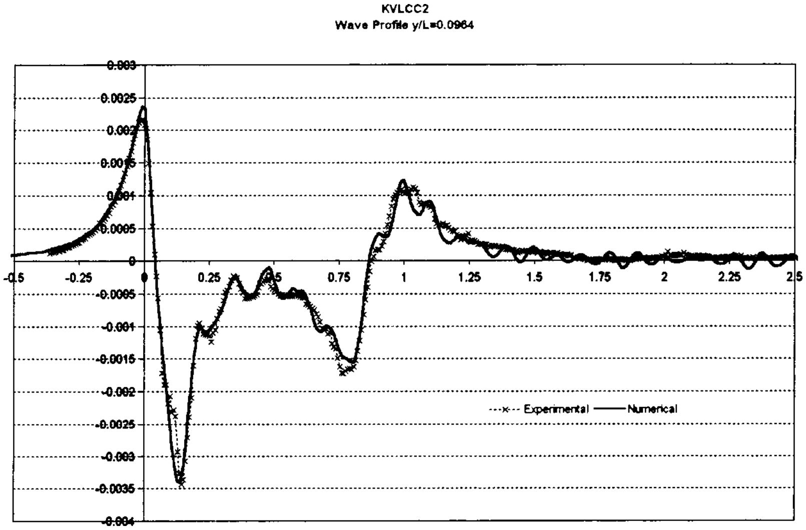

Fig. 10 KVLCC2 model. Wave profile on a cut at $y/L=0.0964$ compared to experimental data, [25]. Thick line shows numerical results.

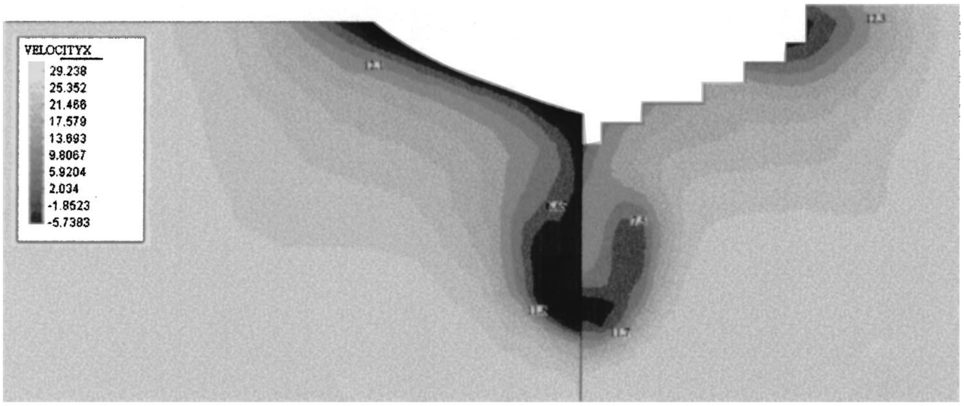

Fig. 11 KVLCC2 model. Map of the *X* component of the velocity on a plane at 2.71 m from the orthogonal aft. Comparison with the experimental data, [25].

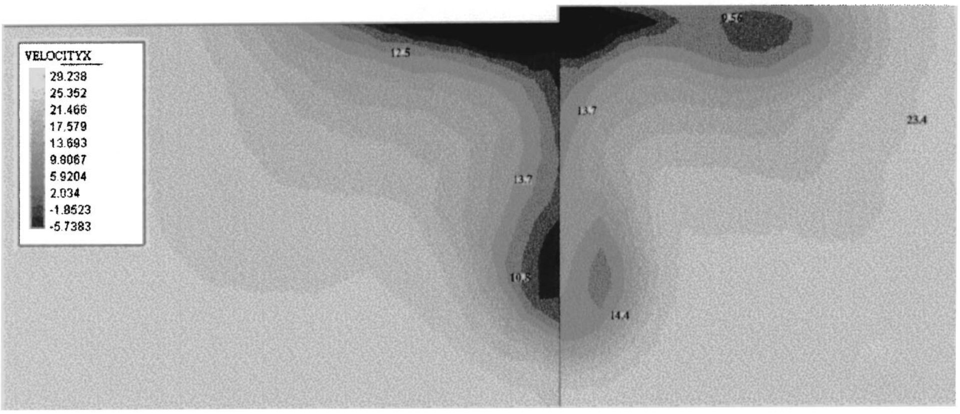

Fig. 12 KVLCC2 model. Map of the *X* component of the velocity on a plane at 2.82 m from the orthogonal aft. Comparison with the experimental data, [25].

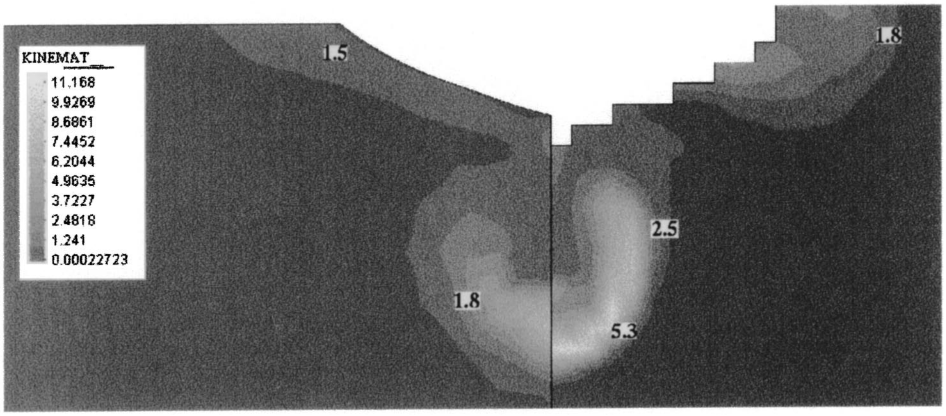

Fig. 13 KVLCC2 model. Map of the eddy kinetic energy (K) on a plane at 2.71 m from the orthogonal aft. Comparison with the experimental data, [25].

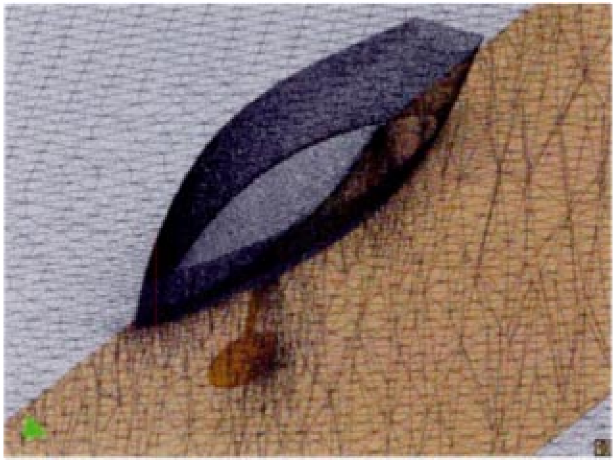

Fig. 14 *Bravo España* sail racing boat. Mesh used in the analysis.

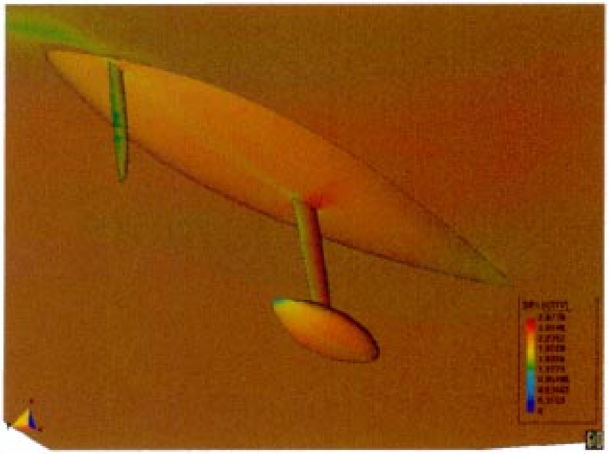

Fig. 15 *Bravo España*. Velocity contours.

for solution of Eq. (13) (viz. Eq. (18)).

Step 3. Solve Eq. (9) for the nodal velocities at time n+1. The Dirichlet boundary conditions on the nodal velocities are imposed when solving Eq. (9).

Step 4. Solve for the new free surface height at time n+1. The new free-surface elevation β^{n+1} in the fluid domain is computed from Eq. (11).

The pressure at the free surface is obtained from the balance of tractions at the surface, [18],

$$n_j\rho\tau_{ij}-n_i\overline{p}=n_j\rho_a\tau^a_{ij}-n_i\overline{p^a}+n_i\frac{\gamma}{R} \tag{22}$$

where $\overline{p}$ is the pressure field on water, $\overline{p^a}$ is the air pressure, τ^a_{ij} is the air viscous stress tensor, ρ_a is the air density, γ is the surface tension coefficient, R is the average curvature radius of the free surface, and n_i is the vector in the normal direction to the free surface. Assuming $\partial\beta/\partial x \ll 1$ and $\partial\beta/\partial y \ll 1$ it can be taken $\mathbf{n}=[0,0,-1]$.

In Eq. (22) the turbulent stresses are neglected close to the free surface as shown experimentally, [18,19].

Assuming that air is at rest ($p^a=0$ and $\tau^a_{ij}=0$), Eq. (22) can be simplified as

$$n_j\rho\tau_{ij}-n_i\overline{p}=n_i\frac{\gamma}{R}. \tag{23}$$

The third component of above equation gives

$$\overline{p}=\rho\tau_{33}+\frac{\gamma}{R}. \tag{24}$$

The dynamic pressure is finally obtained from

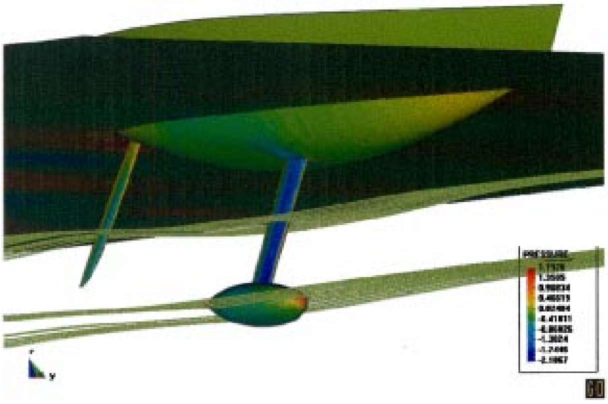

Fig. 16 *Bravo España*. Streamlines.

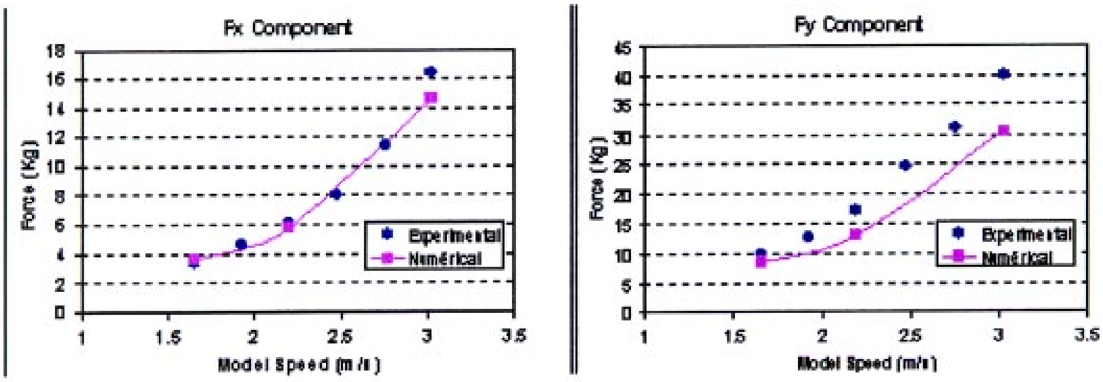

Fig. 17 ***Bravo España*****. Resistance test. Comparison of numerical results with experimental data.**

$$p=\tau_{33}-\frac{\gamma}{\rho R}+g\beta \qquad (25)$$

where g is the modulus of the acceleration of the gravity.

Reaching this point the fluid domain has to be updated due to the new position of the free surface. This is an expensive process and a simplified solution can be found by neglecting the change of the free surface and taking into account its effects by prescribing the pressure acting on the free surface. In order to increase the accuracy of the solution, the free-surface equation is modified by making use of a Taylor series expansion of β in the Oz direction, [20].

Remark 6. The conceptually simplest way to carry out the mesh updating due to the new position of the free surface and of the ship is by remeshing the new fluid domain. A number of algorithms for computation of moving boundaries and interfaces including free-surface flows using interface-tracking and interface-capturing techniques and remeshing algorithms have been proposed in recent years, [13,21]. Indeed, the use of tetrahedra elements and unstructured grids simplifies this process. However, remeshing is nowadays too expensive if industrial applications of the algorithm are sought.

Chiandussi, Bugeda, and Oñate [22] have proposed a simple method for movement of mesh nodes ensuring minimum element distorsion, thereby reducing the need of remeshing. The method is based on the iterative solution of a fictitious linear elastic problem on the mesh domain. In order to minimize mesh deformation the "elastic" properties of each mesh element are adequately selected so that elements suffering greater distortions are stiffer. Applications of this technique to ship hydrodynamic problems can be found in [3,7,9].

Transom Stern Model

It is well known that the transom flow occuring at a sufficient high speed has a singularity for the standard solution of the free-surface Eq. (11). Several authors have proposed solutions to these problem, [23,24], mainly based on experimental observations of this phenomena. Next, a more natural solution to solve the transom flow is presented.

The standard solution of convective equations such as the free-surface equation requires prescribing the Dirichlet conditions at the inflow. As the transom causes a discontinuity in the domain, the solution of the free-surface equation close to this region is inconsistent with the convective nature of the equation. The direct solution of the free surface equation in this case results in the instability of the wave height close to the transom region. This instability is found experimentally for low speeds. The flow at a sufficient high speed is physically more stable although it still cannot be reproduced by standard numerical techniques.

The solution to this problem is to apply adequate free-surface boundary conditions at the transom boundary. The obvious condition is to fix both the free-surface elevation β and its derivative along the corresponding streamline to values given by the transom position and the surface gradient. However, prescribing those values can influence the transition between the transom flux and the lateral flux, resulting in unaccurate wave maps.

The method here proposed is to extend the free surface below the ship. In this way the neccesary Dirichlet boundary conditions imposed at the inflow domain are enough to achieve the well-possessed properties of the problem. We note that is not an ad hoc condition, as Eq. (11) has to be satisfied also in the wetted surface below the ship. Obviously, this way to proceed is valid both for the wetted and dry transom cases and it can be also applied to ships with regular stern. In Fig. 1 the nodes marked with "a" include the standard degrees-of-freedom (β) of the free-surface problem; those nodes marked with "b" introduce the new degrees-of-freedom, while wave elevation β is prescribed at the nodes marked as "c."

Indeed, accounting for every surface element of the wetted ship surface is not neccesary. Just the first row of elements is enough as the rest usually have a fixed wave elevation and will not influence the results.

This scheme can not be used in the case of partially wetted transom when the flow remains adhered to the transom instead of a detatched flow. These phenomena usually appear for highly unsteady flows where wake vortex induces the deformation of the free surface. To favor the convergence of the free surface to a stable state an artificial viscosity term has been added to the free-surface equations in the vecinity of the transom in these cases.

Examples

All examples have been solved in a standard single processor PC using the computer code SHYNE, [25] based on the algorithm here presented and the pre/postprocessor *GiD* developed at CIMNE, [26]. Recent industrial applications of the CFD formulation presented can be found in [27].

Example 1. DTMB 5415 Model. The first case analyzed is the David Taylor Model Basin 5415 benchmark model. The geometry used in the analysis was obtained from the Gothenburg 2000 Workshop database, [28]. The NURBS definition is shown in Fig. 2. The obtained results are compared with experimental data available, [28]. The main characteristics of the analysis are

- length: 5.72 m, beam: 0.5 m, draught: 0.248 m, wetted surface: 4.861 m^2,
- velocity: 2.1 m/seg, Froude number: 0.28, and
- viscosity: 0.001 Kg/mseg, density: 1000 Kg/m^3, Reynolds number: 12.310^6.

The analysis was carried out for three different grids (from 150,000 to 600,000 linear tetrahedra, corresponding to 25,000 and 115,000 nodes) in order to qualitatively analyze the influence of the element size in the solution. Here only the results corresponding to the finest grid are shown. The smallest element size used was 0.002 m and the maximum 0.750 m. The surface mesh of the DTMB 5415 used in the last analysis is shown in Fig. 3. The Smagorinsky turbulence model with the extended law of the wall was chosen. The tramsom stern flow model presented was used.

Figures 4 and 5 show the wave profile on the hull and in a cut at $y/L=0.082$, respectively. Numerical results obtained are compared with the experimental data.

Figure 6 shows the comparison of the wave map obtained with the experimental data available.

Example 2. KVLCC2 Model. The next example is the analysis of the KVLCC2 benchmark model. Here a partially wetted tramsom stern is expected due to the low Froude number of the test. Figure 7 shows the NURBS geometry used obtained from the Hydrodynamic Performance Research team of Korea (KRISO). The obtained results are compared with the experimental data available in the KRISO database, [29].

The smallest element size used was 0.001 m and the largest 0.50 m. The surface mesh chosen is shown in Fig. 8. A total of 550,000 tetrahedra were used in the analysis. The tramsom stern flow model presented in the previous section was used.

Test 1. Wave pattern calculation. The main characteristics of the analysis are listed below:

- length: 5.52 m, beam (at water plane): 0.82 m, draught: 0.18 m, wetted surface: 8.08 m^2,
- velocity: 1.05 m/seg, Froude number: 0.142, and
- viscosity: 0.00126 Kg/mseg, density: 1000 Kg/m^3, Reynolds number: 4.6310^{6}.

The turbulence model used in this case was the K model. Figures 9 and 10 show the wave profiles on the hull and in a cut at $y/L=0.082$ obtained in Test 1, compared to the experimental data. The obtained results are quantitatively good close to the hull. A lost of accuracy is observed in the profiles away from the hull. This is probably due to the fact that the element sizes are not small enough in this area.

Test 2. Wake analysis at different planes. Several turbulence models were used (Smagorinsky, K, and $K\text{-}\epsilon$ model) in order to verify the quality of the results. Here, only the results from the $K\text{-}\epsilon$ model are shown. We note that the velocity maps obtained even for the simplest Smagorinsky model were qualitatively good, showing the accuracy of the fluid solver scheme used. The main characteristics of this analysis are listed below:

- length: 2.76 m, beam (at water plane): 0.41 m, draught: 0.09 m, wetted surface: 2.02 m^2,
- velocity: 25 m/seg, Froude number: 0.0, and
- viscosity: 3.0510^{-5} Kg/mseg, density: 1.01 Kg/m^3, Reynolds number: 4.6310^{6}.

Figures 11 to 13 present the results corresponding to the Test 2. Figures 11 and 12 show the contours of the axial (X) component of the velocity on planes at 2.71 m and 2.82 m from the orthogonal aft, respectively. Figure 13 shows the maps of the kinetic energy on the first of these planes. Experimental results are shown for comparison in all cases.

Example 3. AMERICAN CUP BRAVO ESPAÑA Model The final example is the analysis of the Spanish American Cup racing sail boat *Bravo España*. The finite element mesh used is shown in Fig. 14. The results presented in Figs. 15–17 correspond to the analysis of a nonsymmetrical case including appendages. Good comparison between the experimental data and the numerical results was again obtained.

Conclusions

The finite calculus method provides modified forms of the governing differential equations for a viscous fluid with a free surface. Solution of the modified equations with a semi-implicit fractional step finite element method provides a straight forward and stable algorithm for analysis of ship hydrodynamic problems.

Numerical results obtained in the three-dimensional viscous analysis of complex ship geometries indicate that the proposed numerical method can be used with confidence for practical hydrodynamic design purposes in naval architecture.

Acknowledgments

Financial support for this work was provided by the European Community through projects Brite-Euram BR 967-4342 SHEAKS and Esprit 24903 FLASH. Thanks are given to Dr. H. Sierra from many useful suggestions. The authors are also grateful to Copa America Desafio Español SA for providing the geometry and experimental data of the racing boat analyzed.

Thanks are also given to Mr. J.A. Arráez for his help in computing some of the examples presented.

The authors also thank Prof. S. Idelsohn, Prof. R. Lohner, and Dr. C. Sacco for many useful discussions.

References

[1] García, J., Oñate, E., Sierra, H., Sacco, C., and Idelsohn, S., 1998, "A Stabilized Numerical Method for Analysis of Ship Hydrodynamics," *ECCOMAS98*, K. Papaliou et al., eds., John Wiley and Sons, New York.

[2] Oñate, E., Idelsohn, S., Sacco, C., and García, J., 1998, "Stabilization of the Numerical Solution for the Free Surface Wave Equation in Fluid Dynamics," *ECCOMAS98*, K. Papaliou et al., eds., John Wiley and Sons, New York.

[3] Oñate, E., and García, J., 1999, "A Methodology for Analysis of Fluid-Structure Interaction Accounting for Free Surface Waves," European Conference on Computational Mechanics (ECCM99), Aug. 31–Sept. 3, Munich, Germany.

[4] Oñate, E., 1998, "Derivation of Stabilized Equations for Advective-Diffusive Transport and Fluid Flow Problems," Comput. Methods Appl. Mech. Eng., **151**, pp. 233–267.

[5] Oñate, E., García, J., and Idelsohn, S., 1997, "Computation of the Stabilization Parameter for the Finite Element Solution of Advective-Diffusive Problems," Int. J. Numer. Methods Fluids, **25**, pp. 1385–1407.

[6] Oñate, E., García, J., and Idelsohn, S., 1998, "An Alpha-Adaptive Approach for Stabilized Finite Element Solution of Advective-Diffusive Problems With Sharp Gradients," *New Adv. in Adaptive Comp. Met. in Mech.*, P. Ladeveze and J. T. Oden, eds., Elsevier, New York.

[7] García, J., 1999, "A Finite Element Method for Analysis of Naval Structures," Ph.D. thesis, Univ. Politècnica de Catalunya, Dec. (in Spanish).

[8] Oñate, E., 2000, "A Stabilized Finite Element Method for Incompressible Viscous Flows Using a Finite Increment Calculus Formulation," Comput. Methods Appl. Mech. Eng., **182**, pp. 1–2, 355–370.

[9] Oñate, E., and García, J., 2001, "A Finite Element Method for Fluid-Structure Interaction With Surface Waves Using a Finite Calculus Formulation," Comput. Methods Appl. Mech. Eng., **191**, pp. 635–660.

[10] Oñate, E., 2001, "Possibilities of Finite Calculus in Computational Mechanics," presented at the First Asian-Pacific Congress on Computational Mechanics, APCOM'01 Sydney, Australia, Nov. 20–23.

[11] Tezduyar, T. E., 1991, "Stabilized Finite Element Formulations for Incompressible Flow Computations," Adv. Appl. Mech., **28**, pp. 1–44.

[12] Zienkiewicz, O. C., and Codina, R., 1995, "A General Algorithm for Compressible and Incompressible Flow. Part I: The Split Characteristic Based Scheme," Int. J. Numer. Methods Fluids, **20**, pp. 869–885.

[13] Tezduyar, T. E., 2001, "Finite Element Methods for Flow Problems With Moving Boundaries and Interfaces," Arch. Comput. Methods Eng., **8**, pp. 83–130.

[14] Codina, R., 2001, "Pressure Stability in Fractional Step Finite Element Methods for Incompressible Flows," J. Comput. Phys., **170**, pp. 112–140.

[15] Zienkiewicz, O. C., and Taylor, R. C., 2000, *The Finite Element Method*, 5th Ed., Butterworth-Heinemann, Stonetam, MA.

[16] Hughes, T. J. R., and Mallet, M., 1986, "A New Finite Element Formulations for Computational Fluid Dynamics: III. The Generalized Streamline Operator for Multidimensional Advective-Diffusive Systems," Comput. Methods Appl. Mech. Eng., **58**, pp. 305–328.

[17] Perot, J. B., 1993, "An Analysis of the Fractional Step Method," J. Comput. Phys., **108**, pp. 51–58.

[18] Alessandrini, B., and Delhommeau, G., 1999, "A Fully Coupled Navier-Stokes Solver for Calculation of Turbulent Incompressible Free Surface Flow Past a Ship Hull," Int. J. Numer. Methods Fluids, **29**, pp. 125–142.

[19] Celik, I., Rodi, W., and Hossain, M. S., 1982, "Modelling of Free Surface Proximity Effects on Turbulence," *Proc. Refined Modelling of Flows*, Paris.

[20] Idelsohn, S., Oñate, E., and Sacco, C., 1999, "Finite Element Solution of Free

Surface Ship-Wave Problem,'' Int. J. Numer. Methods Eng., **45**, pp. 503–508.
[21] Löhner, R., Yang, C., Oñate, E., and Idelsohn, S., 1999, ''An Unstructured Grid-Based Parallel Free Surface Solver,'' Concr. Library Int., **31**, pp. 271–293.
[22] Chiandusi, G., Bugeda, G., and Oñate, E., 2000, ''A Simple Method for Update of Finite Element Meshes,'' Commun, Numer. Meth. Engng., **16**, pp. 1–9.
[23] Matusiak, J., Tingqiu, L., and Lehtimäki, R., 1999, ''Numerical Simulation of Viscous Flow With Free Surface Around Realistic Hull Forms With Free Surface Around Realistic Hull Forms With Transform,'' Report of Ship Laboratory, Helsinki University of Technology, Finland.
[24] Raven, H. C., 1996, ''A Solution Method for Ship Wave Resistance Problem,'' Ph.d. thesis, University of Delft, June.
[25] García, J., 2002, ''SHYNE Manual,'' available at www.cimne.upc.es/shyne.
[26] ''GiD,'' 2001, The Personal Pre/Postprocessor, user manual available at www.gid.cimne.upc.es.
[27] Tdyn, 2002, ''A Finite Element Code for Fluid-Dynamic Analysis,'' COMPASS Ingeniería y Sistemas SA, www.compassis.com.
[28] David Taylor Model Basis 5415 Model Database, http://www.iihr.uiowa.edu/gothenburg2000/5415/combatant.html.
[29] Korea Research Institute of Ships and Ocean Engineering (KRISO), http://www.iihr.uiowa.edu/gothenburg2000/KVLCC/tanker.html.

Numerical Solutions of Cauchy-Riemann Equations for Two and Three-Dimensional Flows

M. Hafez

J. Housman

Department of Mechanics and Aerospace Engineering,
University of California,
Davis, CA 95616

For two-dimensional flows, the conservation of mass and the definition of vorticity comprise a generalized Cauchy-Riemann system for the velocity components assuming the vorticity is given. If the flow is compressible, the density is a function of the speed and the entropy, and the latter is assumed to be known. Introducing artificial time, a symmetric hyperbolic system can be easily constructed. Artificial viscosity is needed for numerical stability and is obtained from a least-squares formulation. The augmented system is solved explicitly with a standard point relaxation algorithm which is highly parallelizable. For an extension to three-dimensional flows the continuity equation is combined with the definitions of two vorticity components, and are solved for the three velocity components. Second-order accurate results are compared with exact solutions for incompressible, irrotational, and rotational flows around cylinders and spheres. Results for compressible (subsonic) flows are also included. [DOI: 10.1115/1.1530632]

1 Introduction

Numerical flow simulations are usually based on the solutions of Euler and Navier-Stokes equations in terms of primitive or conservative variables. Alternative formulations based on the vector potential or in terms of velocity—vorticity equations are not popular because of the associated difficulties and limitations. Recently there are some efforts to construct numerical schemes based on decoupling the kinematics and the dynamics of the motion. The motivations and the advantages of such formulations are discussed in Ref. [1].

In this work we are interested in calculating the velocity field using the continuity equation and the definition of vorticity. For steady, incompressible, inviscid, irrotational flow the two velocity components can be obtained from the standard Cauchy-Riemann system. The two first-order equations are equivalent to one second-order Laplace equation in terms of the potential or the stream function. Also, a least-squares procedure results in two Laplace equations for the two velocity components.

If the flow is not irrotational and there are also sources in the field, the nonhomogeneous Cauchy-Riemann equations are not reducible to a single second-order equation. The velocity vector can be represented as the gradient of a potential plus the curl of another vector. The first component is curl-free and the second component is divergence-free. This decomposition is always possible under very general conditions according to the Helmholtz theorem. However, for general three-dimensional flows, the boundary conditions are complicated. On the other hand, the least-squares procedure produces three second-order equations for the three velocity components. It is not clear, however, how to impose easily the entropy condition, in such a formulation, in order to exclude expansion shocks for simulation of transonic flows.

The least-squares formulation has other problems as well, even for incompressible flows. First the spurious solution must be excluded via imposing the first-order equations on the boundary. Moreover mass may not be conserved at the discrete level. Special arrangements, for example, staggered grids may be necessary to ensure conservation of numerical fluxes. For the vorticity, obtained from the curl of the momentum equations, special treatment is required to guarantee that its divergence vanishes identically at the discrete level.

In the following we will solve generalized Cauchy-Riemann equations embedded in an artificial time process governed by a symmetric hyperbolic system leading to a well-posed initial boundary value problem. Since we are interested only in the steady-state solution, the accuracy of the transient behavior is not an issue. Standard convergence acceleration techniques such as multigrid can be employed to improve the efficiency of the calculations (see Appendix A).

To avoid odd and even decoupling and to insure numerical stability, artificial viscosity must be introduced. To guarantee second-order accuracy (for incompressible and subsonic flow), artificial viscosity based on the least-squares formulation is used (see Hughes et al. [2] and Tezduyar and Hughes [3]). The scheme is also similar to Lerat's recent work, [4], at least for subsonic flows. The second-order terms vanish identically at the continuous level since they are consistent with the Cauchy-Riemann equations. At the discrete level they produce higher-order dissipation. Such a construction can be viewed as a compact method to replace the commonly used fourth order dissipation schemes proposed by McCormack [5] and by Jameson [6].

The paper is organized in four sections; governing relations, numerical algorithms, numerical results, and conclusions with some general remarks.

2 Governing Equations and Boundary Conditions

The equations for flow over a cylinder and over a sphere written in cylindrical and spherical coordinates are given.

Flow Over a Cylinder

Continuity Equation.

$$\frac{1}{\rho}\left[\frac{1}{r}\frac{\partial(r\rho v_r)}{\partial r}+\frac{1}{r}\frac{\partial(\rho v_\theta)}{\partial\theta}\right]=0. \tag{1}$$

Contributed by the Applied Mechanics Division of THE AMERICAN SOCIETY OF MECHANICAL ENGINEERS for publication in the ASME JOURNAL OF APPLIED MECHANICS. Manuscript received by the ASME Applied Mechanics Division, Aug. 24, 2001; final revision, June 11, 2002. Associate Editor: T. E. Tezduyar. Discussion on the paper should be addressed to the Editor, Prof. Robert M. McMeeking, Department of Mechanical and Environmental Engineering University of California–Santa Barbara, Santa Barbara, CA 93106-5070, and will be accepted until four months after final publication of the paper itself in the ASME JOURNAL OF APPLIED MECHANICS.

Vorticity Definition.

$$\frac{1}{r}\frac{\partial(rv_\theta)}{\partial r}-\frac{1}{r}\frac{\partial(v_r)}{\partial\theta}=\omega_z. \tag{2}$$

Three-Dimensional Flow Around a Sphere

Continuity Equation.

$$\frac{1}{\rho}\left[\frac{1}{r^2}\frac{\partial(r^2\rho v_r)}{\partial r}+\frac{1}{r\sin\theta}\frac{\partial(\sin\theta\rho v_\theta)}{\partial\theta}+\frac{1}{r\sin\theta}\frac{\partial\rho v_\phi}{\partial\phi}\right]=0. \tag{3}$$

Vorticity Definitions.

$$\frac{1}{r\sin\theta}\frac{\partial v_r}{\partial\phi}-\frac{1}{r}\frac{\partial(rv_\phi)}{\partial r}=\omega_\theta \tag{4}$$

$$\frac{1}{r}\frac{\partial(rv_\theta)}{\partial r}-\frac{1}{r}\frac{\partial v_r}{\partial\theta}=\omega_\phi \tag{5}$$

and the boundary conditions are

$$v_r=0 \quad \text{at } r=r_i \tag{6}$$

$$v_\theta \quad \text{and } v_\phi \quad \text{are given at } r=r_o, \tag{7}$$

where r_i and r_o are the radii of inner and outer spheres.

Table 1 Shown are the total number of iterations and final max norm error of (v_r, v_θ, v_ϕ) for the computed solution where the error is the difference between the exact analytic solution and the numerical results

	ϵ	Number of Iterations	Absolute Error
System 1		1757	0.0084
System 2	1	1805	0.0147
System 3	$\frac{\Delta r}{2}$	381	0.0309

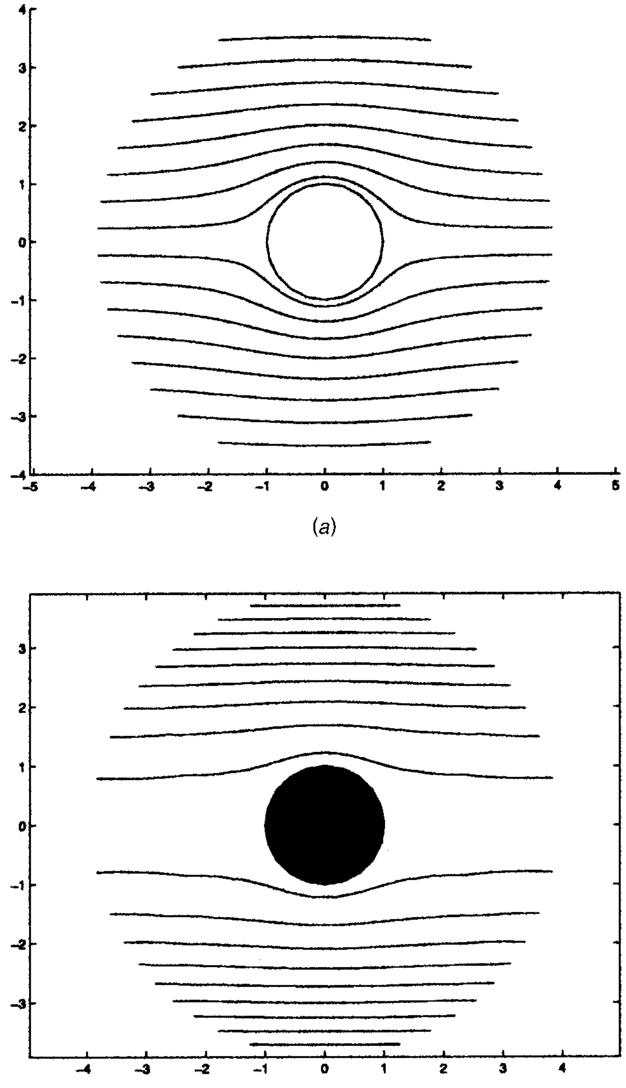

(*a*)

(*b*)

Fig. 1 (*a*) Streamlines for incompressible flow over a cylinder with $\omega_z=0$. (*b*) Streamlines for incompressible axisymmetric flow around a sphere with $\omega_\phi=0$.

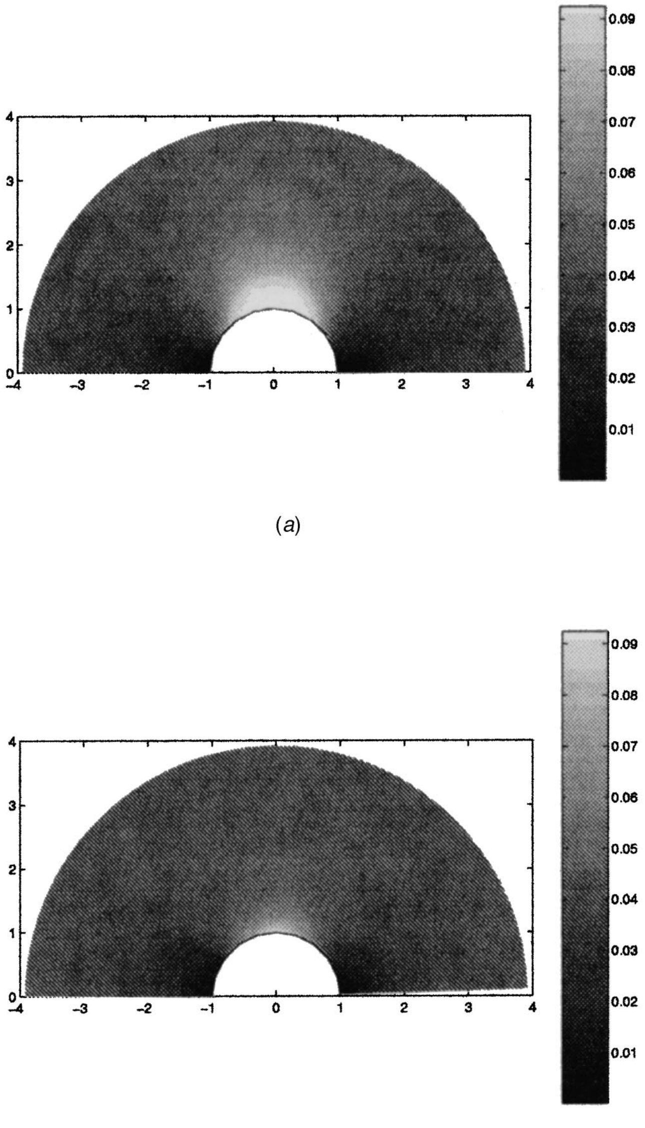

(*a*)

(*b*)

Fig. 2 (*a*) Plot of the local Mach number for compressible flow around a cylinder with $M_\infty=0.2$. (*b*) Plot of the local Mach number for compressible flow over sphere with $M_\infty=0.2$. (*c*) Example 2: Convergence history for the $\|r\|_\infty$ norm for systems 1 and 2. (*d*) Convergence history for the $\|r\|_\infty$ norm for systems 1 and 2.

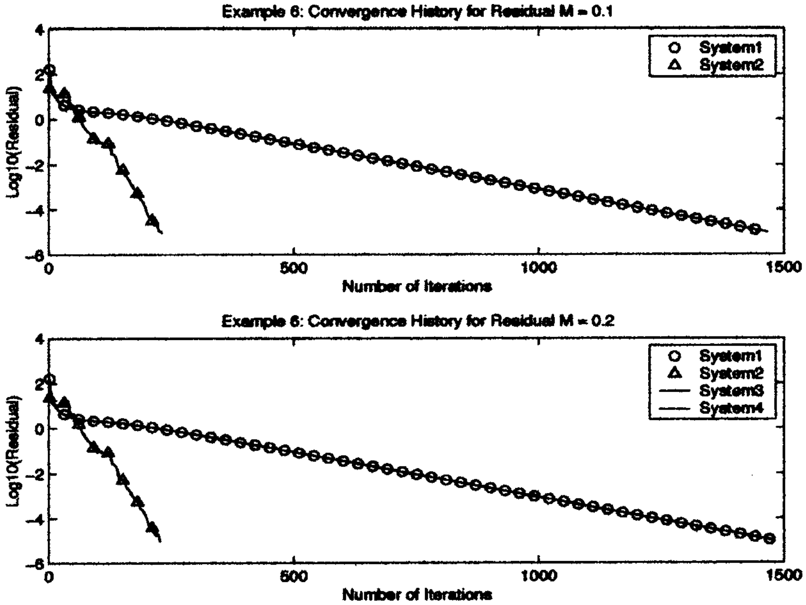

(c)

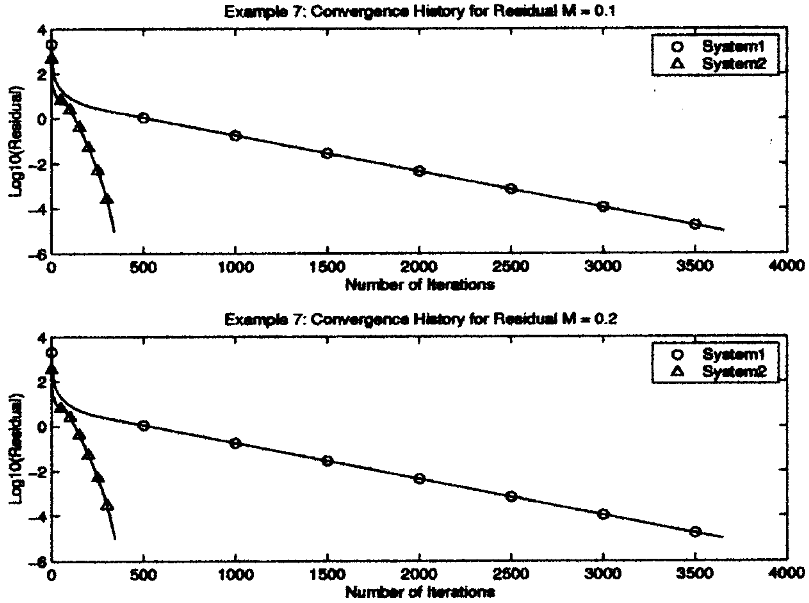

(d)

Fig. 2 (**continued**)

In case of irrotational, isentropic flows the vorticity vanishes identically and the density is related to the speed according to Bernoulli's law:

$$\rho=\left[1-\frac{\gamma-1}{2}M_{\infty}^{2}(|q|^{2}-1)\right]^{1/\gamma-1}, \tag{8}$$

where M_∞ is the freestream Mach number. For incompressible flows $M_\infty=0$.

3 Numerical Methods

Incompressible and compressible (subsonic) flows around cylinder and spheres are calculated using a least-squares formulation

Table 2 Shown are the total number of iterations to reach a residual tolerance of 10^{-5} for the computed solutions with $\epsilon=1$ and $\epsilon=\Delta r/2$ and freestream Mach numbers 0.1 and 0.2

	ϵ	Iterations(M=0.1)	Iterations(M=0.2)
System 1	1	1467	1481
System 2	$\Delta r/2$	231	228

Table 3 Shown are the total number of iterations to reach a residual tolerance of 10^{-5} for the computed solutions with $\epsilon=1$ and $\epsilon=\Delta r/2$ and freestream Mach numbers 0.1 and 0.2

	ϵ	Iterations(M=0.1)	Iterations(M=0.2)
System 1	1	3657	3647
System 2	$\Delta r/2$	341	344

Table 4 Convergence results

N	V-Cycle Iterations	$\|e\|_\infty$	Time(sec.)	Point Relaxation Iterations	$\|e\|_\infty$	Time(sec.)
32^2	15	1.40e-2	3	532	1.40e-2	58
64^2	15	3.52e-3	12	1754	3.52e-3	823
128^2	20	8.80e-4	69	6787	8.89e-4	11810
256^2	23	2.19e-4	337	26982	2.27e-4	107622

as well as Cauchy-Riemann equations embedded in a symmetric hyperbolic system which is augmented by artificial viscosity. All spatial derivatives are discretized using second-order accurate finite volume schemes. The time derivative terms are discretized via first-order time differences. The discretized systems are solved using a point Gauss-Seidel relaxation scheme. The source code is implemented in C++ and run on an HP-Visualize C3000 workstation. In the following, the problems we solved are stated. (Transonic flows with shocks are calculated in [7] using similar schemes but with linearized boundary conditions.)

The governing equations, denoted

$$L(\underset{\sim}{w}), \tag{9}$$

can be imbedded in the following system:

$$\partial_t \underset{\sim}{w} = L(\underset{\sim}{w}) + \epsilon L^* L(\underset{\sim}{w}) \tag{10}$$

where L^* is the adjoint of the operator L. For cartesian coordinates and incompressible irrotational flows, $L^*L(\underset{\sim}{w})$ are the Laplacians of the $\underset{\sim}{w}$ components.

The boundary conditions we imposed are

On Solid Surface: A Dirchlet condition is used for the radial velocity v_r and a Neumann condition derived from the vorticity equation is used for the angular velocity v_θ (and v_ϕ).

Far-Field: A Dirchlet condition is used for the angular velocity v_θ (and v_ϕ) and a Neumann condition derived from the continuity equation is used for the radial velocity v_r.

Flow Field: Periodic boundary conditions are used within the flow field for both v_r and v_θ (and v_ϕ).

4 Numerical Results

4.1 Incompressible Flow. We tested the present formulation for cases with analytical solutions, for example, flow with circulation over a cylinder, uniform and shear, as well as a cylinder in a rotating fluid (see Bachelor [8]). We have also calculated flow over a sphere using axisymmetric as well as the full three-dimensional equations. In Fig. 1, the streamlines are plotted for incompressible flows over a cylinder and a sphere. In all the above cases, the results are satisfactory in terms of accuracy and convergence. For example the results of flow calculations over a sphere are as follows.

Example 1. In this example we assume axisymmetric irrotational flow around a sphere, but we solve for each of the velocity components (v_r, v_θ, v_ϕ), as in a fully three-dimensional flow. Numerical solutions are computed in a spherical coordinate system with three space dimensions. The grid spacings used are $\Delta r = 0.1$, $\Delta\theta = \pi/18$, and $\Delta\phi = \pi/18$. The grid dimensions are $36 \times 19 \times 37$ and the radius of the sphere is nondimensionalized to 1. The program is ran until a residual tolerance of 1.0e-5 is met and the results are shown in Table 1.

4.2 Compressible Flow

Example 2. We solve for compressible flow over a cylinder with and without density in the least-squares formulation using $\epsilon = 1$ and $\epsilon = \Delta r/2$ for a cylindrical coordinate system in two space dimensions. The grid spacing is $\Delta r = 0.1$ and $\Delta\theta = \pi/18$. The grid dimensions are 36×37 and the radius of the cylinder is nondimensionalized to 1, the circulation around the cylinder is kept at $\Gamma = 0$, the vorticity $\omega_z = 0.0$, and Mach numbers of 0.1 and 0.2 are used. The program is run until a residual tolerance of 1.0e-5 is met. (See Figs. 2(a,c) and Table 2.)

Example 3. We solve for compressible flow over a sphere using $\epsilon = 1$ and $\epsilon = \Delta r/2$ for a spherical coordinate system in two space dimensions. The grid spacing is $\Delta r = 0.1$ and $\Delta\theta = \pi/18$. The grid dimensions are 36×37 and the radius of the sphere is nondimensionalized to 1, the vorticity $\omega_z = 0.0$, and Mach numbers of 0.1 and 0.2 are used. The program is run until a residual tolerance of 1.0e-5 is met. (See Figs. 2(b,d) and Table 3.)

All of the above results are obtained using constant artificial viscosity, ϵ. In general, however, ϵ can vary from point to point and from iteration to iteration and it can be optimized, depending on local flow conditions, to accelerate the convergence of the calculations.

5 Concluding Remarks

Given the vorticity and the density, the velocity components for two and three-dimensional flows can be calculated from a generalized system of Cauchy-Riemann equations. Standard numerical algorithms are applicable to achieve the expected accuracy and efficiency. For a complete flow simulation, the dynamics of the motion must be included to provide the entropy and the total enthalpy and hence the vorticity. The full simulation is still under progress and will be reported separately.

Appendix

Multigrid Convergence Results. The convergence of the point relaxation schemes can be enhanced by implementing a multigrid V-Cycle scheme. The V-Cycle scheme from Briggs, Henson, and McCormick [9] was modified to compute the incompressible, irrotational flow over a cyclinder using the Cauchy-Riemann equations with $\epsilon = \pi/8$. The fine grids used for the computations are $N = 32^2, 64^2, 128^2, 256^2$. The coarsest grid used for each run is $N = 8^2$. A comparison of point relaxation and V-Cycle $(\nu 1, \nu 2)$ is shown below. The parameters $\nu 1 = 1$ is the number of relaxations used going down the grids and $\nu 2 = 2$ is the number of relaxations used coming up the grids. The comparison includes the number of iterations until convergence of $\|r\|_\infty < 10\text{e-}5$, the absolute error $\|\mathrm{e}\|_\infty$ between the computed solution and the analytic solution, and the CPU runtime. (See Table 4.)

References

[1] Tang, C., and Hafez, M., 2003, "Numerical Simulation of Steady Compressible Flows Using a Zonal Formulation," Comput. Fluids, to appear.

[2] Hughes, T.J.R., Franca, L.P., and Hulbert, G.M., 1989, "A New Finite Element Formulation for Computational Fluid Dynamics: VIII. The Galerkin/Least Squares Method for Advective-Diffusive Equations," Comput. Methods Appl. Mech. Eng., **73**, pp. 173–189.

[3] Tezduyar, T.E., and Hughes, T.J.R., 1983, "Finite Element Formulations for Convection Dominated Flows With Particular Emphasis on the Compressible Euler Equations," AIAA (83-0125), January Paper No. 83-0125.

[4] Lerat, A., and Corre, C., 2003, "Residual-Based Compact Schemes for Multidimensional Hyperbolic Systems of Conservation Laws," Comput. Fluids, to appear.

[5] McCormack, R.W., and Paullay, A.J., 1974, "The Influence of the Computa-

tional Mesh on Accuracy for Initial Value Problems With Discontinuous or Non-linear Solutions,'' Comput. Fluids, **2**, pp. 339–361.
[6] Jameson, A., Schmidt, W., and Turkel, E., 1981, ''Numerical Solutions for the Euler Equations by Finite Volume Methods Using Runge-Kutta Time-Stepping Schemes.'' AIAA Paper No. 81-1259.
[7] Roy, J., Hafez, M., and Chattot, J., 2003, ''Explicit Methods for the Solution of the Generalized Cauchy Riemann Equations and Simulation of Invicid Rotational Flows,'' Comput. Fluids, to appear.
[8] Bachelor, G.K., 1967, *An Introduction to Fluid Dynamics*. Cambridge University Press, Cambridge, UK.
[9] Briggs, W.L., Hensen, V.E., and McCormick, S.F., 2000, *A Multigrid Tutorial*. SIAM.

C. Kato
Professor,
Institute of Industrial Science,
University of Tokyo,
Tokyo, Japan
e-mail: ckato@iis.u-tokyo.ac.jp

M. Kaiho
Senior Researcher,
Mechanical Engineering Research Laboratory,
Hitachi Ltd.,
Ibaraki, Japan

A. Manabe
Senior Engineer,
Research & Development Laboratory,
Hitachi Industries Co., Ltd.,
Ibaraki, Japan

An Overset Finite-Element Large-Eddy Simulation Method With Applications to Turbomachinery and Aeroacoustics

A numerical method for the prediction of an unsteady fluid flow in a complex geometry that involves moving boundary interfaces is presented in this paper. The method is also applicable to the prediction of the far-field sound that results from an unsteady fluid flow. The flow field is computed by large-eddy simulation (LES), while surface-pressure fluctuations obtained by the LES are used to predict the far-field sound. To deal with a moving boundary interface in the flow field, a form of the finite element method in which overset grids are applied from multiple dynamic frames of reference has been developed. The method is implemented as a parallel program by applying a domain-decomposition programming model. The validity of the proposed method is shown through two numerical examples: prediction of the internal flows of a hydraulic pump stage and prediction of the far-field sound that results from unsteady flow around an insulator mounted on a high-speed train. [DOI: 10.1115/1.1530637]

1 Introduction

Computational fluid dynamics has already become an indispensable tool for turbomachinery design mainly because of the advances in numerical methods for turbomachinery (see, for example, Moore et al. [1], Dawes [2], Hah et al. [3], and Denton [4]) and the remarkable progress in the performance of high-end computers. Regarding internal flow simulations of a hydraulic pump, where our primary interest lies, Goto [5] used the incompressible version of Dawes' three-dimensional Navier-Stokes code (Dawes [2]) to investigate the internal flows of a mixed-flow pump impeller with various tip clearances. Although the overall loss tends to be underestimated, the Euler head as well as the flow patterns at the impeller's exit are reasonably well predicted. Takemura and Goto [6] applied the Denton's viscous code LOSS3D and its multistage version, MULTISTAGE14 (Denton [4]) to compute the internal flows of a low-specific-speed bowl pump stage. Despite the highly distorted nature of the diffuser flow, Takemura and Goto [6] found that the distributions of the total pressure predicted by the stage computations qualitatively agree with the measured equivalent. Kaupert et al. [7] computed the internal flows of a high-specific-speed radial pump impeller by using a commercial code, TASCflow version 2.3. Their computations successfully predicted the discontinuities in the measured impeller's head-flow characteristics, including the hysteresis of the flow rate at which the discontinuities take place. Although the internal flows of a pump are essentially unsteady, the steady Reynolds-averaged Navier-Stokes (RANS) equations were used as the governing equations in all the computations mentioned above. More recently, Shi and Tsukamoto [8] applied the unsteady form of the RANS equations for computing unsteady interactions that take place in the region between the impeller blades and diffuser vanes. The static pressure fluctuations predicted by their computations agreed quantitatively with the measured ones. He and Sato [9] developed a new time-stepping method for the computation of incompressible flows in turbomachinery, and applied the method to predict the internal flows in a centrifugal pump stage. A reasonably good agreement has been obtained between the predicted and measured values of the impeller's exit flow.

Because the RANS equations are in terms of time averages, however, RANS computation has inherent limitations in predicting the unsteady nature of a flow field. Solutions from the RANS equations usually deteriorate when the flow field of interest involves the large-scale separations that are often encountered in internal flows in turbomachinery particularly at off-design points. On the other hand, large-eddy simulation (LES), in which turbulent eddies of a scale larger than the computational grid are directly computed, has the potential to predict unsteady flows and/or flow fields that include regions of large-scale separation much more accurately than RANS-based computation does in general. Since the first achievement of LES of a turbulent channel flow by Deardorff [10], numerous researchers have investigated the subgrid-scale models (Germano et al. [11], Lilly [12], Jordan [13], and Hughes et al. [14]), initial and boundary conditions (Lund [15], Smirnov et al. [16]), and numerical methods (see, for example, Piomelli [17]) for LES, by using relatively simple flow geometries such as homogeneous turbulence or a plane channel flow. Little work, however, can be found in the literature concerning industrial applications of LES, in particular for turbomachinery. The ultimate goal of our study is therefore to develop a practical engineering tool that is based on LES, with a particular emphasis on internal-flow simulations of turbomachinery and simulations of aeroacoustics (Kato et al. [18,19]).

The simulation of aeroacoustics is a promising area for LES application (Tam [20], and Wells and Renaut [21]) since information on the unsteady flow fields that generate sound is essential for many applications. The work that has been published regarding low-speed wake sound, where our primary interest lies, is relatively sparse compared to that on aeroacoustics resulting from high-speed flows. The key issue in aeroacoustics resulting from low-speed flows is how accurately one can compute the fluctua-

---

Contributed by the Applied Mechanics Division of THE AMERICAN SOCIETY OF MECHANICAL ENGINEERS for publication in the ASME JOURNAL OF APPLIED MECHANICS. Manuscript received by the Applied Mechanics Division, July 30, 2001; final revision, June 11, 2002. Associate Editor: T. E. Tezduyar. Discussion on the paper should be addressed to the Editor, Prof. Robert M. McMeeking, Chair, Department of Mechanics and Environmental Engineering, University of California–Santa Barbara, Santa Barbara, CA 93106-5070, and will be accepted until four months after final publication in the paper itself in the ASME JOURNAL OF APPLIED MECHANICS.

tions in the flow field that compose the source term of the acoustics computations. After pioneering work done by Hardin and Lamkin [22], who computed aerodynamic sound generated from a laminar wake of a circular cylinder by using acoustic analogy proposed by Howe [23], several researchers (Akishita et al. [24] Haruna et al. [25], and Adachi et al. [26]) applied essentially the same method as Hardin and Lamkin [22] to compute the aerodynamic sound that is generated from a turbulent wake of a wing. They all used a third-order upwind finite difference scheme to compute unsteady flow fields. Although the overall tendency of the aerodynamic sound could be captured through their computations, the agreement between the computed sound spectra and the measured equivalent was not very satisfactory. Kato and Ikegawa [27] first applied LES in the finite element context to simulate the unsteady turbulent wake of a circular cylinder at a subcritical Reynolds number. Kato et al. [28] also computed the far-field sound that is generated from such a wake by using an acoustic analogy proposed by Curle [29] (see also Lighthill [30] in this regard). They compared the predicted sound-pressure spectra to their wind-tunnel measurements and obtained fairly good agreement up to a Strouhal frequency of about 2.0 (a frequency ten times as high as the Karman vortex shedding frequency). But, again, their computations were limited to a relatively simple flow geometry such as a cylinder wake. Recently, Siegert et al. [31] attempted to simulate aerodynamic sound generated from a more realistic flow field, such as a flow around an automobile mirror. However, their computation indicated that considerable room for improvement remains concerning our capability to predict aerodynamic sound. Our work described here therefore concentrates on improving prediction accuracy regarding the aerodynamic sound generated from a complex flow field geometry.

For turbomachinery simulations, it is necessary to deal with moving boundary interfaces between flow fields, such as those that appear between a rotating impeller and a stationary casing. In our study, the moving boundary interface is taken into account by using overset grids from dual frames of reference. In this method, the overall grid is composed of several (usually from two to five) grid sets and appropriate transactions take place at the interface regions. The overset-grid approach is also applied to increase the grid resolution around the body of interest for computations in the field of aeroacoustics. This is essential as a way of obtaining an accurate sound-pressure spectrum. In consideration of its applications to a complex geometry, the finite element method is used to discretize the governing equations of the flow field. It is implemented for parallel processing, therefore enabling us to complete a large-scale flow-field computation within a practical period of computation on a current-model distributed-memory parallel computer.

In what follows, the governing equations of the flow field and the acoustic field will be explained in Section 2. The numerical method, including the overset-grid approach, the formulation of finite elements, and the implementation for parallel processing, will then be described in Section 3. Finally, in Section 4, two numerical examples, one from turbomachinery-related computation and the other from computations of aeroacoustics, will be given to demonstrate the validity of the proposed method.

2 Governing Equations

2.1 Flow-Field Computation. The governing equations on which the present study is based are the spatially filtered continuity Eq. (1) and the Navier-Stokes Eqs. (2) for the flow of an incompressible fluid, as represented in Cartesian coordinates

$$\frac{\partial \overline{u_i}}{\partial x_i}=0 \tag{1}$$

$$\frac{\partial}{\partial t}\overline{u_i}+\frac{\partial}{\partial x_j}\overline{u_i}\,\overline{u_j}=-\frac{1}{\rho}\frac{\partial \overline{p}}{\partial x_i}+\frac{\partial}{\partial x_j}\left\{\nu\left(\frac{\partial \overline{u_i}}{\partial x_j}+\frac{\partial \overline{u_j}}{\partial x_i}\right)-\overline{u_i' u_j'}\right\}+f_i \tag{2}$$

where $\overline{u_i}$ $(i=1,2,3)$ is the grid-scale velocity component in the x_i-direction, $\overline{p}$ is the grid-scale static pressure, ρ is the density, and ν is the kinematic viscosity.

f_i is the inertial force associated with the motion of the frames of reference. In particular, for a stationary frame of reference,

$$f_i=0 \qquad :i=1,2,3 \tag{3}$$

while for a rotational frame of reference the centrifugal forces and Coriolis forces must be added:

$$f_1=\Omega^2 x_1+2\Omega\overline{u_2}; \quad f_2=\Omega^2 x_2-2\Omega\overline{u_1}; \quad f_3=0 \tag{4}$$

where Ω is the angular velocity of the frame of reference, which is assumed to be rotating about the positive x_3-axis.

The effects of eddies that are not resolved by the grid (subgrid-scale eddies) are modeled after Smagorinsky [32], and incorporated with the Van-Driest wall-damping function that represents the near-wall effects:

$$-\overline{u_i' u_j'}+\frac{1}{3}\delta_{ij}\overline{u_k' u_k'}=\nu_{\mathrm{SGS}}\left(\frac{\partial \overline{u_i}}{\partial x_j}+\frac{\partial \overline{u_j}}{\partial x_i}\right) \tag{5}$$

$$\nu_{\mathrm{SGS}}=(C_S f\Delta)^2(2\overline{S_{ij}}\,\overline{S_{ij}})^{0.5}; \quad \overline{s_{ij}}=\frac{1}{2}\left(\frac{\partial \overline{u_i}}{\partial x_j}+\frac{\partial \overline{u_j}}{\partial x_i}\right) \tag{6}$$

$$f=1-\exp\left(-\frac{y^+}{A^+}\right); \quad A^+=25.0. \tag{7}$$

The model coefficient C_s is fixed to 0.15, which is a standard value for flows with large separation, and the filter size Δ is computed as the cube-root of the volume of each finite element.

Detailed explanations of both the frames of reference and the boundary conditions will be given in Sections 3 and 4.

2.2 Computation of the Acoustic Field. In this study, the aerodynamic sound is assumed to be generated by flows, at relatively low Mach numbers, around an object. The far-field sound radiated from a flow at a low Mach number can be calculated from Lighthill-Curle's equation, [29,30]:

$$p_a=\frac{1}{4\pi}\frac{\partial^2}{\partial x_i x_j}\int_V \frac{T_{ij}(y,t-r/a)}{r}d^3y + \frac{1}{4\pi}\frac{\partial}{\partial x_i}\int_S \frac{n_i p(y,t-r/a)}{r}dS \tag{8}$$

where a denotes the speed of sound in the ambient fluid, p the static pressure in the flow field, p_a the far-field sound pressure, x_i the location of the sound-observation point, y the coordinates at the noise source, r the distance between the noise source and the sound-observation point, and n_j the outward unit vector normal to the solid boundaries. In the above expression, the assumption that the flow has a high Reynolds number makes the contribution of viscous stresses to the surface integral negligible.

T_{ij} in the volume integral denotes Lighthill's acoustic tensor and can be written as

$$T_{ij}=\rho u_i u_j+(p-a^2\rho)\delta_{ij}+\mu_{ij} \tag{9}$$

$$\mu_{ij}=\mu\left(\frac{\partial u_i}{\partial x_j}+\frac{\partial u_j}{\partial x_i}\right)-\frac{2}{3}\mu\delta_{ij}\frac{\partial u_k}{\partial x_k}. \tag{10}$$

The volume integral in Eq. (8) represents the contribution to the sound of the vortices in the flow field (quadrupole sources), while the surface integral represents the contribution of the sound scattering at the solid boundaries in the flow field (dipole sources). For low-frequency sound generated from a flow at a low Mach number, which is of our primary interest, the contribution of the quadrupole sources to the far-field sound is, in general, negligible in comparison with the contribution of dipole sources, [29]. Moreover, if the dimensions of the body are much smaller than the

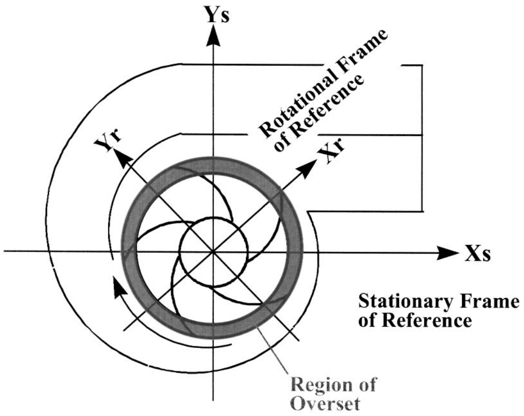

Fig. 1 Schematic view of an example of overset grids from dual frames of reference

wavelength of the sound, as is the case in this study, the dipole term can be converted to the time-derivative form as follows:

$$p_a = \frac{1}{4\pi a} \frac{x_i}{r^2} \frac{\partial}{\partial t} \int_S n_i p(y, t - r/a) dS. \tag{11}$$

Thus, we can calculate the far-field sound from the fluctuating surface pressure obtained by LES.

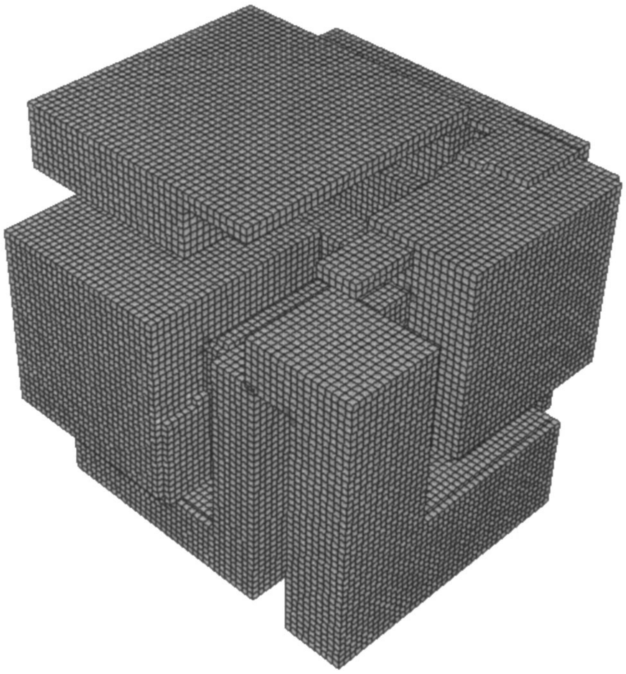

Fig. 2 Example of a subdomain mesh partitioned by the RGB method (computational mesh for flow in a cubic cavity partitioned into eight subdomains)

3 Numerical Method

3.1 Overset Grids From Multiple Dynamic Frames of Reference. In this study, a moving boundary interface in the flow field is treated with overset grids from multiple dynamic frames of reference. The application of this method to the interaction between a rotating impeller and a stationary casing in a pump is schematically depicted in Fig. 1. A computational mesh that rotates along with the impeller is used to compute the flow within the impeller. On the other hand, a dedicated stationary computational mesh for each part computes the flow in stationary parts of the pump, such as the inlet whirl-stop, vaned diffuser, and discharge casing. Each mesh includes appropriate margins of overlap with its neighboring meshes upstream and downstream. At every time-step, the velocity components and static pressure within each such margin are the values interpolated in the computational mesh of the corresponding neighbor. Element-wise trilinear functions are used to interpolate both the velocity components and the static pressure. When velocity components are overset, an appropriate coordinate transformation must be applied to take the differences between the frames of reference into account. For the impeller, because of its rotation, the finite elements at the interface between the stationary and rotating parts, at which the given interpolations take place, change for every time-step. The interaction between the stationary and rotating parts is thus taken into account.

Numerous methods that are able to deal with moving and/or deforming boundaries in fluid flow have been proposed in the finite element context (see, for example, Tezduyar [33]). A great advantage of our method is its flexibility. Computational meshes are generated for parts, and the meshes can then be combined with each other to investigate a flow field in which one has a particular interest. In fact, the method is thus also applicable to the simulation of multistage turbomachinery.

The margin of overlap and the procedure for interpolation have been discussed in detail by Ikegawa et al. [34] and Kaiho et al. [35].

3.2 Finite Element Formulation. The accuracy and stability of the discretizing method is of great importance in LES because the motion of large eddies has to be directly computed. The first-order upwind methods and hybrid methods that are often used for RANS-based computations are, in general, not appropriate for use in LES. The excessive numerical dissipation that is associated with such schemes almost invariably dampens the motion of large eddies. Instead, we used a streamline-upwind finite element formulation, which was previously reported by one of the authors (Kato and Ikegawa [27]), to discretize the governing equations of the flow field. This formulation is based on the SU-PG method originally proposed by Brooks and Hughes [36] and Tezduyar and Hughes [37], which shifts the governing equations in the streamwise direction by modifying the weighting function. Our formulation combines the SU-PG method and the Taylor-Galerkin method proposed by Donea et al. [38], which recursively uses the governing equations to modify their discretized form. This combination results in a shift of the governing equations with a magnitude equal to one-half of the time increment multiplied by the magnitude of the local flow velocity. This shift exactly cancels out the negative numerical dissipation that is otherwise the result of applying the conventional first-order explicit Euler's method and guarantees stability and the accuracy of solutions. The proposed formulation essentially possesses second-order accuracy in terms of both time and space, and has been successfully applied to the LES of external as well as internal flows (Kato et al. [18,28]).

The pressure algorithm is based on the ABMAC method proposed by Viecelli [39], in which the velocity components and static pressure are simultaneously corrected until the maximum divergence of the flow field decreases to less than a prescribed critical value.

Details of this formulation, along with the results of validation studies, have been given by Kato and Ikegawa [27] and Kato et al. [28].

3.3 Parallel Implementation. Most flow fields encountered in engineering applications are complex and their Reynolds numbers are generally high (usually in the range 10^5-10^8). An LES for such a flow field requires a huge number of grid cells. We have, therefore, implemented the formulation described in the previous sections as a parallel program by using the domain-decomposition

Table 1 Results of benchmark tests (CPU time needed to advance by a single time-step in a cubic-cavity flow simulation on Hitachi's SR8000)

Number of Processing Nodes	Number of Elements	Seconds Taken by CPU per Time-Step	Performance (GFLOPS) Peak $[A]$	Performance (GFLOPS) Sustained $[B]$	Ratio $[B]/[A]$
1	1.0 M	3.45	14.4	2.03	14.1%
2	2.0 M	3.62	28.8	3.87	13.4%
4	4.0 M	3.89	57.6	7.23	12.6%
8	8.0 M	3.99	115.2	14.04	12.2%
16	16.0 M	4.06	230.4	27.60	12.0%

programming model, so that the implementation efficiently uses the resources of a distributed-memory parallel computer and is thus suitable for computing large-scale problems.

In the domain-decomposition programming model, the global computational domain is partitioned into a prescribed number of subdomains, and each of the subdomains is assigned to a dedicated processing node. Computation in the various subdomains is unified by implementing appropriate forms of inter-subdomain communication. Various partitioning algorithms (see Simon [40] and Farhat and Lesoinne [41] for details) have been evaluated in terms of the quality of their partitioning and of the memory and CPU time required by the partitioning process. From this extensive comparative study, we have concluded that the recursive graph-bisection (RGB) algorithm is best suited to the present study. A simple example of the partitioning of a computational mesh using this algorithm is shown in Fig. 2.

The communicating pairs and/or local coordinates where interpolations are taking place change at the moving-boundary interfaces for every time step, as was briefly described in Subsection 3.1. The usual (unsophisticated) parallel implementation therefore includes broadcast communications at each time-step as the processing node searches for its new communication pairs. This communication overhead seriously degrades the overall parallel computing performance on most hardware platforms. In our study, the communication pairs are searched for in advance by serial computation and fed to the parallel flow solver as input data at each time-step. This procedure not only avoids the otherwise inevitable communications overhead but also brings in greater flexibility with the flow solver. By preparing appropriate input data for the moving-boundary interfaces, the flow solver is capable of computing flow fields with an arbitrary number of moving-boundary interfaces that move in an arbitrary (but defined) manner.

The performance of the proposed method in terms of parallel computing was evaluated on various hardware platforms. Table 1 shows one such example, where the method was tested on Hitachi's SR8000 supercomputer, which has a theoretical peak performance of 14.4 GFLOPS per processing node. In this benchmark test, the number of finite elements per processing node was fixed to one million and the total number of finite elements was increased to 16 million (with 16 processing nodes). The results are shown in terms of the time needed to advance by one time-step, the sustained overall performance, and the ratio of the sustained performance to the peak performance. As the number of processing nodes increased, the ratio of the sustained performance to the peak performance gradually deteriorated. The sustained performance, however, ranged from 12% to 14% of the peak performance. This is a fairly high value for a finite-element-based flow solver, which generally requires the indirect and random-access loading of data from memory. Figure 3 is a plot of the overall sustained performance against the number of processing nodes for the same benchmark test. A parallel computing efficiency of over 85% was achieved on this platform, which confirmed that a large-scale computation of flow with a grid containing more than 10 million divisions can be completed within a practical period of time on a high-end computer of the current generation.

4 Simulation Examples

After ensuring the validity of the LES code we developed by applying it to the calculation of basic flows of various types (Kato and Ikegawa [27] and Kato et al. [28]), the code is now being

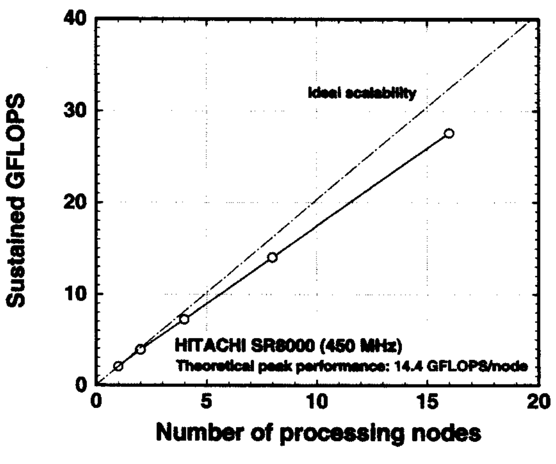

Fig. 3 Sustained parallel computing performance

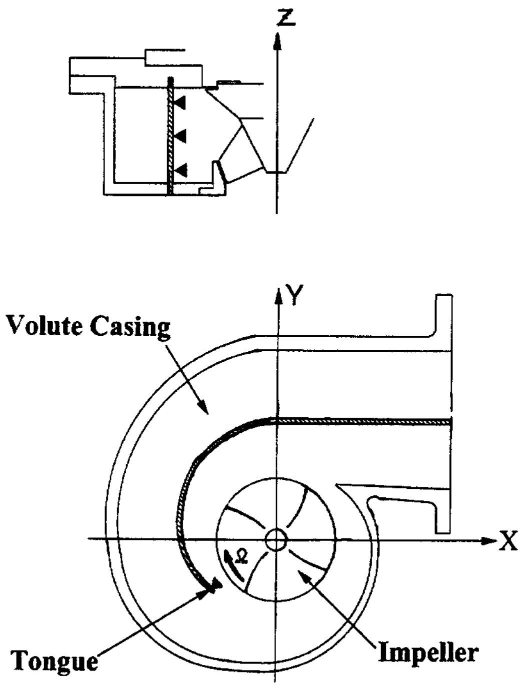

Fig. 4 Cross-sectional views of the test pump (note: arrowheads in the figure indicate the positions where pressure fluctuations were measured)

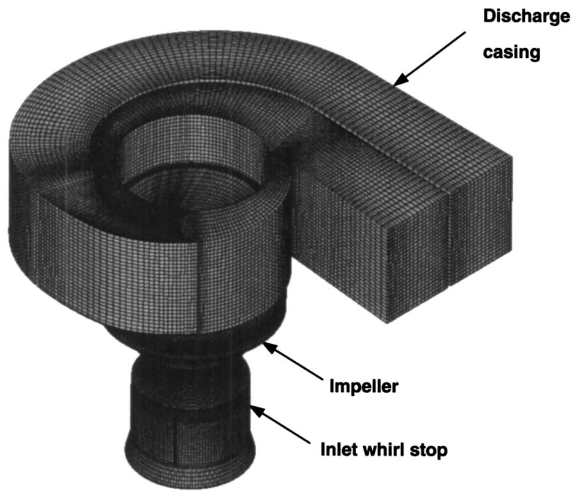

Fig. 5 Computational mesh for a mixed-flow pump, composed of meshes for an inlet whirl-stop, an impeller, and a double-volute discharge casing

tested on real-world problems. Two examples will be described below: one from the simulation of turbomachinery and the other from aeroacoustical simulations.

4.1 Simulation of Unsteady Flow in a Mixed-Flow Pump

Configuration of the Test Pump. The internal flow in a mixed-flow pump stage that has a high specific-speed was computed under two operating conditions: at the design point ($Q/Q_d = 100\%$) and at an off-design point ($Q/Q_d = 60\%$) (Kato et al. [18]). Horizontal and vertical cross sections through the test pump are shown in Fig. 4. This pump is composed of an inlet whirl-stop (not shown), a four-blade open-shroud mixed-flow impeller, and a double-volute discharge casing. The designed specific speed ω_s of the pump is 2.1. Such a pump is typically used for drainage purposes, and can pump a huge amount of water (up to 50 m^3/s) from a river at a lower level. Therefore, it is important to evaluate the steady and unsteady fluid forces on the impeller, since they may sometimes cause problems of vibration and/or noise. To obtain comparative data for use in validation, load cells were placed in the bearing housings to measure the axial and radial fluid forces acting on the impeller and semiconductor pressure transducers were installed in the casing walls to measure static pressures.

The Computational Mesh and Its Boundary Conditions. The computational mesh used in this study is shown in Fig. 5. The overall mesh is composed of the meshes for each of three parts: an inlet whirl-stop, a mixed-flow impeller, and a double-volute casing. These are overset as described in Section 3. The actual impeller has a tip clearance of 0.1% of the impeller diameter, but this clearance was not taken into account in the simulation. The num-

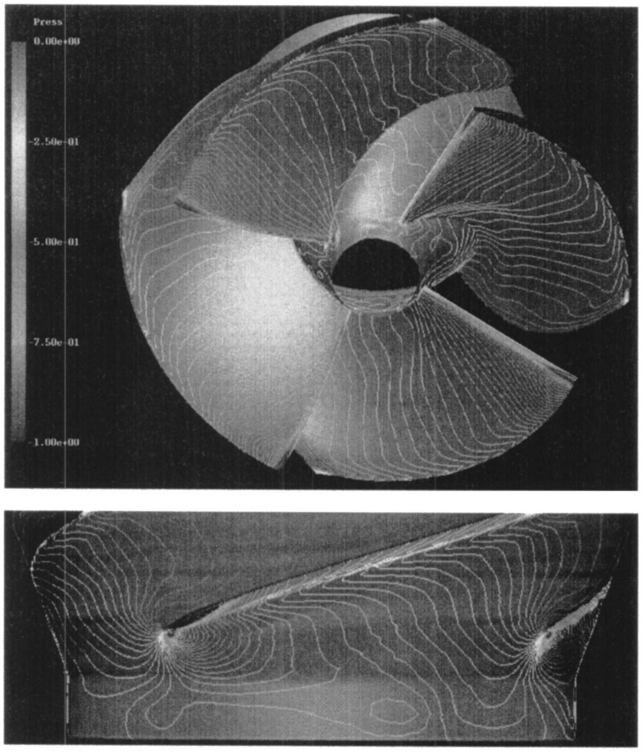

Fig. 6 Computed instantaneous distributions of surface pressure ($Q/Q_d = 100\%$)

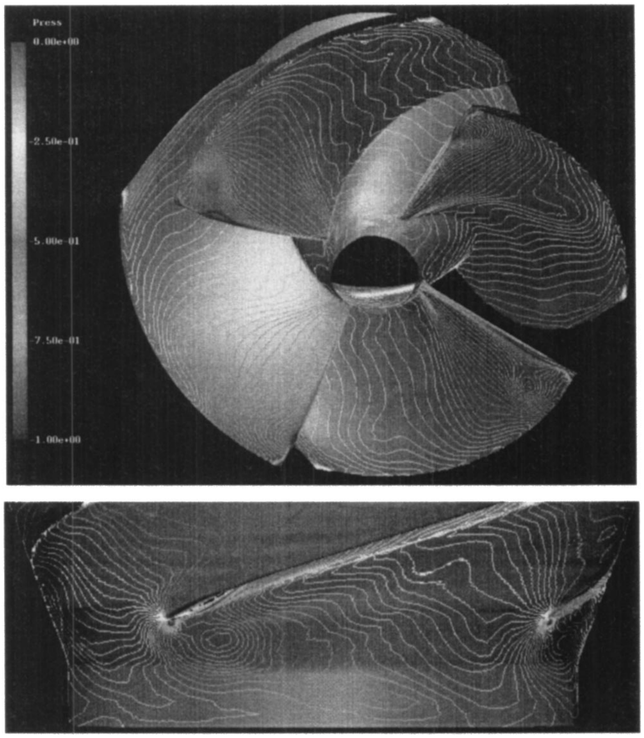

Fig. 7 Computed instantaneous distributions of surface pressure ($Q/Q_d = 60\%$)

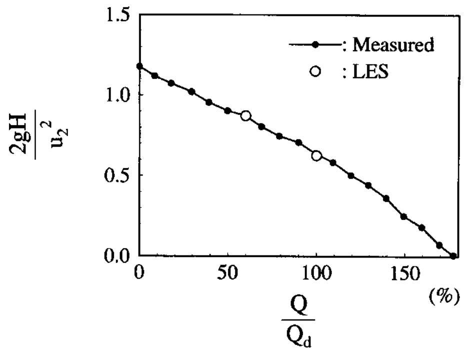

Fig. 8 Comparison of head-flow characteristics

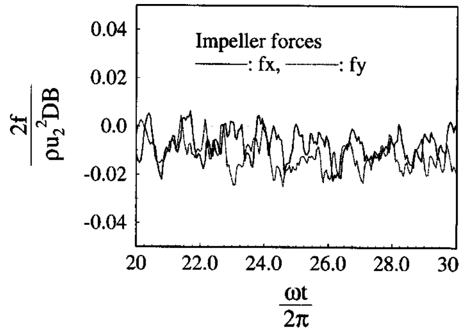

Fig. 9 Computed fluid forces acting on the impeller (Q/Q_d =100%)

bers of grid points are approximately 150,000 for the inlet whirl-stop, 500,000 for the impeller, and 200,000 for the volute casing, for a total of about 850,000 grid points.

The boundary conditions were as follows. A uniform distribution of velocity was assumed for the upstream boundary of the inlet-whirl-stop mesh. The pre-rotation was assumed to be zero and the boundary layer at the inlet was not considered. At the downstream boundary of the volute-casing mesh, the fluid traction was assumed to be zero in all three directions. On the solid walls, a no-slip boundary condition was prescribed, and was incorporated with the Van-Driest damping function described in Subsection 2.1. Note that the wall of the casing liner of the impeller mesh is moving in the negative-Ω direction in the rotational frame of reference, thus the wall velocity was given in this form. The resolution of the grid near the wall's surface was not necessarily fine enough for the no-slip wall boundary condition to actually be correct. However, since reliable wall-stress boundary conditions that are applicable to the LES of complex turbulent flows have not been proposed, the no-slip wall condition was used in this study.

The time increment for the computation was set so that 4000 time-steps corresponded to a single revolution of the impeller. Starting from an initial flow field in which all of the velocity components and the static pressure were set to zero, the flow field in the pump stage became statistically stable within about ten revolutions of the impeller and remained in a statistical state of equilibrium after that. The total pump head, the fluctuating fluid forces, and the fluctuating static pressures were calculated by averaging the flow field during the subsequent ten revolutions of the impeller. The computations were carried out by using four processing nodes on the Hitachi SR8000 supercomputer. The required CPU time was about one second per time-step. The total CPU time for a single operating condition was thus about 22 hours.

Computed Instantaneous Flow Fields. For a typical flow field, Fig. 6 shows the instantaneous static pressure distributions on the suction surface of the impeller blades and on the casing liner for the design-point case, and Fig. 7 shows the corresponding distributions for the off-design-point case.

Table 2 Comparisons of normalized thrust forces on impeller (Q/Q_d=100%)

	Radial Thrust		Axial Thrust	
	Average	RMS	Average	RMS
Measured	0.0189	0.0156	0.449	0.0117
LES	0.0178	0.0143	0.340	0.0096

The static pressure is normalized by twice the dynamic pressure that corresponds to the circumferential velocity u_2 at the impeller exit diameter D. The interval between the contour lines of the normalized values is 0.02. At the design point, the impeller blade was almost uniformly loaded in the spanwise direction. No significant differences in the flow field were seen between blade passages. On the other hand, in the off-design case, each blade was highly loaded near its tip due to the positive incidence of the incoming flow. The boundary layers on the suction side of the blades separated from the blades just after the leading edge and formed separation bubbles in that region. However, this separation did not lead to stall conditions. This is also confirmed by the head-flow characteristics as described below. This was probably due to the relatively small pitch/chord ratio of this particular pump. Note also that the pressure distributions on each blade exhibit a nonuniformity that appears to be associated with the unsteady flow field in the off-design case.

Computed Head-Flow Characteristics. The computed total pump heads, together with their measured equivalents, are plotted in Fig. 8 where they are normalized by using the circumferential velocity u_2 at the impeller exit diameter. Although only two points were computed in this study, the predicted pump heads quantitatively agree with the values measured at the corresponding points, which is quite encouraging.

Computed Fluctuations of Fluid Force on the Impeller. Figure 9 shows the fluid forces computed as acting on the impeller at the design point over a time period that corresponds to ten impeller revolutions. In this figure, B is the width of the impeller's exit, and f_x and f_y, respectively, denote the fluid forces exerted on the impeller in the x and y-directions of the stationary frame of reference. The power spectra of the computed fluid forces are shown in Fig. 10, where f_R and f_Z, respectively, denote the radial and axial thrust forces. For both components, the higher harmonics of the blade passing frequency (BPF) are also computed. Table 2 compares, for the design-point case, the computed and measured values of radial and axial fluid forces. Except for the time-averaged axial thrust force, the computed fluid forces agree with the experimental results within a maximum difference of 12%.

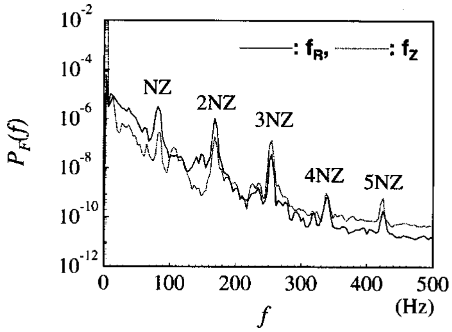

Fig. 10 Computed power spectra of fluid forces on the impeller (Q/Q_d=100%)

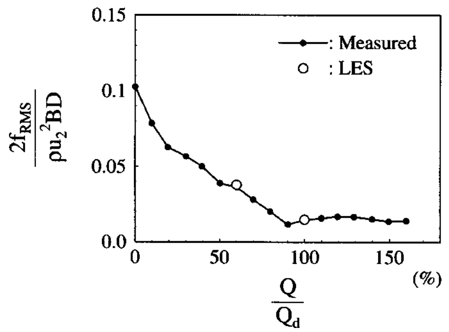

Fig. 11 Comparison of fluctuations in radial thrust force on the impeller

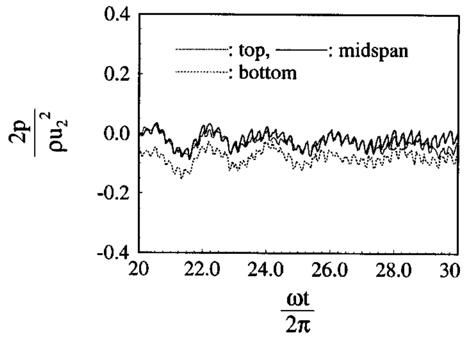

Fig. 12 Computed static-pressure fluctuations at the inner tip of the tongue ($Q/Q_d=100\%$)

Table 3 Comparison between measured and calculated values of normalized fluctuations in static pressure at the inner tip of the tongue ($Q/Q_d=100\%$, rms values)

	Bottom	Midspan	Top
Measured	0.0144	0.0200	0.0152
LES	0.0171	0.0187	0.0166

The large discrepancy seen in the time-averaged axial thrust force is probably due to not including the gaps between the impeller's shroud and casing wall in the computation model. Figure 11 is a plot of the computed and measured values for fluctuations in radial fluid forces against the flow-rate ratio. At both flow-rate ratios (60% and 100%), the computed and measured fluid forces are in very good agreement. This implies that the changes in the internal flow in response to changes in the flow rate ratio have been accurately captured by these computations, and that the unsteady nature of the flow fields has been taken into account.

Computed Fluctuations in Static Pressure at the Inner Tip of the Tongue. Figure 12 shows the computed fluctuations in static pressure at the inner tip of the tongue (see Fig. 4) where the fluctuations in pressure are most pronounced. The rms values of the computed and measured pressure fluctuations are given in Table 3. The computed pressure fluctuations agree with the measured values, to within about 5% to 15%.

Although the data presented in this paper are limited to the computation of the flows in a particular mixed-flow pump stage, the computed results are in good agreement with the measured values in some important respects. These results are quite encour-

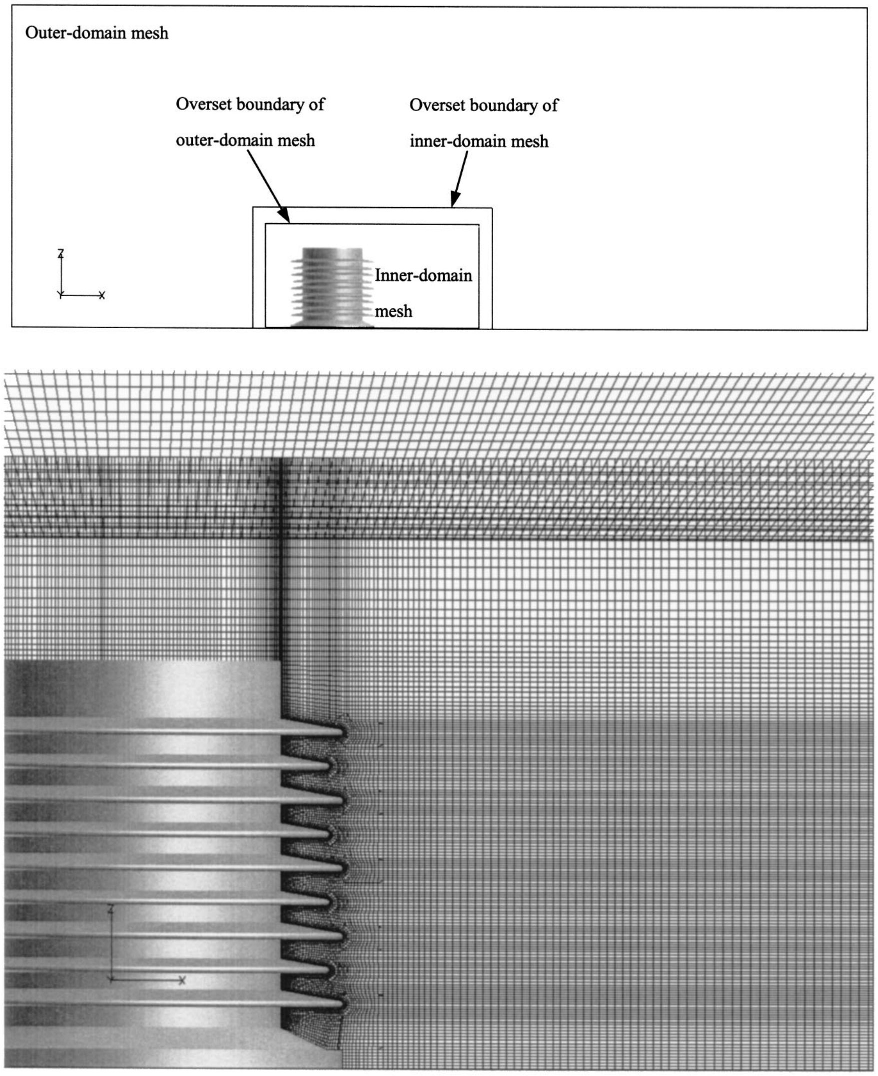

Fig. 13 Overset meshes for flow around an insulator (fine-mesh case)

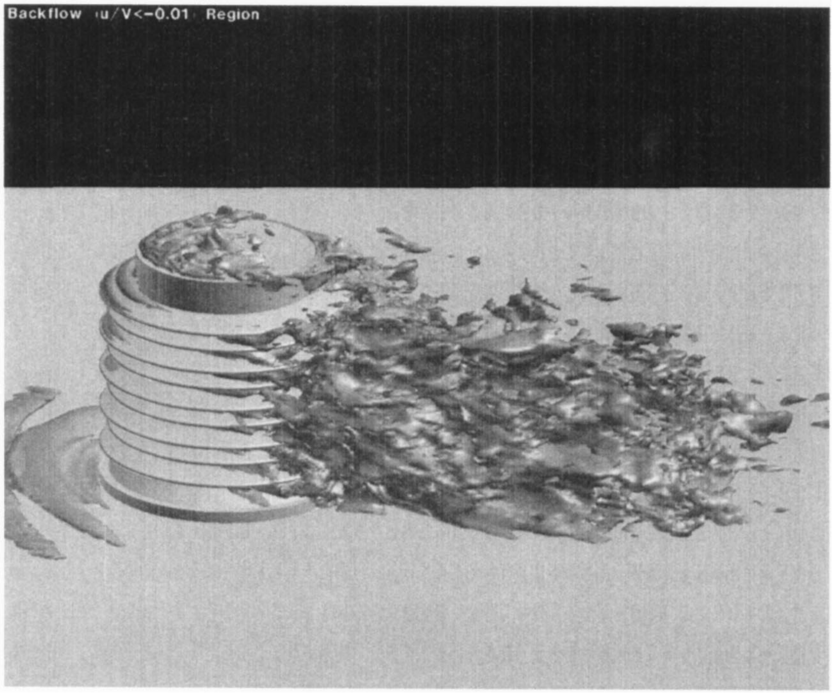

Fig. 14 Regions of instantaneous reverse flow

aging and the proposed method thus seems promising as a candidate for use as a research and design tool for mixed-flow pumps, or for turbomachinery in general.

4.2 Aeroacoustical Simulation of a Pantograph Insulator

Computational Model. To further increase the speeds of high-speed trains, which currently run at 300 km/h in Japan, the aerodynamic noise generated by the pantograph (the electric-current collector on the train's roof) must be reduced, and this has become a matter of great concern in terms of the aerodynamic design of the vehicle. Research has indicated that, among the various noise sources of a pantograph, the insulator provides the dominant contribution to the overall noise level. We have therefore simulated the near-wake of flow around an insulator and the resulting far-field sound, with the particular aim of identifying the primary source of noise. We hope this will lead us to a new concept enabling further reductions in noise levels.

Figure 13 shows an overset mesh for the near-wake LES of the

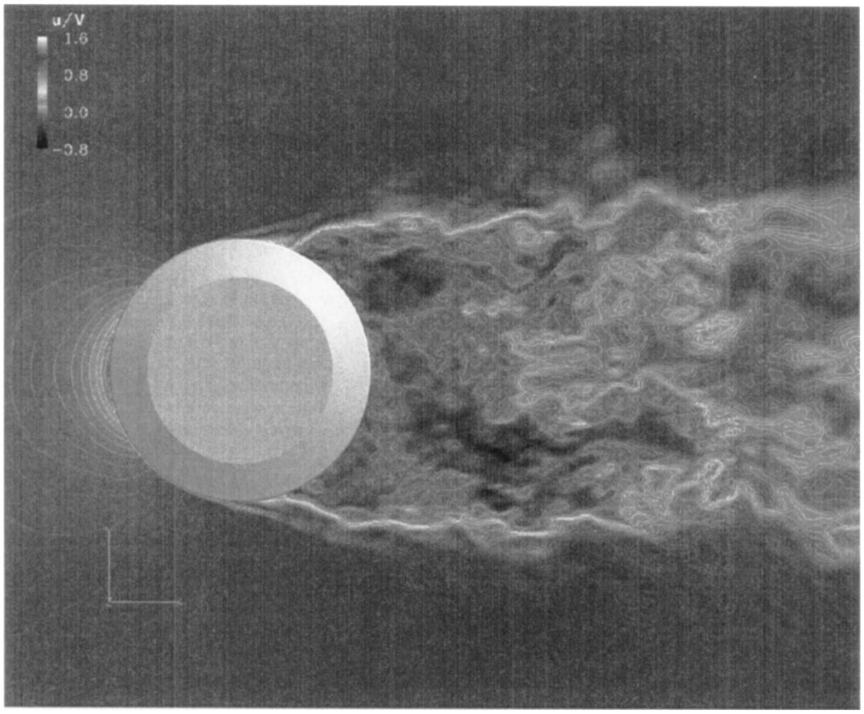

Fig. 15 Instantaneous distribution of streamwise-velocity in the insulator's mid-height plane

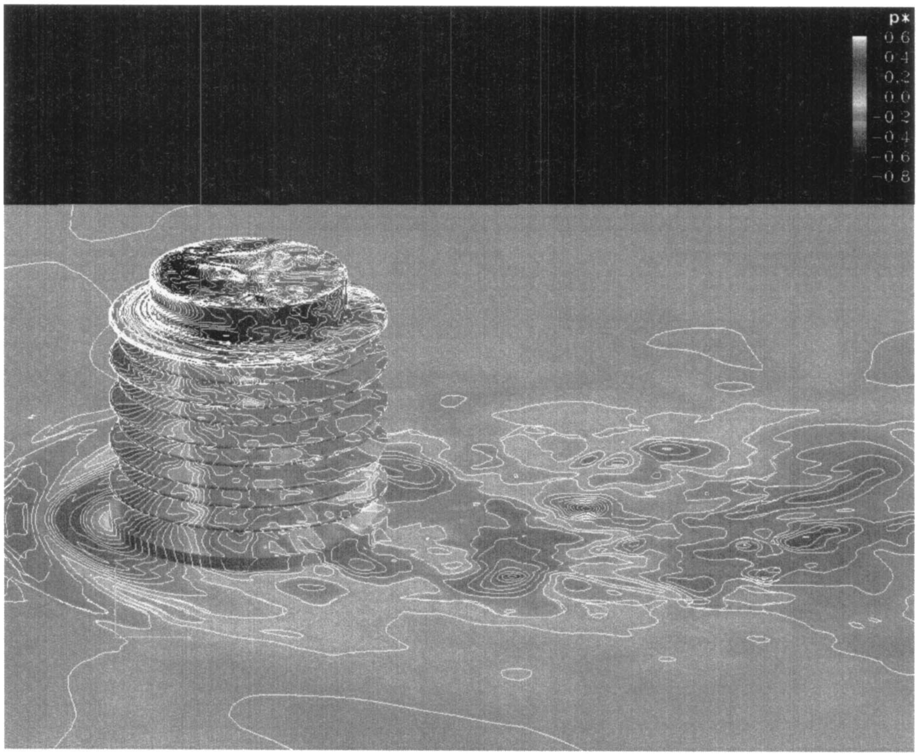

Fig. 16 Instantaneous distribution of surface pressure

insulator that was simulated in our study. The insulator is composed of a main circular cylinder with a diameter of 220 mm and 9 circular disks that guarantee an appropriate creepage distance.

Two sets of overset grids with different resolution were used in the LES and the effects of grid resolution on the fluctuations in the near wake as well as on the resulting far-field sound were investigated. The numbers of elements were approximately 2 million for the coarse mesh and 6 million for the fine mesh.

The boundary conditions correspond to the situation in a wind tunnel test where a 1:6 scale model of the actual insulator is placed on a flat plate in a uniform flow of air with a wind velocity of 50 m/s (180 km/h). That is, a uniform velocity with no turbulence components is prescribed for the upstream section of the outer-domain mesh. A no-slip wall condition, incorporated with the Van-Driest damping function, is given for the surface of the insulator as well as for the flat plate. The traction-free condition is applied at all of the remaining boundaries to avoid nonphysical blockage effects.

The Reynolds number based on this uniform wind velocity and the representative diameter of the model insulator is 1.4×10^5. The computation was mainly carried out by using 16 processing nodes on the Hitachi SR8000 supercomputer. The CPU-time required was about 2.3 seconds per time-step for the fine-mesh case. The total CPU-time taken for integrating 64,000 time-steps, during which the time-averaged, rms, and spectral values of the flow field and far-field sound were calculated, was thus approximately 40 hours for the fine-mesh case.

Instantaneous Flow Field Around the Insulator. In the following sections, we present results from the fine-mesh LES unless we state otherwise. To illustrate the temporal wake structure, regions of instantaneous reverse flow are shown in Fig. 14. The boundary layer that develops on the surface of the insulator separates from the surface while the flow is still laminar, but a transition to turbulence takes place soon after that because of the pronounced three-dimensional structure created by the circular disks.

Figure 15 shows an instantaneous distribution of streamwise velocity in the insulator's midheight plane. The wake still possesses a large vortical structure, similar to the well-known Karman vortex, but this large structure is rather weak due to the enhancement of spanwise mixing effects by the circular disks. Note also that no apparent discontinuity in the velocity is visible in the overset region that lies about one and a half diameters downstream from the insulator.

Figure 16 shows the instantaneous distribution of surface pressure around the insulator and base plate. The time sequence of the surface-pressure fluctuations is fed to the acoustical computation to obtain the far-field sound-pressure fluctuation at some point of interest. Therefore, the smallest scale that is adequately captured in terms of the surface-pressure fluctuation essentially determines the frequency range over which the resulting SPL may accurately be predicted. It seems that rather small-scale fluctuations in surface pressure are captured by this LES because of the relatively fine resolution of the inner grid.

Velocity Fluctuations in the Near Wake. Typical fluctuations in streamwise velocity in the near wake and their power spectra, for both the coarse and fine-mesh cases, are shown in Fig. 17. The sample point is $x=1D$, $y=0$, $z=0.4D$, where D denotes the representative diameter of the insulator while x, y, and z, respectively, denote the streamwise, lateral, and spanwise coordinates from the origin, which is set at the bottom-center of the insulator. The frequency range that is resolvable by the coarse-mesh LES has its upper bound at a Strouhal number of approximately 1.0 (five times the usual Karman vortex frequency). The upper bound is extended to a Strouhal number of about 6 by the fine-mesh LES. Note also that the time-averaged value is higher for the fine-mesh LES than for the coarse-mesh LES. This is because the former gives a narrower region of reverse flow than the latter, and this is probably due to the improved mixing effects in the upper portion of the wake.

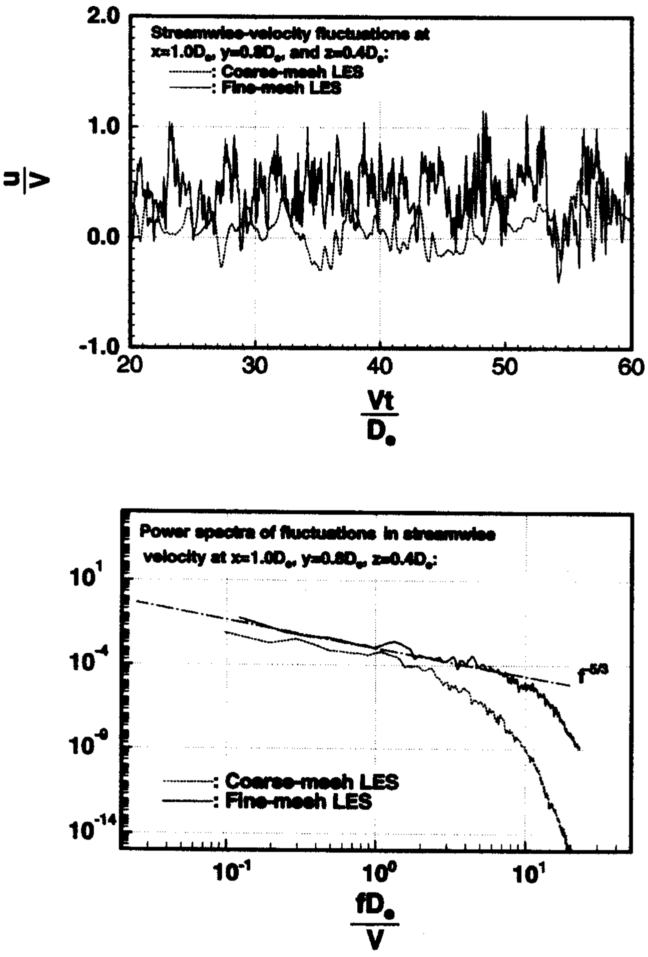

Fig. 17 Fluctuations in streamwise velocity in the near wake (upper) and the power spectra of these fluctuations (lower)

Simulated Far-Field Sound and the Distribution of Source The fluctuations in far-field sound pressure and the power spectra of these fluctuations are shown in Fig. 18, for both the coarse-mesh and fine-mesh cases, together with experimental values measured in a low-noise-level wind tunnel. The sound was evaluated at a point 1 m, as expressed at the model's scale, from the center of the insulator $(x=0, y=1\text{ m}, z=0)$. For convenience, the sound pressure is converted to actual values that correspond to a vehicle speed of 350 km/h (97.2 m/s) by assuming Reynolds number similarity of the flow fields for the model and for the actual structure.

The sound-pressure levels predicted by the coarse-mesh LES and the fine-mesh LES are surprisingly different. The fine-mesh LES provides a reasonably good prediction of the sound-pressure level at frequencies up to about 2.5 kHz, which corresponds to a Strouhal number of 6.4. This is approximately identical to the resolved frequency range for the near-wake velocity fluctuations. For the coarse-mesh LES, which successfully resolved the near-wake velocity fluctuation up to a Strouhal number of about 1.0 (390 Hz), the predicted sound-pressure level deviates from the measured value throughout the frequency range. This implies that there is some threshold in terms of the resolution of a mesh around an object, above which the accurate prediction of far-field sound becomes possible. The overset LES presented in this paper seems to be one way of meeting such criteria within a reasonable computational cost.

Finally, the instantaneous sound-source distributions were investigated according to Powell's equation (Powell [42]), as shown as follows:

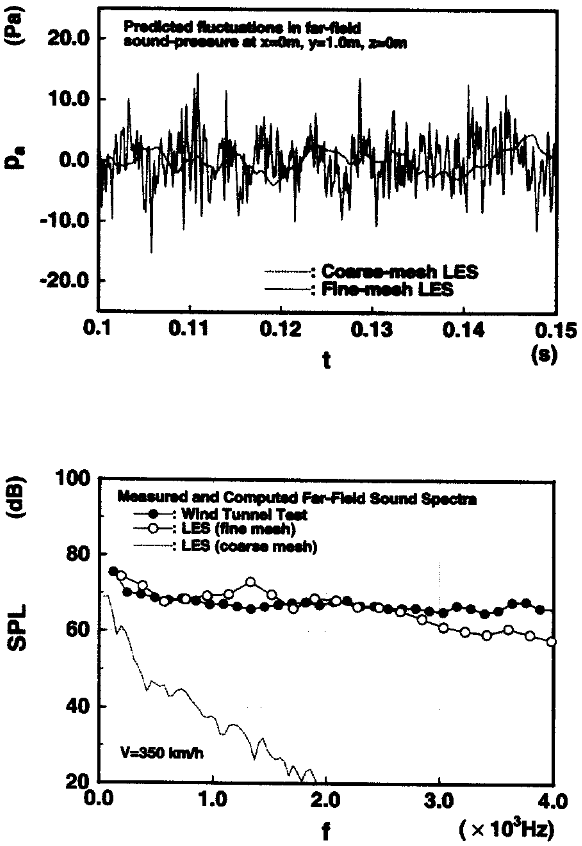

Fig. 18 Computed far-field sound-pressure fluctuations (upper) and their power spectra (lower)

$$\left(\frac{\partial^2}{\partial t^2}-a^2\nabla^2\right)\rho=\nabla\cdot(\rho\boldsymbol{\omega}\times\mathbf{u}). \tag{12}$$

This equation directly shows the contributions to the sound generation from the vortical motions in the flow. Figure 19 shows the instantaneous values for the right side of Eq. (12), which were obtained from the flow-field computation. By examining these sound-source distributions, the longitudinal vortices generated by the circular disks are identified as being primarily responsible for the generation of sound by this flow.

The two examples mentioned above (and many others not given here) have clearly indicated that LES is now beginning to serve as a vital design tool in at least some cases of mechanical engineering.

5 Conclusions

This paper proposes a numerical method that is capable of predicting unsteady flow fields with large-scale separations in a complex geometry that involves an arbitrary number of moving boundary interfaces. The method is also applicable to the prediction of the fluctuations in far-field sound pressure that result from an unsteady turbulent wake. The flow field is computed by a large-eddy simulation (LES), implemented with the standard Smagorinsky model, while the far-field sound is predicted by the surface-pressure fluctuations obtained by the LES.

The method is based on a streamline-upwind finite element formulation with second-order accuracy in both time and space, and incorporates the application of overset grids from multiple and dynamic frames of reference. The overall flow field of interest is covered by using several grid sets, each of which is dedicated to the computation of some portion of the flow field and has a frame of reference that is appropriate to that particular portion. The method is implemented as a parallel program by a domain-

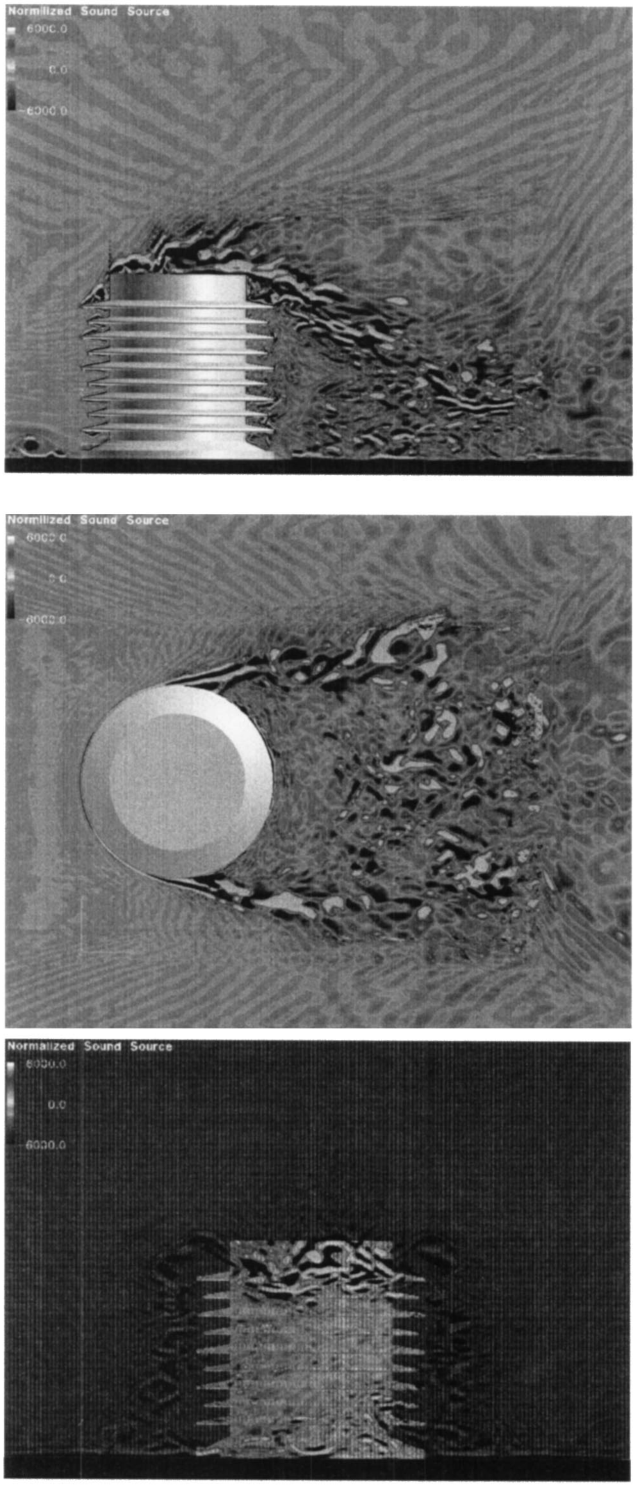

Fig. 19 Instantaneous sound-source distributions in the near wake: centerline plane (top), midheight plane (middle), and a plane one diameter downstream from the insulator (bottom)

decomposition programming model; therefore, a large-scale flow-field computation with over ten million grid cells can be completed within a reasonable period of computation on a current high-end distributed-memory parallel computer.

Initially, the internal flow of a high-specific-speed mixed-flow pump stage $(\omega_s = 2.1)$ was simulated, as a way to evaluate the validity of the proposed method, under two operating conditions: the design point $(Q/Q_d = 100\%)$ and an off-design point $(Q/Q_d = 60\%)$. In both cases, the predicted total pump head and unsteady fluid forces on the impeller were in good agreement with the measured values.

The near wake and the resulting far-field sound were then computed for flow around an insulator that would be mounted on a high-speed train. The predicted sound-pressure level was in reasonably good agreement with the wind-tunnel measurement at Strouhal frequencies of up to about 6. The sound sources in the near wake were analyzed according to Powell's equation and the longitudinal vortices were identified as being primarily responsible for the generation of sound by this flow.

The proposed method thus seems to be a promising candidate for use as an aerodynamic/aeroacoustic design tool.

References

[1] Moore, J., Moore, J. G., and Timmis, P. H., 1984, ''Performance Evaluation of Centrifugal Compressor Impellers Using Three-Dimensional Viscous Flow Calculations,'' ASME J. Eng. Gas Turbines Power, **106**, pp. 475–481.

[2] Dawes, W. N., 1988, ''Development of a 3D Navier-Stokes Solver for Application to All Types of Turbomachinery,'' ASME Paper No. 88-GT-70.

[3] Hah, C., Bryans, A. C., Moussa, Z., and Tomsho, M. E., 1988, ''Application of Viscous Flow Computations for the Aerodynamic Performance of a Back-Swept Impeller at Various Operating Conditions,'' ASME J. Turbomach., **110**, pp. 303–311.

[4] Denton, J. D., 1992, ''The Calculation of Three-Dimensional Viscous Flow Through Multistage Turbomachinery,'' ASME J. Turbomach., **114**, pp. 18–26.

[5] Goto, A., 1992, ''Study of Internal Flows in a Mixed-Flow Pump Impeller at Various Tip Clearances Using Three-Dimensional Viscous Flow Computations,'' ASME J. Turbomach., **114**, pp. 373–382.

[6] Takemura, T., and Goto, A., 1996, ''Experimental and Numerical Study of Three-Dimensional Flows in a Mixed-Flow Pump Stage,'' ASME J. Turbomach., **118**, pp. 552–561.

[7] Kaupert, K. A., Holbein, P., and Staubli, T., 1996, ''A First Analysis of Flow Field Hysteresis in a Pump Impeller,'' ASME J. Fluids Eng., **118**, pp. 685–691.

[8] Shi, F., and Tsukamoto, H., 2001, ''Numerical Study of Pressure Fluctuations Caused by Impeller-Diffuser Interaction in a Diffuser Pump Stage,'' ASME J. Fluids Eng., **123**, pp. 466–474.

[9] He, L., and Sato, K., 2001, ''Numerical Solution of Incompressible Unsteady Flows in Turbomachinery,'' ASME J. Fluids Eng., **123**, pp. 680–685.

[10] Deardorff, J., 1970, ''A Numerical Study of Three-Dimensional Turbulent Channel Flow at Large Reynolds Number,'' J. Fluid Mech., **41**, pp. 453–480.

[11] Germano, M., Piomelli, U., Moin, P., and Cabot, W. H., 1991, ''A Dynamic Sub-Grid-Scale Eddy Viscosity Model,'' Phys. Fluids, **3**(7), pp. 1760–1765.

[12] Lilly, D. K., 1992, ''A Proposed Modification of the Germano Sub-Grid-Scale Closure Method,'' Phys. Fluids, **4**(3), pp. 633–635.

[13] Jordan, S. A., 2001, ''Dynamic Sibgrid-Scale Modeling for Large-Eddy Simulations in Complex Topologies,'' ASME J. Fluids Eng., **123**, pp. 619–623.

[14] Hughes, T. J. R., Oberai, A. A., and Mazzei, L., 2001, ''Large Eddy Simulation of Turbulent Channel Flows by the Variational Multiscale Method,'' Phys. Fluids, **13**, pp. 1884–1799.

[15] Lund, T., 1998, ''Generation of Turbulent Inflow Data for Spatially-Developing Boundary Layer Simulations,'' J. Comput. Phys., **140**, p. 233.

[16] Smirnov, A., Shi, S., and Celik, I., 2001, ''Random Flow Generation Technique for Large Eddy Simulations and Particle-Dynamics Modeling,'' ASME J. Fluids Eng., **123**, pp. 359–371.

[17] Piomelli, U., 1999, ''Large-Eddy Simulation: Achievements and Challenges,'' Prog. Aeronaut. Sci., **35**, p. 335.

[18] Kato, C., Shimizu, H., and Okamura, T., 1999, ''Large Eddy Simulation of Unsteady Flow in a Mixed-flow Pump,'' *Proceedings of 3rd ASME/JSME Joint Fluids Engineering Conference*, FEDSM99-7802.

[19] Kato, C., et al., 2000, ''Numerical Simulation of Aerodynamic Sound Source in the Wake of a Complex Object,'' AIAA Paper 2000-1942.

[20] Tam, C. K. W., 1995, ''Computational Aeroacoustics: Issues and Methods,'' AIAA J., **33**(10), pp. 1788–1796.

[21] Wells, V. L., and Renaut, R. A., 1997, ''Computing Aerodynamically Generated Noise,'' Annu. Rev. Fluid Mech., **29**, pp. 161–199.

[22] Hardin, J. C., and Lamkin, S. L., 1984, ''Aeroacoustics Computation of Cylinder Wake Flow,'' AIAA J., **22**(1), pp. 51–57.

[23] Howe, M. S., 1975, ''The Generation of Sound by Aerodynamic Sources in an Inhomogeneous Steady Flow,'' J. Fluid Mech., **67**(3), pp. 597–610.

[24] Akishita, S., et al., 1987, ''Numerical Simulation of Aerodynamic Sound Radiation from a Two-Dimensional Wing,'' AIAA Paper No. 87-2672.

[25] Haruna, S., et al., 1992, ''Numerical Study of Aerodynamic Noise Radiated From a Three-Dimensional Wing,'' SAE Paper No. 920341.

[26] Adachi, S., et al., 1992, ''Computation of Aerodynamic Sound Radiation from Flows past a Wing,'' DGLR/AIAA Paper No. 92-02-157.

[27] Kato, C., and Ikegawa, M., 1991, ''Large Eddy Simulation of Unsteady Turbulent Wake of a Circular Cylinder Using the Finite Element Method,'' *Advances in Numerical Simulation of Turbulent Flows*, ASME, New York, ASME FED- Vol. 117, pp. 49–56.

[28] Kato, C., Iida, A., Takano, Y., Fujita, H., and Ikegawa, M., 1993, ''Numerical

Prediction of Aerodynamic Noise Radiated From Low Mach Number Turbulent Wake,'' AIAA Paper No. 93-0145.

[29] Curle, N., 1955, ''The Influence of Solid Boundaries Upon Aerodynamic Sound,'' Proc. R. Soc. London, Ser. A, **A231**, pp. 505–514.

[30] Lighthill, M. J., 1951, ''On Sound Generated Aerodynamically: Part I. General Theory,'' Proc. R. Soc. London, Ser. A, **A211**, pp. 564–587.

[31] Siegert, R., Schwarz, V., and Reichenberger, J., 1999, ''Numerical Simulation of Aeroacoustic Sound Generated by Generic Bodies Placed on a Plate: Part II—Prediction of Radicated Sound Pressure,'' AIAA Paper No. 99-1985.

[32] Smagorinsky, J., 1963, ''General Circulation Experiments with Primitive Equations,'' Mon. Weather Rev., **91**(3), pp. 99–164.

[33] Tezduyar, T. E., 2001, ''Finite Element Methods for Flow Problems With Moving Boundaries and Interfaces,'' Arch. Comput. Methods Eng., **8**(2), pp. 83–130.

[34] Ikegawa, M., Kaiho, M., and Kato, C., 1994, ''FEM/FDM Composite Scheme for Viscous Incompressible Flow Analysis,'' Comput. Methods Appl. Mech. Eng., **112**, pp. 149–163.

[35] Kaiho, M., Ikegawa, M., and Kato, C., 1997, ''Parallel Overlapping Scheme for Viscous Incompressible Flows,'' Int. J. Numer. Methods Fluids, **24**, pp. 1341–1352.

[36] Brooks, A. N., and Hughes, T. G. R., 1982, ''Streamline Upwind/Petrov-Galerkin Formulations for Convection Dominated Flows With Particular Emphasis on the Incompressible Navier-Stokes Equations,'' Comput. Methods Appl. Mech. Eng., **32**, pp. 199–259.

[37] Tezduyar, T. E., and Hughes, T. J. R., 1983, ''Finite Element Formulations for Convection Dominated Flows With Particular Emphasis on the Compressible Euler Equations,'' *Proceedings of AIAA 21st Aerospace Sciences Meeting*, AIAA Paper No. 83-0125.

[38] Donea, J. et al., 1984, ''Time Accurate Solution of the Advection-Diffusion Problems by Finite Elements,'' Comput. Methods Appl. Mech. Eng., **45**, pp. 123–145.

[39] Viecelli, J. A., 1971, ''A Computing Method for Incompressible Flows Bounded by Walls,'' J. Comput. Phys., **8**, pp. 119–143.

[40] Simon, H., 1991, ''Partitioning of Unstructured Problems for Parallel Processing,'' Comput. Syst. Eng., **2**, pp. 135–148.

[41] Farhat, C., and Lesoinne, M., 1993, ''Automatic Partitioning of Unstructured Meshes for the Parallel Solution of Problems in Computer Mechanics,'' Int. J. Numer. Methods Eng., **36**, pp. 745–764.

[42] Powell, A., 1964, ''The Theory of Vortex Sound,'' J. Acoust. Soc. Am., **33**, pp. 177–195.

Hierarchical Divergence-Free Bases and Their Application to Particulate Flows

V. Sarin[1]
Department of Computer Science,
Texas A&M University,
College Station, TX 77843
e-mail: sarin@cs.tamu.edu

A. H. Sameh
Department of Computer Science,
Purdue University,
West Lafayette, IN 47907
e-mail: sameh@cs.purdue.edu

The paper presents an algebraic scheme to construct hierarchical divergence-free basis for velocity in incompressible fluids. A reduced system of equations is solved in the corresponding subspace by an appropriate iterative method. The basis is constructed from the matrix representing the incompressibility constraints by computing algebraic decompositions of local constraint matrices. A recursive strategy leads to a hierarchical basis with desirable properties such as fast matrix-vector products, a well-conditioned reduced system, and efficient parallelization of the computation. The scheme has been extended to particulate flow problems in which the Navier-Stokes equations for fluid are coupled with equations of motion for rigid particles suspended in the fluid. Experimental results of particulate flow simulations have been reported for the SGI Origin 2000.

[DOI: 10.1115/1.1530633]

1 Introduction

The simulation of incompressible fluid flow is a computationally intensive application that has challenged high-performance computing technology for several decades. The ability to solve large, sparse linear systems arising from Navier-Stokes equations is critical to the success of such simulations. Linear systems of equations are typically solved by iterative methods that have the advantage of requiring storage proportional to the number of unknowns only. One can use the conjugate gradients method (CG), [1], for symmetric positive definite systems and the generalized minimum residual method (GMRES), [2], for nonsymmetric systems. Although these methods are memory-efficient in comparison to direct methods such as Gaussian elimination, the rate of convergence to the solution can be unacceptably slow. Often one needs to accelerate convergence by using some preconditioning strategy that computes an approximate solution at each step of the iterative method. It is well known that commonly used preconditioning schemes such as those based on incomplete factorization (see, e.g., [3]) may not be effective for indefinite linear systems with eigenvalues on both sides of the imaginary axis. Since the eigenvalue distribution of linear systems arising from the Navier-Stokes equations could produce such systems, it is a challenge to devise robust and effective preconditioners for incompressible flows.

The Navier-Stokes equations governing incompressible fluid are given as follows:

$$\rho \frac{\partial u}{\partial t} + \rho u \cdot \nabla u = \rho g - \nabla p + \nabla \cdot \tau, \tag{1}$$

$$\nabla \cdot u = 0, \tag{2}$$

where u denotes fluid velocity, p denotes pressure, ρ denotes fluid density, g represents gravity, and τ represents the extra-stress tensor. For Newtonian flows, τ takes the form

$$\tau = \mu(\nabla u + \nabla u^T). \tag{3}$$

After appropriate linearization and discretization, the following system must be solved:

$$\begin{bmatrix} A & B \\ B^T & 0 \end{bmatrix} \begin{bmatrix} u \\ p \end{bmatrix} = \begin{bmatrix} f \\ 0 \end{bmatrix}, \tag{4}$$

where u is the velocity vector, p is the pressure vector, B^T and B are discrete operators for divergence and gradient, respectively. The matrix A denotes the discrete operator on velocity in (1). This linear system is indefinite due to the incompressibility constraint on velocity which is enforced by $B^T u = 0$ in (4).

A convenient way to circumvent the indefiniteness of the linear system due to these constraints is to restrict the fluid velocity to divergence-free subspace. There are a number of techniques to construct divergence-free velocity functions. These include discretely divergence-free functions obtained from specially constructed finite element spaces, [4,5], as well as continuous functions derived from solenoidal functions such as those used in vortex methods. The problem is reduced to solving the momentum equation for divergence-free velocity functions without the need to include continuity constraints. In many cases, the resulting reduced linear systems are no longer indefinite. Furthermore, these reduced systems can be preconditioned to accelerate the convergence of iterative solvers.

The existing schemes for divergence-free functions are complicated and difficult to generalize to arbitrary discretizations. In this paper, we present an algebraic scheme to compute a basis for discretely divergence-free velocity. Our scheme constructs a basis for the null space of the matrix representing the linear constraints imposed on fluid velocity by (2). The algebraic nature of the scheme ensures applicability to a wide variety of methods including finite difference, finite volume, and finite elements methods. Since the choice of the basis preconditions the reduced linear system implicitly, it is possible to compute an optimal basis that leads to rapid convergence of the iterative solver. A more modest target is to compute a well-conditioned basis that preconditions the reduced system to some degree. The paper presents an algorithm to construct a hierarchical basis of divergence-free functions that is well conditioned too.

The paper is organized as follows: Section 2 presents the algorithm for hierarchical divergence-free basis and discusses computational aspects. Section 3 outlines the extension of the scheme to particulate flow problems. In Section 4, we describe the behavior of our scheme on benchmark problems in particulate flows. Conclusions are presented in Section 5.

---

[1] To whom correspondence should be addressed.

Contributed by the Applied Mechanics Division of THE AMERICAN SOCIETY OF MECHANICAL ENGINEERS for publication in the ASME JOURNAL OF APPLIED MECHANICS. Manuscript received by the ASME Applied Mechanics Division, July 2, 2001; final revision, Apr. 9, 2002. Associate Editor: T. E. Tezduyar. Discussion on the paper should be addressed to the Editor, Prof. Robert M. McMeeking, Department of Mechanical and Environmental Engineering University of California–Santa Barbara, Santa Barbara, CA 93106-5070, and will be accepted until four months after final publication of the paper itself in the ASME JOURNAL OF APPLIED MECHANICS.

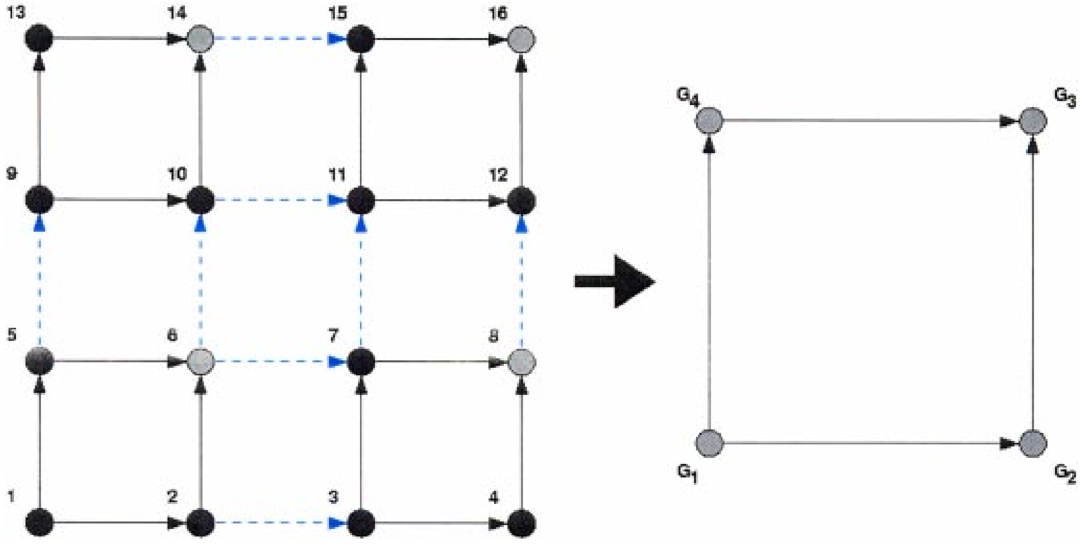

Fig. 1 The coarsening of a 4×4 mesh to a 2×2 mesh

2 Hierarchical Divergence-Free Basis

A straightforward way to construct discretely divergence-free bases is to compute the null space of the discrete divergence operator matrix B^T. This null space can be computed via full QR factorization or singular value decomposition (SVD) of B^T, [6]. For an m by n matrix $(m<n)$, the computation is proportional to m^2n while storage is proportional to mn. For the matrix B^T, the number of rows m corresponds to the number of pressure basis functions and the number of columns n corresponds to the number of velocity basis functions. Since B^T is large and sparse with nonzeros proportional to m, both QR factorization and SVD are unsuitable due to the prohibitive requirements of computation and storage.

The nonzero structure of B^T can be exploited to construct a null-space basis efficiently. The following outline of the algorithm to construct a hierarchical divergence-free basis follows the description in [7]. Suppose one can reorder the columns of B^T such that

$$B^T=[B_{\text{in}}^T \quad B_{\text{out}}^T], \tag{5}$$

where B_{in}^T is a block diagonal matrix with "small" nonzero blocks on the diagonal. Given the following singular value decomposition of B_{in}:

$$B_{\text{in}}=\text{USV}^T=[U_1 \quad U_2]\begin{bmatrix} S_1 & \\ & 0 \end{bmatrix}[V_1 \quad V_2]^T, \tag{6}$$

where S_1 is a nonzero diagonal matrix, B^T can be represented as follows:

$$B^T=VV^T[B_{\text{in}}^T \quad B_{\text{out}}^T]\begin{bmatrix} UU^T & \\ & I \end{bmatrix}=[V_1 \quad V_2]\left[\begin{array}{cc|c} S_1 & 0 & V_1^TB_{\text{out}}^T \\ 0 & 0 & V_2^TB_{\text{out}}^T \end{array}\right] \times\begin{bmatrix} U^T & \\ & I \end{bmatrix}. \tag{7}$$

Since

$$\left[\begin{array}{cc|c} S_1 & 0 & V_1^TB_{\text{out}}^T \\ 0 & 0 & V_2^TB_{\text{out}}^T \end{array}\right]\left[\begin{array}{cc} 0 & -S_1^{-1}V_1^TB_{\text{out}}^T \\ I & 0 \\ \hline 0 & I \end{array}\right]=\begin{bmatrix} 0 & 0 \\ 0 & V_2^TB_{\text{out}}^T \end{bmatrix}, \tag{8}$$

the null-space basis of B^T is given by

$$P=\begin{bmatrix} U & \\ & I \end{bmatrix}\begin{bmatrix} 0 & -S_1^{-1}V_1^TB_{\text{out}}^T \\ I & 0 \\ 0 & I \end{bmatrix}\begin{bmatrix} I & 0 \\ 0 & P^{(1)} \end{bmatrix}, \tag{9}$$

where $P^{(1)}$ is a null-space basis of the matrix $B^{(1)^T}=V_2^TB_{\text{out}}^T$. With this transformation, the problem of computing the null-space of the original matrix B^T is reduced to a problem of smaller size. By applying the same technique to compute the null-space of $B^{(1)^T}$, one gets a recursive strategy for constructing the null-space of B^T.

The preceding approach is viable only if the transformation is inexpensive and the reduced matrix $B^{(1)^T}$ is easy to compute and process subsequently. These criteria are met simultaneously by exploiting the relation of the nonzero structure of B^T with the discretization mesh. The pressure nodes in the mesh are clustered into groups of a few nodes each, and the velocity basis functions with support within a cluster are placed in B_{in} whereas those with support across clusters are placed in B_{out}. The resulting matrix B_{in} is block diagonal with small block sizes. Each diagonal block represents the divergence operator for the corresponding cluster of nodes. Due to the small size of the diagonal blocks, the SVD can be computed very efficiently.

To illustrate the technique, we reproduce an example of a 4 ×4 mesh from [8] (see Fig. 1). Pressure unknowns are defined at the nodes. The x-component of velocity is defined on the horizontal edges and y-component of velocity is defined on the vertical edges. The nodes are clustered into four groups: $G_1=\{1,2,5,6\}$, $G_2=\{3,4,7,8\}$, $G_3=\{9,10,13,14\}$, and $G_4=\{11,12,15,16\}$. The solid edges indicate velocity unknowns for B_{in} and the dashed edges indicate velocity unknowns for B_{out}. The associated matrices are

$$B_{\text{in}}=\begin{bmatrix} B_1 & & & \\ & B_2 & & \\ & & B_3 & \\ & & & B_4 \end{bmatrix},$$

$$B_{\text{out}}=\begin{bmatrix} -C_1 & C_2 & & \\ & & -C_1 & C_2 \\ -C_3 & & C_4 & \\ & -C_3 & & C_4 \end{bmatrix}, \tag{10}$$

in which

$$B_i=\begin{bmatrix}-1 & 1 & 0 & 0\\ 0 & 0 & -1 & 1\\ -1 & 0 & 1 & 0\\ 0 & -1 & 0 & 1\end{bmatrix},\quad i=1,\ldots,4, \tag{11}$$

and

$$C_1=\begin{bmatrix}0 & 1 & 0 & 0\\ 0 & 0 & 0 & 1\end{bmatrix}, C_2=\begin{bmatrix}1 & 0 & 0 & 0\\ 0 & 0 & 1 & 0\end{bmatrix},$$

$$C_3=\begin{bmatrix}0 & 0 & 1 & 0\\ 0 & 0 & 0 & 1\end{bmatrix}, C_4=\begin{bmatrix}1 & 0 & 0 & 0\\ 0 & 1 & 0 & 0\end{bmatrix}. \tag{12}$$

The SVD of each block in B_{in} is given as

$$B_i=U_iS_iV_i^T=\begin{bmatrix}-1/2 & 1/2 & -1/2 & 1/2\\ 1/2 & 1/2 & -1/2 & -1/2\\ -1/2 & 1/2 & 1/2 & -1/2\\ 1/2 & 1/2 & 1/2 & 1/2\end{bmatrix}\begin{bmatrix}2 & & & \\ & \sqrt{2} & & \\ & & \sqrt{2} & \\ & & & 0\end{bmatrix}$$

$$\times\begin{bmatrix}1/2 & -\sqrt{2} & 0 & 1/2\\ -1/2 & 0 & -\sqrt{2} & 1/2\\ -1/2 & 0 & \sqrt{2} & 1/2\\ 1/2 & \sqrt{2} & 0 & 1/2\end{bmatrix}^T, \tag{13}$$

that yields

$$B^{(1)^T}=V_2^TB_{\text{out}}^T$$

$$=\frac{1}{2}\begin{bmatrix}-1 & -1 & 0 & 0 & -1 & -1 & 0 & 0\\ 1 & 1 & 0 & 0 & 0 & 0 & -1 & -1\\ 0 & 0 & -1 & -1 & 1 & 1 & 0 & 0\\ 0 & 0 & 1 & 1 & 0 & 0 & 1 & 1\end{bmatrix}. \tag{14}$$

Note that the rows of $B^{(1)^T}$ correspond to the nodes 6, 8, 14, and 16 of the original mesh, and the columns correspond to the cross-cluster edges. It is easy to see that $B^{(1)^T}$ is a divergence matrix for the coarse mesh shown in Fig. 1. Since columns $2j$-1 and $2j$ are identical for $j=1,\ldots 4$, the columns of $B^{(1)^T}$ can be reduced to four nonzero columns by multiplying with an orthogonal matrix from the right. The resulting matrix is the divergence matrix of a 2×2 mesh which has been scaled by $1/\sqrt{2}$.

In general, the nonzero structure of the matrix $B^{(1)^T}$ retains the structure of a coarse mesh obtained from grouping clusters into single nodes. Furthermore, $B^{(1)^T}$ may be considered equivalent to a divergence operator matrix for the coarse mesh. Thus, the recursive strategy can be applied in a straightforward manner. Since $B^{(1)^T}$ can also be computed efficiently from the SVD of B_{in}, each step of the recursive algorithm is very efficient.

The recursive algorithm to construct the divergence-free basis gives rise to a hierarchical basis that consists of basis functions defined on each level of the mesh hierarchy. In the actual implementation of the algorithm, the null-space matrix is never computed explicitly. It is available only in the form of product of matrices constructed from the SVD matrices and the equivalent divergence operator matrix $B^{(*)^T}$ at each level of the mesh hierarchy.

The size of meshes in the hierarchy decreases geometrically from the finest mesh to the coarsest mesh. Since the size of $B^{(*)^T}$ is proportional to the mesh size at each level, the cost of computing and storing SVDs is also proportional to the mesh size at the corresponding level. Thus, the overall computation and storage is proportional to the size of B^T. This is a significant improvement over the QR and SVD algorithms. However, it should be noted that this reduction in computational complexity is gained at the expense of generating a basis that is not orthonormal. The reader is referred to [7] for more details of this method.

Once the divergence-free basis P has been constructed, the linear system in (4) is transformed to the following reduced system:

$$P^TAPx=P^Tf,\quad u=Px, \tag{15}$$

which is solved by GMRES to obtain x. When A is symmetric and positive definite, one can use CG instead of GMRES. Pressure can be computed correctly by solving the least-squares problem

$$Bp\approx f-Au, \tag{16}$$

which is consistent since $P^T(f-Au)=0$. At each iteration, one needs to compute matrix-vector products of the form $y=Px$ and $z=P^Tw$. The computation follows a recursive structure in which matrix-vector products are computed at each level of the mesh hierarchy. The computation proceeds from the coarsest mesh to the finest mesh for the product $y=Px$ and in the reverse direction for the product $z=P^Tw$. Since the computational complexity of each product is proportional to the size of B^T, the cost of computing the matrix-vector product for the reduced system in (15) is proportional to the number of velocity unknowns. Furthermore, the concurrency in the hierarchical structure of this algorithm can be exploited to develop high-performance software for incompressible flows. Details of an efficient parallel formulation are presented in [9].

3 Particulate Flows

Divergence-free velocity basis can be used to solve linear systems arising in solid-fluid mixtures that consist of rigid particles suspended in incompressible fluids. The solution of these linear systems is extremely computationally intensive and accounts for majority of the simulation time. The motion of particles is governed by Newton's equations whereas the fluid obeys Navier-Stokes equations. Assuming no-slip on the surface of the particle, the fluid velocity at any point on the particle surface is a function of the particle velocity. For the sake of simplicity, this discussion assumes spherical particles. For the ith particle, the position X_i and velocity U_i is obtained by solving the following equations:

$$M_i\frac{dU_i}{dt}=F_i, \tag{17}$$

$$\frac{dX_i}{dt}=U_i, \tag{18}$$

where U_i includes both translation and angular components of the particle, M_i represents the generalized mass matrix, and F_i represents the force and torque acting on the particles by the fluid as well as gravity. Fluid velocity at the surface of the particle is related to the particle velocity as follows:

$$u_j=U_{t,i}+r_j\times U_{r,i} \tag{19}$$

where $U_{t,i}$ and $U_{r,i}$ are the translation and angular velocity components, respectively, and r_j is the position vector of the jth point relative to the center of the particle.

A simple way to represent the linear system arising in particulate flows is as follows. The systems for fluid and particles are written independently along with the constraint in (19) that forces fluid velocity on a particle surface to be dependent on the particle velocity. Thus,

$$\begin{bmatrix}A & B & 0\\ B^T & 0 & 0\\ 0 & 0 & C\end{bmatrix}\begin{bmatrix}u\\ p\\ U\end{bmatrix}=\begin{bmatrix}b\\ 0\\ g\end{bmatrix},\quad\text{where}\quad u=\begin{bmatrix}u_f\\ u_p\end{bmatrix}=\begin{bmatrix}I & \\ & W\end{bmatrix}\begin{bmatrix}u_f\\ U\end{bmatrix}, \tag{20}$$

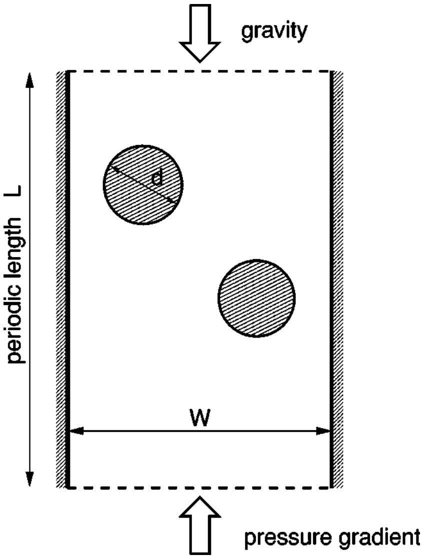

Fig. 2 Particles moving in a periodic channel

in which u_f is the fluid velocity in the interior of the fluid and W is the linear transformation from particle velocity U to fluid velocity u_p on particle surface given by (19). Using subscripts f and p to denote fluid interior and particle surface, respectively, the preceding system can be transformed to the following system:

$$\begin{bmatrix} I & 0 & 0 & 0 \\ 0 & W^T & 0 & I \\ 0 & 0 & I & 0 \end{bmatrix} \begin{bmatrix} A_{ff} & A_{pf} & B_f & 0 \\ A_{fp} & A_{pp} & B_{fp} & 0 \\ B_f^T & B_{fp}^T & 0 & 0 \\ 0 & 0 & 0 & C \end{bmatrix} \begin{bmatrix} I & 0 & 0 \\ 0 & W & 0 \\ 0 & 0 & I \\ 0 & I & 0 \end{bmatrix} \begin{bmatrix} u_f \\ U \\ p \end{bmatrix} = \begin{bmatrix} b_f \\ g+W^T b_p \\ 0 \end{bmatrix}, \tag{21}$$

which can be simplified further to obtain the following system:

$$\begin{bmatrix} A_{ff} & A_{pf}W & B_f \\ W^T A_{fp} & W^T A_{pp} W + C & W^T B_{fp} \\ B_f^T & B_{fp}^T W & 0 \end{bmatrix} \begin{bmatrix} u_f \\ U \\ p \end{bmatrix} = \begin{bmatrix} b_f \\ g+W^T b_p \\ 0 \end{bmatrix}. \tag{22}$$

Note that this system has a form similar to the linear system in (4).

A hierarchical divergence-free basis can be computed for (22) without any difficulty. In this case, the null-space is computed for the constraint matrix $[B_f^T \; B_{fp}^T W]$. The basic algorithm remains unchanged although care has to be taken when coarsening the mesh with particles. The fluid nodes on the particle surface are absent from the mesh in this system. The presence of particles introduces a single node that is connected to all the fluid nodes that are adjacent to the particle surface. The algebraic scheme for computing the divergence-free basis ensures that the algorithm applies without any change to particulate flows as well.

4 Experiments

The hierarchical divergence-free basis method has been used to solve the linear systems arising in particulate flow simulations. The simulations involved incompressible fluid in a two-dimensional channel with a number of rigid particles moving freely under the action of gravitational force as well as force from the surrounding fluid (see Fig. 2).

The physical system is evolved from an initial state by the implicit backward Euler method. The first-order accuracy of this scheme was adequate because the time step was severely constrained by particle dynamics. At each time-step, a nonlinear system of equations was solved by an inexact Newton's method, [10]. At each iteration, a linear system of the form (22) was solved for the Jacobian of the nonlinear equations. In general, this Jacobian matrix is a saddle-point system with a nonsymmetric matrix A which tends to be real positive for a sufficiently small Reynolds number. The hierarchical divergence-free basis approach is used to transform the system in (22) to the reduced form shown in (15). The reduced system is solved by the GMRES method. The adaptive tolerance proposed in [11] was used as a stopping criteria.

The differential equations are approximated by the mixed finite elements method in which fluid velocity and pressure are represented by the P2/P1 pair of elements. The choice of quadratic velocity elements is necessary to capture the behavior of closely spaced particles. A nonuniform mesh is used to discretize the fluid domain resulting in a linear system that is large and sparse. The scheme proposed in [12] is used in an arbitrary Lagrange-Euler (ALE) framework to accommodate moving particles.

The parallel simulation code was developed using Petsc, [13]. Communication between processes was done by MPI, [14]. The mesh is generated using Triangle, [15] and partitioned using Parallel METIS, [16]. Further implementation details are available in [17].

Simulations were conducted for rigid particles falling in a 3.2 in. wide and 30 in. long two-dimensional vertical channel with a solid impenetrable bottom. The particles were assumed to be circular disks of diameter 0.25 in. and specific gravity 1.14. The initial position of particles was specified.

4.1 Single Particle Sedimentation. This benchmark simulates the sedimentation of a single particle from rest whose center is at a distance of 0.8 in. from the left wall and 30 in. from the bottom of the channel. At the first time-step, the computational mesh had 2461 elements and 1347 nodes. The number of unknowns in the unconstrained problem was 9418. Figure 3 shows

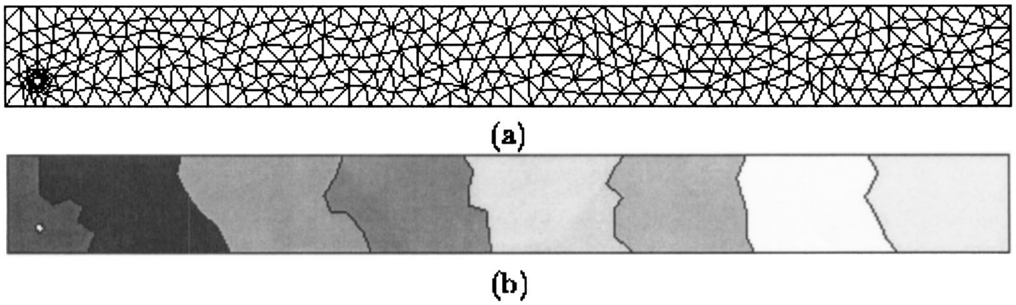

Fig. 3 Sedimentation of a single particle: (*a*) mesh with 2461 elements and 1347 nodes, (*b*) partitioning into eight domains. The gravitational force pulls the particles towards the right.

Table 1 Single particle sedimentation on the SGI origin 2000.

Processors	Time	Speedup	Efficiency
1	1819 s	1.0	1.00
2	822 s	2.2	1.11
4	502 s	3.6	0.91
8	334 s	5.3	0.66

Table 2 Multiple particle sedimentation on the SGI origin 2000

Processors	Time	Speedup	Efficiency
1	3066 s	1.0	1.00
2	1767 s	1.7	0.85
4	990 s	3.0	0.75
8	570 s	5.3	0.66

the initial mesh and the associated partitioning into eight subdomains.

To illustrate the numerical and parallel performance of the algorithm, the experiment was restricted to the first five time-steps starting with the particle and fluid at rest. Each time-step was 0.01 sec. Table 1 presents the performance of the algorithm on eight processors of the SGI Origin 2000 multiprocessor. The parallel efficiency is expected to be much higher for a larger problem. In this experiment, superlinear speedup is observed due to effective cache utilization when data on individual processors is small enough to fit within the cache.

4.2 Multiple Particle Sedimentation. The next benchmark simulates the sedimentation of 240 particles arranged in a stationary *crystal*. The crystal consists of an array of 240 particles in 20 rows and 12 columns. The centers of the particles coincide with the nodes of a uniform mesh with 20 rows and 12 columns. The centers of the particles are approximately 0.06154 in. apart in each direction. The distance between the walls and the nearest particles is also 0.06154 in. The top of the crystal is 30 in. above the channel bottom. Figure 4 shows the initial mesh and the associated partitioning into eight subdomains.

At the first time-step, the computational mesh had 8689 elements and 6849 nodes, giving rise to 43,408 unknowns in the unconstrained problem. The simulation was run for five time-steps starting with the particles and fluid at rest. Each time step was 0.01 sec. Table 2 presents the performance of the algorithm on eight processors of the SGI Origin 2000.

It is instructive to see the breakdown of the computational time into important steps. Table 3 presents the computational cost of critical steps. The nonlinear system solution time consists of the following main steps: calculation of the Jacobian matrix, application of the nonlinear operator, formation of the hierarchical divergence-free basis, and the solution of the linear system. The time to solve the linear system is dominated by matrix-vector multiplication with the Jacobian, application of the hierarchical basis, and orthogonalization of the Krylov subspace vectors in GMRES. The nonlinear solver takes most of the time, and its parallelization is critical to the overall performance.

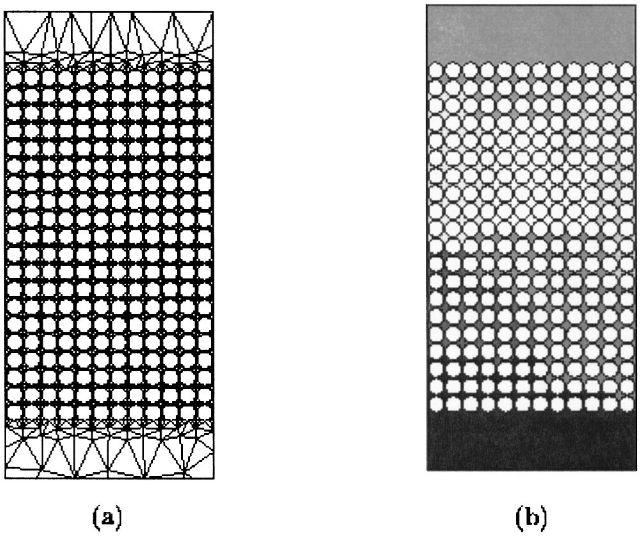

Fig. 4 Sedimentation of multiple particles: (*a*) mesh with 8689 elements and 6849 nodes, and (*b*) partitioning into eight domains. Only the region of interest is shown.

4.3 Additional Remarks. The parallel implementation of the algorithm demonstrates good parallel efficiency even for small-sized problems. The overall speedup of 5.3 on eight processors shown in Table 2 includes nonparallelizable components of the code as well as preconditioning effects that slowed the convergence of iterative solver on larger number of processors. The detailed view in Table 3 shows that the speedup in critical steps is 5.9 on eight processors. The computation of divergence-free velocity in the hierarchical basis is very efficient even on the small problem considered here. The relatively modest speedup in matrix-vector products is due to the structure of computation involving multiplication with the matrices of the hierarchical basis. As discussed in Section 2, this requires matrix-vector products with matrices defined on meshes whose size decreases geometrically from the finest to the coarsest level. In addition, it may be noted that parallel efficiency can be increased by replacing the orthogonalization step in GMRES with a variant that has a smaller serial component.

The preceding benchmark experiments define *speedup* as the improvement in speed over the *best* implementation of the algorithm on a uniprocessor. This implies that although the parallel algorithm demonstrates good *speed improvement* on multiple processors, the speedup may be modest. The code attempts to achieve high parallel performance by adopting an aggressive partitioning strategy which is aimed at good load balance in the overall computation. This particular implementation of the hierachical divergence-free basis algorithm computes a basis that changes with the number of processors. This has resulted in weaker preconditioning which has caused a growth in the number of iterations when the number of processors is increased. The deterioration in numerical efficiency of the algorithm can be eliminated by using the *same* basis on multiple processors. In this case, however, there is a marginal decrease in parallel efficiency which is offset by superior numerical convergence. The reader is referred to [9] for a scalable parallel implementation of this approach.

5 Conclusions

This paper describes an algorithm to compute discrete divergence-free velocity functions for incompressible fluid flow problems. The proposed scheme computes a basis for the null-space of the constraint matrix used to enforce incompressibility in the linearized Navier-Stokes equations. A multilevel recursive algebraic transformation of this constraint matrix yields a hierarchical basis for the required divergence-free functions. The algebraic nature of the scheme allows easy extension to particulate flow problems in which rigid particles are coupled with the surrounding fluid by no-slip condition on the particle surface. The paper outlines the extension of the hierarchical basis method for particulate flow problems. The effectiveness of the proposed scheme is demonstrated by a set of benchmark experiments with single and multiple sedimenting particles. The algorithm is designed to be parallelizable. The resulting implementation on the SGI Origin 2000 parallel computer demonstrates good parallel performance

Table 3 Parallel performance of important steps in the nonlinear solver for multiple particle sedimentation

	P=1		P=8		
Simulation Step	**Time**	**Percent**	**Time**	**Percent**	**Speedup**
Matrix assembly	224	11	33	10	6.8
Hierarchical Basis	1010	49	143	41	7.1
Matrix-vector multiplication	452	22	86	25	5.3
GMRES orthogonalization	360	18	83	24	4.3
Total	2046	100	345	100	5.9

even on small sized problems. For larger problems, the algorithm is expected to have significantly better parallel performance.

Acknowledgments

The authors wish to thank Dr. Knepley for providing the experimental data in Sections 4.1 and 4.2. This work was supported in part by the NSF through the grants ECS-9527123, CTS 9873236, CCR-9972533, and the infrastructure grant EIA 9871053. Sarin was also partially supported by the NSF grant CCR 9984400. Computational resources were provided by NCSA, University of Illinois at Urbana-Champaign.

References

[1] Hestenes, M. R., and Stiefel, E., 1952, ''Methods of Conjugate Gradients for Solving Linear Systems,'' J. Res. Natl. Bur. Stand., **49**, pp. 409–436.
[2] Saad, Y., and Schultz, M. H., 1986, ''GMRES: A Generalized Minimum Residual Algorithm for Solving Nonsymmetric Linear Systems,'' SIAM (Soc. Ind. Appl. Math.) J. Sci. Stat. Comput., **7**, pp. 856–869.
[3] Meijerink, J. A., and Van der vorst, H. A., 1977, ''An Iterative Solution Method for Linear Equation Systems of Which the Coefficient Matrix is a Symmetric M-Matrix,'' Math. Comput., **31**, pp. 148–162.
[4] Gustafson, K., and Hartman, R., 1983, ''Divergence-Free Bases for Finite Element Schemes in Hydrodynamics,'' SIAM (Soc. Ind. Appl. Math.) J. Numer. Anal., **20**(4), pp. 697–721.
[5] Hall, C. A., Peterson, J. S., Porsching, T. A., and Sledge, F. R., 1985, ''The Dual Variable Method for Finite Element Discretizations of Navier-Stokes Equations,'' Int. J. Numer. Methods Eng., **21**, pp. 883–898.
[6] Golub, G. H., and Van Loan, C. F., 1996, *Matrix Computations* 3rd Ed., Johns Hopkins University Press Ltd., London.
[7] Sarin, V., and Sameh, A. H., 1998, ''An Efficient Iterative Method for the Generalized Stokes Problem,'' SIAM J. Sci. Comput. (USA), **19**(1), pp. 206–226.
[8] Sameh, A. H., and Sarin, V., 2002, ''Parallel Algorithms for Indefinite Linear Systems,'' Parallel Comput., **28**, pp. 285–299.
[9] Sarin, V., 1997, ''Efficient Iterative Methods for Saddle Point Problems,'' Ph.D. thesis, University of Illinois, Urbana-Champaign.
[10] Dembo, R. S., Eisenstat, S. C., and Steihaug, T., 1982, ''Inexact Newton Methods,'' SIAM (Soc. Ind. Appl. Math.) J. Numer. Anal., **19**(2), pp. 400–408.
[11] Eisenstat, S. C., and Walker, H. F., 1996, ''Choosing the Forcing Terms in an Inexact Newton Method,'' SIAM J. Sci. Comput. (USA), **17**(1), pp. 16–32.
[12] Hu, H., 1996, ''Direct Simulation of Flows of Solid-Liquid Mixtures,'' Int. J. Multiphase Flow, **22**.
[13] Smith, B. F., Gropp, W. D., McInnes, L. C., and Balay, S., 1995, ''Petsc 2.0 Users Manual,'' Technical Report TR ANL-95/11, Argonne National Laboratory.
[14] Gropp, W. D., Lusk, E., and Skjellum, A., 1994, *Using MPI: Portable Parallel Programming With the Message Passing Interface*, M.I.T. Press, Cambridge, MA.
[15] Shewchuk, J. R., 1996. ''Triangle: Engineering a 2D Quality Mesh Generator and Delaunary Triangulator,'' *First Workshop on Applied Computational Geometry*, ACM, Philadelphia, PA, pp. 124–133.
[16] Karypis, G., and Kumar, V., 1996. ''Parallel Multilevel *k*-Way Partitioning Scheme for Irregular Graphs,'' Technical Report 96-036, University of Minnesota.
[17] Knepley, M. G., Sarin, V., and Sameh, A. H., 1998. ''Parallel Simulation of Particulate Flows,'' *Proc. of the 5th Intl. Symp., IRREGULAR '98*, LNCS 1457, Springer, Berlin, pp. 226–237.

K. Stein
Department of Physics,
Bethel College,
St. Paul, MN 55112

T. Tezduyar

V. Kumar

S. Sathe

Mechanical Engineering,
Rice University,
MS 321,
Houston, TX 77005

R. Benney
Natick Soldier Center,
Natick, MA 01760

E. Thornburg

C. Kyle

U.S. Military Academy,
West Point, NY 10996

T. Nonoshita
Nepon, Inc.,
Kanagawa, Japan

Aerodynamic Interactions Between Parachute Canopies

Aerodynamic interactions between parachute canopies can occur when two separate parachutes come close to each other or in a cluster of parachutes. For the case of two separate parachutes, our computational study focuses on the effect of the separation distance on the aerodynamic interactions, and also focuses on the fluid-structure interactions with given initial relative positions. For the aerodynamic interactions between the canopies of a cluster of parachutes, we focus on the effect of varying the number and arrangement of the canopies. [DOI: 10.1115/1.1530634]

1 Introduction

The performance of a parachute might be influenced by the aerodynamic and fluid-structure interactions of its canopy with other parachute canopies. In this paper, we describe our computational model for such interactions, and present numerical results from simulations for two different types of interactions. In the first case, our investigation focuses on the aerodynamic and fluid-structure interactions between the canopies of two separate parachutes coming close to each other. We study how the aerodynamic interactions depend on the horizontal distance between the parachutes. We also study how such interactions are influenced when our computational model includes the fluid-structure interactions (FSI) between the parachute canopy and the surrounding flow field. For this, we start with given initial relative positions. In the second case, we investigate the aerodynamic interactions between the canopies of a cluster of parachutes. We simulate the interactions for clusters with three, four, five, and six canopies, and investigate how such interactions depend on the number of canopies as well as the spatial arrangement of these canopies.

These simulations, in addition to providing some initial results for the aerodynamic and fluid-structure interactions between parachute canopies, show how the computational methods described can be used for parachute applications. The interaction between the parachute canopy and the surrounding flow field is an essential component of a realistic parachute simulation, and thus the ability to predict parachute FSI is recognized as an important challenge within the parachute research community, [1–5]. In our follow-on studies, we plan to take more extensively into account the complex FSI involved at various stages of parachute systems, from initial deployment to landing.

For the cases simulated in this paper, the parachutes are operating at sufficiently low speeds, and, therefore, the aerodynamics is governed by the Navier-Stokes equations of incompressible flows. For the problems where we limit our attention to the aerodynamic interaction between the parachute canopies, the canopies are not experiencing any shape changes or relative motions. Therefore, in those simulations, the fluid dynamics computations are based on a stabilized semi-discrete finite element formulation, [6]. For the cases that involve fluid-structure interactions, on the other hand, the canopies undergo shape changes. In such cases, because the spatial domain occupied by the fluid is varying (i.e., deforming) with respect to time, we use the Deforming-Spatial-Domain/Stabilized Space-Time (DSD/SST) formulation, [6–8], which was developed for flow problems with moving boundaries and interfaces. Both the semi-discrete and space-time methods have been implemented for parallel computing, and the results presented here are from simulations carried out on a CRAY T3E-1200 supercomputer.

2 Computational Model

2.1 Fluid Dynamics. Let $\Omega_t \subset \mathbb{R}^{n_{sd}}$ be the spatial fluid mechanics domain with boundary Γ_t at time $t \in (0,T)$, where the

---

Contributed by the Applied Mechanics Division of THE AMERICAN SOCIETY OF MECHANICAL ENGINEERS for publication in the ASME JOURNAL OF APPLIED MECHANICS. Manuscript received by the ASME Applied Mechanics Division, Aug. 23, 2001; final revision, Mar. 18, 2002. Associate Editor: W. T. Wheeler. Discussion on the paper should be addressed to the Editor, Prof. Robert M. McMeeking, Department of Mechanical and Environmental Engineering University of California–Santa Barbara, Santa Barbara, CA 93106-5070, and will be accepted until four months after final publication of the paper itself in the ASME JOURNAL OF APPLIED MECHANICS.

subscript t indicates the time-dependence of the spatial domain and its boundary. The Navier-Stokes equations of incompressible flows can be written on Ω_t and $\forall t \in (0,T)$ as

$$\rho\left(\frac{\partial \mathbf{u}}{\partial t}+\mathbf{u}\cdot\boldsymbol{\nabla}\mathbf{u}-\mathbf{f}\right)-\boldsymbol{\nabla}\cdot\boldsymbol{\sigma}=0, \tag{1}$$

$$\boldsymbol{\nabla}\cdot\mathbf{u}=0, \tag{2}$$

where ρ, $\mathbf{u}$, and $\mathbf{f}$ are the density, velocity, and the external force, respectively. The stress tensor $\boldsymbol{\sigma}$ is defined as

$$\boldsymbol{\sigma}(p,\mathbf{u})=-p\mathbf{I}+2\mu\boldsymbol{\varepsilon}(\mathbf{u}). \tag{3}$$

Here p, $\mathbf{I}$, and μ are the pressure, identity tensor, and the viscosity, respectively. The strain rate tensor is defined as

$$\boldsymbol{\varepsilon}(\mathbf{u})=\frac{1}{2}((\boldsymbol{\nabla}\mathbf{u})+(\boldsymbol{\nabla}\mathbf{u})^T). \tag{4}$$

Both Dirichlet and Neumann-type boundary conditions are accounted for:

$$\mathbf{u}=\mathbf{g}\ \text{ on }\ (\Gamma_t)_g, \quad \mathbf{n}\cdot\boldsymbol{\sigma}=\mathbf{h}\ \text{ on }\ (\Gamma_t)_h. \tag{5}$$

Here $(\Gamma_t)_g$ and $(\Gamma_t)_h$ are complementary subsets of the boundary Γ_t, $\mathbf{n}$ is the unit normal vector at the boundary, and $\mathbf{g}$ and $\mathbf{h}$ are given functions. A divergence-free velocity field is specified as the initial condition.

2.2 Structural Dynamics. Let $\Omega_t^s \subset \mathbb{R}^{n_{xd}}$ be the spatial domain bounded by Γ_t^s, where $n_{xd}=2$ for membranes and $n_{xd}=1$ for cables. The boundary Γ_t^s is composed of $(\Gamma_t^s)_g$ and $(\Gamma_t^s)_h$. Here, the superscript "s" corresponds to the structure. The equations of motion for the structural system are

$$\rho^s\left(\frac{d^2\mathbf{y}}{dt^2}+\eta\frac{d\mathbf{y}}{dt}-\mathbf{f}^s\right)-\boldsymbol{\nabla}\cdot\boldsymbol{\sigma}^s=\mathbf{0}, \tag{6}$$

where $\mathbf{y}$ is the displacement, ρ^s is the material density, $\mathbf{f}^s$ are the external body forces, $\boldsymbol{\sigma}^s$ is the Cauchy stress tensor, and η is the mass-proportional damping coefficient. The damping provides additional stability and is used for problems where time accuracy is not important.

We use a total Lagrangian formulation of the problem. Thus, stresses are expressed in terms of the second Piola-Kirchoff stress tensor $\mathbf{S}$, which is related to the Cauchy stress tensor through a kinematic transformation. Under the assumption of large displacements and rotations, small strains, and no material damping, the membranes and cables are treated as Hookean materials with linear elastic properties. For membranes, under the assumption of plane stress, $\mathbf{S}$ becomes

$$S^{ij}=(\overline{\lambda}_m G^{ij}G^{kl}+\mu_m[G^{il}G^{jk}+G^{ik}G^{jl}])E_{kl}, \tag{7}$$

where for the case of isotropic plane stress

$$\overline{\lambda}_m=\frac{2\lambda_m\mu_m}{(\lambda_m+2\mu_m)}. \tag{8}$$

Here, E_{kl} are the components of the Cauchy-Green strain tensor, G^{ij} are the components of the contravariant metric tensor in the original configuration, and λ_m and μ_m are Lamé constants. For cables, under the assumption of uniaxial tension, $\mathbf{S}$ becomes

$$S^{11}=E_c G^{11}G^{11}E_{11}, \tag{9}$$

where E_c is the cable Young's modulus. To account for stiffness-proportional material damping, the Hookean stress-strain relationships defined by Eqs. (7) and (9) are modified, and E_{kl} is replaced by $\hat{E}_{kl}$, where

$$\hat{E}_{kl}=E_{kl}+\zeta\dot{E}_{kl}. \tag{10}$$

Here, ζ is the stiffness proportional damping coefficient and $\dot{E}_{kl}$ is the time derivative of E_{kl}.

2.3 Semi-Discrete Formulation of Fluid Dynamics. Let us consider a fixed spatial domain Ω and its boundary Γ, where subscript t is dropped from both Ω_t and Γ_t. The domain Ω is discretized into subdomains Ω^e, $e=1,2,\cdots,n_{el}$, where n_{el} is the number of elements. For this discretization, the finite element trial function spaces $\mathcal{S}_u^h$ for velocity and $\mathcal{S}_p^h$ for pressure, and the corresponding test function spaces $\mathcal{V}_u^h$ and $\mathcal{V}_p^h$ are defined as follows:

$$\mathcal{S}_u^h=\{\mathbf{u}^h|\mathbf{u}^h\in[H^{1h}(\Omega)]^{n_{sd}},\mathbf{u}^h\doteq\mathbf{g}^h\ \text{ on }\ \Gamma_g\}, \tag{11}$$

$$\mathcal{V}_u^h=\{\mathbf{w}^h|\mathbf{w}^h\in[H^{1h}(\Omega)]^{n_{sd}},\mathbf{w}^h\doteq\mathbf{0}\ \text{ on }\ \Gamma_g\}, \tag{12}$$

$$\mathcal{S}_p^h=\mathcal{V}_p^h=\{q^h|q^h\in H^{1h}(\Omega)\}. \tag{13}$$

Here $H^{1h}(\Omega)$ is the finite-dimensional function space over Ω. The stabilized formulation is written as follows: Find $\mathbf{u}^h\in\mathcal{S}_{\mathbf{u}}^h$ and $p^h\in\mathcal{S}_p^h$ such that $\forall\mathbf{w}^h\in\mathcal{V}_{\mathbf{u}}^h$ and $q^h\in\mathcal{V}_p^h$:

$$\begin{aligned}
&\int_\Omega \mathbf{w}^h\cdot\rho\left(\frac{\partial\mathbf{u}^h}{\partial t}+\mathbf{u}^h\cdot\boldsymbol{\nabla}\mathbf{u}^h-\mathbf{f}^h\right)d\Omega\\
&\quad+\int_\Omega\boldsymbol{\varepsilon}(\mathbf{w}^h):\boldsymbol{\sigma}(p^h,\mathbf{u}^h)d\Omega-\int_{\Gamma_h}\mathbf{w}^h\cdot\mathbf{h}^h d\Gamma\\
&\quad+\int_\Omega q^h\boldsymbol{\nabla}\cdot\mathbf{u}^h d\Omega\\
&\quad+\sum_{e=1}^{n_{el}}\int_{\Omega^e}\frac{1}{\rho}[\tau_{\text{SUPG}}\rho\mathbf{u}^h\cdot\nabla\mathbf{w}^h+\tau_{\text{PSPG}}\nabla q^h]\\
&\quad\times[\text{Ł}(p^h,\mathbf{u}^h)-\rho\mathbf{f}^h]d\Omega\\
&\quad+\sum_{e=1}^{n_{el}}\int_{\Omega^e}\tau_{\text{LSIC}}\boldsymbol{\nabla}\cdot\mathbf{w}^h\rho\boldsymbol{\nabla}\cdot\mathbf{u}^h d\Omega=0,
\end{aligned} \tag{14}$$

where

$$\text{Ł}(q^h,\mathbf{w}^h)=\rho\left(\frac{\partial\mathbf{w}^h}{\partial t}+\mathbf{u}^h\cdot\boldsymbol{\nabla}\mathbf{w}^h\right)-\boldsymbol{\nabla}\cdot\boldsymbol{\sigma}(q^h,\mathbf{w}^h). \tag{15}$$

In this formulation, τ_{SUPG}, τ_{PSPG}, and τ_{LSIC} are the stabilization parameters, [6,9].

2.4 DSD/SST Formulation of Fluid Dynamics. In discretization of the space-time domain, the time interval $(0,T)$ is partitioned into subintervals $I_n=(t_n,t_{n+1})$, where t_n and t_{n+1} belong to an ordered series of time levels $0=t_0<t_1\cdots<t_N=T$. Let $\Omega_n=\Omega_{t_n}$ and $\Gamma_n=\Gamma_{t_n}$ to simplify the notation. The space-time slab Q_n is defined as the domain enclosed by the surfaces Ω_n, Ω_{n+1}, and P_n, where P_n is the lateral surface of Q_n described by the boundary Γ_n as t traverses I_n.

The Dirichlet and Neumann-type boundary conditions are specified over $(P_n)_g$ and $(P_n)_h$. For this discretization, the finite element trial function spaces $(\mathcal{S}_{\mathbf{u}}^h)_n$ for velocity and $(\mathcal{S}_p^h)_n$ for pressure, and the corresponding test function spaces $(\mathcal{V}_{\mathbf{u}}^h)_n$ and $(\mathcal{V}_p^h)_n$ are defined as follows:

$$(\mathcal{S}_{\mathbf{u}}^h)_n=\{\mathbf{u}^h|\mathbf{u}^h\in[H^{1h}(Q_n)]^{n_{sd}},\mathbf{u}^h\doteq\mathbf{g}^h\ \text{ on }\ (P_n)_g\}, \tag{16}$$

$$(\mathcal{V}_{\mathbf{u}}^h)_n=\{\mathbf{w}^h|\mathbf{w}^h\in[H^{1h}(Q_n)]^{n_{sd}},\mathbf{w}^h\doteq\mathbf{0}\ \text{ on }\ (P_n)_g\}, \tag{17}$$

$$(\mathcal{S}_p^h)_n=(\mathcal{V}_p^h)_n=\{q^h|q^h\in H^{1h}(Q_n)\}. \tag{18}$$

Here $H^{1h}(Q_n)$ is the finite-dimensional function space over the space-time slab Q_n. Over the element domain, this space is formed by using first-order polynomials in both space and time. The interpolation functions are continuous in space but discontinuous in time.

The DSD/SST formulation is written as follows: Given $(\mathbf{u}^h)_n^-$, find $\mathbf{u}^h\in(\mathcal{S}_{\mathbf{u}}^h)_n$ and $p^h\in(\mathcal{S}_p^h)_n$ such that $\forall\mathbf{w}^h\in(\mathcal{V}_{\mathbf{u}}^h)_n$ and $q^h\in(\mathcal{V}_p^h)_n$:

$$\int_{Q_n}\mathbf{w}^h\cdot\rho\left(\frac{\partial\mathbf{u}^h}{\partial t}+\mathbf{u}^h\cdot\boldsymbol{\nabla}\mathbf{u}^h-\mathbf{f}^h\right)dQ$$

$$+\int_{Q_n}\boldsymbol{\varepsilon}(\mathbf{w}^h):\boldsymbol{\sigma}(p^h,\mathbf{u}^h)dQ-\int_{(P_n)_h}\mathbf{w}^h\cdot\mathbf{h}^h dP$$

$$+\int_{Q_n}q^h\boldsymbol{\nabla}\cdot\mathbf{u}^h dQ$$

$$+\int_{\Omega_n}(\mathbf{w}^h)_n^+\cdot\rho((\mathbf{u}^h)_n^+-(\mathbf{u}^h)_n^-)d\Omega$$

$$+\sum_{e=1}^{(n_{el})_n}\int_{Q_n^e}\frac{\tau_{\mathrm{LSME}}}{\rho}\boldsymbol{\mathcal{L}}(q^h,\mathbf{w}^h)\cdot$$

$$[\boldsymbol{\mathcal{L}}(p^h,\mathbf{u}^h)-\rho\mathbf{f}^h]dQ$$

$$+\sum_{e=1}^{n_{el}}\int_{Q_n^e}\tau_{\mathrm{LSIC}}\boldsymbol{\nabla}\cdot\mathbf{w}^h\rho\boldsymbol{\nabla}\cdot\mathbf{u}^h dQ=0. \tag{19}$$

This formulation is sequentially applied to all space-time slabs $Q_0, Q_1, Q_2, \ldots, Q_{N-1}$. The computation starts with

$$(\mathbf{u}^h)_0^-=\mathbf{u}_0, \quad \boldsymbol{\nabla}\cdot\mathbf{u}_0=0 \quad \text{on } \Omega_0. \tag{20}$$

Here τ_{LSME} is the stabilization parameter (see [9,10]). For an earlier, detailed reference on this formulation see [6].

2.5 Structural Dynamics Formulation. The semi-discrete finite element formulation for the structural dynamics is based on the principle of virtual work:

$$\int_{\Omega_0^s}\rho^s\frac{d^2\mathbf{y}^h}{dt^2}\cdot\mathbf{w}^h d\Omega^s+\int_{\Omega_0^s}\eta\rho^s\frac{d\mathbf{y}^h}{dt}\cdot\mathbf{w}^h d\Omega^s+\int_{\Omega_0^s}\mathbf{S}^h:\delta\mathbf{E}(\mathbf{w}^h)d\Omega^s$$

$$=\int_{\Omega_t^s}(\mathbf{t}+\rho^s\mathbf{f}^s)\cdot\mathbf{w}^h d\Omega^s. \tag{21}$$

Here the weighting function $\mathbf{w}^h$ is also the virtual displacement. The air pressure force on the canopy surface is represented by vector $\mathbf{t}$. The pressure term is a "follower force" (since it "follows" the deforming structural geometry) and thus increases the overall nonlinearity of the formulation. The left-hand-side terms of Eq. (21) are referred to in the original configuration and the right-hand-side terms for the deformed configuration at time t.

Upon discretization using appropriate function spaces, a nonlinear system of equations is obtained at each time-step. In solving that nonlinear system with an iterative method, we use the following incremental form:

$$\left[\frac{\mathbf{M}}{\beta\Delta t^2}+\frac{(1-\alpha)\gamma\mathbf{C}}{\beta\Delta t}+(1-\alpha)\mathbf{K}\right]\Delta\mathbf{d}^i=\mathbf{R}^i, \tag{22}$$

where

$$\mathbf{C}=\eta\mathbf{M}+\zeta\mathbf{K}. \tag{23}$$

Here $\mathbf{M}$ is the mass matrix, $\mathbf{K}$ is the consistent tangent matrix associated with the internal elastic forces, $\mathbf{C}$ is a damping matrix, $\mathbf{R}^i$ is the residual vector at the ith iteration, and $\Delta\mathbf{d}^i$ is the ith increment in the nodal displacements vector $\mathbf{d}$. In Eq. (22), all of the terms known from the previous iteration are lumped into the residual vector $\mathbf{R}^i$. The parameters α, β, γ are part of the Hilber-Hughes-Taylor, [11], scheme, which is used here for time-integration.

2.6 Mesh Update Method. How the mesh should be updated depends on several factors, such as the complexity of the moving boundary or interface and overall geometry, how unsteady the moving boundary or interface is, and how the starting mesh was generated. In general, the mesh update could have two components: moving the mesh for as long as it is possible, and full or partial remeshing (i.e., generating a new set of elements, and sometimes also a new set of nodes) when the element distortion becomes too high.

In mesh moving strategies, the only rule the mesh motion needs to follow is that at the moving boundary or interface the normal velocity of the mesh has to match the normal velocity of the fluid. Beyond that, the mesh can be moved in any way desired, with the main objective being to reduce the frequency of remeshing. In three-dimensional simulations, if the remeshing requires calling an automatic mesh generator, the cost of automatic mesh generation becomes a major reason for trying to reduce the frequency of remeshing. Furthermore, when we remesh, we need to project the solution from the old mesh to the new one. This introduces projection errors. Also, in three-dimensional, the computing time consumed by this projection step is not a trivial one. All these factors constitute a strong motivation for designing mesh update strategies which minimize the frequency of remeshing.

In some cases where the changes in the shape of the computational domain allow it, a special-purpose mesh moving method can be used in conjunction with a special-purpose mesh generator. In such cases, simulations can be carried out without calling an automatic mesh generator and without solving any additional equations to determine the motion of the mesh. One of the earliest examples of that, two-dimensional computation of sloshing in a laterally vibrating container, can be found in [6]. Extension of that concept to three-dimensional parallel computation of sloshing in a vertically vibrating container can be found in [12].

In general, however, we use an automatic mesh moving scheme, [13], to move the nodal points, as governed by the equations of linear elasticity, and where the smaller elements enjoy more protection from mesh deformation. The motion of the internal nodes is determined by solving these additional equations, with the boundary conditions for these mesh motion equations specified in such a way that they match the normal velocity of the fluid at the interface. In computation of fluid-structure interactions of parachute systems reported here we use this automatic mesh moving technique.

3 Numerical Examples

For fluid dynamics equations we use tetrahedral meshes. The parachute canopy surface is representative of a C-9 parachute for cases with only aerodynamic interactions, and a T-10 parachute for cases with fluid-structure interactions. In simulation of the aerodynamic interactions between two parachutes, the parachute model consists of the canopy and a paratrooper. For the fluid-structure interactions of two parachutes and for the aerodynamic interactions in clusters of parachutes, we only consider the canopies. Figure 1 shows the parachute canopy surface mesh and and the paratrooper. The simulations are carried out at a Reynolds number (based on the canopy diameter) of approximately 5 million.

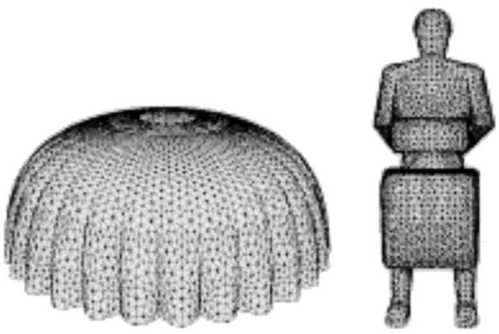

Fig. 1 Aerodynamic interactions of two parachutes. Parachute canopy (left), paratrooper (right).

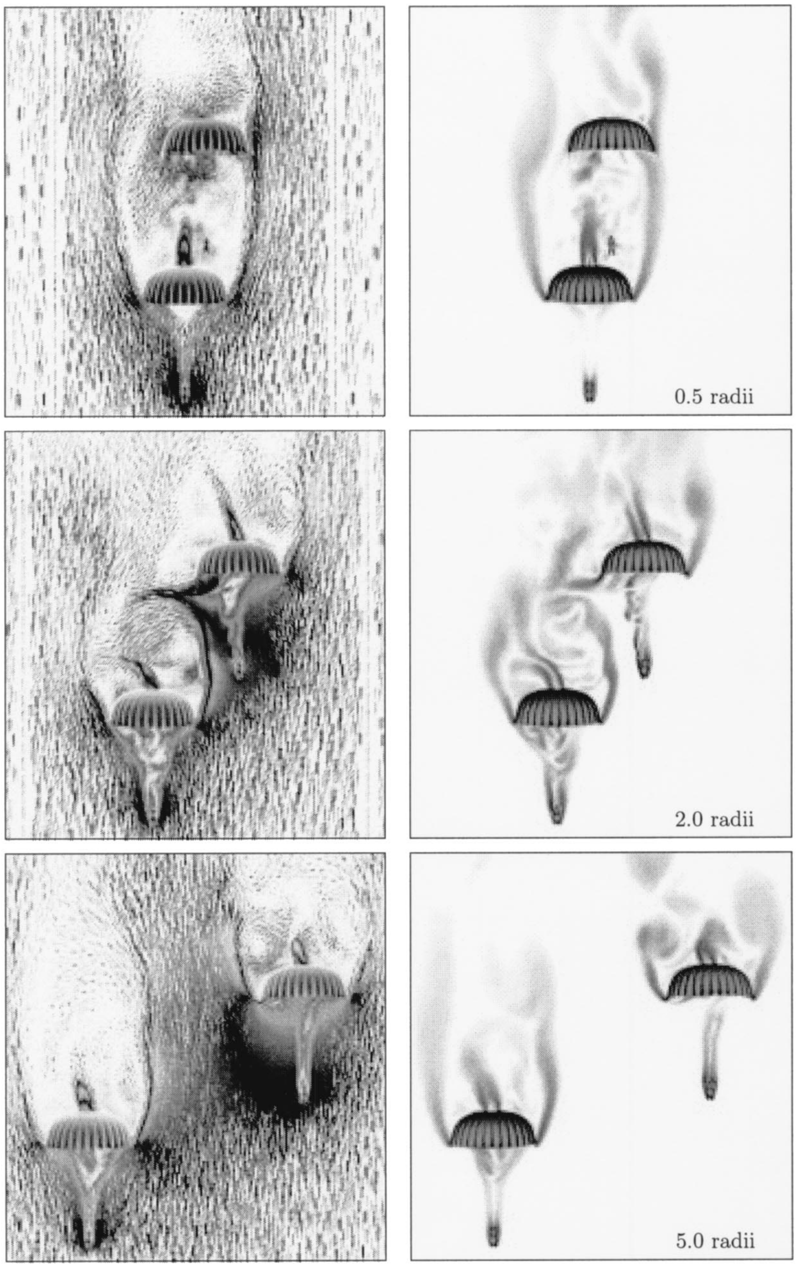

Fig. 2 Aerodynamic interactions of two parachutes. Velocity (left), vorticity (right).

3.1 Aerodynamic Interactions of Two Parachutes. A series of simulations are carried out for the aerodynamic interactions between two separate parachutes, where each parachute consists of a round canopy and a paratrooper. The horizontal spacings, defined to be along the x-axis, range from zero to five (inflated) parachute radii. Vertical spacings are held constant at approximately 3.3 feet between the apex of the lower canopy and the feet of the paratrooper. The parachute model is representative of a 28-foot diameter and 28-gore C-9 personnel parachute. Representation of the canopy geometry comes from a separate structural dynamics simulation with a prescribed pressure distribution. Surface representations for the paratrooper and other boundaries in the fluid dynamics model are obtained using a variety of in-house modeling tools. Separate unstructured volume meshes are generated for each case studied. For each of the examples, the two paratrooper and canopy systems are identical, with 8288 triangular faces describing both the upper and lower canopy surfaces, and 11,714 triangular faces representing the paratrooper. The size of the volume meshes varies from case to case. For the case with horizontal spacing of 0.5 radii, we have approximately 1.8 million elements and 300,000 nodes, resulting in approximately 1.2 million coupled equations. In each of the meshes, the mesh refinement is controlled around the paratroopers and canopies and in the wake and interaction regions, so that we have a larger concentration of elements in these regions. Descent velocities of 22 ft/s are represented by imposing a uniform upstream boundary condition at the lower boundary. Other boundary conditions are, no-slip conditions on the paratrooper and canopy surfaces, zero normal velocity and zero shear stress conditions at the side boundaries, and traction-free conditions at the outflow boundary.

The simulations show a strong, adverse interaction between the upper and lower parachutes for spacings of 1.0 radius and less. In these cases, the upper canopy ‘‘loses its wind,’’ and experiences negative drag for spacings of 0.5 radii and less. This indicates a

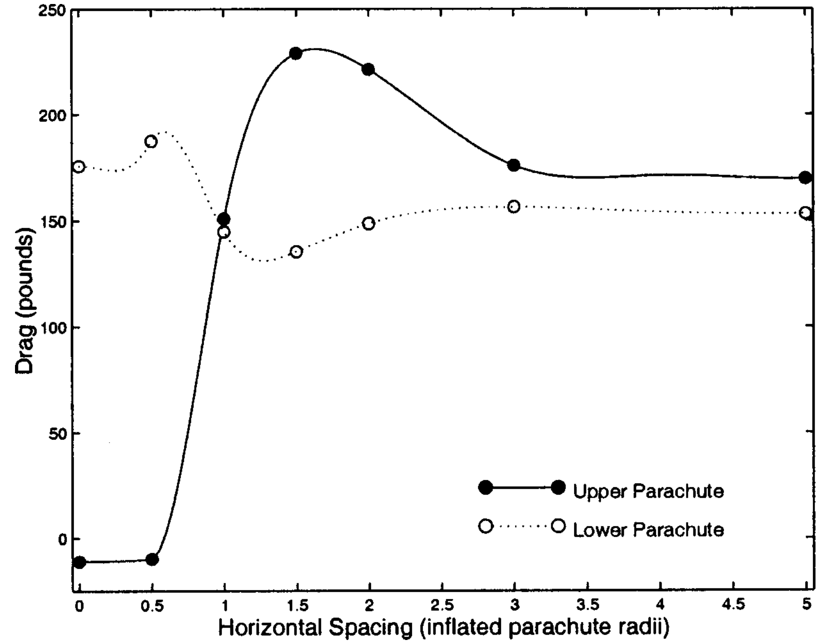

Fig. 3 Aerodynamic interactions of two parachutes. Influence of horizontal spacing on drag, *D*.

potential for parachute collapse. The flow fields for horizontal spacings of 0.5, 2.0, and 5.0 radii are shown in Fig. 2, with the velocity vectors on the left and the vorticity on the right. For horizontal spacing of 0.5 radii, we clearly see that the upper canopy is caught in the wake of the lower one. For horizontal spacing of 5.0 radii, on the other hand, very little interaction is seen between the two parachute flow fields. The 2.0 radii separation case shows a clear interaction between the two parachutes, but without the upper canopy being trapped in the wake of the lower one.

The interaction between the two parachutes for different horizontal spacings is further understood when we look at the aerodynamic forces acting on the individual canopies. Time-averaged force values were obtained for each horizontal spacing over equivalent time periods, and after the flow fields were fully established. Figure 3 shows, for the lower and upper canopies and for spacings ranging from 0.0 to 5.0 radii, the time-averaged drag (D). The forces shown in these figures are scaled from the computed values based on the C-9 physical dimensions, the prescribed descent velocity, and the air density (these scalings differ from the scaling that was initially presented, [14]). For both canopies, the drag values are fitted to a curve using cubic splines and assuming that the curve (a) is symmetric at zero horizontal spacing and (b) approaches a constant value as the horizontal spacing becomes

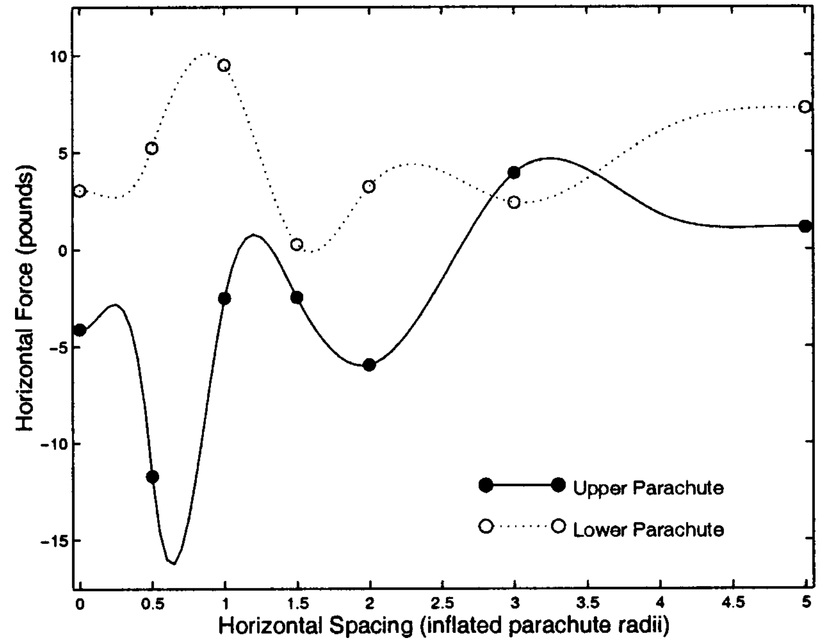

Fig. 4 Aerodynamic interactions of two parachutes. Influence of horizontal spacing on F_x.

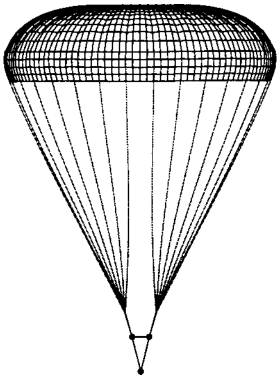

Fig. 5 Fluid-structure interactions of two parachutes. T-10 parachute structural model.

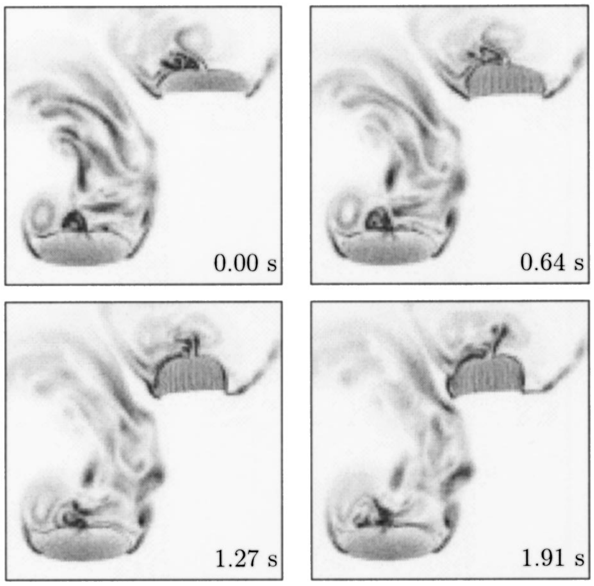

Fig. 6 Fluid-structure interactions of two parachutes. Vorticity at four instants.

large. At large horizontal spacings, the drag for the lower canopy is expected to approach the same value as the drag for the upper canopy. We see that the drag on the upper parachute can become negative for severe interactions between the parachutes, such as for spacing of 0.5 radii and less. For the 2.0 radii separation case, the drag on the upper canopy remains positive. However, in this case there is a clear interaction between the two parachutes, which could possibly lead to severe structural responses in the fluid-structure interactions of the upper parachute. For the 5.0 radii separation, minimal interaction is seen in the drag history plots, with minor difference in drag for the two parachutes. The proximity of the parachutes to the side and outflow boundaries has some role in the presence of these differences. Extending the boundaries further out and carrying out the computations further in time would make the differences in the time-averaged values of D for the two parachutes even smaller.

Figure 4 shows the time-averaged values of the horizontal force component, F_x. Again, the force histories are fitted to a curve using cubic splines to only show the qualitative trends for the horizontal forces acting on the two parachutes as function of their horizontal separation. For cases with no interaction between the two canopies, the average value of F_x is expected to be zero. The horizontal forces acting on the two canopies are mostly attractive, and are more substantially so for spacings of 2.0 radii and less. For the spacings of 3.0 radii and more, the interaction becomes less evident and the difference between F_x for the upper and lower canopies begins to decrease. The flow field in the wake of each parachute is very unsteady and shows no discernible time-periodic behavior. For these larger spacings, extending the boundaries further out and carrying out the computations further in time would bring the time-averaged values of F_x closer to zero.

3.2 Fluid-Structure Interactions of Two Parachutes. In this simulation, initially the two parachutes have a horizontal spacing of 42 ft, which is approximately 3 (inflated) radii, and a vertical spacing of 56 ft. Here, the parachute model is representative of a standard U.S. Army T-10 personnel parachute. The T-10 is a ‘‘flat extended skirt canopy’’ composed of a 35-foot diameter canopy and 30 suspension lines each 29.4 ft long. The canopy is called a ‘‘flat extended skirt canopy’’ because in its constructed (or unstressed) configuration it is composed of a main circular section with a circular vent at the apex and an inverted flat ring section, which lies under the main section and is connected to the main section at the outer radius. The lines connect to four risers which attach the payload (or paratrooper). The suspension lines continue as 30 gore-to-gore reinforcements through the parachute canopy and meet at the apex. For the T-10, the vent diameter and the skirt width are both 3.5 ft.

Here the lower canopy is treated as a rigid body, while the upper canopy is allowed to deform due to the response of the parachute structure to the fluid dynamics forces. The structural dynamics model is divided into six distinct material groups; a membrane group, three cable groups, a truss group, and a concentrated mass group. The parachute canopy is composed of 780 biquadratic membrane elements. We have distinct cable groups for the suspension lines, the canopy radial reinforcements, and the risers. The truss and concentrated mass groups define the payload, which has a total weight of 250 pounds. The structure is allowed to fall completely unconstrained.

The parachute canopies are represented as interior surfaces in the fluid mesh (with 17,490 triangular faces on both the upper and

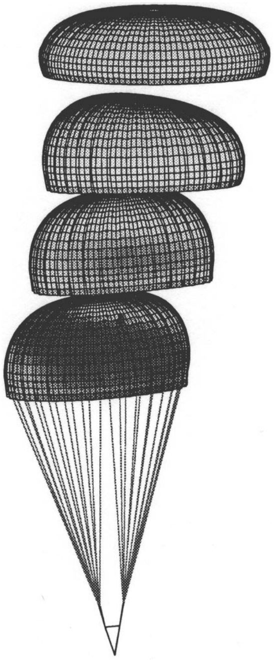

Fig. 7 Fluid-structure interactions of two parachutes. Structural motion and differential pressure distribution at $t=0.00$, 0.64, 1.27, and 1.91 seconds.

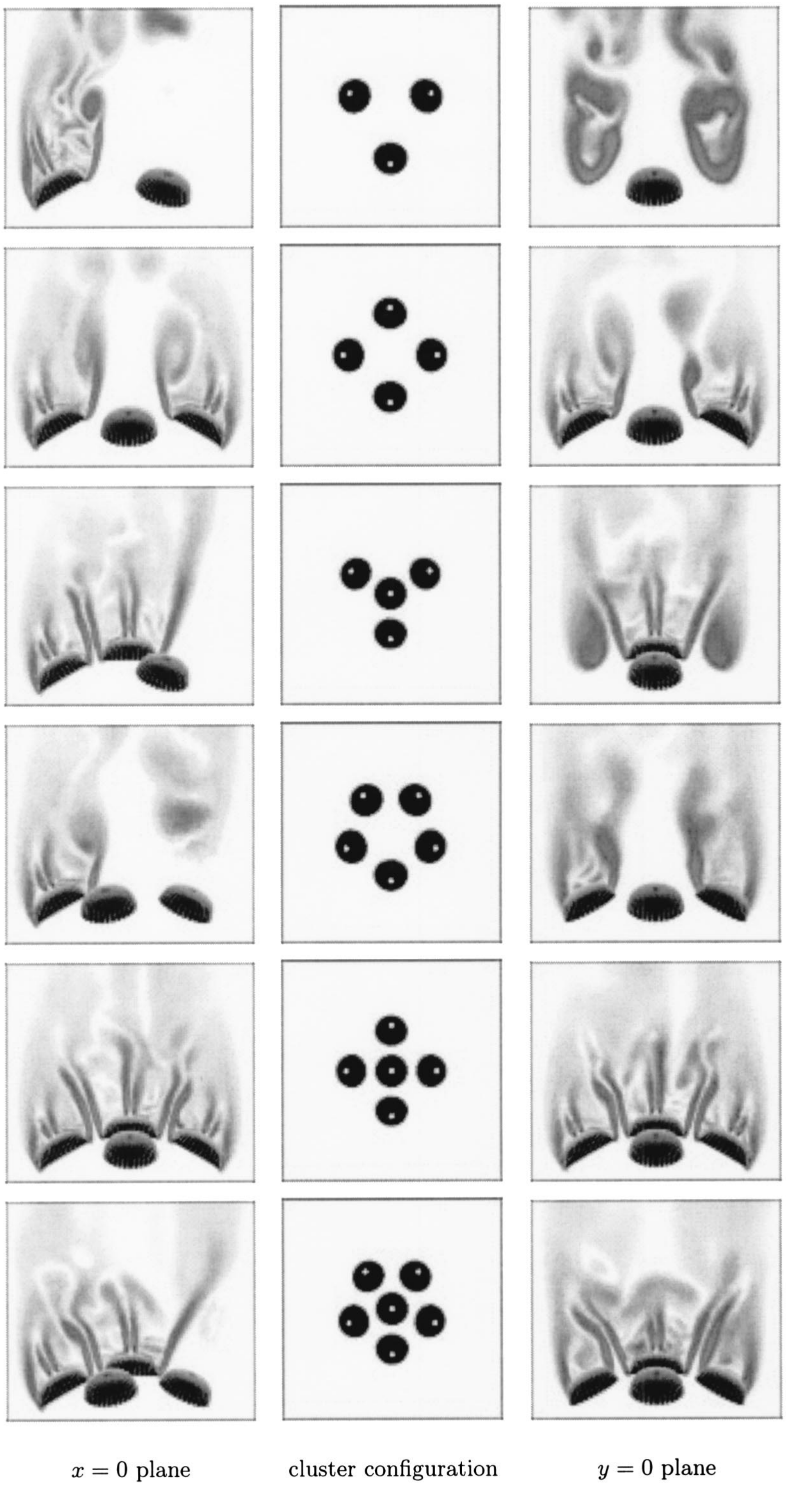

Fig. 8 Aerodynamic interactions in parachute clusters. Vorticity.

lower canopy surfaces). The typical size of the volume mesh is approximately 3.5 million elements and 580 thousand nodes, resulting in approximately 4.6 million coupled equations with the DSD/SST formulation. The automatic mesh update method described earlier is employed to handle the canopy shape changes, with occasional remeshing of the fluid domain. The surface for the upper canopy is assigned a no-slip boundary condition, with velocities coming from the structural dynamics solution. The boundary conditions for the lower canopy and at the outer boundaries are identical to the conditions used in the previous example.

The coupling is achieved iteratively, by transferring the information between the fluid and structure with a least-squares projection. Figure 5 shows the parachute structural model used at the start of the simulation.

Figure 6 shows, at four instants during the simulation, the vorticity field surrounding the two parachutes. The deformation and motion of the upper canopy is evident. Figure 7 shows, at the same four instants, the structural dynamics of the upper parachute.

3.3 Aerodynamic Interactions in Parachute Clusters. A series of simulations are carried out for the aerodynamic interactions between the canopies in a cluster of parachutes, for three to six canopies. For these simulations, the parachute model is represented by a set of identical C-9 canopies that are positioned and oriented relative to a prescribed confluence point. Two types of configurations are prescribed. First, 3, 4, and 5-canopy clusters are defined with the canopies uniformly distributed at a prescribed angle about the azimuthal axis. Secondly, 4, 5, and 6-canopy clusters are defined with a single canopy in the center and the remaining canopies distributed uniformly at a prescribed angle about the azimuthal axis. The size of the volume mesh varies from case to case. For the 5-canopy cluster with a parachute in the center, we have approximately 2.5 million elements and 450,000 nodes, resulting in approximately 1.9 million coupled equations. Mesh refinement is controlled around the canopies and in the wake and interaction regions. As with the previous example, descent velocities of 22.0 ft/s are represented by imposing a uniform upstream boundary condition at the lower boundary, and no-slip conditions are imposed on the canopy surfaces.

The computed flow fields at the end of the simulations from these preliminary simulations are shown in Fig. 8, with the cluster configurations in the middle column and the corresponding vorticity magnitudes in two cutting planes ($x=0$ and $y=0$) in the left and right columns. These initial simulations qualitatively demonstrate the interactions between the canopies in different cluster arrangements. Further analysis is needed to better understand the other effects influencing the interactions in clusters, such as the preferred arrangements for the canopies, blockage effects due to the finite computational domain, and ultimately the FSI effects. For the examples presented, blockage effects are evident and increase with the number of canopies in the cluster. Experimental studies have been conducted to provide empirical correction factors for blockage effects, [15]. However, these data are dependent on the type of parachute, FSI, and other factors. Further simulations are now being carried out to numerically obtain correction factors for the cases studied.

Additionally, the examples presented neglect the structural response between the canopies in the clusters. The DSD/SST method is now being used to study the dynamics interactions between the canopies in the cluster, treating the individual canopies as rigid bodies. Numerical simulations, [16], have been conducted previously to predict the equilibrium configuration for clusters of three half-scale C-9 parachutes in comparison with experimental data, [17]. In these simulations, equilibrium configurations were determined using a quasi-static approach and imposing a symmetry configuration for the three canopies. The DSD/SST formulation, along with an appropriate mesh-update strategy, allows us to study the interaction of canopies in a cluster in a dynamic fashion. Follow-on simulations will be carried out to predict equilibrium configurations for the 3-canopy cluster with and without an imposed symmetry. Additional simulations will be carried out to study the interactions for the 4, 5, and 6-canopy clusters. Initially, these studies will treat the canopies as rigid bodies, with later simulations including FSI effects.

4 Concluding Remarks

We have described our computational methods for simulation of aerodynamic and fluid-structure interactions between parachute canopies. We considered two different types of problems. In the first case, we focused on the aerodynamic and fluid-structure interactions between the canopies of two separate parachutes in close proximity to one another. We studied the dependence of the aerodynamic interactions on the horizontal distance separating the two parachutes. In this study we observed significant interactions when the horizontal spacing between the parachutes is two canopy radii or less. We also studied how the interactions between the two parachutes are influenced when we include in our computational model the fluid-structure interactions (FSI). The significant amount of structural response we observe in this study for the upper parachute makes it clear that the FSI play a key role in making this class of simulations more realistic. In the second case, we focused on the aerodynamic interactions between the canopies of a cluster of parachutes, and investigated the nature of these interactions for three, four, five, and six canopies. In this study, we were able to see the dependence of these interactions not only on the number of canopies but also on the spatial arrangement of these canopies.

This class of simulations can provide a better understanding of the interactions between parachute canopies and help identify the scenarios under which the interactions are most severe. In the cases of severe interactions, more sophisticated fluid-structure interaction models would be required to accurately represent the response of the parachute structure.

Acknowledgment

The work reported in this paper was partially sponsored by NASA JSC, AFOSR, and by the Natick Soldier Center.

References

[1] Peterson, C. W., Strickland, J. H., and Higuchi, H., 1996, ''The Fluid Dynamics of Parachute Inflation,'' Annu. Rev. Fluid Mech., **28**, pp. 361–387.

[2] Benney, R. J., and Stein, K. R., 1996, ''A Computational Fluid Structure Interaction Model for Parachute Inflation,'' J. Aircr., **33**, pp. 730–736.

[3] Stein, K. R., Benney, R. J., Kalro, V., Johnson, A. A., and Tezduyar, T. E., 1997, ''Parallel Computation of Parachute Fluid-Structure Interactions,'' AIAA Paper No. 97-1505.

[4] Stein, K., Benney, R., Kalro, V., Tezduyar, T., Leonard, J., and Accorsi, M., 1999, ''3-D Computation of Parachute Fluid-Structure Interactions: Performance and Control,'' AIAA Paper No. 99-1714.

[5] Ibos, C., Lacroix, C., Goy, A., and Bordenave, P., 1999, ''Fluid-Structure Simulation of 3D ram Air Parachute With Sinpa Software,'' AIAA Paper No. 99-1713.

[6] Tezduyar, T. E., 1991, ''Stabilized Finite Element Formulations for Incompressible Flow Computations,'' Adv. Appl. Mech., **28**, pp. 1–44.

[7] Tezduyar, T. E., Behr, M., and Liou, J., 1992, ''A New Strategy for Finite Element Computations Involving Moving Boundaries and Interfaces—The Deforming-Spatial-Domain/Space-Time Procedure: I. The Concept and the Preliminary Tests,'' Comput. Methods Appl. Mech. Eng., **94**, pp. 339–351.

[8] Tezduyar, T. E., Behr, M., Mittal, S., and Liou, J., 1992, ''A New Strategy for Finite Element Computations Involving Moving Boundaries and Interfaces—The Deforming-Spatial-Domain/Space-Time Procedure: II. Computation of Free-Surface Flows, Two-Liquid Flows, and Flows With Drifting Cylinders,'' Comput. Methods Appl. Mech. Eng., **94**, pp. 353–371.

[9] Tezduyar, T. E., and Osawa, Y., 1999, ''Methods for parallel computation of complex flow problems,'' Parallel Comput., **25**, pp. 2039–2066.

[10] Behr, M., and Tezduyar, T. E., 1994, ''Finite element solution strategies for large-scale flow simulations,'' Comput. Methods Appl. Mech. Eng., **112**, pp. 3–24.

[11] Hilber, H. M., Hughes, T. J. R., and Taylor, R. L., 1977, ''Improved Numerical Dissipation for Time Integration Algorithms in Structural Dynamics,'' Earthquake Eng. Struct. Dyn., **5**, pp. 283–292.

[12] Tezduyar, T., Aliabadi, S., Behr, M., Johnson, A., and Mittal, S., 1993, ''Parallel Finite-Element Computation of 3D Flows,'' IEEE Computer, **26**, pp. 27–36.

[13] Tezduyar, T. E., Behr, M., Mittal, S., and Johnson, A. A., 1992, ''Computation of Unsteady Incompressible Flows With the Finite Element Methods—Space-Time Formulations, Iterative Strategies and Massively Parallel Implementations,'' *New Methods in Transient Analysis*, P. Smolinski, W. K. Liu, G. Hulbert, and K. Tamma, eds. AMD-Vol.143, ASME, New York, pp. 7–24.

[14] Stein, K., Benney, R., Tezduyar, T., Kumar, V., Thornburg, E., Kyle, C., and Nonoshita, T., 2001, ''Aerodynamic Interaction Between Multiple Parachute Canopies,'' *Proceedings of the First MIT Conference on Computational Fluid and Solid Mechanics*, M.I.T. Press, Cambridge, MA.

[15] Macha, J. M., and Buffington, R. J., 1989, ''Wall-Interference Corrections for Parachutes in a Closed Wind Tunnel,'' AIAA Paper No. 89-0900.

[16] Sahu, J., and Benney, R., 1997, ''Prediction of Terminal Descent Characteristics of Parachute Clusters Using CFD,'' AIAA Paper No. 97-1453.

[17] Lee, C. K., Lanza, J., and Buckley, J., 1996, ''Apparatus and Method for Measuring Angular Positions of Parachute Canopies,'' J. Aircr., **33**, pp. 1197–1199.

K. Stein
Department of Physics,
Bethel College,
St. Paul, MN 55112

T. Tezduyar
Mechanical Engineering,
Rice University,
MS 321,
Houston, TX 77005

R. Benney
Natick Soldier Center,
Natick, MA 01760

Mesh Moving Techniques for Fluid-Structure Interactions With Large Displacements

In computation of fluid-structure interactions, we use mesh update methods consisting of mesh-moving and remeshing-as-needed. When the geometries are complex and the structural displacements are large, it becomes even more important that the mesh moving techniques are designed with the objective to reduce the frequency of remeshing. To that end, we present here mesh moving techniques where the motion of the nodes is governed by the equations of elasticity, with selective treatment of mesh deformation based on element sizes as well as deformation modes in terms of shape and volume changes. We also present results from application of these techniques to a set of two-dimensional test cases. [DOI: 10.1115/1.1530635]

1 Introduction

Computation of flows with fluid-structure interactions was one of the objectives in development of the Deforming-Spatial-Domain/Stabilized Space-Time (DSD/SST) formulation, [1–3], for flows with moving boundaries and interfaces. This is an interface-tracking technique, and as such requires that the mesh be updated to track the moving interfaces as the spatial domain occupied by the fluid is varying (i.e., deforming) with respect to time. In computations with the arbitrary Lagrangian-Eulerian method, which is another interface-tracking method, one faces the same requirement. In general, mesh update consists of moving the mesh for as long as it is possible, and full or partial remeshing (i.e., generating a new set of elements, and sometimes also a new set of nodes) when the element distortion becomes too high.

As the mesh moves, the normal velocity of the mesh at the interface has to match the normal velocity of the fluid. With this condition met, our main objective in designing a mesh update technique becomes reducing the remeshing frequency. This is very important in three-dimensional computations with complex geometries, because remeshing in such cases typically requires calling an automatic mesh generator and projecting the solution from the old mesh to the new one. Both of these steps involve large computational costs.

In selecting a category of mesh moving techniques, geometric complexity is one of the major determining factors. Sometimes the overall problem geometry, including the interface geometry, is simple enough so that the mesh can be generated by a special-purpose mesh generation technique. In such cases, the mesh can be updated by using a special-mesh moving technique, without calling an automatic mesh generator and without solving any additional equations to determine the motion of the mesh. This approach involves virtually no mesh update cost, and one of its earliest examples, two-dimensional computation of sloshing in a laterally vibrating container, can be found in [1].

In most practical problems, such as the parachute fluid-structure interactions, the overall problem geometry would be too complex to use a special-purpose mesh generation technique. The mesh produced with an automatic mesh generator would require an au-

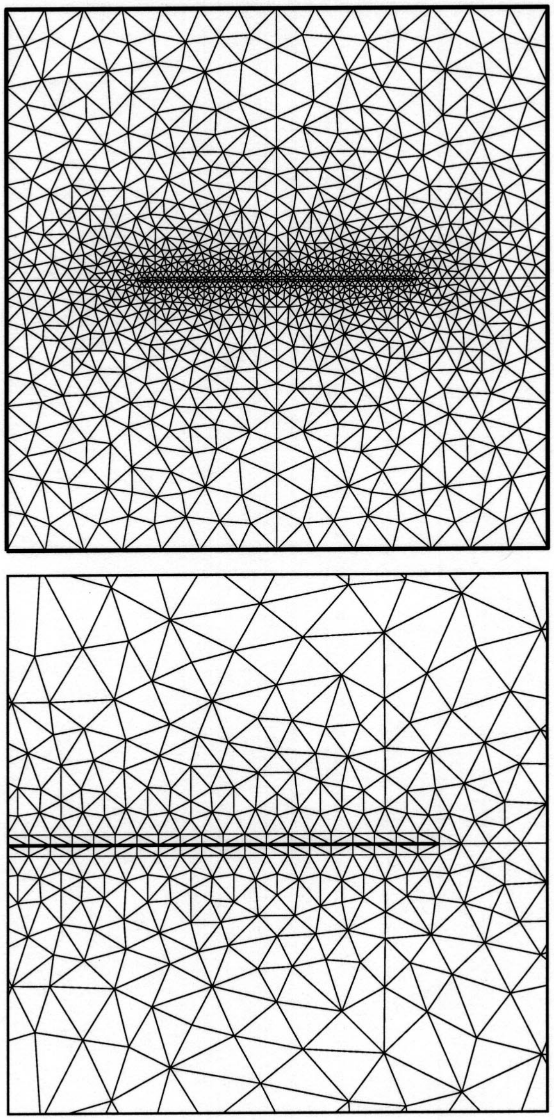

Fig. 1 Two-dimensional test mesh

Contributed by the Applied Mechanics Division of THE AMERICAN SOCIETY OF MECHANICAL ENGINEERS for publication in the ASME JOURNAL OF APPLIED MECHANICS. Manuscript received by the ASME Applied Mechanics Division, Dec. 4, 2001; final revision, Mar. 4, 2002. Associate Editor: L. T. Wheeler. Discussion on the paper should be addressed to the Editor, Prof. Robert M. McMeeking, Department of Mechanical and Environmental Engineering University of California–Santa Barbara, Santa Barbara, CA 93106-5070, and will be accepted until four months after final publication of the paper itself in the ASME JOURNAL OF APPLIED MECHANICS.

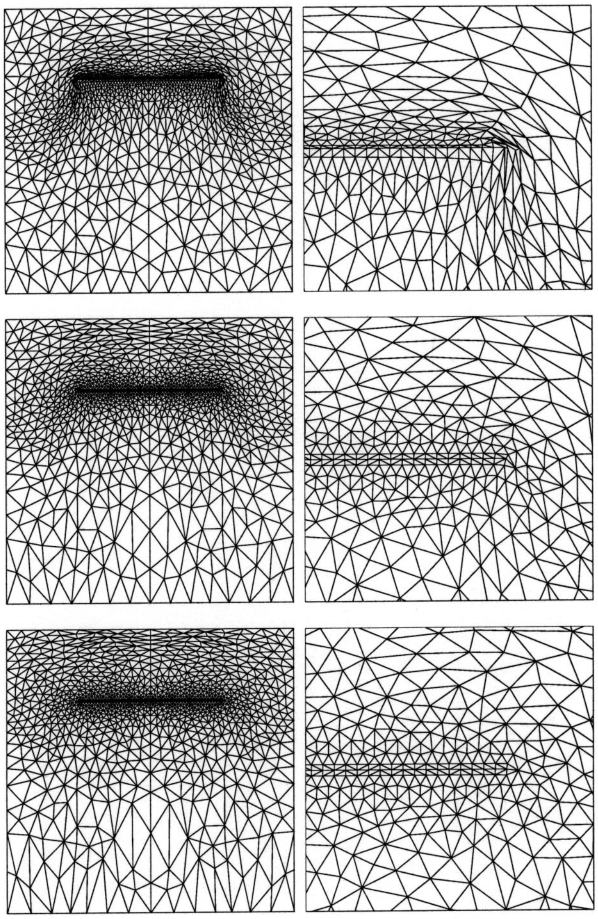

Fig. 2 Translation tests. Deformed mesh for $\chi=0.0,1.0,2.0$.

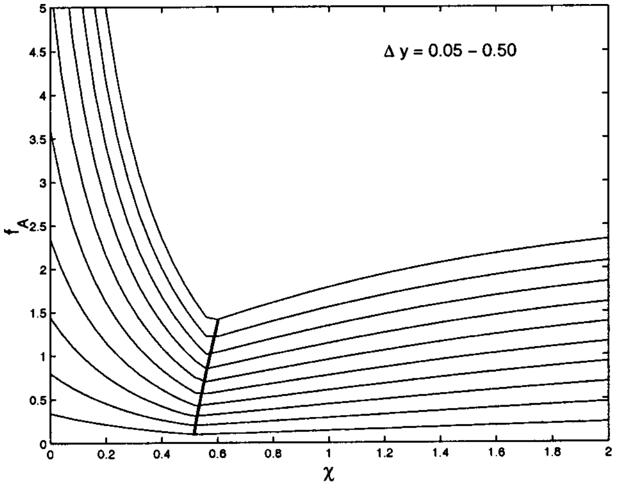

Area Change

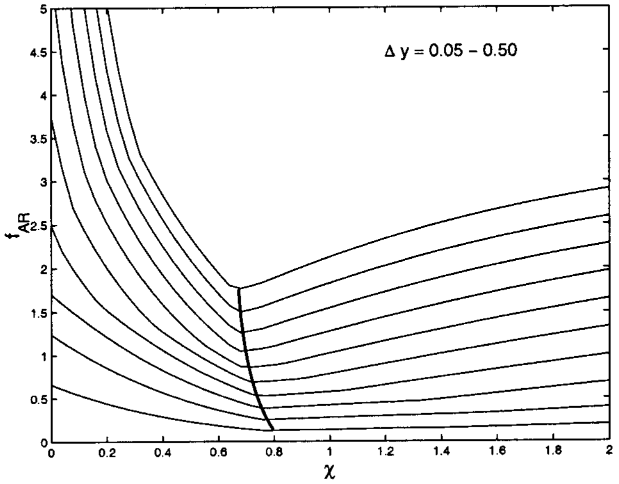

Shape Change

Fig. 3 Translation tests. Mesh quality as function of stiffening power.

tomatic mesh moving technique. We use the technique introduced in [4], where the motion of the nodes is governed by the equations of elasticity, and the mesh deformation is dealt with selectively based on the sizes of the elements and also the deformation modes in terms of shape and volume changes. The motion of the internal nodes is determined by solving these additional equations. As boundary condition, the motion of the nodes at the interfaces is specified to match the normal velocity of the fluid at the interface. Mesh moving techniques with comparable features were introduced in [5].

In the technique introduced in [4], selective treatment of the mesh deformation based on shape and volume changes is implemented by adjusting the relative values of the Lamé constants of the elasticity equations. The objective would be to stiffen the mesh against shape changes more than we stiffen it against volume changes. Selective treatment based on element sizes, on the other hand, is implemented by simply altering the way we account for the Jacobian of the transformation from the element domain to the physical domain. In this case, we would like the smaller elements to be stiffened more than the larger ones.

In this paper, we augment the method described in [4] to a more extensive kind, where we introduce a stiffening power that determines the degree by which the smaller elements are rendered stiffer than the larger ones. When the stiffening power is set to zero, the method reduces back to an elasticity model with no Jacobian-based stiffening. When it is set to one, the method is identical to the one introduced in [4]. Our studies here include seeking optimum values of this stiffening power with the objective of reducing the deformation of the smaller elements, typically placed near solid surfaces. In this context, by varying the stiffening power, we generate a family of mesh moving techniques, and test these techniques on fluid meshes where the structure undergoes three different types of prescribed motion or deformation.

2 Mesh Moving Model

2.1 Equations of Linear Elasticity. Let $\Omega\subset\mathbb{R}^{n_{sd}}$ be the spatial domain bounded by Γ, where n_{sd} is the number of space dimensions. Corresponding to the Dirichlet and Neumann-type boundary conditions, the boundary Γ is composed of Γ_g and Γ_h. The equations governing the displacement of the internal nodes can then be written as

$$\nabla\cdot\boldsymbol{\sigma}+\mathbf{f}=\mathbf{0}\quad\text{on }\Omega, \tag{1}$$

where $\boldsymbol{\sigma}$ is the Cauchy stress tensor and $\mathbf{f}$ is the external force. For linear elasticity, $\boldsymbol{\sigma}$ is defined as

$$\boldsymbol{\sigma}=\lambda\,\mathrm{tr}(\boldsymbol{\varepsilon}(\mathbf{y}))\mathbf{I}+2\mu\boldsymbol{\varepsilon}(\mathbf{y}), \tag{2}$$

where $\mathbf{y}$ is the displacement, tr( ) is the trace operator, λ and μ are the Lamé constants, $\mathbf{I}$ is the identity tensor, and $\boldsymbol{\varepsilon}(\mathbf{y})$ is the strain tensor:

$$\boldsymbol{\varepsilon}(\mathbf{y})=\frac{1}{2}(\nabla\mathbf{y}+(\nabla\mathbf{y})^{\mathbf{T}}). \tag{3}$$

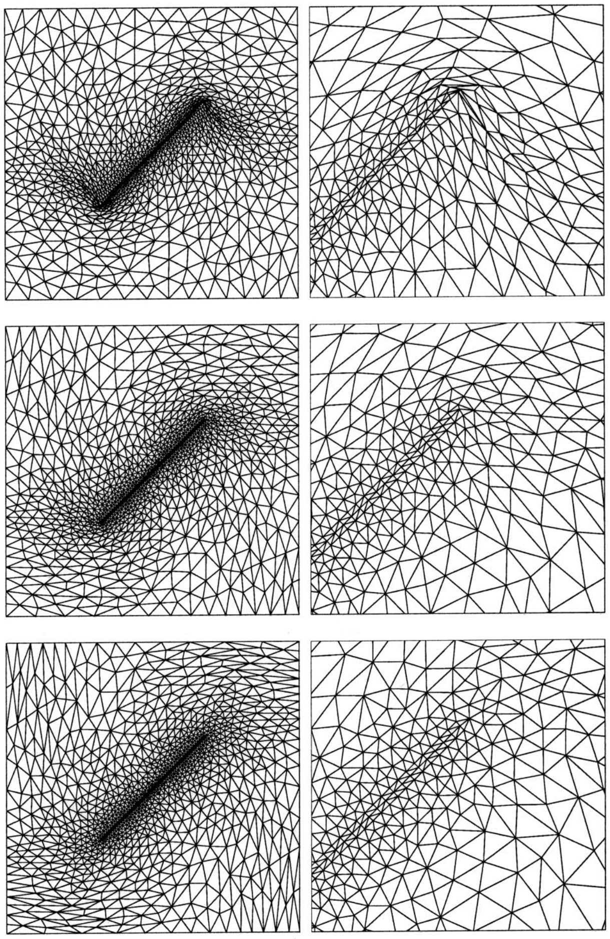

Fig. 4 Rotation tests. Deformed mesh for $\chi=0.0,1.0,2.0$.

The Dirichlet and Neumann-type boundary conditions are represented as

$$\mathbf{y}=\mathbf{g} \quad \text{on } \Gamma_g,$$

$$\mathbf{n}\cdot\boldsymbol{\sigma}=\mathbf{h} \quad \text{on } \Gamma_h. \tag{4}$$

2.2 Finite Element Formulation. In writing the finite element formulation for Eq. (1), we first define the finite element trial and test function spaces $\mathcal{S}^h$ and $\mathcal{V}^h$:

$$\mathcal{S}^h=\{\mathbf{y}^h|\mathbf{y}^h\in[H^{1h}(\Omega)]^{n_{sd}},\mathbf{y}^h\doteq\mathbf{g}^h \quad \text{on } \Gamma_g\}, \tag{5}$$

$$\mathcal{V}^h=\{\mathbf{w}^h|\mathbf{w}^h\in[H^{1h}(\Omega)]^{n_{sd}},\mathbf{w}^h\doteq\mathbf{0} \quad \text{on } \Gamma_g\}. \tag{6}$$

Here, $H^{1h}(\Omega)$ is the finite-dimensional function space over Ω. The finite element formulation for Eq. (1) is then written as follows: find $\mathbf{y}^h\in\mathcal{S}^h$ such that $\forall\mathbf{w}^h\in\mathcal{V}^h$

$$\int_\Omega \boldsymbol{\varepsilon}(\mathbf{w}^h):\boldsymbol{\sigma}(\mathbf{y}^h)d\Omega-\int_\Omega \mathbf{w}^h\cdot\mathbf{f}d\Omega=\int_{\Gamma_h}\mathbf{w}^h\cdot\mathbf{h}d\Gamma. \tag{7}$$

By assigning appropriate values to the ratio λ/μ, we can produce to a certain extent the desired effect in terms of volume and shape changes for the elements during the mesh motion. This approach becomes more clear if we rewrite the term that generates the stiffness matrix as

$$\boldsymbol{\varepsilon}(\mathbf{w}^h):\boldsymbol{\sigma}(\mathbf{y}^h)$$
$$=\left(\lambda+\frac{2}{n_{sd}}\mu\right)\text{tr}(\boldsymbol{\varepsilon}(\mathbf{w}^h))\text{tr}(\boldsymbol{\varepsilon}(\mathbf{y}^h))+2\mu\boldsymbol{\varepsilon}'(\mathbf{w}^h):\boldsymbol{\varepsilon}'(\mathbf{y}^h), \tag{8}$$

where

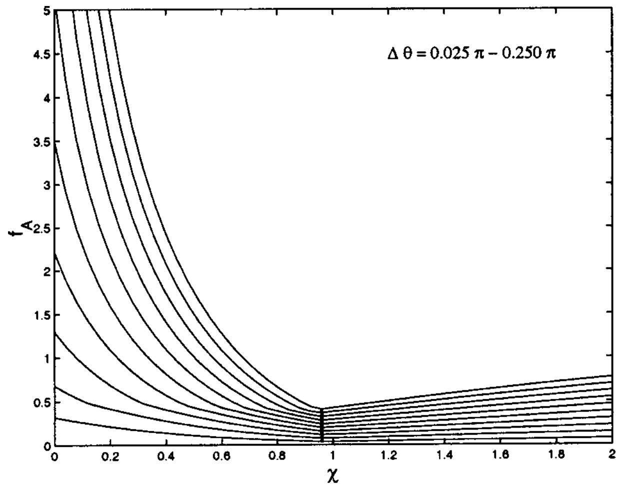

Area Change

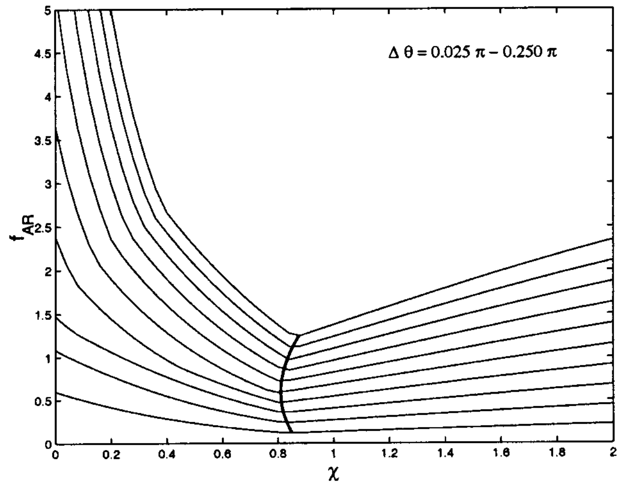

Shape Change

Fig. 5 Rotation tests. Mesh quality as function of stiffening power.

$$\boldsymbol{\varepsilon}'(\mathbf{y}^h)=\boldsymbol{\varepsilon}(\mathbf{y}^h)-\frac{1}{n_{sd}}\text{tr}(\boldsymbol{\varepsilon}(\mathbf{y}^h))\mathbf{I}. \tag{9}$$

The two terms on the right-hand side of Eq. (8) can be recognized as those corresponding, respectively, to the volume and shape change components of the stiffness matrix. In this context, the relative values of $(\lambda+2/n_{sd}\,\mu)$ and 2μ can be adjusted to produce to a certain extent the desired effect in terms of stiffening the mesh against volume or shape changes.

Although a selective treatment of the mesh deformation can be incorporated also into the force vector **f** by providing an appropriate definition for the forcing function, in our case we set it equal to zero.

2.3 Jacobian Options. A selective treatment of the mesh deformation based on the element sizes can be implemented by simply altering the way we account for the Jacobian of the transformation from the element domain to the physical domain. This method was first introduced in [4], where the Jacobian is dropped from the finite element formulation, resulting in the smaller elements being stiffened more than the larger ones. Here we augment

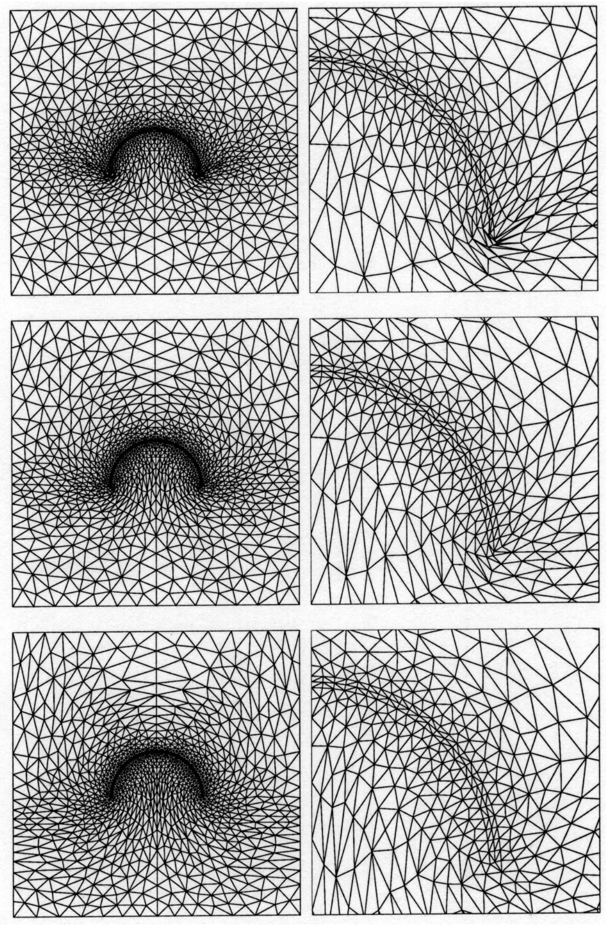

Fig. 6 Bending tests. Deformed mesh for $\chi = 0.0, 1.0, 2.0$.

that method to a more extensive kind. To describe this approach, we first write the global integrals generated by the terms in Eq. (8) as

$$\int_{\Omega}[\ldots]d\Omega=\sum_{e}\int_{\Xi}[\ldots]^{e}J^{e}d\Xi, \tag{10}$$

where $[\ldots]$ symbolically represents what is being integrated, Ξ is the finite element (parent) domain, and the Jacobian for element e is defined as

$$J^{e}=\det\left(\frac{\partial \mathbf{x}}{\partial \boldsymbol{\xi}}\right)^{e}. \tag{11}$$

Here $\mathbf{x}$ represents the physical coordinates, and $\boldsymbol{\xi}$ represents the element (local) coordinates.

We alter the way we account for the Jacobian as follows:

$$\int_{\Xi}[\ldots]^{e}J^{e}d\Xi\mapsto\int_{\Xi}[\ldots]^{e}J^{e}\left(\frac{J^{0}}{J^{e}}\right)^{\chi}d\Xi, \tag{12}$$

where χ, a non-negative number, is the stiffening power, and J^0, an arbitrary scaling parameter, is inserted into the formulation to make the alteration dimensionally consistent. With $\chi = 0.0$, the method reduces back to an elasticity model with no Jacobian-based stiffening. With $\chi = 1.0$, the method is identical to the one first introduced in [4]. In the general case of $\chi \neq 1.0$, the method stiffens each element by a factor of $(J^e)^{-\chi}$, and χ determines the degree by which the smaller elements are rendered stiffer than the larger ones.

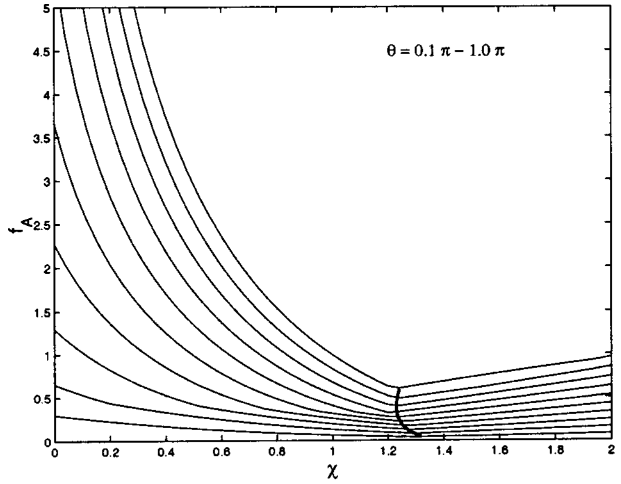

Area Change

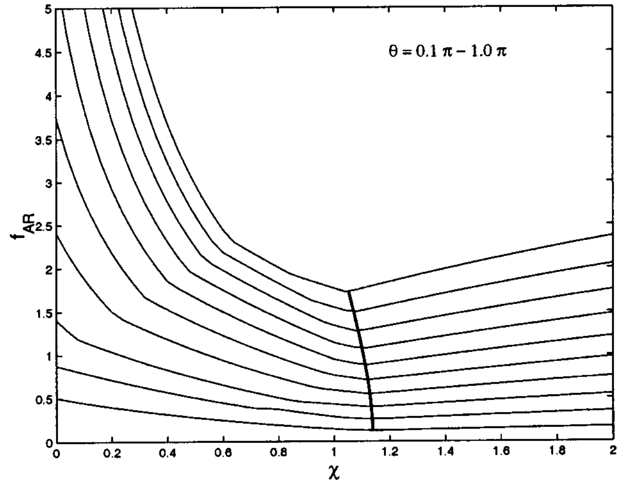

Shape Change

Fig. 7 Bending tests. Mesh quality as function of stiffening power.

3 Test Cases

The test cases are all based on a two-dimensional unstructured mesh consisting of triangular elements and an embedded structure with zero thickness. The mesh spans a region of $|x| \leqslant 1.0$ and $|y| \leqslant 1.0$. The structure spans $y = 0.0$ and $|x| \leqslant 0.5$. A thin layer of elements (with $\ell_y = 0.01$) are placed along both sides of the structure, with 50 element edges along the structure (i.e., $\ell_x = 0.02$). Figure 1 shows the mesh and its close up view near the structure.

The test cases involve three different types of prescribed motion or deformation for the structure: rigid-body translation in the y-direction, rigid-body rotation about the origin, and prescribed bending. In the case of prescribed bending, the structure deforms from a line to a circular arc, with no stretch in the structure and no net vertical or horizontal displacement. The tests are carried out with the Jacobian-based stiffening technique defined by Eq. (12), where χ ranges from 0.0 (no stiffening) to 2.0.

3.1 General Test Conditions and Mesh Quality Measures

In all test cases the maximum displacement or deformation is reached over 50 increments. The mesh over which the elasticity equations are solved is updated at each increment. This update is based on the displacements calculated over the current mesh that

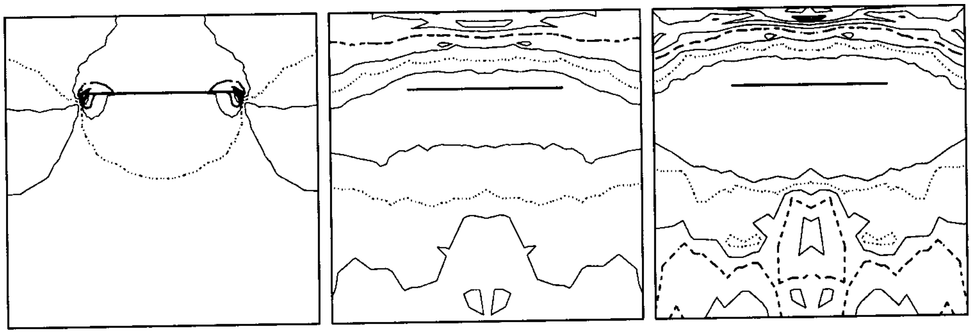

Translation

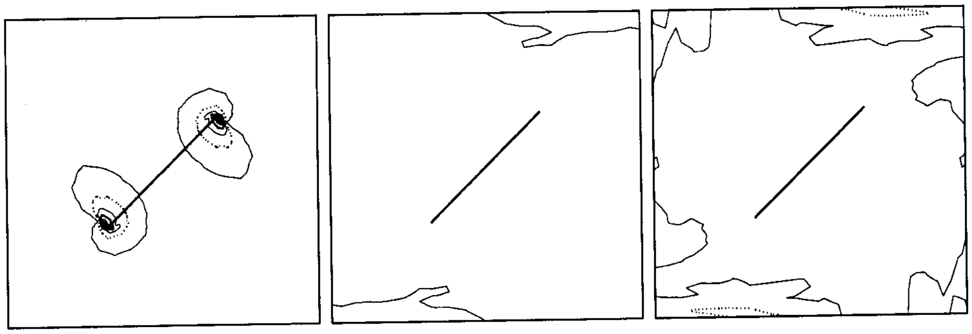

Rotation

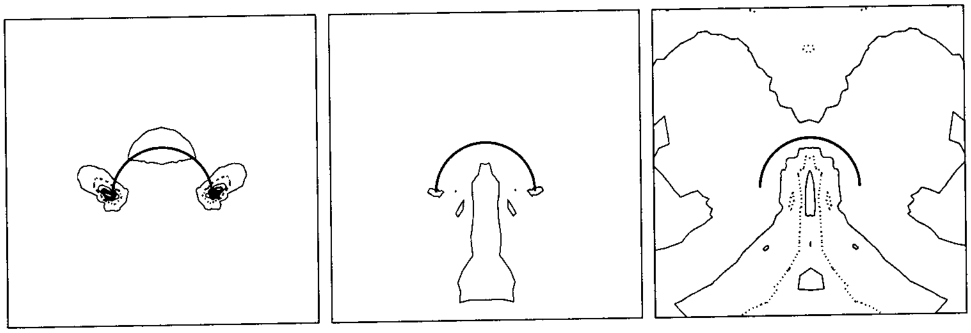

Bending

$\chi = 0.0$ $\chi = 1.0$ $\chi = 2.0$

Fig. 8 Element area change (f_A^e)

has been selectively stiffened. That way, the element Jacobians used in stiffening are updated every time the mesh deforms. As a result, the most current size of an element is used in determining how much it is stiffened. Also as a result, as an element approaches a tangled state, its Jacobian approaches zero, and its stiffening becomes very large.

To evaluate the effectiveness of different mesh moving techniques, two measures of mesh quality are defined based on those used in [6]. They are *element area change* (f_A^e) and *element shape change* (f_{AR}^e):

$$f_A^e = \left| \log\left(\frac{A^e}{A_o^e}\right) / \log(2.0) \right|, \tag{13}$$

$$f_{AR}^e = \left| \log\left(\frac{AR^e}{AR_o^e}\right) / \log(2.0) \right|. \tag{14}$$

Here subscript "o" refers to the undeformed mesh (i.e., the mesh obtained after the last remesh) and AR^e is the element aspect ratio, defined as

$$AR^e = \frac{(l^e{}_{\max})^2}{A^e}, \tag{15}$$

where $l^e{}_{\max}$ is the maximum edge length for element e. For a given mesh, global area and shape changes (f_A and f_{AR}) are defined to be the maximum values of the element area and shape changes, respectively.

3.2 Test Results. In the translation tests, the prescribed translation is in the y-direction, with the displacement magnitudes ranging from $\Delta y = 0.05$ to 0.5. Figure 2 shows the deformed mesh for the maximum translation of $\Delta y = 0.5$. It is evident that the small elements near the structure respond poorly for $\chi = 0.0$, resulting in severe stretching of the row of elements adjacent to the structure, and tangling of elements near the structure tips. For $\chi=1.0$ and $\chi=2.0$, the small elements near the structure experience no tangling and significantly less deformation. For $\chi=2.0$, the small elements near the structure undergo almost rigid-body motion. However, the behavior of the larger elements deteriorates as the smaller elements are stiffened. This is most apparent for $\chi=2.0$ where the larger element tangle near the upper boundary of the mesh. Figure 3 shows the values of f_A and f_{AR} as functions of χ and for different magnitudes of translation. The bold curve crossing the contours denotes the value of χ that results in minimum global mesh deformation. For example, for a displacement of 0.05 the optimal value of f_A is obtained when χ is approximately 0.5. For larger displacements, the optimal value of χ is slightly greater. The optimal value of f_{AR} is obtained at $\chi\approx 0.8$ for a displacement of 0.05 and at $\chi\approx 0.7$ for a displacement of 0.5.

In the rotation tests, the rotation magnitudes range from $\Delta\theta=0.025\pi$ to 0.25π. For $\chi=0.0$ the mesh experiences significant stretching and tangling near the structure tips. No tangling is seen for the cases with element stiffening, but for $\chi=2.0$ the large elements near the outer boundaries experience significant distortion. Figure 4 shows the deformed mesh for the maximum rotation of $\pi/4$. Figure 5 shows the values of f_A and f_{AR} as functions of χ and for different magnitudes of rotation. The minimum deformation of the mesh is seen for values of χ around 0.8. The mesh quality deteriorates more rapidly as χ decreases from 1.0 than when χ increases from 1.0.

In the bending tests, the bending magnitudes range from $\theta=0.1\pi$ to π, where θ denotes the arc length (in radians) for the deformed structure. Figure 6 shows the deformed mesh when the structure bends to a half-circle (i.e., $\theta=\pi$). For $\chi=0.0$, we see tangling near the structure tips. As the element stiffening increases, tangling at the tips disappears, but severe element distortion arises in the interiors. Figure 7 shows the values of f_A and f_{AR} as functions of χ and for different magnitudes of prescribed bending. The minimum deformation of the mesh is seen for values of χ around 1.1.

Figure 8 shows, for different deformation modes, the contours of f_A^e for stiffening power of $\chi=0.0$, 1.0, and 2.0. The contours corresponding to $f_A^e=0.5$, 1.0, and 2.0 are denoted with dotted, dashed, and bold lines, respectively.

4 Concluding Remarks

We have presented automatic mesh moving techniques for fluid-structure interactions with large displacements. In these techniques, the motion of the nodes is governed by the equations of elasticity, and deformation of the elements are treated selectively based on element sizes as well as deformation modes in terms of shape and volume changes. Smaller elements, typically placed near solid surfaces, are stiffened more than the larger ones. This is implemented by altering the way we account for the Jacobian of the transformation from the element domain to the physical domain. The degree by which the smaller elements are stiffened more than the larger ones is determined by a stiffening power introduced into the formulation. When the stiffening power is set to zero, the method reduces back to a model with no Jacobian-based stiffening. The two-dimensional test cases we presented here for three different structural deformation modes show that the stiffening power approach substantially improves the deformed mesh quality near the solid surfaces, even when the displacements are large. The test cases also show that the optimal stiffening power is somewhat problem-dependent. It is higher for the bending tests ($\chi\approx 1.1$) than it is for the rotation ($\chi\approx 0.8$) and translation ($\chi\approx 0.7$) tests.

Acknowledgment

The work reported in this paper was partially sponsored by NASA JSC and by the Natick Soldier Center.

References

[1] Tezduyar, T. E., 1991, ‘‘Stabilized Finite Element Formulations for Incompressible Flow Computations,’’ Adv. Appl. Mech., **28**, pp. 1–44.
[2] Tezduyar, T. E., Behr, M., and Liou, J., 1992, ‘‘A New Strategy for Finite Element Computations Involving Moving Boundaries and Interfaces—The Deforming-Spatial-Domain/Space-Time Procedure: I. The Concept and the Preliminary Tests,’’ Comput. Methods Appl. Mech. Eng., **94**, pp. 339–351.
[3] Tezduyar, T. E., Behr, M., Mittal, S., and Liou, J., 1992, ‘‘A New Strategy for Finite Element Computations Involving Moving Boundaries and Interfaces—The Deforming-Spatial-Domain/Space-Time Procedure: II. Computation of Free-Surface Flows, Two-Liquid Flows, and Flows With Drifting Cylinders,’’ Comput. Methods Appl. Mech. Eng., **94**, pp. 353–371.
[4] Tezduyar, T. E., Behr, M., Mittal, S., and Johnson, A. A., 1992, ‘‘Computation of Unsteady Incompressible Flows With the Finite Element Methods—Space-Time Formulations, Iterative Strategies and Massively Parallel Implementations,’’ *New Methods in Transient Analysis*, P. Smolinski, W. K. Liu, G. Hulbert, and K. Tamma, eds., ASME, New York, AMD-Vol. 143, pp. 7–24.
[5] Masud, A., and Hughes, T. J. R., 1997, ‘‘A Space-Time Galerkin/Least-Squares Finite Element Formulation of the Navier-Stokes Equations for Moving Domain Problems,’’ Comput. Methods Appl. Mech. Eng., **146**, pp. 91–126.
[6] Johnson, A. A., and Tezduyar, T. E., 1996, ‘‘Simulation of Multiple Spheres Falling in a Liquid-Filled Tube,’’ Comput. Methods Appl. Mech. Eng., **134**, pp. 351–373.

A Method for Particle Simulation

Z. Zhang

A. Prosperetti[1]
Fellow ASME

Department of Mechanical Engineering,
The Johns Hopkins University,
Baltimore, MD 21218

This paper extends a recent approach to the direct numerical simulation of particle flows to the case in which the particles are not fixed. The basic idea is to use a local analytic representation valid near the particle to "transfer" the no-slip condition from the particle surface to the adjacent grid nodes. In this way the geometric complexity arising from the irregular relation between the particle boundary and the underlying mesh is avoided and fast solvers can be used. The results suggest that the computational effort increases only slowly with the number of particles so that the method is efficient for large-scale simulations. The focus here is on the two-dimensional case (cylindrical particles), but the same procedure, to be developed in forthcoming papers, applies to three dimensions (spherical particles). [DOI: 10.1115/1.1530636]

1 Introduction

The importance of direct numerical simulation in the study of fluid flows with suspended particles has long been recognized. The computational task is considerable and the earlier models treated the particles as points (see, e.g., Refs. [1–3]). This approximation is justified for dilute systems such as dusty gases, particle-laden gas jets, and other situations in which the major part of the particle interaction with the fluid takes place through drag, and possibly lift, forces. In concentrated systems, or liquid-particle flows, however, the fact that the particles have a finite size plays a determinant role in the physics of the problem and cannot be neglected. For this reason, the last few years have seen a greater effort in this direction. Examples are the early calculations of Joseph and collaborators (see, e.g., Refs. [4–6]) the more recent work of this group (see, e.g., Refs. [7–9]), the "immersed boundary" approach of Refs. [10], [11], the finite element calculations of Refs. [12], [13], the CHIMERA method (see, e.g., Refs. [14], [15]), and others. Other recent methods are based on lattice-Boltzmann formulations, [16–18].

The present paper extends a recent method, PHYSALIS, based on an approach rather different from the ones used before, [19,20]. Very briefly, the basic idea can be explained in the following terms. Because of the boundary conditions on its surface, a particle induces a specific structure in the neighboring flow which manifests itself in certain nonlocal relations among the flow fields (velocity, pressure, vorticity). Rather than solving the problem with the particle in place, one can therefore impose this relationship directly on the nodes of a fixed regular grid and effectively remove the particle. Thus, the actual boundary of the particle, with its usually complex relation to the underlying regular grid, can in principle be replaced by a simpler boundary consisting of grid nodes although, in practice, it is possible to eliminate entirely this internal boundary by exploiting the iterative nature of the algorithm. With this step, all internal boundaries are eliminated and, if the external boundary of the computational domain is regular, fast solvers can be used. It should be stressed that the procedure in no way implies approximating the particle shape, as in some other approaches (see, e.g., Ref. [18]). In particular, unlike other methods, the no-slip condition at the particle surface is enforced exactly and, as the number of degrees-of-freedom per particle is increased, the error decreases faster than algebraically.

Another useful feature of the method is that, for a given computational domain, the computation time is only weakly dependent on the total number of particles, which permits relatively large computations to be carried out with modest computational resources. A preliminary analysis of the convergence properties of this approach is presented in Ref. [21].

In past work we have demonstrated PHYSALIS for potential flow past spheres, [19], and Navier-Stokes flow past fixed cylinders, [20], with some preliminary examples of Navier-Stokes flow past spheres, [22]. In all these examples the particles were stationary. It is the purpose of the present paper to illustrate the performance of the method in the presence of moving cylindrical particles. The three-dimensional case of spheres can be treated analogously.

2 Reduction to the Rest Frame

The method requires the consideration of the flow in the neighborhood of each particle separately. Let $\mathbf{U}$ be the flow velocity in the inertial frame, and $\mathbf{w}$, $\mathbf{\Omega}$ the translational and angular velocity of a particle. The first step is to express the Navier-Stokes equations in the particle rest frame, where the flow velocity $\mathbf{u}$ is related to $\mathbf{U}$ by

$$\mathbf{U}=\mathbf{u}+\mathbf{w}+\mathbf{\Omega}\times\mathbf{x}, \tag{1}$$

in which $\mathbf{x}$ is the position relative to the particle center. In this frame the momentum equation is

$$\rho\left[\frac{\partial\mathbf{u}}{\partial t}+(\mathbf{u}\cdot\nabla)\mathbf{u}+2\mathbf{\Omega}\times\mathbf{u}\right]=-\nabla p+\mu\nabla^2\mathbf{u}+\rho\mathbf{g} -\rho[\dot{\mathbf{w}}+\dot{\mathbf{\Omega}}\times\mathbf{x}+\mathbf{\Omega}\times(\mathbf{\Omega}\times\mathbf{x})], \tag{2}$$

to be solved subject to the incompressibility constraint and to the boundary condition $\mathbf{u}=0$ on the particle surface. In (2) ρ and μ are the fluid density and viscosity, p is the pressure, and $\mathbf{g}$ the body force; dots denote Lagrangian time derivatives following the particle.

The change of variables

$$\mathbf{u}=\tilde{\mathbf{u}}+\frac{r^4-a^4}{8\nu r^2}\dot{\mathbf{\Omega}}\times\mathbf{x},\quad p=\tilde{p}+\frac{1}{2}\rho(\mathbf{\Omega}\times\mathbf{x})^2-\rho(\dot{\mathbf{w}}-\mathbf{g})\cdot\mathbf{x}, \tag{3}$$

brings (2) into the form

$$\rho\left[\frac{\partial\mathbf{u}}{\partial t}+(\mathbf{u}\cdot\nabla)\mathbf{u}+2\mathbf{\Omega}\times\mathbf{u}\right]=-\nabla\tilde{p}+\mu\nabla^2\tilde{\mathbf{u}}, \tag{4}$$

with $\tilde{\mathbf{u}}=0$ on the particle surface. Since $\mathbf{u}=0$ on the particle surface, by continuity, it will be small near the particle and, therefore,

---

[1] Also, Faculty of Applied Physics and Twente Institute of Mechanics, University of Twente, AE 7500 Enschede, The Netherlands, and Burgerscentrum, The Netherlands.

Contributed by the Applied Mechanics Division of THE AMERICAN SOCIETY OF MECHANICAL ENGINEERS for publication in the ASME JOURNAL OF APPLIED MECHANICS. Manuscript received by the Applied Mechanics Division, Dec. 4, 2001; final revision, Mar. 26, 2002. Associate Editor: T. E. Tezduyar. Discussion on the paper should be addressed to the Editor, Prof. Robert M. McMeeking, Chair, Department of Mechanics and Environmental Engineering, University of California–Santa Barbara, Santa Barbara, CA 93106-5070, and will be accepted until four months after final publication in the paper itself in the ASME JOURNAL OF APPLIED MECHANICS.

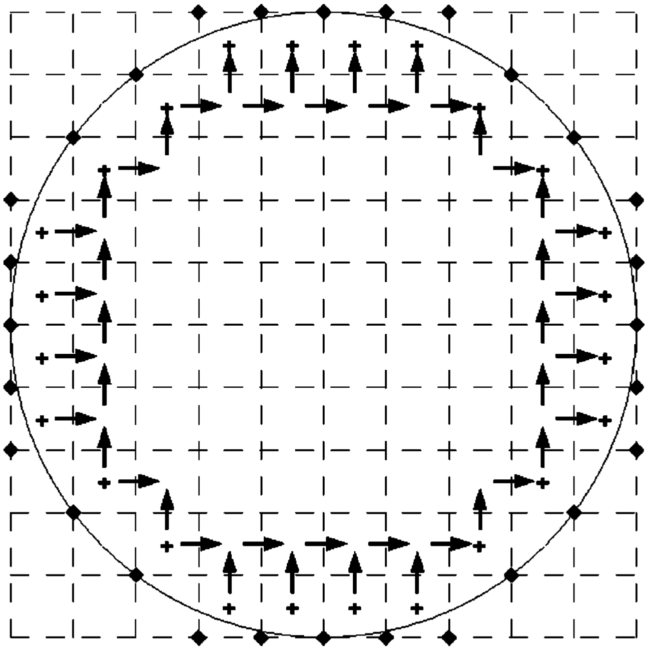

Fig. 1 Example of cage around a particle: crosses: pressure nodes; diamonds: vorticity nodes; arrows: velocity nodes

Table 1 Comparison among three different calculation of the force on a line of cylinders held between two moving walls

L/D	$a/\Delta x$	Nodes per Cylinder	f_c Present	 Ref. [18]	 Ref. [25]
11.8	10.8	10	1.034	1.053	0.966
6.1	20.8	10	1.224	1.251	1.158
2.09	60.8	20	2.079	2.093	2.067

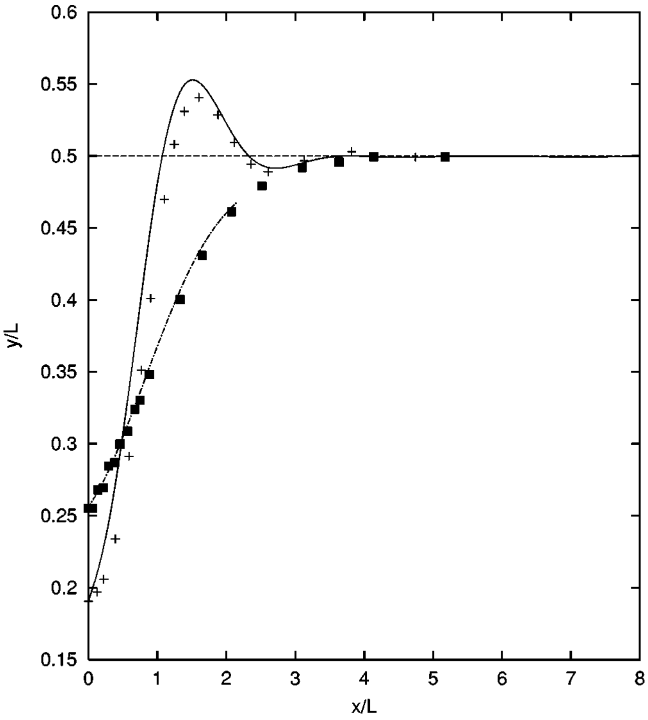

Fig. 2 Two particles falling (left to right) between two parallel plates separated by four particle diameters with final Reynolds numbers of 1.03 (dotted line and squares) and 8.33 (continuous line and crosses). The lines are the present results and the symbols the results of Ref. [6].

there is a region adjacent to the particle where the left-hand side of (4) is small. Thus, locally, $(\tilde{\mathbf{u}},\tilde{p})$ approximately satisfy

$$-\nabla\tilde{p}+\mu\nabla^2\tilde{\mathbf{u}}=0, \quad \nabla\cdot\tilde{\mathbf{u}}=0, \tag{5}$$

i.e., the Stokes equations. Naturally, the extent of the spatial region where (5) are a good approximation to (4) becomes smaller and smaller as the Reynolds number increases but, for any finite Reynolds number, there is a nonvanishing region where (5) are applicable with but a small error.

The general solution of the Stokes Eqs. (5) subject to the condition of vanishing velocity on the particle surface is readily found in terms of a dimensionless stream function ψ, defined so that $\tilde{\mathbf{u}}=\nabla\times(\nu\psi\mathbf{k})$ (with $\mathbf{k}$ the unit vector normal to the flow plane and ν is the kinematical viscosity), and is

$$\psi=\nu(s^2-2\log s-1)A_0+\nu\sum_{n=1}^{\infty}[\psi_n(A_n\cos n\theta+\tilde{A}_n\sin n\theta)$$
$$+\tilde{\psi}_n(B_n\cos n\theta+\tilde{B}_n\sin n\theta)], \tag{6}$$

where

$$\psi_1=s^3-2s+\frac{1}{s}, \quad \tilde{\psi}_1=s\log s-\frac{s}{2}+\frac{1}{2s} \tag{7}$$

$$\psi_n=ns^{n+2}-(n+1)s^n+s^{-n}, \quad \tilde{\psi}_n=ns^{-n+2}-(n-1)s^{-n}-s^n, \tag{8}$$

with $s=r/a$. An important point to stress is that, thanks to the as yet undetermined coefficients A_n, B_n, $\tilde{A}_n$, $\tilde{B}_n$ (different for each particle), the stream function (6) is able to accommodate any (locally Stokes) flow in the neighborhood of the particle. Thus, no assumptions or restrictions about this flow (in particular, about its behavior far from the particle) have been introduced. These coefficients will be determined iteratively by matching the velocity field given by (6) to the numerically computed flow away from the particle.

The pressure and vorticity fields corresponding to (6) are

$$\tilde{p}=p_0+\frac{\mu\nu}{a^2}\left\{8s(-A_1\sin\theta+\tilde{A}_1\cos\theta)+\frac{2}{s}(B_1\sin\theta-\tilde{B}_1\cos\theta)\right.$$
$$+\sum_{n=2}^{\infty}[4n(n+1)s^n(-A_n\sin n\theta+\tilde{A}_n\cos n\theta)$$
$$\left.+4n(n-1)s^{-n}(\tilde{B}_n\cos n\theta-B_n\sin n\theta)]\right\}, \tag{9}$$

where p_0 is a constant, different for each particle, and

$$\tilde{\omega}=\frac{\nu}{a^2}\left\{-4A_0-8s(A_1\cos\theta+\tilde{A}_1\sin\theta)-\frac{2}{s}(B_1\cos\theta\right.$$
$$+\tilde{B}_1\sin\theta)-\sum_{n=2}^{\infty}[4n(n+1)s^n(A_n\cos n\theta+\tilde{A}_n\sin n\theta)$$
$$\left.+4n(-n+1)s^{-n}(B_n\cos n\theta+\tilde{B}_n\sin n\theta)]\right\}. \tag{10}$$

In the original inertial frame, the hydrodynamic force $\mathbf{F}$ and couple $\mathbf{L}$ (per unit length) acting on the particle are

$$\mathbf{F}=\rho v(\dot{\mathbf{w}}-\mathbf{g})+4\pi\frac{\mu\nu}{a}(\tilde{B}_1,-B_1), \quad \mathbf{L}=-8\pi\mu\nu A_0\mathbf{k}+\rho v a^2\dot{\mathbf{\Omega}}. \tag{11}$$

3 Implementation

The general idea described in the Introduction can now be made more precise.

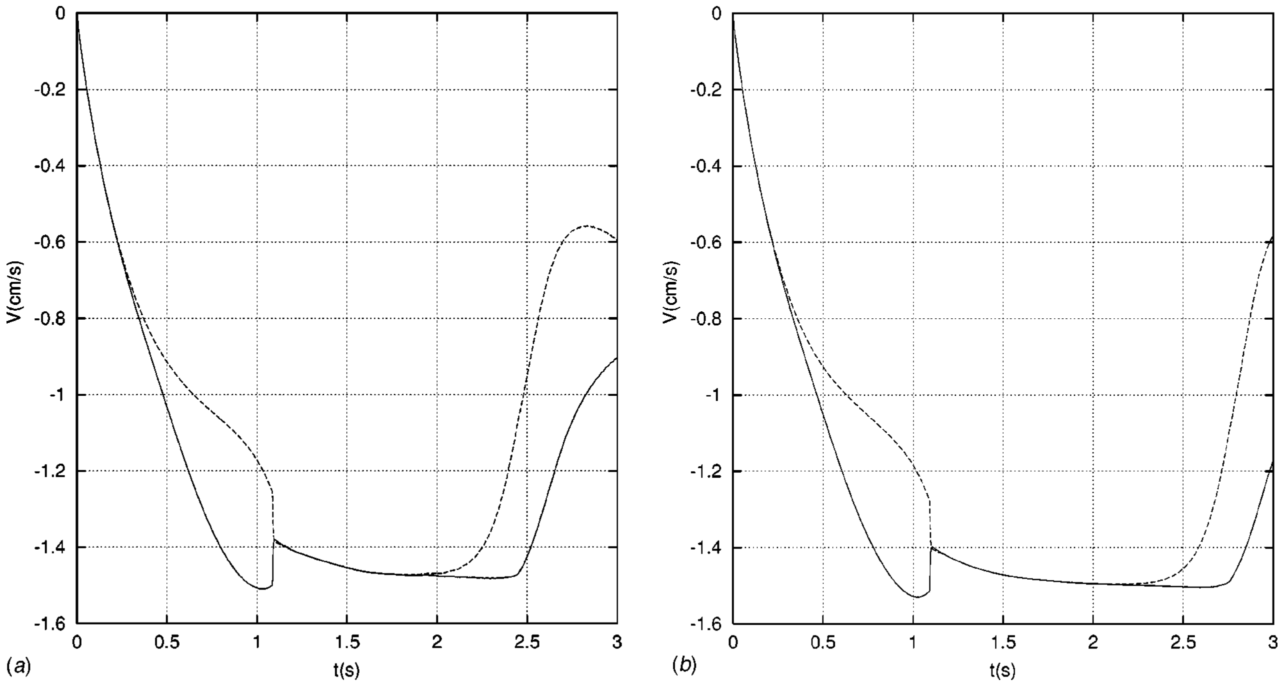

Fig. 3 **Vertical velocity versus time for two particles aligned vertically and released: while the distance is large enough the fall velocity is nearly equal. As the upper particle gets caught in the wake of the lower one it accelerates (drafting); the two particles interact (kissing), until they tumble and separate. The calculation shown on the left was done with 19.2 nodes per particle diameter, that on the right with 28.8 (courtesy of Prof. T. W. Pan, University of Houston).**

The entire domain, irrespective of the presence of the bodies, is covered by a regular finite difference grid. Each cylinder is surrounded by a cage of cells straddling the body surface; an example is shown in Fig. 1 and the algorithm used to construct the cage is described later. We use a standard staggered grid arrangement, with pressure at cell centers (crosses) and velocities at the midpoints of cell sides (arrows). Vorticity is calculated from

$$\omega_{ij}=\frac{1}{\Delta x\Delta y}\oint \mathbf{u}\cdot d\mathbf{l}\simeq\frac{v_{i+1,j}-v_{i,j}}{\Delta x}-\frac{u_{i,j+1}-u_{i,j}}{\Delta y}, \qquad (12)$$

where Δx and Δy are the mesh spacings, and, therefore, it resides on the grid nodes (diamonds).

The procedure can be summarized as follows. Suppose that a provisional estimate of velocity and pressure fields is available

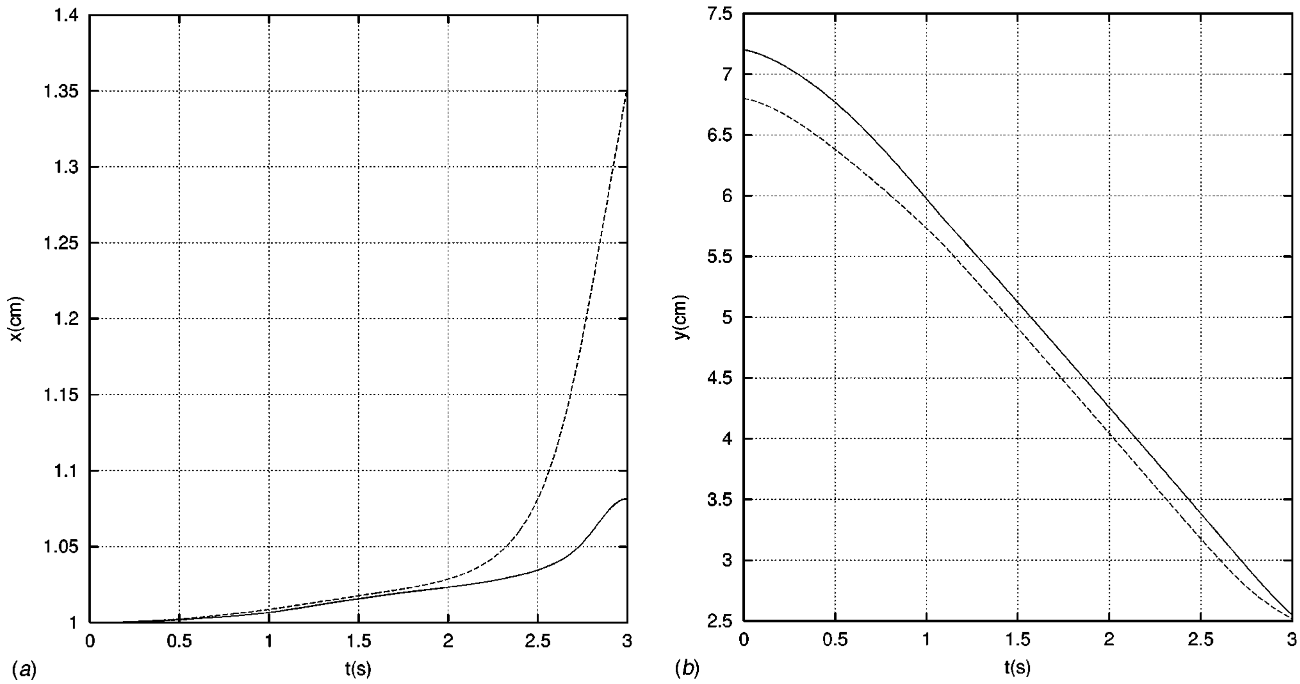

Fig. 4 **Position versus time for the two particles of the previous figure as calculated with the finer discretization (courtesy of Prof. T. W. Pan, University of Houston)**

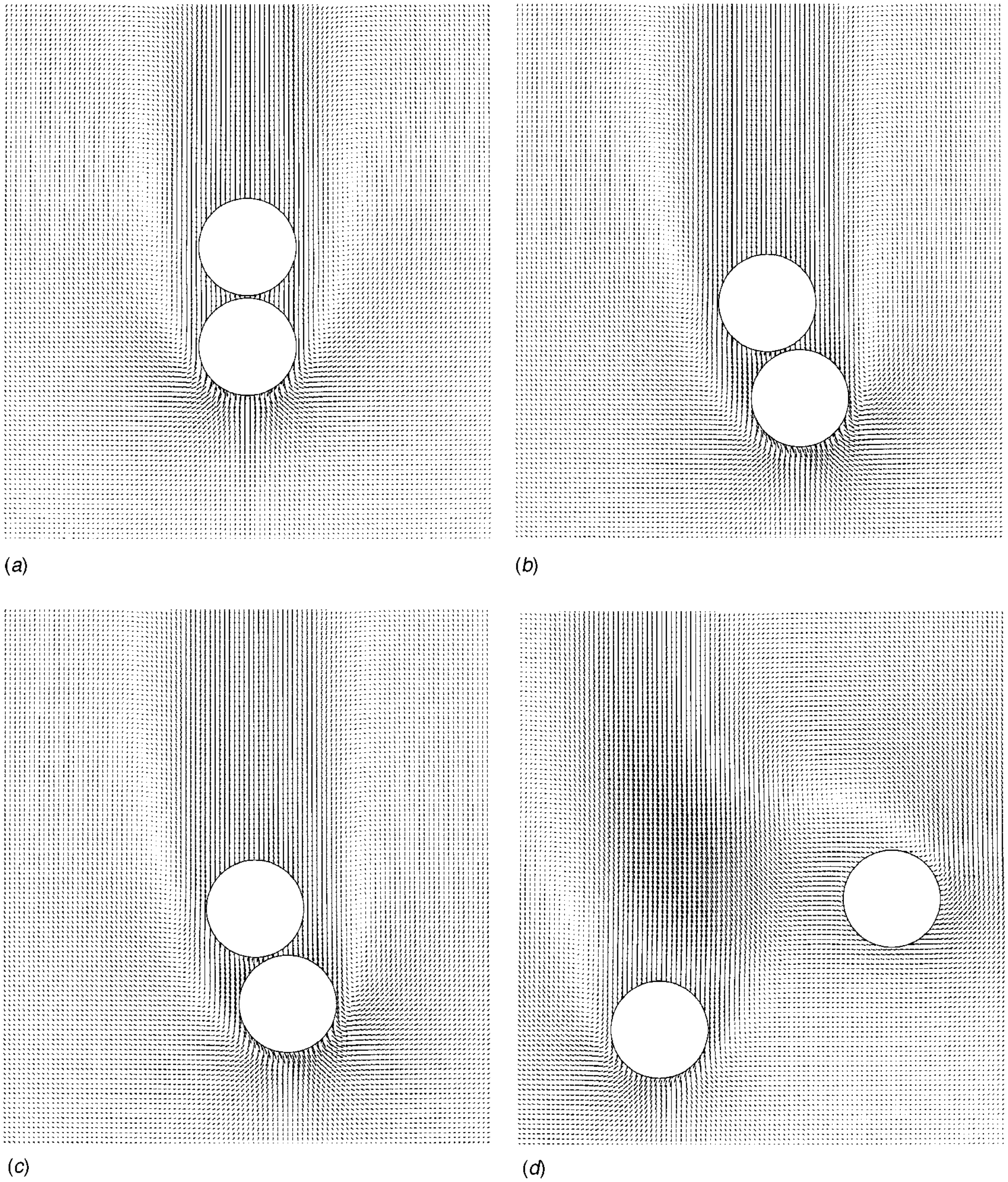
(*a*) (*b*) (*c*) (*d*)

Fig. 5 Snapshots of the two falling cylinders of Figs. 6 and 7 at times $t=1.312$, 2.272, 2.521, and 2.971 s as given by the present method

(this could be, for example, the velocity field at the previous time-step). Then, after truncating the summations in (6), (9), and (10) to a finite number of terms N_c and calculating the vorticity from (12):

1 For each particle, let $1, 2, \ldots, N_p$ be the pressure nodes and $1, 2, \ldots, N_\omega$ the vorticity nodes of the cage; match the provisional $\tilde{p}$ and $\tilde{\omega}$ to the analytic expressions (9) and (10) to generate a linear system for the coefficients A_n, B_n, $\tilde{A}_n$, $\tilde{B}_n$ of the particle. In principle, the maximum number of coefficients that can be determined in this way equals the number of cage nodes, although in practice we use fewer and solve this system in a least square sense (see below).

2 Using the values of the coefficients determined at the previous step, compute from the analytic formulas the velocity at the velocity points $1, 2, \ldots, N_v$ of the cage surrounding the particle.

3 Solve the full Navier-Stokes equations on the finite difference grid imposing this velocity field as boundary condition on the velocity nodes of the cage of each particle.

4 Calculate the corresponding vorticity, return to Step 1, and repeat until convergence.

As will be explained in the next section, in executing Step 3, it is efficient to solve for the flow field over the entire grid, disregarding the presence of the particles. The velocity field outside the cages is the one that is desired. The field inside the cages is the correct solution of another flow problem, in which the flow is driven by the imposed velocity on the cage nodes: This solution is not unphysical—it is simply irrelevant for the purposes of the calculation and can be disregarded. The final flow field is given by the finite difference solution outside the cages, and by the analytic representation in the thin region between each particle and the

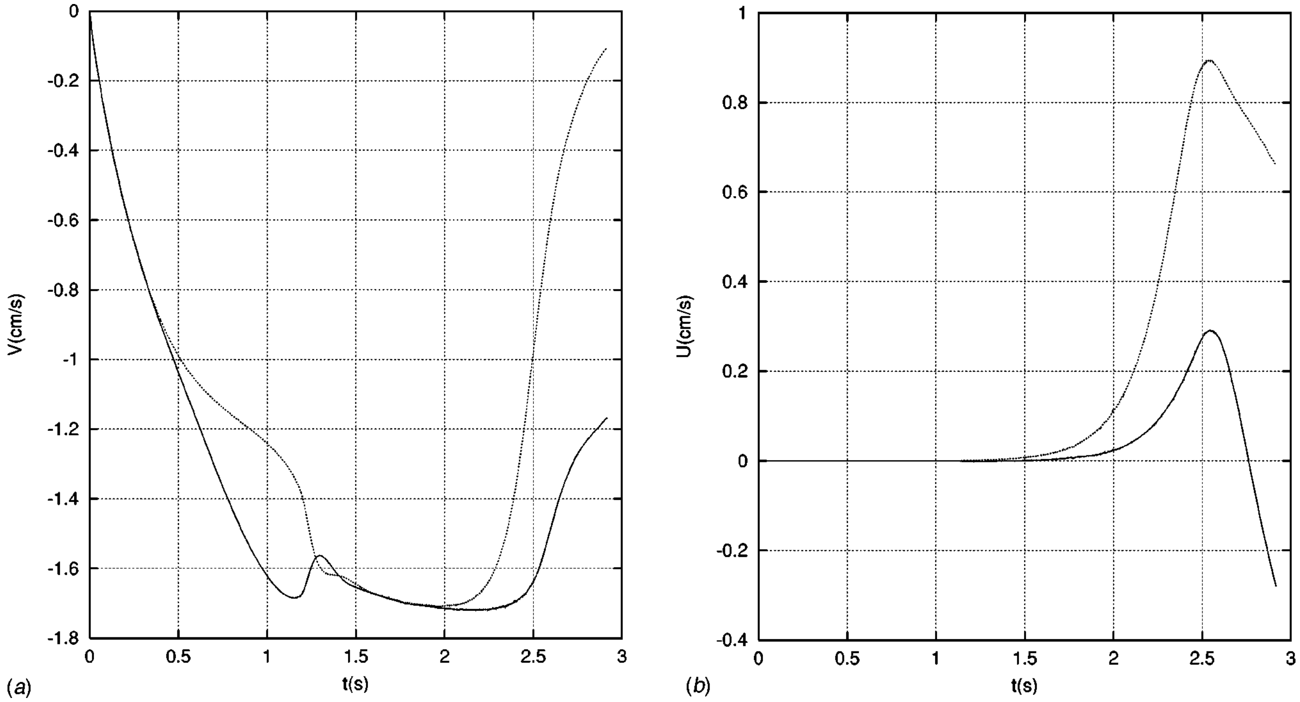

Fig. 6 Vertical (left) and horizontal (right) velocity versus time for the two particles of Fig. 3 as computed by the present method with $\Delta t = 1$ ms

surrounding cage. It should be stressed that the solution procedure is devised in such a way that, other than for satisfying a common velocity boundary conditions at the cage nodes, the solutions inside and outside the cages are completely unrelated, so that any "contamination" of the latter by the former is avoided. In particular, there is no continuity or other relation satisfied by the stresses across the cage surface.

A possible criticism of the method is its reliance on an approximate solution in the fluid regions between the particle and the surrounding cage. The associated error can be reduced by refining the grid, which has the effect of putting the cage nodes closer and closer to the particle surface. Another possibility (which we have not yet explored) would be to improve on the Stokes flow solution by approximating the solution of the full nonlinear Eq. (4) by a

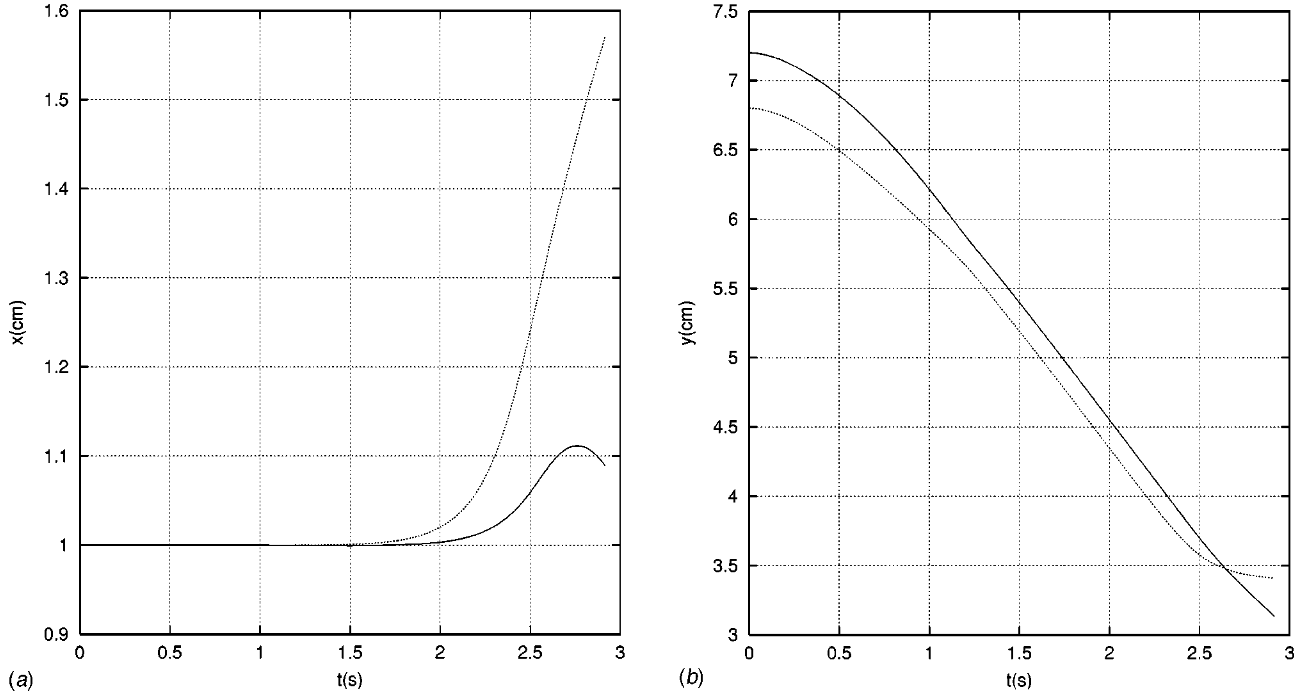

Fig. 7 Vertical (left) and horizontal (right) position versus time for the two particles of Fig. 4 as computed by the present method with $\Delta t = 1$ ms

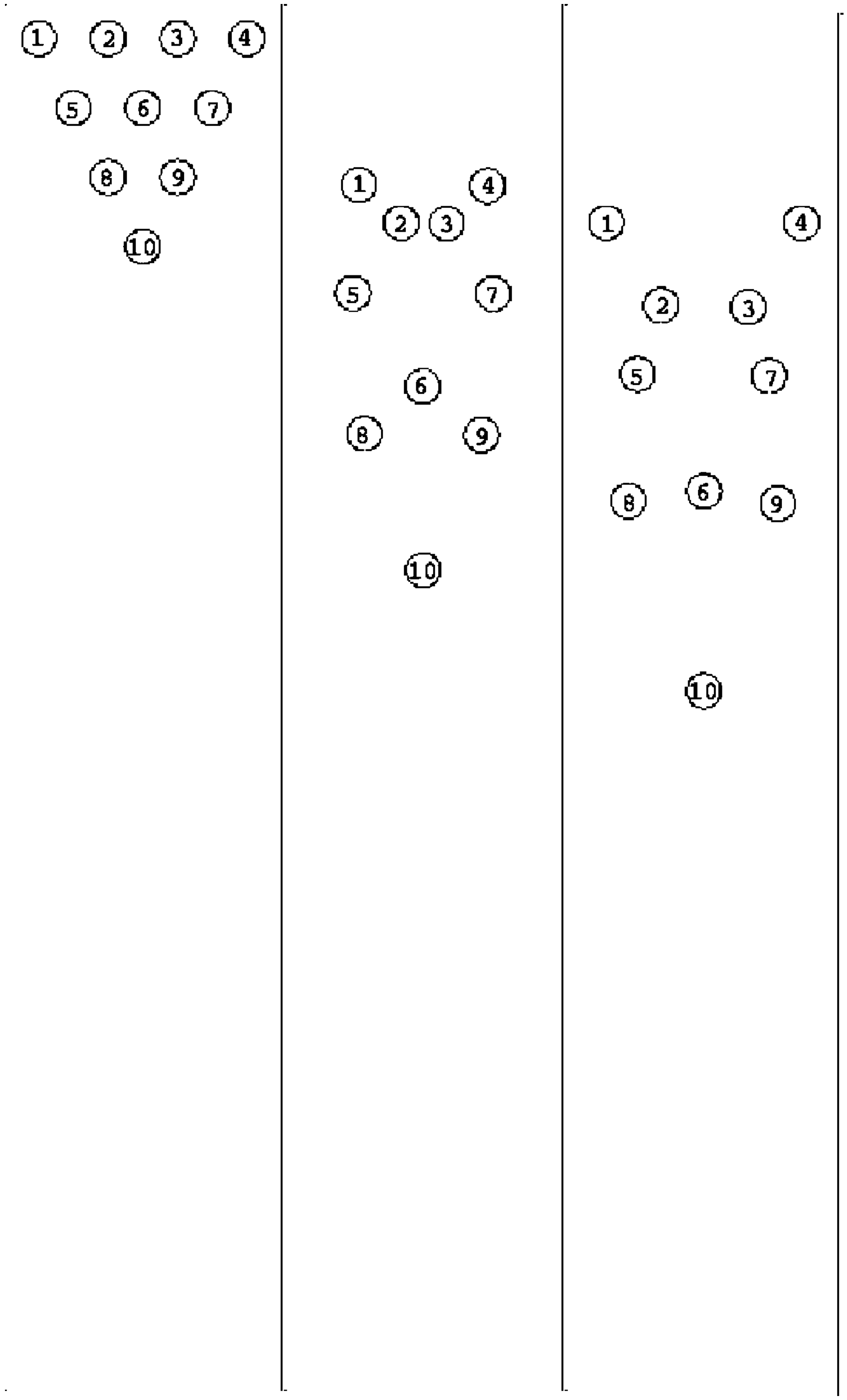

Fig. 8 Fall of a cluster of ten particles as computed with the present method at $\nu t/a = 0$, 3.0, and 4.0

regular perturbation expansion. It may be noted, however, that in practice some control of the error is built into the procedure as convergence requires that all the flow fields be described by the *same* set of coefficients (A_k, B_k). In the presence of strong nonlinear effects, which are not accounted for in the analytic solution (6), this condition would not be satisfied and the iterative procedure would not converge as we have indeed found by purposely putting the cage nodes too far from the particle surface.

A rough idea of the grid size Δ necessary for a good numerical accuracy may be found by noting that the grid points should be inside the boundary layer for the Stokes approximation to be valid. If the boundary layer thickness is estimated as $a/\sqrt{\mathrm{Re}}$, where Re is the Reynolds number expressed in terms of a characteristic velocity and the cylinder diameter, we thus have that $N_\Delta = 2a/\Delta$ should be sufficiently larger than $\sqrt{\mathrm{Re}}$. This limit is not different from that applicable to a standard finite difference calculation.

We now turn to some details of the implementation; additional information can be found in [20].

3.1 Flow Solver. As is clear from the previous description, each computational cycle consists of two steps: an inner one that updates the coefficients, and an outer one that calculates the flow field for a given set of coefficients.

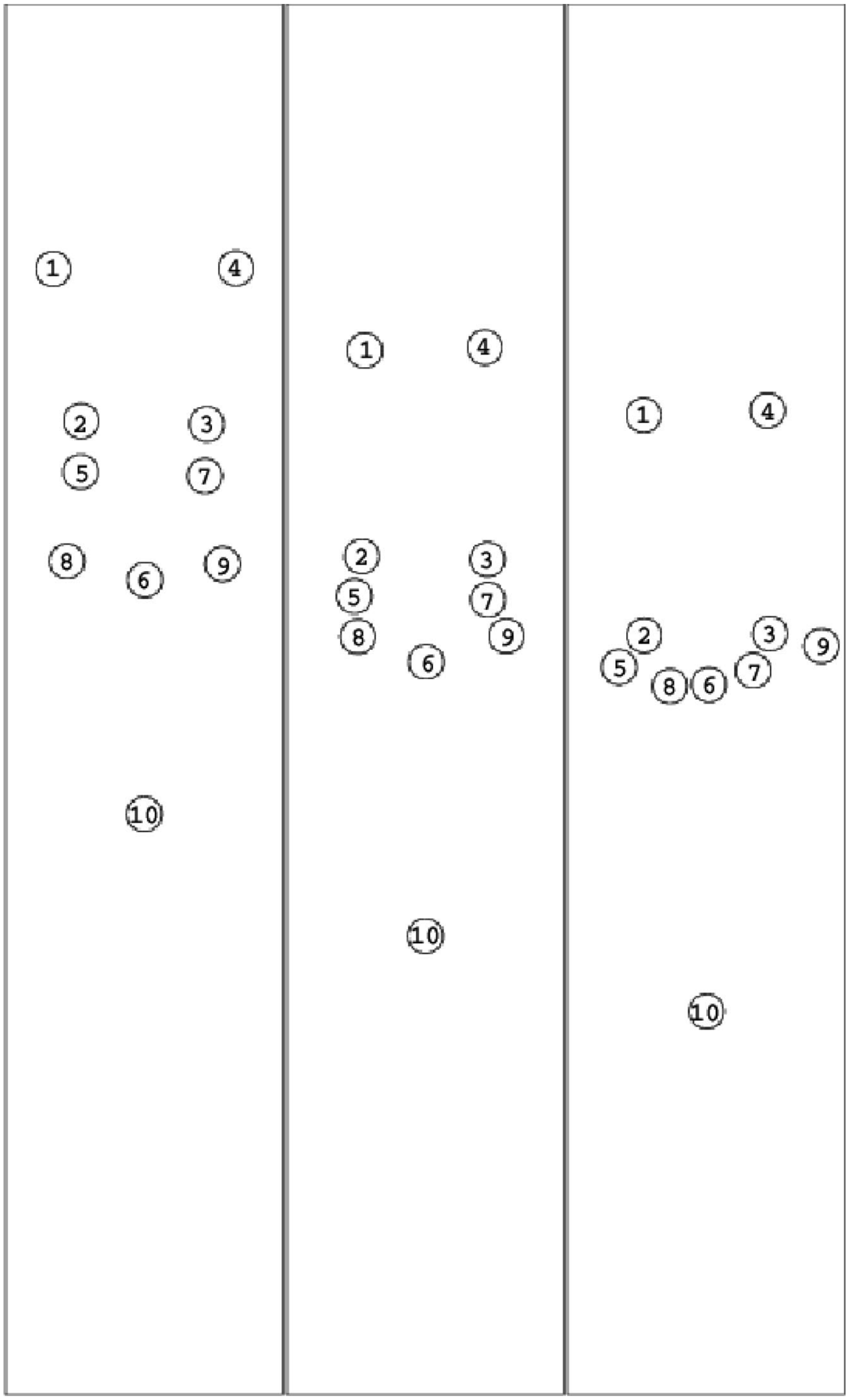

Fig. 9 **Continuation of the previous figure showing the ten falling particles at $\nu t/a=5.0$, 6.0, and 6.62. The terminal velocity of the leading particle (No. 10) corresponds to $\mathrm{Re}\simeq 14$, while the maximum Re reached in the simulation is about 17.**

The outer step is executed by a suitably modified first-order-accurate projection method which rests on writing the time-discretized Navier-Stokes equation as

$$\frac{\mathbf{u}^{n+1}-\mathbf{u}^{n}}{\Delta t}=\mathcal{N}(\mathbf{u}^{n})-\frac{1}{\rho}\boldsymbol{\nabla} p^{n+1}, \tag{13}$$

where $\mathcal{N}$ stands for all the terms that need not be shown explicitly; the superscripts n, $n+1$ denote time levels and we assume that everything is known at time level n. The modification to the usual procedure is rendered necessary by the fact that the velocity

Table 2 **Dimensionless force components for flow past a cylinder at Re=30 in dependence of the number N_Δ of points per cylinder diameter and number of modes N_c**

N_Δ	N_c	$aF_x/4\pi\mu\nu$	$aF_y/4\pi\mu\nu$
20	4	41.019	−0.0131
30	4	41.089	0.00302
40	2	41.374	0.0379
40	4	41.081	0.00331
40	6	41.094	−0.000493
40	8	41.093	0.000127

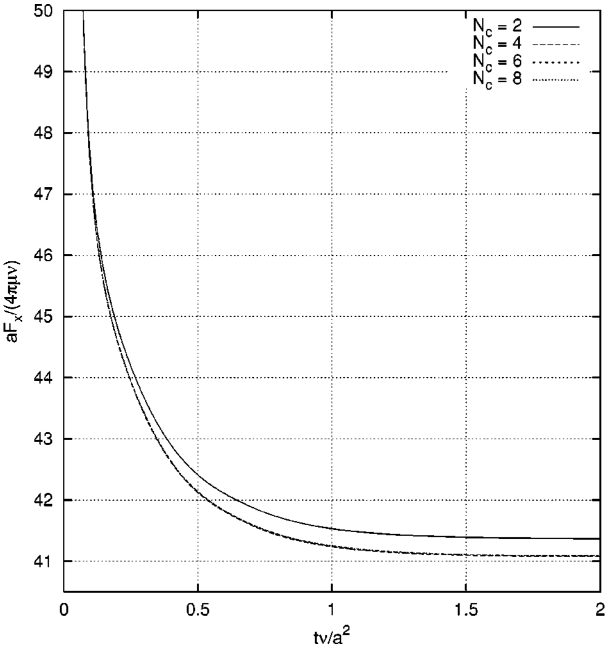

Fig. 10 **Dimensionless force component $aF_x/4\pi\mu\nu$ in the direction of the flow versus time at Re=30 in dependence of the number N_c of modes retained in the summations in (6), (9), and (10); the number of points per cylinder diameter is $N_\Delta=40$**

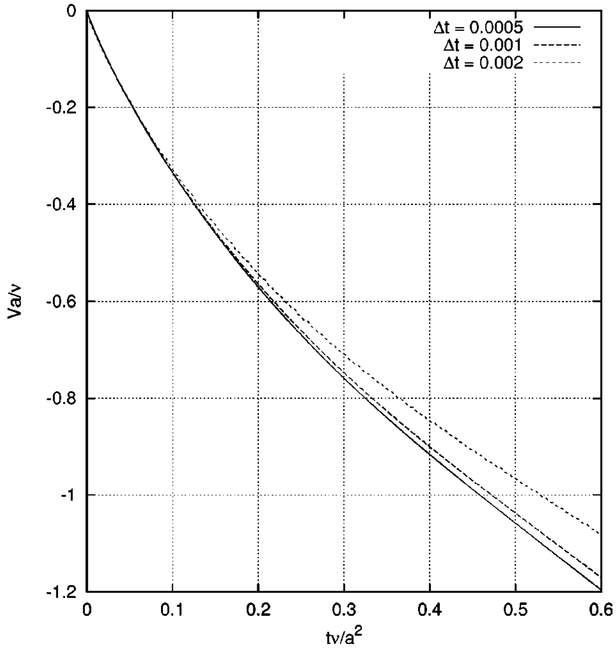

Fig. 12 **Vertical velocity of the leading particle for the simulation of Fig. 5 as computed with $\Delta t=0.5$, 1, and 2 ms**

boundary condition on the cages depends on the coefficients of the expansions which are only determined as part of the iteration procedure. Denote by κ the index of this iteration, and write, for brevity, $\mathbf{u}^\kappa$, p^κ, and $\mathbf{A}^\kappa$ in place of $\mathbf{u}^{n+1,\kappa}$, $p^{n+1,\kappa}$, and $(A_k^\kappa, B_k^\kappa, \tilde{A}_k^\kappa, \tilde{B}_k^\kappa)$. As in the usual method, we define $\mathbf{u}_*^\kappa$ at interior nodes by

$$\frac{\mathbf{u}_*^\kappa - \mathbf{u}^n}{\Delta t} = \mathcal{N}(\mathbf{u}^n), \tag{14}$$

and, since approximate values $\mathbf{A}^{\kappa-1}$ of the coefficients are available, we use these values to set $\mathbf{u}_*^\kappa$ on the cage nodes (see below for a further note on this step).

Before taking the divergence of (13) as in the usual implementation of the projection method, we multiply this equation by the characteristic function χ of the domain external to the cages. Near the generic particle α we may take $\chi=H(S^\alpha)$, where H is the Heaviside distribution and $S^\alpha(\mathbf{x})=0$ is the cage surrounding particle α, with $S^\alpha>0$ outside the cage. The result is

$$H\nabla^2 p^{\kappa+1} + \nabla H\cdot\nabla p^{\kappa+1} = \frac{\rho}{\Delta t}[H\nabla\cdot\mathbf{u}_*^\kappa + (\mathbf{u}^{n+1}-\mathbf{u}_*^\kappa)\cdot\nabla H]. \tag{15}$$

Thanks to the factor ∇H, the last term of the equation only contributes on the cage where, at convergence, $\mathbf{u}^{n+1}=\mathbf{u}_*$; thus we drop this term and further approximate (15) by evaluating the second term at iteration level κ rather than $\kappa+1$:

$$H\nabla^2 p^{\kappa+1} = \frac{\rho}{\Delta t}H\nabla\cdot\mathbf{u}_*^\kappa - \nabla H\cdot\nabla p^\kappa. \tag{16}$$

The solution of this equation gives a new estimate $p^{\kappa+1}$ of p^{n+1}, which enables us to calculate $\mathbf{u}^{\kappa+1}$ from

$$\frac{\mathbf{u}^{\kappa+1}-\mathbf{u}_*^\kappa}{\Delta t} = -\frac{1}{\rho}\nabla p^{\kappa+1}, \tag{17}$$

from which new coefficients $\mathbf{A}^{\kappa+1}$ can be found by matching, and so on.

If (16) were solved as it stands, it would be necessary to implement a procedure to skip the nodes inside the inner cage, which would prevent the use of a fast solver. This potential source of inefficiency can, however, be avoided as explained in [20].

After convergence, the position $\mathbf{y}$, velocity $\mathbf{w}$, and angular velocity Ω of each particle are updated from

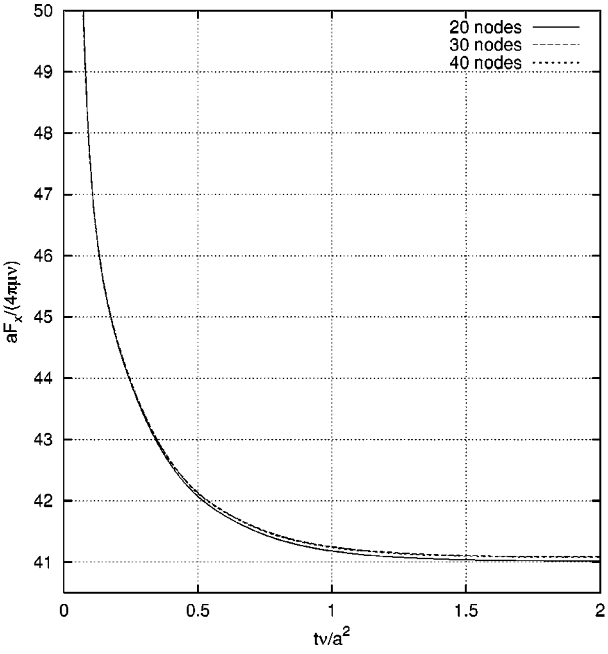

Fig. 11 **Dimensionless force component $aF_x/4\pi\mu\nu$ in the direction of the flow versus time at Re=30 in dependence of the number of points per cylinder diameter; the number of modes is $N_c=4$**

$$\mathbf{w}^{n+1}=\mathbf{w}^n+\frac{\Delta t}{2m}(\mathbf{F}^{n+1}+\mathbf{F}^n), \quad \mathbf{y}^{n+1}=\mathbf{y}^n+\frac{\Delta t}{2}(\mathbf{w}^{n+1}+\mathbf{w}^n), \tag{18}$$

$$\Omega^{n+1}=\Omega^n+\frac{\Delta t}{2I}(L^{n+1}+L^n), \tag{19}$$

where m and I are the particle mass and moment of inertia. It should be noted that this procedure is only $O(\Delta t)$ accurate as the flow fields used to calculate $\mathbf{F}^{n+1}$ and $\mathbf{L}^{n+1}$ are based on the old (at time t^n) position and velocity of the particles. Use of (18) and (19) enhances stability.

3.2 Matching. According to Step 1 of the procedure described before, once $\mathbf{u}^{\kappa+1}$ has been determined, it is necessary to update the coefficients $(A_k, B_k, \tilde{A}_k, \tilde{B}_k)$. This step involves solving a linear system and, in principle, one could retain as many coefficients as there are pressure and vorticity points in the cage. In practice, however, on a finite difference discretization with cells of side Δ, the shortest feature that can be resolved has a length scale $\sim 2\Delta$ so that, retaining modes with a shorter wavelength, would contaminate the calculation with aliasing errors rather than increase accuracy. Truncating the summation in (6) at N_c is equivalent to allowing a shortest wavelength of the order of $2a/N_c$. Thus we expect that a near-optimal choice would be $2a/N_c \simeq 2\Delta$, or $N_c \simeq 1/2N_\Delta$, where $N_\Delta = 2a/\Delta$ is the number of mesh lengths per diameter. Since the number of available grid points is of the order of $2\pi a/\Delta \simeq 6N_\Delta$, and the number of coefficients $\simeq 4N_c$, in a typical calculation there are about three times as many grid points as coefficients. The system determining the coefficients has therefore a rectangular matrix, and we solve it by the Singular Value Decomposition algorithm, which is equivalent to a least-squares procedure when all singular values are retained (see, e.g., Refs. [23,24]).

It is apparent that the accuracy of the method can be increased arbitrarily by increasing the number of nodes (with the effect, among others, of reducing the extent of the region where applicability of the Stokes equations is assumed) and the number of coefficients in the exact solution. It may also be noted that, for a smooth velocity field, the analytic expansion (6) converges faster than algebraically and therefore the present method makes an efficient use of the degrees-of-freedom retained for each particle. Another significant advantage is that the force and torque on each particle are found directly from (11) once the low-order coefficients A_0, B_1, $\tilde{B}_1$ are known. This avoids the difficulty encountered with some other methods which require high-order extrapolations to obtain the stress distribution on the particle.

3.3 Cage. The algorithm used to generate the particle cage is as follows. For each particle, at each time-step, the grid node closest to the particle center $\mathbf{y}$ is identified. A square centered at this node, with sides equal to the number of grid nodes per particle plus 1 (so as to make sure that the particle is entirely contained in it), is then constructed. All the cells contained in this square are then examined in turn, and the fraction of their area occupied by the particle is computed: if this fraction is between 50% and 100%, the cell is assigned to the cage; note that, in this way, the pressure point at the center of the cell is guaranteed to be inside the particle. For each cage cell, the node farthest from the particle center is taken as vorticity point, while the velocity nodes are taken at the midpoints of the cell sides closest to the particle center. Additional vorticity nodes are then inserted to ensure that no gaps are left. This construction is repeated each time a particle is moved.

Many of the points used in the algorithm thus fall inside the particle, but this does not create any difficulty—practical or conceptual—as, in principle, the functions defined by (6), (9), and (10) are defined for r both greater and smaller than the particle radius (provided, of course, that $r>0$). As a matter of fact, the possibility of placing the cage mostly inside the particle permits two particles to come in very near contact as will be demonstrated below.

4 Some Examples

Our first example is reproduced from [20]. It consists of the flow induced by a line of stationary cylinders held between two parallel walls both moving with velocity U; the Reynolds number is defined as $\mathrm{Re}=2aU/\nu$, where a is the particle radius. This case was simulated in Ref. [25] by a finite element method and in Ref. [18] by a lattice-Boltzmann method. The cylinders are spaced by a distance L, D denotes the spacing between the walls, and $f_c = |\mathbf{F}|/2\pi\rho U^2 a$, with $\mathbf{F}$ the total fluid-dynamic force. Table 1 illustrates the near-perfect agreement among the three computations for a case with Re=1. Here the column labeled $a/\Delta x$ refers to the computations of Refs. [18] and [25]; the third column denotes the conditions for the present computation. Note that in the last two cases our results have been obtained with 1/2 and 1/3 of the nodes of the lattice-Boltzmann calculation, respectively. For these simulations we took $N_c=4$, and periodicity boundary conditions were applied to the boundaries of the computational domain perpendicular to the moving planes, and no-slip conditions on the planes. Other examples of this type are given in [20]. We now turn to cases with moving particles which were not considered in the earlier papers. We first compare our results with those obtained by others, and conclude with an example with many particles.

Reference [6] reports results of a simulation in which a cylinder falls under the action of gravity between two parallel vertical walls spaced by $L=8a$. Our results for two of their cases are shown in Fig. 2, in which gravity acts from left to right. For the first case (dotted line and squares) the particle to fluid density is $\rho_P/\rho_L=1.003$ and the final Reynolds number 1.03; for the other case (solid line and crosses) $\rho_P/\rho_L=1.03$ with a final Reynolds number 8.33. The figure compares the trajectories of the center of the cylinder when it is released from a distance $0.255L$ and $0.19L$ from the lower wall as computed by the present method (lines) with the results of Ref. [6] (symbols). The two calculations are in close agreement. Here, as in Ref. [6], the computational domain had a total length of $80a$; for Re=8.33 we used $\Delta x=\Delta y=0.125$, and $2a/\Delta x=16$ with 64×640 nodes, a time-step $\nu\Delta t/a^2=0.002$, and $N_c=4$. For the smaller Reynolds number case we found that our method required a somewhat finer discretization, $2a/\Delta x=20$, with $\nu\Delta t/a^2=0.001$. No-slip boundary conditions were applied on all boundaries.

Figure 3 is the ''drafting, kissing, and tumbling'' example of Fig. 3 of Ref. [8] as kindly recalculated for us by Prof. T. W. Pan. Here two particles are allowed to fall along the centerline of a domain having a width $L=20a$ and height $80a$. The particles have a radius of 1 mm and are released at distances $72a$ and $68a$ above the horizontal bottom of the domain. The liquid kinematic viscosity is 0.01 cm^2/s, the liquid density $\rho_L=1$ g/cm^3, and the particle density $\rho_P=1.01$ g/cm^3. The two figures differ in the discretization: 19.2 nodes per particle diameter for the figure on the left, and 28.8 for that on the right; in both cases the time-step was 1 ms. The higher particle falls faster and catches up with the lower one (drafting), after which the two particles fall with nearly the same velocity (kissing), until they tumble and separate. It can be seen upon comparing the two figures that the duration of the ''kiss'' is longer with the finer discretization; also, the results shown here differ rather markedly from those in Fig. 3 of Ref. [8]. The problem is that, with mathematically smooth particles and infinite-precision arithmetic, the two particles would remain aligned indefinitely approaching without ever touching. In the numerical calculation, due to the necessarily finite time-step, it is necessary to introduce an artificial repulsion force to prevent the particles from overlapping and, depending on how this force is specified and on the details of the numerics, the results may very rather widely as can be seen by comparing the two results in Fig. 3 and with those in Fig. 3 of Ref. [8]. The horizontal and vertical positions of the particle centers with the finer discretization are shown in Fig. 4. Another numerical effect is apparent here: the particles drift sideways (x-direction), in spite of the fact that, at this relatively low Reynolds number, single-particle wakes are symmetric and steady. This effect is probably due to the use of a grid of similarly oriented triangles (see [7]).

In our simulation, we imposed no-slip conditions on all the bounding surfaces and took $2a/\Delta x = 2a/\Delta y = 20$. In order to prevent particle collisions, we use the same procedure as suggested in Ref. [7]: It is assumed that a repulsive force $\mathbf{F}_p$ exists between the particles i and j given by

$$\mathbf{F}_c = \begin{cases} 0 & d > 2a + \delta \\ \epsilon_p^{-1}(\mathbf{y}_i - \mathbf{y}_j)(2a + \delta - d)^2 & d \leqslant 2a + \delta \end{cases} \tag{20}$$

where $d = |\mathbf{y}_i - \mathbf{y}_j|$ is the distance between the particle centers, δ is the thickness of a "security zone" (equal to two mesh sizes for the calculations of Figs. 3 and 4) around the particles, and ϵ_p specifies the magnitude of the force. Our results have been obtained with 20 nodes per particle diameter $\delta/a = 0.2$ and $\epsilon_p = 8 \times 10^{-5}$ cm^{3}s^2/g; the time-step was initially set at 1 ms, decreased to 0.6 ms during the time the force (20) was active, and then again increased to 1 ms after the particles separated. We also ran a simulation with a 0.5 ms time-step finding very nearly the same results.

Qualitatively, one notes oscillations during the particle-particle interaction, a feature which is also present in Fig. 10 of [7], who used (20), but not in Fig. 3 where a slightly different form was used:

$$\mathbf{F}_c = \begin{cases} 0 & d > 2a + \delta \\ \epsilon_p^{-1}(\mathbf{y}_i - \mathbf{y}_j)((2a + \delta)^2 - d^2) & d \leqslant 2a + \delta, \end{cases} \tag{21}$$

with $\epsilon_p = 10^{-3}$. The sensitivity to the precise form of the force can be explained by noting that, while they interact, the particle behavior is similar to a damped nonlinear oscillator and, if the damping is not sufficiently strong with respect to the restoring force, oscillations will be produced. Indeed, we have found that these oscillations are strongly affected by the magnitude of δ and ϵ_p; for example, in preliminary calculations in which, following the lead of Ref. [9], the interaction force is turned on only when the particles touch, they disappear. The strong effect of the collision force is also apparent from the very significant differences among the results of [8] and those of Fig. 3 of Professor Pan. Unfortunately, this state of affairs appears to be inherent in this type of simulations: mathematically, the particle interaction is the result of an instability while, physically, it is the result of imperfections of the particle surface. Thus, even in principle, there is little hope of ever developing the "right" interaction force. On the other hand, if interest lies in the simulation of many particles, it may be expected that, on average, the behavior of the system would be rather robust and insensitive to such details. On a more positive note, it may be noted that this type of calculations is still in its infancy and much still remains to be learned.

The maximum vertical velocity in our calculation is reached somewhat later than in Fig. 3; it exceeds by about 10% the result of Fig. 3 and by about 5 percent that of [8]. Figure 5 shows four snapshots of the falling cylinders at times $t = 1.312$, 2.272, 2.521, and 2.971 s; initially the cylinders are located at $y = 7.2$ cm and 6.8 cm, both with $x = 1$ cm.

A significant point worth stressing is that the PHYSALIS algorithm works well even when the particles get closer than one mesh length. For Figs. 6 and 7 the minimum distance between the particle surfaces was $0.0376a$, i.e., less than 1/3 of the mesh length.

As a final example, we show in Figs. 8 and 9 a simulation of the falling of ten cylinders; here the particle diameter is 1 cm, $\rho_P = 1.05$, $\rho = 1$ g/cm^3, and $\nu = 1$ cm^2/s; time is given as $t^* = \nu t/a^2$. The domain width and length were 8 and 40 particle diameters, respectively, with no slip boundary conditions applied on all boundaries; 16 nodes per cylinder diameter were used, $N_c = 4$, $\Delta t = 2$ ms, and $\delta/a = 0.4$. In the last frame of Figs. 9, the leading particle (No. 10) has a terminal velocity corresponding to Re$\simeq$14, while the maximum Re reached in the simulation was about 17.

As long as there are no collisions, the particle arrangement remains symmetric about the midplane of the channel, which implies an absence of bias in the numerics. Symmetry is lost after the particles start undergoing collisions, as a consequence of the instability mentioned before.

The computational times for this multiparticle simulation and the single-particle simulation of Fig. 2 were comparable. In the latter case the domain was half the width as in the former, but the computation was stopped at a value of t^* twice as large as for the multiparticle simulation. The time-step and number of nodes per particle were the same in the two cases, and the Reynolds numbers were similar. Thus, the very weak dependence of the computational time on the number of particles that we have reported in [20] is confirmed by the present results.

5 Some Considerations on Convergence

The numerical results depend on the number of nodes per particle diameter, N_Δ, the number $4N_c + 2$ of coefficients retained in the summations (6), (9), and (10), and the time-step Δt. It was argued earlier that the avoidance of aliasing errors in the summations puts an upper limit on N_c of about $1/2N_\Delta$ and that N_Δ should be sufficiently larger than $\sqrt{\mathrm{Re}}$ to have adequate resolution in the boundary layer.

To illustrate the dependence of our results on these parameters we show in Table 2 the calculated force components on a periodic system of cylinders separated by $12a$ along a line perpendicular to an incoming uniform flow with Re$=30$ (x-axis). The cylinder center is on the midplane of the computational domain at a distance of $10a$ from the upstream boundary; the length of the computational domain in the direction of the flow is $40a$. By symmetry, F_y should be zero and, therefore, F_y/F_x may be taken as a measure of the error on the total force. The results are all very close to each other and appear to be more sensitive to N_c than to the other parameters.

The time evolution of the dimensionless force $aF_x/4\pi\mu\nu$ in the flow direction for different parameter values is shown in Figs. 10 and 11. At $t = 0$ the cylinder is placed in a steady uniform flow, which then adjusts in time to the presence of the bodies. Figure 10 is for 40 nodes per cylinder diameter with $N_c = 2$, 4, 6, 8 modes, i.e. 10, 18, 26, and 34 coefficients. Only the curve corresponding to the smallest number of modes can be distinguished. The effect of the number of nodes, with $N_c = 4$, is shown in Fig. 11. The curves are all very close to each other and only that corresponding to $N_\Delta = 20$ can be distinguished.

Finally, to illustrate the effect of the time-step, we return to the drafting, kissing, and tumbling example of Fig. 6 and show in Fig. 12 the vertical velocity of the leading particle as computed with $\Delta t = 0.5$, 1, and 2 ms during the initial stages of the process. Convergence of the results is clear from this example.

Acknowledgment

We are indebted with Prof. T. W. Pan (University of Houston) for graciously permitting us to publish the results of his simulations in Figs. 3 and 4. It is also a pleasure to thank Prof. D. D. Joseph (University of Minnesota) for helpful advice.

This study has been supported by DOE under grant DE-FG02-99ER14966.

References

[1] Elghobashi, S., and Truesdell, G. C., 1993, "On the Two-Way Interaction Between Homogeneous Turbulence and Dispersed Solid Particles, I: Turbulence Modification," Phys. Fluids A, **5**, pp. 1790–1801.

[2] Stock, D. E., 1996, "Particle Dispersion in Flowing Gases," ASME J. Fluids Eng., **118**, pp. 4–17.

[3] Crowe, C. T., Troutt, T. R., and Chung, J. N., 1996, "Numerical Models for Two-Phase Turbulent Flows," Annu. Rev. Fluid Mech., **28**, pp. 11–41.

[4] Fortes, A., Joseph, D. D., and Lundgren, T. S., 1987, ‘‘Nonlinear Mechanics of Fluidization of Beds of Spherical Particles,’’ J. Fluid Mech., **177**, pp. 467–483.

[5] Hu, H. H., Joseph, D. D., and Crochet, M. J., 1992, ‘‘Direct Simulation of Fluid-Particle Motions,’’ Theor. Comput. Fluid Dyn., **3**, pp. 285–306.

[6] Feng, J., Hu, H. H., and Joseph, D. D., 1994, ‘‘Direct Simulation of Initial Value Problems for the Motion of Solid Bodies in a Newtonian Fluid, Part 1. Sedimentation,’’ J. Fluid Mech., **261**, pp. 95–134.

[7] Glowinski, R., Pan, T. W., Hesla, T. I., and Joseph, D. D., 1999, ‘‘A Distributed Lagrange Multiplier/Fictitious Domain Method for Particulate Flows,’’ Int. J. Multiphase Flow, **25**, pp. 755–794.

[8] Patankar, N. A., Singh, P., Joseph, D. D., Glowinski, R., and Pan, T.-W., 2000, ‘‘A New Formulation of the Distributed Lagrange Multiplier/Fictitious Domain Method for Particulate Flows,’’ Int. J. Multiphase Flow, **26**, pp. 1509–1524.

[9] Singh, P., Hesla, T. I., and Joseph, D. D., 2001, ‘‘Modified Distributed Lagrangian Multiplier/Fictitious Domain Method for Particulate Flows With Collisions,’’ preprint.

[10] Pan, Y., and Banerjee, S., 1997, ‘‘Numerical Investigation of the Effect of Large Particles on Wall Turbulence,’’ Phys. Fluids, **9**, pp. 3786–3807.

[11] Takiguchi, S., Kajishima, T., and Miyake, Y., 1999, ‘‘Numerical Scheme to Resolve the Interaction Between Solid Particles and Fluid Turbulence,’’ JSME Int. J., **B42**, pp. 411–418.

[12] Johnson, A. A., and Tezduyar, T., 1996, ‘‘Simulation of Multiple Spheres Falling in a Liquid-Filled Tube,’’ Comput. Methods Appl. Mech. Eng., **134**, pp. 351–373.

[13] Johnson, A. A., and Tezduyar, T., 1997, ‘‘3-D Simulation of Fluid-Particle Interactions With the Number of Particles Reaching 100,’’ Comput. Methods Appl. Mech. Eng., **145**, pp. 301–321.

[14] Chattot, J. J., and Wang, Y., 1998, ‘‘Improved Treatment of Intersecting Bodies With the Chimera Method and Validation With a Simple and Fast Flow Solver,’’ Comput. Fluids, **27**, pp. 721–740.

[15] Nirschl, H., Dwyer, H. A., and Denk, V., 1995, ‘‘Three-Dimensional Calculations of the Simple Shear Flow Around a Single Particle Between Two Moving Walls,’’ J. Fluid Mech., **283**, pp. 273–285.

[16] Chen, S., and Doolen, G. D., 1998, ‘‘Lattice Boltzmann Method in Fluid Flows,’’ Annu. Rev. Fluid Mech., **30**, pp. 329–364.

[17] Aidun, C. K., Lu, Y., and Ding, E.-J., 1998, ‘‘Direct Analysis of Particulate Suspensions With Inertia Using the Discrete Boltzmann Equation,’’ J. Fluid Mech., **37**, pp. 287–311.

[18] Inamuro, T., Maeba, K., and Ogino, F., 2000, ‘‘Flow Between Parallel Walls Containing the Lines of Neutrally Buoyant Circular Cylinders,’’ Int. J. Multiphase Flow, **26**, pp. 1981–2004.

[19] Prosperetti, A., and Og̃uz, H. N., 2001, ‘‘PHYSALIS: A New $o(N)$ Method for the Numerical Simulation of Disperse Flows of Spheres, Part I: Potential Flow,’’ J. Comput. Phys., **167**, pp. 196–216.

[20] Takagi, S., Og̃uz, H. N., Zhang, Z., and Prosperetti, A., 2002, ‘‘PHYSALIS: A New Method Particle Simulation, Part II: Two-Dimensional Navier-Stokes Flow Around Cylinders,’’ J. Comput. Phys., submitted for publication.

[21] Huang, H., and Takagi, S., 2002, ‘‘PHYSALIS: A New Method for Particle Flow Simulation, Part III: Convergence Analysis,’’ J. Comput. Phys., submitted for publication.

[22] Ory, E., Og̃uz, H. N., and Prosperetti, A., 2000, ‘‘PHYSALIS: A New Numerical Method for Particle Simulations,’’ *Proceedings of the ASME FED Summer Meeting*, ASME, New York.

[23] Kress, R., 1989, *Linear Integral Equations*, Springer, Berlin.

[24] Press, W. H., Vetterling, W. T., Teukolsky, S. A., and Flannery, B. P., 1992, *Numerical Recipes in FORTRAN*, 2nd Ed; Cambridge University Press, Cambridge, UK.

[25] Aidun, C. K., and Lu, Y., 1995, ‘‘Lattice Boltzmann Simulation of Solid Particles Suspended in a Fluid,’’ J. Stat. Phys., **81**, pp. 49–61.

Shear Buckling of Sandwich, Fiber Composite and Lattice Columns, Bearings, and Helical Springs: Paradox Resolved

Z. P. Bažant
McCormick School Professor
and Walter P. Murphy Professor of Civil
Engineering and Materials Science,
McCormick School of Engineering
and Applied Science,
Northwestern University,
2145 Sheridan Road,
Evanston, IL 60208
e-mail: z-bazant@northwestern.edu
Fellow ASME

As shown three decades ago, in situations where the initial stresses before buckling are not negligible compared to the elastic moduli, the geometrical dependence of the tangential moduli on the initial stresses must be taken into account in stability analysis, and the stability or bifurcation criteria have different forms for tangential moduli associated with different choices of the finite strain measure. So it has appeared paradoxical that, for sandwich columns, different but equally plausible assumptions yield different formulas, Engesser's and Haringx' formulas, even though the axial stress in the skins is negligible compared to the axial elastic modulus of the skins and the axial stress in the core is negligible compared to the shear modulus of the core. This apparent paradox is explained by variational energy analysis. It is shown that the shear stiffness of a sandwich column, provided by the core, generally depends on the axial force carried by the skins if that force is not negligible compared to the shear stiffness of the column (if the column is short). The Engesser-type, Haringx-type, and other possible formulas associated with different finite strain measures are all, in principle, equivalent, although a different shear stiffness of the core, depending linearly on the applied axial load, must be used for each. The Haringx-type formula, however, is most convenient because it represents the only case in which the shear modulus of the core can be considered to be independent of the axial force in the skins and to be equal to the shear modulus measured in simple shear tests (e.g., torsional test). Extensions of the analysis further show that Haringx's formula is preferable for a highly orthotropic composite because a constant shear modulus of the soft matrix can be used for calculating the shear stiffness of the column, and further confirm that Haringx's buckling formula with a constant shear stiffness is appropriate for helical springs and built-up columns (laced or battened). [DOI: 10.1115/1.1509486]

1 Introduction

During the 1960s, there used to be lively polemics among the proponents of different three-dimensional stability formulations associated variationally with different finite strain measures (see, e.g., the preface of Biot's book [1]), different objective stress rates, and different incremental differential equations of equilibrium (proposed by Hadamard, Biot, Trefftz, Truesdell, Pearson, Hill, Biezeno, Hencky, Neuber, Jaumann, Southwell, Cotter, Rivlin, Engesser, Haringx, etc.—see [2] (p. 732 and Chap. 11) and [3]). These polemics were settled in 1971 by the demonstration, [4], that all these formulations are equivalent because the tangential elastic moduli of the material cannot be taken the same but must rather have different values in each formulation. It was also concluded that these differences matter only if the initial stresses at the critical state of buckling are not negligible compared to the elastic moduli ([2], Sec. 11.4), [4].

For most buckling problems, the differences between various stability criteria are insignificant because the initial stresses are negligible compared to the tangential moduli. One exception is the buckling of rubber and other elastomers. Others are the buckling of composites with a highly orthotropic fiber reinforcement and a very soft matrix, or built-up columns (battened or lattice columns), large regular frameworks treated in a smeared manner as a continuum, and elastomeric bearings used for bridges and for seismic isolation of buildings.

For sandwich plates, which are very sensitive to buckling, [5–11], the initial axial stress in the skins of a sandwich column is negligible compared to the elastic modulus of the skins, and the initial axial stress in the foam core is zero. Consequently, it may at first seem that the shear stiffness of the core should not depend on the axial force in the skins, which would imply that there should be no differences among the critical load formulas associated with different finite strain measures.

So, it came as a surprise that the Engesser-type, [12–14], buckling formula for sandwich columns, which is associated with the Doyle-Ericksen finite strain tensor of order $m=2$, [2], gave, for short sandwich columns, much smaller critical loads than the Haringx-type, [15,16], formula, which is associated with the Doyle-Ericksen tensor of order $m=-2$. The discrepancy was vehemently debated at several recent symposia on composites (especially at those sponsored by ONR at the ASME Congresses in Orlando (2000) and in New York (2001)). Using constant and the same shear stiffness values for both formulas, Kardomateas [17–22] and Simitses and Shen [23] showed that the Haringx-type buckling formula gave results closer to the experiments on sandwich columns and to three-dimensional finite element simulations. But, in view of the smallness of stresses in both the core and the skins, the reason for the difference has been seen as a paradox. To explain it, is the purpose of this paper. The explanation will also clarify the shear stiffness to be used for buckling of highly orthotropic composites and explain why Haringx's formula is the correct buckling formula for helical springs.

Contributed by the Applied Mechanics Division of THE AMERICAN SOCIETY OF MECHANICAL ENGINEERS for publication in the ASME JOURNAL OF APPLIED MECHANICS. Manuscript received by the Applied Mechanics Division, Jan. 30, 2002; final revision, May 9, 2002. Associate Editor: A. Needleman. Discussion on the paper should be addressed to the Editor, Prof. Robert M. McMeeking, Chair, Department of Mechanics and Environmental Engineering, University of California–Santa Barbara, Santa Barbara, CA 93106-5070, and will be accepted until four months after final publication in the paper itself in the ASME JOURNAL OF APPLIED MECHANICS.

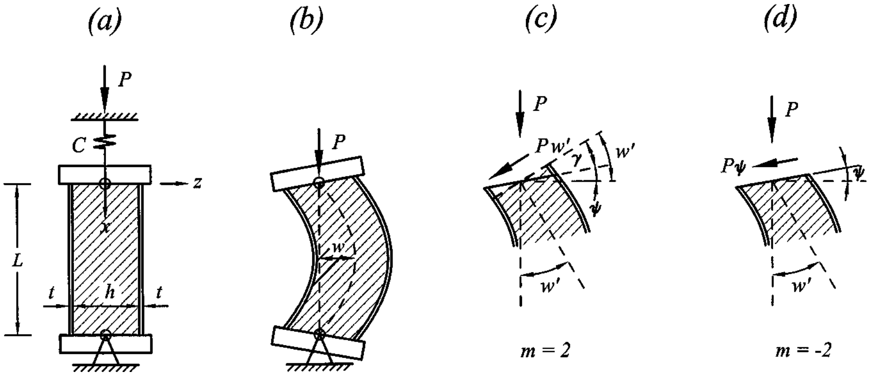

Fig. 1 Sandwich column in (*a*) initial state and (*b*) deflected state; (*c,d*) cross-section rotation, shear angle and shear force due to axial load

In applications to built-up (battened or laced (latticed)) columns and to fiber composites, the difference between the Engesser and Haringx shear buckling formulas has been discussed for about 60 years; e.g., [2,4,24–34]. Ziegler [27], for example, tended to favor Engesser's formula and Reissner, [28,29], Haringx's formula. However, no consensus on the theory has yet emerged, [25,26], although the experiments on helical springs, [16], elastomeric bearings, [35], and latticed columns, [32], clearly favor Haringx's formula.

2 Tangential Moduli Associated With Different Finite Strain Measures

To discuss buckling with shear, we need to recall the dependence of the tangential stiffness tensor of a material on the choice of the finite strain measure (Bažant [4]). A broad class of equally admissible finite strain measures which comprises practically all of those ever used is represented by the Doyle-Ericksen tensors $\boldsymbol{\epsilon}=(\mathbf{U}^m-\mathbf{I})/m$ (also called Hill's family of strains, see, e.g., [2], Section 9.1)); m can be any real number, $\mathbf{I}$=unit tensor, and $\mathbf{U}$=right-stretch tensor. The second-order approximation of these tensors is, in component form,

$$\epsilon_{ij}^{(m)}=e_{ij}+\frac{1}{2}u_{k,i}u_{k,j}-\alpha e_{ki}e_{kj}, \quad e_{ki}=\frac{1}{2}(u_{k,i}+u_{i,k}),$$

$$\alpha=1-\frac{1}{2}m. \tag{1}$$

Here e_{ij} is the small (linearized) strain tensor; the subscripts refer to Cartesian coordinates x_i, $i=1, 2, 3$) and repetition of tensorial subscripts implies summation. In all the formulations up to now, $-2\leqslant m\leqslant 2$.

It was shown in [4] and, didactically, in [2], Sec. 11.4, that the stability criteria expressed in terms of any of these strain measures are mutually equivalent if the tangential moduli associated with different m-values are related as follows:

$$C_{ijkl}^{(m)}=C_{ijkm}+\frac{1}{4}(2-m)(S_{ik}\delta_{jl}+S_{jk}\delta_{il}+S_{il}\delta_{jk}+S_{jl}\delta_{ik}) \tag{2}$$

([4] and [2] p. 727). Here C_{ijkl} are the tangential moduli associated with Green's Lagrangian strain ($m=2$), and S_{ij}=current stress (Cauchy stress). Obviously, the differences among the $C_{ijkl}^{(m)}$ values for different m are insignificant if the (suitable) norms

$$\|S_{ij}(\mathbf{x})\|\ll\|C_{ijkl}^{(m)}(\mathbf{x})\| \quad \text{(for every } \mathbf{x}\text{; } m \text{ bounded)} \tag{3}$$

where $\mathbf{x}$=coordinate vectors of points in the structure. This inequality is satisfied for sandwich columns, which is why the discrepancy between the two existing sandwich buckling formulas has seemed paradoxical.

3 Classical Paradox in Buckling of Columns Weak in Shear

Engesser in 1889 [12–14] and Haringx in 1942 [15] presented different formulas for the first critical load in buckling of columns exhibiting significant shear deformations (Fig. 1(*a,b*)). They read

$$P_{cr}=\frac{P_E}{1+(P_E/GA)} \quad \text{(Engesser)} \tag{4}$$

$$P_{cr}=\frac{GA}{2}\left(\sqrt{1+\frac{4P_E}{GA}}-1\right) \quad \text{(Haringx)} \tag{5}$$

(see also [24]); E,G=elastic Young's and shear moduli, $P_E=(\pi^2/l^2)EI$=Euler's critical load, l=effective buckling length, and EI,GA=bending stiffness and shear stiffness of the cross section (note that, in general, $A=\kappa A_0$ where A_0=actual cross-section area and κ=Timoshenko's shear correction factor, which is greater than but close to 1; for a sandwich $\kappa\approx1$). Each of these two formulas can be regarded as a different and equally plausible generalization of the Timoshenko beam theory ([36]), which does not deal with finite strain effects and applies only to beams carrying negligible axial force.

The discrepancy between these two formulas used to be, until 1971, regarded as a paradox. Then it was shown, [2,4], that this classical paradox is caused by a dependence of the tangential shear modulus $C_{1212}=G$ on the axial stress $S_{11}=-P/A$, which inevitably is different for different choices of the finite strain measure, i.e., for different m. It turns out that Engesser's formula corresponds to Green's Lagrangian strain tensor ($m=2$), and Haringx's formula to the Lagrangian Almansi strain tensor ($m=-2$). Properly the shear moduli in (4) and (5) should be labeled as $G^{(2)}$ and $G^{(-2)}$, respectively, and (2) indicates that

$$G^{(2)}=G^{(-2)}+P/A. \tag{6}$$

Equation (2) further indicates a difference in the E-values, however, that difference can be neglected because the axial stress is always negligible compared to E. Replacing G in Engesser's formula with $G+P_{cr}/A$ and solving P_{cr} from the resulting equation, one obtains Haringx's formula ([2], p. 738), which makes the equivalence blatant.

Equation (6) shows that if the shear modulus is constant (independent of stress $-P/A$) for one formula, it cannot be considered constant for the other formula. For a homogeneous material for which these two buckling formulas give different results, the case of a constant shear modulus would be one chance among infinitely many possible stress-dependences of the shear modulus, and so a constant shear modulus is highly unlikely for either formula.

The difference in shear moduli in (6), of course, becomes significant only if the axial stress $S_{11}=-P/A$ is not negligible compared to G. Such a situation arises for built-up columns (consisting either of a regular pin-jointed lattice or a regular moment-resisting framework) approximated by a homogenizing continuum, or for highly orthotropic columns, e.g., columns made of a fiber composite with a very soft matrix. With a proper definition of the dependence of G on the axial stress, both formulas are equivalent. However, even though the equivalence of both formulas along with (6) was demonstrated three decades ago, a false perception of contradiction between these formulas has been widespread.

The relationship between the G values for two different m is linear in stress $S^0 = -P/A$. Thus, if the dependence of $G^{(m)}$ on S^0 is linear, there must exist one m value for which $G^{(m)}$ is constant. The formulation for this m is the the most convenient one for practical use. On the other hand, if the dependence of G on S^0 were nonlinear, there would exist no m for which G could be constant.

4 New Apparent Paradox for Sandwich Buckling

In this study, we focus attention on elastic sandwich columns, for which a similar but not identical paradox has arisen as a consequence of various recent studies, [19–23,32], and was debated at several recent conferences (especially the ASME congresses in Orlando in 2000, and in New York in 2001). Explanation of this new apparent paradox is the objective of our analysis.

Let L denote the length of the column, l its effective length, and P the axial force. The core has thickness h and shear modulus G. The skins have thickness t and are, in general, orthotropic, with axial elastic modulus E (Fig. 1(a)). Since Young's modulus of the core is negligible compared to E for the skins, the entire axial force and bending moment are carried by the skins. On the other hand, since we may generally assume that $t \ll h$, the entire shear force is carried by the core. Therefore, one may substitute $EI = Ebt(h+t)^2/2 + Ebt^3/6 \approx Ebth^2/2 =$ bending stiffness of the sandwich ($t \ll h$), and $GA = Gbh =$ shear stiffness of the sandwich, b being the cross section width in the y-direction. With these substitutions, the Engesser and Haringx formulas become

$$P_{cr} = \frac{P_E}{1 + (P_E/Gbh)} \quad \text{(Engesser type)} \tag{7}$$

$$P_{cr} = \frac{Gbh}{2}\left[\sqrt{1 + \frac{4P_E}{Gbh}} - 1\right] \quad \text{(Haringx type)} \tag{8}$$

where P_E is the Euler load,

$$P_E = \frac{\pi^2}{l^2} EI \approx \frac{\pi^2}{l^2} \frac{Ebth^2}{2}. \tag{9}$$

Similar to (6), one may check that, by making the replacement

$$G_{\text{core}} \leftarrow G_{\text{core}} - \frac{2t}{h} \sigma_{\text{skins}} \tag{10}$$

where $\sigma_{\text{skins}} = -P_{cr}/2bt$ and $G = G_{\text{core}} =$ shear modulus of the core, the Engesser-type formula (7) gets transformed into the Haringx-type formula (8).

Although the foregoing replacement works, it is, however, purely formalistic, with no physical basis. It is certainly paradoxical that the shear modulus in the *core* should depend on the axial stress in the *skins*. Therefore, the reason for the discrepancy between these two formulas cannot be caused by the differences in the shear modulus G of the core material, as given by (6). Besides, there is no reason for the G-moduli associated with different strain measures to differ because the axial stress in the core is negligible compared to the shear modulus of core.

We thus have a different kind of paradox, which we must explain. To this end, we must not limit consideration to the material level, as in (10). Rather, we must consider from the outset a sandwich column constrained by the hypothesis that (in slender enough columns) the cross sections of the core must remain plane.

5 Adaptation of Previous General Analysis to Sandwich Column

To clarify the differences between the Engesser-type and Haringx-type formulas, Bažant's [4] general analysis of a column with shear needs to be adapted to a sandwich column. In stability analysis, the incremental potential energy of the column must be expressed accurately up to the second order in displacement gradients. Since the critical axial stress S^0 is not small, finite strain expressions that are accurate up to the second order must be used in the incremental energy expression.

To check whether there is any difference between the P_{cr}-values for axial loads P applied under load control (e.g., gravity) and under displacement control (i.e., with a prescribed axial displacement u_0 at column top), it is convenient to consider a general loading in which P is applied through a spring of stiffness C, attached on top (Fig. 1(a)). We introduce Cartesian coordinates x_i ($i = 1,2,3$, $x_1 = x$, $x_2 = y$, $x_3 = z$), positioned so that $x_1 =$ axial coordinate of column (Fig. 1(a)). The components of the incremental displacements from the stressed initial undeflected state are u_i; $u_3 = w(x) =$ small lateral deflection (displacement of the neutral axis in the direction of coordinate x_3), and $u_1 = u(x,y,z) =$ small incremental axial displacement; ψ a small rotation of the cross section, assumed to remain plane but generally not normal to the deflected beam axis (Fig. 1(c,d)). The shear angle $\gamma = \theta - \psi$ (Fig. 1(c,d)) where $\theta = w' =$ slope of the deflection curve (the primes denote derivatives with respect to x).

Obviously, the incremental axial strain in the neutral axis is distributed uniformly along the column; $e_{11}^0 = u_0/L$. The second-order incremental potential energy $\delta^2 \mathcal{W}$ for small deflections $w(x)$ and small axial displacements $u(x)$ is

$$\delta^2 \mathcal{W} = \int_0^L \int_A \left[S^0(y,z)(\epsilon_{11}^{(m)} - e_{11}) + \frac{1}{2} E^{(m)}(y,z) e_{11}^2 + \frac{1}{2} G^{(m)}(y,z) \gamma^2 \right] \mathrm{d}A \ \mathrm{d}x + \int_A \int_0^L \frac{1}{2} E^{(m)}(y,0)(u_0/L)^2 \mathrm{d}A \ \mathrm{d}x + \frac{1}{2} C u_0^2 \tag{11}$$

where the factor $(\epsilon_{11}^{(m)} - e_{11})$ is justified in [2] (Chap. 11); $y = x_2$ and $z = x_3 =$ coordinates of the cross section whose area is A; $\mathrm{d}A = \mathrm{d}y\mathrm{d}z$; $S^0(y,z) =$ initial axial normal stress in the straight column before deflection; $E^{(m)}(y,z)$ and $G^{(m)}(y,z)$ are the tangential elastic moduli at point (y,z); $E^{(m)}(y,z) =$ axial elastic modulus (taken, in the case of a sandwich, to be nonzero only for the skins, which normally are orthotropic), $G^{(m)}(y,z) =$ shear modulus (taken into account, for a sandwich, only for the core); and $E^{(m)}(y,0)$ is the value at the neutral plane (midthickness of core). The superscript $^{(m)}$ indicates that, for different m, these values may in general be different, as implied by (2).

Since the skin thickness $t \ll h$, we consider the skins to possess only axial stiffness; the bending and shear stiffnesses of the skins are negligible, and we may also consider $\gamma = 0$ within the skins. Accordingly,

$$u = u_1 = -z\psi, \quad u_{1,3} = -\psi, \quad u' = u_{1,1} = e_{11} = -z\psi', \tag{12}$$

$$u_{1,3} = -\psi, \quad u_{3,1} = w' = \theta, \quad 2e_{13} = 2e_{31} = u_{1,3} + u_{3,1} = \gamma = w' - \psi \tag{13}$$

$$\epsilon_{11}^{(m)} - e_{11} = \frac{1}{2}(u_{1,1}^2 + u_{3,1}^2) - \alpha(e_{11}^2 + e_{31}^2) = \frac{1}{2}(z^2\psi'^2 + w'^2) - \alpha\left[z^2\psi'^2 + \frac{1}{4}(w' - \psi)^2\right] \tag{14}$$

(since we consider deflections from the initial state of loaded column before buckling, the expression $u_1 = -z\psi$ does not include

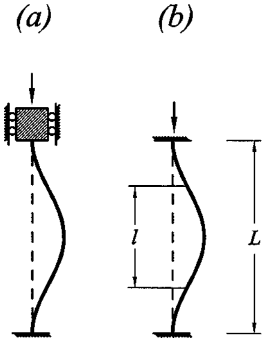

Fig. 2 Column loaded (*a*) under load control (e.g., by gravity) and (*b*) displacement control

the axial displacement at column axis, corresponding to displacement u_0 at the top). After these substitutions, (11) becomes

$$\delta^2\mathcal{W}=\frac{1}{2}\int_0^L\int_A\left\{[(m-1)S^0(y,z)+E^{(m)}(y,z)]z^2\psi'^2 + S^0(y,z)w'^2 + \left[G^{(m)}(y,z)-\frac{1}{4}(2-m)S^0(y,z)\right](w'-\psi)^2\right\}\mathrm{d}A\,\mathrm{d}x + \int_0^L\int_A\frac{1}{2}E^{(m)}(y,z)(u_0/L)^2\mathrm{d}A\,\mathrm{d}x+\frac{1}{2}Cu_0^2. \tag{15}$$

Note that none of the terms containing δu_0 contains also $w(x)$. Thus it is clear that the stiffness of the spring will have no effect on the critical load for lateral buckling. So we will from now on ignore the terms containing C, which is equivalent to considering $C\to\infty$, or to setting $u_0=\delta u_0=0$. As the displacement control (Fig. 2) of axial loading of the column is equivalent to $C\to\infty$ and the load control to $C=0$ (Fig. 1(*a,b*)), it follows that the critical loads of lateral buckling are the same for both types of load control (which is, in principle, well known).

Now we may integrate (15) over the cross section. Noting that the elastic modulus $E^{(m)}$ is negligibly small within the core, that the $G^{(m)}$ of the skins may be neglected because they carry a negligible portion of the shear force, and that the bending stiffness of the skins is negligible, we obtain in the integration process the following cross-section stiffness expressions and resultants:

$$\int_A E^{(m)}(y,z)z^2\mathrm{d}A=R^{(m)}=E^{(m)}\frac{1}{2}bth^2,$$

$$\int_A G^{(m)}(y,z)\mathrm{d}A=H^{(m)}=G^{(m)}bh \tag{16}$$

$$\int_A S^0(y,z)\mathrm{d}A=-P,\qquad \int_A S^0(y,z)z^2\mathrm{d}A=-\frac{1}{2}Ph^2. \tag{17}$$

Here $E^{(m)}$ is the value for the skins and $G^{(m)}$ the value for the core; $R^{(m)}$ and $H^{(m)}$ are the bending and shear stiffnesses of the cross section. A simplification can be obtained by noting that

$$|(m-1)S^0(y,z)|\ll E^{(m)} \tag{18}$$

because the magnitude of the axial compressive stress in the skin is always negligible compared to the axial elastic modulus of the skin. Setting also $\alpha=1-m/2$, we thus obtain

$$\delta^2\mathcal{W}=\frac{1}{2}\int_0^L\left\{R^{(m)}\psi'^2+\left[H^{(m)}+\frac{1}{4}(2-m)P\right](w'-\psi)^2 - Pw'^2\right\}dx. \tag{19}$$

The necessary condition of stability loss and bifurcation is that the first variation of the second-order work $\delta^2\mathcal{W}$ during any kinematically admissible deflection variations $\delta w(x)$, $\delta u(x)$, δu_0 must vanish (Trefftz condition [2]). So,

$$\delta(\delta^2\mathcal{W})=\int_0^L\left\{R^{(m)}\psi'\,\delta\psi'+\left[H^{(m)}+\frac{1}{4}(2-m)P\right](w'-\psi)\times(\delta w'-\delta\psi)-Pw'\,\delta w'\right\}\mathrm{d}x=0. \tag{20}$$

Now we may integrate the first term by parts to eliminate the derivative of the variation $\delta\psi(x)$;

$$\delta(\delta^2\mathcal{W})=\int_0^L\left\{\left[H^{(m)}+\frac{1}{4}(2-m)P\right](w'-\psi)-Pw'\right\}\delta w'(x)\mathrm{d}x - \int_0^L\left\{R^{(m)}\psi''+\left[H^{(m)}+\frac{1}{4}(2-m)P\right]\times(w'-\psi)\right\}\delta\psi(x)\mathrm{d}x + [\ \ldots\ ]_0^L \tag{21}$$

where the boundary terms, $[\ \ldots\ ]_0^L$, need not be written out in detail for our purpose. The last variational equation must be satisfied for any kinematically admissible variations $\delta\psi(x)$ and $\delta w'(x)$. This condition requires that

$$Pw'-\left[H^{(m)}+\frac{1}{4}(2-m)P\right](w'-\psi)=0 \tag{22}$$

$$R^{(m)}\psi''+\left[H^{(m)}+\frac{1}{4}(2-m)P\right](w'-\psi)=0. \tag{23}$$

Consider now simple supports at ends (in which case $l=L$; Fig. 2). Upon adding the last two equations, we may integrate them and, in view of the boundary conditions of simple supports, we get:

$$R^{(m)}\psi'+Pw=0. \tag{24}$$

This equation together with (22) represents a system of two linear homogeneous first-order ordinary differential equations for $w(x)$ and $\psi(x)$. They can further be reduced to one second-order homogeneous equation by differentiating (22) and substituting ψ' expressed from (24). The result is

$$w''+k^2w=0 \tag{25}$$

where

$$k^2=\frac{P\left[H^{(m)}+\frac{1}{4}(2-m)P\right]}{R^{(m)}\left[H^{(m)}-\frac{1}{4}(2+m)P\right]}. \tag{26}$$

The solution of differential Eq. (25) satisfying the boundary conditions of a simply supported column (Fig. 1(*b*)) is $w(x)=a\sin kx$ where a is any real number. The boundary conditions require that $k^2=\pi^2/L^2$ for the first critical load. If we substitute this into (26), we acquire the following equation for the first critical load P at which buckling takes place:

$$\frac{1}{4}(2-m)P^2+\left[H^{(m)}+\frac{1}{4}(2+m)P_E^{(m)}\right]P-H^{(m)}P_E^{(m)}=0 \tag{27}$$

where P_E is the Euler load, i.e.,

$$P_E^{(m)} = \pi^2 R^{(m)}/L^2. \tag{28}$$

Equation (27) is a quadratic equation, which has for $m=2$ and $m=-2$ the following positive solutions analogous to Engesser's and Haringx's formulas:

$$\text{for } m=2: \quad P_{cr} = \frac{P_E^{(2)}}{1+(P_E^{(2)}/H^{(2)})} \quad \text{with } P_E^{(2)} = \frac{\pi^2}{l^2}R^{(2)}$$

$$\text{for } m=-2: \quad P_{cr} = \frac{H^{(-2)}}{2}\left[\sqrt{1+\frac{4P_E^{(-2)}}{H^{(-2)}}}-1\right] \tag{29}$$

$$\text{with } P_E^{(-2)} = \frac{\pi^2}{L^2}R^{(-2)}. \tag{30}$$

It has been shown in 1971, [4], (and with more detailed explanations in [2]) that the case $m=2$ is associated by work with Truesdell's objective stress rate, and the case $m=-2$ with Cotter and Rivlin's (convected) objective stress rate.

One could further obtain from (27) an infinite number of sandwich buckling formulas, each associated with any chosen value of m. Curiously, however, no investigators proposed critical load formulas associated with other m values, although many investigators (e.g., Biot [1], Biezeno, Hencky, Neuber, Jaumann, Southwell, Oldroyd, Truesdell, Cotter, and Rivlin—see [2], Chap. 11) introduced formulations for objective stress rates, three-dimensional stability criteria, surface buckling, internal buckling, and incremental differential equations of equilibrium associated with $m=1$, 0 and -1.

6 Paradox Resolution: Shear Stiffness Definition for Stressed Sandwich

In analogy to (6) and in similarity to (10), one may expect the shear stiffnesses for the Engesser's and Haringx's formulas to be related as

$$H^{(2)} = H^{(-2)} + Ph/2t. \tag{31}$$

Indeed, when this relation is substituted into (29) and the resulting equation is solved for $P=P_{cr}$, formula (30) results. However, unlike homogeneous columns weak in shear, the foregoing transformation cannot be physically justified in the sense of (10), i.e., on the basis of the general transformation of tangential moduli in (2) nor its special case in (6). The reason is that the axial stress S^0 in the core in much less than $E^{(m)}$ in the core and negligible. From this viewpoint, the transformation appears illogical: Why should the shear modulus of the core be adjusted according to the axial stress in the skins?

This has become a new apparent paradox, which must be resolved. To this end, we need take a closer look at the definition of the shear stiffness H of a sandwich, which we do next.

Let us imagine a homogeneous pure shear deformation of an element Δx of the sandwich column;

$$u_1 = u_{1,1} = u_{1,3} = e_{11} = 0, \quad u_{3,1} = \gamma, \quad e_{13} = e_{31} = \gamma/2. \tag{32}$$

After substitution into (11), the second-order incremental potential energy of the element is obtained as

$$\delta^2\mathcal{W} = \Delta x \int_A \left[-\frac{P}{2bt}\left(\frac{1}{2}u_{k,1}u_{k,1} - \alpha e_{k1}e_{k1}\right) + \frac{1}{2}G_m\gamma^2\right]\mathrm{d}A \tag{33}$$

or

$$\delta^2\mathcal{W} = bh\Delta x\left(G^{(m)} - \frac{2+m}{4}\,\frac{P}{bh}\right)\frac{\gamma^2}{2}. \tag{34}$$

In particular, for $m=2$ (Engesser type) and $m=-2$ (Haringx type),

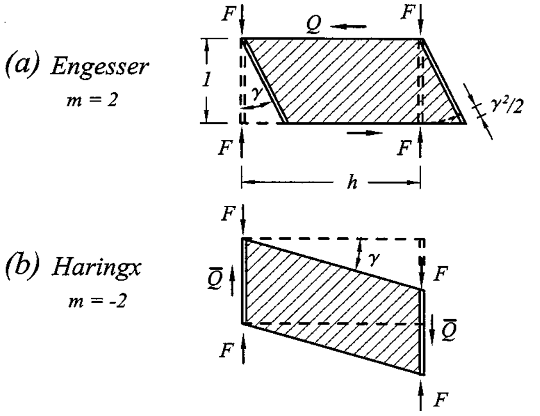

Fig. 3 Shear deformation of an element of sandwich column under initial axial forces $F=P/2$; (a) with second-order axial extension $\gamma^2/2$, and (b) at no axial extension

$$\delta^2\mathcal{W} = \begin{cases} bh\Delta x\ [G^{(2)} - (P/bh)]\gamma^2/2 & (\text{Engesser type } G) \\ bh\Delta x\ G^{(-2)}\gamma^2/2 & (\text{Haringx type } G) \end{cases}. \tag{35}$$

Since the foam core in an axially loaded sandwich column carries no appreciable axial stresses, it is convenient to use that definition of $G^{(m)}$ for which the shear stiffness of the core requires no correction for the effect of the axial force P carried by the skins. As we see, that is the latter, Haringx-type, expression (for $m=-2$). In that case, the shear modulus $G^{(-2)}$ is the same as that obtained in a pure shear test without normal stress, for example, in the torsion test of thin-wall tube made of the rigid foam.

The solutions for $m \neq -2$, including the Engesser-type formula, are of course equivalent. But if they are used the shear modulus of the core must be corrected for the effect of the axial forces $F=P/2$ carried by the skins. It would be wrong to use in them the G value measured in a pure shear test of the foam, in which no normal force acts on the shear plane.

Intuitive understanding can be gained from Fig. 3, which shows two kinds of shear deformation of an element (of height $\Delta x=1$) of a sandwich column. In the first kind (Fig. 3(a)), corresponding to the deformation described by (32), small shearing of the element is accompanied by a second-order small axial extension of the skins, equal to $1-\cos\gamma \approx \gamma^2/2$ (per unit height). If the initial forces F were negligible, this second-order small extension would make no difference but since they are not, one must take into account the work of the initial forces of F on this extension, which is $(2F\gamma^2/2)bh$ or $-bhS^0(-\gamma^2/2)$ (per unit height, $\Delta x=1$). This work must be added to the work of the shear stresses, $(G\gamma^2/2)bh$, in order to obtain the complete second-order work expression. In the second kind of shear deformation (Fig. 3(b)), the initial forces F do no work. So, the incremental second-order work expressions for these two kinds of shear deformation, respectively, are

$$\delta^2\mathcal{W} = \begin{cases} bh(G^{(2)} + S^0)\gamma^2/2 & (\text{case a}) \\ G^{(-2)}\gamma^2/2 & (\text{case b}). \end{cases} \tag{36}$$

These two cases (Fig. 3) give the same incremental second-order work if $G^{(2)} = G^{(-2)} - S^0$ or $G^{(2)} = G^{(-2)} + 2F/bh$. We see that these relations coincide with (6).

From the foregoing comparisons and the discussion of Fig. 3, it is now obvious that a constant shear modulus G, equal to the shear modulus measured in a shear test of the foam (e.g, a torsional test of a hollow tube), can be used only in the Haringx-type formula ($m=-2$).

Recently Simitses and Shen [23], Kardomateas [19,20,22] and Kardomateas and Huang [21], studied the differences between the Engesser-type and Haringx-type formulas experimentally and by finite element analysis. They concluded that the Haringx-type formula gives better predictions. Since they tacitly adopted a constant value of incremental modulus *G*, this is indeed the conclusion that they should have obtained. The present theoretical analysis explains why.

When can the differences between the column solutions for different *m*, and particularly between the formulas of Engesser and Haringx, be ignored? They can if

$$P \ll H^{(m)} = G^{(m)} bh. \tag{37}$$

7 Ambiguity in Deriving Differential Equations of Equilibrium

The Engesser and Haringx formulas can also be derived from the differential equations of equilibrium. This is discussed for a homogeneous column weak in shear on p. 738 in [2], and we will now indicate it for a sandwich. Fig. 1(*c,d*) shows two kinds of cross sections of a sandwich column in a deflected position: (a) the cross section that is normal to the deflected column axis, on which the shear force due to axial load is

$$Q = Pw' \tag{38}$$

and (b) the cross section that was normal to the column axis in the initial undeflected state, on which the shear force due to axial load is

$$\bar{Q} = P\psi. \tag{39}$$

From equilibrium, for a simply supported (hinged) column, the bending moment is $M = -Pw$ in both cases. The force-deformation relations are $M = Ebth^2\psi'/2$ and Q or $\bar{Q} = Gbh\gamma = Gbh(w' - \psi)$ in case a or b, respectively. Eliminating *M*, γ, ψ and Q or $\bar{Q}$ from the foregoing relations, we get a differential equation of the form $w'' + k^2 w = 0$, same as (25), where

$$k^2 = \frac{GbhP}{E(bth^2/2)(Gbh - P)} \tag{40}$$

or

$$k^2 = \frac{P^2 + GbhP}{E(bth^2/2)Gbh}, \tag{41}$$

respectively. Setting again $k = \pi/l$ and solving for *P*, we find the former equation to lead to Engesser's formula (4) and the latter to Haringx's formula (5).

We see that Engesser's formula $(m=2)$ is obtained when the shear deformation γ is assumed to be caused by the shear force acting on the cross section that is normal to the deflected axis of column, and Haringx's formula $(m=-2)$ when caused by the shear force acting on the rotated cross section that was normal to the beam axis in the initial state.

The foregoing equilibrium derivation, however, does not show that the values of shear stiffness in both formulas must be different. Especially, it does not show that the shear stiffness in the direction of the rotated cross section can be kept constant, while the shear stiffness in the direction of normal to the deflected axis must be considered to depend on the axial force. This has been a perennial source of confusion. To dispel it, the work of the shear forces must be considered. So, an energy approach is appropriate.

8 Implications for Highly Orthotropic Composites

Orthotropic composite plates or columns, reinforced by fibers in one or two directions, can have a shear modulus *G* much smaller then the axial elastic modulus *E* (typically 25 times smaller). The shear modulus of the composite can be determined in two ways: (1) by calculation from the measured shear and axial moduli G_p, E_p of the polymeric matrix and the elastic modulus E_f of the fibers, or (2) by direct testing of the composite in tension and torsion.

In the former way, moduli G_p, E_p, and E_f may be taken as constant because the stresses in the matrix and fibers are too small compared to the respective moduli. Since in Fig. 3(*a,b*) we can imagine the skins acting like two adjacent fibers in an element of a composite column, and the core like the matrix between these fibers, the situation is similar to that analyzed for the sandwich. It immediately follows that Haringx's formula (5), with a constant value of G_p, is the appropriate one. Engesser's formula (4) could nevertheless be used to get identical results if G_p of the matrix were transformed as a linear function of the initial stress S_f in the fibers, similar to formula (36a) or (10).

In the latter way, the incremental $G^{(m)}$ value of the composite depends in general on the initial axial force in the tube being tested, if any is applied. However, the special case of Haringx's formula $(m=-2)$ employs a *G* modulus that corresponds, as already shown, to the shearing in torsion at constant length of tube (Fig. 3(*a*)), in which the axial stress S_f in the fibers does no work. So, in that special case, the incremental $G^{(m)}(m=-2)$ should be independent of S_f.

Therefore, the *G* value in Haringx's formula (5) for an orthotropic composite can be taken as constant. On the other hand, the *G* value in Engesser's formula must be considered to depend on P_{cr} (linearly, in the manner of (31)). This makes P_{cr} an unknown, and so the formula becomes an equation (a quadratic one) for P_{cr}. The solution of course leads to the Haringx-type formula.

9 Remarks on Helical Springs, Built-Up Columns, and Bridge Bearings

As another obvious ramification, the present analysis explains why Haringx's formula, [15], is the correct one for helical springs, which were the objective of Haringx's original study. It suffices to note that, in the case of springs, the rotated, initially normal, cross section lies symmetrically within a single pitch of the spiral, halving the separation between the pitches at the point diametrically opposite to the point of intersection of the cross section with the deformed spiral (see "Haringx" in Fig. 4). The stiffness for this cross section can be calculated easily. By contrast, a cross section normal to the deflected axis of the helix does not exhibit this kind of symmetry and may even cut through more than one pitch of the helix (see "Engesser" in Fig. 4). The shear stiffness for such a cross section must depend on the axial force in the spring. Its calculation would be messy and unsuitable for practice.

In bridge bearings that consist of a stack of horizontal steel plates separated by bonded elastomeric layers (Fig. 4 right), the shear force that determines the shear deformation of each elastomeric layer is parallel to the steel plate, and thus to the cross section that was horizontal before deflection, and not to the cross section that is normal to the current deflected axis of the bearing. This again implies that a constant shear modulus can be used only with Haringx's formula (provided, of course, that the layers of elastomer behave elastically).

The built-up columns are normally approximated in a smeared manner as continuous columns (Fig. 5). They can consist of (i) a single-bay regular rectangular frame (flanges joined by battens), which resists the shear force predominantly through the bending of the flanges and the batten in each repetitive cell of the column, or (ii) a lattice, which is idealized as pin-jointed and resists the shear force predominantly by axial forces in the members of each lattice cell.

For both cases, the equivalent shear stiffness *H* of the continuum approximation of a built-up column may be calculated from the shear deformation of one repetitive cell of the column ([2], p. 739, Fig. 11.6b,c). A constant shear stiffness can be used if the shear deformation of the cell is calculated at constant length of the vertical flange, as shown in Fig. 5 (bottom). In that case, Haringx's formula is appropriate.

On the other hand, if the shear stiffness of the cell is calculated from the shear deformation in Fig. 5, the work that forces $F=$

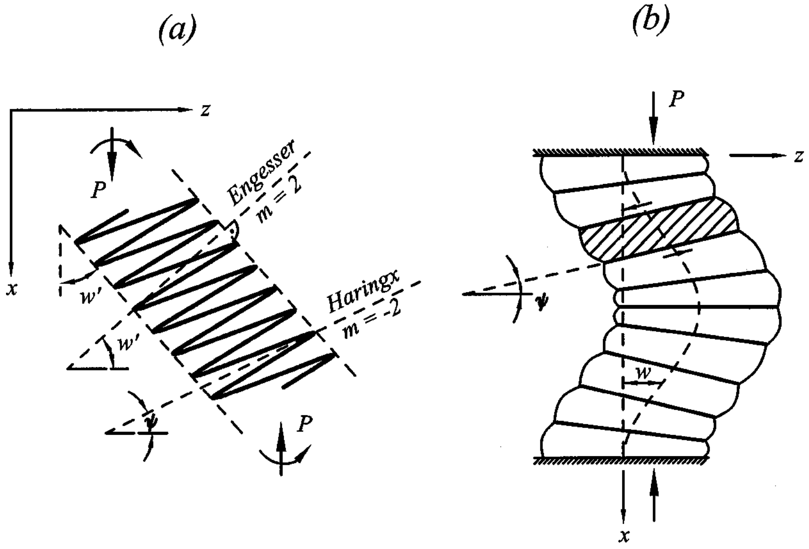

Fig. 4 (***a***) **Lateral view of a helical spring and cross sections on which the shear force is defined in Haringx and Engesser theories; (*b*) shear buckling of an elastomeric bridge bearing**

$-P/2$ in the flanges do on the second-order axial extension $\gamma^2/2$ must be taken into account. This leads to Engesser's formula. But the shear stiffness in that formula must of course be considered to depend on P.

Haringx's formula with a constant effective shear stiffness is obviously also appropriate for the overall shear buckling of large regular multi-bay multi-story frames as used in tall buildings (Section 2.9 in [2]).

10 Summary and Conclusions

1. In the case where the initial stresses before buckling are not negligible in comparison to the elastic moduli, the dependence of the tangential moduli on the initial stresses must be taken into account in stability analysis, and the stability or bifurcation criteria have different forms for tangential moduli associated with different choices of the finite strain measures, [4]. It has been regarded as paradoxical that sandwich columns apparently defy this condition—equilibrium analyses based on different but equally plausible assumptions yield different formulas (Engesser's and Haringx' formulas) even though the axial stress in the skins is negligible compared to the axial and shear moduli of the skins and the axial stress in the core is negligible compared to the axial and shear moduli of the core. Here it is shown by variational energy analysis that the aforementioned condition for the stress dependence of the tangential moduli needed for stability analysis is only a sufficient condition but not a necessary one. Another condition applies to sandwich structures—if the normal stress in a stiff component of the cross section, the skins, is not negligible compared to the shear

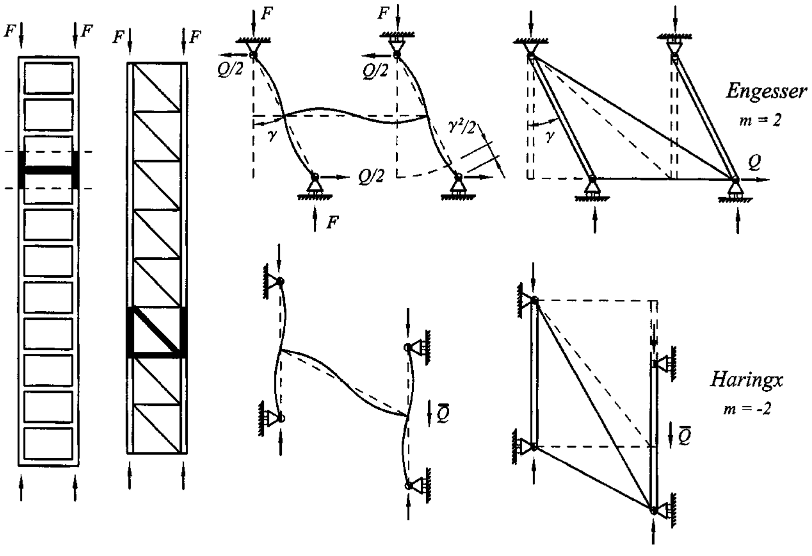

Fig. 5 Left: Column with battens and pin-jointed lattice column. Middle: Shearing of a cell of batten column. Right: Shearing of a cell of lattice column. Top: Shearing with second-order axial extension. Bottom: Shearing with no axial extension.

modulus in an adjacent soft component, the foam core, then this stress influences the shear stiffness of the sandwich cross section.

2. The shear stiffness of the core is in general a linear function of the axial forces carried by the skins, and this function is different for stability theories associated with different finite strain measures. The corresponding definitions of the shear force caused by the applied axial load are also different.
3. The Engesser-type buckling formula and the Haringx-type buckling formula are both, in principle, correct and mutually equivalent. But a different shear stiffness of the core of the sandwich column, in general depending linearly on the applied axial load, must be used in each.
4. The Haringx-type formula represents a special case in which the shear modulus of the foam core can be taken as independent of the axial force in the skins and equal to the shear modulus measured in a simple shear test (e.g., the torsional test of a thin-wall foam tube). For the Engesser-type formula, the shear stiffness of the core must be considered to depend on the unknown axial force. Therefore, the Haringx-type formula is more convenient for practice.
5. The foregoing conclusion is in agreement with the recent findings of Simitses, Kardomateas and co-workers who used a constant shear modulus for the core of sandwich columns in both the Engesser-type and Haringx-type buckling formulas and found that the latter gave results closer to experiments as well as three-dimensional finite element calculations.
6. An extension of the analysis further shows that Haringx's formula is preferable for highly orthotropic composites. If, and only if, that formula is used, a constant shear modulus of the soft matrix can be used for calculating the shear stiffness of column. For Engesser's formula, the shear modulus of the matrix must be considered to depend on the axial stress in the fibers.
7. As further ramifications, the effective shear stiffness of helical springs, elastomeric bridge bearings, built-up (battened or laced) columns and multi-bay multi-story frames can be considered to be constant only if Haringx's formula is used.
8. The difference between the Engesser-type and Haringx-type formulas for a sandwich (or orthotropic fiber composite) can be ignored only when the axial force carried by the skins (or the fibers) is much less then the shear stiffness of the core (or the matrix).
9. For orthotropic materials whose tangential shear modulus is a nonlinear function of the normal stress, both the Engesser-type and Haringx-type formulas necessitate the use of a variable shear stiffness, and in that case none of them is more convenient than the other.
10. For general structures, condition (3) is only a necessary one for making the differences among various choices of the finite strain measure $\epsilon^{(m)}$ irrelevant. A condition that is sufficient is

$$\max_{(\mathbf{x})}\|S_{ij}(\mathbf{x})\| \ll \min_{(\mathbf{x})}\|C^{(m)}_{ijkl}(\mathbf{x})\| \quad (m \text{ bounded}). \tag{42}$$

This condition appears to be both sufficient and necessary when the maximum and minimum are taken within any single cross section of a slender beam, but not necessary for a general body with the maximum and mimimum taken over the whole body. The reason that the inequality $\|S_{ij}(\mathbf{x})\| \ll \|C^{(m)}_{ijkm}(\mathbf{x})\|$ for a material point is insufficient is the interaction within the cross section, reflected in the hypothesis of cross sections of slender beams remaining plane.

Acknowledgment

Grateful acknowledgment is due to the ONR (Office of Naval Research) for partial financial support under grant N00014-91-J-1109 (monitored by Yapa D. S. Rajapakse) to Northwestern University.

References

[1] Biot, M. A., 1965, *Mechanics of Incremental Deformations*. John Wiley and Sons, New York.
[2] Bažant, Z. P., and Cedolin, L., 1991, *Stability of Structures: Elastic, Inelastic, Fracture and Damage Theories*, Oxford University Press, New York (and 2nd updated Ed., Dover, New York, 2002).
[3] Bažant, Z. P., 1968, "Conditions of Deformation Instability of a Continuum and Their Application to Thick Slabs and a Half Space" (in Czech, with English summary), Stavebnícky Časopis (SAV, Bratislava), **16**, pp. 48–64.
[4] Bažant, Z. P., 1971, "A Correlation Study of Incremental Deformations and Stability of Continuous Bodies," ASME J. Appl. Mech., **38**, pp. 919–928.
[5] Goodier, J. N., and Hsu, C. S., 1954, "Nonsinusoidal Buckling Modes of Sandwich Plates," J. Aeronaut. Sci., **21**, pp. 525–532.
[6] Plantema, F. J., 1966, *Sandwich Construction: The Bending and Buckling of Sandwich Beams, Plates and Shells*, John Wiley and Sons, New York.
[7] Allen, H. G., 1969, *Analysis and Design of Sandwich Panels*, Pergamon Press, Oxford, UK.
[8] Kovařík, V., and Šlapák, P., 1973, *Stability and Vibrations of Sandwich Plates*, Academia, Prague (in Czech).
[9] Michiharu, O., 1976, "Antisymmteric and Symmetric Buckling of Sandwich Columns Under Compressive Loads," Trans., Jap. Soc. of Aeronaut. Space Sci., **19**, pp. 163–178.
[10] Chong, K. P., Wang, K. A., and Griffith, G. R., 1979, "Analysis of Continuous Sandwich Panels in Building Systems," *Building and Environment* 44.
[11] Frostig, Y., and Baruch, M., 1993, "Buckling of Simply Supported Sandwich Beams With Transversely Flexible Core—A High Order Theory," J. Eng. Mech. **119**, pp. 955–972.
[12] Engesser, F., 1889, "Die Knickfestigkeit gerader Stäbe," Zentralblatt des Bauverwaltung., **11**, p. 483–486.
[13] Engesser, F., 1889, "Die Knickfestigkeit gerader Stäbe," Z. Architekten und Ing. Verein zu Hannover, **35**, p. 455.
[14] Engesser, F., 1891, "Die Knickfestigkeit gerader Stäbe," Zentralblatt der Bauverwaltung, **11**, pp. 483–486.
[15] Haringx, J. A., 1942, "On the Buckling and Lateral Rigidity of Helical Springs," *Proc., Konink. Ned. Akad. Wetenschap.*, **45**, p. 533.
[16] Haringx, J. A., 1948–1949, *Phillips Research Reports*, Vols. 3–4, Phillips Research Laboratories, Eindhoven.
[17] Kardomateas, G. A., 1995, "Three Dimensional Elasticity Solution for the Buckling of Transversely Isotropic Rods: The Euler Load Revisited," ASME J. Appl. Mech., **62**, pp. 346–355.
[18] Kardomateas, G. A., and Dancila, D. S., 1997, "Buckling of Moderately Thick Orthotropic Columns: Comparison of an Elasticity Solution With the Euler and Engesser/Haringx/Timoshenko Formulas," Int. J. Solids Struct., **34**(3), pp. 341–357.
[19] Kardomateas, G. A., 2001, "Elasticity Solutions for Sandwich Orthotropic Cylindrical Shell Under External Pressure, Internal Pressure and Axial Force," AIAA J., **39**(4), pp. 713–719.
[20] Kardomateas, G. A., 2001, "Three-Dimensional Elasticity Solutions for the Buckling of Sandwich Columns," *ASME Intern. Mechanical Engrg. Congress*, pp. 1–6.
[21] Kardomateas, G. A., and Huang, H., 2002, "Buckling and Initial Postbuckling Behavior of Sandwich Beams Including Transverse Shear," AIAA J., in press.
[22] Kardomateas, G. A., Simitses, G. J., Shen, L., and Li, R., 2002, "Buckling of Sandwich Wide Columns," Int. J. Non-Linear Mech., (special issue on "Nonlinear Stability of Structures"), in press.
[23] Simitses, G. J., and Shen, L., 2000, "Static and Dynamic Buckling of Sandwich Columns," *Mechanics of Sandwich Structures*, Y. D. S. Rajapakse et al., eds., ASME, New York, AD-Vol. 62/AMD-Vol. 245, pp. 41–50.
[24] Timoshenko, S. P., and Gere, J. M., 1961, *Theory of Elastic Stability*, McGraw-Hill, New York, pp. 135, 142.
[25] Bažant, Z. P., 1992, discussion of "Stability of Built-up Columns," by A. Gjelsvik, J. Eng. Mech., **118**(6), pp. 1279–1281.
[26] Bažant, Z. P., 1993, discussion of "Use of Engineering Strain and Trefftz Theory in Buckling of Columns," by C. M. Wang and W. A. M. Alwis ASME J. Appl. Mech., **119**(12), pp. 2536–2537.
[27] Ziegler, F., 1982, "Arguments for and Against Engesser's Buckling Formulas," Ingenieur-Archiv, **52**, pp. 105–113.
[28] Reissner, E., 1972, "On One-Dimensional Finite-Strain Beam Theory: The Plane Problem," J. of Applied Mathematics and Physics, **23**, pp. 795–804.
[29] Reissner, E., 1982, "Some Remarks on the Problem of Column Buckling," Ingenieur-Archiv, **52**, pp. 115–119.
[30] Simo, J. C., and Kelly, J. M., 1984, "The Analysis of Multilayer Elastomeric Bearings," ASME J. Appl. Mech., **51**, pp. 256–262.

[31] Simo, J. C., Hjelmstad, K. D., and Taylor, R. L., 1984, ''Numerical Formulation of Elasto-Viscoplastic Response of Beams Accounting for the Effect of Shear,'' Comput. Methods Appl. Mech. Eng., **42**, pp. 301–330.
[32] Gjelsvik, A., 1991, ''Stability of Built-Up Columns,'' J. Eng. Mech., **117**(6), pp. 1331–1345.
[33] Wang, C. M., and Alwis, W. A. M., 1992, ''Use of Engineering Strain and Trefftz Theory in Buckling of Columns,'' J. Eng. Mech., **118**(10), pp. 2135–2140.
[34] Attard, M. A., 2002, draft of a manuscript on ''Finite Strain Beam Theory,'' University of New South Wales, Australia (private communication to Bažant, 2002).
[35] Buckle, I., Nagarajaiah, S., and Ferell, K., 2002, ''Stability of Elastomeric Isolation Bearings: Experimental Study,'' J. Eng. Mech., **128**(1), pp. 3–11.
[36] Timoshenko, S. P., 1921, ''On the Correction for Shear in the Differential Equation of Transverse Vibrations of Prismatic Bars,'' Philos. Mag., **21**, p. 747.

Residual Stress-Induced Center Wave Buckling of Rolled Strip Metal

F. D. Fischer
Institute of Mechanics,
Montanuniversitat Loeben,
Franz-Josef-Str. 18,
A-8700 Loeben, Austria

F. G. Rammerstorfer

N. Friedl

Institute of Lightweight Structures
and Aerospace Engineering,
Vienna University of Technology,
Gusshausstrasse 27–29,
A-1040 Vienna, Austria

In this paper computational and analytical treatments of the center wave buckling phenomenon in thin strips under in-plane loads which typically appear during cold rolling of sheet metal, are presented. Buckling due to self-equilibrating residual stresses, caused by the rolling process, in conjunction with global tensile stresses (due to the traction force acting on the strip) is considered. The shape of the distribution of the residual stresses over the width of the strip influences the buckling mode. Furthermore, it is shown that an increasing global tension force leads not only to increased critical residual stress intensities but also to shorter buckling waves concentrated towards the center of the strip. Taking these facts into account, a proper combination of the information gained from measuring the global tensile force at which buckling appears, the wave length, and some characteristic shape parameters of the buckling pattern allows the estimation of the intensity and the type of the residual membrane force distribution in the strip. By introducing dimensionless quantities, diagrams are provided which can be used for the determination of critical loading combinations, wave lengths, and shape parameters.

[DOI: 10.1115/1.1532322]

1 Introduction

It is well known in the metal forming community that residual stresses can lead to buckling of the strips during the rolling process. Such residual stresses can be caused by thickness reductions which are not exactly homogeneous over the width of the strip. If the thickness reduction is more pronounced in the middle of the width of the strip, then compressive residual stresses will appear there, and center wave buckling can be expected. Consequently, thickness reductions which are larger in the edge areas than in the middle region more likely cause edge wave buckling. Certainly, these thickness reductions are the result of large plastic deformations. However, the resulting residual stresses—even in combination with the global traction force—are typically in the elastic range. In most situations, particularly for thin strips, if buckling happens it is an elastic bifurcation process. Even very small residual stresses (with magnitudes less than some MPa's) may lead to buckling and to considerably high amplitudes of the transversal deformations in the post-buckling pattern if the global traction force is reduced. Since during this post-buckling processes the residual stresses are released by the transversal deflections the whole deformation history; i.e., buckling and post-buckling, can be treated as an elastic process.

A survey of the literature dealing with these phenomena can be found in [1]. Further treatments of buckling during rolling of sheet metal are presented for instance in [2,3] and, more recently, in [4,5]. The character and the shape of the buckling mode and, consequently, the post-buckling pattern depend on the shape of the distribution of the residual membrane force over the width of the strip and on the ratio between the intensity of the residual membrane forces and that of the traction force at which the trivial, i.e., plane, configuration loses its stability; see Fig. 1.

In [4,5] the authors presented the principal features of these buckling phenomena; moreover, analytical approaches were derived and discussed. In those papers results have been presented only for situations in which so-called edge wave buckling appears. This paper deals with center wave buckling.

2 Formulation of the Mathematical Model

The formulation of the mathematical model follows in its principal features what has been presented in [5]. However, in this paper the combination of analytical and finite element analysis is of particular importance: The buckling modes obtained from eigenvalue analyses in finite element computations were crucial for determining proper trial functions in the Ritz-Ansatz approximating the buckling pattern for the analytical approach. The analytical approach achieved this way is generally applicable and no further finite element analysis is required. Because the analytical results can be achieved in a dimensionless form, the analytical procedure leads to a tool which can be easily used in practice.

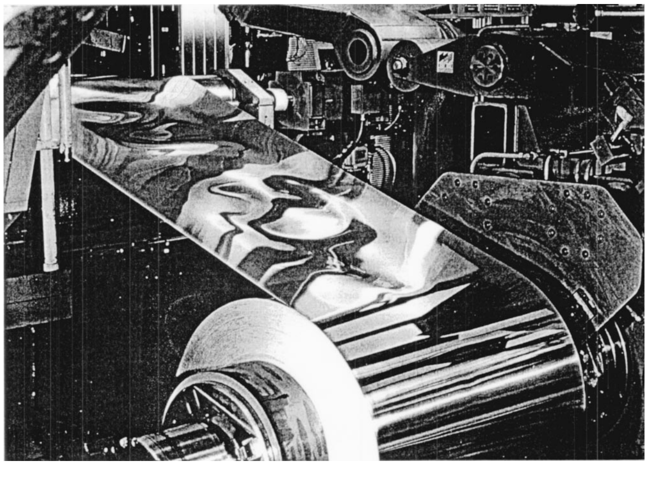

Fig. 1 Center wave buckling of a rolled strip metal (courtesy of VOEST ALPINE Industrieanlagenbau, Linz, Austria)

Contributed by the Applied Mechanics Division of THE AMERICAN SOCIETY OF MECHANICAL ENGINEERS for publication in the ASME JOURNAL OF APPLIED MECHANICS. Manuscript received by the ASME Applied Mechanics Division, Jan. 16, 2001; final revision, July 26, 2002. Associate Editor: N. Triantafyllidis. Discussion on the paper should be addressed to the Editor, Prof. Robert M. McMeeking, Department of Mechanical and Environmental Engineering University of California–Santa Barbara, Santa Barbara, CA 93106-5070, and will be accepted until four months after final publication of the paper itself in the ASME JOURNAL OF APPLIED MECHANICS.

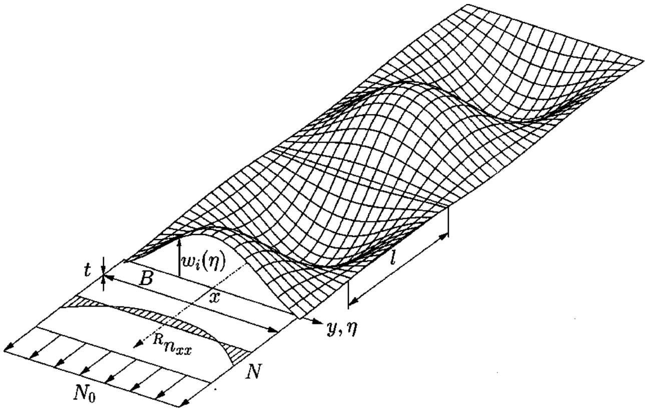

Fig. 2 The strip under residual membrane force distribution and global tension

2.1 Description of the Residual Stress Field. A strip of infinite length (representing a sheet metal in the rolling path) with the width B and a plate bending stiffness $K = Et^3/12(1-\nu^2)$ (with E being Young's modulus, ν Poisson's ratio, t the thickness), is loaded by a self-equilibrating residual membrane force distribution $^R n_{xx}(y) = N\hat{g}(y)$ and a constant global tension force N_0; see Fig. 2. Independent of the longitudinal coordinate x, the membrane force distribution is given by

$$n_{xx}(y) = N\hat{g}(y) + N_0. \tag{1}$$

The following dimensionless quantities are introduced:

$$\eta = y/B, \quad \text{with} \quad -B/2 \leqslant y \leqslant B/2, \quad -1/2 \leqslant \eta \leqslant 1/2,$$

$$\hat{g}(y) \to g(\eta), \quad n_{xx} \to n_{xx}(\eta) = Ng(\eta) + N_0, \tag{2}$$

$$\tilde{N} = \frac{NB^2}{K\pi^2}, \quad \tilde{N}_0 = \frac{N_0 B^2}{K\pi^2}.$$

($\tilde{N}_0$ values within the range up to 1000 are typically of interest in cold rolling of metal strips.)

Because $^R n_{xx}$ must be self-equilibrated, the following condition must hold:

$$\int_{-1/2}^{+1/2} g(\eta)\, d\eta = 0,$$

$$\text{i.e., for symmetrical } g(\eta): \quad \int_0^{1/2} g(\eta)\, d\eta = 0. \tag{3}$$

In order to capture a wide range of symmetrical residual membrane force distributions which typically lead to "center wave buckling," i.e., a buckling pattern showing waves with maximum wave heights at the center of the strip, the following distributions are assumed:

a. Cosine distribution:

$$g^c(\eta) = 1 - C_m \cos^m \pi\eta \quad \text{with} \quad m = 1,2,\ldots$$
$$\text{and} \quad -1/2 \leqslant \eta \leqslant 1/2. \tag{4}$$

The equilibrium condition for $^R n_{xx}(\eta)$ leads to

$$C_m = \frac{1}{2}\left[\int_0^{1/2} \cos^m \pi\eta\, d\eta\right]^{-1}. \tag{5}$$

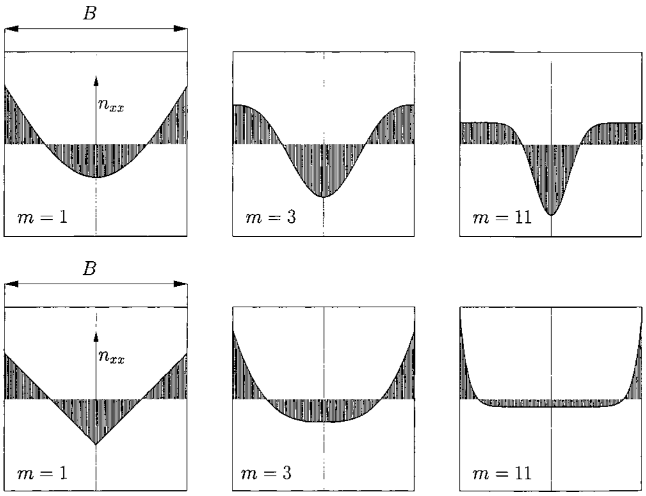

Fig. 3 Schematic representations of typical residual stress distributions; top: according to Eq. (4), bottom: according to Eq. (6)

b. Polynomial distribution:

$$g^p(\eta) = \frac{1}{m}\left[(m+1)(2|\eta|)^m - 1\right] \quad \text{with} \quad m = 1,2,\ldots\ldots, \tag{6}$$

which also fulfils the equilibrium condition (3).

Here and in the following the superscripts "c" and "p" refer to the cosine and the polynomial residual membrane force distributions, respectively.

Due to the variable exponent m in $g^c(\eta)$ and $g^p(\eta)$, respectively, the required large variability of residual stress distributions can be provided, see Fig. 3.

From this figure one can see that by consideration of cosine distributions with $m = 11$ and $m = 1$ as well as polynomial distributions with $m = 11$ the field of very much and moderately concentrated as well as smoothly distributed compressive residual membrane forces, respectively, is captured. This is the reason why the results for these cases are presented in the figures of this paper.

Both distributions, i.e., the cosine and the polynomial one, lead to

$$g(\eta = \pm 1/2) = 1. \tag{7}$$

This means that a positive value of N in Eq. (1) corresponds to tensile residual membrane forces in the edge regions and compressive residual membrane forces in the center regions of the strip. In other words, the residual membrane force intensity N is expressed by the tensile residual membrane force at the edges of the strip.

2.2 Determination of Proper Trial Functions for the Buckling Pattern. In order to apply the Ritz approach as described in [4,5] we have to find a proper Ritz-Ansatz, i.e., trial functions, for the buckling pattern. For center wave buckling this task is not as easy as in the case of edge wave buckling.

In order to find appropriate trial functions an extensive finite element study of the problem under consideration was performed. Strips of sufficient length having a width $B = 1.5$ m, and a thickness $t = 0.5$ mm, made of aluminum ($E = 7 \times 10^4$ N/mm^2, $\nu = 0.33$) were discretized by finite shell elements. The different kinds of nominal residual membrane force distributions, i.e., cosine or polynomial (according to Eqs. (4) or (6)), were introduced via fictitious temperature loads. Additionally, different values of the global tensile force N_0 were applied. Linear eigenvalue analyses led to the critical values of the membrane force intensity N as functions of the global tensile force N_0 and to the corresponding

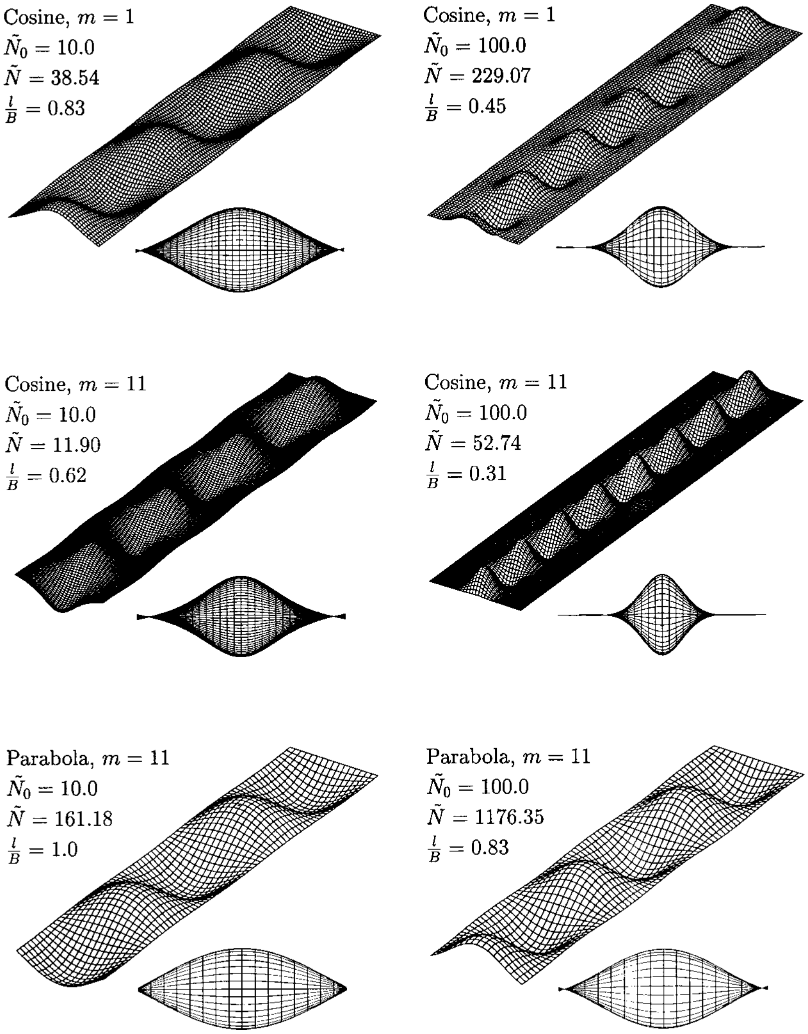

Fig. 4 Buckling modes for cosine-distributed residual membrane forces (with $m=1$ and $m=11$) and for polynomially distributed residual membrane forces (with $m=11$)

buckling modes. For cosine residual membrane force distributions the exponent m was chosen to be 1 and 11 and for polynomial distributions $m=11$ was considered. These three cases capture the most characteristic cases within the wide field of varieties.

Figure 4 shows some typical results for cosine-distributed (with $m=1$ and $m=11$) as well as for polynomial distributions (with $m=11$) for two values of the global tensile force, expressed in dimensionless quantities according to Eqs. (2). For reasons of comparison, sections of equal length are cut out from the typically longer finite element models.

From the results of the finite element buckling analyses some principal features of the buckling pattern can be drawn: The higher the global tensile force $\tilde{N}_0$ the more the buckles are concentrated at the center of the strip and the smaller is their wave length. For small values of $\tilde{N}_0$ two cases have to be distinguished: one in which the amplitude values of the buckling waves at the center and at the edges are opposite to each other, and one in which these signs are the same. Higher values of $\tilde{N}_0$ lead to buckling modes with straight edges of the strip. Furthermore, transversal distributions of the amplitude function of the buckling mode with and without points of inflexion were found. In the case of center wave buckling just symmetric buckling modes appear. With these results the following two alternative trial functions for the Ritz-Ansatz approximating the buckling pattern were chosen:

$$w(x,\eta)=qw_a(x,\eta), \quad w_a(x,\eta)=\cos(a\pi\eta)\cos\left(\frac{\pi x}{l}\right) \tag{8}$$

or

$$w(x,\eta)=qw_n(x,\eta), \quad w_n(x,\eta)=(1-12\eta^2+16\eta^3)^n\cos\left(\frac{\pi x}{l}\right). \tag{9}$$

By these trial functions the whole field of varieties of buckling modes is approximated to a high degree of accuracy, provided that the parameters $|a|<2.0$ in Eq. (8) and $n\geqslant 1.0$ in Eq. (9) are properly chosen. The finite element results show that buckling modes according to Eq. (8) are only relevant for values of the global tensile membrane force N which are too small to be of practical relevance. This statement is confirmed also by the results of the analytical model as described below. Therefore, the main emphasis is laid on the solutions with trial functions according to Eq. (9).

Both the half-wave length l and the parameter a or the exponent n, respectively, have to be determined such that the Ritz approach leads to the relevant, i.e., the minimum, critical membrane force intensity as a function of the global tension force: $N^c(N_0)$ or $N^p(N_0)$ for a given exponent m in Eq. (4) or (6), respectively.

3 Analysis

The Ritz approach in combination with the concept of minimization of the total potential energy ϕ determines the buckling load as that eigenvalue of the residual membrane force intensity at which a nontrivial equilibrium path bifurcates from the trivial, i.e., the flat, one.

Just for consistency's sake the principal features of this energy approach are repeated from, [5]: The total potential energy ϕ of a thin plate deformed in a nontrivial way, i.e., also in the direction normal to the middle surface, and subjected to a membrane force state ${}^{R}n_{xx}+N_0$ can be taken from the literature (see, e.g., [6]) and reads, specialized for the considered situation, as follows:

$$\phi_B=\frac{K}{2}\int_\Omega\left\{\left(\frac{\partial^2 w}{\partial x^2}+\frac{\partial^2 w}{\partial y^2}\right)^2 -2(1-\nu)\left[\frac{\partial^2 w}{\partial x^2}\,\frac{\partial^2 w}{\partial y^2}-\left(\frac{\partial^2 w}{\partial x\,\partial y}\right)^2\right]\right\}d\Omega, \tag{10}$$

$$\phi_M=\frac{1}{2}\int_\Omega({}^{R}n_{xx}+N_0)\left(\frac{\partial w}{\partial x}\right)^2 d\Omega, \tag{11}$$

$$\phi_{N_0}=-\frac{N_0^2 LB}{2Et},\qquad \phi=\phi_B+\phi_M+\phi_{N_0}. \tag{12}$$

The application of Gauss' theorem leads to the following modified formulation of ϕ_B:

$$\phi_B=\frac{K}{2}\int_\Omega\left(\frac{\partial^2 w}{\partial x^2}+\frac{\partial^2 w}{\partial y^2}\right)^2 d\Omega+K(1-\nu)\int_{\partial\Omega}\frac{\partial w}{\partial x}\,\frac{\partial}{\partial y}\left(\frac{\partial w}{\partial s}\right)ds. \tag{13}$$

ϕ_B is the contribution to ϕ due to bending, ϕ_M that due to the membrane forces, and ϕ_{N_0} is the potential energy of the boundary force N_0 at $x=0$ and $x=L\gg B$.

Since we are dealing with single-term shape functions we have just one degree-of-freedom, which is related to the amplitude q of the buckling mode; see Eq. (8) or (9).

Stationarity of $\phi(qw_i)$ requires $\partial\phi/\partial q=0$, which immediately leads to the equation

$$\phi_B(w_i)+\phi_M(w_i)=0. \tag{14}$$

w_i stands for the trial function with $i=\mathrm{a}$ if Eq. (8) is used and $i=n$ if Eq. (9) is used.

If we now insert the membrane state according to Eq. (4) or (6), respectively, which depends on a positive constant N, see Eq. (1), the Eq. (14) can be rewritten with the dimensionless entities defined by Eq. (2):

$$\tilde{N}\phi'_{M,N}(w_i)+\tilde{N}_0\phi'_{M,N_0}(w_i)+\phi_B(w_i)=0, \tag{15}$$

where $\phi'_{M,N}$ and ϕ'_{M,N_0} are the contributions to ϕ_M due to $\tilde{N}=1$ and $\tilde{N}_0=1$, respectively. This leads to

$$\tilde{N}_i=-\frac{\phi_B(w_i)+\tilde{N}_0\phi'_{M,N_0}(w_i)}{\phi'_{MN}(w_i)} \tag{16}$$

as critical residual membrane force intensity corresponding to the Ritz-Ansatz with parameter a or exponent n, respectively.

The right-hand side of Eq. (16) contains a further unknown quantity, namely the half-wave length l in the x-direction. Since we look for the minimum possible value of the buckling parameter $\tilde{N}_i$ (i becomes a or n), we find l by minimizing $\tilde{N}_i$ with respect to this quantity:

$$\frac{d\tilde{N}_i}{dl}=0. \tag{17}$$

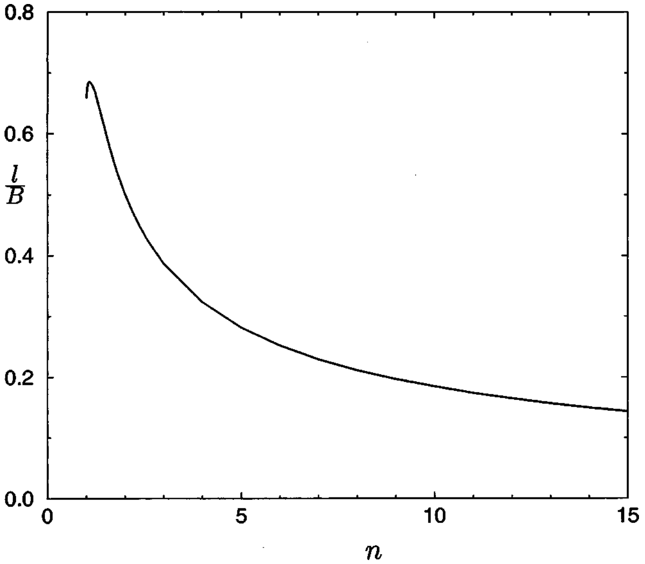

Fig. 5 Half-wave length of the relevant buckling mode as a function of *n* in Eq. (9)

This additional relation allows to find $l_{\min}$ and, as a consequence, $\tilde{N}_{a^{\min}}(\tilde{N}_0)$ and $\tilde{N}_{n^{\min}}(\tilde{N}_0)$ for given values of a and n, respectively. In the following text these quantities will be used without the subscript "min". The relevant parameter a or exponent n will be determined below.

For the more relevant case, i.e., based on Eq. (9), the dependence of the half-wave length of the relevant buckling mode on the exponent n is shown in Fig. 5. This result holds true independent of the shape of the residual membrane force distribution, i.e., Eqs. (4) or (5). Certainly, the relevant exponent n depends on this distribution shape, and, thus, also l does.

Similar to the solution obtained in [5] for edge wave buckling, l/B as a function of n shows a maximum. In the case under consideration this maximum is at $n^*\approx 1.1$. For $n>n^*$ increasing n leads to decreasing l. The interval $[1.0,n^*]$ appears to be unphysical; however, it is of no relevance because the solutions with $n\in[1.0,n^*]$ lead to larger critical residual membrane force intensities than those obtained with trial functions according to Eq. (8), and are therefore not relevant.

Equation (16) in combination with (17) leads to the following solution for the critical residual membrane force intensity for a given exponent m in Eqs. (4) or (6):

$$\tilde{N}_i^k(\tilde{N}_0)=F_1^k(i)+F_2^k(i)\tilde{N}_0. \tag{18}$$

The index k denotes the character of the residual membrane forces: cosine-distributed $(k=c)$ or polynomially $(k=p)$, while the index (or the variable) i indicates a or n, depending on the choice of the trial function (8) or (9).

The functions F_1 and F_2 are determined in analytical form.

For a given type of residual membrane force distribution (characterized by Eq. (4) or (6) and a given value of the exponent m) the critical intensity $\tilde{N}_i(\tilde{N}_0)$ represents for every parameter a or exponent n a straight line in the $\tilde{N}-\tilde{N}_0$-diagram (Eq. (18) is a linear relation). These straight lines intersect each other. As discussed in detail in [5] for the case of edge wave buckling, the relevant value of $\tilde{N}(\tilde{N}_0)$, i.e.,

$$\tilde{N}(\tilde{N}_0)=\min_i \tilde{N}_i(\tilde{N}_0) \tag{19}$$

is represented by the inner envelope as formed by the manifold of straight lines $\tilde{N}_i(\tilde{N}_0)$ with a continuously varying parameter a or exponent n.

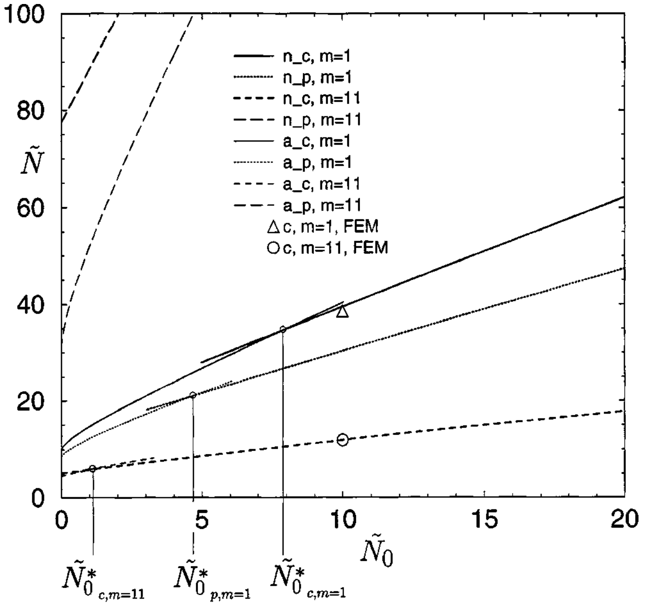

Fig. 6 Functions $\tilde N_i(\tilde N_0)$, $i=a,n$, for small values of $\tilde N_0$. The notation i_k denotes the combinations of buckling modes and membrane force distribution. $i=a$ means cosine mode according to Eq. (8), and $i=n$ stands for Hermitean based mode according to Eq. (9); $k=c$ points to cosine and $k=p$ to polynomial distributions of the residual membrane forces.

This envelope is, for given m, implicitly described by

$$G(\tilde N,\tilde N_0,i)=\tilde N-F_1(i)-F_2(i)\tilde N_0=0. \tag{20}$$

Therefore, the condition for the envelope

$$\frac{\partial G}{\partial i}=-\frac{dF_1}{di}-\frac{dF_2}{di}\tilde N_0=0, \tag{21}$$

yields

$$\tilde N_0=-\frac{dF_1}{di}\bigg/\frac{dF_2}{di}=\tilde N_0(i). \tag{22}$$

This way the critical intensity can be expressed as a function of i ($i=a$ or n) only instead of $\tilde N(\tilde N_0)$:

$$\tilde N(i)=F_1(i)-F_2(i)\left(\frac{dF_1}{di}\bigg/\frac{dF_2}{di}\right). \tag{23}$$

Finally, $\tilde N(\tilde N_0)$ can be determined by evaluating Eqs. (22) and (23) for continuously varying i. In this way also the relevant values of the parameters $i=a$, n are found.

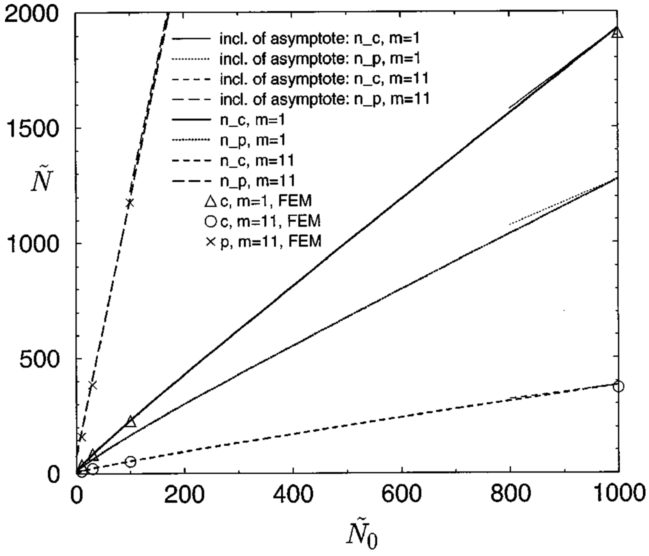

Fig. 8 Dependence of the critical residual membrane force intensity $\tilde N$ on the global strip tension $\tilde N_0$ for different distributions of the membrane forces. Comparison between analytical and finite element results.

Equations (22) and (23) require the first derivatives of $F_1(i)$ and $F_2(i)$, which can be calculated numerically.

For every membrane force distribution two envelopes exist for the Ritz-Ansatz approximating the buckling pattern: $\tilde N_a(\tilde N_0)$ for the buckling mode according to Eq. (8), and $\tilde N_n(\tilde N_0)$ for the buckling mode approximated by Eq. (9). Of course, the minimum of $\tilde N_i(\tilde N_0)$, $i=a,n$, is physically relevant. Thus, $\tilde N_a(\tilde N_0)$ is the relevant curve until it crosses the $\tilde N_n(\tilde N_0)$-curve at a certain value of $\tilde N_0=\tilde N_0^*$; see Fig. 6. To allow a comparison, finite element solutions, obtained as described in Section 2.2, are also included in Fig. 6.

For $\tilde N_0 \geqslant \tilde N_0^*$ the $\tilde N_n(\tilde N_0)$-curve is relevant. Certainly, the nonsmooth transition from the one curve to the other does not really indicate a mode-jump but reflects the approximate character of the Ritz approach used in the estimations. This becomes also obvious if one compares the trial functions, determined by minimizing the eigenvalues resulting from the Ritz approach as described above, with the corresponding finite element solutions—see Fig. 7. In Fig. 8 just the relevant curves are included.

This figure shows transversal amplitude functions of the buckling modes, derived on the basis of Eqs. (8) or (9) with the appropriately determined parameters $i=a$ for cosine distributed buckling pattern—Eq. (8), and $i=n$ for Hermitean buckling pattern—Eq. (9). Finite element solutions are also presented. With

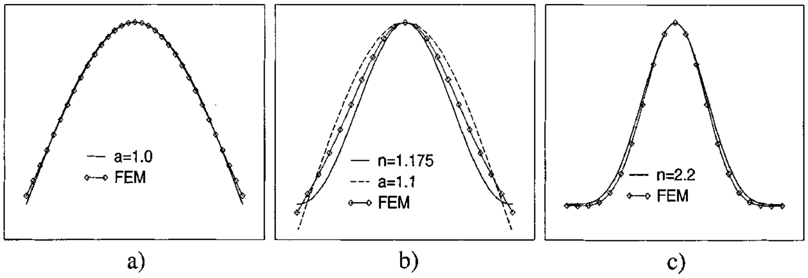

a) b) c)

Fig. 7 Transversal amplitude functions of the buckling modes. Analytical and finite element solutions. (*a*) Polynomially ($m=11$) distributed membrane force, $\tilde N_0=10$, (*b*) cosine($m=1$) distributed membrane force, $\tilde N_0=10$, (*c*) cosine ($m=1$) distributed membrane force, $\tilde N_0=100$.

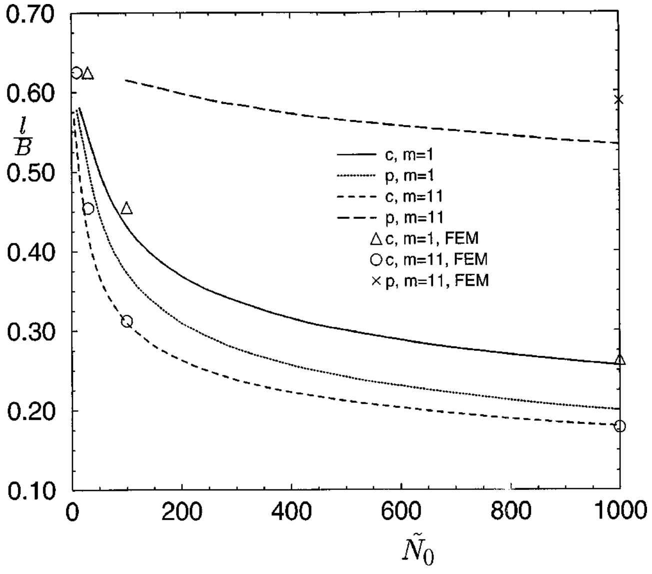

Fig. 9 Dependence of the half-wave length l/B on the global strip tension $\tilde{N}_0$ for different distributions of the residual membrane force

the exception of the region of transition between the two kinds of buckling mode, $\tilde{N}_0 \approx \tilde{N}_0^*$ (Fig. 7(*b*), which represents the situation corresponding to the triangular symbol in Fig. 6), the determined trial functions correspond considerably well with the finite element solutions (Fig. 7(*a*, *c*), representing situations which correspond to the lowest cross symbol and to the highest triangular symbol, respectively, in Fig. 8).

As mentioned earlier, very small values of $\tilde{N}_0$ are only of limited practical relevance. Therefore, the authors did not put too much effort into improving the trial functions in the transition regime around $\tilde{N}_0 \approx \tilde{N}_0^*$.

Figure 8 shows the critical residual membrane force intensities $\tilde{N}(\tilde{N}_0)$ for the practically relevant regime of $\tilde{N}_0$. The correspondence between the analytically obtained solutions and the finite element solutions is excellent.

In Fig. 8 also the asymptotic solution for $F_2^k(n)$, $k=c,p$ is included by showing the inclination of the tangent to the curves approximated by $F_2^k(n)$ for large values of $\tilde{N}_0$, i.e., large values of *n*. From this one can see that in many cases the relation $\tilde{N}_i(\tilde{N}_0)$ becomes nearly linear for large values of $\tilde{N}_0$. Asymptotic considerations for both $F_1^k(n)$ and $F_2^k(n)$ can be found in the Appendix.

Figure 9 shows how the half-wave length l/B decreases with increasing $\tilde{N}_0$ for different kinds of distributions of residual membrane forces. As expectable and also indicated by the finite element analyses, the residual membrane force distribution with compressive stresses almost over the complete width of the strip, i.e., *p*, $m=11$, the polynomial one with exponent $m=11$, leads to rather large wave lengths, while residual membrane forces which have their compressive stresses concentrated in the center region of the strip, i.e. $\cos^m(\pi\eta)$, $m=11$, have comparably short buckling waves. The analytical solutions obtained with trial functions according to Eq. (9), i.e., Hermitean-type functions, correspond well with finite element results as long as $\tilde{N}_0$ is sufficiently large. For smaller $\tilde{N}_0$-values the analytical determination of l/B would have to be carried out with trial functions according to Eq. (8), which has not been done because of the irrelevance for practical applications.

4 Conclusions

This paper deals with buckling phenomena caused by residual membrane force distributions in rolled metal strips which are symmetrical with respect to the midaxis of the strip, showing longitudinal compressive forces in the center regions and tensile forces in the edge regions. It has been shown that the intensities of different residual stress distributions which are critical with respect to center buckling of the strip metal can be determined in dependence of the global tension force based on analytical solutions. A wide range of characteristic residual stress distributions has been considered.

Increased global strip tension leads to an increase of the critical membrane force intensity accompanied by a decrease of the half-wave length and to buckling waves concentrated more and more towards the center of the strip. The derived analytical solutions in dimensionless form provide diagrams which—on the one hand—allow a simple and quick estimation of the critical residual stress intensities, and—on the other hand—allow to estimate the character of the residual stress distribution by measuring the half-wave length in combination with that global strip tension at which buckling appears. The finite element solutions computed for a selected set of parameters prove the correctness of the analytical solutions.

Appendix

The Mathematical Structure of $\tilde{N}$—Asymptotic Considerations. For not too small values of $\tilde{N}_0$ only $\tilde{N}(n)$, i.e., the solution for Hermitean based trial functions, is relevant. Relation (18),

$$\tilde{N}(n)=F_1(n)+F_2(n)\tilde{N}_0, \qquad (A1)$$

is the starting equation. For $n \gg 1$ an asymptotic relation for $F_1(n)$ can be found after some mathematical operations as

$$f_1(n)=\frac{48}{\pi^2}\left(\sqrt{\frac{11}{4}}+\frac{1}{2}\right)\left(\frac{1}{g^k(0)}\right); \quad F_1(n)=f_1 n. \qquad (A2)$$

For $g^k(0)$ and *m*, see Eqs. (4) and (5):

$$k=c:, \quad m=1: \quad g^c(0)=\pi/2-1,$$

$$k=c:, \quad m=11: \quad g^c(0)=(693/512)\pi-1, \qquad (A3)$$

$$k=p:, \quad g^p(0)=1/m.$$

$F_2(n)$ does not allow a similar mathematical treatment. However, starting with $n \sim 1$, a surprisingly accurate curve fitting of the numerical results can be presented as

$$F_2(n)=1/g^k(0)+f_2/n^a \qquad (A4)$$

$$k=c, \quad m=1: \quad f_2=0{,}6277, \quad \alpha=1,$$

$$k=c, \quad m=11: \quad f_2=0{,}4638, \quad \alpha=1,$$

$$k=p, \quad m=1: \quad f_2=0{,}8571, \quad \alpha=0{,}68,$$

$$k=p, \quad m=11: \quad f_2=0{,}0962, \quad \alpha=3{,}72. \qquad (A5)$$

According to Eqs. (21), (22), and (23), $\tilde{N}$ can finally be expressed with (*A*2) and (*A*4) as

$$\tilde{N}=(f_1\beta_1+f_2/\beta_1^{\alpha})\tilde{N}_0^{1/(\alpha+1)}+\tilde{N}_0/g^k(0), \quad \beta_1=\alpha f_2/f_1. \qquad (A6)$$

Relation (*A*6) can be used for practical applications and considered as an approximation of the lines in Fig. 8. However, to find f_2 and α for any *k* and *m*, it is necessary to perform the extensive numerical analysis as outlined in Chap. 3.

Finally, also an approximation for l/B can be found according to Eq. (17) as

$$l/B=\frac{\pi}{2\sqrt{6}}\frac{1}{\sqrt{\beta_1}}\tilde{N}_0^{-1/2(\alpha+1)}. \tag{A7}$$

References

[1] Tarnopolskaya, T., and de Hoog, F. R., 1998, ''An Efficient Method for Strip Flatness Analysis in Cold Rolling,'' Math. Eng. Indust., **7**, pp. 71–95.

[2] Tomita, Y., and Shao, H., 1993, ''Buckling Behavior in Thin Sheet Metal Subjected to Nonuniform Membrane-Type Deformation,'' *Advances in Engineering Plasticity and Its Applications*, W. B. Lee, Elsevier, Amsterdam, pp. 923–930.

[3] Komori, K., 1998, ''Analysis of Cross and Vertical Buckling in Sheet Metal Rolling,'' Int. J. Mech. Sci., **40**, pp. 1235–1246.

[4] Fischer, F. D., Rammerstorfer, F. G., Friedl, N., and Wieser, W., 2000, ''Buckling Phenomena Related to Rolling and Levelling of Sheet Metal,'' Int. J. Mech. Sci., **42**, pp. 1887–1910.

[5] Rammerstorfer, F. G., Fischer, F. D., and Friedl, N., 2001, ''Buckling of Free Infinite Strips Under Residual Stresses and Global Tension,'' ASME J. Appl. Mech., **68**, pp. 399–404.

[6] Yuan, S., and Jin, Y., 1998, ''Computation of Elastic Buckling Loads of Rectangular Thin Plates Using the Extended Kantorovich Method,'' Comput. Struct., **66**, pp. 861–867.

Generalized Framework for Three-Dimensional Upper Bound Limit Analysis in a Tresca Material

A. M. Puzrin[1]
School of Civil and Environmental Engineering,
Georgia Institute of Technology,
Atlanta, GA 30332

M. F. Randolph
Center for Offshore Foundation Systems,
The University of Western Australia,
Nedlands, WA 6907, Australia

A new method is proposed for deriving kinematically admissible velocity fields (KAVFs) for three-dimensional upper bound limit analyses in a Tresca material using coordinate transformations. The method allows the incompressibility condition to be satisfied simply by imposing certain requirements on the analytical form of velocity magnitudes. This allows for new classes of velocity fields to be derived solely using standard procedures. These new classes of fields include: KAVFs with new streamline shapes; new planar but non-plane-strain KAVFs; new radial but nonaxisymmetric KAVFs. The method allows the expression of local dissipation of plastic work in any field to be derived in a closed form. The proposed method makes an attempt to expand the applicability of three-dimensional upper bound limit analysis by introducing more realistic shapes of KAVFs, while maintaining simplicity and clear engineering meaning. [DOI: 10.1115/1.1507764]

1 Introduction

Three-dimensional upper bound limit analysis is a powerful tool for solving bearing capacity problems in perfectly plastic media. Ingenuity is required in this approach from the need to devise velocity fields satisfying kinematic admissibility conditions and yet producing a sufficiently low value for the upper bound of the collapsed load. In spite of the power of modern finite element techniques, upper bound limit analysis still has certain advantages, particularly with respect to identifying failure mechanisms and conducting parametric studies for different loading combinations or where the material is nonhomogeneous. In many cases, the approach can lead to much simpler mathematical calculations, although this will depend on the choice of kinematically admissible velocity field (KAVF) and coordinate system. The aim in this paper is to demonstrate how careful choice of these can lead to easily calculable expressions for dissipation of plastic work.

Most velocity fields presented so far in the literature for upper bound analysis consist of rigid blocks and distortional shear zones with either straight or circular velocity fields. With a few exceptions (e.g., Murff and Hamilton [1]) the mechanisms are either plane strain (e.g., Shield and Drucker [2]) or axisymmetric (e.g., Levin [3]). Although Levin proposed an ingenious method for construction of more general nonsymmetrical KAVFs in cylindrical coordinates, he was not able to present any results apart from for the axisymmetric case because of limited computational resources at that time.

Advances in finite element analysis, particularly for three-dimensional problems, suggest a new paradigm for limit analysis, whereby velocity fields are deduced from the kinematic fields from the finite element analysis (e.g., Bransby and Randolph [4]). The velocity fields may then be used as a basis to explore effects of geometry variations, or heterogeneity of material properties, using upper bound limit analysis. An appealing approach to avoid complex velocity fields is to make use of existing (simple) fields that are applicable to specific conditions, superimposing different fields in order to obtain improved solutions for the general case. This can lead to rounding of the corner where two separate upper bound solutions intersect ([5,6]). However, new, more complex, velocity fields are also needed, but how can we make sure that these are (i) kinematically admissible, and (ii) calculable?

The present paper addresses this question by developing a generalized framework for the construction of three-dimensional velocity fields that are both kinematically admissible and easily calculable. This will allow for much greater flexibility in the generation of new KAVFs, and the approximation of velocity fields obtained from finite element analysis. A key feature of the approach is to adopt a local curvilinear coordinate system where one axis is directed along the streamline of the velocity field.

2 Upper Bound Limit Analysis With Tresca's Criterion

A general method for determining the upper bound collapse load for assemblages of rigid and elastic-perfectly plastic bodies was developed by Drucker et al. [7] and Shield and Drucker [2]. The term ''collapse'' is used to describe conditions for which plastic flow would occur under constant loads if the accompanying change in the geometry of the body were disregarded. The upper bound limit analysis approach in the form required in the present study is briefly outlined here.

Consider an assemblage of rigid and elastic-perfectly plastic bodies under the action of a set of surface tractions. Strain rates can be derived from any given velocity field. Considering the strain rates as purely plastic, the internal rate of plastic work can be calculated. (Note, we have deliberately avoided using the word ''dissipation,'' since plastic work is often referred to as dissipation of energy, which is an incorrect term. Energy never dissipates, as postulated by the First Law of Thermodynamics; it simply transforms from one form into another. In our case, mechanical plastic work is ''dissipated'' as heat.)

A velocity field is said to be kinematically admissible for plastic deformation governed by Tresca's yield criterion if

- the velocity components satisfy the incompressibility condition;

---

[1] Formerly at Department of Civil Engineering, Technion–Israel Institute of Technology.

Contributed by the Applied Mechanics Division of THE AMERICAN SOCIETY OF MECHANICAL ENGINEERS for publication in the ASME JOURNAL OF APPLIED MECHANICS. Manuscript received by the ASME Applied Mechanics Division, July 20, 2001; final revision, Mar. 15, 2002. Associate Editor: E. Arruda. Discussion on the paper should be addressed to the Editor, Prof. Robert M. McMeeking, Department of Mechanical and Environmental Engineering University of California–Santa Barbara, Santa Barbara, CA 93106-5070, and will be accepted until four months after final publication of the paper itself in the ASME JOURNAL OF APPLIED MECHANICS.

and

- the velocity components satisfy any imposed velocity boundary condition.

A kinematically admissible velocity field may contain discontinuities in the tangential velocities across fixed surfaces. This type of discontinuity is an idealization of a continuous large variation in velocity across a thin transition layer.

In the absence of inertial effects, the rate at which the applied tractions do work (determined by the velocities at their points of application) must equal the rate of internal plastic work. The following theorem has been formulated for the case where all surface tractions increase proportionally ([2]):

The Upper Bound Theorem. *Collapse will occur under the smallest values of the surface tractions for which it is possible to find a kinematically admissible velocity field.*

This theorem provides a method for determining upper bounds for the limiting values of surface tractions. For Tresca's yield criterion of constant maximum shearing stress, c_u, Shield and Drucker [2] showed that the upper bound solution for the surface traction $\mathbf{T}=\{T_x,T_y,T_z\}^T$ is calculated from the following equation:

$$\int_S \mathbf{T}^T\mathbf{v}dS=W(\mathbf{T},\mathbf{v})=D(\mathbf{v})=\int_V 2c_u|\dot{\boldsymbol{\varepsilon}}|_{\max}dV+\int_{S_D} c_u|\Delta v|dS \tag{1}$$

where

$\mathbf{v}$ = $\{v_x,v_y,v_z\}^T$–the kinematically admissible velocity field;
$W(\mathbf{T},\mathbf{v})$ = rate of work done by the surface tractions;
$D(\mathbf{v})$ = rate of internal plastic work;
$|\dot{\boldsymbol{\varepsilon}}|_{\max}$ = absolutely largest principal component of the plastic strain rate;
Δv = velocity jump across any discontinuity;
S = surface that bounds the body or the assemblage of the bodies;
V = volume of the assemblage of the bodies; and
S_D = surfaces of all discontinuities.

Any variation in the maximum shearing stress, c_u, between the bodies in the assemblage, within the volume of the bodies, and along discontinuities, must be taken into account in the evaluation of plastic work in Eq. (1). Obviously, rigid bodies in the assemblage contribute nothing to the volume integration since the strain rate is zero for a rigid body.

3 General Framework

Consider a velocity field $\mathbf{v}=\{U,V,W\}^T$ in orthogonal Cartesian coordinates (X, Y, Z), such that the velocity components of this field are defined through the following equations:

$$U=U(X,Y,Z)\quad V=V(X,Y,Z)\quad W=W(X,Y,Z). \tag{2}$$

This velocity field defines a family of streamlines. Let us narrow our analysis to a class of velocity fields, where each of the streamlines results from the intersection of two perpendicular surfaces (examples will be given later):

$$\begin{cases} y(X,Y,Z)=y_i=\text{const} \\ z(X,Y,Z)=z_i=\text{const.} \end{cases} \tag{3}$$

The orthogonality of these two surfaces is expressed by the following condition:

$$y_{,X}z_{,X}+y_{,Y}z_{,Y}+y_{,Z}z_{,Z}=0 \tag{4}$$

where the notation $a_{,b}=\partial a/\partial b$ is adopted.

Each pair of constants (y_i,z_i) defines a different streamline. Next, consider the third surface:

$$x(X,Y,Z)=x_i=\text{const} \tag{5}$$

which is perpendicular to all the streamlines, so that

$$\begin{cases} x_{,X}y_{,X}+x_{,Y}y_{,Y}+x_{,Z}y_{,Z}=0 \\ x_{,X}z_{,X}+x_{,Y}z_{,Y}+x_{,Z}z_{,Z}=0 \end{cases}. \tag{6}$$

Intersection of the ith streamline with the surface $x(X,Y,Z)=x_i$ $=\text{const}$ will produce a point. Coordinates of this point in the Cartesian system $\{X, Y, Z\}$ are obtained by solving Eqs. (3) together with Eq. (5). However, the three constants (x_i,y_i,z_i) would also define the position of this point uniquely, and therefore they can be used as alternative coordinates, defined in the following curvilinear orthogonal coordinate system:

$$\begin{cases} x=x(X,Y,Z) \\ y=y(X,Y,Z) \\ z=z(X,Y,Z). \end{cases} \tag{7}$$

The original velocity field, when presented in curvilinear coordinates (x, y, z), will have a different set of components $\mathbf{v}$ $=\{u,v,w\}^T$ in coordinate directions x, y and z, respectively:

$$u=u(x,y,z)\quad v=v(x,y,z)\quad w=w(x,y,z). \tag{8}$$

An important property of the curvilinear orthogonal coordinate system defined above is that the coordinate line x coincides with the streamline. Therefore, the only nonzero component of velocity in the (x, y, z) coordinate system is u. Components of the small strain rate tensor in general orthogonal curvilinear coordinates are given by the following expressions ([8]):

$$\begin{aligned} \dot{\varepsilon}_x&=\frac{1}{\alpha}\left(u_{,x}+\alpha_{,y}\frac{v}{\beta}+\alpha_{,z}\frac{w}{\gamma}\right) & 2\dot{\varepsilon}_{xy}&=\frac{\alpha}{\beta}\left(\frac{u}{\alpha}\right)_{,y}+\frac{\beta}{\alpha}\left(\frac{v}{\beta}\right)_{,x} \\ \dot{\varepsilon}_y&=\frac{1}{\beta}\left(\beta_{,x}\frac{u}{\alpha}+v_{,y}+\beta_{,z}\frac{w}{\gamma}\right) & 2\dot{\varepsilon}_{yz}&=\frac{\beta}{\gamma}\left(\frac{v}{\beta}\right)_{,z}+\frac{\gamma}{\beta}\left(\frac{w}{\gamma}\right)_{,y} \\ \dot{\varepsilon}_z&=\frac{1}{\gamma}\left(\gamma_{,x}\frac{u}{\alpha}+\gamma_{,y}\frac{v}{\beta}+w_{,z}\right) & 2\dot{\varepsilon}_{xz}&=\frac{\alpha}{\gamma}\left(\frac{u}{\alpha}\right)_{,z}+\frac{\gamma}{\alpha}\left(\frac{w}{\gamma}\right)_{,x} \end{aligned} \tag{9}$$

where

$$\begin{aligned} \alpha&=\sqrt{(X_{,x})^2+(Y_{,x})^2+(Z_{,x})^2} \\ \beta&=\sqrt{(X_{,y})^2+(Y_{,y})^2+(Z_{,y})^2} \\ \gamma&=\sqrt{(X_{,z})^2+(Y_{,z})^2+(Z_{,z})^2}. \end{aligned} \tag{10}$$

These equations are derived by calculating the rate of incremental change of length of the deformed element in two different coordinate systems (Cartesian and curvilinear) and comparing the corresponding components.

Functions $X=X(x,y,z)$, $Y=Y(x,y,z)$ and $Z=Z(x,y,z)$ are defined by solving Eqs. (7). Substitution of the special property v $=w=0$ of our curvilinear coordinate system into expressions (9) yields the following expression for the strain rate tensor:

$$\dot{\varepsilon}=\begin{bmatrix} \dfrac{u_{,x}}{\alpha} & \dfrac{\alpha}{2\beta}\left(\dfrac{u}{\alpha}\right)_{,y} & \dfrac{\alpha}{2\gamma}\left(\dfrac{u}{\alpha}\right)_{,z} \\ \dfrac{\alpha}{2\beta}\left(\dfrac{u}{\alpha}\right)_{,y} & \dfrac{\beta_{,x}}{\beta}\dfrac{u}{\alpha} & 0 \\ \dfrac{\alpha}{2\gamma}\left(\dfrac{u}{\alpha}\right)_{,z} & 0 & \dfrac{\gamma_{,x}}{\gamma}\dfrac{u}{\alpha} \end{bmatrix}. \tag{11}$$

The incompressibility condition is equivalent to the following differential equation:

$$\frac{u_{,x}}{\alpha}+\frac{\beta_{,x}}{\beta}\frac{u}{\alpha}+\frac{\gamma_{,x}}{\gamma}\frac{u}{\alpha}=0 \tag{12}$$

which, upon integration, yields the following functional form for the velocity component u:

$$u(x,y,z)=\frac{f(y,z)}{\beta\gamma} \tag{13}$$

where $f(y,z)$ is an arbitrary function of y and z. It follows that the incompressibility condition does not place any restrictions on variation of the velocity with y and z-coordinates, but its variation with the x-coordinate depends on the functional form of β and γ.

The characteristic equation for the strain rate tensor (11), satisfying condition (12), is

$$\dot{\varepsilon}^3-p\dot{\varepsilon}-q=0 \tag{14}$$

where

$$p=s^2\left[\left(\frac{\beta_{,x}}{\beta}\right)^2+\frac{\beta_{,x}}{\beta}\frac{\gamma_{,x}}{\gamma}+\left(\frac{\gamma_{,x}}{\gamma}\right)^2+\left(\frac{\alpha}{2\beta}\frac{s_{,y}}{s}\right)^2+\left(\frac{\alpha}{2\gamma}\frac{s_{,z}}{s}\right)^2\right] \tag{15}$$

$$q=s^3\left[\left(\frac{\beta_{,x}}{\beta}\right)^2\frac{\gamma_{,x}}{\gamma}+\left(\frac{\alpha}{2\beta}\frac{s_{,y}}{s}\right)^2\frac{\gamma_{,x}}{\gamma}+\left(\frac{\gamma_{,x}}{\gamma}\right)^2\frac{\beta_{,x}}{\beta}+\left(\frac{\alpha}{2\gamma}\frac{s_{,z}}{s}\right)^2\frac{\beta_{,x}}{\beta}\right] \tag{16}$$

$$s=\frac{u}{\alpha}=\frac{f(y,z)}{\alpha\beta\gamma}. \tag{17}$$

The absolutely largest value of the principal strain rate is obtained in closed form after solving the cubic Eq. (14) ([9]):

$$|\dot{\varepsilon}|_{\max}=2\sqrt{\frac{p}{3}}\cos\left(\frac{1}{3}\arccos\frac{3\sqrt{3}|q|}{2\sqrt{p^3}}\right). \tag{18}$$

By substituting this expression into Eq. (1) and expressing an infinitesimal volume in curvilinear orthogonal coordinates

$$dV=\alpha\beta\gamma dxdydz \tag{19}$$

we can calculate the volume integral in Eq. (1) using simple numerical or analytical integration.

The surface integral in Eq. (1) is taken over the discontinuity surfaces. In many cases these discontinuity surfaces coincide with the coordinate surfaces x, y, or z, in which case the infinitesimal area of the discontinuity is given by one of the following three expressions:

$$dS_x=\beta\gamma dydz \quad dS_y=\alpha\gamma dxdz \quad dS_z=\alpha\beta dxdy \tag{20}$$

where dS_x, dS_y, and dS_z are the infinitesimal areas of the coordinate surfaces x, y, and z, respectively. The velocity jump Δv across the discontinuity is calculated as a vector difference between the tangential components of the two velocity vectors at both sides of discontinuity. In a case where the discontinuity coincides with the coordinate surface x, one of these two vectors is perpendicular to the discontinuity and its tangential component is zero. In cases where the discontinuity coincides with the coordinate surface y or z, one of these two vectors lies entirely within the discontinuity; its tangential component is parallel to the x-coordinate line and has a length u, defined by expression (13). This simplifies the calculation for $|\Delta v|$ in the surface integral in Eq. (1), allowing for simple numerical or analytical integration.

As is seen from the above derivations, use of a curvilinear orthogonal coordinate system simplifies integration of the rate of internal plastic work. Consequently, the upper bound surface traction can be calculated easily for the chosen KAVF.

4 Derivation of Streamlines

Applicability of the above method to a chosen KAVF depends entirely on our ability to obtain a closed-form solution for the system of Eqs. (7). This requirement, however, involves severe restrictions on the possible shapes of KAVFs. In order to avoid complications arising from this requirement, let us invert the problem and consider some transformation of coordinates

$$\begin{cases} X=X(x,y,z)\\ Y=Y(x,y,z)\\ Z=Z(x,y,z)\end{cases} \tag{21}$$

satisfying uniqueness and orthogonality conditions:

$$J=\begin{vmatrix} X_{,x} & Y_{,x} & Z_{,x}\\ X_{,y} & Y_{,y} & Z_{,y}\\ X_{,z} & Y_{,z} & Z_{,z}\end{vmatrix}\neq 0 \tag{22}$$

$$\begin{cases} X_{,x}X_{,y}+Y_{,x}Y_{,y}+Z_{,x}Z_{,y}=0\\ X_{,z}X_{,y}+Y_{,z}Y_{,y}+Z_{,z}Z_{,y}=0\\ X_{,x}X_{,z}+Y_{,x}Y_{,z}+Z_{,x}Z_{,z}=0.\end{cases} \tag{23}$$

Then, a family of non intersecting streamlines can be associated with the x-coordinate lines. In this case it is not really necessary to resolve the system of Eqs. (21)—the streamlines can be defined in a parametric form.

To illustrate this approach, let us consider a class of velocity fields where each streamline in the field lies entirely within some plane. We shall refer to these fields as *planar* velocity fields. Streamlines in velocity fields can never intersect except along axes with zero velocity. In planar velocity fields this condition is automatically satisfied in the following two cases:

Case I: *Plane* velocity fields—where all the planes are parallel to each other;

Case II: *Radial* velocity fields—where all the planes intersect along the same straight line.

In the following we illustrate derivation of the coordinate surfaces for these two cases.

4.1 Plane Velocity Fields. Let us choose the Z-axis of the Cartesian coordinate system in such a way that all the planes containing streamlines are orthogonal to it. The coordinate surface z is then a plane given by $z=Z-Z_0$, so that $Z_{,x}=Z_{,y}=0$ and $Z_{,z}=1$. The uniqueness condition (22) becomes

$$X_{,x}Y_{,y}-Y_{,x}X_{,y}\neq 0 \tag{24}$$

and it follows that, in order to have a nontrivial solution, orthogonality conditions (23) must be reduced to

$$\begin{cases} X_{,x}X_{,y}+Y_{,x}Y_{,y}=0\\ X_{,z}=Y_{,z}=0.\end{cases} \tag{25}$$

Table 1 gives details of three simple coordinate transformations satisfying both uniqueness (24) and orthogonality conditions (25) (actual examples illustrating these fields graphically are given in Sections 5 and 6 of this paper). The streamlines in the three cases considered comprise: (a) straight parallel lines inclined to any $Y=\text{const}$ plane by angle ψ; (b) concentric circular arcs centred at the point $\{X_0,Y_0\}$; and (c) involute curves arising from an evolute circle of radius R centered at the point $\{X_0,Y_0\}$. The last of these is included as an example of a curved, but noncircular, family of streamlines, which has found application in the flow of material past a cylindrical object ([10]).

In the first two cases, the coordinate transformation leads to an explicit expression for the coordinate surfaces y (see Table 1). In the third case the surface is contained implicitly in parametric form (with x as the parameter) in the coordinate transformation equations. In all cases, analytical expressions are given in Table 1 for the maximum principal strain rate, in terms of a streamline velocity that is some general function of coordinates y and z.

4.2 Radial Velocity Fields. Let us choose the Y-axis of the Cartesian coordinate system in such a way that it belongs to all the planes containing streamlines. In this case the coordinate surface z is a plane given by $Z=X\tan z$, so that

Table 1 Key functions for plane velocity fields

	Straight	Circular	Involute
Coordinate transformations	$X=X_0+x\cos\psi-y\sin\psi$ $Y=Y_0+x\sin\psi+y\cos\psi$ $Z=Z_0+z$	$X=X_0+y\cos x$ $Y=Y_0+y\sin x$ $Z=Z_0+z$	$X=X_0+R(\cos x+(x-y)\sin x)$ $Y=Y_0+R(\sin x-(x-y)\cos x)$ $Z=Z_0+z$
Coordinate surface, y	$y=(Y-Y_0)\cos\psi-(X-X_0)\sin\psi$	$y=\sqrt{(Y-Y_0)^2+(X-X_0)^2}$	From first two equations above
Scaling parameters α, β, γ	$\alpha=\beta=\gamma=1$	$\alpha=y;\ \beta=\gamma=1$	$\alpha=R(x-y)\ ;\ \beta=R\ ;\ \gamma=1$
Streamline functions s, u	$s=u\ ;\ u=f(y,z)$	$s=u/y\ ;\ u=f(y,z)$	$s=\dfrac{u}{R(x-y)};\ u=f(y,z)/R$
Principal strain rate	$\lvert\dot{\varepsilon}\rvert_{\max}=\frac{1}{2}\sqrt{s_{,y}^2+s_{,z}^2}$	$\lvert\dot{\varepsilon}\rvert_{\max}=\frac{y}{2}\sqrt{s_{,y}^2+s_{,z}^2}$	$\lvert\dot{\varepsilon}\rvert_{\max}=\frac{x-y}{2}\sqrt{s_{,y}^2+R^2s_{,z}^2}$
Volumetric element	$dV=dxdydz$	$dV=y\,dxdydz$	$dV=R^2(x-y)dxdydz$

$$\begin{cases} Z_{,x}=X_{,x}\tan z \\ Z_{,y}=X_{,y}\tan z \\ Z_{,z}=X_{,z}\tan z+X(1+\tan^2 z). \end{cases} \tag{26}$$

The uniqueness condition (22) becomes

$$\begin{cases} X_{,x}Y_{,y}-Y_{,x}X_{,y}\neq 0 \\ X\neq 0 \end{cases} \tag{27}$$

and it follows that, in order to have a nontrivial solution, the orthogonality conditions (23) must be reduced to

$$\begin{cases} X_{,x}X_{,y}(1+\tan^2 z)+Y_{,x}Y_{,y}=0 \\ X_{,z}=-X\tan z \\ Y_{,z}=0 \end{cases}. \tag{28}$$

Table 2 gives details of three coordinate transformations satisfying the equation $Z=X\tan z$, and both uniqueness (27) and orthogonality conditions (28). Similar to the examples for plane velocity fields, the streamlines comprise: (a) straight parallel lines inclined to any $Y=\text{const}$ plane by angle ψ; (b) concentric circular arcs

Table 2 Key functions for radial velocity fields

	Straight	Circular	Involute
Coordinate transformations	$X=(x\cos\psi-y\sin\psi+R_0)\cos z$ $Y=Y_0+x\sin\psi+y\cos\psi$ $Z=(x\cos\psi-y\sin\psi+R_0)\sin z$	$X=(y\cos x+R_0)\cos z$ $Y=Y_0+y\sin x$ $Z=(y\cos x+R_0)\sin z$	$X=(R_0+R(\cos x+(x-y)\sin x))\cos z$ $Y=Y_0+R(\sin x-(x-y)\cos x)$ $Z=(R_0+R(\cos x+(x-y)\sin x))\sin z$
Coordinate surface, y	$y=(Y-Y_0)\cos\psi-\left(\sqrt{X^2+Z^2}-R_0\right)\sin\psi$	$y=\sqrt{(Y-Y_0)^2+\left(\sqrt{X^2+Z^2}-R_0\right)^2}$	Equations (29)
Scaling parameters α, β, γ	$\alpha=\beta=1;$ $\gamma=x\cos\psi-y\sin\psi+R_0$	$\alpha=y$, $\beta=1$ and $\gamma=y\cos x+R_0$	$\alpha=R(x-y)$, $\beta=R$ and $\gamma=R_0+R\cos x+R(x-y)\sin x$
Streamline functions s, u	$s=u$ and $u=f(y,z)/(x\cos\psi-y\sin\psi+R_0)$	$s=u/y$ and $u=f(y,z)/(y\cos x+R_0)$	$s=\dfrac{u}{R(x-y)}$ and $u=\dfrac{f(y,z)}{R(R\cos x+R(x-y)\sin x+R_0)}$
Principal strain rate	$\lvert\dot{\varepsilon}\rvert_{\max}=\sqrt{a}\cos\left(\frac{1}{3}\arccos b\right)$ where: $a=\dfrac{4(s\cos\psi)^2+s_{,z}^2+c^2s_{,y}^2}{3c^2}$ $b=\dfrac{3\sqrt{3}\lvert s\cos\psi\rvert s_{,y}^2c^2}{\sqrt{\left(4(s\cos\psi)^2+s_{,z}^2+c^2s_{,y}^2\right)^3}}$ $c=x\cos\psi-y\sin\psi+R_0$	$\lvert\dot{\varepsilon}\rvert_{\max}=y\sqrt{b}\cos\left(\frac{1}{3}\arccos b\right)$ where: $a=\dfrac{4(s\sin x)^2+s_{,z}^2+c^2s_{,y}^2}{3c^2}$ $b=\dfrac{3\sqrt{3}\lvert s\sin x\rvert s_{,y}^2c^2}{\sqrt{\left(4(s\sin x)^2+s_{,z}^2+c^2s_{,y}^2\right)^3}}$ $c=y\cos x+R_0$	$\lvert\dot{\varepsilon}\rvert_{\max}=(x-y)\sqrt{a}\cos\left(\frac{1}{3}\arccos b\right)$ where: $a=\dfrac{4(Rs\cos x)^2+R^2s_{,z}^2+c^2s_{,y}^2}{3c^2}$ $b=\dfrac{3\sqrt{3}\lvert s\cos x\rvert s_{,y}^2c^2}{\sqrt{\left(4(Rs\cos x)^2+R^2s_{,z}^2+c^2s_{,y}^2\right)^3}}$ $c=R\cos x+R(x-y)\sin x+R_0$
Volumetric element	$dV=(x\cos\psi-y\sin\psi+R_0)dxdydz$	$dV=y(y\cos x+R_0)dxdydz$	$dV=R^2(x-y)$ $(R\cos x+R(x-y)\sin x+R_0)dxdydz$

centered at the point $\{R_0 \cos z, Y_0, R_0 \sin z\}$; and (c) involute curves derived from an evolute circle of radius R centered at the point $\{R_0 \cos z, Y_0, R_0 \sin z\}$ ([11]).

For the involute curves, the coordinate surfaces y cannot be obtained analytically, but are given in a parametric form by equations

$$\begin{cases} \sqrt{X^2+Z^2}=R_0+R(\cos x+(x-y)\sin x) \\ Y=Y_0+R(\sin x-(x-y)\cos x) \end{cases} \tag{29}$$

where x is a parameter.

4.3 Discussion. The general framework presented above allows for derivation of the three-dimensional kinematically admissible velocity fields from any unique orthogonal transformation of Cartesian coordinates $\{X, Y, Z\}$. In fact, each transformation can generate three different families of streamlines, depending which of the coordinate lines are chosen to act as streamlines, with new fields being derived from the same transformation (21) by interchanging variables x, y, and z. For example, by interchanging variables x and y in the coordinate transformation for straight streamlines in Table 1, we obtain a new family of straight, but radial, streamlines emanating from the center $\{X_0, Y_0\}$.

The coordinate surfaces y are obtained by resolving the modified transformation equations to give $(Y-Y_0)=(X-X_0)\tan y$. From Eqs. (10) it follows that $\beta=x$ and $\alpha=\gamma=1$, and their substitution into Eqs. (15)–(19) produces

$$|\dot{\varepsilon}|_{\max}=\sqrt{\frac{4s^2+s_{,y}^2+x^2s_{,z}^2}{3x^2}}\cos\left(\frac{1}{3}\arccos\frac{3\sqrt{3}|s|s_{,z}^2x^2}{\sqrt{(4s^2+s_{,y}^2+x^2s_{,z}^2)^3}}\right) \tag{30}$$

$$dV=x\,dx\,dy\,dz \tag{31}$$

where $s=u$ and $u=f(y,z)/x$ is some function describing a particular velocity field.

This section has covered virtually all shapes of streamlines presented so far in the literature. Derivation of these fields using the proposed approach has allowed closed-form expressions of the maximum absolute values of principal strain rates to be obtained by means of a standard procedure. This reduces calculations of the upper bounds to simple numerical integration, while in some cases closed-form upper bound solutions may be obtained.

However, the benefits of the proposed approach extend far beyond simplifications in calculations. In this paper we will demonstrate some potential applications of the approach, namely

- derivation of KAVFs with new streamline shapes;
- derivation of new plane KAVFs (non-plane-strain);
- derivation of new radial KAVFs (nonaxisymmetric).

5 Applications: Fields With New Streamline Shapes

In order to demonstrate application of the proposed approach to derivation of KAVFs with new streamline shapes, let us consider the following simple bearing capacity problem.

5.1 Bearing Capacity Problem of a Rough Strip Footing Near a Rigid Obstacle. Consider a rigid rough strip footing of width $2b$ on saturated clay between two rigid rough obstacles at a distance of $(1+d)b$ from either edge of the footing, and subjected to an average pressure, p (Fig. 1).

Due to symmetry, only half of the problem will be considered below. Clearly, when $d \geqslant 1$, the upper bound bearing capacity of the footing under vertical load is given by the Prandtl solution $p=(2+\pi)c_u$, which also happens to be the exact solution. The corresponding kinematic mechanism, consisting of two rigid blocks ABO and ACD and a fan shear zone ABC is shown in Fig. 2(*a*). However, for obstacles located closer than that (i.e., when $d<1$) the Prandtl mechanism is not kinematically admissible, because the passive block ACD will collide with the obstacle. For cases when $0<d<1$, one possible solution of the problem would be to modify the Prandtl mechanism by adjusting the passive region ACD in such a way that it avoids collision with the obstacle (Fig. 2(*b*)). This may be achieved through new shapes of streamlines, e.g., hyperbolic streamlines.

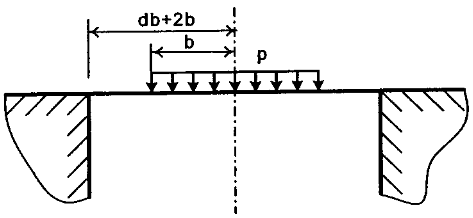

Fig. 1 Schematic layout of the bearing capacity problem

5.2 Hyperbolic Streamlines. Let us consider a plane coordinate transformation

$$\begin{cases} X=X_0+\sqrt{-x^2+\sqrt{x^4+(y+y_0)^4}} \\ Y=Y_0+\sqrt{x^2+\sqrt{x^4+(y+y_0)^4}} \\ Z=Z_0+z. \end{cases} \tag{32}$$

This coordinate transformation satisfies both uniqueness (24) and orthogonality (25) conditions. Coordinate surfaces y are obtained by resolving Eqs. (32) to give $(y+y_0)^2=(X-X_0)/(Y-Y_0)$ and their intersection with the plane z produces a family of hyperbolic streamlines. From Eqs. (10) it follows that

$$\alpha=\frac{\sqrt{2}x}{\sqrt[4]{x^4+(y+y_0)^4}} \quad \beta=\frac{\sqrt{2}(y+y_0)}{\sqrt[4]{x^4+(y+y_0)^4}} \quad \gamma=1 \tag{33}$$

and their substitution into Eqs. (15)–(17) produces

$$q=\frac{-x^5ss_{,z}^2}{2\sqrt{(x^4+(y+y_0)^4)^3}} \tag{34}$$

$$p=\frac{x^6s^2}{(x^4+(y+y_0)^4)^2}+\frac{x^2s_{,z}^2}{2\sqrt{(x^4+(y+y_0)^4)}}+\frac{x^2s_{,y}^2}{4(y+y_0)^2} \tag{35}$$

where

$$s=\frac{u\sqrt[4]{x^4+(y+y_0)^4}}{\sqrt{2}x} \quad \text{and} \quad u=\frac{f(y,z)\sqrt[4]{x^4+(y+y_0)^4}}{\sqrt{2}(y+y_0)} \tag{36}$$

are some functions describing a particular velocity field. For a plane-strain case, u and s are independent of z, reducing expression (34) to $q=0$ and simplifying expression (35), which after substitution into (18) and (19) produce

$$|\dot{\varepsilon}|_{\max}=\sqrt{\frac{x^6s^2}{(x^4+(y+y_0)^4)^2}+\frac{s_{,y}^2}{4(y+y_0)^2}};$$

$$dV=\frac{2x(y+y_0)}{\sqrt{x^4+(y+y_0)^4}}dx\,dy\,dz. \tag{37}$$

5.3 Solution. Let us construct a hyperbolic velocity field in a passive shear zone ACD (Fig. 3). The origin of the Cartesian coordinate system X0Y is chosen at point C. Substituting $X_0=Y_0=y_0$ into Eqs. (32) and resolving them with respect to x and y we obtain

$$\begin{cases} (y+y_0)^2=(X-y_0)(Y-y_0) \\ 2x^2=(Y-y_0)^2-(X-y_0)^2 \end{cases}. \tag{38}$$

The first Eq. (38) produces a family of hyperbolic streamlines:

$$Y=\frac{y^2+y_0(X+2y)}{X-y_0}. \tag{39}$$

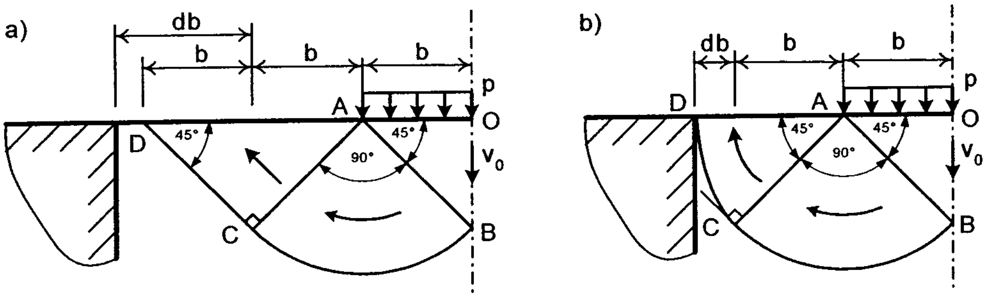

Fig. 2 Failure mechanisms: (*a*) $d \geqslant b$; (*b*) $0 < d < b$

The streamline passing through the origin is defined by $y=0$. This streamline also represents a discontinuity separating the passive shear zone ACD from the rigid half-space and emerges to the surface at point D with coordinates $X=-db$ and $Y=b$. Parameter y_0 is defined by substituting these coordinates and $y=0$ into Eq. (39):

$$y_0=\frac{-db}{1-d} \tag{40}$$

so that the hyperbolic discontinuity surface is described by

$$Y=\frac{-dbX}{X(1-d)+db}. \tag{41}$$

In Fig. 3(*a*), a family of these curves bounding the passive shear zone is shown for varying parameter *d*. As is seen, this family covers a wide range of shapes, from the original Prandtl triangle at $d=1$ to half of this triangle at $d=0$, with a smooth hyperbolic boundary for any intermediate value of *d*.

Once the boundary is established and parameter y_0 is defined from Eq. (40), the whole family of streamlines is defined by substituting y_0 into (39). In Fig. 3(*b*), this family of streamlines is shown for $d=0.4$ for various values of curvilinear coordinate *y*. The first streamline in the family passes through the point C with Cartesian coordinates (0, 0) and is defined by $y_{\mathrm{CD}}=0$. The last streamline in the family passes through the point A with Cartesian coordinates $X=Y=b$ and substitution of these coordinates into (39) produces $y_{\mathrm{A}}=-b$. All the streamlines are perpendicular to the radius AC bounding the fan zone ABC.

Because in the proposed method integration of plastic work in the volume ACD will be carried out in curvilinear coordinates *x* and *y*, it is necessary to define integration limits in these coordinates. As is clear from the previous paragraph, coordinate *y* changes within $-b \leqslant y \leqslant 0$. Coordinate *x* changes between its respective values along lines AC and AD. Along the line AC, $X=Y$ and from the second Eq. (38): $x_{\mathrm{AC}}=0$. Along the line AD, $Y=b$ and after eliminating *X* from Eqs. (38) we obtain

$$x_{\mathrm{AD}}=\frac{(b-y_0)}{\sqrt{2}}\sqrt{1-\frac{(y+y_0)^4}{(b-y_0)^4}}. \tag{42}$$

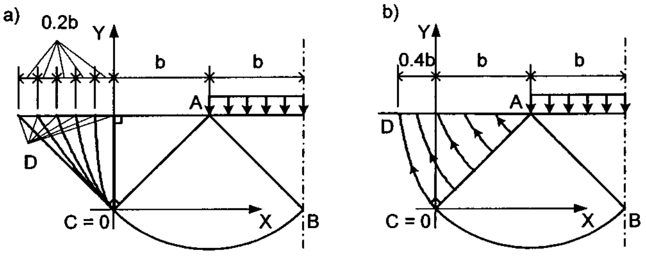

Fig. 3 Examples of hyperbolic velocity fields: (*a*) discontinuity surfaces bounding the passive shear zone for various values of *d*; (*b*) hyperbolic streamlines for $d=0.4$

The velocity field is defined by the second Eq. (36), where an arbitrary function $f(y)$ is defined from the velocity continuity condition between the fan shear zone ABC and the hyperbolic shear zone ACD. Along the radius AC, $u_{\mathrm{AC}}=v_0/\sqrt{2}$ and $x_{\mathrm{AC}}=0$, where v_0 is the vertical velocity of the footing, which after substitution into the second Eq. (36) produces $f(y)=v_0$. This leads to

$$s=\frac{v_0\sqrt{x^4+(y+y_0)^4}}{2x(y+y_0)} \quad \text{and} \quad u=\frac{v_0\sqrt[4]{x^4+(y+y_0)^4}}{\sqrt{2}(y+y_0)}. \tag{43}$$

Substituting (43) into (37) we obtain

$$|\dot{\varepsilon}|_{\max}=\frac{\sqrt{x^4+(y+y_0)^4}}{4(y+y_0)^3}; \quad dV=\frac{2x(y+y_0)}{\sqrt{x^4+(y+y_0)^4}}\,dx\,dy\,dz \tag{44}$$

and integration of (37) over the volume ACD according to (1), gives an expression for the plastic work in this volume:

$$D_{\mathrm{ACD}}=v_0c_u\int_{y_{\mathrm{DC}}=-b}^{y_{\mathrm{AA}}=0}\int_{x_{\mathrm{AC}}=0}^{x_{\mathrm{AD}}}\frac{x}{(y+y_0)^2}\,dx\,dy. \tag{45}$$

Substituting x_{AD} from (42), integrating Eq. (45) and substituting for y_0 from (40), we obtain

$$D_{\mathrm{ACD}}=\frac{4-(1+d)(1+d^2)}{12d}\,v_0c_ub. \tag{46}$$

Plastic work along the discontinuity CD is calculated using the fact that the discontinuity surface coincides with one of the *y*-coordinate surfaces, namely $y=0$, giving

$$D_{\mathrm{CD}}=c_u\int_{x_{\mathrm{AC}}=0}^{x_{\mathrm{AD}}|_{y=0}}|u_{\mathrm{CD}}|_{y=0}\,dS_y. \tag{47}$$

Substitution of Eqs. (20), (40), (42), and (43) into (47), and subsequent integration yields

$$D_{\mathrm{CD}}=v_0c_u\int_{x_{\mathrm{AC}}=0}^{x_{\mathrm{AD}}|_{y=0}}\frac{x}{y_0}\,dx=\frac{(1+d)(1+d^2)}{4d}\,v_0c_ub. \tag{48}$$

Total plastic work in the passive shear zone is $D=D_{\mathrm{CD}}+D_{\mathrm{ACD}}=[2+(1+d)(1+d^2)]/6d\;v_0c_ub$, so that the upper bound of the collapse pressure in the entire mechanism is

$$p=\left(1+\pi+\frac{1}{2d}+\frac{1+d+d^2}{6}\right)c_u. \tag{49}$$

5.4 Discussion. Remarkably, the new hyperbolic shear zone produced a simple closed-form solution (49), which paradoxically contains a hyperbolic term! For $d=1$ this solution is identical to

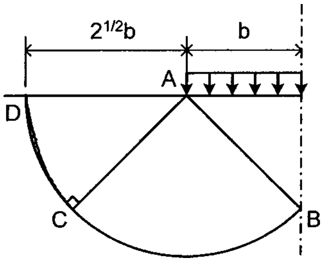

Fig. 4 Comparison of different velocity fields in the passive zone

the Prandtl (exact) solution, because in this extreme case the hyperbolic shear zone degenerates into a rigid block. Derivation of the plastic work in this zone looks rather elaborate, due to the necessity to demonstrate clearly the proposed procedure. However, once derived, the hyperbolic shear zone can be used in construction of the kinematic mechanisms in a way similar to that of the fan shear zones and rigid blocks in a search for sharper upper bounds.

For example, in the particular case $d=\sqrt{2}-1$ of our problem of a strip footing near the rigid obstacle, the mechanism constructed by extending the fan shear zone ABC into the passive zone ACD (external arc CD in Fig. 4) produces the upper bound $p=(1+3\pi/2)c_u \approx 5.71c_u$. By contrast, the hyperbolic shear zone ACD (internal hyperbola CD in Fig. 4) produces a sharper upper bound: $p=(2+\pi+\sqrt{2}/3)c_u \approx 5.61c_u$. Both of these are lower than a finite element solution, which yields $p=5.81c_u$ (compared with $5.17c_u$ for the case of $d>1$).

While the present solution gives unrealistically infinite capacity as d approaches zero, in principal the approach could be extended for rigid walls that approach right to the edge of the footing, by reducing the present fan angle below $\pi/2$ again matching the hyperbolic streamlines to the velocities emerging from the fan zone. This is outside the scope of the present paper, but the example has served to demonstrate the general approach, and also that (a) closed-form expressions for the dissipation terms can sometimes be achieved, and (b) the method can lead to improved upper bounds compared with existing mechanisms.

6 Applications: Plane But Non-Plane-Strain Fields

There are certain classes of problem where it is reasonable to assume streamlines that lie in parallel planes, but where the velocity fields vary in the direction normal to the planes. Such cases are referred to here as "plane but not plane-strain velocity fields."

In order to demonstrate application of the proposed approach to derivation of non-plane-strain KAVFs, let us consider the bearing capacity problem of a rigid smooth square footing of width $2b$ on saturated clay subjected to undrained moment loading $\mathbf{M}$ (Fig. 5). The form of the failure surface is identical to that proposed by Shield and Drucker [2] for purely vertical loading of a square footing, which led to an upper bound for the vertical load, V, of $\mathbf{V}=[4\sqrt{6}+\pi(2+\sqrt{6})]b^2c_u \approx 23.78b^2c_u$. Under moment loading, the footing rotates and the soil within the fields OBCDI and OLMNJ is assumed to move in vertical planes parallel to NOD. (Note that, although the footing is smooth, a symmetric mechanism is assumed at this stage, with soil beneath the trailing half of the footing moving upwards as the footing rotates; the case where the soil breaks from the footing and remains stationary in OLMNJ and OFGHJ merely reduces the final dissipation (and resulting ultimate moment) by a factor of 2.) At the sides of the footing, soil within the fields OFGHI and OFGHJ is assumed to move in vertical planes parallel to OH, with zero velocity in the plane OEHGF.

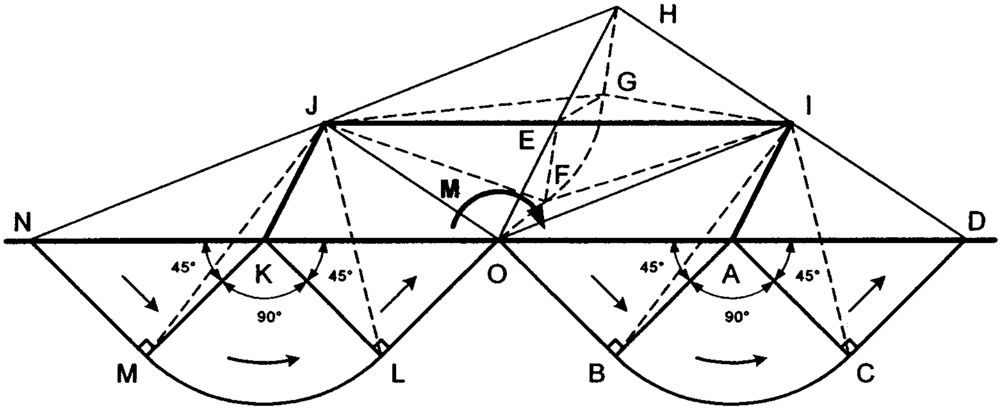

Fig. 5 Rotation of a smooth square footing

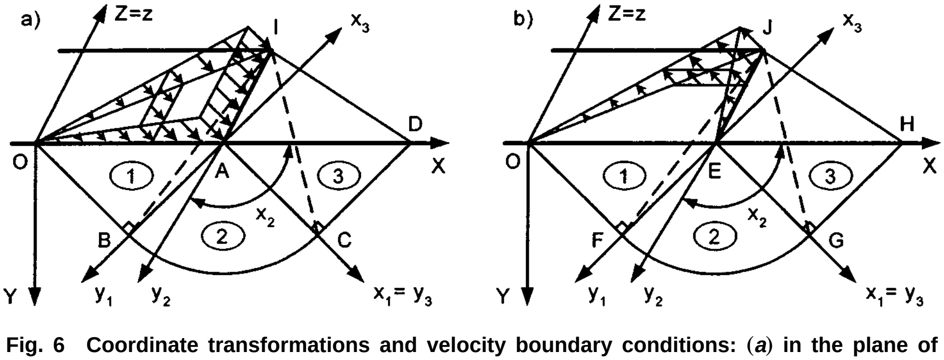

Fig. 6 Coordinate transformations and velocity boundary conditions: (*a*) in the plane of rotation; (*b*) perpendicular to the plane of rotation

Table 3 Internal plastic work for square footing under moment loading

	In plane of rotation	Normal to plane of rotation
Region 1: Table 1 (Straight)	$D_1 = 2c_u\int_0^b\int_0^{\frac{b-z}{\sqrt{2}}}\int_{-y_1}^{0}\lvert\dot{\varepsilon}\rvert_{\max}\,dx_1dy_1dz = \frac{1}{6}b^3c_u\dot{\theta}_0$	$D_1 = 2c_u\int_0^b\int_0^{\frac{b-z}{\sqrt{2}}}\int_{-y_1}^{0}\lvert\dot{\varepsilon}\rvert_{\max}\,dx_1dy_1dz = \frac{\sqrt{2}}{12}b^3c_u\dot{\theta}_0$
Region 1: Interface	$D_{OBI} = c_u\int_0^b\int_{-\frac{b-z}{\sqrt{2}}}^{0}\lvert u_1\rvert dx_1d\sqrt{\frac{3}{2}}z = \frac{1}{2\sqrt{6}}b^3c_u\dot{\theta}_0$	$D_{OFJ} = c_u\int_0^b\int_{-\frac{b-z}{\sqrt{2}}}^{0}\lvert u_1\rvert dx_1d\sqrt{\frac{3}{2}}z = \frac{1}{2\sqrt{6}}b^3c_u\dot{\theta}_0$
Region 2: Table 1 (Circular)	$D_2 = 2c_u\int_0^b\int_0^{\frac{b-z}{\sqrt{2}}}\int_{\pi/4}^{3\pi/4}\lvert\dot{\varepsilon}\rvert_{\max}\,y_2dx_2dy_2dz = \frac{\pi}{4}b^3c_u\dot{\theta}_0$	$D_2 = 2c_u\int_0^b\int_0^{\frac{b-z}{\sqrt{2}}}\int_{\pi/4}^{3\pi/4}\lvert\dot{\varepsilon}\rvert_{\max}\,y_2dx_2dy_2dz =$ $\frac{\pi}{108\sqrt{2}}\left(3+6\sqrt{2}+2\sqrt{3}\ln\frac{\sqrt{6}+2}{\sqrt{3}-1}\right)b^3c_u\dot{\theta}_0$
Region 2: Interface	$D_{BCI} = c_u\int_0^b\int_{\pi/4}^{3\pi/4}\lvert u_2\rvert\frac{b-z}{\sqrt{2}}dx_2\sqrt{\frac{3}{2}}dz = \frac{\pi}{4\sqrt{6}}b^3c_u\dot{\theta}_0$	$D_{FGJ} = c_u\int_0^b\int_{\pi/4}^{3\pi/4}\lvert u_2\rvert\frac{b-z}{\sqrt{2}}dx_2\sqrt{\frac{3}{2}}dz = \frac{\pi}{4\sqrt{6}}b^3c_u\dot{\theta}_0$
Region 3: Table 1 (Straight)	$D_3 = 2c_u\int_0^b\int_0^{\frac{b-z}{\sqrt{2}}}\int_0^{y_3}\lvert\dot{\varepsilon}\rvert_{\max}\,dx_3dy_3dz = \frac{1}{6}b^3c_u\dot{\theta}_0$	$D_3 = 2c_u\int_0^b\int_0^{\frac{b-z}{\sqrt{2}}}\int_0^{y_3}\lvert\dot{\varepsilon}\rvert_{\max}\,dx_3dy_3dz = \frac{\sqrt{2}}{12}b^3c_u\dot{\theta}_0$
Region 3: Interface	$D_{CDI} = c_u\int_0^b\int_0^{\frac{b-z}{\sqrt{2}}}\lvert u_3\rvert dx_3d\sqrt{\frac{3}{2}}z = \frac{1}{2\sqrt{6}}b^3c_u\dot{\theta}_0$	$D_{GHJ} = c_u\int_0^b\int_0^{\frac{b-z}{\sqrt{2}}}\lvert u_3\rvert dx_3d\sqrt{\frac{3}{2}}z = \frac{1}{2\sqrt{6}}b^3c_u\dot{\theta}_0$

Let us start with the field OBCDI. As is seen from Fig. 6(*a*), in a section through a plane parallel to the plane of rotation, the field is built of two triangular shear zones 1 and 3 with straight streamlines, and one fan shear zone 2 with circular streamlines. The Cartesian coordinate system is chosen with the origin at the center of the footing and axis Z perpendicular to the plane of rotation. In shear zone 1, a new coordinate system x_1y_1z with the origin at the point A is obtained from the transformation for straight streamlines in Table 1, with $\psi=\pi/4$, $X_0=b$ and $Y_0=Z_0=0$. A similar transformation, but with $\psi=-\pi/4$, yields coordinate system x_3y_3z in shear zone 3. In the fan shear zone 2, the coordinate system x_2y_2z with the origin at the point A is obtained from the transformation for circular streamlines in Table 1, with $X_0=b$ and $Y_0=Z_0=0$. The velocity fields in the three zones are all parallel to the x_j axes, with velocity magnitudes given by $u_i(y_i,z)=\sqrt{2}\dot{\theta}_0(b-\sqrt{2}y_i)$, where $\dot{\theta}_0$ is the rotational velocity of the footing. On the interfaces OBI, BCI, and CDI, the velocities simplify to $u_i(y_i,z)=\sqrt{2}\dot{\theta}_0z$. Using the expressions in Table 1, the maximum principal strain rates are $|\dot{\varepsilon}|_{\max}=\dot{\theta}_0$ in shear zones 1 and 3, and $|\dot{\varepsilon}|_{\max}=b\dot{\theta}_0/(y_2\sqrt{2})$ in shear zone 2. The expressions for the internal plastic work in each zone and the corresponding interfaces are summarized in Table 3.

The total plastic work in the field OBCDI is then obtained by summing the plastic work in each zone to give

$$D_{\mathrm{OBCDI}}=\left[\frac{1}{3}+\frac{\pi}{4}+\frac{1}{\sqrt{6}}\left(1+\frac{\pi}{4}\right)\right]b^3c_u\dot{\theta}_0. \tag{50}$$

Next, let us consider the field OFGHJ. As is seen from Fig. 6(*b*), in a section by a plane perpendicular to the plane of rotation, this field is also built of two triangular shear zones 1 and 3, and one fan shear zone 2. The Cartesian coordinate system is chosen with the origin at the center of the footing and axis Z parallel to the plane of rotation (but rotated in absolute terms relative to Fig. 6(*a*), so that the streamlines lie within the $Z=\text{const}$ planes). The coordinate transformations are identical to those for the field OBCDI, while the velocities in the three zones and the corresponding interfaces are given by $u_i(z)=\sqrt{2}\dot{\theta}_0z$.

The maximum principal strain rates are $|\dot{\varepsilon}|_{\max}=\dot{\theta}_0/\sqrt{2}$ in the triangular shear zones 1 and 3, and $|\dot{\varepsilon}|_{\max}=\dot{\theta}_0\sqrt{y_2^2+z^2}/(y_2\sqrt{2})$ in the fan shear zone 2. The expressions for the internal plastic work in each zone and the corresponding interfaces are summarized in Table 3.

The total plastic work in the field OFGHJ is calculated by summing the plastic work in each zone to give

$$D_{\mathrm{OFGHJ}}=\left[\frac{\sqrt{2}+\sqrt{6}}{6}+\frac{\pi\sqrt{2}}{216}\left(3+6\sqrt{2}+9\sqrt{3}+2\sqrt{3}\ln\frac{\sqrt{6}+2}{\sqrt{3}-1}\right)\right]\times b^3c_u\dot{\theta}_0. \tag{51}$$

Finally, Eq. (1) in our case can be written as

$$\mathbf{M}\dot{\theta}_0=4(D_{\mathrm{OBCDI}}+D_{\mathrm{OFGHJ}}) \tag{52}$$

and after substitution of (50) and (51) we obtain an upper bound for the collapse moment:

$$M=\left[\frac{4+2\sqrt{2}+4\sqrt{6}}{3}+\frac{\pi\sqrt{2}}{54}\left(3+33\sqrt{2}+18\sqrt{3}+2\sqrt{3}\ln\frac{\sqrt{6}+2}{\sqrt{3}-1}\right)\right]\times b^3c_u\approx 12.71b^3c_u. \tag{53}$$

This upper bound may be compared with a value of $M=13.41b^3c_u$ using the mechanism adopted by Paolucci and Pecker [12], some 5% above the above solution. The present solution may be improved by adjusting angles AOB and DAC, but the main advantage of adopting a similar mechanism for rotational motion as for vertical translation ([2]), is that excellent upper bound solutions may be obtained for combinations of vertical and moment loading.

7 Applications: Nonaxisymmetrical Fields

In order to demonstrate application of the proposed approach to deriving nonaxisymmetric KAVFs, let us consider the bearing capacity problem of a rigid rough circular footing of radius b on saturated clay subjected to undrained moment loading **M** (Fig. 7).

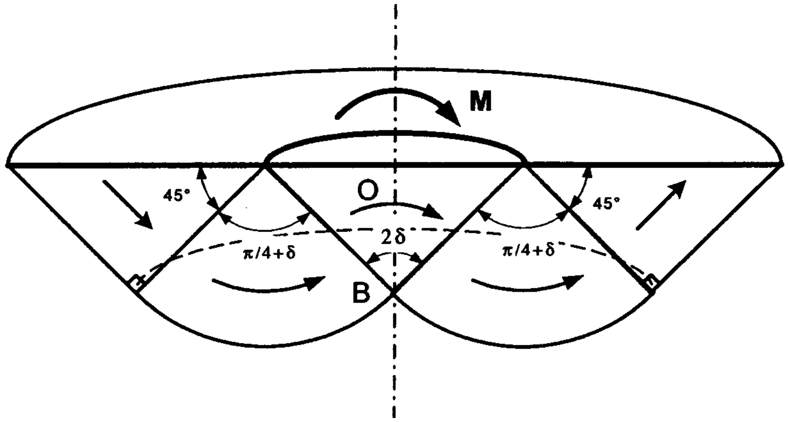

Fig. 7 Rotation of a rough circular footing

The footing rotates around an axis parallel to the ground surface and passing through point B and the kinematic mechanism under consideration (of a shape proposed in [13] for vertical loading) is shown in Fig. 7. The mechanism consists of a rigid conical block based on the footing with the tip of the cone located at point B and two shear zones. As is seen from Fig. 8, in a section trough the axis of symmetry of the footing, the field is built of a fan shear zone 1 and a triangular shear zone 2. Figure 8 also shows velocity boundary conditions for the fan shear zone 1 in the plane of rotation. In other planes, rotation of the rigid cone produces more complex velocity boundary conditions, including circumferential velocity components as will be described below.

The Cartesian coordinate system is chosen with the origin at the center of the footing and axis Z perpendicular to the plane of rotation. In the fan shear zone 1, a new coordinate system x_1y_1z with origin at point A is obtained from the transformation for circular streamlines in Table 2, with $R_0=b$ and $Y_0=0$. Velocity boundary conditions on the cone surface AB are defined by analyzing the three-dimensional velocity field from rotation of the rigid cone, giving

$$u_{x_1}=\dot{\theta}_0\cos(z)\left(\frac{b}{\sin\delta}-y_1\right);\quad u_{y_1}=0;$$

$$u_z=\dot{\theta}_0\sin(z)\cos\delta\left(\frac{b}{\sin\delta}-y_1\right) \tag{54}$$

where $\dot{\theta}_0$ is the rotational velocity of the footing; u_{x_1}, u_{y_1}, and u_z are boundary velocity components in x_1, y_1, and z-directions, respectively. The velocity field, satisfying these boundary conditions and incompressibility condition, is given by circular streamlines parallel to the x_1-curvilinear coordinate, with magnitude given by

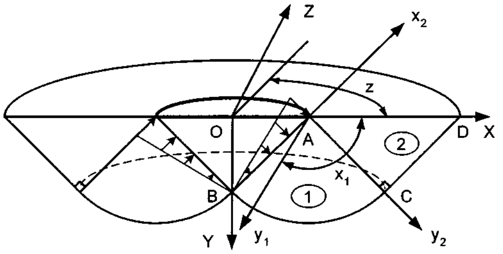

Fig. 8 Coordinate transformations and velocity boundary condition

$$u_1(x_1,y_1,z)=\dot{\theta}_0\cos(z)\left(\frac{b}{\sin\delta}-y_1\right)\frac{y_1\cos(\pi/2+\delta)+b}{y_1\cos x_1+b} \tag{55}$$

so that at $x_1=\pi/2+\delta$: $u_1(\pi/2+\delta,y_1,z)=u_{x_1}(y_1,z)$. Then, $|\dot{\varepsilon}|_{\max}$ is calculated using the expression in Table 2 (circular streamlines), with plastic work in fan shear zone 1 given by

$$D_1=2c_u\int_0^{2\pi}\int_0^{b/\sin\delta}\int_{\pi/4}^{\pi/2+\delta}|\dot{\varepsilon}|_{\max}y_1(y_1\cos x_1+b)\,dx_1dy_1dz. \tag{56}$$

Discontinuity surface AB is in fact the $x_1=\pi/2+\delta$ coordinate surface. Therefore, plastic work on this surface is calculated using Eqs. (20) and (54) to give

$$D_{\mathrm{AB}}=c_u\int_0^{2\pi}\int_0^{b/\sin\delta}|u_z|\left(y_1\cos\left(\frac{\pi}{2}+\delta\right)+b\right)dy_1dz$$

$$=\frac{4\cos\delta}{3\sin^2\delta}b^3c_u\dot{\theta}_0. \tag{57}$$

Finally, in the shear zone 2, a new coordinate system x_2y_2z with origin at point A is obtained from the transformation for straight streamlines in Table 2, with $\psi=-\pi/4$, $R_0=b$ and $Y_0=0$. The velocity field, satisfying boundary and incompressibility conditions, is parallel to the x_2-axis, with magnitude given by

$$u_2(x_2,y_2,z)=\dot{\theta}_0\cos(z)\left(\frac{b}{\sin\delta}-y_2\right)$$

$$\times\frac{y_2\cos(\pi/2+\delta)+b}{x_2\cos(\pi/4)+y_2\sin(\pi/4)+b}. \tag{58}$$

Equation (58) satisfies both the incompressibility condition and continuity of velocities $u_1(\pi/4,y_1,z)=u_2(0,y_2,z)$ at the boundary AC between the shear zones 1 and 2, defined by $x_1=\pi/4$, $x_2=0$ and $y_1=y_2$. Then, $|\dot{\varepsilon}|_{\max}$ is calculated using the expression in Table 2 (straight streamlines), with plastic work in shear zone 2 given by

$$D_2=2c_u\int_0^{2\pi}\int_0^{b/\sin\delta}\int_0^{y2}|\dot{\varepsilon}|_{\max}(x_2\cos(\pi/4)+y_2\sin(\pi/4)+b)$$

$$\times dx_2dy_2dz. \tag{59}$$

Finally, Eq. (1) in our case can be written as

$$\mathbf{M}\dot{\theta}_0=D_1+D_{\mathrm{AB}}+D_2 \tag{60}$$

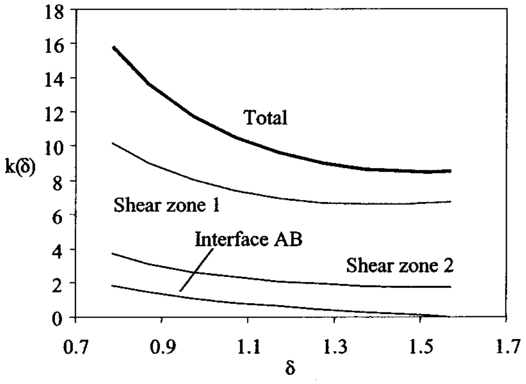

Fig. 9 Bearing capacity coefficient

and after numerical integration of Eqs. (56) and (59) and their substitution together with (57) into Eq. (60), we obtain an upper bound for the collapse moment:

$$\mathbf{M} = k(\delta) b^3 c_u \tag{61}$$

where $k(\delta)$ is a coefficient given in Fig. 9 for a range of $\delta \in [\pi/4; \pi/2]$. The minimum value of $k(\delta)$ is 8.47, and occurs for $\delta = 1.517$. This value is approximately twice as high as can be obtained with a spherical scoop mechanism, which yields $\mathbf{M} = 4.21 b^3 c_u$. However, the mechanism considered here, since it is similar to the optimal mechanism under purely vertical load, yields the sharpest upper bound for combinations of moment and high vertical load, making use of the superposition technique of [6].

8 Concluding Remarks

The proposed method of derivation of kinematically admissible velocity fields (KAVFs) using coordinate transformations provides significant flexibility for three-dimensional upper bound limit analysis in a Tresca material. The main feature of this method is that it allows the incompressibility condition to be satisfied simply by imposing certain requirements on the analytical form of velocity magnitudes. This allows for new classes of velocity fields to be derived solely using standard procedures. These new classes of fields include: KAVFs with new streamline shapes; new plane but non-plane-strain KAVFs; new radial but nonaxisymmetric KAVFs. An additional advantage of the method is that it allows for expressions of local plastic work in any field to be derived in closed form. When these expressions can be integrated analytically, we obtain analytical solutions for upper bounds of collapse loads, but even numerical integration of these expressions does not constitute a problem of significant complexity and can be easily performed. The proposed method makes an attempt to expand applicability of three-dimensional upper bound limit analysis by introducing more realistic shapes of KAVFs, while maintaining simplicity and the clear engineering meaning of this approach.

Acknowledgments

The research was supported by an IREX grant from the Australian Research Council and by the Technion Foundation of the Vice President for Research. Their support is gratefully acknowledged.

References

[1] Murff, J. D., and Hamilton, J., 1993, "P-Ultimate for Undrained Analysis of Laterally Loaded Piles," J. Geotech. Eng., **119**, pp. 91–107.

[2] Shield, R. T., and Drucker, D. C., 1953, "The Application of Limit Analysis to Punch Indentation Problems," ASME J. Appl. Mech., **20**, pp. 453–460.

[3] Levin, A., 1955, "Indentation Pressure of a Smooth Circular Punch," Quart. Appl. Math., , **13**, pp. 381–389.

[4] Bransby, M. F., and Randolph, M. F., 1998, "Combined Loading on Skirted Foundations," Geotechnique, **48**, pp. 637–655.

[5] Puzrin, A. M., 2001, "On the Superposition of Work Dissipation in Coulomb's Soil," Int. J. Solids Struct., in press.

[6] Puzrin, A. M., and Randolph, M. F., 2001, "On the Superposition of Plastically Dissipated Work in Upper Bound Limit Analysis," Proc. R. Soc. London, Ser. A, **457**, pp. 567–586.

[7] Drucker, D. C., Greenberg, H. J., and Prager, W., 1951, "The Safety Factor of an Elastic-Plastic Body in Plane Strain," ASME J. Appl. Mech., **73**, pp. 371–378.

[8] Boresi, A. P., and Chong, K. P., 2000, *Elasticity in Engineering Mechanics*, John Wiley and Sons, New York.

[9] Abramovitz, M., and Stegun, I. A., eds., 1973, *Handbook of Mathematical Functions*, Dover, New York.

[10] Randolph, M. F., and Houlsby, G. T., 1984, "The Limiting Pressure on a Circular Pile Loaded Laterally in Cohesive Soil," Geotechnique, **34**, pp. 613–623.

[11] Randolph, M. F., Martin, C. M., and Hu, Y., 2000, "Limiting Resistance of a Spherical Penetrometer in Cohesive Material," Geotechnique, **50**, pp. 573–582.

[12] Paolucci, R., and Pecker, A., 1997, "Soil Inertia Effects on the Bearing Capacity of Rectangular Foundations on Cohesive Soils," Eng. Struct., **19**(8), pp. 637–643.

[13] Kusakabe, O., Suzuki, H., and Nakase, A., 1986, "An Upper-Bound Calculation on Bearing Capacity of a Circular Footing on a Non-homogeneous Clay," Soils Found., **26**, pp. 143–148.

Three-Dimensional Green's Functions in an Anisotropic Half-Space With General Boundary Conditions

E. Pan[1]
Structures Technology, Inc.
543 Keisler Drive,
Cary, NC 27511
Mem. ASME

This paper derives, for the first time, the complete set of three-dimensional Green's functions (displacements, stresses, and derivatives of displacements and stresses with respect to the source point), or the generalized Mindlin solutions, in an anisotropic half-space $(z>0)$ *with general boundary conditions on the flat surface* $z=0$*. Applying the Mindlin's superposition method, the half-space Green's function is obtained as a sum of the generalized Kelvin solution (Green's function in an anisotropic infinite space) and a Mindlin's complementary solution. While the generalized Kelvin solution is in an explicit form, the Mindlin's complementary part is expressed in terms of a simple line-integral over* $[0,\pi]$*. By introducing a new matrix* **K**, *which is a suitable combination of the eigenmatrices* **A** *and* **B**, *Green's functions corresponding to different boundary conditions are concisely expressed in a unified form, including the existing traction-free and rigid boundaries as special cases. The corresponding generalized Boussinesq solutions are investigated in details. In particular, it is proved that under the general boundary conditions studied in this paper, the generalized Boussinesq solution is still well-defined. A physical explanation for this solution is also offered in terms of the equivalent concept of the Green's functions due to a point force and an infinitesimal dislocation loop. Finally, a new numerical example for the Green's functions in an orthotropic half-space with different boundary conditions is presented to illustrate the effect of different boundary conditions, as well as material anisotropy, on the half-space Green's functions.* [DOI: 10.1115/1.1532570]

Introduction

Green's functions (due to a concentrated source) are of great interests in both theoretical and applied mechanics ([1–3]). With increasing popularity of the integral equation method among different engineering fields, research on various Green's functions is increasing. The half-space Green's function alone has been applied in materials science ([4–6]), rock engineering ([7,8]), inverse problem [6], and contact mechanics ([9–12]). However, because of complexity, most three-dimensional half-space Green's functions are for the traction-free boundary condition only, including the isotropic half-space solution by Mindlin [13], transversely isotropic half-space solution by Pan and Chou [14], and anisotropic half-space solution by Willis [9], Barnett and Lothe [4], Barber and Sturla [15], Ting [2], Wu [16], and Pan and Yuan [17]. While the half-space Green's functions with a rigid surface can also be reduced from the corresponding bimaterial Green's functions, no Green's function solution exists in an anisotropic half-space with any mixed surface boundary conditions, with the exception of the transversely isotropic half-space Green's solution by Yu et al. [18] for the slippery boundary condition, which includes the isotropic solution of Dundurs and Hetenyi [19] as a special case.

While the traction-free and rigid boundary conditions on the surface of a half-space are perhaps the most common ones in engineering applications, the mixed boundary conditions, in particular the slippery condition, have been also used in various practical problems ([20,21]). For example, in rock and foundation engineering, the slippery boundary condition has been used to model a large-size soil deposit underlain by a hard bedrock base ([22]). In plate theory, the roller or simple supported condition resembles the slippery surface condition ([23]). The slippery condition has been also used to describe the connection between an ideal fluid and a solid in material science ([24]), and to model the bone implants in biomechanics ([25]).

Besides its applications in conventional engineering, Green's function method now becomes an essential tool in the numerical studies of strained semiconductor quantum devices where the strain-induced quantum dot growth in semiconductor nanostructures is crucial to the electronic performance ([26–28]). While under two-dimensional deformation, the strain-induced elastic and electric fields can be easily analyzed by the analytical solution of Ru ([29,30]), for those in the three-dimensional space, the Green's functions, as embedded in the Eshelby tensor ([5,31]), are required in the corresponding studies.

In Green's function solutions involving material anisotropy, the Stroh formalism has been shown to be mathematically elegant and technically powerful ([2,32,33]). Under two-dimensional deformation, Ting and co-workers ([2,34,35]) first derived the Green's functions in anisotropic half-plane with general boundary conditions. Two new eigenmatrices were introduced to replace the original eigenmatrices **A** and **B**, and the solution of the general boundary value problems was expressed in terms of a new single Stroh formalism ([2,34]). The general boundary conditions considered by Ting and co-workers ([2,34,35]) include, as special cases, the traction-free, rigid, and slippery boundary conditions, and their solution covers at least eight different sets of boundary conditions (to be defined later). While the two-dimensional deformation in terms of the Stroh formalism is relatively easy, the

---

[1] Currently at the Department of Civil Engineering, University of Akron, Akron, OH 44325-3905. e-mail: pan2@uakron.edu

Contributed by the Applied Mechanics Division of THE AMERICAN SOCIETY OF MECHANICAL ENGINEERS for publication in the ASME JOURNAL OF APPLIED MECHANICS. Manuscript received by the ASME Applied Mechanics Division, Feb. 19, 2001; final revision, Mar. 5, 2002. Associate Editor: D. A. Kouris. Discussion on the paper should be addressed to the Editor, Prof. Robert M. McMeeking, Department of Mechanical and Environmental Engineering, University of California–Santa Barbara, Santa Barbara, CA 93106-5070, and will be accepted until four months after final publication of the paper itself in the ASME JOURNAL OF APPLIED MECHANICS.

corresponding three-dimensional deformation is much more complicated. Although in recent years, the Stroh formalism was extended to certain three-dimensional Green's function solutions ([2,16,17]) no literature exists on generalizing the Stroh formalism to the three-dimensional problem with general boundary conditions.

In this paper, the author shows that, similar to the two-dimensional case, the Green's function in an anisotropic half-space with general boundary conditions can also be derived in terms of the extended Stroh formalism. The present study follows a recent development on three-dimensional Green's function solution in anisotropic bimaterials with perfectly bonded interface ([17]). It is found that, similar to the three-dimensional bimaterial case, the three-dimensional half-space Green's function with general boundary conditions can also be expressed as a sum of the generalized Kelvin Green's functions (the infinite-space Green's functions) and a Mindlin's complimentary part. While the former has an explicit expression ([36–39]), the latter can be expressed in terms of a simple line integral over $[0,\pi]$. Furthermore, a new matrix, named **K**, which is a suitable combination of the eigenmatrices **A** and **B**, is introduced so that the Green's functions corresponding to different boundary conditions can be concisely expressed in a unified form, including the existing traction-free and rigid boundaries as special cases. Also studied for the first time are the limit cases of the Green's functions when the source and/or field points are on the surface of the half-space with general boundary conditions. It is proved that even for these special cases, the corresponding Green's function solutions, the generalized Boussinesq solutions in particular, are still well defined. To enhance our understanding, a physical explanation for these solutions are also offered in terms of the equivalent concept of the Green's functions due to a point force and an infinitesimal dislocation loop. Finally, a new numerical example for the Green's functions in an orthotropic half-space with different boundary conditions is presented to illustrate the effect of different boundary conditions, as well as material anisotropy, on the half-space Green's functions.

In the following discussion, the three-dimensional Green's functions due to an interior point force in an anisotropic half-space with general boundary conditions will be also called the generalized Mindlin solutions. When the source point is located on the surface of the half-space, the corresponding Green's functions will be then called generalized Boussinesq solutions (i.e., the generalized surface Green's functions, see e.g., [4,15]. Also, by Green's functions, we mean the Green's displacements, stresses, and derivatives of displacements and stresses with respect to the source point.

Problem Description

Consider an anisotropic half-space occupying domain $x_3>0$ bounded by the $x_3=0$ plane. Let a point force $\mathbf{f}=(f_1,f_2,f_3)$ be applied in the half-space at source point $\mathbf{d}\equiv(d_1,d_2,d_3\equiv d)$ with $d_3>0$ and the field point be denoted by $\mathbf{x}\equiv(x_1,x_2,x_3\equiv z)$.[2] As usual, the problem domain is artificially divided into two regions: $z>d$ and $0\leqslant z<d$.

In the two regions of the half-space, the equations of equilibrium in terms of displacements u_k in the absence of body forces are written as

$$C_{ijkl}u_{k,lj}=0 \tag{1}$$

where C_{ijkl} is the elastic stiffness tensor of the half-space.

In this paper, the following eight different sets of boundary conditions on the surface $z=0$ ([2,34]) will be discussed. In other words, the half-space Green's functions are required to satisfy one of the eight sets of boundary conditions:

$$u_1=0;\; u_2=0;\; u_3=0 \tag{2a}$$

$$t_1=0;\; u_2=0;\; u_3=0 \tag{2b}$$

$$u_1=0;\; t_2=0;\; u_3=0 \tag{2c}$$

$$u_1=0;\; u_2=0;\; t_3=0 \tag{2d}$$

$$t_1=0;\; t_2=0;\; t_3=0 \tag{2e}$$

$$u_1=0;\; t_2=0;\; t_3=0 \tag{2f}$$

$$t_1=0;\; u_2=0;\; t_3=0 \tag{2g}$$

$$t_1=0;\; t_2=0;\; u_3=0 \tag{2h}$$

where the vector $\mathbf{t}(t_1,t_2,t_3)$ is the traction on the $z=$constant plane defined as

$$\mathbf{t}=(\sigma_{13},\sigma_{23},\sigma_{33}). \tag{3}$$

Similar to the corresponding two-dimensional analysis ([2,34]), we unify Equations (2*a–h*) by the following simple vector equation:

$$\mathbf{I}_u\mathbf{u}+\mathbf{I}_t\mathbf{t}=\mathbf{0} \tag{4}$$

where $\mathbf{I}_u$ and $\mathbf{I}_t$ are 3×3 diagonal matrices whose elements are either one or zero, and satisfy conditions

$$\mathbf{I}_u+\mathbf{I}_t=\mathbf{I};\quad \mathbf{I}_u\mathbf{I}_t=\mathbf{0} \tag{5}$$

with **I** being the unit matrix.

It is seen that Equations (2*a*) and (2*e*) corresponds to the rigid and traction-free boundary conditions, respectively, with $(\mathbf{I}_u,\mathbf{I}_t)=(\mathbf{I},\mathbf{0})$ and $(\mathbf{I}_u,\mathbf{I}_t)=(\mathbf{0},\mathbf{I})$. On the other hand, the slippery surface condition is represented by Equation (2*h*) and $\mathbf{I}_u=\mathrm{diag}[0,0,1]$ and $\mathbf{I}_t=\mathrm{diag}[1,1,0]$. We remark that instead of the displacement and stress function vectors $(\mathbf{u},\boldsymbol{\phi})$ adopted in the two-dimensional analysis ([2,34]), the displacement and traction vectors $(\mathbf{u},\mathbf{t})$ are used in this paper.

At the source level $z=d$ where the point force is applied, the displacement and traction vectors are required to satisfy the following conditions:

$$\mathbf{u}|_{z=d^-}=\mathbf{u}|_{z=d^+}$$
$$\mathbf{t}|_{z=d^-}-\mathbf{t}|_{z=d^+}=\delta(x_1-d_1)\,\delta(x_2-d_2)\mathbf{f} \tag{6}$$

along with the radiation condition so that the solution in the half-space vanishes as $|\mathbf{x}|$ approaches infinity.

Stroh Formalism in the Transformed Domain

To solve the problem described in the previous section, the two-dimensional Fourier transform (i.e., for the displacement)

$$\tilde{u}_k(y_1,y_2,z;\mathbf{d})=\int\int u_k(x_1,x_2,z;\mathbf{d})e^{iy_\alpha x_\alpha}dx_1dx_2 \tag{7}$$

is applied to Eq. (1). In Eq. (7), α takes the summation from 1 to 2.

A general solution to the Fourier transformed equation of (1) can be expressed as ([2,17])

$$\tilde{\mathbf{u}}(y_1,y_z,z;\mathbf{d}=\mathbf{a}e^{-ip\eta z} \tag{8}$$

with p and **a** satisfying the eigenrelation

$$[\mathbf{Q}+p(\mathbf{R}+\mathbf{R}^T)+p^2\mathbf{T}]\mathbf{a}=0. \tag{9}$$

The superscript T denotes matrix transpose, and

$$Q_{ik}=C_{ijks}n_jn_s,\;\; R_{ik}=C_{ijks}n_jm_s,\;\; T_{ik}=C_{ijks}m_jm_s \tag{10}$$

with

$$(n_1,n_2,n_3)\equiv(\cos\theta,\sin\theta,0) \tag{11}$$

$$(m_1,m_2,m_3)\equiv(0,0,1).$$

---

[2] Thereafter, the scalar variables z and d will be used exclusively for the third field coordinate x_3 and the third source coordinate d_3, respectively.

Note that a polar coordinate transform, defined below, has been used:

$$\begin{aligned} y_1 &= \eta \cos\theta \\ y_2 &= \eta \sin\theta. \end{aligned} \tag{12}$$

It is observed that Eq. (9) is the Stroh eigenrelation for the oblique plane spanned by **n** and **m** defined in Eq. (11). It has been also shown (see i.e., [2]) that its eigenvalues are either complex or purely imaginary due to the positive requirement on the strain energy density.

Using the Stroh eigenvalues and the corresponding eigenvectors, the traction vector **t** on the z=constant plane and the in-plane stress vector **s**, namely

$$\mathbf{t} = (C_{13kl}u_{k,l}, C_{23kl}u_{k,l}, C_{33kl}u_{k,l}) \tag{13}$$

$$\begin{aligned} \mathbf{s} &\equiv (\sigma_{11}, \sigma_{12}, \sigma_{22}) \\ &= (C_{11kl}u_{k,l}, C_{12kl}u_{k,l}, C_{22kl}u_{k,l}) \end{aligned} \tag{14}$$

can be expressed in the Fourier-transformed domain as ([17])

$$\tilde{\mathbf{t}} = -i\eta \mathbf{b} e^{-ip\eta\zeta} \tag{15}$$

$$\tilde{\mathbf{s}} = -i\eta \mathbf{c} e^{-ip\eta\zeta} \tag{16}$$

with

$$\begin{aligned} \mathbf{b} &= (\mathbf{R}^T + p\mathbf{T})\mathbf{a} = -\frac{1}{p}(\mathbf{Q} + p\mathbf{R})\mathbf{a} \\ \mathbf{c} &= \mathbf{D}\mathbf{a}. \end{aligned} \tag{17}$$

The matrix **D** is defined by

$$\mathbf{D} = \begin{bmatrix} C_{111\alpha}n_\alpha + pC_{1113} & C_{112\alpha}n_\alpha + pC_{1123} & C_{113\alpha}n_\alpha + pC_{1133} \\ C_{121\alpha}n_\alpha + pC_{1213} & C_{122\alpha}n_\alpha + pC_{1223} & C_{123\alpha}n_\alpha + pC_{1233} \\ C_{221\alpha}n_\alpha + pC_{2213} & C_{222\alpha}n_\alpha + pC_{2223} & C_{223\alpha}n_\alpha + pC_{2233} \end{bmatrix}. \tag{18}$$

If p_j, $\mathbf{a}_j$, and $\mathbf{b_j}$ $(j = 1,2,\ldots 6)$ are the eigenvalues and the associated eigenvectors, we let

$$\begin{gathered} \mathrm{Im}p_j > 0, \;\; p_{j+3} = \overline{p_j}, \;\; \mathbf{a}_{j+3} = \overline{\mathbf{a}_j}, \;\; \mathbf{b}_{j+3} = \overline{\mathbf{b}_j}, \;\; \mathbf{c}_{j+3} = \overline{\mathbf{c}_j} \\ (j = 1,2,3) \\ \mathbf{A} = [\mathbf{a}_1, \mathbf{a}_2, \mathbf{a}_3], \;\; \mathbf{B} = [\mathbf{b}_1, \mathbf{b}_2, \mathbf{b}_3], \;\; \mathbf{C} = [\mathbf{c}_1, \mathbf{c}_2, \mathbf{c}_3] \end{gathered} \tag{19}$$

where Im stands for the imaginary part and the overbar denotes the complex conjugate. It is further assumed that p_j are distinct and the eigenvectors $\mathbf{a}_j$, and $\mathbf{b}_j$ satisfy the following normalization relation:

$$\mathbf{b}_i^T\mathbf{a}_j + \mathbf{a}_i^T\mathbf{b}_j = \delta_{ij} \tag{20}$$

with δ_{ij} being the Kronecker delta.

It is worthwhile mentioning that should repeated eigenvalues occur, i.e., for transversely isotropic or isotropic materials, a slight perturbation on the material stiffness tensor would make them distinct with negligible error ([40]). Therefore, the unified and simple solution presented in this paper can be applied to materials with any material symmetry.

Half-Space Green's Functions in the Fourier Transformed Domain

For the anisotropic half-space, the general boundary conditions (4) on the surface $z = 0$ and the condition (6) at the source level $z = d$, become, in the Fourier transformed domain, as

$$\mathbf{I}_u\tilde{\mathbf{u}} + \mathbf{I}_t\tilde{\mathbf{t}} = \mathbf{0} \tag{21}$$

and

$$\begin{aligned} \tilde{\mathbf{u}}|_{z=d^-} &= \tilde{\mathbf{u}}|_{z=d^+} \\ \tilde{\mathbf{t}}|_{z=d^-} - \tilde{\mathbf{t}}|_{z=d^+} &= \mathbf{f}e^{iy_\alpha d_\alpha}. \end{aligned} \tag{22}$$

Using these conditions as well as the requirement that the solution should vanish as $|\mathbf{x}|$ approaches infinity, the half-space Green's function in the Fourier transformed domain can be derived as ([2,17]) follows:

For $0 \leqslant z < d$:

$$\begin{aligned} \tilde{\mathbf{u}}(y_1, y_2, z; \mathbf{d}) &= i\eta^{-1}\mathbf{A}\langle e^{-ip_*\eta(z-d)}\rangle\mathbf{q}^\infty - i\eta^{-1}\overline{\mathbf{A}}\langle e^{-i\overline{p}_*\eta z}\rangle\mathbf{q} \\ \tilde{\mathbf{t}}(y_1, y_2, z; \mathbf{d}) &= \mathbf{B}\langle e^{-ip_*\eta(z-d)}\rangle\mathbf{q}^\infty - \overline{\mathbf{B}}\langle e^{-\overline{p}_*\eta z}\rangle\mathbf{q} \\ \tilde{\mathbf{s}}(y_1, y_2, z; \mathbf{d}) &= \mathbf{C}\langle e^{-ip_*\eta(z-d)}\rangle\mathbf{q}^\infty - \overline{\mathbf{C}}\langle e^{-i\overline{p}_*\eta z}\rangle\mathbf{q}. \end{aligned} \tag{23}$$

For $z > d$:

$$\begin{aligned} \tilde{\mathbf{u}}(y_1, y_2, z; \mathbf{d}) &= -i\eta^{-1}\overline{\mathbf{A}}\langle e^{-ip_*\eta(z-d)}\rangle\overline{\mathbf{q}}^\infty - i\eta^{-1}\overline{\mathbf{A}}\langle e^{-i\overline{p}_*\eta z}\rangle\mathbf{q} \\ \tilde{\mathbf{t}}(y_1, y_2, z; \mathbf{d}) &= -\overline{\mathbf{B}}\langle e^{-ip_*\eta(z-d)}\rangle\overline{\mathbf{q}}^\infty - \overline{\mathbf{B}}\langle e^{-i\overline{p}_*\eta z}\rangle\mathbf{q} \\ \tilde{\mathbf{s}}(y_1, y_2, z; \mathbf{d}) &= -\overline{\mathbf{C}}\langle e^{-ip_*\eta(z-d)}\rangle\overline{\mathbf{q}}^\infty - \overline{\mathbf{C}}\langle e^{-i\overline{p}_*\eta z}\rangle\mathbf{q}. \end{aligned} \tag{24}$$

where

$$\mathbf{q}^\infty = \mathbf{A}^T\mathbf{f}e^{iy_\alpha d_\alpha} \tag{25}$$

and

$$\langle e^{-ip*\eta z}\rangle = diag[e^{-ip_1\eta z}, e^{-ip_2\eta z}, e^{-ip_3\eta z}]. \tag{26}$$

The complex vector **q** in Eqs. (23) and (24) is to be determined.

Motivated by the unified and elegant expression for the Green's function in an anisotropic half-plane with general boundary conditions ([2]), we have found that if we introduce a new matrix **K** defined as

$$\mathbf{K} = \mathbf{I}_u\mathbf{A} + \mathbf{I}_t\mathbf{B} \tag{27}$$

then the complex vector **q** for the eight different sets of boundary conditions (2*a*–*h*) can be expressed, in a single vector equation, as

$$\mathbf{q} = \overline{\mathbf{K}}^{-1}\mathbf{K}\langle e^{ip_*\eta d}\rangle\mathbf{A}^T\mathbf{f}e^{iy_\alpha d_\alpha}. \tag{28}$$

It is also observed that the new matrix **K**, like **A** and **B**, is independent of the radial variable η, an important feature to be used later. Equation (28) is a very surprising result and will be the key factor when deriving the physical-domain Green's functions.

Substituting Eq. (28) into Eqs. (23) and (24) gives the half-space Green's displacements and stresses in the Fourier transformed domain, which possess the following important features:

1. As discussed by Pan and Yuan [17], the first terms in Eqs. (23) and (24) are the Fourier transformed-domain Green's functions for a homogeneous and anisotropic full space. Inverse of these Green's functions, i.e., the physical-domain solution, has been obtained by Tewary [36], Ting and Lee [37], Sales and Gray [38], and Tonon et al. [39] in an explicit form. Therefore, the inverse Fourier transform needs to be carried out only for the second terms of the solution, which resemble the complementary part of the Mindlin solution ([13]).
2. These unified Fourier transformed-domain solutions (Eqs. (23) and (24)) include the eight different sets of the boundary conditions (2*a*–*h*). Thus, to solve for the Green's function in an anisotropic half-space with different boundary conditions, one only needs to assign the matrix **K** defined by Eq. (28) with the corresponding boundary conditions, a remarkably simple result parallel to its two-dimensional counterpart ([2]).
3. In deriving the Fourier transformed-domain solution, the matrix **K** has been assumed to be nonsingular. This can be proved following a procedure similar to the corresponding two-dimensional analysis ([2]).

Generalized Mindlin Solution

Having obtained the Green's functions in the Fourier transformed domain, we now apply the inverse Fourier transform to Eqs. (23) and (24). To handle the double infinite integrals, the polar coordinate transform (12) is introduced so that the infinite integral with respect to the radial variable η can be carried out exactly. Thus, the final half-space Green's function in the physical domain, i.e., the generalized Mindlin solution, can be expressed as a sum of a Kelvin's part in an explicit form and a Mindlin's complementary part in terms of a line integral over $[0,2\pi]$. The integral for the latter can actually be further reduced to an integral over $[0,\pi]$. In what follows, we will use only the displacement solution to illustrate the derivation and list the final results for other Green's functions. Assumption will be also made that the source point **d** is interior to the half-space. The limit case, namely, the corresponding Boussinesq solution (when the source point **d** is on the surface) will be discussed later.

Applying the inverse Fourier transform, the Green's displacement in Eq. (24) becomes

$$\begin{aligned}\mathbf{u}(x_1,x_2,z;\mathbf{d})=&-\frac{i}{4\pi^2}\int\int\{\eta^{-1}\overline{\mathbf{A}}\langle e^{-i\bar{p}_*\eta(z-d)}\rangle\\&\times\overline{\mathbf{q}}^{\infty}e^{-i(x_\alpha-d_\alpha)y_\alpha}\}dy_1dy_2\\&-\frac{i}{4\pi^2}\int\int\{\eta^{-1}\overline{\mathbf{A}}\langle e^{-i\bar{p}_*\eta z}\rangle\\&\times\mathbf{q}e^{-i(x_\alpha-d_\alpha)y_\alpha}\}dy_1dy_2.\end{aligned}\tag{29}$$

The first integral in Eq. (29) corresponds to the full-space Green's displacement that is already available in an explicit form ([36–39]). Consequently, the inverse transform needs to be carried out only for the second integral, or the complementary part. Denoting the full-space Green's function tensor by $\mathbf{U}^{\infty}(\mathbf{x};\mathbf{d})$ with its row and column indices corresponding to the displacement component and point-force direction, respectively, and introducing the polar coordinate transform (12), the half-space Green's displacement tensor can be rewritten as

$$\begin{aligned}\mathbf{U}(\mathbf{x};\mathbf{d})=\mathbf{U}^{\infty}(\mathbf{x};\mathbf{d})-&\frac{i}{4\pi^2}\int_0^{2\pi}d\theta\int_0^{\infty}\overline{\mathbf{A}}\langle e^{-i\bar{p}_*\eta z}\rangle\\&\times\overline{\mathbf{K}}^{-1}\mathbf{K}\langle e^{ip_*\eta d}\rangle e^{-i\eta[(x_1-d_1)\cos\theta+(x_2-d_2)\sin\theta]}\mathbf{A}^{T}d\eta.\end{aligned}\tag{30}$$

Since the matrices **A** (also **B** and **C**) and $\overline{\mathbf{K}}^{-1}\mathbf{K}$ are independent of the radial variable η, integral with respect to η can therefore be performed analytically, resulting in the following compact form:

$$\mathbf{U}(\mathbf{x};\mathbf{d})=\mathbf{U}^{\infty}(\mathbf{x};\mathbf{d})+\frac{1}{2\pi^2}\int_0^{\pi}\overline{\mathbf{A}}\mathbf{G}_1\mathbf{A}^{\mathbf{T}}d\theta\tag{31}$$

where[3]

$$(\mathbf{G}_1)_{ij}=\frac{(\overline{\mathbf{K}}^{-1}\mathbf{K})_{ij}}{-\bar{p}_iz+p_jd-[(x_1-d_1)\cos\theta+(x_2-d_2)\sin\theta]}.\tag{32}$$

It is noticed that the integral interval in Eq. (31) has been reduced from $[0,2\pi]$ to $[0,\pi]$ based upon certain properties of the integrand as a function of θ ([41]), plus a new relation for the matrix $\overline{\mathbf{K}}^{-1}\mathbf{K}$, i.e., $\overline{\mathbf{K}}^{-1}\mathbf{K}(\theta+\pi)=-\mathbf{K}^{-1}\overline{\mathbf{K}}(\theta)$. Similar properties have also been used to derive the Green's stresses, derivatives of Green's displacements and stresses.

Following a similar procedure, the half-space Green's stress tensors can be derived and the results are listed as

$$\mathbf{T}(\mathbf{x};\mathbf{d})=\mathbf{T}^{\infty}(\mathbf{x};\mathbf{d})+\frac{1}{2\pi^2}\int_0^{\pi}\overline{\mathbf{B}}\mathbf{G}_2\mathbf{A}^{T}d\theta\tag{33a}$$

$$\mathbf{S}(\mathbf{x};\mathbf{d})=\mathbf{S}^{\infty}(\mathbf{x};\mathbf{d})+\frac{1}{2\pi^2}\int_0^{\pi}\overline{\mathbf{C}}\mathbf{G}_2\mathbf{A}^{T}d\theta.\tag{33b}$$

In Eqs. (33*a*) and (33*b*), $\mathbf{T}^{\infty}(\mathbf{x};\mathbf{d})$ and $\mathbf{S}^{\infty}(\mathbf{x};\mathbf{d})$ are the full-space Green's stress tensors ([39]), and

$$(\mathbf{G}_2)_{ij}=\frac{(\overline{\mathbf{K}}^{-1}\mathbf{K})_{ij}}{\{-\bar{p}_iz+p_jd-[(x_1-d_1)\cos\theta+(x_2-d_2)\sin\theta]\}^2}.\tag{34}$$

Derivatives of the Green's displacements and stresses (tensors) with respect to the source point (d_1,d_2,d_3) are found to be

$$\frac{\partial\mathbf{U}(\mathbf{x};\mathbf{d})}{\partial d_j}=\frac{\partial\mathbf{U}^{\infty}(\mathbf{x};\mathbf{d})}{\partial d_j}-\frac{1}{2\pi^2}\int_0^{\pi}\overline{\mathbf{A}}\mathbf{G}_2\langle g_j\rangle\mathbf{A}^{T}d\theta\tag{35}$$

$$\begin{aligned}\langle g_1\rangle&=diag[\cos\theta,\cos\theta,\cos\theta]\\\langle g_2\rangle&=diag[\sin\theta,\sin\theta,\sin\theta]\\\langle g_3\rangle&=diag[p_1,p_2,p_3]\end{aligned}\tag{36}$$

$$\frac{\partial\mathbf{T}(\mathbf{x};\mathbf{d})}{\partial d_j}=\frac{\partial\mathbf{T}^{\infty}(\mathbf{x};\mathbf{d})}{\partial d_j}-\frac{1}{2\pi^2}\int_0^{\pi}\overline{\mathbf{B}}\mathbf{G}_3\langle g_j\rangle\mathbf{A}^{T}d\theta\tag{37a}$$

$$\frac{\partial\mathbf{S}(\mathbf{x};\mathbf{d})}{\partial d_j}=\frac{\partial\mathbf{S}^{\infty}(\mathbf{x};\mathbf{d})}{\partial d_j}-\frac{1}{2\pi^2}\int_0^{\pi}\overline{\mathbf{C}}\mathbf{G}_3\langle g_j\rangle\mathbf{A}^{T}d\theta\tag{37b}$$

$$(\mathbf{G}_3)_{ij}=\frac{(\overline{\mathbf{K}}^{-1}\mathbf{K})_{ij}}{\{-\bar{p}_iz+p_jd-[(x_1-d_1)\cos\theta+(x_2-d_2)\sin\theta]\}^3}.\tag{38}$$

Equations (31), (33), (35), and (37) are the *complete* Green's functions in an anisotropic half-space with general boundary conditions, or the generalized Mindlin solutions. It is emphasized that these Green's functions are presented in a unified and very simple form so that the eight different sets of the boundary conditions (2*a–h*) are all included. To find the Green's functions for a given set of boundary conditions, one only needs to assign the corresponding **K** matrix. For example, for **K**=**B**, the present half-space Green's displacements and stresses will then reduce to the existing solution ([2,4,16,17]) for the traction-free boundary condition case. Since the present solution includes all the eight different sets of the boundary conditions, it is therefore particularly convenient when investigating the effect of different boundary conditions on the problem solution based on the Green's function method.

Considering the complexity of the problem and yet the simplicity of the final physical-domain Green's function expressions for all the eight sets of the boundary conditions, it is seen that, by resorting to the Mindlin's superposition approach, the extended (three-dimensional) Stroh formalism is indeed a very powerful and elegant method. A direct application of the Fourier transform method, without employing the Stroh formalism, would require three-dimensional Fourier inverse integrals for the infinite Green's function, and four-dimensional Fourier inverse integrals for the complementary part ([42]).

Besides their concise expressions, the present half-space Green's functions (generalized Mindlin solutions) also possess the following important features:

1. Similar to the bimaterial Green's functions with perfectly bonded interface ([17]), the half-space Green's displacements, stresses and derivatives of displacements, and derivatives of stresses are inversely proportional to, respectively, a linear, quadratic, and cubic combination of the field and source coordinates. This feature resembles the behavior of the full-space Green's displacements ($\propto 1/r$), stresses and derivatives of displacements ($\propto 1/r^2$), and derivatives of stresses ($\propto 1/r^3$), with r being the distance between the source and field points.
2. Different to either the bimaterial Green's functions with perfectly bonded interface or the half-space Green's functions with traction-free boundary conditions (2*e*) where the source point **d**

---

[3] Thereafter, the indices i and j take the range from 1 to 3.

can directly approach the interface or the surface for all the three point-force directions, the half-space Green's functions with other seven sets of boundary conditions need special attention when approaching the surface, a very interesting feature to be discussed in the next section.

3. Since the source point is not on the surface of the half-space (i.e., $d \neq 0$), the integrals in Eqs. (31), (33), (35), and (37) for performing the complementary part of the half-space Green's functions are regular and thus can be easily carried out by a standard numerical integral method such as the Gauss quadrature.

Generalized Boussinesq Solution

In the previous section, we derived the generalized Mindlin solution in an anisotropic half-space with general boundary conditions (2*a*–*h*). While the field point **x** can be anywhere in the half space, the source point **d** is assumed to be interior to the half-space (i.e., $d \neq 0$). We recall that in the Mindlin solution ([13]) to an isotropic half-space with traction-free boundary conditions, both field and source points (**x** and **d**) can be arbitrary, and the corresponding Boussinesq solution (for a point force in any direction on the surface; see, [43]) can be directly reduced from Mindlin solution by taking the source point to the surface (i.e., $d=0$). Furthermore, the special half-space surface Green's function where the field and source points are both on the surface (i.e., $z=0$ and $d=0$), can also be obtained either from Mindlin solution with $z=0$ and $d=0$ for from Boussinesq solution with $z=0$. Actually, this feature also holds for the Mindlin solution in a transversely isotropic ([14]) and general anisotropic half-space ([2,4,15–17]). It is important at this point to emphasize that this feature is based upon the condition that the surface of the half-space is traction-free (i.e., Eq. (2*e*)). Then, it is natural to ask the question: Can one safely take the source point to the surface (i.e., $d=0$) in the generalized Mindlin solution to obtain the corresponding generalized Boussinesq solution? The answer is yes!

First, it is observed that if the *i*-th component of the traction vector is zero (i.e., $t_i=0$) on the surface, with boundary conditions in other two directions being properly given, then the corresponding generalized Boussinesq solution exists for a surface point force acting in the *i*th direction. Furthermore, this solution can be directly obtained from the generalized Mindlin solution by letting $d=0$. We point out that the field point is assumed to be interior to the half-space (i.e., $z \neq 0$), leaving the case of $d=0$ and $z=0$ being treated separately in the next section. It is very interesting that Boussinesq (see [43]) derived solutions in an isotropic half-space subjected to two general types of boundary conditions to which the present boundary condition sets (2*d*) and (2*h*) have direct connection. Therefore, for example, for the boundary condition set (2*d*), the generalized Boussinesq solution to a normal point force (i.e., in the x_3-direction) on the surface with fixed tangential displacements (i.e., $u_1=0$ and $u_2=0$) is well-defined and can be directly reduced from the generalized Mindlin solution by taking $d=0$.

Now, let us examine the case where the *i*th component of the displacement vector is zero (i.e., $u_i=0$) on the surface, which is also subjected to a surface point force in the *i*th direction at the origin. Since the displacement component $u_i=0$ is described on the whole surface while a concentrated traction component $t_i(=-\delta(\mathbf{x}))$ is also given at the surface point $\mathbf{x}=(0,0,0)$, the resulting boundary condition is over imposed at $\mathbf{x}=(0,0,0)$! However, if we release the displacement condition at $\mathbf{x}=(0,0,0)$ for u_i, due to the fact that this is a concentrated force at $\mathbf{x}=(0,0,0)$, then the boundary value problem will be well defined. Actually, from a mathematical point of view, i.e., from Eqs. (31)–(38), it can be proved that when $d=0$, these Boussinesq solutions are still well defined and regular as long as $z \neq 0$. It is noted that the first terms in Eqs. (31), (33), (35), and (37) are the infinite-space Green's functions that are regular and become singular if and only if the field and source points are coincident to each other (i.e., $\mathbf{x}=\mathbf{d}$). The second terms in these equations are proportional to one of the $\mathbf{G}_i$ matrices defined by Eqs. (32), (34), and (38), which are again regular and well defined. Therefore, in conclusion, the generalized Boussinesq solutions with general boundary conditions are still well defined and regular (if $z \neq 0$).

To enhance our understanding, we now offer a physical explanation to the generalized Boussinesq solutions in terms of the equivalent concept of the Green's functions due to a point force and an infinitesimal dislocation loop. Using the Betti's reciprocity, it can be shown ([44–46]) that the following important equivalent between the Green's function of a unit point force and that of a unit infinitesimal dislocation loop holds (in a dimensionless form):

$$u_j^{uik}(\mathbf{d};\mathbf{x}) = \sigma_{ik}^{fj}(\mathbf{x};\mathbf{d}) \tag{39}$$

While the right-hand side of Eq. (39) denotes the Green's stress component (i,k) at the field point **x** due to a point force in the *j*th direction at **d**, the left-hand side denotes the displacement in the *j*th direction at the field point **d** due to an infinitesimal dislocation loop, with index (i,k) for the dislocation direction and the normal of the dislocation plane, at the source point **x**. Therefore, the stress field due to a point force can be equivalently considered as a displacement field due to an infinitesimal dislocation loop. The latter is well defined with an apparent physical meaning: The displacement response on the surface of the half-space **d** (since $d=0$) due to an interior infinitesimal dislocation loop at the source point **x** (since $z \neq 0$). A very interesting consequence of Eq. (39) is that if the boundary condition is rigid (2*a*), then the stress field within the whole half-space, due to a point force in any direction on the surface, is zero! Furthermore, our numerical tests have shown that for such a case, the displacement field is indeed zero. The only nonzero components are the derivatives of the displacement and stress with respect to the third source coordinate *d*. While whether or not this special Boussinesq solution (with rigid boundary condition) has any application is unknown to the author, it is worth mentioning that these numerically obtained features on the displacements, stresses, and derivatives of displacements and stresses are consistent with those in the corresponding two-dimensional half-plane ([2]) where analytical solutions exist.

Yet, another limit case is when the field and source points are both on the surface (i.e., $z=d=0$). The corresponding response is a special case of the surface Green function, and it is discussed and presented in the following section.

Special Surface Green's Function

When both the field and source points are on the surface (i.e., $z=d=0$), the half-space Green's functions are reduced (from either the generalized Mindlin or Boussinesq solutions) to a particular class of Green's functions called special surface Green's functions. Similar to the generalized Mindlin or Boussinesq solutions, these special surface Green's functions can be expressed as a sum of the generalized Kelvin solution in an explicit form and a Mindlin's complementary part. For the complementary part, however, the involved one-dimensional integral becomes singular and exists only in the sense of finite-part principle value ([47–49]). Assuming that the field and source coordinates on the surface are (x_1,x_2) and (d_1,d_2), respectively, and expressing their relative position in terms of the polar coordinate as $x_1-d_1=r\cos\theta_0; x_2-d_2=r\sin\theta_0$, then these special surface Green's functions are obtained as ([50])

$$\mathbf{U}(\mathbf{x};\mathbf{d}) = \mathbf{U}^{\infty}(\mathbf{x};\mathbf{d}) - \frac{1}{2\pi r}\left\{\frac{1}{\pi}\int_0^{\pi}\frac{\overline{\mathbf{AK}}^{-1}\mathbf{KA}^T}{\cos(\theta-\theta_0)}d\theta + i[\overline{\mathbf{AK}}^{-1}\mathbf{KA}^T]_{\theta=\theta_0+\pi/2}\right\} \tag{40}$$

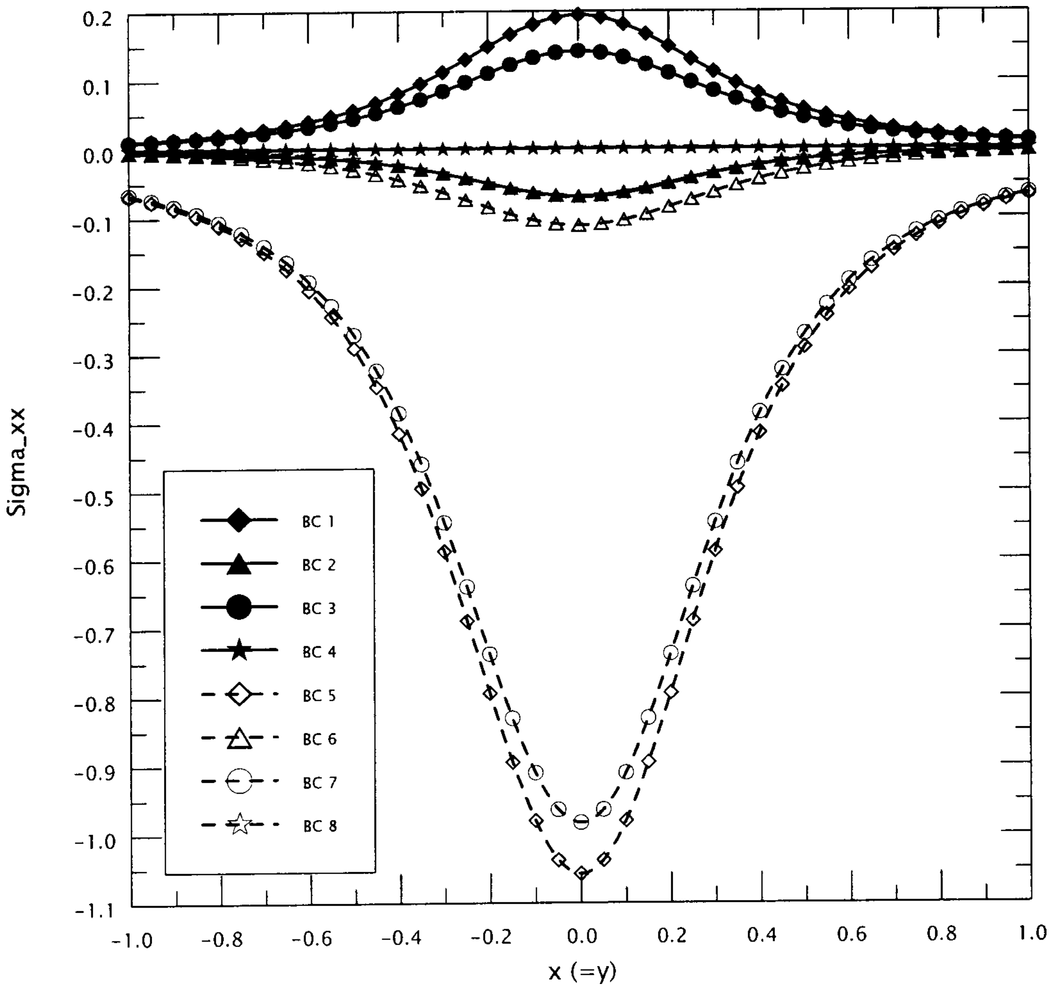

Fig. 1 Variation of in-plane stress component σ_{xx} along the line $x=y$ on the surface $z=0$, caused by the point force f=(0,0,1) and d=(0,0,1). Labels BC 1 to BC 8 correspond to the eight different sets of boundary conditions (2*a*–*h*).

$$\frac{\partial\mathbf{U}(\mathbf{x};\mathbf{d})}{\partial d_j}=\frac{\partial\mathbf{U}^{\infty}(\mathbf{x};\mathbf{d})}{\partial d_j}-\frac{1}{2\pi r^2}\left\{\frac{1}{\pi}\int_0^{\pi}\frac{\overline{\mathbf{AK}}^{-1}\mathbf{K}(g_j\rangle\mathbf{A}^T}{\cos^2(\theta-\theta_0)}d\theta\right.$$
$$\left.-i\,\frac{d[\overline{\mathbf{AK}}^{-1}\mathbf{K}\langle g_j\rangle\mathbf{A}^T]}{d\theta}\right|_{\theta=\theta_0+\pi/2}\Bigg\}\tag{41}$$

$$\mathbf{T}(\mathbf{x};\mathbf{d})=\mathbf{T}^{\infty}(\mathbf{x};\mathbf{d})+\frac{1}{2\pi r^2}\left\{\frac{1}{\pi}\int_0^{\pi}\frac{\overline{\mathbf{BK}}^{-1}\mathbf{KA}^T}{\cos^2(\theta-\theta_0)}d\theta\right.$$
$$\left.-i\,\frac{d[\overline{\mathbf{BK}}^{-1}\mathbf{KA}^T}{d\theta}\right|_{\theta=\theta_0+\pi/2}\Bigg\}\tag{42}$$

$$\frac{\partial\mathbf{T}(\mathbf{x};\mathbf{d})}{\partial d_j}=\frac{\partial\mathbf{T}^{\infty}(\mathbf{x};\mathbf{d})}{\partial d_j}+\frac{1}{2\pi r^3}\left\{\frac{2}{\pi}\int_0^{\pi}\frac{\overline{\mathbf{BK}}^{-1}\mathbf{K}\langle g_j\rangle\mathbf{A}^T}{\cos^3(\theta-\theta_0)}d\theta\right.$$
$$+i\left[\frac{d^2[\overline{\mathbf{BK}}^{-1}\mathbf{K}\langle g_j\rangle\mathbf{A}^T]}{d^2\theta}\right.$$
$$\left.\left.+[\overline{\mathbf{BK}}^{-1}\mathbf{K}\langle g_j\rangle\mathbf{A}^T]\right]\right|_{\theta=\theta_0+\pi/2}\Bigg\}\tag{43}$$

$$\mathbf{S}(\mathbf{x};\mathbf{d})=\mathbf{S}^{\infty}(\mathbf{x};\mathbf{d})+\frac{1}{2\pi r^2}\left\{\frac{1}{\pi}\int_0^{\pi}\frac{\overline{\mathbf{CK}}^{-1}\mathbf{KA}^T}{\cos^2(\theta-\theta_0)}d\theta\right.$$
$$\left.-i\,\frac{d[\overline{\mathbf{CK}}^{-1}\mathbf{KA}^T]}{d\theta}\right|_{\theta=\theta_0+\pi/2}\Bigg\}\tag{44}$$

$$\frac{\partial\mathbf{S}(\mathbf{x};\mathbf{d})}{\partial d_j}=\frac{\partial\mathbf{S}^{\infty}(\mathbf{x};\mathbf{d})}{\partial d_j}+\frac{1}{2\pi r^3}\left\{\frac{2}{\pi}\int_0^{\pi}\frac{\overline{\mathbf{CK}}^{-1}\mathbf{K}\langle g_j\rangle\mathbf{A}^T}{\cos^3(\theta-\theta_0)}d\theta\right.$$
$$+i\left[\frac{d^2[\overline{\mathbf{CK}}^{-1}\mathbf{K}\langle g_j\rangle\mathbf{A}^T]}{d^2\theta}\right.$$
$$\left.\left.+[\overline{\mathbf{CK}}^{-1}\mathbf{K}\langle g_j\rangle\mathbf{A}^T]\right]\right|_{\theta=\theta_0+\pi/2}\Bigg\}.\tag{45}$$

Several features regarding to the special surface Green's functions with general boundary conditions are observed:

1. Similar to the interfacial Green's functions in anisotropic bimaterial with perfectly bonded interface ([50]), the surface displacements, stresses and derivatives of displacements, and derivatives of stresses are inversely proportional, respectively, to r, r^2, and r^3, where r is the distance between the field and source points on the surface ($z=d=0$), a generalized consequence of self-

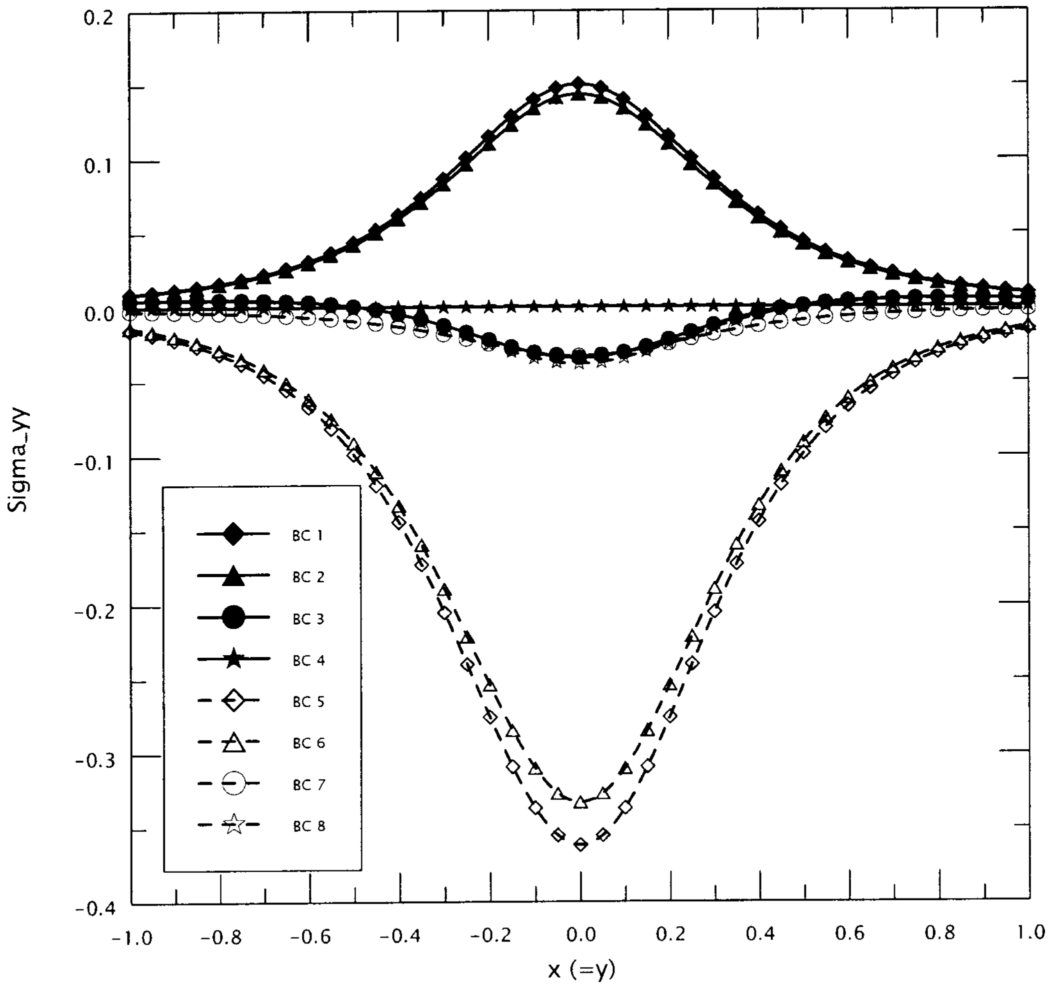

Fig. 2 Variation of in-plane stress component σ_{yy} along the line $x=y$ on the surface $z=0$, caused by the point force f=(0,0,1) at d=(0,0,1). Labels BC 1 to BC 8 correspond to the eight different sets of boundary conditions (2*a–h*).

similarity [9,15]. For the special surface Green's function component which is inversely proportional to r, r^2, and r^3, the corresponding finite-part integral has singular order of one $(1/\cos\theta)$, two $(1/\cos^2\theta)$, and three $(1/\cos^3\theta)$, respectively; therefore, the special surface Green's functions are completely determined by the values on a unit circle on the surface $z=d=0$ (with field point on the unit circle and source point at the center of the circle). The finite-part integrals can be carried out accurately and efficiently using an adaptive scheme proposed recently by Pan and Yang [50].

2. For the traction-free boundary conditions (2*e*), the corresponding special surface Green's function was discussed previously by Willis [9], Barnett and Lothe [4], Barber and Sturla [15], Ting [2], Wu [16], and Pan and Yuan [17]. Even for this case, the complete special surface Green's functions are not available in the literature until very recently ([50]).

3. All the special surface Green's functions corresponding to the boundary conditions (2*a–d*) and (2*f–h*) are new.

Numerical Examples

For an anisotropic half space with general boundary conditions (2*a–h*), no previous solution is available except for the traction-free (2*e*) and rigid (2*a*) cases. While for the former, the Green's displacements and stresses were studied previously by Barrett and Lothe [4], Tine [2], Wu [16], and Pan and Yuan [17], the Green's functions for the latter can be numerically reduced from the bimaterial Green's functions of Pan and Yuan [17] for a perfectly bonded interface by letting the elastic tensor C_{ijkl} in the $z<0$ half-space being much stiffer than that in the concerned half-space region $z>0$. Although the isotropic ([19]) and transversely isotropic ([18]) half-space Green's solutions were studied before for the slippery surface boundary conditions (2*h*), no numerical result is available. Nevertheless, the present generalized Mindlin solutions have been self-checked for the boundary conditions (2*a*) and (2*e*), and for two of the mixed boundary conditions, namely conditions (2*d*) and (2*h*), to be discussed below.

Boussinesq (see [43]) derived the solution in an isotropic half-space when its boundary is subjected to two general types of boundary conditions: namely, the normal traction t_z and tangential displacements (u_x and u_y), and normal displacement u_z and tangential tractions (t_x and t_y). If, for the former, we assume a unit normal point force at the original and let the tangential displacements be zero (i.e., $u_x=u_y=0$), then the dilatation at any field point $\mathbf{x}=(x,y,z)$ of the half-space caused by this normal point force is found to be

$$\Delta=u_{i,i}=\frac{-z}{2\pi(\lambda+2\mu)(x^2+y^2+z^2)^{3/2}} \tag{46}$$

where λ and μ are the two Lame constants.

Similarly, for the latter, if we assume a unit point force in the x-direction at the original, traction-free in the y-direction (t_y

Table 1 Reduced and normalized stiffness matrix C_{ij} in the half-space

1.0352019	.0523837	.0523837	.0	.0	.0
	.1153771	.0405268	.0	.0	.0
		.1153771	.0	.0	.0
			.0333333	.0	.0
				.0333333	.0
					.0333333

$=0$), and zero-displacement in the z-direction $(u_z=0)$, then the dilatation at any field point $\mathbf{x}=(x,y,z)$ of the half-space caused by this tangential point force is obtained as

$$\Delta=u_{i,i}=\frac{-x}{2\pi(\lambda+2\mu)(x^2+y^2+z^2)^{3/2}}. \tag{47}$$

It is seen that while Boussinesq solution (46) corresponds to the present Green's function with boundary condition (2*d*), solution (47) corresponds to that with the boundary condition (2*h*). For the former, the point force is in the z-direction and for the latter it is in the x-direction.

In the numerical testing, a Young's modulus $E=2.6$ and Poisson's ratio $\nu=0.3$ were assumed for the isotropic half-space. For the field point at $(x,y,z)=(1/\sqrt{3},1/\sqrt{3},1/\sqrt{3})$, both Eqs. (46) and (47) give the same dilatation value $\Delta=-0.026254$, while that predicted by the present Green's function solutions for the two cases is $\Delta=-0.026251$. This result not only has validated some of the present Green's functions, but also has shown that even the isotropic case can be easily handled by the present Stroh formalism using a slightly perturbed elastic property ([40]). For instance, to use the present Stroh formalism for the isotropic material, an orthotropic material was assumed with one of the three Poisson's ratios being perturbed to $\nu=0.2999$ while the other two being kept at $\nu=0.3$.

Next, the effect of different boundary conditions as well as material anisotropy, on the surface stress field is studied for an orthotropic half-space. The stiffness matrix (in its reduced and normalized form) from Pan and Yang [50] is given in Table 1. For this example, the source is fixed at $\mathbf{d}=(0,0,1)$ while the field point varies on the surface of the half-space as $\mathbf{x}=(x,x,0)$, with $\mathbf{x}\in[-1,1]$. While Figs. 1 and 2 show the variation of the normal stresses σ_{xx} and σ_{yy} caused by a unit point force in the z-direction, Figs. 3 and 4 show the variation of these normal stresses (σ_{xx} and σ_{yy}) due to a unit point force in the x-direction. In these figures, results for the eight different sets of boundary conditions (2*a–h*) are labeled as BC 1 and BC 8, respectively. These numerical results are believed to be new and possess the following interesting features:

1. For the given material (orthotropic), the surface normal stresses σ_{xx} and σ_{yy} are either symmetric (Figs. 1 and 2) or anti-

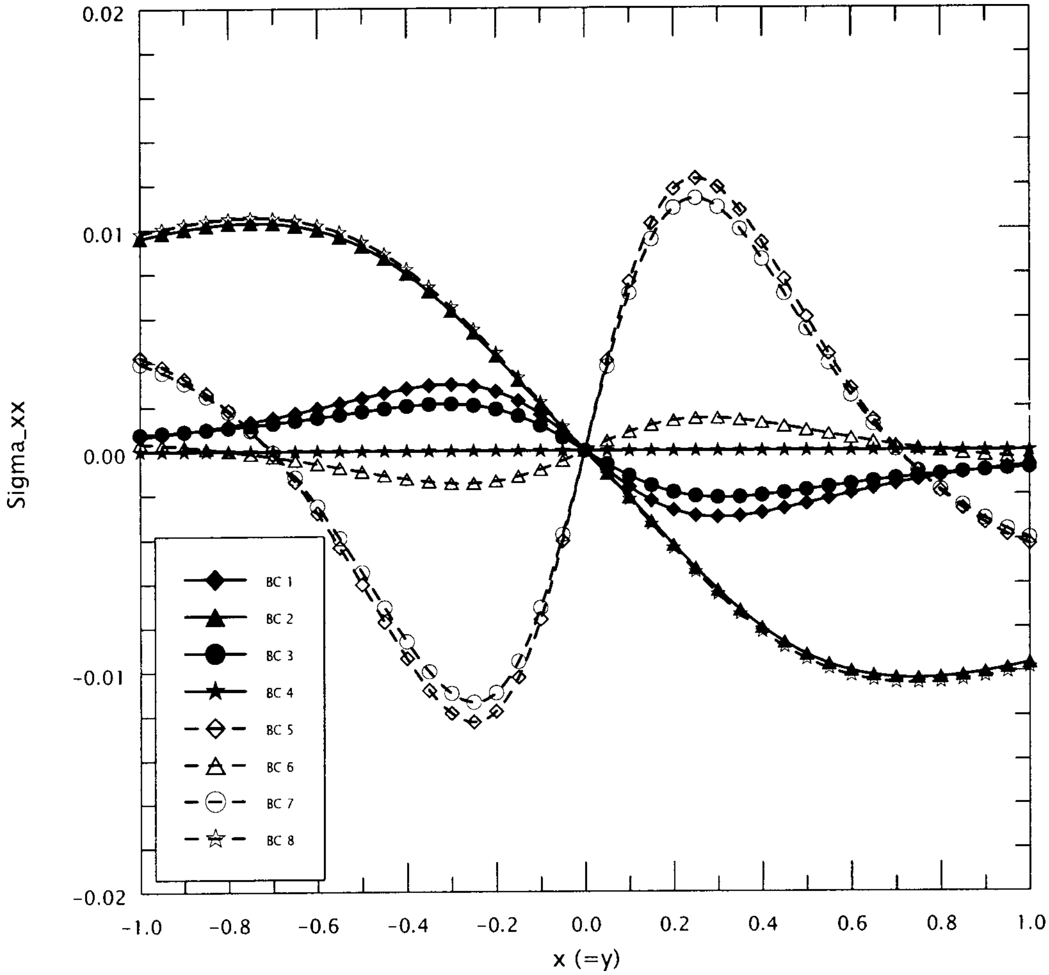

Fig. 3 Variation of in-plane stress component σ_{xx} along the line $x=y$ on the surface $z=0$, caused by the point force f=(1,0,0) at d=(0,0,1). Labels BC 1 to BC 8 correspond to the eight different sets of boundary conditions (2*a–h*).

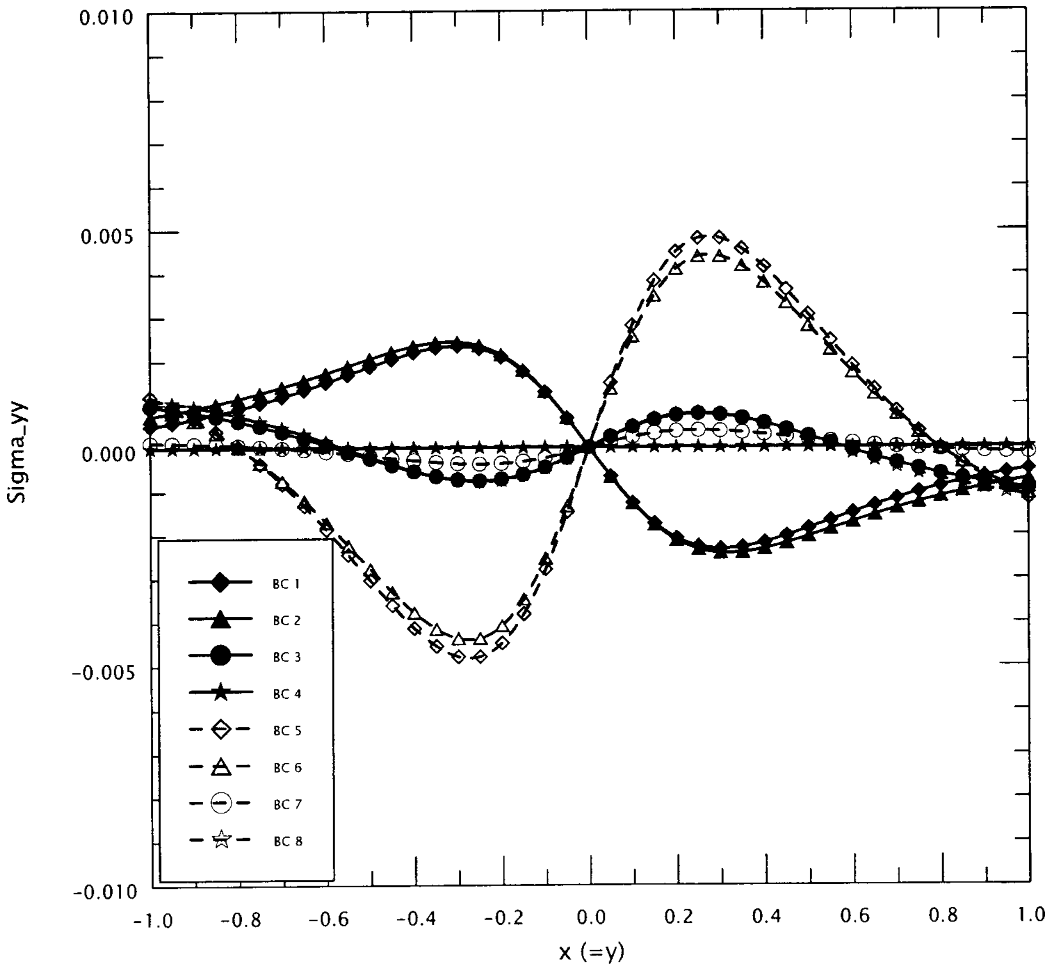

Fig. 4 Variation of in-plane stress component σ_{yy} along the line $x=y$ on the surface $z=0$, caused by the point force f=(1,0,0) at d=(0,0,1). Labels BC 1 to BC 8 correspond to the eight different sets of boundary conditions (2*a*–*h*).

symmetric (Figs. 3 and 4), a general feature also associated with the Mindlin solution in an isotropic half-space with traction-free boundary conditions.

2. The effect of material anisotropy on the surface normal stresses can be clearly see by comparing Fig. 1 to Fig. 2. For BC 1 and BC 5, both normal stresses σ_{xx} and σ_{yy} should be the same if the material is isotropic. However, the magnitudes are much different in the orthotropic half space for σ_{xx} and σ_{yy} under boundary condition BC 1 or BC 5.

3. It is of particular interest to order the normal stresses σ_{xx} and σ_{yy} at the surface point $\mathbf{x}=\mathbf{0}$, i.e., the symmetric point) from the largest tension (maximum) to the largest compression (minimum) according to the different sets of boundary conditions. While for those in Fig. 1, the descent order is BC 1, BC 3, BC 4, BC 2, BC 8, BC 6, BC 7, and BC 5, for those in Fig. 2, it is BC 1, BC 2, BC 4, BC 7, BC 3, BC 8, BC 6, and BC 5. It is observed that the boundary condition case BC 4 (Eq. (2*d*)) is in neutral for which the normal stresses σ_{xx} and σ_{yy} along the line $x=y$ on the surface are zero. While BC 1 and BC 3 predict a tensile and BC 2, BC 5–8 a compressive value for the normal stress σ_{xx}, BC 1 and BC 2 predict a tensile and BC 3, BC 5–8 a compressive value for the normal stress σ_{yy}.

Conclusions

In this paper, the complete set of three-dimensional Green's functions (displacements, stresses, and derivatives of displacements and stresses with respect to the source points), due to a point force in an anisotropic half-space with general boundary conditions, also called the generalized Mindlin solutions, are derived for the first time. Applying the Mindlin's superposition method, the half-space Green's function is obtained as a sum of the generalized Kelvin solution (Green's function in an anisotropic infinite space) and a Mindlin's complementary solution. While the generalized Kelvin solution is in an explicit form, the Mindlin's complementary part is expressed in terms of a simple line-integral over $[0,\pi]$. To handle the eight different sets of boundary conditions, a new matrix $\mathbf{K}$, a combination of the eigenmatrices $\mathbf{A}$ and $\mathbf{B}$, has been introduced so that the Green's functions corresponding to the eight different sets of boundary conditions can be expressed in a unified form, including the existing traction-free and rigid boundaries as the special cases.

The corresponding generalized Boussinesq solutions (for source point on the surface) and the special surface Green's functions (for both the source and field points on the surface) have been studied in details. In particular, it has been proved that under the general boundary conditions studied in this paper, the generalized Boussinesq solution is still well-defined, along with a physical explanation in terms of the equivalent concept of the Green's functions due to a point force and an infinitesimal dislocation loop.

A typical numerical example has been also presented for the Green's functions in an orthotropic half-space with the eight different sets of boundary conditions. The new numerical result illustrates clearly the effect of the boundary conditions, as well as material anisotropy, on the half-space Green's stresses. It is believed that the present complete Green's function solutions should be of interest to various boundary/contact designs and of particular value to various mechanical engineering and quantum device analyses based upon the integral equation method using Green's function.

Acknowledgments

The author would like to thank Prof. C. Q. Ru of the University of Alberta for discussions during the course of this study and the reviewer for his constructive comments, which lead to improvements of the earlier version of this article.

References

[1] Barber, J. R., 1992, *Elasticity*, Kluwer Academic Publishers, Dordrecht, The Netherlands.

[2] Ting, T. C. T., 1996, *Anisotropic Elasticity*, Oxford University Press, Oxford, UK.

[3] Davis, R. O., and Selvadurai, A. P. S., 1996, *Elasticity and Geomechanics*, Cambridge University Press, Cambridge, MA.

[4] Barnett, D. M., and Lothe, J., 1975, ''Line Force Loadings on Anisotropic Half-Spaces and Wedges,'' Phys. Norv., **8**, pp. 13–22.

[5] Mura, T., 1987, *Micromechanics of Defects in Solids*, 2nd Ed., Martinus Nijhof, Dordrecht, The Netherlands.

[6] Vlassak, J. J., and Nix, W. D., 1994, ''Measuring the Elastic Properties of Anisotropic Materials by Means of Indentation Experiments,'' J. Mech. Phys. Solids, **42**, pp. 1223–1245.

[7] Liao, J.J., and Wang, C. D., 1998, ''Elastic Solutions for a Transversely Isotropic Half-Space Subjected to a Point Load,'' Int. J. Numer. Analyt. Meth. Geomech., **22**, pp. 425–447.

[8] Wang, C. D., and Liao, J. J., 1999, ''Elastic Solutions for a Transversely Isotropic Half-Space Subjected to Buried Asymmetric-Loads,'' Int. J. Numer. Analyt. Meth. Geomech., **23**, pp. 115–139.

[9] Willis, J. R., 1966, ''Hertzian Contact of Anisotropic Bodies,'' J. Mech. Phys. Solids, **14**, pp. 163–176.

[10] Gladwell, G. M. L., 1980, *Contact Problems in the Classical Theory of Elasticity*, Sithoff and Noordhoff, The Netherlands.

[11] Barber, J. R., and Ciavarella, M., 2000, ''Contact Mechanics,'' Int. J. Solids Struct. **37**, pp. 29–43.

[12] Yu, H. Y., 2001, ''A Concise Treatment of Indentation Problems in Transversely Isotropic Half Spaces,'' Int. J. Solids Struct., **38**, pp. 2213–2232.

[13] Mindlin, R. D., 1936, ''Force at a Point in the Interior of a Semi-Infinite Solid,'' Physics (N.Y.), **7**, pp. 195–202.

[14] Pan, Y. C., and Chou, T. W., 1979, ''Green's Function Solutions for Semi-Infinite Transversely Isotropic Materials,'' Int. J. Eng. Sci. **17**, pp. 545–551.

[15] Barber, J. R., and Sturla, F. A., 1992, ''Application of the Reciprocal Theorem to Some Problems for the Elastic Half-Space'' J. Mech. Phys. Solids, **40**, pp. 17–25.

[16] Wu, K. C., 1998, ''Generalization of the Stroh Formalism to 3-Dimensional Anisotropic Elasticity,'' J. Elast., **51**, pp. 213–225.

[17] Pan, E., and Yuan, F. G., 2000, ''Three-Dimensional Green's Functions in Anisotropic Bimaterials,'' Int. J. Solids Struct., **37**, pp. 5329–5351.

[18] Yu, H. Y., Sanday, S. C., Rath, B. B., and Chang, C. I., 1995, ''Elastic Fields due to Defects in Transversely Isotropic Half Spaces,'' Proc. R. Soc. London, Ser. A, **A449**, pp. 1–30.

[19] Dundurs, J., and Hetenyi, M., 1965, ''Transmission of Force Between Two Semi-Infinite Solids,'' ASME J. Appl. Mech., **32**, pp. 671–674.

[20] Fabrikant, I., 1989, *Applications of Potential Theory in Mechanics: A Selection of New Results*, Kluwer Academic Publishers, Dordrecht, The Netherlands.

[21] Fabrikant, V. I., 1991, *Mixed Boundary Value Problems of Potential Theory and Their Applications in Engineering*, Kluwer Academic Publishers, Dordrecht, The Netherlands.

[22] Craig, R. F., 1992, *Soil Mechanics*, 5th Ed., Chapman & Hall, New York.

[23] Timoshenko, S., and Woinowsky-Krieger, S., 1987 *Theory of Plates and Shells*, 2nd Ed., McGraw-Hill, New York.

[24] Shilkrot, L. E., and Srolovitz, D. J., 1998, ''Elastic Analysis of Finite Stiffness Bimaterial Interfaces: Application to Dislocation-Interface Interactions,'' Acta Mater., **46**, pp. 3063–3075.

[25] Gharpuray, V. M., Dundurs, J., and Keer, L. M., 1991, ''A Crack Terminating at a Slipping Interface Between Two Materials,'' ASME J. Appl. Mech., **58**, pp. 960–963.

[26] Davies, J. H., and Larkin, I. A., 1994, ''Theory of Potential Modulation in Lateral Surface Superlattices,'' Phys. Rev. B, **B49**, pp. 4800–4809.

[27] Larkin, I. A., Davies, J. H., Long, A. R., and Cusco, R., 1997, ''Theory of Potential Modulation in Lateral Surface Superlattices, II. Piezoelectric Effect,'' Phys. Rev. B, **B56**, pp. 15,242–15,251.

[28] Holy, V., Springholz, G., Pinczolits, M., and Bauer, G., 1999, ''Strain Induced Vertical and Lateral Correlations in Quantum Dot Superlattices,'' Phys. Rev. Lett., **83**, pp. 356–359.

[29] Ru, C. Q., 1999, ''Analytic Solution for Eshelby's Problem of an Inclusion of Arbitrary Shape in a Plane or Half-Plane,'' ASME J. Appl. Mech., **66**, pp. 315–322.

[30] Ru, C. Q., 2000, ''Eshelby's Problem for Two-Dimensional Piezoelectric Inclusion of Arbitrary Shapem,'' Proc. R. Soc. London, Ser. A, **A456**, pp. 1051–1068.

[31] Eshelby, J. D., 1957, ''The Determination of the Elastic Field on an Ellipsoidal Inclusion, and Related Problems,'' Proc. R. Soc. London, Ser. A, **A241**, pp. 376–396.

[32] Ting, T. C. T., 2000, ''Recent Developments in Anisotropic Elasticity,'' Int. J. Solids Struct., **37**, pp. 401–409.

[33] Ting, T. C. T., 2001, ''The Wonderful World of Anisotropic Elasticity—An Exciting Theme Park to Visit,'' *Proc. 4th Pacific International Conference on Aerospace Science and Technology*,'' pp. 1–7.

[34] Ting, T. C. T., and Wang, M. Z., 1992, ''Generalized Stroh Formalism for Anisotropic Elasticity for General Boundary Conditions,'' Acta Mech. Sin., **8**, pp. 193–207.

[35] Wang, M. Z., Ting, T. C. T., and Yan, G., 1993, ''The Anisotropic Elastic Semi-Infinite Strip,'' Q. Appl. Math., **51**, pp. 283–297.

[36] Tewary, V. K., 1995, ''Computationally Efficient Representation for Elastostatic and Elastodynamic Green's Functions,'' Phys. Rev. B, **51**, pp. 15,695–15,702.

[37] Ting, T. C. T., and Lee, V. G., 1997, ''The Three-Dimensional Elastostatic Green's Function for General Anisotropic Linear Elastic Solids,'' Q. J. Mech. Appl. Math., **50**, pp. 407–426.

[38] Sales, M. A., and Gray, L. J., 1998, ''Evaluation of the Anisotropic Green's Function and its Derivatives,'' Comput. Struct., **69**, pp. 247–254.

[39] Tonon, F., Pan, E., and Amadei, B., 2001, ''Green's Functions and Boundary Element Method Formulation for 3D Anisotropic Media,'' Comput. Struct., **79**, pp. 469–482.

[40] Pan, E., 1997, ''A General Boundary Element Analysis of 2-D Linear Elastic Fracture Mechanics,'' Int. J. Fract., **88**, pp. 41–59.

[41] Pan, E., 2002, ''Three-Dimensional Green's Functions in Anisotropic Magneto-Electro-Elastic Bimaterials,'' J. Appl. Math Phys., pp. 815–838.

[42] Walker, K. P., 1993, ''Fourier Integral Representation of the Green's Function for an Anisotropic Elastic Half-Space,'' Proc. R. Soc. London, Ser. A, **A443**, pp. 367–389.

[43] Love, A. E. H., 1994, *A Treatise on the Mathematical Theory of Elasticity*, 4th Ed., Dover Publication, New York.

[44] Sokolnikoff, I. S., 1956, *Mathematical Theory of Elasticity*, McGraw-Hill, New York.

[45] Hirth, J. P., and Lothe, J., 1982, *Theory of Dislocations*, 2nd Ed., John Wiley and Sons, New York.

[46] Pan, E., 1991, ''Dislocation in an Infinite Poroelastic Medium,'' Acta Mech., **87**, pp. 105–115.

[47] Paget, D. F., 1981, ''The Numerical Evaluation of Hadamard Finite-Part Intervals,'' Numer. Math., **36**, pp. 447–453.

[48] Monegato, G., 1994, ''Numerical Evaluation of Hypersingular Integrals,'' J. Comput. Appl. Math., **50**, pp. 9–31.

[49] Mastronardi, N., and Occorsio, D., 1996, ''Some Numerical Algorithms to Evaluate Hadamard Finite-Part Integrals,'' J. Comput. Appl. Math., **70**, pp. 75–93.

[50] Pan, E., and Yang, B., 2003, ''Three-Dimensional Interfacial Green's Functions in Anisotropic Bimaterials,'' Appl. Math. Model., in press.

M. Jabbari
Science and Research Campus,
Islamic Azad University,
Tehran, Iran

S. Sohrabpour
Professor,
Mechanical Engineering Department,
Sharif University of Technology,
Tehran, Iran

M. R. Eslami
Professor,
Mechanical Engineering Department,
Amirkabir University of Technology,
Tehran, Iran
Fellow ASME

General Solution for Mechanical and Thermal Stresses in a Functionally Graded Hollow Cylinder due to Nonaxisymmetric Steady-State Loads

In this paper, the general theoretical analysis of two-dimensional steady-state thermal stresses for a hollow thick cylinder made of functionally graded material is developed. The temperature distribution is assumed to be a function of radial and circumferential directions with general thermal and mechanical boundary conditions on the inside and outside surfaces. The material properties, except Poisson's ratio, are assumed to depend on the variable r and they are expressed as power functions of r. The separation of variables and complex Fourier series are used to solve the heat conduction and Navier equations. [DOI: 10.1115/1.1509484]

1 Introduction

Functionally graded materials are new, advanced, heat-resisting materials used in modern technologies as advanced structures. In addition to superb heat properties, they are corrosion and erosion resistant and have high fracture stiffness. The basic concept is to mix the ceramic and metal such that the material properties continuously vary from one constituent material to the other. In effect, the governing equations for the temperature and stress distributions are coordinate dependent, as the material properties are functions of position.

There are some analytical thermal and stress calculations for functionally graded materials in the one-dimensional case for thick spheres and cylinders ([1,2]). The authors have considered the nonhomogeneous material properties as linear functions of r. The thermal and stress analysis of these types of structures are sometimes carried out using the theory of laminated composites ([3–7]). The material properties are, however, continuous functions of position and therefore there are some objections to the analogy of functionally graded materials with composites. Han et al. [8,9] used the layerwise theory of plates to model the wave propagation in a plate made of functionally graded material and used the quadratic element. They showed that the quadratic element may well express the properties of the functionally graded material plates across the thickness. The quadratic layered element method may well express the material properties of the functionally graded material along the graded direction, but it is basically an analytical-numerical technique with approximate solutions.

Using the perturbation technique, Obata and Noda [10] presented a solution for the transient thermal stresses in a plate made of functionally graded material. The same authors used the perturbation technique to derive the thermal stress equations of the thick hollow spheres and plates made of functionally graded materials under different temperature distributions ([11,12]). Obata et al. [13] presented the solution for thermal stresses of a thick hollow cylinder made of functionally graded material under two-dimensional transient temperature distribution. Tanigawa et al. [14,15] solved the thermal stresses for a slab and a semi-infinite body with the assumption that the nonhomogeneous material properties are power functions of the thickness direction, z. These papers, due to their mathematical limitations, have a constraint for power of z in shear modulus of elasticity $G(z)$. In the study of thermal stresses of functionally graded material plates, spheres, cylinders, and semi-infinite bodies in two and three-dimensional cases, the traditional potential function method is used. This method of solution has limitations in choosing the boundary conditions for stresses and displacements.

In the present paper, a direct method of solution of the Navier equations is presented which does not have the limitations of the potential function method as to handle the general types of mechanical and thermal boundary conditions. A thick hollow cylinder made of functionally graded material under two-dimensional steady-state temperature distribution with general types of thermal and mechanical boundary conditions is considered. The functionally graded material properties of the cylinder are assumed to be expressed by power functions in r. None of the limitations considered in the previous references ([14,15]) for the power of material properties are applied in this paper. The Navier equations in terms of displacements are derived and solved analytically by the direct method, so any boundary conditions for stresses and displacements can be satisfied. By setting the power index constants equal to zero, the method of solution and the results are reduced to those of thick cylinders of isotropic material.

2 Derivations of Governing Equations

Consider a thick hollow cylinder of inner radius a and outer radius b made of functionally graded material. The cylinder's material is graded through the r-direction, thus the material properties are functions of r. Let u and v be the displacement components in the radial and circumferential directions, respectively. Then the strain-displacement relations are

$$\begin{aligned}\epsilon_{rr}&=u_{,r}\\ \epsilon_{\theta\theta}&=\frac{v_{,\theta}}{r}+\frac{u}{r}\\ \epsilon_{r\theta}&=\frac{1}{2}\left(\frac{u_{,\theta}}{r}+v_{,r}-\frac{v}{r}\right)\end{aligned}\tag{1}$$

Contributed by the Applied Mechanics Division of THE AMERICAN SOCIETY OF MECHANICAL ENGINEERS for publication in the ASME JOURNAL OF APPLIED MECHANICS. Manuscript received by the Applied Mechanics Division, Oct. 23, 2000; final revision, May 8, 2002. Associate Editor: M.-P. Pindera. Discussion on the paper should be addressed to the Editor, Prof. Robert M. McMeeking, Chair, Department of Mechanics and Environmental Engineering, University of California–Santa Barbara, Santa Barbara, CA 93106-5070, and will be accepted until four months after final publication in the paper itself in the ASME JOURNAL OF APPLIED MECHANICS.

where (,) denotes partial derivative. The stress-strain relations for plane-strain conditions are

$$\begin{aligned}\sigma_{rr}&=(\lambda+2\mu)\epsilon_{rr}+\lambda\epsilon_{\theta\theta}-(3\lambda+2\mu)\alpha T(r,\theta)\\ \sigma_{\theta\theta}&=(\lambda+2\mu)\epsilon_{\theta\theta}+\lambda\epsilon_{rr}-(3\lambda+2\mu)\alpha T(r,\theta)\\ \sigma_{r\theta}&=2\mu\epsilon_{r\theta}\end{aligned}\tag{2}$$

where σ_{ij} and $\epsilon_{ij}(i,j=r,\theta)$ are the stress and strain tensors, $T(r,\theta)$ is the temperature distribution determined from the heat conduction equation, α is the coefficient of thermal expansion, and λ and μ are the Lamé coefficients related to the modulus of elasticity E and Poisson's ratio ν as

$$\begin{aligned}\lambda&=\frac{\nu E}{(1+\nu)(1-2\nu)}\\ \mu&=\frac{E}{2(1+\nu)}.\end{aligned}\tag{3}$$

The equilibrium equations in the radial and circumferential directions, disregarding the body forces and the inertia terms, are

$$\begin{aligned}\sigma_{rr,r}+\frac{1}{r}\sigma_{r\theta,\theta}+\frac{1}{r}(\sigma_{rr}-\sigma_{\theta\theta})&=0\\ \sigma_{r\theta,r}+\frac{1}{r}\sigma_{\theta\theta,\theta}+\frac{2}{r}\sigma_{r\theta}&=0.\end{aligned}\tag{4}$$

To obtain the equilibrium equations in terms of the displacement components for the functionally graded material cylinder, the functional relationship of the material properties must be known. Since the cylinder's material is assumed to be graded along the *r*-direction, the modulus of elasticity and the coefficient of thermal expansion are assumed to be described with power laws as

$$\begin{aligned}E(r)&=E_0r^{m_1}\\ \alpha(r)&=\alpha_0r^{m_2}\end{aligned}\tag{5}$$

where E_0 and α_0 are the material constants and m_1 and m_2 are the power-law indices of the material. We further assume that the Poisson's ratio is constant.

Using the relations (1) to (5), the Navier equations in term of the displacements are

$$\begin{aligned}&u_{,rr}+(m_1+1)\frac{1}{r}u_{,r}+\left(\frac{\nu m_1}{1-\nu}-1\right)\frac{1}{r^2}u+\left(\frac{1-2\nu}{2-2\nu}\right)\frac{1}{r^2}u_{,\theta\theta}\\ &\quad+\left(\frac{1}{2-2\nu}\right)\frac{1}{r}v_{,r\theta}+\left(\frac{(4+2m_1)\nu-3}{2-2\nu}\right)\frac{1}{r^2}v_{,\theta}\\ &=\frac{(1+\nu)\alpha_0}{1-\nu}((m_1+m_2)r^{m_2-1}T+r^{m_2}T_{,r})\end{aligned}\tag{6}$$

$$\begin{aligned}&v_{,rr}+(m_1+1)\frac{1}{r}v_{,r}-(m_1+1)\frac{1}{r^2}v+\left(\frac{2-2\nu}{1-2\nu}\right)\frac{1}{r^2}v_{,\theta\theta}\\ &\quad+\left(\frac{1}{1-2\nu}\right)\frac{1}{r}u_{,r\theta}+\left(\frac{3-4\nu}{1-2\nu}+m_1\right)\frac{1}{r^2}u_{,\theta}\\ &=\left(\frac{2+2\nu}{1-2\nu}\right)\alpha_0r^{m_2-1}T_{,\theta}.\end{aligned}\tag{7}$$

Heat Conduction Problem. The heat conduction equation in the steady-state condition for the two-dimensional problem in polar coordinates and the thermal boundary conditions for a functionally graded material hollow cylinder are given, respectively, as

$$T_{,rr}+\left(\frac{k'}{k}+1\right)\frac{1}{r}T_{,r}+\frac{1}{r^2}T_{,\theta\theta}=0\qquad\begin{array}{c}a\leqslant r\leqslant b\\ -\pi\leqslant\theta\leqslant+\pi\end{array}\tag{8}$$

$$\begin{aligned}C_{11}T(a,\theta)+C_{12}T_{,r}(a,\theta)&=f_1(\theta)\\ C_{21}T(b,\theta)+C_{22}T_{,r}(b,\theta)&=f_2(\theta)\end{aligned}\tag{9}$$

where $k=k(r)$ is the thermal conduction coefficient, the symbol $(')$ denotes derivative with respect to r, a, and b are the inner and outer radii of the hollow cylinder, respectively, and C_{ij} are the constant thermal parameters related to the conduction and convection coefficients. The functions $f_1(\theta)$ and $f_2(\theta)$ are known on the inner and outer radii, respectively.

We assume that the nonhomogeneous thermal conduction coefficient $k(r)$ is a power function of r as

$$k(r)=k_0r^{m_3}\tag{10}$$

where k_0 and m_3 are material parameters. Using Eqs. (8) and (10), the heat conduction equation becomes

$$T_{,rr}+(m_3+1)\frac{1}{r}T_{,r}+\frac{1}{r^2}T_{,\theta\theta}=0.\tag{11}$$

Since $T(r,\theta)$ is a periodic function of θ, it may be written in the form of complex Fourier series as

$$T(r,\theta)=\sum_{n=-\infty}^{\infty}T_n(r)e^{in\theta}\tag{12}$$

where $T_n(r)$ is the coefficient of complex Fourier series of $T(r,\theta)$ and is

$$T_n(r)=\frac{1}{2\pi}\int_{-\pi}^{\pi}T(r,\theta)e^{-in\theta}d\theta.\tag{13}$$

Substituting Eq. (12) into Eq. (11), the following equation is obtained:

$$T_n''(r)+(m_3+1)\frac{1}{r}T_n'(r)-\frac{n^2}{r^2}T_n(r)=0.\tag{14}$$

Equation (14) is the Euler equation and has solutions in the form of

$$T_n(r)=A_nr^{\beta}.\tag{15}$$

Substituting Eq. (15) into Eq. (14), the following characteristic equation is obtained:

$$\beta^2+m_3\beta-n^2=0.\tag{16}$$

The roots of Eq. (16) are

$$\beta_{n1,2}=\frac{-m_3}{2}\mp\left(\frac{m_3^2}{4}+n^2\right)^{1/2}.\tag{17}$$

Thus

$$T_n(r)=A_{n1}r^{\beta_{n1}}+A_{n2}r^{\beta_{n2}}.\tag{18}$$

Substituting Eq. (18) into Eq. (12), gives

$$T(r,\theta)=\sum_{n=-\infty}^{\infty}(A_{n1}r^{\beta_{n1}}+A_{n2}r^{\beta_{n2}})e^{in\theta}.\tag{19}$$

Using the boundary conditions (9) to determine the constants A_{n1} and A_{n2}, yields

$$\begin{aligned}&\sum_{n=-\infty}^{\infty}[(C_{11}a^{\beta_{n1}}+C_{12}\beta_{n1}a^{\beta_{n1}-1})A_{n1}+(C_{11}a^{\beta_{n2}}\\ &\quad+C_{12}\beta_{n2}a^{\beta_{n2}-1})A_{n2}]e^{in\theta}=f_1(\theta)\\ &\sum_{n=-\infty}^{\infty}[(C_{21}b^{\beta_{n1}}+C_{22}\beta_{n1}b^{\beta_{n1}-1})A_{n1}+(C_{21}b^{\beta_{n2}}\\ &\quad+C_{22}\beta_{n2}b^{\beta_{n2}-1})A_{n2}]e^{in\theta}=f_2(\theta).\end{aligned}\tag{20}$$

In Eqs. (20), the right-hand sides are the coefficients of complex Fourier series of left-hand sides as

$$
\begin{aligned}
&(C_{11}a^{\beta_{n1}}+C_{12}\beta_{n1}a^{\beta_{n1}-1})A_{n1}+(C_{11}a^{\beta_{n2}}+C_{12}\beta_{n2}a^{\beta_{n2}-1})A_{n2}\\
&\quad=\frac{1}{2\pi}\int_{-\pi}^{\pi}f_1(\theta)e^{-in\theta}d\theta\\
&(C_{21}b^{\beta_{n1}}+C_{22}\beta_{n1}b^{\beta_{n1}-1})A_{n1}+(C_{21}b^{\beta_{n2}}+C_{22}\beta_{n2}b^{\beta_{n2}-1})A_{n2}\\
&\quad=\frac{1}{2\pi}\int_{-\pi}^{\pi}f_2(\theta)e^{-in\theta}d\theta.
\end{aligned}
\tag{21}
$$

Equations (21) are a system of algebraic equations for the constant coefficients A_{n1} and A_{n2}, where the solution by Cramer's method is

$$
\begin{aligned}
A_{n1}=&\frac{1}{2\pi}\int_{-\pi}^{\pi}[(C_{21}b^{\beta_{n2}}+C_{22}\beta_{n2}b^{\beta_{n2}-1})f_1(\theta)-(C_{11}a^{\beta_{n2}}\\
&+C_{12}\beta_{n2}a^{\beta_{n2}-1})f_2(\theta)]e^{-in\theta}d\theta/(\hat{C}_1-\hat{C}_2)\\
A_{n2}=&\frac{1}{2\pi}\int_{-\pi}^{\pi}[(C_{11}a^{\beta_{n1}}+C_{12}\beta_{n1}a^{\beta_{n1}-1})f_2(\theta)-(C_{21}b^{\beta_{n1}}\\
&+C_{22}\beta_{n1}a^{\beta_{n1}-1})f_1(\theta)]e^{-in\theta}d\theta/(\hat{C}_1-\hat{C}_2)
\end{aligned}
\tag{22}
$$

where

$$
\begin{aligned}
\hat{C}_1&=(C_{11}a^{\beta_{n1}}+C_{12}\beta_{n1}a^{\beta_{n1}-1})(C_{21}b^{\beta_{n2}}+C_{22}\beta_{n2}b^{\beta_{n2}-1})\\
\hat{C}_2&=(C_{11}a^{\beta_{n2}}+C_{12}\beta_{n2}a^{\beta_{n2}-1})(C_{21}b^{\beta_{n1}}+C_{22}\beta_{n1}b^{\beta_{n1}-1}).
\end{aligned}
\tag{23}
$$

Solution of the Navier Equations. To solve the Navier equations, the displacement components $u(r,\theta)$ and $v(r,\theta)$ are expanded in the complex Fourier series as

$$
\begin{aligned}
u(r,\theta)&=\sum_{n=-\infty}^{\infty}u_n(r)e^{in\theta}\\
v(r,\theta)&=\sum_{n=-\infty}^{\infty}v_n(r)e^{in\theta}
\end{aligned}
\tag{24}
$$

where $u_n(r)$ and $v_n(r)$ are the coefficients of complex Fourier series of $u(r,\theta)$ and $v(r,\theta)$, respectively, and are

$$
\begin{aligned}
u_n(r)&=\frac{1}{2\pi}\int_{-\pi}^{\pi}u(r,\theta)e^{-in\theta}d\theta\\
v_n(r)&=\frac{1}{2\pi}\int_{-\pi}^{\pi}v(r,\theta)e^{-in\theta}d\theta.
\end{aligned}
\tag{25}
$$

Substituting Eq. (19) and Eq. (24) into Eq. (6) and Eq. (7), yields

$$
\begin{aligned}
&u_n''+(m_1+1)\frac{1}{r}u_n'+\left(\frac{\nu m_1}{1-\nu}-1-\frac{(1-2\nu)n^2}{2-2\nu}\right)\frac{1}{r^2}u_n\\
&\quad+\left(\frac{in}{2-2\nu}\right)\frac{1}{r}v_n'+in\left(\frac{(4+2m_1)\nu-3}{2-2\nu}\right)\frac{1}{r^2}v_n\\
&\quad=\frac{(1+\nu)\alpha_0}{1-\nu}[(m_1+m_2+\beta_{n1})A_{n1}r^{\beta_{n1}+m_2-1}\\
&\quad+(m_1+m_2+\beta_{n2})A_{n2}r^{\beta_{n2}+m_2-1}]
\end{aligned}
\tag{26}
$$

$$
\begin{aligned}
&v_n''+(m_1+1)\frac{1}{r}v_n'-\left(m_1+1+\frac{(2-2\nu)n^2}{1-2\nu}\right)\frac{1}{r^2}v_n+\left(\frac{in}{1-2\nu}\right)\frac{1}{r}u_n'\\
&\quad+in\left(\frac{3-4\nu}{1-2\nu}+m_1\right)\frac{1}{r^2}u_n=\frac{in(2+2\nu)\alpha_0}{1-2\nu}[A_{n1}r^{\beta_{n1}+m_2-1}\\
&\quad+A_{n2}r^{\beta_{n2}+m_2-1}].
\end{aligned}
\tag{27}
$$

Equations (26) and (27) are a system of ordinary differential equations having general and particular solutions. The general solutions are assumed as

$$
\begin{aligned}
u_n^g(r)&=Br^{\eta}\\
v_n^g(r)&=Cr^{\eta}.
\end{aligned}
\tag{28}
$$

Substituting Eqs. (28) into Eqs. (26) and (27), yields

$$
\begin{aligned}
&\left[\eta(\eta-1)+(m_1+1)\eta+\frac{\nu m_1}{1-\nu}-1-\frac{(1-2\nu)n^2}{2-2\nu}\right]B\\
&\quad+i\left[\frac{\eta}{2-2\nu}+\frac{(4+2m_1)\nu-3}{2-2\nu}\right]nC=0\\
&i\left[\frac{\eta}{1-2\nu}+\frac{3-4\nu}{1-2\nu}+m_1\right]nB+\left[\eta(\eta-1)+(m_1+1)\eta-m_1-1\right.\\
&\quad\left.-\frac{(2-2\nu)n^2}{1-2\nu}\right]C=0.
\end{aligned}
\tag{29}
$$

A nontrivial solution of Eqs. (29) is obtained as

$$
\begin{aligned}
&\left[\eta(\eta-1)+(m_1+1)\eta+\frac{\nu m_1}{1-\nu}-1-\frac{(1-2\nu)n^2}{2-2\nu}\right]\left[\eta(\eta-1)\right.\\
&\quad\left.+(m_1+1)\eta-m_1-1-\frac{(2-2\nu)n^2}{1-2\nu}\right]+n^2\left[\frac{\eta}{2-2\nu}\right.\\
&\quad\left.+\frac{(4+2m_1)\nu-3}{2-2\nu}\right]\left[\frac{\eta}{1-2\nu}+\frac{3-4\nu}{1-2\nu}+m_1\right]=0.
\end{aligned}
\tag{30}
$$

Equation (30) has four roots η_{n1} to η_{n4}. Thus, the general solutions are

$$
\begin{aligned}
u_n^g(r)&=\sum_{j=1}^{4}B_{nj}r^{\eta_{nj}}\\
v_n^g(r)&=\sum_{j=1}^{4}N_{nj}B_{nj}r^{\eta_{nj}}
\end{aligned}
\tag{31}
$$

where N_{nj} is the relation between constants B_{nj} and C_{nj} and is obtained from the first of Eq. (29) as

$$
N_{nj}=\frac{i\left[\eta_{nj}(\eta_{nj}-1)+(m_1+1)\eta_{nj}+\dfrac{\nu m_1}{1-\nu}-1-\dfrac{(1-2\nu)n^2}{2-2\nu}\right]}{n\left[\dfrac{\eta_{nj}}{2-2\nu}+\dfrac{(4+2m_1)\nu-3}{2-2\nu}\right]}
$$

$$
j=1,2,3,4. \tag{32}
$$

For isotropic materials ($m_1=0$) and for $n=1$, Eq. (30) has repeated roots and hence a solution of the form of $\ln r$ must be considered for $u_1^g(r)$ and $v_1^g(r)$.

The particular solutions $u_n^p(r)$ and $v_n^p(r)$ are assumed as

$$
\begin{aligned}
u_n^p(r)&=D_{n1}r^{\beta_{n1}+m_2+1}+D_{n2}r^{\beta_{n2}+m_2+1}\\
v_n^p(r)&=D_{n3}r^{\beta_{n1}+m_2+1}+D_{n4}r^{\beta_{n2}+m_2+1}.
\end{aligned}
\tag{33}
$$

Substituting Eqs. (33) into Eqs. (26) and (27), yields

$$
\begin{aligned}
&d_1D_{n1}r^{\beta_{n1}+m_2-1}+d_2D_{n2}r^{\beta_{n2}+m_2-1}+d_3D_{n3}r^{\beta_{n1}+m_2-1}\\
&\quad+d_4D_{n4}r^{\beta_{n2}+m_2-1}=d_5r^{\beta_{n1}+m_2-1}+d_6r^{\beta_{n2}+m_2-1}
\end{aligned}
\tag{34}
$$

$$d_7 D_{n3} r^{\beta_{n1}+m_2-1} + d_8 D_{n4} r^{\beta_{n2}+m_2-1} + d_9 D_{n1} r^{\beta_{n1}+m_2-1} + d_{10} D_{n2} r^{\beta_{n2}+m_2-1} = d_{11} r^{\beta_{n1}+m_2-1} + d_{12} r^{\beta_{n2}+m_2-1} \tag{35}$$

where constants d_1 to d_{12} are given in the Appendix. Equating the coefficients of the identical powers yields

$$\begin{aligned} d_1 D_{n1} + d_3 D_{n3} &= d_5 \\ d_9 D_{n1} + d_7 D_{n3} &= d_{11} \end{aligned} \tag{36}$$

$$\begin{aligned} d_2 D_{n2} + d_4 D_{n4} &= d_6 \\ d_{10} D_{n2} + d_8 D_{n4} &= d_{12}. \end{aligned} \tag{37}$$

Equations (36) and (37) are a system of algebraic equations, where the solution is given by the Cramer's method as

$$\begin{aligned} D_{n1} &= \frac{d_5 d_7 - d_3 d_{11}}{d_1 d_7 - d_3 d_9} \\ D_{n2} &= \frac{d_6 d_8 - d_4 d_{12}}{d_2 d_8 - d_4 d_{10}} \\ D_{n3} &= \frac{d_1 d_{11} - d_5 d_9}{d_1 d_7 - d_3 d_9} \\ D_{n4} &= \frac{d_2 d_{12} - d_6 d_{10}}{d_2 d_8 - d_4 d_{10}}. \end{aligned} \tag{38}$$

The complete solutions for $u_n(r)$ and $v_n(r)$ are the sum of the general and particular solutions and are

$$\begin{aligned} u_n(r) &= u_n^g(r) + u_n^p(r) \\ v_n(r) &= v_n^g(r) + v_n^p(r). \end{aligned} \tag{39}$$

Thus

$$\begin{aligned} u_n(r) &= \sum_{j=1}^{4} B_{nj} r^{\eta_{nj}} + D_{n1} r^{\beta_{n1}+m_2+1} + D_{n2} r^{\beta_{n2}+m_2+1} \\ v_n(r) &= \sum_{j=1}^{4} N_{nj} B_{nj} r^{\eta_{nj}} + D_{n3} r^{\beta_{n1}+m_2+1} + D_{n4} r^{\beta_{n2}+m_2+1}. \end{aligned} \tag{40}$$

For $n=0$ the coefficient N_{nj} in Eq. (32) is undefined because the system of Eqs. (26) and (27) for $n=0$ is two decoupled ordinary differential equations as

$$\begin{aligned} u_0'' + (m_1+1)\frac{1}{r}u_0' + \left(\frac{\nu m_1}{1-\nu} - 1\right)\frac{1}{r^2}u_0 = \frac{(1+\nu)\alpha_0}{1-\nu} \\ \times ((m_1+m_2+\beta_{01}) \\ A_{01} r^{\beta_{01}+m_2-1} + (m_1+m_2+\beta_{02}) A_{02} r^{\beta_{02}+m_2-1}) \end{aligned} \tag{41}$$

$$v_0'' + (m_1+1)\frac{1}{r}v_0' - (m_1+1)\frac{1}{r^2}v_0 = 0. \tag{42}$$

The solutions of Eqs. (41) and (42) are

$$\begin{aligned} u_0(r) &= \sum_{j=1}^{2} (B_{0j} r^{\eta_{0j}} + D_{0j} r^{\beta_{0j}+m_2+1}) \\ v_0(r) &= \sum_{j=3}^{4} B_{0j} r^{\eta_{0j}} \end{aligned} \tag{43}$$

where

$$\begin{aligned} \eta_{01,2} &= \frac{-m_1}{2} \mp \left(\frac{m_1^2}{4} - \frac{\nu m_1}{1-\nu} + 1\right)^{1/2} \\ \eta_{03} &= 1 \\ \eta_{04} &= -(m_1+1) \end{aligned} \tag{44}$$

$$D_{0j} = \frac{(1+\nu)(\beta_{0j}+m_1+m_2)\alpha_0 A_{0j}}{(1-\nu)\left[(\beta_{0j}+m_2+1)(\beta_{0j}+m_2) + (\beta_{0j}+m_2+1)(m_1+1) + \dfrac{\nu m_1}{1-\nu} - 1\right]} \quad j=1,2.$$

Substituting Eqs. (40) and (43) into Eq. (24) give

$$\begin{aligned} u(r,\theta) = \sum_{j=1}^{2} (B_{0j} r^{\eta_{0j}} + D_{0j} r^{\beta_{01}+m_2+1}) + \sum_{n=-\infty, n\neq 0}^{\infty} \Bigg[\sum_{j=1}^{4} B_{nj} r^{\eta_{nj}} \\ + D_{n1} r^{\beta_{n1}+m_2+1} + D_{n2} r^{\beta_{n2}+m_2+1} \Bigg] e^{in\theta} \end{aligned} \tag{45}$$

$$\begin{aligned} v(r,\theta) = \sum_{j=3}^{4} B_{0j} r^{\eta_{0j}} + \sum_{n=-\infty, n\neq 0}^{\infty} \Bigg[\sum_{j=1}^{4} N_{nj} B_{nj} r^{\eta_{nj}} \\ + D_{n3} r^{\beta_{n1}+m_2+1} + D_{n4} r^{\beta_{n2}+m_2+1} \Bigg] e^{in\theta}. \end{aligned}$$

Substituting Eqs. (45) into Eqs. (1) and (2), the strains and stresses are obtained as

$$\begin{aligned} \epsilon_{rr} = \sum_{j=1}^{2} \Bigg(\eta_{0j} B_{0j} r^{\eta_{0j}-1} + (\beta_{01}+m_2+1) D_{0j} r^{\beta_{0j}+m_2} \\ + \sum_{n=-\infty, n\neq 0}^{\infty} \Bigg[\sum_{j=1}^{4} \eta_{nj} B_{nj} r^{\eta_{nj}-1} + D_{n1}(\beta_{n1}+m_2+1) r^{\beta_{n1}+m_2} \\ + D_{n2}(\beta_{n2}+m_2+1) r^{\beta_{n2}+m_2} \Bigg] e^{in\theta} \end{aligned} \tag{46}$$

$$\begin{aligned} \epsilon_{\theta\theta} = \sum_{j=1}^{2} (B_{0j} r^{\eta_{0j}-1} + D_{0j} r^{\beta_{0j}+m_2}) + \sum_{n=-\infty, n\neq 0}^{\infty} \Bigg[\sum_{j=1}^{4} (inN_{nj} \\ + 1) B_{nj} r^{\eta_{nj}-1} + (inD_{n3} + D_{n1}) r^{\beta_{n1}+m_2} \\ + (inD_{n4} + D_{n2}) r^{\beta_{n2}+m_2} \Bigg] e^{in\theta} \end{aligned} \tag{47}$$

$$\epsilon_{r\theta}=\frac{1}{2}\Biggl((\eta_{04}-1)B_{04}r^{\eta_{04}}+\sum_{n=-\infty,n\neq 0}^{\infty}\Biggl[\sum_{j=1}^{4}(in+(\eta_{nj}-1)N_{nj})B_{nj}r^{\eta_{nj}-1}+(inD_{n1}+(\beta_{n1}+m_2)D_{n3})r^{\beta_{n1}+m_2}+(inD_{n2}+(\beta_{n2}+m_2)D_{n4})r^{\beta_{n2}+m_2}\Biggr]\Biggr)e^{in\theta} \tag{48}$$

$$\sigma_{rr}=\frac{E_0}{(1+\nu)(1-2\nu)}\Biggl(\sum_{j=1}^{2}((1-\nu)\eta_{0j}+\nu)B_{0j}r^{\eta_{0j}+m_1-1}+(\nu\beta_{0j}+\nu m_2+1-(1+\nu)\alpha_0)D_{0j}r^{\beta_{0j}+m_1+m_2}+\sum_{n=-\infty,n\neq 0}^{\infty}\Biggl[\sum_{j=1}^{4}((1-\nu)\eta_{nj}+\nu(inN_{nj}+1))B_{nj}r^{\eta_{nj}+m_1-1}+((1-\nu)(\beta_{n1}+m_2+1)D_{n1}+\nu(inD_{n3}+D_{n1})-(1+\nu)\alpha_0A_{n1})r^{\beta_{n1}+m_1+m_2}+((1-\nu)(\beta_{n2}+m_2+1)D_{n2}+\nu(inD_{n4}+D_{n2})-(1+\nu)\alpha_0A_{n2})r^{\beta_{n2}+m_1+m_2}\Biggr]\Biggr)e^{in\theta} \tag{49}$$

$$\sigma_{\theta\theta}=\frac{E_0}{(1+\nu)(1-2\nu)}\Biggl(\sum_{j=1}^{2}((1-\nu)\eta_{0j}+\nu)B_{0j}r^{\eta_{0j}+m_1-1}+\Biggl((1-\nu)(\beta_{0j}+m_2+1-(1+\nu)\alpha_0)D_{0j}r^{\beta_{0j}+m_1+m_2}+\sum_{n=-\infty,n\neq 0}^{\infty}\Biggl[\sum_{j=1}^{4}(\nu\eta_{nj}+(1-\nu)(inN_{nj}+1))B_{nj}r^{\eta_{nj}+m_1-1}+(\nu(\beta_{n1}+m_2+1)D_{n1}+(1-\nu)(inD_{n3}+D_{n1})-(1+\nu)\times\alpha_0A_{n1})r^{\beta_{n1}+m_1+m_2}+(\nu(\beta_{n2}+m_2+1)D_{n2}+(1-\nu)\times(inD_{n4}+D_{n2})-(1+\nu)\alpha_0A_{n2})r^{\beta_{n2}+m_1+m_2}\Biggr]\Biggr)e^{in\theta} \tag{50}$$

$$\sigma_{r\theta}=\frac{E_0}{(1+\nu)}\Biggl((\eta_{04}-1)B_{04}r^{\eta_{04}+m_1-1}+\sum_{n=-\infty,n\neq 0}^{\infty}\Biggl[\sum_{j=1}^{4}(in+(\eta_{nj}-1)N_{nj})B_{nj}r^{\eta_{nj}+m_1-1}+(inD_{n1}+(\beta_{n1}+m_2)D_{n3})r^{\beta_{n1}+m_1+m_2}+(inD_{n2}+(\beta_{n2}+m_2)D_{n4})r^{\beta_{n2}+m_1+m_2}\Biggr)\Biggr]e^{in\theta}. \tag{51}$$

To determine the constants B_{nj}, we may consider any general from of boundary conditions for displacements and stresses as

$$\begin{aligned}
u(a,\theta)&=g_1(\theta)\\
u(b,\theta)&=g_2(\theta)\\
v(a,\theta)&=g_3(\theta)\\
v(b,\theta)&=g_4(\theta)\\
\sigma_{rr}(a,\theta)&=g_5(\theta)\\
\sigma_{rr}(b,\theta)&=g_6(\theta)\\
\sigma_{r\theta}(a,\theta)&=g_7(\theta)\\
\sigma_{r\theta}(b,\theta)&=g_8(\theta).
\end{aligned} \tag{52}$$

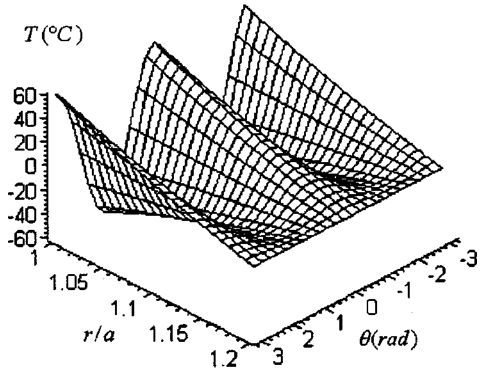

Fig. 1 Temperature distribution in the cross section of a cylinder (example 1)

It is recalled that Eqs. (45) through (51) contain four unknowns B_{n1}, B_{n2}, B_{n3}, and B_{n4}. Therefore, four boundary conditions are required to evaluate the four unknowns. These boundary conditions may be selected from the list of conditions given in Eq. (52).

Assume that the four boundary conditions are specified from the list of Eqs. (52). The boundary conditions may be either the given displacements or stresses, or combinations. Expanding the given boundary conditions in complex Fourier series gives

$$g_j(\theta)=\sum_{n=-\infty}^{\infty}G_j(n)e^{in\theta}\quad j=1,\ldots,4 \tag{53}$$

where

$$G_j(n)=\frac{1}{2\pi}\int_{-\pi}^{\pi}g_j(n)e^{-in\theta}d\theta\quad j=1,\ldots,4. \tag{54}$$

Substituting the four boundary conditions (52) with the help of Eqs. (53) in Eqs. (45), (49), and (51) the constants of integration B_{nj} are calculated.

3 Results

Consider a thick hollow cylinder of inner radius $a=1$ m and outer radius $b=1.2$ m. The Poisson's ratio is assumed 0.3 and the modulus of elasticity and the thermal coefficient of expansion of the inner radius are $E_i=200$ Gpa and $\alpha_i=1.2\times10^{-6}/°\text{C}$, respectively. For simplicity of analysis we consider the power law of material properties be the same as $\dot{m}_1=m_2=m_3=m$. To examine the proposed solution method, two example problems are considered. The first example problem may have some physical interpretation, while the second example is chosen to show the mathematical effectiveness of the proposed method.

As the first example, consider a thick hollow cylinder where the inside boundary is traction-free with given temperature distribution $T(a,\theta)=60\cos 2\theta$°C. The outside boundary is assumed to be radially fixed with zero temperature. Therefore, the assumed boundary conditions yield $\sigma_{rr}(a,\theta)=0$, $\sigma_{r\theta}(a,\theta)=0$, $u(b,\theta)=0$ and $v(b,\theta)=0$. The thermal boundary conditions are substituted in Eq. (19) to obtain the temperature distribution, where the constants of integration are obtained from Eqs. (22). In general, the displacement and stress boundary conditions are substituted in Eqs. (52), and with proper function expansions (53), the constant coefficients of the series expansion are obtained from Eq. (54).

Figure 1 shows the temperature distribution in the wall thickness along the radius and circumferential directions. Figure 2 shows the resulting thermoelastic radial displacement due to the given temperature variations. The resulting circumferential displacement v is shown in Fig. 3. It is noted that, due to the assumed boundary conditions, the u and v-displacements are zero at $r=b$, and follow the pattern of the temperature distribution at the inside surface at $r/a=1$. Figures 4, 5, and 6 show the distribution

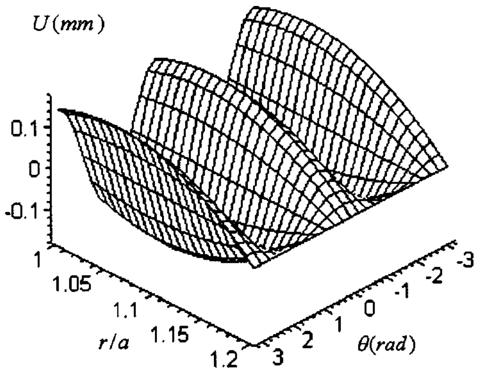

Fig. 2 Radial displacement in the cross section of a cylinder (example 1)

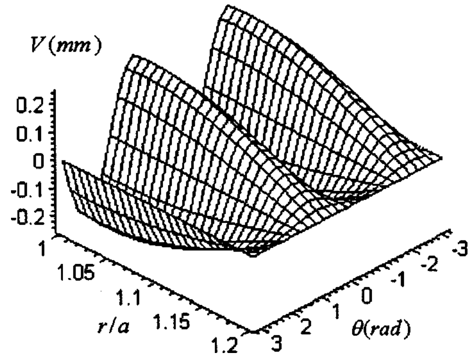

Fig. 3 Circumferential displacement in the cross section of a cylinder (example 1)

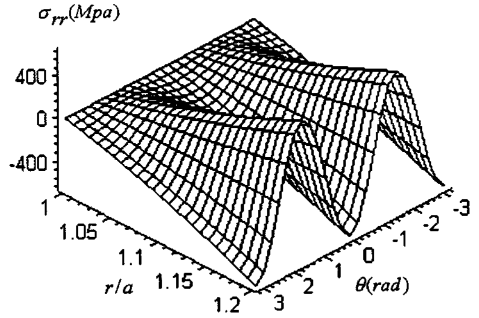

Fig. 4 Radial thermal stress in the cross section of a cylinder (example 1)

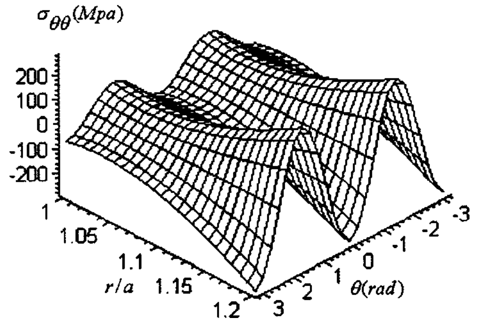

Fig. 5 Hoop thermal stress in the cross section of a cylinder (example 1)

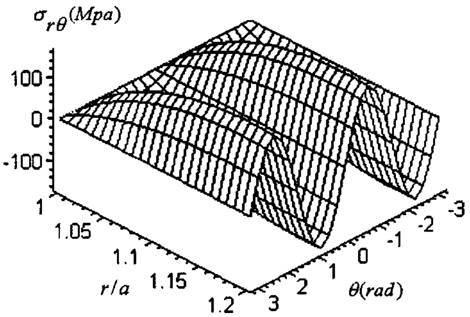

Fig. 6 Shear thermal stress in the cross section of a cylinder (example 1)

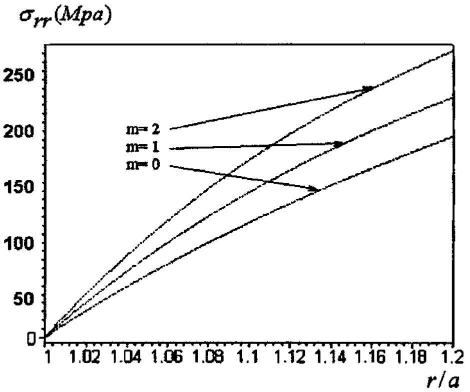

Fig. 7 Radial distribution of radial thermal stress σ_{rr} at $\theta=\pi/3$ (example 1)

of the radial, circumferential, and the shear thermal stresses in the cross section of the cylinder. It is interesting to see that all components of stresses follow a harmonic pattern on the outside surface. The radial and shear stresses are zero at the insider surface, due to the assumed boundary conditions. The effect of the power-law index on the distribution of the radial thermal stress is shown in Fig. 7. This figure is the plot of σ_{rr} versus r/a at $\theta=\pi/3$. It is shown as m increases, the radial thermal stress is increased.

As the second example, a thick-walled cylinder may be assumed with zero temperature distribution ($T(a,\theta)=0$ and $T(b,\theta)=0$), but exposed to mechanical boundary conditions. The stress and displacement boundary conditions are assumed to by

$$\begin{gathered}\sigma_{rr}(a,\theta)=400\sin\left(\frac{\theta^2}{4}-\theta\right)\ \text{MPa}\\ \sigma_{r\theta}(a,\theta)=50\theta^2\cos\theta\ \text{MPa}\\ u(b,\theta)=0\end{gathered}\tag{55}$$

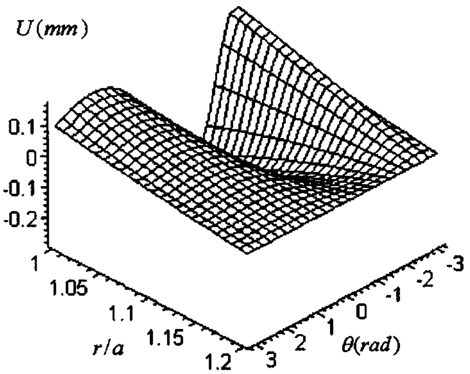

Fig. 8 Radial displacement in the cross section of a cylinder (example 2)

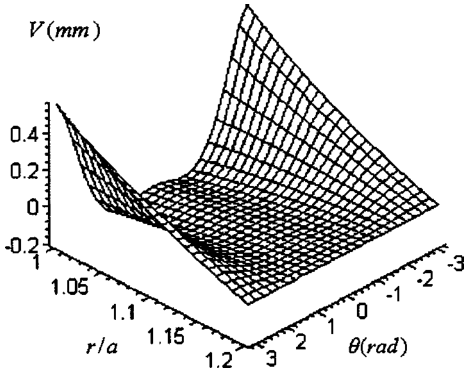

Fig. 9 Circumferential displacement in the cross section of a cylinder (example 2)

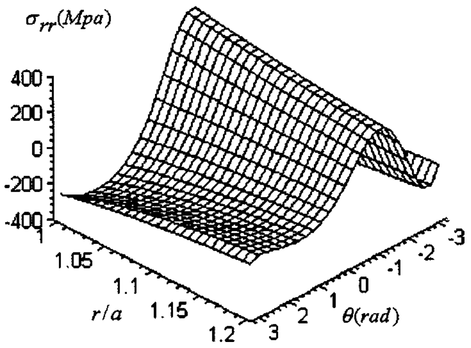

Fig. 10 Radial mechanical stress in the cross section of a cylinder (example 2)

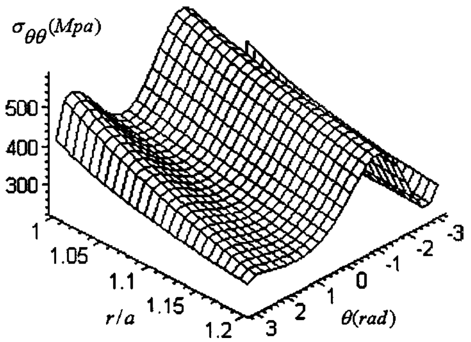

Fig. 11 Hoop mechanical stress in the cross section of a cylinder (example 2)

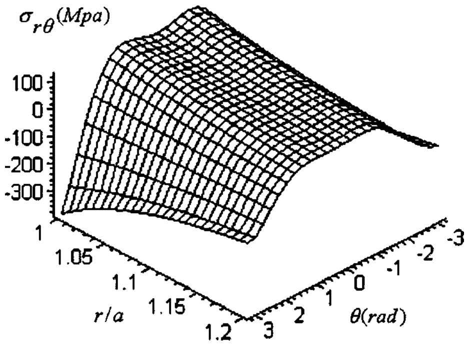

Fig. 12 Shear mechanical stress in the cross section of a cylinder (example 2)

The reason to select such boundary conditions is to examine the mathematical strength of the proposed method. These types of boundary conditions may not be handled with the potential function method. It is examined that series expansion of Eq. (54) rapidly converge after 31 number of terms. Therefore, in the calculations and plotting the figures, 31 terms of each series are considered.

Using Eqs. (52) to (54), the boundary conditions given in Eqs. (55) are expanded by the integral series and the unknown coefficients B_{nj} are determined. Figures 8 and 9 show the radial and circumferential displacements in the cross section of the cylinder. According to the boundary conditions, $u=v=0$ at $r=b$. At the inside surface $r=a$, u, and v are harmonically varying. The stress distributions are shown in Figs. 10–12. Stress patterns in inside and outside surfaces follow harmonic patterns. The given harmonic boundary conditions for σ_{rr} and $\sigma_{r\theta}$ at $r=a$, have general influence on the pattern of stress distributions in the cylinder's cross section, as seen from Figs. 10 through 12.

4 Conclusions

This paper presents the analytical solution for the nonaxisymmetric thermal and mechanical stresses in a thick hollow cylinder made of functionally graded material. The method of solution is based on the direct method and uses power series, rather than the potential function method. The advantage of this method over the potential function method is its generality and mathematical power to handle any type of the mechanical and thermal boundary conditions. It is to be emphasized that the proposed method does not have the mathematical limitations to handle the general types of boundary conditions which are usually countered in the potential function method.

Appendix

The constants d_j defined in Eqs. (34) and (35) are given as

$$\begin{aligned}
d_1&=(\beta_{n1}+m_2+1)(\beta_{n1}+m_2)+(m_1+1)(\beta_{n1}+m_2+1)\\
&\quad+\frac{\nu m_1}{1-\nu}-1-\frac{(1-2\nu)n^2}{2-2\nu}\\
d_2&=(\beta_{n2}+m_2+1)(\beta_{n2}+m_2)+(m_1+1)(\beta_{n2}+m_2+1)\\
&\quad+\frac{\nu m_1}{1-\nu}-1-\frac{(1-2\nu)n^2}{2-2\nu}\\
d_3&=in\left(\frac{\beta_{n1}+m_2+1}{2-2\nu}+\frac{(4+2m_1)\nu-3}{2-2\nu}\right)\\
d_4&=in\left(\frac{\beta_{n2}+m_2+1}{2-2\nu}+\frac{(4+2m_1)\nu-3}{2-2\nu}\right)\\
d_5&=\frac{(1+\nu)(m_1+m_2+\beta_{n1})\alpha_0A_{n1}}{1-\nu}\\
d_6&=\frac{(1+\nu)(m_1+m_2+\beta_{n2})\alpha_0A_{n2}}{1-\nu}\\
d_7&=(\beta_{n1}+m_2+1)(\beta_{n1}+m_2)+(m_1+1)(\beta_{n1}+m_2+1)\\
&\quad-m_1-1-\frac{(2-2\nu)n^2}{1-2\nu}\\
d_8&=(\beta_{n2}+m_2+1)(\beta_{n2}+m_2)+(m_1+1)(\beta_{n2}+m_2+1)\\
&\quad-m_1-1-\frac{(2-2\nu)n^2}{1-2\nu}
\end{aligned}\tag{56}$$

$$d_9 = in\left(\frac{\beta_{n1}+m_2+1}{1-2\nu}+\frac{3-4\nu}{1-2\nu}+m_1\right)$$

$$d_{10} = in\left(\frac{\beta_{n2}+m_2+1}{1-2\nu}+\frac{3-4\nu}{1-2\nu}+m_1\right)$$

$$d_{11} = \frac{in(2+2\nu)\alpha_0 A_{n1}}{1-2\nu}$$

$$d_{12} = \frac{in(2+2\nu)\alpha_0 A_{n2}}{1-2\nu}.$$

References

[1] Lutz, M. P., and Zimmerman, R. W., 1996, ''Thermal Stresses and Effective Thermal Expansion Coefficient of a Functionally Graded Sphere,'' J. Therm. Stresses, **19**, pp. 39–54.

[2] Zimmerman, R. W., and Lutz, M. P., 1999, ''Thermal Stress and Thermal Expansion in a Uniformly Heated Functionally Graded Cylinder,'' J. Therm. Stresses, **22**, pp. 177–188.

[3] Ootao, Y., Fukuda, T., and Tanigawa, Y., 1989, ''Transient Thermal Stress Analysis of a Multi-Layered Composite Laminate Cylinder and Its Analytical Extension of Non-Homogeneous Materials,'' Theor Appl. Mech., **38**, pp. 177–188.

[4] Ootao, Y., Tanigawa, Y., and Fukuda, T., 1991, ''Axisymmetric Transient Thermal Stress Analysis of a Multilayered Composite Hollow Cylinder,'' J. Therm. Stresses, **14**, pp. 201–213.

[5] Ootao, Y., Akai, T., and Tanigawa, Y., 1993, ''Three-Dimensional Transient Thermal Stress of Analysis Nonhomogeneous Circular Cylinder,'' Transationcs. JSME, , **59**, pp. 1684–1690 (in Japanese).

[6] Ootao, Y., Akai, T., and Tanigawa, Y., 1995, ''Three-Dimensional Transient Thermal Stress Analysis of a Nonhomogeneous Hollow Circular Cylinder due to a Moving Heat Source in the Axial Direction,'' J. Therm. Stresses, **18**, pp. 497–512.

[7] Ootao, Y., Tanigawa, Y., and Murakami, H., 1999, ''Transient Thermal Stress and Deformation of a Laminated Composite Beam Due to Partially Distributed Heat Supply,'' J. Therm. Stresses, **13**, pp. 193–206.

[8] Han, X., Liu, G. R., and Lam, K. Y., 2000, ''A Quadratic Layer Element For Analyzing Stress Waves in FGMs and Its Application in Material Characterization,'' J. Sound Vib., **236**(2), pp. 307–321.

[9] Han, X., Liu, G. R., and Lam, K. Y., 2001, ''Transient Waves in Plates of Functionally Graded Materials,'' Int. J. Numer. Methods Eng., **52**, pp. 851–865.

[10] Obata, Y., and Noda, N., 1993, ''Transient Thermal Stress in a Plate of Functionally Gradient Materials,'' Ceramic Transactions, **34**, p. 403.

[11] Obata, Y., and Noda, N., 1995, ''Transient Thermal Stresses in a Hollow Sphere of Functionally Gradient Material,'' *Proceedings of Thermal Stresses*, Shizuola University Press, Hamamatsu, Japan, pp. 335–338.

[12] Obata, Y., and Noda, N., 1997, ''Two-Dimensional Unsteady Thermal Stresses in a Partially Heated Plate Made of Functionally Graded Material,'' *Proceedings of Thermal Stresses*, Rochester Institute of Technology, Rochester, New York, pp. 735–738.

[13] Obata, Y., Kanayama, K., Ohji, T., and Noda, N., 1999, ''Two-Dimensional Unsteady Thermal Stresses in a Partially Heated Circular Cylinder Made of Functionally Graded Material,'' *Proceedings of Thermal Stresses*, Pub. Branti Zew, Krakow, Poland, pp. 595–598.

[14] Tanigawa, Y., Morishita, H., and Ogaki, S., 1999, ''Derivation of Systems of Fundamental Equations for a Three-Dimensional Thermoelastic Field With Nonhomogeneous Material Properties and Its Application to a Semi-Infinite Body,'' J. Therm. Stresses, **22**, pp. 689–711.

[15] Tanigawa, Y., Ootao, Y., and Kawamura, R., 1991, ''Thermal Bending of Laminated Composite Rectangular Plates and Nonhomogeneous Plates due to Partial Heating,'' J. Therm. Stresses, **14**, pp. 285–308.

W.-C. Xie
Professor,
Solid Mechanics Division,
Faculty of Engineering,
University of Waterloo,
Waterloo ON N2L 3G1, Canada
e-mail: xie@uwaterloo.ca

Localization of Vibration Propagation in Two-Dimensional Systems With Multiple Substructural Modes

Localization of vibration propagation in randomly disordered weakly coupled two-dimensional cantilever-mesh-spring arrays, in which multiple substructural modes are considered for each cantilever, is studied in this paper. A method of regular perturbation for a linear algebraic system is applied to determine the localization factors, which are defined in terms of the angles of orientation and characterize the average exponential rates of growth or decay of the amplitudes of vibration in the given directions. Iterative formulations are derived to determine the amplitudes of vibration of the cantilevers. In the diagonal directions, a transfer matrix formulation is obtained. For a given direction of orientation, the localization behavior is similar to that of a one-dimensional cantilever-spring-mesh chain. The effect of the stiffnesses and the disorder in the stiffnesses of the cantilevers on the localization behavior of the system is investigated.
[DOI: 10.1115/1.1507766]

1 Introduction

In engineering applications, there are many structures, such as long satellite antennae or space trusses used in space solar power stations, which are designed to be composed of identically constructed elements assembled end-to-end to form a spatially periodic structure. When analyzing the vibration of these large space structures, they have been traditionally treated as perfectly periodic structures. However, due to defects in manufacture and assembly, these nominally periodic structures can never be perfectly periodic but are in reality randomly disordered. The vibrational behavior of a disordered periodic structure can be significantly different from that of a perfectly periodic structure. For a perfectly periodic structure, the vibration modes are of wavy shapes and extend throughout the structure; whereas, when a structure is disordered, vibration is confined to a small region with the amplitudes decaying exponentially away from the center. The average exponential rate at which the amplitudes of vibration decay is the localization factor.

For one-dimensional monocoupled structures, the transfer matrices are of dimension 2×2, and Furstenberg's theorem [1] for products of random matrices may be applied to determine the localization factors. For multicoupled structures, the dimension of the transfer matrices is higher than 2×2; the multiplicative ergodic theorem of Oseledec [2] has to be employed to obtain the localization factors. The localization factor is related to the smallest positive Lyapunov exponent for the corresponding discrete dynamical system. A one-dimensional monocoupled structure may be regarded as a special case of a multicoupled structure in which there is only one positive Lyapunov exponent. Since the smallest Lyapunov exponent is also the largest for monocoupled structures, the determination of the localization factors is much easier. The method of Green's function ([3,4]) may also be employed to determine the localization factors for both monocoupled and multicoupled one-dimensional structures.

For localization problems in the context of structural dynamics, much work has been done during the past two decades in both theory and experiments. However, because of the inapplicability of the methods of transfer matrix and Green's function, which are formulated for one-dimensional systems, to higher-dimensional systems in their current formulations, the degree of difficulty, and the amount of computation involved in studying higher-dimensional systems, most of the research work on localization in structural dynamics has been restricted to one-dimensional structures. Detailed reviews of literature on localization in one-dimensional systems may be found in the papers and references in the special issue on *Localization Problems in Engineering* [5].

In engineering applications, there are many structures, such as large floor systems of shopping malls and airport terminals, which should be realistically modeled as large plates stiffened in two orthogonal directions, i.e., two-dimensional disordered periodic structures. It is therefore of practical importance to study in detail the localization behavior of disordered two-dimensional periodic systems. However, because of the complexity of mathematical modelling and analysis of large realistic two-dimensional disordered periodic engineering structures, to obtain some general knowledge on the localization behavior of disordered two-dimensional systems, simple models of two-dimensional cantilever-mesh-spring arrays have been considered, which can be studied using elegant analytical approaches.

In an earlier study ([6]), the free-vibration mode localization in two-dimensional cantilever-spring arrays with single substructural mode was investigated. This was the first publication on vibration mode location of two-dimensional structures in the context of structural dynamics. A regular perturbation method for a linear eigenvalue problem was applied to obtain the amplitudes of vibration of the cantilevers and a first-order approximation of the localization factors, which were defined in terms of the angles of orientation and characterized the exponential rates of growth or decay of amplitudes of vibration in the given directions. When plotted in the logarithmic scale, the vibration modes were of hill shape with the amplitudes of vibration decaying linearly away from the cantilever at which vibration was originated. The results

---

Contributed by the Applied Mechanics Division of THE AMERICAN SOCIETY OF MECHANICAL ENGINEERS for publication in the ASME JOURNAL OF APPLIED MECHANICS. Manuscript received by the ASME Applied Mechanics Division, August 6, 2001; final revision, April 3, 2002. Associate Editor: O. O'Reilly. Discussion on the paper should be addressed to the Editor, Prof. Robert M. McMeeking, Department of Mechanical and Environmental Engineering, University of California–Santa Barbara, Santa Barbara, CA 93106-5070, and will be accepted until four months after final publication of the paper itself in the ASME JOURNAL OF APPLIED MECHANICS.

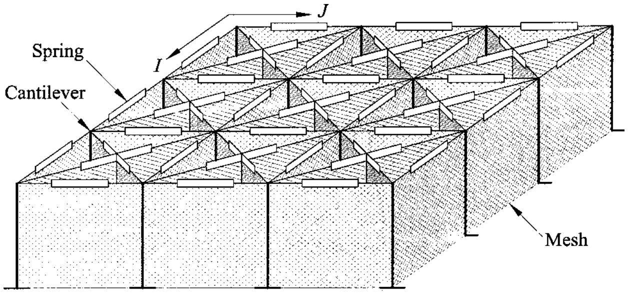

Fig. 1 Two-dimensional cantilever-mesh-spring array

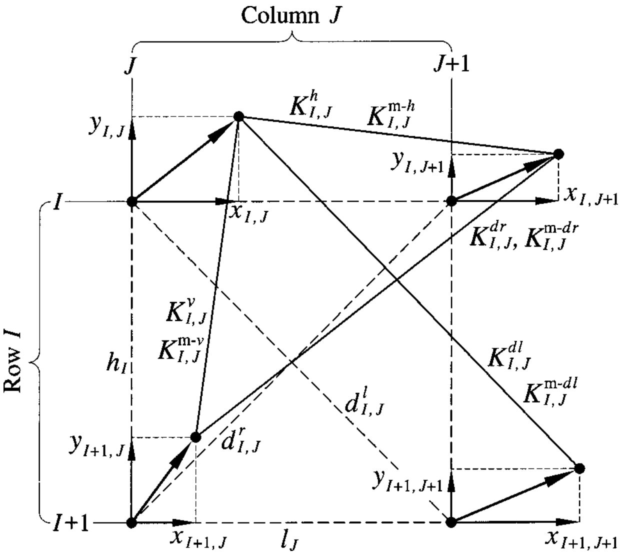

Fig. 2 Parameters and displacements of a two-dimensional cantilever-mesh-spring array

presented in [6] were extended in [7] to the free-vibration mode localization in two-dimensional cantilever-mesh-spring arrays with multiple substructural modes, in which multiple substructural modes are considered for each cantilever.

In Ref. [8], a method of regular perturbation for a linear algebraic system was applied to study localization of vibration propagation in randomly disordered weakly coupled two-dimensional cantilever-spring arrays with a single substructural mode under external harmonic excitations.

In this paper, the work presented in [8] is extended to study localization in vibration propagation in two-dimensional cantilever-mesh-spring arrays with multiple substructural modes, which is a more realistic model of engineering structures, although simplified. Employing a method of regular perturbation for a linear algebraic system in the block matrix form, first-order approximations of the localization factors are obtained.

For a two-dimensional system with a single substructural mode, when the mean values of stiffness of the cantilevers in the x and y-directions are the same, there is only one frequency passband; whereas when they are different, there are two frequency passbands. On the other hand, for a two-dimensional system with S substructural modes, depending on the average values of stiffness of the cantilevers in the x and y-directions, the possible number of frequency passbands is between S and $2S$ with various possible combinations. Therefore, there are many properties of vibration propagation localization for systems with multiple substructural modes that are not observable for systems with a single substructural mode. The objective of this research is to obtain some general knowledge on the localization behavior of vibration propagation in disordered two-dimensional structures using a simplified model.

2 Perturbation Formulation for Vibration Localization

2.1 Equations of Motion. Consider the forced vibration of a two-dimensional cantilever-mesh-spring array as shown in Fig. 1. The system is subjected to harmonic exciting forces $F_0^x e^{i\omega t}$ and $F_0^y e^{i\omega t}$ in the x and y-directions, respectively, applied at the tip of the (I_0,J_0)th cantilever. Each cantilever of length L is connected to its eight neighboring cantilevers by massless meshes and linear springs located at height H. The parameters and displacements of the cantilever-mesh-spring array are shown in Fig. 2. The numbers of columns and rows of cantilevers in the array are N_H and N_V, respectively.

If S substructural modes are considered for each cantilever, the x and y components of the displacement of the (I,J)th cantilever are, respectively,

$$x_{I,J}(z,t)=\mathbf{a}^T_{I,J}(t)\boldsymbol{\phi}(z),\quad y_{I,J}(z,t)=\mathbf{b}^T_{I,J}(t)\boldsymbol{\phi}(z),$$

$$\mathbf{a}_{I,J}(t)=\{a^1_{I,J}(t),\ \ldots,a^S_{I,J}(t)\}^T,$$

$$\mathbf{b}_{I,J}(t)=\{b^1_{I,J}(t),\ \ldots,b^S_{I,J}(t)\}^T,$$

$$\boldsymbol{\phi}(z)=\{\phi_1(z),\ \ldots,\phi_S(z)\}^T,$$

where $\phi_\alpha(z)$, $\alpha=1,\ldots,S$, is the αth normal mode shape of a cantilever given by

$$\phi_\alpha(z)=\cosh\hat{\beta}_\alpha\zeta-\cos\hat{\beta}_\alpha\zeta-\hat{\alpha}_\alpha(\sinh\hat{\beta}_\alpha\zeta-\sin\hat{\beta}_\alpha\zeta),\qquad \zeta=\frac{z}{L}.$$

For the first three cantilever modes, the parameters are $\hat{\alpha}_1=0.73410$, $\hat{\alpha}_2=1.01847$, $\hat{\alpha}_3=0.99922$, $\hat{\beta}_1=1.87510$, $\hat{\beta}_2=4.69409$, $\hat{\beta}_3=7.85476$.

Following [7], the total kinetic energy of the cantilever-mesh-spring array is

$$T=\sum_{I=1}^{N_V}\sum_{J=1}^{N_H}\frac{m_{I,J}}{2}\int_0^L\{[\dot{\mathbf{a}}^T_{I,J}(t)\boldsymbol{\phi}(z)]^2+[\dot{\mathbf{b}}^T_{I,J}(t)\boldsymbol{\phi}(z)]^2\}dz,\tag{1}$$

where $m_{I,J}$ is the mass per unit length of cantilever (I,J). The potential energy due to bending of the cantilevers is

$$V_C=\sum_{I=1}^{N_V}\sum_{J=1}^{N_H}\left\{\frac{EI^x_{I,J}}{2}\int_0^L[\mathbf{a}^T_{I,J}(t)\boldsymbol{\phi}''(z)]^2dz+\frac{EI^y_{I,J}}{2}\int_0^L[\mathbf{b}^T_{I,J}(t)\boldsymbol{\phi}''(z)]^2dz\right\},\tag{2}$$

where $EI^x_{I,J}$ and $EI^y_{I,J}$ are the flexural rigidities of the (I,J)th cantilever in the x and y-directions, respectively.

Considering only small deformations, the potential energy due to the extensions of the springs is

$$V_S=\sum_{I=1}^{N_V}\sum_{J=1}^{N_H}\frac{1}{2}[K^h_{I,J}(\Delta^h_{I,J})^2+K^v_{I,J}(\Delta^v_{I,J})^2+K^{dl}_{I,J}(\Delta^{dl}_{I,J})^2+K^{dr}_{I,J}(\Delta^{dr}_{I,J})^2],\tag{3}$$

where $\Delta^h_{I,J}$, $\Delta^v_{I,J}$, $\Delta^{dl}_{I,J}$, and $\Delta^{dr}_{I,J}$ are the extensions of the horizontal spring $K^h_{I,J}$, vertical spring $K^v_{I,J}$, and diagonal springs $K^{dl}_{I,J}$ and $K^{dr}_{I,J}$, respectively. The potential energy due to the extensions of the meshes is

$$V_M=\sum_{I=1}^{N_V}\sum_{J=1}^{N_H}\frac{1}{2}\left\{K_{I,J}^{m\text{-}h}\int_0^L[\Delta_{I,J}^{m\text{-}h}(z,t)]^2dz\right.$$
$$+K_{I,J}^{m\text{-}v}\int_0^L[\Delta_{I,J}^{m\text{-}v}(z,t)]^2dz+K_{I,J}^{m\text{-}dl}\int_0^L[\Delta_{I,J}^{m\text{-}dl}(z,t)]^2dz$$
$$\left.+K_{I,J}^{m\text{-}dr}\int_0^L[\Delta_{I,J}^{m\text{-}dr}(z,t)]^2dz\right\}, \tag{4}$$

where $\Delta_{I,J}^{m\text{-}h}(z,t)$ is the extension of the horizontal mesh on line I and in column J, $\Delta_{I,J}^{m\text{-}v}(z,t)$ is the extension of the vertical mesh in row I and on line J, $\Delta_{I,J}^{m\text{-}dl}(z,t)$ and $\Delta_{I,J}^{m\text{-}dr}(z,t)$ are the extensions of the left and right-slanting meshes in panel I,J, respectively, and $K_{I,J}^{m\text{-}h}$, $K_{I,J}^{m\text{-}v}$, $K_{I,J}^{m\text{-}dl}$, $K_{I,J}^{m\text{-}dr}$ are the normal stiffnesses per unit length of the corresponding meshes.

The Lagrange's equations of motion are, for $I=1,\ldots,N_V$ and $J=1,\ldots,N_H$,

$$\frac{d}{dt}\left(\frac{\partial T}{\partial \dot{\mathbf{a}}_{I,J}}\right)+\frac{\partial V}{\partial \mathbf{a}_{I,J}}=\mathbf{R}_{I,J}^x,\quad \frac{d}{dt}\left(\frac{\partial T}{\partial \dot{\mathbf{b}}_{I,J}}\right)+\frac{\partial V}{\partial \mathbf{b}_{I,J}}=\mathbf{R}_{I,J}^y, \tag{5}$$

where V is the total potential energy given by $V=V_C+V_S+V_M$, $\mathbf{R}_{I_0,J_0}^x=e^{i\omega t}F_0^x\boldsymbol{\phi}(L)$, $\mathbf{R}_{I_0,J_0}^y=e^{i\omega t}F_0^y\boldsymbol{\phi}(L)$, and $\mathbf{R}_{I,J}^x=\mathbf{R}_{I,J}^y=\mathbf{0}$, for all $I\neq I_0$, $J\neq J_0$.

Substituting Eqs. (1)–(4) into Eqs. (5) results in the equations of motion for forced vibration of the cantilever-mesh-spring array:

$$\mathbf{M}\ddot{\mathbf{x}}+\mathbf{K}\mathbf{x}=\mathbf{F}e^{i\omega t}, \tag{6}$$

in which $\mathbf{M}$ is the mass matrix, $\mathbf{K}$ is the stiffness matrix, and the displacement vector $\mathbf{x}$ and the load vector $\mathbf{F}$ are given by

$$\mathbf{x}=\{\mathbf{a}_{1,1}^T,\mathbf{b}_{1,1}^T;\mathbf{a}_{1,2}^T,\mathbf{b}_{1,2}^T;\ldots;\mathbf{a}_{N_V,N_H}^T,\mathbf{b}_{N_V,N_H}^T\}^T,$$

$$\mathbf{F}=\{\mathbf{0}^T,\mathbf{0}^T;\ldots;\mathbf{0}^T,\mathbf{0}^T;F_0^x\boldsymbol{\phi}^T(L),F_0^y\boldsymbol{\phi}^T(L);\mathbf{0}^T,\mathbf{0}^T;\ldots;\mathbf{0}^T,\mathbf{0}^T\}^T.$$

To nondimensionalize Eq. (6), let

$$\mathbf{x}=L\sqrt{m}\mathbf{M}^{-1/2}\hat{\mathbf{x}}e^{i\omega t},\quad \overline{\mathbf{f}}=\frac{1}{\omega_0^2\sqrt{L^3m}}\mathbf{M}^{-1/2}\mathbf{F},\quad \omega_0^2=\frac{EI^x}{mL^4},$$

where m and EI^x are the average values of the mass densities $m_{I,J}$ and the flexural rigidities $EI_{I,J}^x$ of cantilevers, respectively.

Transform the nodal coordinates (I,J) to the global coordinates i using the following relationships as in Ref. [6]:

$$i=\left\{\begin{array}{ll}2(I-1)N_H+2J-1, & \text{for } x\text{-direction}\\ 2(I-1)N_H+2J, & \text{for } y\text{-direction}\end{array}\right\}\Leftrightarrow$$
$$I=\text{int}\left(\frac{i-1}{2N_H}\right)+1,\ J=\text{int}\left(\frac{i+1}{2}\right)+1.$$

Without loss of generality, it may be assumed that i is an odd number and it corresponds to the x-direction; hence $i+1$ is an even number and it corresponds to the y-direction. Letting $\overline{\mathbf{u}}_i=\hat{\mathbf{a}}_{I,J}$, $\overline{\mathbf{u}}_{i+1}=\hat{\mathbf{b}}_{I,J}$, the nondimensional displacement vector $\hat{\mathbf{x}}$ becomes $\overline{\mathbf{u}}$, where

$$\overline{\mathbf{u}}=\{\overline{\mathbf{u}}_1^T,\overline{\mathbf{u}}_2^T;\ldots;\overline{\mathbf{u}}_{2N_HN_V-1}^T,\overline{\mathbf{u}}_{2N_HN_V}^T\}^T,\quad \overline{\mathbf{u}}_i=\{\overline{u}_{i1},\ldots,\overline{u}_{iS}\}^T,$$

and the nondimensional load vector becomes

$$\overline{\mathbf{f}}=\{\mathbf{0}^T,\mathbf{0}^T;\ldots;\mathbf{0}^T,\mathbf{0}^T;\mathbf{f}_j^T,\mathbf{f}_{j+1}^T;\mathbf{0}^T,\mathbf{0}^T;\ldots;\mathbf{0}^T,\mathbf{0}^T\}^T, \tag{7}$$

where the global coordinates j and $j+1$ correspond to the (I_0,J_0)th cantilever, and

$$\mathbf{f}_j=\overline{f}_x\frac{1}{2}\boldsymbol{\phi}(L),\quad \mathbf{f}_{j+1}=\overline{f}_y\frac{1}{2}\boldsymbol{\phi}(L),\quad \overline{f}_x=\frac{F_0^x}{f_0},\quad \overline{f}_y=\frac{F_0^y}{f_0},$$

$$f_0=\frac{EI^x}{2L^2}\sqrt{\frac{m_{I_0,J_0}}{m}},$$

where $\frac{1}{2}\boldsymbol{\phi}(L)$ is a vector of dimension S give by $(1,-1,1,-1,\ldots)^T$.

The equations of motion become

$$\overline{\mathbf{A}}\overline{\mathbf{u}}=\overline{\mathbf{f}}, \tag{8}$$

where $\overline{\mathbf{A}}=\omega_0^{-2}\mathbf{M}^{-1/2}\mathbf{K}\mathbf{M}^{-1/2}-\nu\mathbf{I}$, $\nu=\omega^2/\omega_0^2$.

For simplicity of presentation, assume that there is no disorder in the geometry of the array, the mass densities of the cantilevers, the meshes and springs connecting the cantilevers, and denote $\hat{K}_{I,J}^h=k^h$, $\hat{K}_{I,J}^v=k^v$, $\hat{K}_{I,J}^{dl}=\hat{K}_{I,J}^{dr}=2k^d$, $\hat{K}_{I,J}^{m\text{-}h}=\kappa^h$, $\hat{K}_{I,J}^{m\text{-}v}=\kappa^v$, $\hat{K}_{I,J}^{m\text{-}dl}=\hat{K}_{I,J}^{m\text{-}dr}=2\kappa^d$, for all values of I, J, in which $\hat{K}_{I,J}^{\text{dir}}=K_{I,J}^{\text{dir}}/(EI^x/L^3)$, $\hat{K}_{I,J}^{\text{m-dir}}=LK_{I,J}^{\text{m-dir}}/(EI^x/L^3)$, where "dir" is h, v, dl, dr. The only sources of disorder are the bending stiffnesses of the cantilevers in both x and y-directions denoted as $k_i^x=EI_{I,J}^x/EI^x$ and $k_{i+1}^y=EI_{I,J}^y/EI^x$.

Therefore, in the block form, matrix $\overline{\mathbf{A}}=[\overline{\mathbf{A}}_{k,l}]$, in which there are $2N_HN_V$ block rows and block columns, respectively, and each block is of dimension $S\times S$. The nonzero block elements in the ith block row (corresponding to the x-direction) are

$$\begin{aligned}\overline{\mathbf{A}}_{i,i}&=k_i^x\hat{\boldsymbol{\beta}}^4+(2k^h+4k^d)\boldsymbol{\Phi}_H+(2\kappa^h+4\kappa^d-\nu)\mathbf{I},\\ \overline{\mathbf{A}}_{i,i-2}&=\overline{\mathbf{A}}_{i,i+2}=-(k^h\boldsymbol{\Phi}_H+\kappa^h\mathbf{I}),\\ \overline{\mathbf{A}}_{i,i-2N_H-2}&=-\overline{\mathbf{A}}_{i,i-2N_H-1}=\overline{\mathbf{A}}_{i,i-2N_H+2}=\overline{\mathbf{A}}_{i,i-2N_H+3}\\ &=\overline{\mathbf{A}}_{i,i+2N_H-2}=\overline{\mathbf{A}}_{i,i+2N_H-1}=\overline{\mathbf{A}}_{i,i+2N_H+2}\\ &=-\overline{\mathbf{A}}_{i,i+2N_H+3}=-(k^d\boldsymbol{\Phi}_H+\kappa^d\mathbf{I}),\end{aligned} \tag{9}$$

and the nonzero block elements in the $(i+1)$th block row (corresponding to the y-direction) are

$$\begin{aligned}\overline{\mathbf{A}}_{i+1,i+1}&=k_{i+1}^y\hat{\boldsymbol{\beta}}^4+(2k^v+4k^d)\boldsymbol{\Phi}_H+(2\kappa^v+4\kappa^d-\nu)\mathbf{I},\\ \overline{\mathbf{A}}_{i+1,i-2N_H+1}&=\overline{\mathbf{A}}_{i+1,i+2N_H+1}=-(k^v\boldsymbol{\Phi}_H+\kappa^v\mathbf{I}),\\ -\overline{\mathbf{A}}_{i+1,i-2N_H-2}&=\overline{\mathbf{A}}_{i+1,i-2N_H-1}=\overline{\mathbf{A}}_{i+1,i-2N_H+2}=\overline{\mathbf{A}}_{i+1,i-2N_H+3}\\ &=\overline{\mathbf{A}}_{i+1,i+2N_H-2}=\overline{\mathbf{A}}_{i+1,i+2N_H-1}=-\overline{\mathbf{A}}_{i+1,i+2N_H+2}\\ &=\overline{\mathbf{A}}_{i+1,i+2N_H+3}=-(k^d\boldsymbol{\Phi}_H+\kappa^d\mathbf{I}),\end{aligned} \tag{10}$$

where $\hat{\boldsymbol{\beta}}^4=\text{diag}\{\hat{\beta}_1^4,\ldots,\hat{\beta}_S^4\}$, $\boldsymbol{\Phi}_H=\boldsymbol{\phi}(H)\boldsymbol{\phi}^T(H)$. For the case when $S=3$ and $H=L$,

$$\hat{\boldsymbol{\beta}}^4=\text{diag}\{12.36236,\ 485.51882,\ 3806.54627\},$$

$$\boldsymbol{\Phi}_H=\boldsymbol{\Phi}_L=\begin{bmatrix}4 & -4 & 4\\ -4 & 4 & -4\\ 4 & -4 & 4\end{bmatrix}.$$

2.2 Perturbation Analysis.

To apply the method of regular perturbation, weak coupling is assumed, i.e., the magnitudes of the off-diagonal elements of $\overline{\mathbf{A}}$, which are functions of the nondimensional stiffnesses of the meshes κ^h, κ^v, and κ^d and the springs k^h, k^v, and k^d, are much smaller than the magnitudes of the diagonal elements of $\overline{\mathbf{A}}$, which are functions of the nondimensional flexural rigidities of the cantilevers k_i^x and k_{i+1}^y. Matrix $\overline{\mathbf{A}}$ may be written as

$$\overline{\mathbf{A}}=\mathbf{A}+\delta\mathbf{A}, \tag{11}$$

where $\mathbf{A}$ is the diagonal matrix obtained from the main diagonal of matrix $\overline{\mathbf{A}}$ and is given by

$$\mathbf{A}=\mathrm{diag}\{\mathbf{A}_{1,1}^{\mathrm{diag}},\mathbf{A}_{2,2}^{\mathrm{diag}},\ldots,\mathbf{A}_{2N_HN_V,2N_HN_V}^{\mathrm{diag}}\},$$

$$\mathbf{A}_{k,k}^{\mathrm{diag}}=\mathrm{diag}\{A_{1,1}^{k},A_{2,2}^{k},\ldots,A_{S,S}^{k}\},\quad k=1,\ldots,2N_HN_V,$$

and for i odd, $\alpha=1,\ldots,S$,

$$\begin{aligned}A_{\alpha,\alpha}^{i}&=k_i^x\hat{\beta}_\alpha^4+(2k^h+4k^d)\Phi_{\alpha\alpha}+(2\kappa^h+4\kappa^d)-\nu,\\A_{\alpha,\alpha}^{i+1}&=k_{i+1}^y\hat{\beta}_\alpha^4+(2k^v+4k^d)\Phi_{\alpha\alpha}+(2\kappa^v+4\kappa^d)-\nu.\end{aligned}\tag{12}$$

In Eq. (11), matrix $\delta\mathbf{A}$ is of the form $\delta\mathbf{A}=[\delta\mathbf{A}_{k,l}]$, where the diagonal blocks are, for i odd,

$$\delta\mathbf{A}_{i,i}=(2k^h+4k^d)\boldsymbol{\Phi}^0,\quad \delta\mathbf{A}_{i+1,i+1}=(2k^v+4k^d)\boldsymbol{\Phi}^0,$$

where $\boldsymbol{\Phi}^0$ equals $\boldsymbol{\Phi}_H$ except all diagonal elements that are set to 0, and the off-diagonal blocks $\delta\mathbf{A}_{k,l}=\overline{\mathbf{A}}_{k,l}$, $k\neq l$, which are given by Eqs. (9) and (10).

The method of regular perturbation for a linear algebraic system in the block form is applied to solve Eq. (8). Expanding the response vector $\overline{\mathbf{u}}$ as

$$\overline{\mathbf{u}}=\mathbf{u}+\delta\mathbf{u}+\cdots+\delta^m\mathbf{u}+\cdots,\tag{13}$$

and substituting Eqs. (11) and (13) into (8) yields

$$\mathbf{Au}+(\mathbf{A}\delta\mathbf{u}+\delta\mathbf{Au})+\cdots+(\mathbf{A}\delta^m\mathbf{u}+\delta\mathbf{A}\delta^{m-1}\mathbf{u})+\cdots=\overline{\mathbf{f}}.$$

The zeroth-order perturbation equation is

$$\mathbf{Au}=\overline{\mathbf{f}}.\tag{14}$$

Substituting Eqs. (12) and (7) into Eq. (14) results in the zeroth-order solution

$$\mathbf{u}=(\mathbf{u}_1^T,\mathbf{u}_2^T;\mathbf{u}_3^T,\mathbf{u}_4^T;\ldots;\mathbf{u}_{2N_HN_V-1}^T,\mathbf{u}_{2N_HN_V}^T)^T,$$

$$\begin{aligned}\mathbf{u}_j&=(\mathbf{A}_{j,j}^{\mathrm{diag}})^{-1}\mathbf{f}_j=\overline{f_x}\{(A_{1,1}^j)^{-1},-(A_{2,2}^j)^{-1},\ldots,(-1)^S(A_{S,S}^j)^{-1}\}^T,\\\mathbf{u}_{j+1}&=(\mathbf{A}_{j+1,j+1}^{\mathrm{diag}})^{-1}\mathbf{f}_{j+1}=\overline{f_y}\{(A_{1,1}^{j+1})^{-1},-(A_{2,2}^{j+1})^{-1},\ldots,\\&\qquad(-1)^S(A_{S,S}^{j+1})^{-1}\}^T,\end{aligned}\tag{15}$$

$$\mathbf{u}_i=\mathbf{u}_{i+1}=\mathbf{0},\quad\text{for}\ i=1,3,\ldots,2N_HN_V-1,\quad\text{and}\quad i\neq j.$$

This result indicates that, in the zeroth-order, only the directly forced (I_0,J_0)th cantilever is excited.

For the Mth-order perturbation, $M=1,2,\ldots$, the perturbation equation is

$$\mathbf{A}\delta^M\mathbf{u}+\delta\mathbf{A}\delta^{M-1}\mathbf{u}=\mathbf{0}.\tag{16}$$

Express the Mth-order amplitude of vibration vector $\delta^M\mathbf{u}$ as a linear combination of the unit vector $\mathbf{u}_{l\beta}$, which is formed by $2N_HN_V$ blocks of dimension S in which the βth element of the lth block is equal to 1 and all other elements are equal to 0, as

$$\delta^M\mathbf{u}=\sum_{l=1}^{2N_HN_V}\sum_{\beta=1}^{S}\varepsilon_{l\beta}^M\mathbf{u}_{l\beta}.\tag{17}$$

Substituting Eq. (17) into (16), multiplying the resulting equation by $\mathbf{u}_{k\alpha}^T$ from the left results in

$$\varepsilon_{k\alpha}^M=-\frac{1}{A_{\alpha,\alpha}^k}\sum_{l=1}^{2N_HN_V}\sum_{\beta=1}^{S}\varepsilon_{l\beta}^{M-1}(\mathbf{u}_{k\alpha}^T\delta\mathbf{A}\mathbf{u}_{l\beta}).\tag{18}$$

It is easy to show that $\mathbf{u}_{k\alpha}^T\delta\mathbf{A}\mathbf{u}_{l\beta}=\delta\mathbf{A}_{k\alpha,l\beta}$, which is the element of $\delta\mathbf{A}$ located on the αth row of the kth row block and the βth column of the lth column block.

Using Eqs. (9) and (10) and after some calculation, the following results are obtained. For $k=i$ odd, which corresponds to the x-direction, Eq. (18) becomes

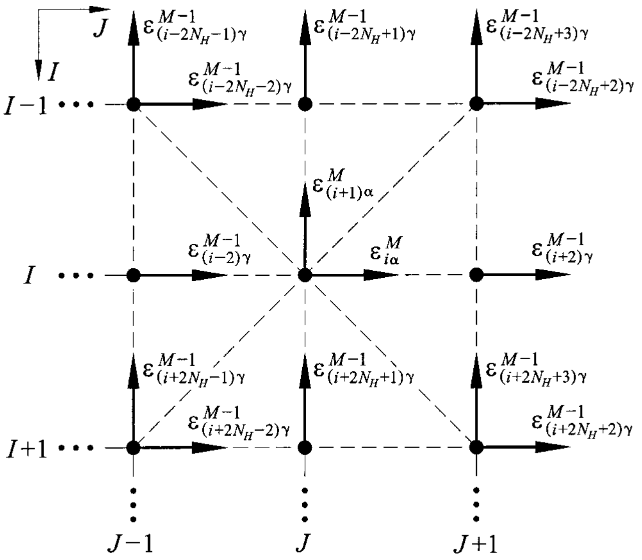

Fig. 3 Coupling of cantilevers in the transfer of vibration

$$\begin{aligned}\varepsilon_{i\alpha}^M=\frac{1}{A_{\alpha,\alpha}^i}\Bigg\{&\sum_{\gamma=1}^{S}(k^h\Phi_{\alpha\gamma}+\kappa^h\delta_{\alpha\gamma})[\varepsilon_{(i-2)\gamma}^{M-1}+\varepsilon_{(i+2)\gamma}^{M-1}]\\&-(2k^h+4k^d)\sum_{\gamma=1}^{S}\Phi_{\alpha\gamma}^0\varepsilon_{i\gamma}^{M-1}-\sum_{\gamma=1}^{S}(k^d\Phi_{\alpha\gamma}+\kappa^d\delta_{\alpha\gamma})\\&\times[-\varepsilon_{(i-2N_H-2)\gamma}^{M-1}+\varepsilon_{(i-2N_H-1)\gamma}^{M-1}-\varepsilon_{(i-2N_H+2)\gamma}^{M-1}\\&-\varepsilon_{(i-2N_H+3)\gamma}^{M-1}-\varepsilon_{(i+2N_H-2)\gamma}^{M-1}-\varepsilon_{(i+2N_H-1)\gamma}^{M-1}\\&-\varepsilon_{(i+2N_H+2)\gamma}^{M-1}+\varepsilon_{(i+2N_H+3)\gamma}^{M-1}]\Bigg\},\end{aligned}\tag{19}$$

and for $k=i+1$ even, which corresponds to the y-direction, Eq. (18) becomes

$$\begin{aligned}\varepsilon_{(i+1)\alpha}^M=\frac{1}{A_{\alpha,\alpha}^{i+1}}\Bigg\{&\sum_{\gamma=1}^{S}(k^v\Phi_{\alpha\gamma}+\kappa^v\delta_{\alpha\gamma})[\varepsilon_{(i-2N_H+1)\gamma}^{M-1}\\&+\varepsilon_{(i+2N_H+1)\gamma}^{M-1}]-(2k^v+4k^d)\sum_{\gamma=1}^{S}\Phi_{\alpha\gamma}^0\varepsilon_{(i+1)\gamma}^{M-1}\\&-\sum_{\gamma=1}^{S}(k^d\Phi_{\alpha\gamma}+\kappa^d\delta_{\alpha\gamma})[\varepsilon_{(i-2N_H-2)\gamma}^{M-1}-\varepsilon_{(i-2N_H-1)\gamma}^{M-1}\\&-\varepsilon_{(i-2N_H+2)\gamma}^{M-1}-\varepsilon_{(i-2N_H+3)\gamma}^{M-1}-\varepsilon_{(i+2N_H-2)\gamma}^{M-1}\\&-\varepsilon_{(i+2N_H-1)\gamma}^{M-1}+\varepsilon_{(i+2N_H+2)\gamma}^{M-1}-\varepsilon_{(i+2N_H+3)\gamma}^{M-1}]\Bigg\}.\end{aligned}\tag{20}$$

Equations (19) and (20) give the relationships between the amplitude of vibration of the (I,J)th cantilever, corresponding to the global coordinates i and $i+1$, in the Mth-order perturbation and those of its eight neighboring cantilevers in the $(M-1)$th-order perturbation. This coupling of cantilevers in the transfer of vibration can be better visualized in Fig. 3.

As shown in Fig. 1, each cantilever is coupled with its eight adjacent cantilevers through meshes and linear springs. In the zeroth-order perturbation, only the (I_0,J_0)th cantilever that is directly forced is vibrating. For the first-order perturbation, the eight neighboring cantilevers on the first layer are brought into motion through coupling; whereas for the second-order perturbation, the 16 cantilevers on the second layer are brought into motion. In

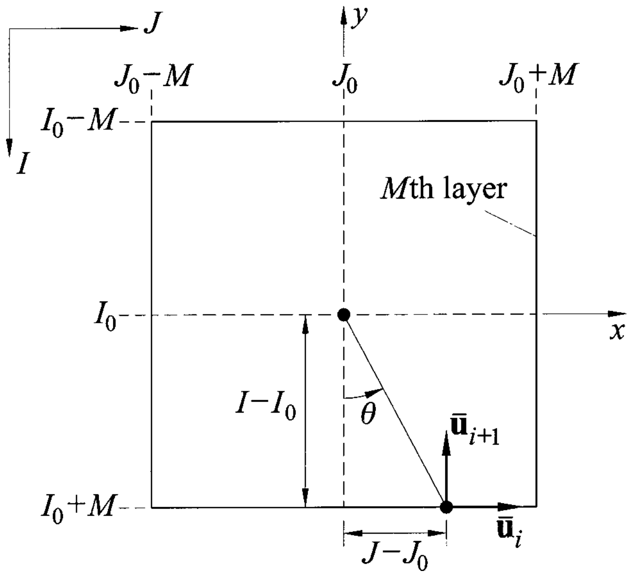

Fig. 4 Definition of the localization factor

general, for the Mth-order perturbation, $8M$ cantilevers on the Mth layer are brought into motion for the first time. As shown in Fig. 4, if the (I,J)th cantilever is on the Mth layer, it satisfies the condition $|I-I_0|=M$ and/or $|J-J_0|=M$. For the mth-order perturbation $(m<M)$, all cantilevers on and outside the Mth layer are at rest ([6]). Therefore, vibration extends or propagates outward a layer for each increment in the order of perturbation and the Mth layer is the farthest layer that vibration can extend to in the Mth-order perturbation. The amplitudes of vibration of the cantilevers on the Mth layer in the Mth-order perturbation are therefore determined by the amplitudes of vibration of the cantilevers on the $(M-1)$th layer in the $(M-1)$th-order perturbation. Hence, if the (I,J)th cantilever, corresponding to the global coordinates i and $i+1$, is on the Mth layer, the terms on the right sides of Eqs. (19) and (20) that correspond to cantilevers not on the $(M-1)$th layer are equal to zero; for example, the second summation terms in Eqs. (19) and (20) are equal to zero.

In Ref. [8], where localization of vibration propagation in a two-dimensional cantilever-spring array with one substructural mode is considered, it is found that the amplitudes of vibration are of hill shapes when plotted in the logarithmic scale. The amplitudes of vibration of the cantilevers decay linearly in a specific direction (angle of orientation) in the logarithmic scale away from the cantilever that is directly forced. This observation suggested the definition of the localization factors for a two-dimensional cantilever-spring array in terms of the angle of orientation ([8]), which are analogous to the localization factors for a one-dimensional randomly disordered system and characterize the average exponential rates of growth or decay of amplitudes of vibration.

A localization factor is defined as

$$\lambda_\theta=-\lim_{M\to\infty}\frac{1}{M}\ln\|\overline{\mathbf{v}}_i\|,\qquad \theta=\tan^{-1}\frac{J-J_0}{I-I_0},\tag{21}$$

where $\overline{\mathbf{v}}_i=(\overline{\mathbf{u}}_i^T,\overline{\mathbf{u}}_{i+1}^T)^T=(\overline{u}_{i1},\ldots,\overline{u}_{iS};\overline{u}_{(i+1)1},\ldots,\overline{u}_{(i+1)S})^T$ is the nondimensional amplitude vector of vibration of the (I,J)th cantilever on the Mth layer (corresponding to the global coordinates i and $i+1$), and θ is the angle of orientation as shown in Fig. 4.

The localization factors defined in Eq. (21) are consistent in the sense that, in numerical simulations, two different values of $M\to\infty$ yield the same value of λ_θ as long as the cantilevers (I,J) on the two different layers correspond to the same angle of orientation θ. This confirms that the exponential decay rate of vibration amplitudes is invariant for a specific direction and it is reasonable to define the localization factors in terms of the angle of orientation.

It may be noted that, when the full linear algebraic system (8) is solved and the true amplitude vector of vibration $\overline{\mathbf{v}}_i$ of the (I,J)th cantilever, which is on the Mth layer, is used in Eq. (21), the exact value of the localization factor λ_θ is obtained when the number of layer M approaches infinity.

On the other hand, when applying the method of regular perturbation, $\overline{\mathbf{v}}_i$ may be written as, following Eq. (13), $\overline{\mathbf{v}}_i=\mathbf{v}_i+\delta\mathbf{v}_i+\delta^2\mathbf{v}_i+\cdots$. Since cantilever (I,J) or the global coordinate i is on the Mth layer, $\delta^m\mathbf{v}_i=\mathbf{0}$ for $m<M$ as discussed above, which results in

$$\overline{\mathbf{v}}_i=\delta^M\mathbf{v}_i+\delta^{M+1}\mathbf{v}_i+\cdots.\tag{22}$$

However, because of the large amount of computation involved, it is difficult to evaluate Eq. (22) beyond the leading term. Hence, in this study, only the leading term in the perturbation series, (22) is taken, i.e., $\overline{\mathbf{v}}_i\approx\delta^M\mathbf{v}_i=\{(\delta^M\mathbf{u}_i)^T,(\delta^M\mathbf{u}_{i+1})^T\}^T$, the elements of which are obtained using Eqs. (19) and (20). The localization factor λ_θ obtained using Eq. (21) with $\overline{\mathbf{v}}_i\approx\delta^M\mathbf{v}_i$ is therefore a first-order approximation.

For the four cantilevers located at the corners of the Mth layer, which correspond to the angles of orientation $\theta=45$ deg, 135 deg, 225 deg, and 315 deg, Eqs. (19) and (20) can be simplified significantly. Because of symmetry, only the diagonal direction $\theta=45$ deg is considered in the following formulation. As discussed above, the amplitudes of vibration of the cantilevers on the Mth layer in the Mth-order perturbation depend only on the amplitudes of vibration of the cantilevers on the $(M-1)$th layer in the $(M-1)$th-order perturbation. Since the cantilever (I_0+M,J_0+M) on the Mth layer, which is located in the direction $\theta=45$ deg, is coupled with only one cantilever on the $(M-1)$th layer, i.e., the cantilever (I_0+M-1,J_0+M-1), the amplitudes of vibration of the cantilever (I_0+M,J_0+M) in the Mth-order perturbation depend only on those of the cantilever (I_0+M-1,J_0+M-1) in the $(M-1)$th-order perturbation. Equations (19) and (20) are simplified as

$$\begin{aligned}\boldsymbol{\varepsilon}_{i\alpha}^{M}&=\frac{1}{A_{\alpha,\alpha}^{i}}\left\{\sum_{\gamma=1}^{S}(k^d\Phi_{\alpha\gamma}+\boldsymbol{\kappa}^d\delta_{\alpha\gamma})[\boldsymbol{\varepsilon}_{(i-2N_H-2)\gamma}^{M-1}-\boldsymbol{\varepsilon}_{(i-2N_H-1)\gamma}^{M-1}]\right\},\\ \boldsymbol{\varepsilon}_{(i+1)\alpha}^{M}&=\frac{1}{A_{\alpha,\alpha}^{i+1}}\left\{\sum_{\gamma=1}^{S}(k^d\Phi_{\alpha\gamma}+\boldsymbol{\kappa}^d\delta_{\alpha\gamma})[-\boldsymbol{\varepsilon}_{(i-2N_H-2)\gamma}^{M-1}\right.\\ &\qquad\left.+\boldsymbol{\varepsilon}_{(i-2N_H-1)\gamma}^{M-1}]\right\},\end{aligned}\tag{23}$$

where $i=j+2M(N_H+1)$. Equation (23) may be written in the matrix form as

$$\begin{Bmatrix}\boldsymbol{\varepsilon}_i^M\\ \boldsymbol{\varepsilon}_{i+1}^M\end{Bmatrix}=\mathbf{T}^M\begin{Bmatrix}\boldsymbol{\varepsilon}_{i-2N_H-2}^{M-1}\\ \boldsymbol{\varepsilon}_{i-2N_H-1}^{M-1}\end{Bmatrix},\tag{24}$$

where $\boldsymbol{\varepsilon}_l^m=\{\varepsilon_{l1}^m,\ldots,\varepsilon_{lS}^m\}^T$, and $\mathbf{T}^M$ is the transfer matrix given by

$$\mathbf{T}^M=\begin{bmatrix}\mathbf{T}_i^M & -\mathbf{T}_i^M\\ -\mathbf{T}_{i+1}^M & \mathbf{T}_{i+1}^M\end{bmatrix},$$

$$\mathbf{T}_l^M=\begin{bmatrix} \dfrac{k^d\,\Phi_{11}+\kappa^d}{A_{1,1}^l} & \dfrac{k^d\Phi_{12}}{A_{1,1}^l} & \cdots & \dfrac{k^d\Phi_{1S}}{A_{1,1}^l} \\ \dfrac{k^d\Phi_{21}}{A_{2,2}^l} & \dfrac{k^d\Phi_{22}+\kappa^d}{A_{2,2}^l} & \cdots & \dfrac{k^d\,\Phi_{2S}}{A_{2,2}^l} \\ \vdots & \vdots & \vdots & \vdots \\ \dfrac{k^d\Phi_{S1}}{A_{S,S}^l} & \dfrac{k^d\Phi_{S2}}{A_{S,S}^l} & \cdots & \dfrac{k^d\Phi_{SS}+\kappa^d}{A_{S,S}^l} \end{bmatrix}.$$

Equation (24) leads to

$$\begin{Bmatrix} \boldsymbol{\varepsilon}_i^M \\ \boldsymbol{\varepsilon}_{i+1}^M \end{Bmatrix}=\mathbf{T}^M\mathbf{T}^{M-1}\cdots\mathbf{T}^1\begin{Bmatrix} \boldsymbol{\varepsilon}_j^0 \\ \boldsymbol{\varepsilon}_{j+1}^0 \end{Bmatrix}, \tag{25}$$

where $\boldsymbol{\varepsilon}_j^0=\mathbf{u}_j$ and $\boldsymbol{\varepsilon}_{j+1}^0=\mathbf{u}_{j+1}$ as given in Eq. (15).

Hence, in the diagonal direction of $\theta=45$ deg, a first-order approximation of the propagation of vibration is expressed in terms of a product of transfer matrices of $2S\times 2S$. This implies that the localization behavior of a two-dimensional cantilever-mesh-spring array in the diagonal direction of $\theta=45$ deg is similar to that of a one-dimensional system with multiple substructural modes ([9]). The numerical method presented in [9] can be applied to determine the localization factors.

The αth frequency passbands corresponding to vibration dominant in the x and y-directions are located around, respectively,

$$\nu_\alpha^x=\mu_{kx}\hat{\beta}_\alpha^4+(2k^h+4k^d)\Phi_{\alpha\alpha}+(2\kappa^h+4\kappa^d),$$

$$\nu_\alpha^y=\mu_{ky}\hat{\beta}_\alpha^4+(2k^v+4k^d)\Phi_{\alpha\alpha}+(2\kappa^v+4\kappa^d),$$

with certain bandwidths.

For weak coupling of the cantilevers, i.e., small values of the nondimensional stiffnesses of the springs k^h, k^v, and k^d and the meshes κ^h, κ^v, and κ^d, the locations of the frequency passbands are given approximately by $\nu_\alpha^x\approx\mu_{kx}\hat{\beta}_\alpha^4$, $\nu_\alpha^y\approx\mu_{ky}\hat{\beta}_\alpha^4$. The following three cases are possible.

Case 1. $\mu_{kx}=\mu_{ky}$

In this case, the frequency passbands corresponding to vibration dominant in the x-direction and the y-direction coincide and are well separated. For example, if $\mu_{kx}=\mu_{ky}=1$ and three substructural modes are taken, i.e., $S=3$, the passbands are located around

for both x and y-directions: 12.36 485.52 3806.55.

Case 2. $\mu_{kx}\neq\mu_{ky}$, without overlap

For certain values of μ_{kx} and μ_{ky}, the frequency passbands corresponding to vibration dominant in the x-direction and the y-direction are well separated. For example, if $\mu_{kx}=1$, $\mu_{ky}=5$, $S=3$, the frequency passbands are located around

x-direction:	12.36		485.52		3806.55	
y-direction:		61.81		2427.59		19032.73.

Case 3. $\mu_{kx}\neq\mu_{ky}$, with overlap

For certain values of μ_{kx} and μ_{ky}, there may be overlaps between the frequency passbands corresponding to vibration dominant in the x-direction and those corresponding to vibration dominant in the y-direction. For example, if $\mu_{kx}=1$, $\mu_{ky}=7.84$, $S=3$, the frequency passbands are located around

x-direction:	12.36		485.52	3806.55	
y-direction:		96.92		3806.47	29843.32

in which the third frequency passband corresponding to vibration dominant in the x-direction and the second frequency passband corresponding to vibration dominant in the y-direction overlap.

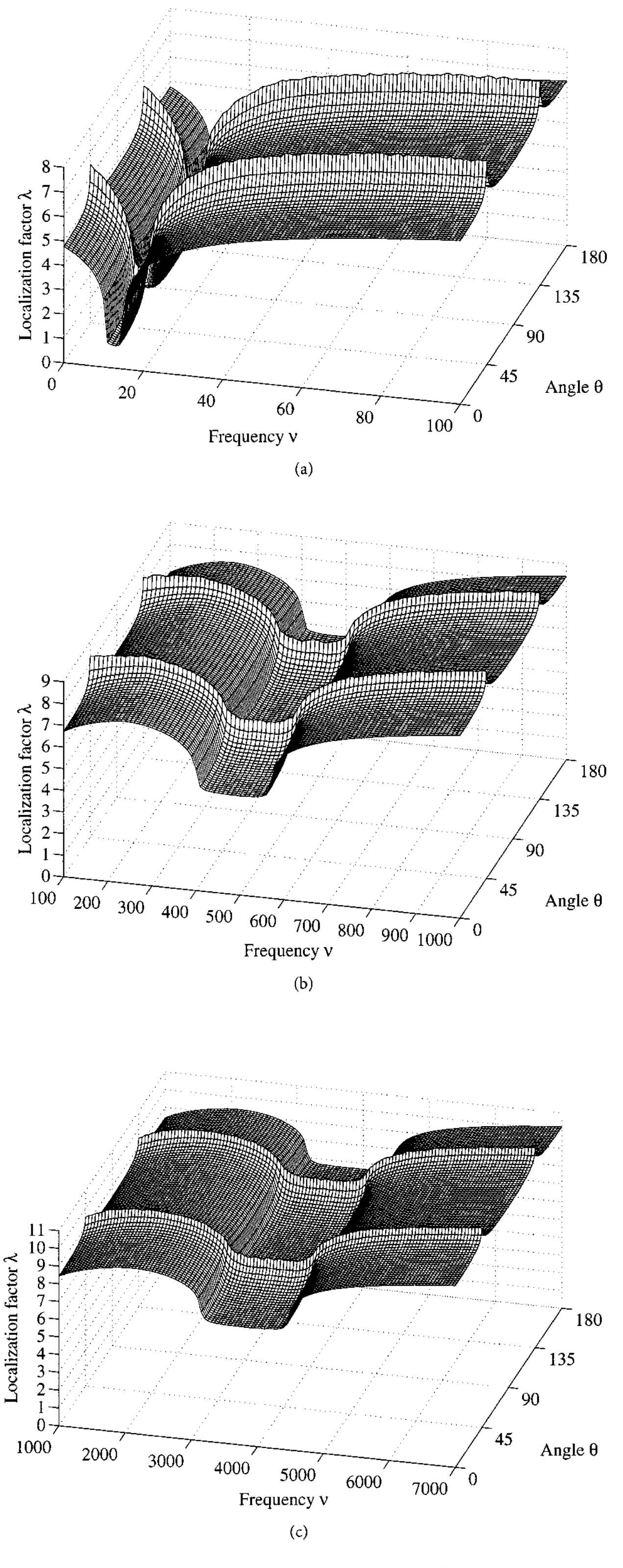

Fig. 5 Localization factors: $\mu_{kx}=\mu_{ky}=1$, $k^h=k^v=k^d=\kappa^h=\kappa^v=\kappa^d=0.01$

3 Numerical Results

Numerical results of the first-order approximation of the localization factors for vibration propagation in disordered two-dimensional cantilever-mesh-spring arrays are presented in this section.

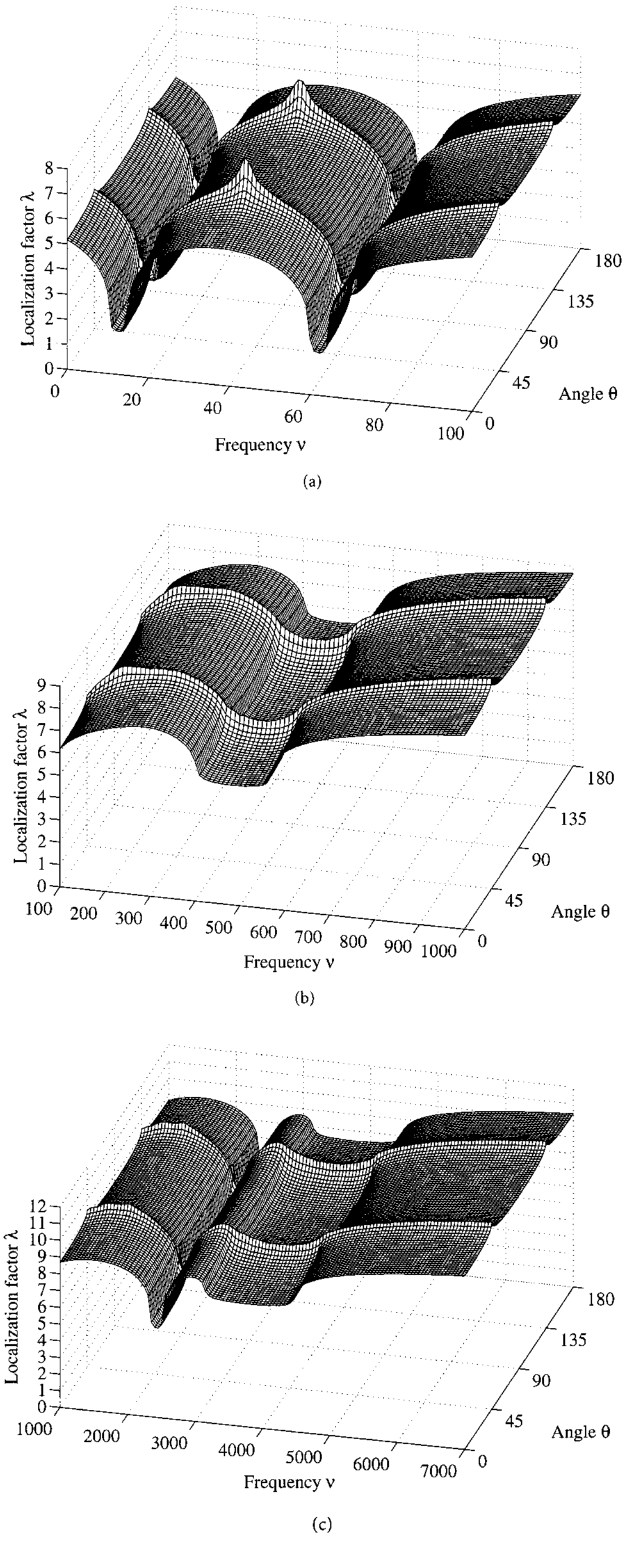

(a)

(b)

(c)

Fig. 6 Localization factors: $\mu_{kx}=1$, $\mu_{ky}=5$, $k^h=k^v=k^d=\kappa^h=\kappa^v=\kappa^d=0.01$

For the purpose of illustration, three substructural modes are considered for each cantilever, i.e., $S=3$. The nondimensional bending stiffnesses of the cantilevers in the x and y-directions k_i^x and k_{i+1}^y are uniformly distributed random numbers with mean values μ_{kx} and μ_{ky} and coefficients of variation δ_{kx} and δ_{ky}, and the exciting forces are taken as $\overline{f_x}=\overline{f_y}=1$.

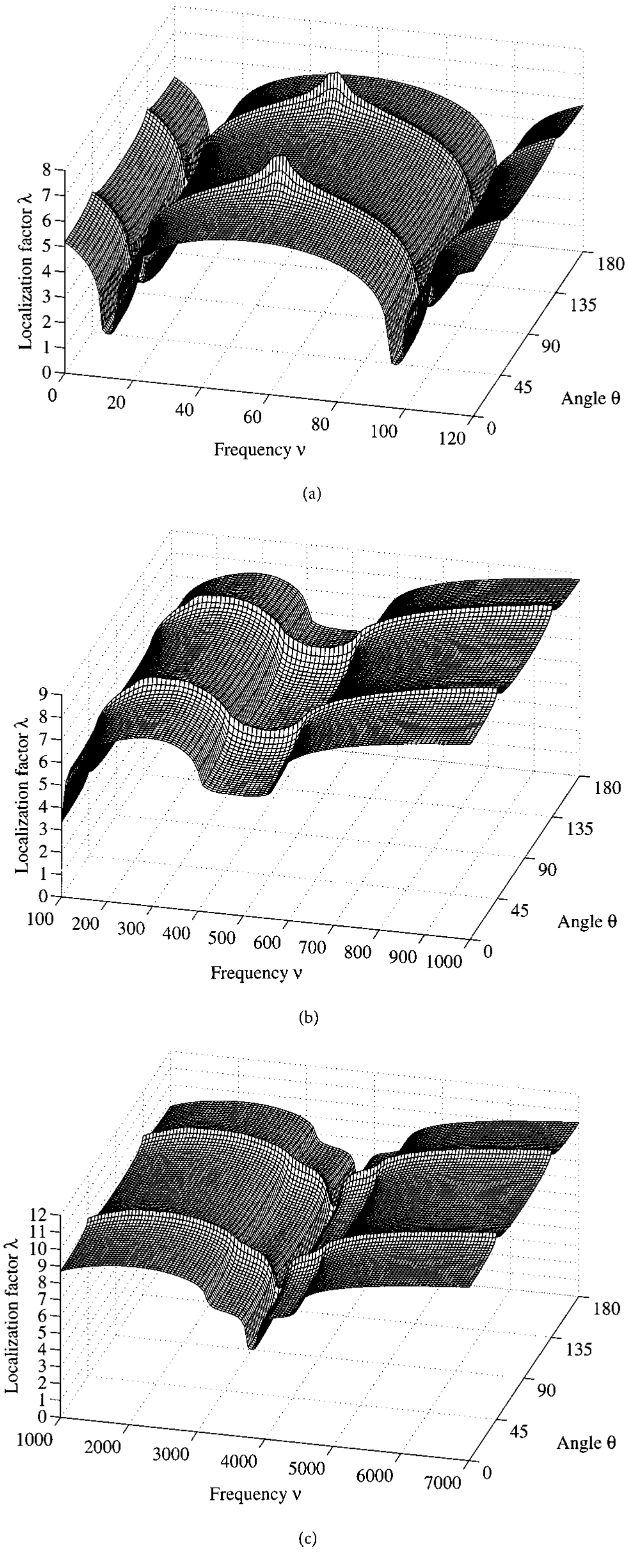

(a)

(b)

(c)

Fig. 7 Localization factors: $\mu_{kx}=1$, $\mu_{ky}=7.84$, $k^h=k^v=k^d=\kappa^h=\kappa^v=\kappa^d=0.01$

Given the nondimensional forces $\overline{f_x}$ and $\overline{f_y}$, and the excitation frequency ν, the zeroth-order approximation of the amplitude of vibration vector $\mathbf{u}$ is given by Eq. (15). Iterative Eqs. (19) and (20) are employed to determine the amplitudes of vibration of all the cantilevers on the Mth layer in the Mth-order perturbation. For each iteration, two independent uniformly distributed random

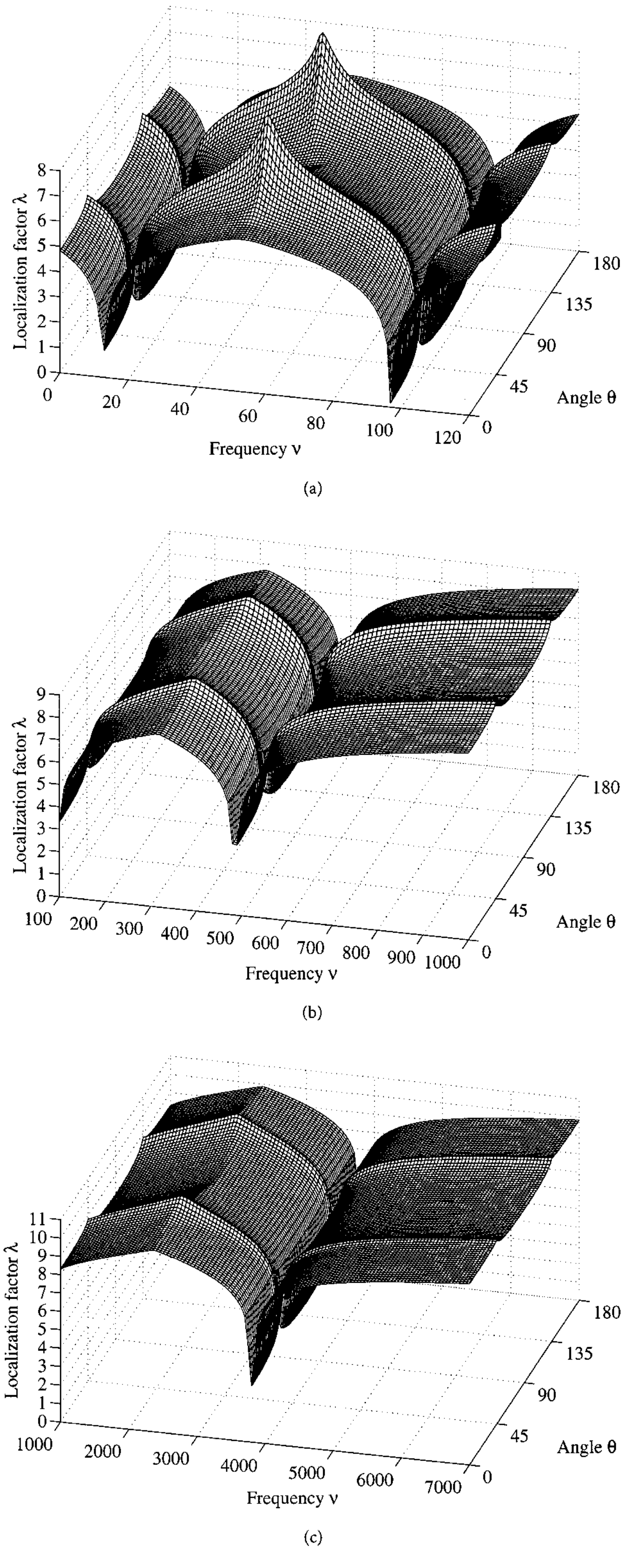

Fig. 8 Localization factors: $\mu_{kx}=1$, $\mu_{ky}=7.84$, $\delta_{kx}=\delta_{ky}=0.01$, $k^h=k^v=k^d=\kappa^h=\kappa^v=\kappa^d=0.01$

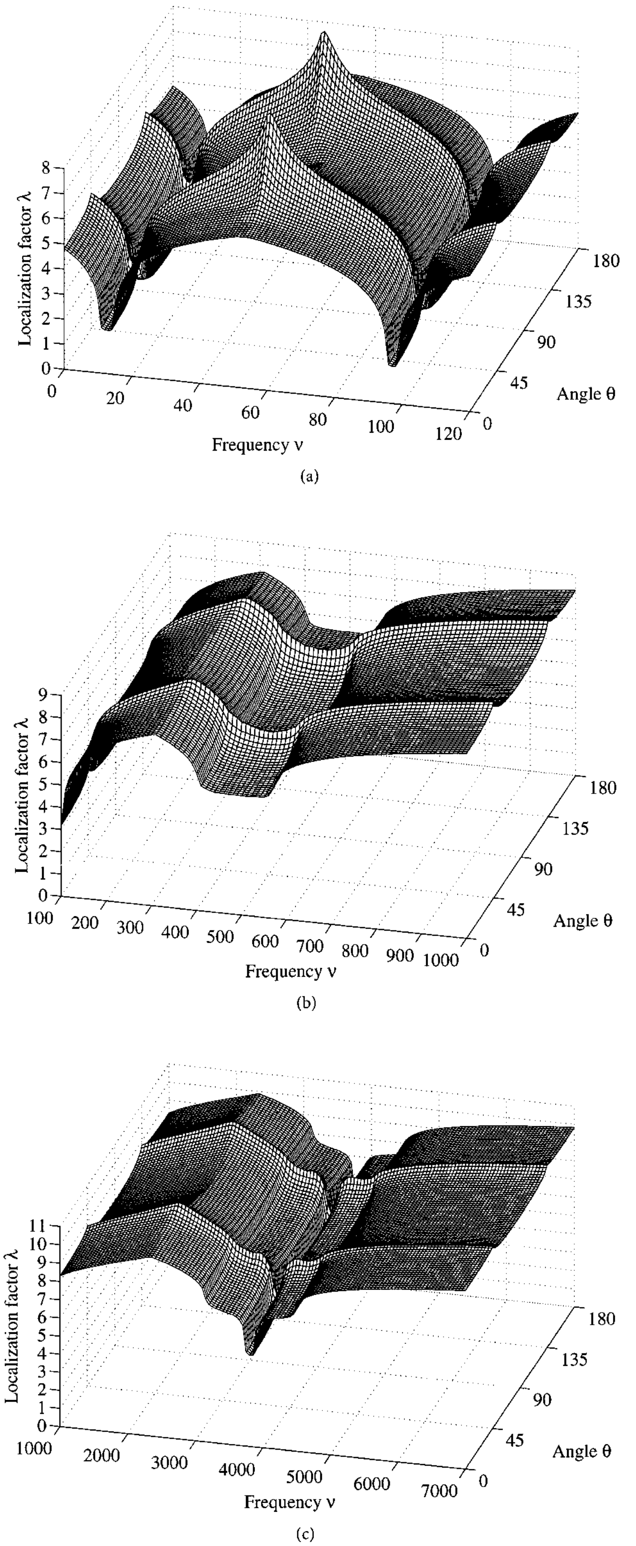

Fig. 9 Localization factors: $\mu_{kx}=1$, $\mu_{ky}=7.84$, $\delta_{kx}=0.1$, $\delta_{ky}=0.01$, $k^h=k^v=k^d=\kappa^h=\kappa^v=\kappa^d=0.01$

numbers are generated for k_i^x and k_{i+1}^y for the cantilever corresponding to the ith global coordinate. Equation (21) is then employed to determine the localization factors λ_θ.

The determination of a first-order approximation of the localization factors requires only the amplitudes of vibrations of cantilevers on the Mth layer in the Mth-order perturbation for M large. All cantilevers outside the Mth layer are at rest in the Mth-order perturbation. Therefore, a large two-dimensional cantilever-mesh-spring array may be imagined as one with $2M+1$ rows and $2M+1$ columns and the cantilever that is directly forced is located at node $(M+1,M+1)$. The localization factors are plotted for 0 deg$\leqslant\theta\leqslant$180 deg only due to their symmetry.

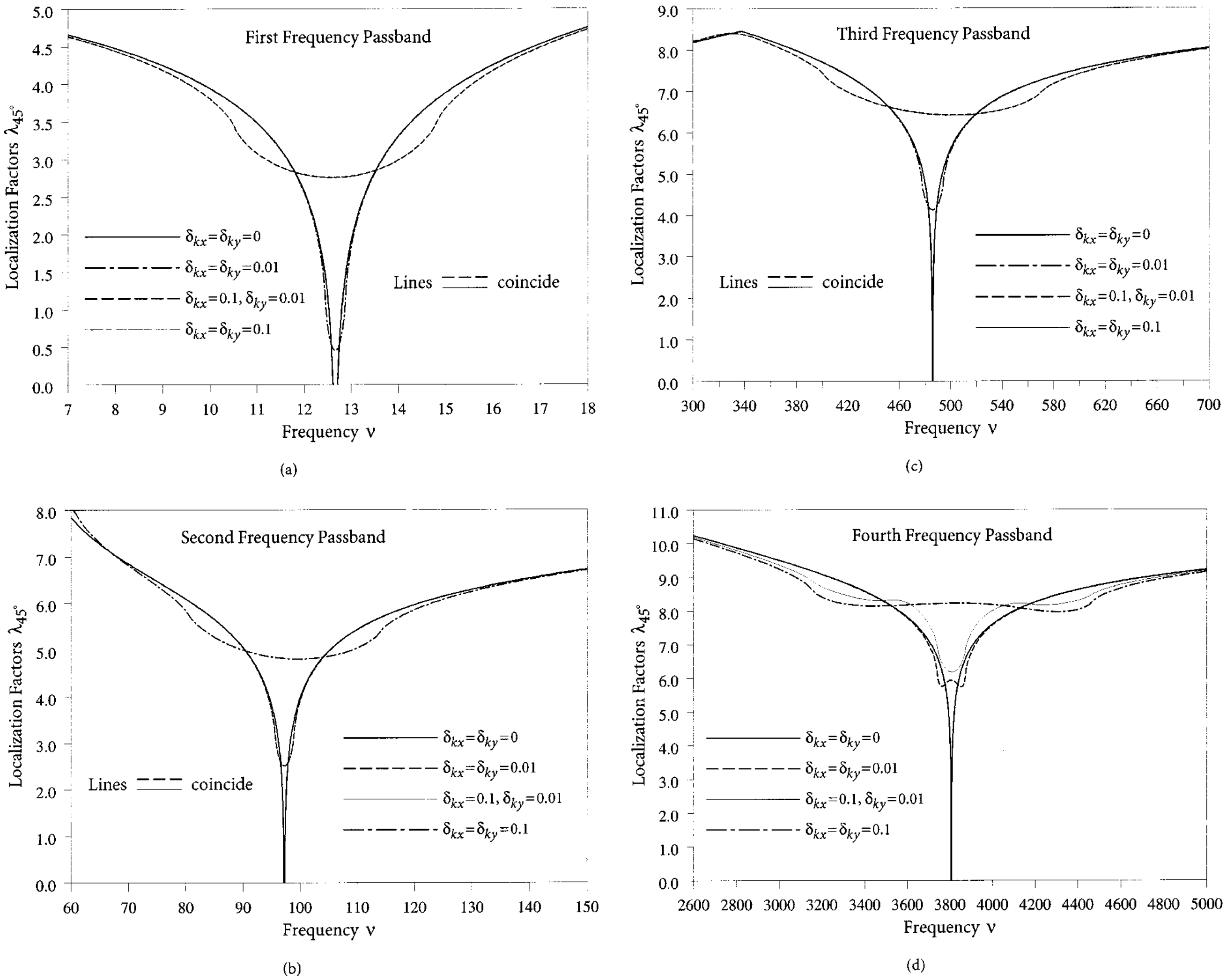

(a) (c)

(b) (d)

Fig. 10 Localization factors in direction $\theta=45$ deg: $\mu_{kx}=1$, $\mu_{ky}=7.84$, $k^h=k^v=k^d=\kappa^h=\kappa^v=\kappa^d=0.01$

First-order approximate localization factors are shown in Fig. 5 for $\mu_{kx}=\mu_{ky}=1$, $\delta_{kx}=\delta_{ky}=0.1$. Since $\mu_{kx}=\mu_{ky}$ and $S=3$, there are three frequency passbands as discussed in Section 2. Because the statistical properties of the cantilever-mesh-spring array in the x-direction are the same as those in the y-direction, the vibration propagation localization behavior in the x-direction ($\theta=90$ deg) is the same as that in the y-direction ($\theta=0$ deg). Furthermore, because of the symmetry of the two-dimensional cantilever-spring-mesh array in the statistical sense, the localization factors are symmetric about the horizontal axis ($\theta=90$ deg), vertical axis ($\theta=0$ deg, 180 deg), and the diagonal lines ($\theta=45$ deg, 135 deg) passing through the cantilever that is directly forced. It is seen that the localization factors are minimum in the x and y-directions ($\theta=0$ deg, 90 deg, and 180 deg) and are maximum in the diagonal directions ($\theta=45$ deg and 135 deg).

When $\mu_{kx}=1$, $\mu_{ky}=5$, $\delta_{kx}=\delta_{ky}=0.1$, the localization factors are shown in Fig. 6. In this case, there are six frequency passbands, three of which correspond to vibration dominant in the x-direction and three of which correspond to vibration dominant in the y-direction. Since $\mu_{kx}<\mu_{ky}$, the coupling in the x-direction is relatively stronger than that in the y-direction. Hence the localization factor in the x-direction ($\theta=90$ deg) is smaller than that in the y-direction ($\theta=0$ deg). The localization factors are symmetric about the horizontal axis ($\theta=90$ deg) and vertical axis ($\theta=0$ deg, 180 deg) but not the diagonal lines ($\theta=45$ deg, 135 deg) passing through the cantilever that is directly forced. It is observed that the localization factors are minimum in the x-direction ($\theta=90$ deg) and maximum in the diagonal directions ($\theta=45$ deg and 135 deg).

When $\mu_{kx}=1$, $\mu_{ky}=7.84$, $\delta_{kx}=\delta_{ky}=0.1$, there are five frequency passbands, in which the third passband corresponding to vibration dominant in the x-direction overlaps with the second passband corresponding to vibration dominant in the y-direction. Numerical results of the localization factors are shown in Fig. 7. The interesting shape of the localization factor plot in the fourth frequency passband around $\nu=3806$ where the overlap of the passbands occurs is noteworthy. In this passband, vibration is dominant in both the x and y directions, and the localization factor in the x-direction ($\theta=90$ deg) is the same as that in the y-direction ($\theta=0$ deg). In other frequency passbands, properties of the localization factors observed for the case $\mu_{kx}=1$, $\mu_{ky}=5$ can also be observed here.

When the stiffnesses of the springs and meshes in the diagonal directions are reduced, the coupling of the cantilevers in the diagonal directions becomes weak, resulting in larger values of the localization factors. Because of the limit in the length of the paper, numerical results are not presented here.

To study the effect of the degree of disorder on the localization behavior of the system, the case of $\delta_{kx}=\delta_{ky}=0.01$ is considered. The localization factors are shown in Fig. 8 for $\mu_{kx}=1$ and $\mu_{ky}=7.84$. It is seen that for smaller values of disorder, the localization factors are small, implying a smaller degree of localization.

This result is expected; as an extreme case when $\delta_{kx}=\delta_{ky}=0$, i.e., for the perfect periodic system, the localization factor is zero in the passband and there is no localization.

The case of $\delta_{kx}=0.1$ and $\delta_{ky}=0.01$, i.e., the disorder in the x-direction is different from that in the y-direction, is considered in the following. The localization factors are shown in Fig. 9 for $\mu_{kx}=1$ and $\mu_{ky}=7.84$.

To further compare the effect of the values of δ_{kx} and δ_{ky} on the localization behavior, the localization factors for the diagonal direction $\theta=45$ deg, which are obtained using Eq. (25) and the method of transfer matrix ([9]), are shown in Fig. 10 for the case of $\mu_{kx}=1$ and $\mu_{ky}=7.84$, and various values of δ_{kx} and δ_{ky}. As is well known, for the perfect system with $\delta_{kx}=\delta_{ky}=0$, the localization factors are zero in the passband and there is not localization. The localization factors increase when the values of δ_{kx} and δ_{ky} are increased.

Consider the case $\mu_{kx}=1$, $\mu_{ky}=7.84$, $\delta_{kx}=0.1$, and $\delta_{ky}=0.01$ as an example of $\mu_{kx}\neq\mu_{ky}$. In the first and the third frequency passbands around $\nu=12.36$ and $\nu=485.52$, vibration is dominant in the x-direction. The statistical properties of the system in the y-direction have little effect on the dynamical behavior of the system. Hence, the localization factors of a system with $\delta_{kx}=0.1$ and $\delta_{ky}=0.01$ are the same as those with $\delta_{kx}=\delta_{ky}=0.1$ near the first and the third frequency passbands. This can be observed in Fig. 10, as the localization factors for both cases concur around the first and the third frequency passbands.

On the other hand, in the second frequency passband around $\nu=96.92$, vibration is dominant in the y-direction. The statistical properties of the system in the x-direction have little effect on the dynamical behavior of the system. Therefore, the localization factor of a system with $\delta_{kx}=0.1$ and $\delta_{ky}=0.01$ is the same as that with $\delta_{kx}=\delta_{ky}=0.01$, which is evident in Fig. 10 as the localization factors for both cases coincide around the second passband.

However, in the fourth passband around $\nu=3806.5$, vibration is dominant in both the x and y-directions. The statistical properties of the system in both the x and y-directions affect the dynamical behavior of the system, which can be observed in Fig. 10 as the localization factors are different for different values of δ_{kx} and δ_{ky} in the fourth frequency passband. The same conclusion can be drawn for the case when $\mu_{kx}=\mu_{ky}=1$ in all three frequency passbands, since the frequency passbands corresponding to vibration dominant in the x-direction and the y-direction coincide.

From Figs. 5–9, it is observed that for a given direction of orientation θ, the localization behavior of the two-dimensional cantilever-mesh-spring array is similar to that of an one-dimensional cantilever-mesh-spring chain. The weaker the coupling of the cantilevers in a given direction, the larger the localization factors.

Since the diagonal elements $A^{i}_{\alpha,\alpha}$ and $A^{i+1}_{\alpha,\alpha}$ in Eq. (12) increase rapidly with $\hat{\beta}^{4}_{\alpha}$ as the substructural mode number α is increased, the αth substructural mode becomes increasingly weakly coupled, resulting in more prominent localization when the frequency passband number is increased. For example, as seen in Figs. 5–10, the localization factors in the second passband are larger than those in the first passband for the same system parameters.

4 Conclusions

In this paper, the localization of forced vibration propagation in two-dimensional cantilever-mesh-spring arrays with multiple substructural modes is studied. A method of regular perturbation for a linear algebraic system in the block form is applied to obtain iteratively the amplitudes of vibration of the cantilevers on the Mth layer in the Mth-order perturbation in terms of the amplitudes of vibration of the cantilevers on the $(M-1)$th layer in the $(M-1)$th-order perturbation. The amplitudes of vibration of the cantilevers on the Mth layer in the Mth-order perturbation for M large are employed to obtain a first-order approximation of the localization factors of the two-dimensional system. The localization factors are defined in terms of the angles of orientation and characterize the exponential rate of growth or decay of the amplitudes of vibration in the given directions. For a given direction of orientation, the localization behavior is similar to that of one-dimensional systems. In the diagonal directions, changes of the amplitudes of vibration of cantilevers can be expressed in terms of a product of random transfer matrices and the localization factors may be determined using the method of transfer matrix. The effect of the stiffnesses and the disorder in the stiffnesses of the cantilevers on the localization behavior of the system is investigated. The general vibration propagation localization behavior observed in the simplified two-dimensional cantilever-mesh-spring arrays is expected to be applicable to more realistic two-dimensional engineering disordered periodic structures.

Acknowledgment

The research for this paper was supported, in part, by the Natural Sciences and Engineering Research Council of Canada through Grant No. OGPO131355. The author is grateful to the referees for the constructive comments which helped to improve the paper.

References

[1] Furstenberg, H., 1963, "Noncommuting Random Products," Trans. Am. Math. Soc., **108**, No. (3), pp. 377–428.

[2] Oseledec, Y. I., 1968, "A Multiplicative Ergodic Theorem. Lyapunov Characteristic Number for Dynamical Systems," Trans. Moscow Math. Soc., **19**, pp. 197–231 (English translation).

[3] Herbert, D. C., and Jones, R., 1971, "Localized States in Disordered Systems," J. Phys. C, **4**(10), pp. 1145–1161.

[4] Thouless, D. J., 1972, "A Relation Between the Density of States and Range of Localization for One Dimensional Random Systems," J. Phys. C, **5**(1), pp. 77–81.

[5] Special issue on "Localization Problems in Engineering," 2000, Chaos, Solitons Fractals, **11**, No. (10).

[6] Xie, W.-C., and Wang, Xing, 1997, "Vibration Mode Localization in Two-Dimensional System," AIAA J., **35**, pp. 1653–1659.

[7] Xie, W.-C., 2001, "Vibration Mode Localization in Two-Dimensional Systems With Multiple Substructural Modes," Chaos, Solitons Fractals, **12**, pp. 551–570.

[8] Xie, W.-C., 2000, "Localization of Vibration Propagation in Two-Dimensional Systems," Chaos, Soliton Fractals, **11**, pp. 1505–1518.

[9] Xie, W.-C., and Ariaratnam, S. T., 1996, "Vibration Mode Localization in Disordered Cyclic Structures, II: Multiple Substructure Modes," J. Sound Vib., **189**, pp. 647–660.

Feedback Stabilization of Quasi-Integrable Hamiltonian Systems

W. Q. Zhu
Professor

Z. L. Huang
Associate Professor

Department of Mechanics,
Zhejiang University,
Hangzhou 310027, P. R. China

A procedure for designing a feedback control to asymptotically stabilize with probability one quasi-integrable Hamiltonian system is proposed. First, a set of averaged Itô stochastic differential equations for controlled first integrals is derived from given equations of motion of the system by using the stochastic averaging method for quasi-integrable Hamiltonian systems. Second, a dynamical programming equation for infinite horizon performance index with unknown cost function is established based on the stochastic dynamical programming principle. Third, the asymptotic stability with probability one of the optimally controlled system is analyzed by evaluating the largest Lyapunov exponent of the fully averaged Itô equations for the first integrals. Finally, the cost function and feedback control law are determined by the requirement of stabilization of the system. An example is worked out in detail to illustrate the application of the proposed procedure and the effect of optimal control on the stability of the system. [DOI: 10.1115/1.1483833]

Introduction

The feedback stabilization of stochastic systems is an important problem in control theory. Although the basic formulation and fundamental equations of stochastic stabilization have been known since the 1960s ([1]), the only results of any significance for a long period were those pertaining to linear stochastic systems and employing quadratic control criteria ([2]). For nonlinear stochastic systems, the progress on stochastic stabilization has been plagued by a fundamental technical obstacle in the Lyapunov analysis. In recent years, the stabilization of nonlinear stochastic systems has received much attention and several interesting results have been obtained. Particularly, the concept of stochastic control Lyapunov function has been introduced and the sufficient conditions for feedback stabilization have been derived by Florchinger [3,4]. The stochastic stabilization problem for strict-feedback systems was solved and a systematic backstepping design scheme was developed by Pan and Basar [5]. The inverse optimal stabilization of strict-feedback systems was designed and extended to output-feedback systems by Deng and Krstic [6–8]. Notable advances on input-to-state stabilization were also made by Tsinias [9].

A recent trend in the study of stochastic stability is to employ Lyapunov exponent rather than Lyapunov function. According to multiplicative ergodic theorem due to Oseledec [10], the necessary and sufficient condition for the asymptotic stability with probability one of a linear stochastic system is that its largest Lyapunov exponent is negative. A procedure for evaluating the largest Lyapunov exponent of linear system of Itô stochastic differential equations was proposed by Khasminskii [11] and the procedure has been successfully applied to certain two-dimensional linear stochastic systems. The direct use of Khasminskii's procedure to the system of dimension higher than two has not met with much success principally due to the difficulty of discussing diffusion process occurring on surface of unit hypersphere in higher dimensional space. However, the stochastic averaging method may be used to reduce the dimension of stochastic systems. Thus, a combination of the stochastic averaging method and the Khasminskii's procedure is a powerful approach to evaluating the largest Lyapunov exponent of higher-dimensional stochastic systems ([12,13]). Especially, the combination of the stochastic averaging method for quasi-integrable Hamiltonian systems ([14]) and the Khasminskii's procedure may be applied to higher-dimensional nonlinear stochastic systems ([13,15]).

At the same time, a nonlinear stochastic optimal control strategy for quasi-Hamiltonian systems was proposed recently by the present first author and his co-workers ([16–18]) based on the stochastic averaging method for quasi-Hamiltonian systems ([14,19]) and the stochastic dynamical programming principle. It has been shown that the strategy has several advantages over existing ones and is very promising.

In the present paper, a procedure for designing a feedback control law to asymptotically stabilize with probability one quasi integrabe Hmiltonian systems is proposed. The procedure is a nontrivial combination of the nonlinear stochastic optimal control strategy and the approach to stochastic stability of quasi integrable Hamiltonian systems. An example is worked out in detail to illustrate the proposed procedure.

Stochastic Averaging

Consider an *n*-degree-of-freedom controlled quasi-Hamiltonian system governed by the following *n* pairs of equations of motion:

$$\dot{Q}_i = \frac{\partial H'}{\partial P_i}$$

$$\dot{P}_i = -\frac{\partial H'}{\partial Q_i} - c'_{ij}\frac{\partial H'}{\partial P_j} + u_i + f_{ik}W_k(t)$$

$$i,j=1,2,\cdots,n;\quad k=1,2,\cdots,m \tag{1}$$

where Q_i and P_i are generalized displacements and momenta, respectively; $H' = H'(\mathbf{Q},\mathbf{P})$ is twice differentiable Hamiltonian; $c'_{ij} = c'_{ij}(\mathbf{Q},\mathbf{P})$; $u_i = u_i(\mathbf{Q},\mathbf{P})$; $f_{ik} = f_{ik}(\mathbf{Q},\mathbf{P})$; $W_k(t)$ are Gaussian white noises in the sense of Stratonovich with correlation functions $E[W_k(t)W_l(t+\tau)] = 2D_{kl}\delta(\tau)$; c'_{ij}, u_i, and $f_{ik}f_{jl}D_{kl}$ are assumed to be of the same order of ε, where ε is a small parameter. The system governed by Eq. (1) is generally nonlinear. The first summation terms on the right-hand side of Eq. (1) represent dissipation while the second summation terms the multiplicative excitations of Gaussian white noises. u_i are the feedback control forces.

Contributed by the Applied Mechanics Division of THE AMERICAN SOCIETY OF MECHANICAL ENGINEERS for publication in the ASME JOURNAL OF APPLIED MECHANICS. Manuscript received by the ASME Applied Mechanics Division, July 12, 2000; final revision, January 15, 2002. Associate Editor: A. A. Ferri. Discussion on the paper should be addressed to the Editor, Professor Robert M. McMeeking, Department of Mechanical and Environmental Engineering University of California–Santa Barbara, Santa Barbara, CA 93106-5070, and will be accepted until four months after final publication of the paper itself in the ASME JOURNAL OF APPLIED MECHANICS.

Equation (1) is equivalent to the following set of Itô equations:

$$dQ_i=\frac{\partial H'}{\partial P_i}dt$$

$$dP_i=-\left(\frac{\partial H'}{\partial Q_i}+c'_{ij}\frac{\partial H'}{\partial P_j}-D_{kl}f_{jl}\frac{\partial f_{ik}}{\partial P_j}+u_i\right)dt+\sigma_{ik}dB_k(t) \tag{2}$$

$$i,j=1,2,\cdots,n;\quad k,l=1,2,\cdots,m$$

where $B_k(t)$ are unit-independent Wiener processes and $\boldsymbol{\sigma\sigma}^T=2\mathbf{fDf}^T$. The double summation terms on the right-hand side of Eq. (2) are known as the Wong-Zakai correction terms ([20]). These terms usually can be split into a conservative part and a dissipative part. The conservative part can be combined with $-\partial H'/\partial Q_i$ to form overall effective conservative terms $-\partial H/\partial Q_i$ with a modified Hamiltonian $H=H(\mathbf{Q,P})$ and $\partial H/\partial P_i=\partial H'/\partial P_i$. The dissipative part can be combined with $-c'_{ij}\partial H'/\partial P_j$ to constitute effective dissipative terms $-c_{ij}\partial H/\partial P_j$ with $c_{ij}=c_{ij}(\mathbf{Q,P})$. With these accomplished, Eq. (2) can be rewritten as

$$dQ_i=\frac{\partial H}{\partial P_i}dt$$

$$dP_i=-\left(\frac{\partial H}{\partial Q_i}+c_{ij}\frac{\partial H}{\partial P_j}-u_i\right)dt+\sigma_{ik}dB_k(t) \tag{3}$$

$$i,j=1,2,\cdots,n;\quad k=1,2,\cdots,m.$$

The Hamiltonian system with modified Hamiltonian H governed by Eq. (3) with $c_{ij}=u_i=\sigma_{ik}=0$ is assumed to be integrable. That is, there exit n-independent first integrals, $H_1,H_2,\cdots,H_n$, which are in involution. This last term means that any two of them commute each other, i.e.,

$$[H_i,H_j]=0,\quad i,j=1,2,\cdots,n \tag{4}$$

where

$$[H_i,H_j]=\frac{\partial H_i}{\partial p_k}\frac{\partial H_j}{\partial q_k}-\frac{\partial H_i}{\partial q_k}\frac{\partial H_j}{\partial p_k},\quad k=1,2,\cdots,n \tag{5}$$

is the Poisson bracket of H_i and H_j. The Hamiltonian system is assumed to be nonresonant. So, the motion of the system is almost periodic and the orbits of the system are uniformly distributed on n-dimensioned torus.

Introduce transformations

$$H_r=H_r(\mathbf{Q,P}),\quad r=1,2,\cdots,n. \tag{6}$$

The Itô equations for H_r are obtained from Eq. (3) by using Itô differential rule as follows:

$$dH_r=\left(-c_{ij}\frac{\partial H}{\partial P_j}\frac{\partial H_r}{\partial P_i}+\frac{1}{2}\sigma_{ik}\sigma_{jk}\frac{\partial^2 H_r}{\partial P_i\partial P_j}+u_i\frac{\partial H_r}{\partial P_i}\right)dt+\frac{\partial H_r}{\partial P_i}\sigma_{ik}dB_k(t)$$

$$i,j,r=1,2,\cdots,n;\quad k=1,2,\cdots,m. \tag{7}$$

Take $Q_1,Q_2,\cdots,Q_n$ and $H_1,H_2,\cdots,H_n$ as the new state variables of the system. Then the system is governed by Eq. (7) and the n equations for Q_i in Eq. (3) with P_i replaced by H_r and Q_i in all these equations according to the transformations (6). It is seen that Q_i are rapidly varying processes while H_r slowly varying processes. According to the Khasminskii's theorem ([21]), the H_r converge weakly to an n-dimensional diffusion process as $\varepsilon\to 0$ in a time interval $0\leqslant t\leqslant T$, where $T\sim o(\varepsilon^{-1})$. The Itô equations for averaged H_r are of the form

$$dH_r=\left[F_r(\mathbf{H})+\left\langle u_i\frac{\partial H_r}{\partial P_i}\right\rangle\right]dt+G_{rk}(\mathbf{H})dB_k(t)$$

$$r,i=1,2,\cdots,n;\quad k=1,2,\cdots,m \tag{8}$$

where

$$\mathbf{H}=[H_1,H_2,\cdots,H_n]^T,$$

$$F_r(\mathbf{H})=\left\langle c_{ij}\frac{\partial H}{\partial P_j}\frac{\partial H_r}{\partial P_i}+\frac{1}{2}\sigma_{ik}\sigma_{jk}\frac{\partial^2 H_r}{\partial P_i\partial P_j}\right\rangle$$

$$b_{rs}(\mathbf{H})=G_{rk}(\mathbf{H})G_{sk}(\mathbf{H})=\left\langle\sigma_{ik}\sigma_{jk}\frac{\partial H_r}{\partial P_i}\frac{\partial H_s}{\partial P_j}\right\rangle \tag{9}$$

and

$$\langle[\cdot]\rangle=\lim_{T\to\infty}\frac{1}{T}\int_{t_0}^{t_0+T}[\cdot]dt \tag{10}$$

denoting a time-averaging operation. The time-averaging in Eq. (8) and (9) may be replaced by space-averaging using the ergodic property of the associated integrable and nonresonant Hamiltonian system on n-dimensional torus ([14]). The averaging of term $u_i\partial H_r/\partial P_i$ will be completed later since u_i are unknown so far.

Dynamical Programming Equation

Consider the n-dimensional controlled diffusion process $\mathbf{H}(t)$ governed by Eq. (8) on an infinite time interval $[0,\infty)$. Assume that the stationary solution exists in the system. Then we may formulate an ergodic control problem: finding Markov feedback control law $u_i=u_i(\mathbf{Q,P})$ to minimize the expected average cost function

$$J=\lim_{T\to\infty}\frac{1}{T}E\left[\int_0^T(f(\mathbf{H})+\langle\mathbf{u}^T\mathbf{Ru}\rangle)dt\right] \tag{11}$$

where $E[\cdot]$ denotes expectation operation, $\mathbf{u}=[u_1,u_2,\cdots,u_n]^T$ and $\mathbf{R}$ is a positive definite matrix; or, simply to minimize the average cost function

$$J=\lim_{T\to\infty}\frac{1}{T}\int_0^T(f(\mathbf{H})+\langle\mathbf{u}^T\mathbf{Ru}\rangle)dt \tag{12}$$

when $\mathbf{H}(t)$ is ergodic. The dynamical programming equation for this ergodic control problem can be established based on the dynamical programming principle as follows ([22]):

$$\min_{\mathbf{u}}\left\{f(\mathbf{H})+\langle\mathbf{u}^T\mathbf{Ru}\rangle+\frac{\partial V}{\partial H_r}\left[F_r(\mathbf{H})+\left\langle u_i\frac{\partial H_r}{\partial P_i}\right\rangle\right]+\frac{1}{2}b_{rs}(\mathbf{H})\frac{\partial^2 V}{\partial H_r\partial H_s}\right\}=\gamma \tag{13}$$

where

$$\gamma=\lim_{T\to\infty}\frac{1}{T}\int_0^T[f(\mathbf{H})+\langle\mathbf{u}^{*T}\mathbf{Ru}^*\rangle]dt \tag{14}$$

is the optimal average cost function and $\mathbf{u}^*$ is the optimal control.

The necessary conditions for minimizing the left-hand side of Eq. (13) are

$$\frac{\partial}{\partial u_i}\left\langle\mathbf{u}^T\mathbf{Ru}+u_i\frac{\partial V}{\partial H_r}\frac{\partial H_r}{\partial P_i}\right\rangle=0$$

$$i,r=1,2,\cdots,n. \tag{15}$$

The optimal feedback control law is thus obtained from Eq. (15) as follows:

$$u_i^*=-\frac{1}{2}(\mathbf{R}^{-1})_{ij}\frac{\partial H_r}{\partial P_j}\frac{\partial V}{\partial H_r}$$

$$i,j,r=1,2,\cdots,n \tag{16}$$

where $(\mathbf{R}^{-1})_{ij}$ is the i,j element of $\mathbf{R}^{-1}$. If $\mathbf{R}$ is a diagonal matrix with elements R_i, then Eq. (16) is reduced to

$$u_i^* = -\frac{1}{2R_i}\frac{\partial H_r}{\partial P_i}\frac{\partial V}{\partial H_r}$$

$$i,r=1,2,\cdots,n. \tag{17}$$

Substituting Eq. (16) or (17) into Eq. (13) and averaging the terms involving u_i^* lead to the final dynamical programming equation. For example, in the case of diagonal $\mathbf{R}$, the dynamical programming equation is of the form

$$f(\mathbf{H})+F_r(\mathbf{H})\frac{\partial V}{\partial H_r}-\frac{1}{4R_s}\left\langle\left(\frac{\partial H_r}{\partial P_s}\right)^2\right\rangle\left(\frac{\partial V}{\partial H_r}\right)^2$$

$$+\frac{1}{2}b_{rs}(\mathbf{H})\frac{\partial^2 V}{\partial H_r\partial H_s}=\gamma$$

$$r,s=1,2,\cdots,n. \tag{18}$$

For given $f(\mathbf{H})$ and $\mathbf{R}$, the optimal control law is obtained from solving Eq. (18) and then substituting the resulting $\partial V/\partial H_r$ into Eq. (17). Note that u_i^* are generally nonlinear in Q_i and P_i. For the problem of feedback stabilization, $f(\mathbf{H})$ and $\mathbf{R}$ will be determined by the requirement of stochastic stabilization as shown in the following section.

Stochastic Stabilization

The asymptotic stability with probability one of quasi-integrable Hamiltonian systems without control has been studied by evaluating the largest Lyapunov exponent of the averaged Itô equations for first integrals ([13,15]). Here we extend the result to controlled quasi-integrable Hamiltonian systems.

Substituting u_i^* obtained from Eq. (17) and (18) into Eq. (8) to replace u_i and averaging $u_i^*\partial H_r/\partial P_i$ lead to the following averaged Itô equations for controlled first integrals:

$$dH_r=\overline{F}_r(\mathbf{H})dt+G_{rk}(\mathbf{H})dB_k(t)$$

$$r=1,2,\cdots,n;\quad k=1,2,\cdots,m \tag{19}$$

where

$$\overline{F}_r(\mathbf{H})=F_r(\mathbf{H})-\frac{1}{2R_s}\left\langle\left(\frac{\partial H_r}{\partial P_s}\right)^2\right\rangle\left(\frac{\partial V}{\partial H_r}\right). \tag{20}$$

Let $\overline{H}$ be sum of n independent first integrals, i.e.,

$$\overline{H}=\sum_{r=1}^{n}H_r(\mathbf{Q},\mathbf{P}). \tag{21}$$

For example, for mechanical systems the total energy of the system is a sum of n component energies. Since the stochastic excitations in Eq. (1) are pure parametric (multiplicative), there will be

$$F_r(\mathbf{0})=0,\quad G_{rk}(\mathbf{0})=0. \tag{22a}$$

That is, $\mathbf{0}$ is the trivial solution of the uncontrolled system. Let $\langle(\partial H_r/\partial P_s)^2\rangle(\partial V/\partial H_r)|_{\mathbf{H=0}}=0$. Furthermore, assume that the drift and diffusion coefficients of fully averaged Itô Eqs. (19) satisfy the following conditions:

$$k\overline{F}_r(\mathbf{H})=\overline{F}_r(k\mathbf{H}),\quad kG_{rk}(\mathbf{H})=G_{rk}(k\mathbf{H}) \tag{22b}$$

$$(\mathbf{G}(\mathbf{H})\mathbf{G}^T(\mathbf{H})\mathbf{a},\mathbf{a})\geqslant c|\mathbf{H}|^2|\mathbf{a}|^2 \tag{23}$$

where $\mathbf{a}$ is an arbitrary vector and $c>0$ is a scalar. Equations (22*a*,*b*) and (23) imply that the drift and diffusion coefficients are homogeneous in H_r of degree one and the diffusion process $\mathbf{H}(t)$ is nonsingular, respectively. In the case where Eq. (19) does not satisfy conditions (22*b*), we may linearize Eq. (19). These assumptions permit us to derive an expression for the largest Lyapumov exponent of Eq. (19) using a procedure similar to that due to Khasminskii [11].

To this end, introduce the following new variables:

$$\rho=\frac{1}{2}\ln\overline{H} \tag{24}$$

and

$$\alpha_r=H_r/\overline{H},\quad r=1,2,\cdots n. \tag{25}$$

The Itô equations for ρ and α_r are obtained from Eq. (19) by using Itô differential rule as follows:

$$d\rho=\overline{Q}(\boldsymbol{\alpha})dt+\Sigma_k(\boldsymbol{\alpha})dB_k(t) \tag{26}$$

$$d\alpha_r=\overline{m}_r(\boldsymbol{\alpha})dt+\sigma_{rk}(\boldsymbol{\alpha})dB_k(t)$$

$$r=1,2,\cdots,n;\quad k=1,2,\cdots,m \tag{27}$$

where $\boldsymbol{\alpha}=[\alpha_1,\alpha_2,\cdots,\alpha_n]^T$,

$$\overline{Q}(\boldsymbol{\alpha})=\frac{1}{2}\sum_{s=1}^{n}\overline{F}_s(\boldsymbol{\alpha})-\frac{1}{4}\sum_{s,s'=1}^{n}\sum_{k=1}^{m}G_{sk}(\boldsymbol{\alpha})G_{s'k}(\boldsymbol{\alpha})$$

$$\overline{m}_r(\boldsymbol{\alpha})=-\alpha_r\sum_{s=1}^{n}\overline{F}_s(\boldsymbol{\alpha})+\overline{F}_r(\boldsymbol{\alpha})+\frac{1}{2}\alpha_r\sum_{s,s'=1}^{n}\sum_{k=1}^{m}G_{sk}(\boldsymbol{\alpha})G_{s'k}(\boldsymbol{\alpha})$$

$$-\frac{1}{2}\sum_{s=1}^{n}\sum_{k=1}^{m}G_{rk}(\boldsymbol{\alpha})G_{sk}(\boldsymbol{\alpha})$$

$$\sigma_{rk}(\boldsymbol{\alpha})=G_{rk}(\boldsymbol{\alpha})-\alpha_r\sum_{s=1}^{n}G_{sk}(\boldsymbol{\alpha}). \tag{28}$$

Note that $\Sigma_{r=1}^{n}\alpha_r=1$. So, only $n-1$ equations for α_r in Eq. (27) are independent. In the following the $n-1$ equations for $\alpha_1,\alpha_2,\cdots,\alpha_{n-1}$ are taken as independent ones. Let $\boldsymbol{\alpha}'=[\alpha_1,\alpha_2,\cdots,\alpha_{n-1}]^T$ and α_n be replaced by $1-\Sigma_{r=1}^{n-1}\alpha_r$.

Define the Lyapunov exponent of averaged system (19) as the asymptotic rate of the exponential growth of the square root of $\overline{H}$, i.e.,

$$\overline{\lambda}=\lim_{T\to\infty}\frac{1}{2T}\ln\overline{H}. \tag{29}$$

This definition is essentially the same as the Lyapunov exponent usually defined in terms of Euclidean norm when the associated Hamiltonian systems is linear but different when it is nonlinear. However, it is physically meaningful and it simplifies the evaluation of the largest Lyapunov exponent.

Following a derivation similar to that in [13] yields the following expression for the largest Lyapunov exponent of controlled system (19):

$$\overline{\lambda}_{\max}=\int\overline{Q}(\boldsymbol{\alpha}')\overline{p}(\boldsymbol{\alpha}')d\boldsymbol{\alpha}' \tag{30}$$

where $\overline{Q}(\boldsymbol{\alpha}')$ is obtained from $\overline{Q}(\boldsymbol{\alpha})$ in Eq. (28) with α_n replaced by $1-\Sigma_{r=1}^{n-1}\alpha_r$ and $\overline{p}(\boldsymbol{\alpha}')$ is the stationary probability density of $\boldsymbol{\alpha}'$ obtained from solving the reduced Fokker-Planck equation associated with Itô Eq. (27) with α_n replaced by $1-\Sigma_{r=1}^{n-1}\alpha_r$. In the derivation of Eq. (30), it is assumed that $\boldsymbol{\alpha}'$ is ergodic on the entire intervals $0<\alpha_r<1$, $r=1,2,\cdots,n$. In the case $\boldsymbol{\alpha}'$ is not ergodic on the entire intervals, special investigation is necessary (see, for example, [12]). The necessary and sufficient condition for asymptotic stability with probability one of the trivial solution of Eq. (19) is $\overline{\lambda}_{\max}<0$. This is also the approximate condition for asymptotic stability with probability one of the trivial solution of original system (1). The boundary between stability and instability regions of original system (1) is determined approximately by $\overline{\lambda}_{\max}=0$.

The differences between uncontrolled and controlled averaged systems are in drift coefficients

$$\overline{F}_r(\mathbf{H})-F_r(\mathbf{H})=-\frac{1}{2R_i}\left\langle\left(\frac{\partial H_r}{\partial P_i}\right)^2\right\rangle\left(\frac{\partial V}{\partial H_r}\right)$$

$$r,i=1,2,\cdots,n. \tag{31}$$

These differences will stabilize the system studied and they are determined by dynamical programming Eq. (18) for given $f(\mathbf{H})$ and $\mathbf{R}$ subject to the restrictions in Eq. (22*a*,*b*). In the designing feedback stabilization, $f(\mathbf{H})$ and $\mathbf{R}$ are so selected that $\overline{\lambda}_{\max}<0$. In the following an example is given to illustrate in detail the designing procedure.

Example

Consider the feedback stabilization of a linear oscillator coupled with a nonlinear oscillator by dampings and stochastically parametric excitations. The equations of motion of the system are of the form

$$\ddot{X}_1+\beta_{11}\dot{X}_1+\beta_{12}\dot{X}_2+\omega_1^2X_1=C_{11}\dot{X}_1W_1(t)+C_{12}\dot{X}_2W_2(t)+u_1$$

$$\ddot{X}_2+\beta_{21}\dot{X}_1+\beta_{22}\dot{X}_2+\gamma|X_2|^{\delta}\mathrm{sign}X_2=C_{21}\dot{X}_1W_1(t)$$

$$+C_{22}\dot{X}_2W_2(t)+u_2 \tag{32}$$

where X_i are generalized coordinates; β_{ij} are damping coefficients; C_{ij} are constants; ω_1 is the natural frequency of the linear oscillator; γ, $\delta>0$ are constants; $W_k(t)$ are independent Gaussian white noises in the senses of Stratonovich with intensities $2D_k$. Assume that β_{ij}, $C_{ik}D_k$, and u_i are of the same order of ε.

Let $X_i=Q_i$, $\dot{X}_i=P_i$, $i=1$, 2. Equation (32) can be rewritten as the following Itô equations:

$$dQ_1=P_1dt$$

$$dP_1=[-\omega_1^2Q_1-(\beta_{11}-C_{11}^2D_1)P_1-(\beta_{12}-C_{12}C_{22}D_2)P_2+u_1]dt$$

$$+C_{11}\sqrt{2D_1}P_1dB_1(t)+C_{12}\sqrt{2D_2}P_2dB_2(t)$$

$$dQ_2=P_2dt$$

$$dP_2=[-\gamma|Q_2|^{\delta}\mathrm{sign}Q_2-(\beta_{21}-C_{21}C_{11}D_1)P_1-(\beta_{22}$$

$$-C_{22}^2D_2)P_2+u_2]dt+C_{21}\sqrt{2D_1}P_1dB_1(t)$$

$$+C_{22}\sqrt{2D_2}P_2dB_2(t). \tag{33}$$

The Wong-Zakai correction terms contain no conservative part. The Hamiltonian associated with Eq. (33) is

$$H=H_1+H_2 \tag{34}$$

where

$$H_1=(P_1^2+\omega_1^2Q_1^2)/2$$

$$H=P_2^2/2+\gamma|Q_2|^{\delta+1}/(\delta+1). \tag{35}$$

The Itô equations for H_1 and H_2 are obtained from Eq. (33) by using Itô differential rule as follows:

$$dH_1=[-(\beta_{11}-C_{11}^2D_1)P_1^2-(\beta_{12}-C_{12}C_{22}D_2)P_1P_2+u_1P_1$$

$$+C_{11}^2D_1P_1^2+C_{12}^2D_2P_2^2]dt+C_{11}^2\sqrt{2D_1}P_1^2dB_1(t)$$

$$+C_{12}\sqrt{2D_2}P_1P_2dB_2(t)$$

$$dH_2=[-(\beta_{21}-C_{11}C_{21}D_1)P_1P_2-(\beta_{22}-C_{22}^2D_2)P_2^2+u_2P_2$$

$$+C_{21}^2D_1P_1^2+C_{22}^2D_2P_2^2]dt+C_{21}\sqrt{2D_1}P_1P_2dB_1(t)$$

$$+C_{22}\sqrt{2D_2}P_2^2dB_2(t). \tag{36}$$

Following the derivation from Eq. (7) to Eq. (8), the following averaged Itô equations for H_1 and H_2 can be obtained:

$$dH_1=(F_1(\mathbf{H})+\langle u_1P_1\rangle)dt+G_{11}dB_1(t)+G_{12}dB_2(t)$$

$$dH_2=(F_2(\mathbf{H})+\langle u_2P_2\rangle)dt+G_{21}dB_1(t)+G_{22}dB_2(t) \tag{37}$$

where $\mathbf{H}=[H_1,H_2]^T$,

$$F_1(\mathbf{H})=F_{11}H_1+F_{12}H_2$$

$$F_2(\mathbf{H})=F_{21}H_1+F_{22}H_2$$

$$b_{11}(\mathbf{H})=(\mathbf{GG}^T)_{11}=b_{11}^{(1)}H_1^2+b_{11}^{(2)}H_1H_2$$

$$b_{22}(\mathbf{H})=(\mathbf{GG}^T)_{22}=b_{22}^{(1)}H_1H_2+b_{22}^{(2)}H_2^2$$

$$b_{12}(\mathbf{H})=b_{21}(\mathbf{H})=0 \tag{38}$$

and

$$F_{11}=2C_{11}^2D_1-\beta_{11},\quad F_{12}=2C_{12}^2D_2(\delta+1)/(\delta+3)$$

$$F_{21}=C_{21}^2D_1,\quad F_{22}=2(2C_{22}^2D_2-\beta_{22})(\delta+1)/(\delta+3)$$

$$b_{11}^{(1)}=3C_{11}^2D_1,\quad b_{11}^{(2)}=4C_{12}^2D_2(\delta+1)/(\delta+3)$$

$$b_{22}^{(1)}=4C_{21}^2D_1(\delta+1)/(\delta+3),$$

$$b_{22}^{(2)}=24C_{22}^2D_2(\delta+1)^2/[(\delta+3)(3\delta+5)]. \tag{39}$$

For uncontrolled system, $u_i=0$. Equation (34) is a special case of Eq. (21), and F_i and G_{ik} in Eq. (38) satisfy the conditions in Eq. (22*a*,*b*) and (23). Introducing the transformations in Eq. (24) and (25), we obtain the following equations for ρ and α_1:

$$d\rho=Q(\alpha_1)dt+\Sigma(\alpha_1)dB(t) \tag{40}$$

$$d\alpha_1=m(\alpha_1)dt+\sigma(\alpha_1)dB(t) \tag{41}$$

where

$$Q(\alpha_1)=\lambda_1\alpha_1+\lambda_2(1-\alpha_1)+\tfrac{1}{4}\varphi(\alpha_1)+b_{22}^{(1)}\alpha_1(1-\delta)/8(1+\delta)$$

$$m(\alpha_1)=2(\lambda_1-\lambda_2)\alpha_1(1-\alpha_1)+\tfrac{1}{2}(1-2\alpha_1)\varphi(\alpha_1)$$

$$-b_{22}^{(1)}\alpha_1^2(1-\delta)/4(1+\delta)$$

$$\sigma^2(\alpha_1)=\alpha_1(1-\alpha_1)\varphi(\alpha_1) \tag{42}$$

and

$$\lambda_1=F_{11}/2-b_{11}^{(1)}/4,\quad \lambda_2=F_{22}/2-b_{22}^{(2)}/4$$

$$\varphi(\alpha_1)=a\alpha_1^2+b\alpha_1+c$$

$$a=b_{11}^{(2)}+b_{22}^{(1)}-b_{11}^{(1)}-b_{22}^{(2)}$$

$$b=b_{11}^{(1)}+b_{22}^{(2)}-2b_{11}^{(2)}$$

$$c=b_{11}^{(2)}$$

$$\Delta=b^2-4ac=(b_{11}^{(1)}+b_{22}^{(2)})^2-4b_{11}^{(2)}b_{22}^{(1)}. \tag{43}$$

Since $\sigma^2(\alpha_1)=0$ at two boundaries $\alpha_1=0$, 1, α_1 is singular at these two boundaries. It can be further identified by evaluating diffusion exponent and character value and by using Table 4.5.2 in ([23]) that $\alpha_1=0$ is an entrance and $\alpha_1=1$ is an entrance when $\delta<1$ and regular when $\delta>1$. α_1 is nonsingular and ergodic in the interval $0<\alpha_1<1$. The stationary probability density $p(\alpha_1)$ exists and it is obtained from solving the reduced Fokker-Planck equation associated with Itô Eq. (41) as follows:

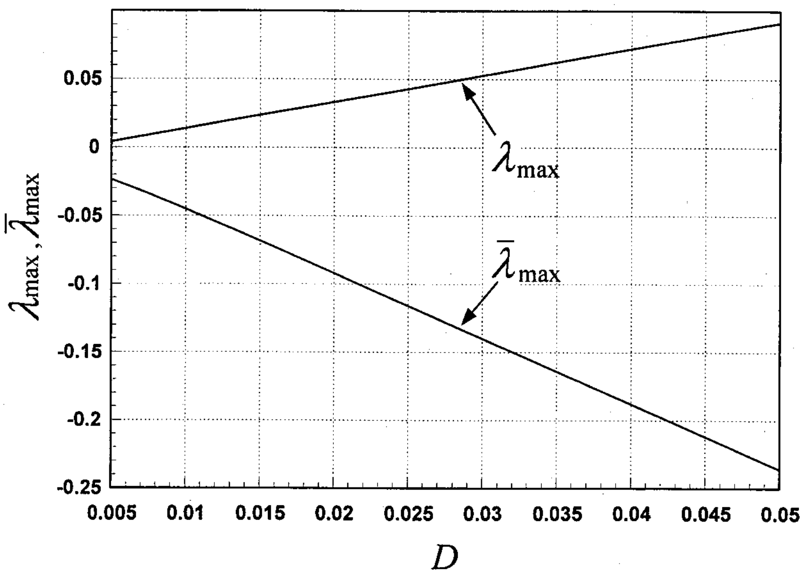

Fig. 1 The largest Lyapunov exponents $\lambda_{\max}$ and $\bar{\lambda}_{\max}$ of uncontrolled and optimally controlled system (32) versus intensity $D_1=D_2=D$ of stochastic excitations. $\omega=1.0$, $\gamma=1.0$, $\delta=3$, $\beta_{11}=\beta_{22}=0.01$, $\beta_{12}=\beta_{21}=0.0$, $c_{11}=c_{22}=1.0$, $c_{12}=c_{21}=2.0$, $f_1=f_2=0.0005$, $R_1=R_2=1.0$.

$$p(\alpha_1)=\frac{C(1-\alpha_1)^{(1-\delta)/2(1+\delta)}}{(\varphi(\alpha_1))^{1+(1-\delta)/4(1+\delta)}} \times\exp\left[\frac{4(\lambda_1-\lambda_2)+(b_{11}^{(1)}+b_{22}^{(2)})(1-\delta)/4(1+\delta)}{\sqrt{\Delta}} \times\ln\left|\frac{2a\alpha_1+b-\sqrt{\Delta}}{2a\alpha_1+b+\sqrt{\Delta}}\right|\right] \quad \text{for } \Delta>0 \tag{44}$$

$$p(\alpha_1)=\frac{C(1-\alpha_1)^{(1-\delta)/2(1+\delta)}}{(\varphi(\alpha_1))^{1+(1-\delta)/4(1+\delta)}} \times\exp\left[\frac{8(\lambda_1-\lambda_2)+(b_{11}^{(1)}+b_{22}^{(2)})(1-\delta)/2(1+\delta)}{\sqrt{-\Delta}} \times tg^{-1}\frac{2a\alpha_1+b}{\sqrt{-\Delta}}\right] \quad \text{for } \Delta<0 \tag{45}$$

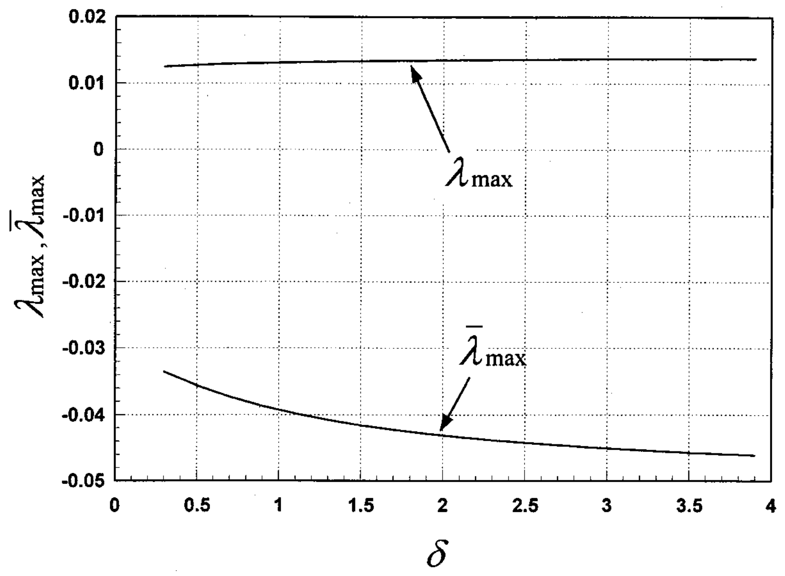

Fig. 2 The largest Lyapunov exponents $\lambda_{\max}$ and $\bar{\lambda}_{\max}$ of uncontrolled and optimally controlled system (32) versus intensity δ of nonlinearity. $\omega=1.0$, $\gamma=1.0$, $\beta_{11}=\beta_{22}=0.01$, $\beta_{12}=\beta_{21}=0.0$, $c_{11}=c_{22}=1.0$, $c_{12}=c_{21}=2.0$, $f_1=f_2=0.0005$, $R_1=R_2=1.0$, $D_1=D_2=0.01$.

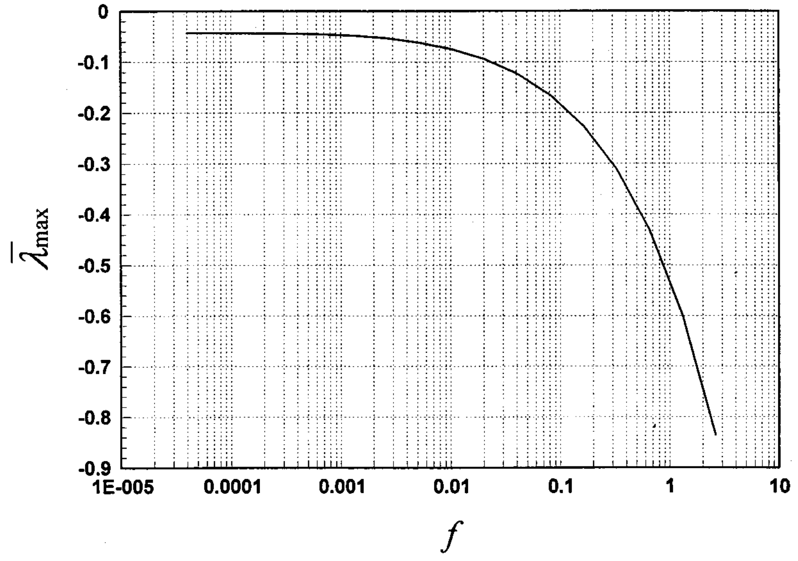

Fig. 3 The largest Lyapunov exponent $\bar{\lambda}_{\max}$ of optimally controlled system (32) versus $f_1=f_2=f$. $\omega=1.0$, $\gamma=1.0$, $\delta=3$, $\beta_{11}=\beta_{22}=0.01$, $\beta_{12}=\beta_{21}=0.0$, $c_{11}=c_{22}=1.0$, $c_{12}=c_{21}=2.0$, $R_1=R_2=1.0$, $D_1=D_2=0.01$.

$$p(\alpha_1)=\frac{C(1-\alpha_1)^{(1-\delta)/2(1+\delta)}}{(\varphi(\alpha_1))^{1+(1-\delta)/4(1+\delta)}}$$

$$\times\exp\left[-\frac{8(\lambda_1-\lambda_2)+(b_{11}^{(1)}+b_{22}^{(2)})(1-\delta)/2(1+\delta)}{2a\alpha_1+b}\right]$$

$$\text{for}\quad \Delta=0 \tag{46}$$

where C is a normalization constant. The largest Lyapunov exponent of uncontrolled system (32) is then

$$\lambda_{\max}=\int_0^1 Q(\alpha_1)p(\alpha_1)d\alpha_1. \tag{47}$$

Now consider the controlled system (32). From Eq. (35),

$$\frac{\partial H_1}{\partial P_1}=P_1,\quad \frac{\partial H_2}{\partial P_2}=P_2. \tag{48}$$

It is seen from Eq. (20) that in order to satisfy the conditions in Eq. (22*a*,*b*), $\partial V/\partial H_r$ should be constant. That is, V should be linear function of H_1 and H_2. Then, it is seen from dynamical programming Eq. (18) that $f(\mathbf{H})-\gamma$ should also be linear function of H_1 and H_2. Let

$$f(H)-\gamma=f_1H_1+f_2H_2$$

$$V(H)=k_1H_1+k_2H_2. \tag{49}$$

Substituting Eq. (49) into Eq. (18) leads to the following equations:

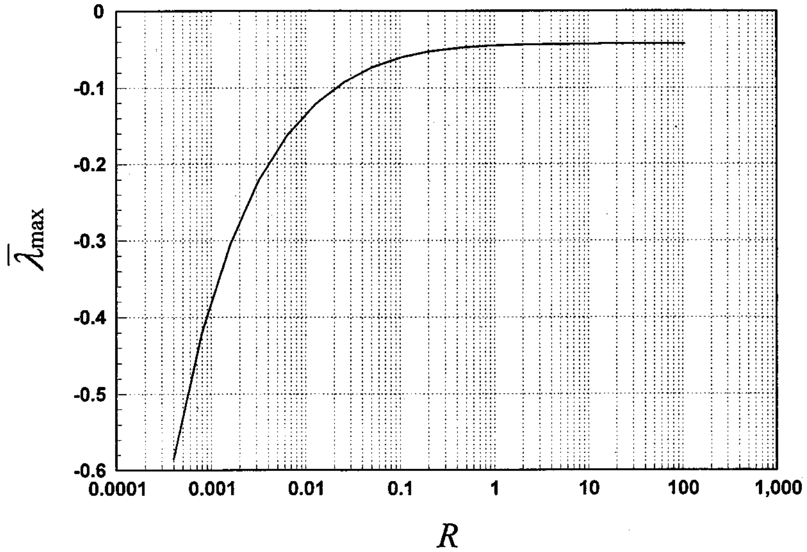

Fig. 4 The largest Lyapunov exponent $\bar{\lambda}_{\max}$ of optimally controlled system (32) versus $R_1=R_2=R$. $\omega=1.0$, $\gamma=1.0$, $\delta=3$, $\beta_{11}=\beta_{22}=0.01$, $\beta_{12}=\beta_{21}=0.0$, $c_{11}=c_{22}=1.0$, $c_{12}=c_{21}=2.0$, $f_1=f_2=0.0005$, $D_1=D_2=0.01$.

$$f_1+F_{11}k_1+F_{21}k_2-\frac{1}{4R_1}k_1^2=0$$

$$f_2+F_{12}k_1+F_{22}k_2-\frac{\delta+1}{2R_2(\delta+3)}k_2^2=0. \tag{50}$$

k_1 and k_2 can be solved from Eq. (50) for given f_i and R_i ($i=1,2$). The optimal control u_i^* are then obtained from Eq. (17) as follows:

$$u_i^*=-\frac{k_i}{2R_i}P_i=-\frac{k_i}{2R_i}\dot{Q}_i, \quad i=1,2. \tag{51}$$

Substituting u_i^* into Eq. (37) and then averaging $u_i^*P_i$ yield the following averaged drift coefficients for controlled first integrals:

$$\overline{F}_1(\mathbf{H})=\left(F_{11}-\frac{k_1}{2R_1}\right)H_1+F_{12}H_2$$

$$\overline{F}_2(\mathbf{H})=F_{21}H_1+\left(F_{22}-\frac{(\delta+1)k_2}{(\delta+3)R_2}\right)H_2. \tag{52}$$

Let

$$\overline{\lambda}_1=\lambda_1-\frac{k_1}{4R_1}, \quad \overline{\lambda}_2=\lambda_2-\frac{(\delta+1)k_2}{2(\delta+3)R_2}. \tag{53}$$

Following the derivation similar to that from Eq. (37) to Eq. (47), the following expression for the largest Lyapunov exponent of controlled averaged system can be obtained:

$$\overline{\lambda}_{\max}=\int_0^1\overline{Q}(\alpha')\overline{p}(\alpha')d\alpha' \tag{54}$$

where $\overline{Q}(\alpha')$ and $\overline{p}(\alpha')$ are obtained from $Q(\alpha')$ in Eq. (42) and from $p(\alpha')$ in Eq. (44)–(46), respectively, by replacing λ_1 and λ_2 with $\overline{\lambda}_1$ and $\overline{\lambda}_2$, respectively.

Equation (50) can be reduced to the following quadruplicate algebraic equation for k_1:

$$k_1^4+a_1k_1^3+a_2k_1^2+a_3k_1+a_4=0 \tag{55}$$

where

$$a_1=-\frac{2F_{11}}{d_1}$$

$$a_2=\frac{1}{d_1^2d_2}(d_2{F_{11}}^2-2d_1d_2f_1-d_1F_{21}F_{22})$$

$$a_3=\frac{1}{d_1^2d_2}(2d_2F_{11}f_1+F_{11}F_{22}F_{21}-F_{12}{F_{21}}^2)$$

$$a_4=\frac{1}{d_1^2d_2}(d_2{f_1}^2-{F_{21}}^2f_2+F_{21}F_{22}f_1)$$

$$d_1=\frac{1}{4k_1}, \quad d_2=\frac{\delta+1}{2(\delta+3)R_2} \tag{56}$$

while k_2 can be obtained from k_1 as follows:

$$k_2=\frac{1}{F_{21}}(d_1{k_1}^2-F_{11}k_1-f_1), \quad F_{21}\neq 0. \tag{57}$$

The feedback stabilization of system (32) is to determine f_i and R_i ($i=1,2$) such that the largest Lyapunov exponent determined by Eq. (54) is negative. It is seen from Eq. (51) that if $k_i>0$ ($i=1,2$), then u_i^* are really negative feedback control and the system may be stabilized by the control. Extensive computational results show that there are always positive real solutions for k_1 and k_2 in Eq. (50) provided f_i are positive. It is verified in Figs. 1 and 2, where the largest Lyapunov exponent $\lambda_{\max}$ of uncontrolled system (32) is positive while the largest Lyapunov exponent $\overline{\lambda}_{\max}$ of optimally controlled system (32) is negative. It is noted that the absolute value of negative largest Lyapunov exponent can be taken as a measure of stability margin. Figure 1–4 show that feedback stabilization is more effective for stronger nonlinearity and stochastic excitations and with larger f_i or smaller R_i.

Conclusions

In the present paper a procedure for designing feedback control to asymptotically stabilize with probability one quasi integrable Hamiltonian systems has been proposed. The procedure consists of deriving the averaged equations for first integrals, establishing the dynamical programming equation for an ergodic control problem, and determining the stability by evaluating the largest Lyapunov exponent of the averaged system. One example has been worked out in detail to illustrate the procedure. It has been shown that the procedure is relatively simple. It has also been shown that a quasi-integrable Hamiltonian system can always be stabilized by the control via proper choice of the cost function.

Acknowledgment

The work reported in this paper was supported by the National Natural Science Foundation of China under Grant Nos 19972059, 10002015.

References

[1] Kushner, J., 1967, *Stochastic Stability and Control*, Academic Press, New York.

[2] Khasminskii, R. Z., 1980, *Stochastic Stability of Differential Equation*, Sijthoff & Noordhoff, Alphen ann den Rijn.

[3] Florchinger, D., 1995, ''Lyapunov-Like Technique for Stochastic Stability,'' SIAM J. Control Optim., **33**, pp. 1151–1169.

[4] Florchinger, D., 1997, ''Feedback Stabilization of Affine in the Control Stochastic Differential Systems by the Control Lyapunov Function Method,'' SIAM J. Control Optim., **35**, pp. 500–511.

[5] Pan, Z., and Basar, T., 1999, ''Backstepping Controller Design for Nonlinear Stochastic Systems Under a Risk-Sensitive Cost Criterion,'' SIAM J. Control Optim., **37**, pp. 957–995.

[6] Deng, H., and Krstic, M., 1997, ''Stochastic Nonlinear Stabilization—Part II: Inverse Optimality,'' Syst. Control Lett., **32**, pp. 151–159.

[7] Deng, H., and Krstic, M., 1999, ''Output-Feedback Stochastic Nonlinear Stabilization,'' IEEE Trans. Autom. Control, **44**, pp. 328–333.

[8] Deng, H., and Krstic, M., 2000, ''Output-Feedback Stabilization of Stochastic Nonlinear Systems Driven by Noise of Unknown Covariance,'' Syst. Control Lett., **39**, pp. 173–182.

[9] Tsinias, J., 1998, ''Stochastic Input-to-State Stability and Applications to Global Feedback Stabilization,'' Int. J. Control, **71**, pp. 905–930.

[10] Oseledec, V. I., 1968, ''A Multiplicative Ergodic Theorem: Lyapunov Characteristic Number for Dynamical Systems,'' Trans. Moscow Mathematical Society, **19**, pp. 197–231.

[11] Khasminskii, R. Z., 1967, ''Necessary and Sufficient Conditions for the Asymptotic Stability of Linear Stochastic Systems,'' Theor. Probab. Appl., **12**, pp. 144–147.

[12] Ariaratnam, S. T., and Xie, W. C., 1992, ''Lyapunov Exponents and Stochastic Stability of Coupled Linear Systems Under Real Noise Excitation,'' ASME J. Appl. Mech., **59**, pp. 664–673.

[13] Zhu, W. Q., and Huang, Z. L., 1999, ''Lyapunov Exponents and Stochastic Stability of Quasi-Integrable-Hamiltonian Systems,'' ASME J. Appl. Mech., **66**, pp. 211–217.

[14] Zhu, W. Q., Huang, Z. L., and Yang, Y. Q., 1997, ''Stochastic Averaging of Quasi-Integrable-Hamiltonian Systems,'' ASME J. Appl. Mech., **64**, pp. 975–984.

[15] Huang, Z. L., and Zhu, W. Q., 2000, ''Lyapunov Exponent and Almost Sure Asymptotic Stability of Quasi-Linear Gyroscopic Systems,'' Int. J. Non-Linear Mech., **35**, pp. 645–655.

[16] Zhu, W. Q., and Ying, Z. G., 1999, ''Optimal Nonlinear Feedback Control of Quasi Hamiltonian Systems,'' Sci. China, Ser. A: Math., Phys., Astron., **42**, pp. 1213–1219.

[17] Zhu, W. Q., Ying, Z. G., Ni, Y. Q., and Ko, J. M., 2000, ''Optimal Nonlinear Stochastic Control of Hysteretic Systems,'' J. Eng. Mech., **126**, pp. 1027–1032.

[18] Zhu, W. Q., Ying, Z. G., and Soong, T. T., 2001, ''An Optimal Nonlinear Feedback Control Strategy for Randomly Excited Structural Systems,'' Nonlinear Dyn., **24**, pp. 31–51.

[19] Zhu, W. Q., and Yang, Y. Q., 1997, ''Stochastic Averaging of Quasi-Nonintegrable-Hamiltonian Systems,'' ASME J. Appl. Mech., **64**, pp. 157–164.
[20] Wong, E., and Zakai, M., 1965, ''On the Relation Between Ordinary and Stochastic Equations,'' Int. J. Eng. Sci., **3**, pp. 213–229.
[21] Khasminskii, R. Z., 1968, ''On the Averaging Principle for Stochastic Differential Equation,'' Kibernetika, **4**, pp. 260–279 (in Russian).
[22] Kushner, J., 1978, ''Optimality Conditions for the Average Cost Per Unit Time Problem With a Diffusion Model,'' SIAM J. Control Optim., **16**, pp. 330–346.
[23] Lin, Y. K., and Cai, G. Q., 1995, *Probabilistic Structure Dynamics, Advanced Theory and Applications*, McGraw-Hill, New York.

Journal of Applied Mechanics

Brief Notes

A Brief Note is a short paper that presents a specific solution of technical interest in mechanics but which does not necessarily contain new general methods or results. A Brief Note should not exceed 2500 words *or equivalent* (a typical one-column figure or table is equivalent to 250 words; a one line equation to 30 words). Brief Notes will be subject to the usual review procedures prior to publication. After approval such Notes will be published as soon as possible. The Notes should be submitted to the Editor of the JOURNAL OF APPLIED MECHANICS. Discussions on the Brief Notes should be addressed to the Editorial Department, ASME International, Three Park Avenue, New York, NY 10016-5990, or to the Editor of the JOURNAL OF APPLIED MECHANICS. Discussions on Brief Notes appearing in this issue will be accepted until two months after publication. Readers who need more time to prepare a Discussion should request an extension of the deadline from the Editorial Department.

Squeeze Film Force Using an Elliptical Velocity Profile

R. Usha
e-mail: ushar@iitm.ac.in

P. Vimala

Department of Mathematics, Indian Institute of
Technology, Madras, Channei 600 036, India

The squeeze film force in a circular Newtonian squeeze film has been theoretically predicted by using the elliptical velocity profile assumption in the squeeze film by three different approximation methods. As examples, the numerical results for the sinusoidal squeeze motion, constant velocity squeezing state, and constant force squeezing state have been obtained and the results have been found to be in good agreement with those obtained using experimental test coefficients predicted by the spectral analysis techniques for Newtonian circular squeeze film geometry. The validity of applying the energy integral method (EIM) or the successive approximation method (SAM) has been justified and the effectiveness of EIM or SAM in predicting squeeze film force using the elliptical velocity profile assumption in the squeeze film for large-amplitude motion has been demonstrated.

[DOI: 10.1115/1.1526124]

1 Introduction

The study of the dynamics of liquid squeeze films is important in many practical engineering applications. The squeeze film force that arises due to the motion of two surfaces separated by a viscous fluid is highly nonlinear in nature and hence it is difficult to obtain exact closed form solutions including the effects of fluid inertia. The studies based on Reynolds equation neglect the inertia effects completely, in predicting the squeeze film force. But, the approximation methods like the successive approximation method (SAM), momentum integral method (MIM), and energy integral method (EIM) include the inertial effects in predicting theoretically the squeeze film performance. These methods require a knowledge of the velocity profile in the squeeze film. Usually, a parabolic velocity profile is assumed and the expression for the squeeze film force is obtained.

However, the parabolic velocity profile assumption in the squeeze film is derived by neglecting the inertial effects and hence the resulting solution obtained for the squeeze film force is not valid for large amplitude motion of the squeeze film. Further, the experimental results on the squeeze film force in heat exchangers between a tube and its cylindrical support (Lu and Rogers [1,2]) and the experimental and the simulated results on the squeeze film force components in a circular geometry (Esmonde et al. [3] and Esmonde [4]) show that the temporal inertia force dominates the convective inertia and the viscous forces for large-amplitude motion and hence again the parabolic velocity profile assumption is inadequate.

Therefore, in order to accurately predict the squeeze film force for large-amplitude motion, it is necessary to assume the shape of a velocity profile that takes into account the inertial effects. Gross et al. [5] have suggested the use of elliptical velocity profile assumption in such cases where the inertia cannot be neglected.

In view of this, the axisymmetric problem of squeeze film in a circular geometry is analyzed by the approximation methods using an elliptical velocity profile assumption and the squeeze film force is theoretically predicted. The results obtained are compared with those predicted using other velocity profile assumptions for sinusoidal squeeze motion, constant velocity squeezing state, and constant force squeezing state for large-amplitude motion. The effectiveness of SAM or EIM in predicting the squeeze film force using the elliptical velocity profile assumption is demonstrated by comparing the present results with (i) those obtained using the experimental test coefficients predicted by spectral analysis techniques by Esmonde et al. [3] for Newtonian circular squeeze film geometry and (ii) the exact similarity solution due to Wang [6].

2 Mathematical Analysis

The equation of continuity and the Navier-Stokes equations in cylindrical polar coordinates, simplified using the order of magnitude analysis (Tichy and Winer [7]) for axisymmetric flow, are

$$\frac{\partial u}{\partial r}+\frac{u}{r}+\frac{\partial w}{\partial z}=0 \tag{1}$$

$$\frac{\partial p}{\partial r}=-\rho\frac{\partial u}{\partial t}-\rho\left(u\frac{\partial u}{\partial r}+w\frac{\partial u}{\partial z}\right)+\mu\frac{\partial^2 u}{\partial z^2} \tag{2}$$

$$\frac{\partial p}{\partial z}=0 \tag{3}$$

Contributed by the Applied Mechanics Division of THE AMERICAN SOCIETY OF MECHANICAL ENGINEERS for publication in the ASME JOURNAL OF APPLIED MECHANICS. Manuscript received by the ASME Applied Mechanics Division June 2, 2000, final revision, August 26, 2002. Associate Editor: K. T. Ramesh.

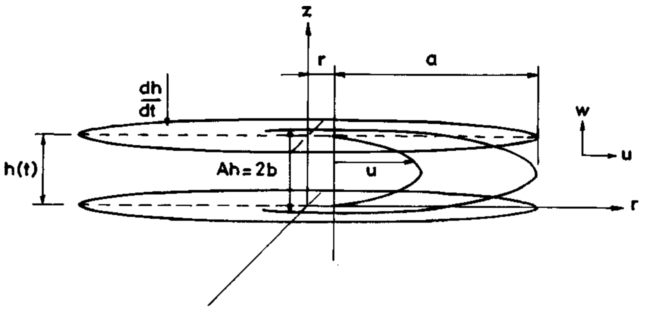

Fig. 1 Geometry of the parallel circular squeeze film and elliptical velocity profile

where u and w are the components of velocity in the radial and axial directions. Figure 1 shows the squeeze film configuration of the axisymmetric flow between two parallel circular disks of radius r_a located at $z=0$ and $z=h(t)$. The disk at $z=0$ is fixed and the other at $z=h(t)$ has motion only in the axial direction.

An elliptical velocity profile in the squeeze film with semi-major axis "a" and semi-minor axis "b" is assumed in the form

$$u^2(r,z,t)+B(r,t)z^2+C(r,t)u(r,z,t)+D(r,t)z+E(r,t)=0 \tag{4}$$

where B, C, D, and E are determined using the no-slip conditions

$$u=0 \quad \text{on} \quad z=0; \quad u=0 \quad \text{on} \quad z=h(t) \tag{5}$$

$$w=0 \quad \text{on} \quad z=0; \quad w=\dot{h} \quad \text{on} \quad z=h(t) \tag{6}$$

and $(\cdot)$ refers to derivative with respect to t. The condition (5) gives the equation of the elliptical velocity profile as

$$\frac{\left(u+\dfrac{C}{2}\right)^2}{\left(\dfrac{C^2}{4}+\dfrac{Bh^2}{4}\right)}+\frac{\left(z-\dfrac{h}{2}\right)^2}{\dfrac{1}{B}\left(\dfrac{C^2}{4}+\dfrac{Bh^2}{4}\right)}=1. \tag{7}$$

Equating the semi-major axis and the semi-minor axis to a and b, respectively, where $b=Ah/2$, $(A\geqslant 1)$, A is a constant parameter introduced to specify that part of the ellipse which is used to describe the velocity profile, and C and B are obtained as

$$C=\frac{a}{b}\sqrt{4b^2-h^2}, \quad B=\frac{a^2}{b^2} \tag{8}$$

so that the elliptical velocity profile in the squeeze film is given by (Fig. 2)

$$u=\frac{a}{Ah}\left[\sqrt{(Ah)^2-(2z-h)^2}-\sqrt{(Ah)^2-(h)^2}\right]. \tag{9}$$

The equation of continuity (1) and the condition (6) then yield the semi-major axis and the radial and axial components of velocity as

$$a=-\frac{A\dot{h}}{h}\,\frac{r}{A^2\sin^{-1}\left(\dfrac{1}{A}\right)-\sqrt{A^2-1}} \tag{10}$$

$$u=-\frac{\dot{h}r}{h^2}\,\frac{\left[\sqrt{(Ah)^2-(2z-h)^2}-h\sqrt{A^2-1}\right]}{\left[A^2\sin^{-1}\left(\dfrac{1}{A}\right)-\sqrt{A^2-1}\right]} \tag{11}$$

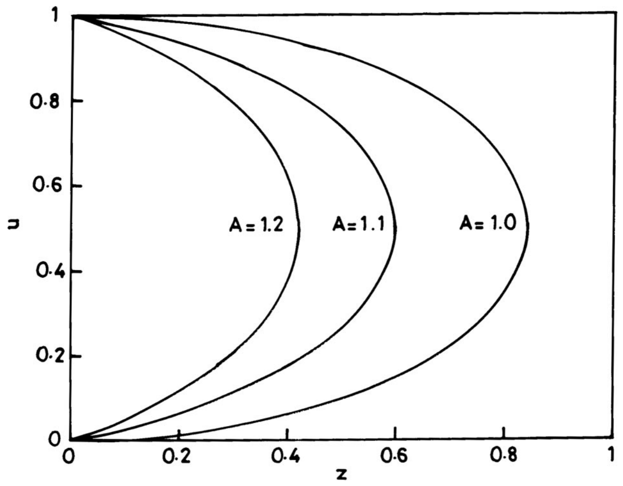

Fig. 2 Elliptical velocity profiles at a radial location for different values of A

$$w=\frac{A^2\dot{h}}{2}\,\frac{\left\{\sin^{-1}\left(\dfrac{2z-h}{Ah}\right)+\sin^{-1}\left(\dfrac{1}{A}\right)\right\}}{\left[A^2\sin^{-1}\left(\dfrac{1}{A}\right)-\sqrt{A^2-1}\right]}-\frac{\dot{h}}{2h}\,\frac{(4z-h)\sqrt{A^2-1}}{\left[A^2\sin^{-1}\left(\dfrac{1}{A}\right)-\sqrt{A^2-1}\right]}+\frac{\dot{h}}{2h^2}\,\frac{(2z-h)\sqrt{(Ah)^2-(2z-h)^2}}{\left[A^2\sin^{-1}\left(\dfrac{1}{A}\right)-\sqrt{A^2-1}\right]}. \tag{12}$$

The elliptical velocity profile thus obtained is used in the different approximation methods (SAM, MIM, and EIM) to get the average radial pressure gradient, and the squeeze film force is then obtained from

$$F=\int_0^{r_a}(p-p_a)|_{(z=h(t))}r\ \ dr \tag{13}$$

where r_a is the radius of the disk and p_a is the pressure at $r=r_a$.

3 Approximation Methods

There are three basic approaches to the integration of the Navier-Stokes equations to determine the average radial pressure gradient. In the MIM, the average radial pressure gradient is obtained by integrating the expression for the local pressure gradient across the squeeze film, so that

$$\frac{\partial p}{\partial r}=-\frac{\rho}{h}\int_0^h\left(\frac{\partial u}{\partial t}+u\frac{\partial u}{\partial r}+w\frac{\partial u}{\partial z}\right)dz+\frac{\mu}{h}\int_0^h\frac{\partial^2 u}{\partial z^2}dz. \tag{14}$$

In the EIM, the Navier-Stokes equation is first multiplied by the radial velocity u and then the resulting equation is integrated across the squeeze film to obtain the average radial pressure gradient. This gives

$$\frac{\partial p}{\partial r} = -\frac{\rho}{\int_0^h u\,dz}\int_0^h\left(u\frac{\partial u}{\partial t} + u^2\frac{\partial u}{\partial r} + uw\frac{\partial u}{\partial z}\right)dz$$

$$+\frac{\mu}{\int_0^h u\,dz}\int_0^h u\frac{\partial^2 u}{\partial z^2}dz. \tag{15}$$

The expressions for the assumed velocity profile in the squeeze film are substituted for u and w that appear on the right-hand side of (14) and (15) and the resulting average radial pressure gradient is then integrated to give the pressure in the squeeze film.

In the SAM, the Navier-Stokes equation is rewritten as

$$\frac{\partial^2 u}{\partial z^2} = \frac{1}{\mu}\frac{\partial p}{\partial r} + \frac{\rho}{\mu}\left(\frac{\partial u}{\partial t} + u\frac{\partial u}{\partial r} + w\frac{\partial u}{\partial z}\right) \tag{16}$$

and is then linearized using the assumed velocity profile in the squeeze film. The equation of continuity expressed in the form

$$\int_0^h u \quad dz = -\frac{\dot{h}r}{2} \tag{17}$$

is then used to find the radial pressure gradient.

In the present investigation, the elliptical velocity profile given in (11) and (12) are used on the right-hand side of (14), (15), and (16). The squeeze film force F is then obtained from (13) by the three approximation methods as

$$F = \lambda\left[-\frac{\alpha\ddot{h}}{h} + \frac{\beta\dot{h}^2}{h^2} - \frac{\gamma\nu\dot{h}}{h^3}\right] \tag{18}$$

where $\lambda = \rho\pi r_a^4/8$ and

$$\alpha = 1;\quad \beta = \frac{6\left[A^2\left\{1-\sqrt{A^2-1}\,\sin^{-1}\left(\frac{1}{A}\right)\right\}-\frac{1}{3}\right]}{\left(A^2\sin^{-1}\left(\frac{1}{A}\right)-\sqrt{A^2-1}\right)^2}$$

$$\gamma = \frac{8}{\left(A^2\sin^{-1}\left(\frac{1}{A}\right)-\sqrt{A^2-1}\right)\sqrt{A^2-1}}. \tag{19}$$

For MIM,

$$\alpha = -\frac{8\left\{-\frac{A^2}{2}+\frac{1}{6}+\frac{A^2}{2}\sqrt{A^2-1}\,\sin^{-1}\left(\frac{1}{A}\right)\right\}}{\left(A^2\sin^{-1}\left(\frac{1}{A}\right)-\sqrt{A^2-1}\right)^2}$$

$$\beta = -\frac{4\left\{-\frac{A^2}{2}+\frac{1}{6}+\frac{A^2}{2}\sqrt{A^2-1}\,\sin^{-1}\left(\frac{1}{A}\right)\right\}}{\left(A^2\sin^{-1}\left(\frac{1}{A}\right)-\sqrt{A^2-1}\right)^2}$$

$$-\frac{4\left\{\sin^{-1}\left(\frac{1}{A}\right)\left(-\frac{15}{4}A^4+3A^2\right)+\sqrt{A^2-1}\left(\frac{15}{4}A^2-\frac{1}{2}\right)\right\}}{\left(A^2\sin^{-1}\left(\frac{1}{A}\right)-\sqrt{A^2-1}\right)^3}$$

$$\gamma = \frac{8\left\{A\ln\left(\frac{A+1}{A-1}\right)-2\right\}}{\left(A^2\sin^{-1}\left(\frac{1}{A}\right)-\sqrt{A^2-1}\right)^2}. \tag{20}$$

For EIM and for SAM,

$$\alpha = \frac{\left\{3A^2(4-A^2)\sin^{-1}\left(\frac{1}{A}\right)+(3A^2-10)\sqrt{A^2-1}\right\}}{8\left(A^2\sin^{-1}\left(\frac{1}{A}\right)-\sqrt{A^2-1}\right)}$$

$$\beta = \frac{\left\{3A^2(A^2-4)\sin^{-1}\left(\frac{1}{A}\right)-(3A^2+14)\sqrt{A^2-1}+24A\right\}}{4\left(A^2\sin^{-1}\left(\frac{1}{A}\right)-\sqrt{A^2-1}\right)}$$

$$+\frac{\left\{1+5A^2\left(-A^2+\frac{4}{3}\right)+A^2(5A^2-8)\sqrt{A^2-1}\,\sin^{-1}\left(\frac{1}{A}\right)\right\}}{\left(A^2\sin^{-1}\left(\frac{1}{A}\right)-\sqrt{A^2-1}\right)^2}$$

$$+\frac{3A\left\{\left(A^3\left(\sin^{-1}\left(\frac{1}{A}\right)\right)^2-2A^2\sin^{-1}\left(\frac{1}{A}\right)+2\sqrt{A^2-1}\right)\right\}}{\left(A^2\sin^{-1}\left(\frac{1}{A}\right)-\sqrt{A^2-1}\right)^2}$$

$$\gamma = 12. \tag{21}$$

Table 1 Force coefficients for different velocity profiles using different methods * Elkouh [8]; ◦ Kuzma [9]; Tichy and Winer [7] (perturbation solution up to first order)

Method	Profile	α	β	γ
MIM	Elliptical $A=1.0$	1.0000	1.6211	-
	$A=1.1$	1.0000	1.7200	18.9247
	$A=1.2$	1.0000	1.7430	15.9691
EIM	Elliptical $A=1.0$	1.0808	1.7564	-
	$A=1.1$	1.1468	1.9627	12.6821
	$A=1.2$	1.1620	2.0133	12.3072
SAM	Elliptical $A=1.0$	1.1250	1.8308	12
	$A=1.1$	1.1704	2.0016	12
	$A=1.2$	1.1796	2.0421	12
* MIM	Parabolic	1.0	1.8	12
* EIM		1.2	2.1429	12
◦ SAM		1.2	2.1429	12
MIM	Uniform	1.0	1.5	0
EIM		1.0	1.5	0
SAM		1.0	1.5	0
Esmonde et al. [3]	Experimental test coefficients using spectral analysis techniques	1.22	0.8	8.85

4 Results and Discussion

The values of the coefficients α, β and γ obtained by the three methods, using the elliptical velocity profile (11) and (12) in the squeeze film are presented in Table 1, for different values of the profile factor A. In order to facilitate comparison, the results obtained (Elkouh [8]; Kuzma, [9]; and Tichy and Winer [7]) using the parabolic velocity profile $(u=(3\dot{h}r/h^3)(z^2-hz);w=(-6\dot{h}/h^3)(z^3/3-hz^2/2))$ and the uniform velocity profile $(u=r\dot{h}/2h;w=-\dot{h}z/h)$ for the circular squeeze film geometry by the three approximation methods, are presented in Table 1. The experimental test coefficients obtained using spectral analysis techniques by Esmonde et al. [3] are also presented for comparison.

From Table 1 it is observed that the temporal inertia force coefficient α takes the value one for different velocity profile assumptions in the squeeze film by MIM. This implies that the choice of the assumed velocity profile in the squeeze film does not affect the temporal inertia coefficient α when MIM is employed to predict the squeeze film force. On the other hand, in the case of EIM or SAM, the value of α depends upon the use of the assumed velocity profile in the squeeze film. This suggests that the tempo-

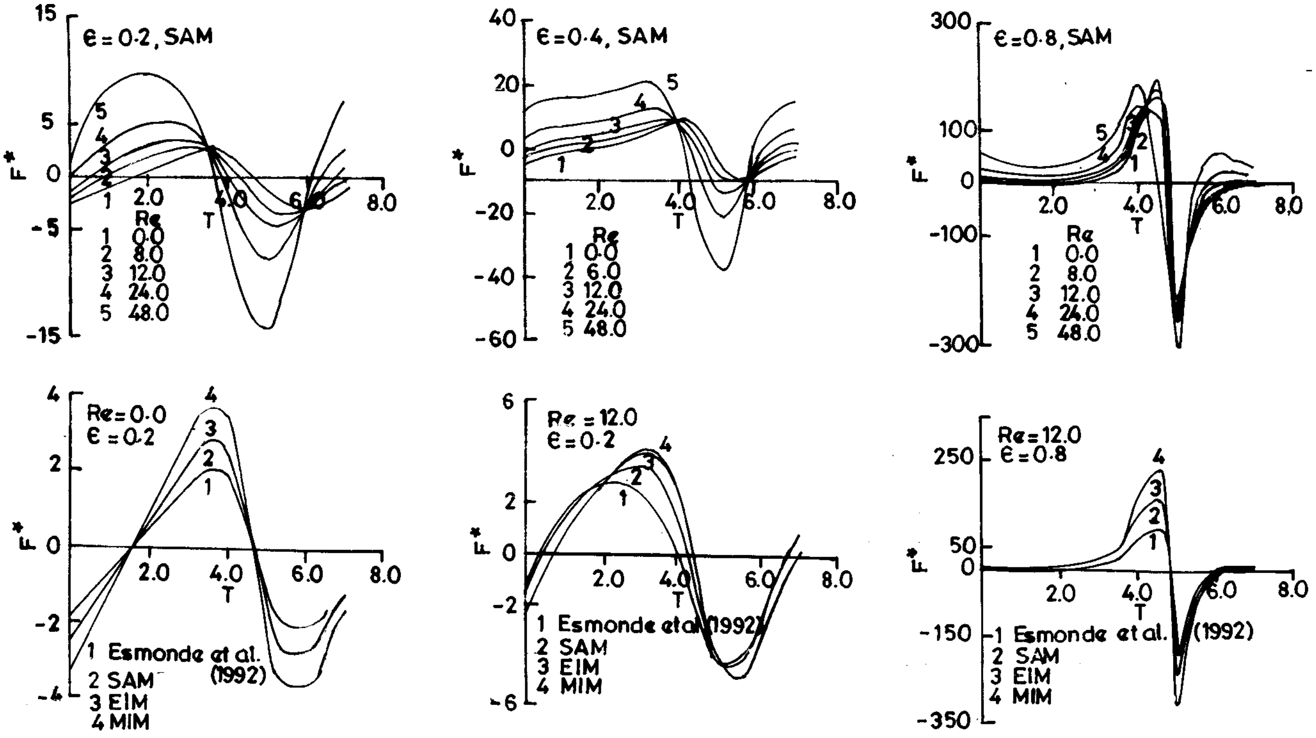

Fig. 3 Effects of fluid inertia on the squeeze film force using elliptical velocity profile under sinusoidal squeezing

ral inertia force in the circular squeeze film might be reasonably accurately predicted if either SAM or EIM is employed. Also, it is observed from Table 1 that the value of α given by either EIM or SAM using elliptical velocity profile (for different values of the profile factor A) lie between those predicted by uniform velocity profile and parabolic velocity profile assumptions.

With regard to the convective inertia force coefficient β and the viscous force coefficient γ, it is observed from Table 1 that the values of β and γ predicted by EIM or SAM using elliptical velocity profile are close to those obtained by any of the three methods using parabolic velocity profiles. Further, the viscous force coefficient γ predicted by all the methods using uniform velocity profile has the value zero. Such a prediction would be valid only for very low-viscosity fluids.

The temporal inertia coefficient predicted by the experimental results of Esmonde et al. [3] for the circular squeeze film geometry is higher than that predicted using parabolic profile by successive approximation method (Table 1). Comparison of the current results with the experimental results by Esmonde et al. [3] show that simulated values for temporal inertia coefficient are also greater than that obtained using elliptic velocity profile with either EIM or SAM.

Thus, the results presented in Table 1 and the deductions based on these values as given above imply that the use of either SAM or EIM with elliptical velocity profile assumptions in the squeeze film might predict reasonably accurate values of the squeeze film force for large-amplitude motion. In view of this, the results are presented for sinusoidal squeeze motion, constant velocity squeezing state and constant force squeezing state using elliptical velocity profile in the squeeze film by SAM and are compared with the other methods and other velocity profiles.

Figure 3 presents the results obtained for sinusoidal squeeze motion ($h^*(T)=1+\epsilon \sin T$; h^* is the dimensionless gap width given by $h^*=h/h_0$, where $h(t)=h_0+e \sin \omega t$, h_0 is the initial squeeze film thickness, $\epsilon=e/h_0$ and T is the dimensionless time

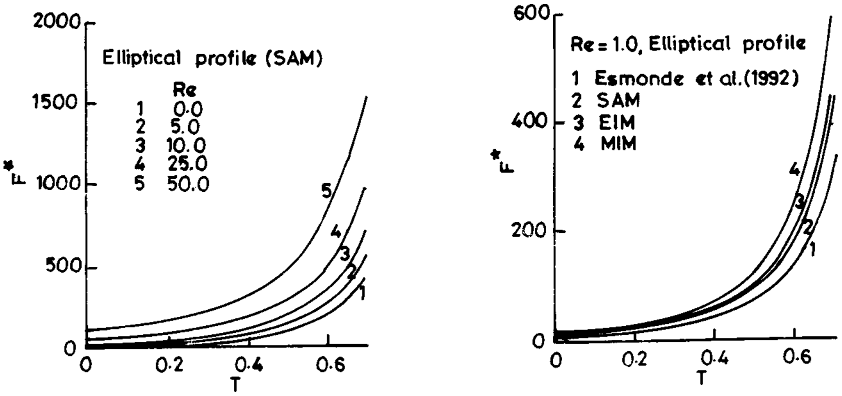

Fig. 4 Effects of fluid inertia on the squeeze film force for constant velocity squeezing state

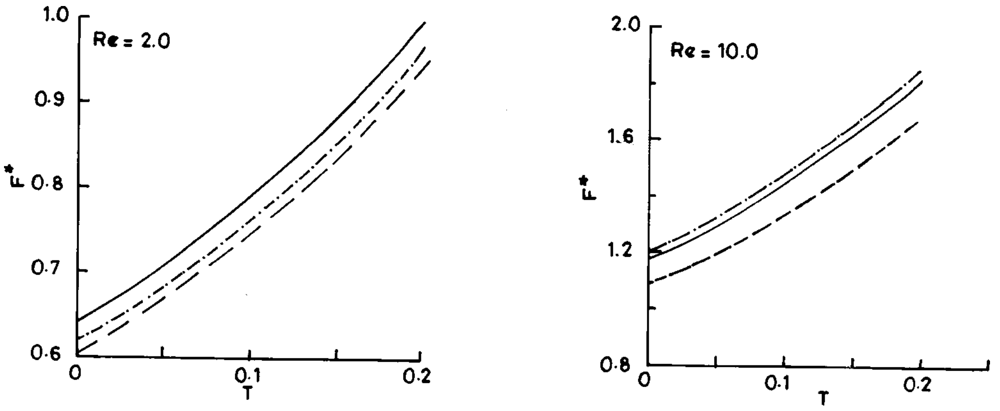

Fig. 5 Comparison of squeeze film force variation with Wang's [6] results. ——Wang, —·—· EIM, — — MIM.

given by $T=\omega t$) of the circular geometry using elliptical velocity profile by different methods, for different values of Reynolds numbers. It is observed that except for small values of ϵ and Re, there is a significant distortion in the waveform of the fluctuating force and phase shift. The comparison is made with reference to the waveform of the force obtained for the doubly limiting case $\epsilon\rightarrow 0$ and $\mathrm{Re}\rightarrow 0$. ($F^*\propto\cos T$, $\mathrm{Re}=\rho h_0^2\omega/\mu$ is the Reynolds number and $F^*=F/\pi r_a^2 p_a$ is the dimensionless force). It is also noted that phase shift is remarkable as Re increases and this may be attributed to the effect of fluid inertia. The distortion in waveform is magnified as ϵ increases and this is due to the change in the gapwidth.

Figure 4 presents the comparison of the results obtained using elliptical velocity profile by different methods and by using SAM with different values of Reynolds numbers for the constant velocity squeezing state. The dimensionless squeeze film force increases with the increase of Re for elliptical velocity profile assumptions using SAM. Further, the dimensionless squeeze film force obtained by EIM and SAM do not differ significantly when elliptical velocity profile assumption is used and the values lie between those of MIM and the results of Esmonde et al. [3].

The squeeze film force obtained using elliptical velocity profile assumption using MIM and EIM is compared (Fig. 5) with the exact similarity solution presented by Wang [6]. It is observed that the solution obtained by EIM using elliptical velocity profile is in good agreement with that of Wang's results.

In the case of constant force squeezing state, it is evident from Fig. 6 that the gapwidth decreases considerably with the increase in force and that the effect of inertia is to increase the normal force on the upper disk.

5 Conclusion

The squeeze film force in a circular Newtonian squeeze film has been theoretically predicted by using the elliptical velocity profile assumption in the squeeze film using three different approximation methods, and the numerical results for sinusoidal squeeze motion, constant velocity squeezing state, and constant force squeezing state have been obtained. Motivated by the suggestion by Gross et al. [5] and the investigation by Han and Rogers [10] on two-dimensional squeeze film geometry, the elliptical velocity profile in the film has been derived by taking into account the inertial effects. It has been observed by Esmonde et al. [3] that the various physical phenomena associated with the circular squeeze film for different film sizes for sinusoidal excitation obtained using spectral simulation agree well with their experimental results. In view of this, the present results have been compared with the exact similarity solution of Wang [6] and with those predicted by Esmonde [4] using experimental test coefficients obtained from the spectral analysis techniques and have been found to be in good agreement. It has been observed that the squeeze film force predicted by EIM or SAM using the elliptical velocity profile might be accepted as reasonably accurate for large-amplitude motion.

The investigations by Elkouh [11] for steady flow in a hydrostatic thrust bearing, Kuzma [9] and Elkouh [8] for flow in a Newtonian circular squeeze film, Turns [12] for flow in a Newtonian annular squeeze film, and Gupta and Kapur [13] for flow in

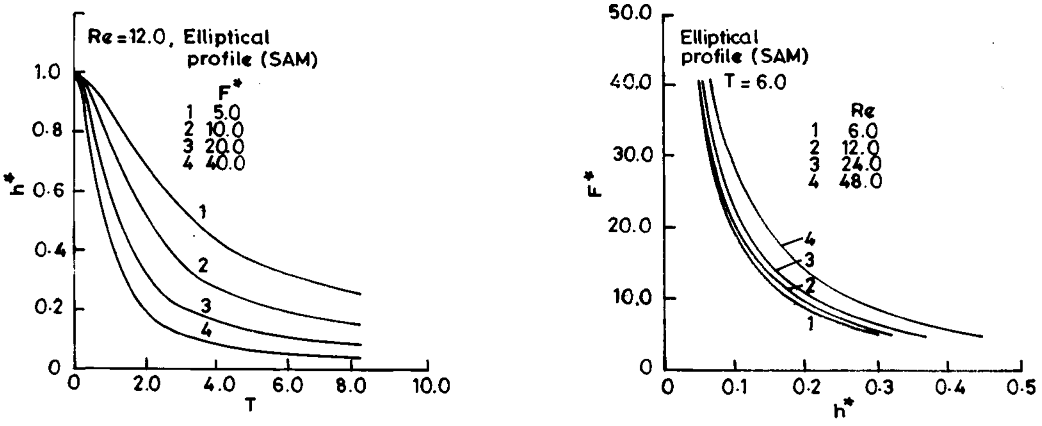

Fig. 6 Effects of fluid inertia on the squeeze film force under constant force squeezing state

a Newtonian curved squeeze film using SAM or EIM have been shown to be in good agreement either with experimental results (Tichy and Winer, [7]) or with the numerical solution (Grimm [14]) and have thus justified the validity of applying SAM or EIM in lubrication problems, in particular, in squeeze flow problems. These investigations have assumed a parabolic velocity profile assumption in the squeeze film and hence the results are valid for small to moderate Reynolds numbers. The success of these approximation methods in predicting theoretically the squeeze film force has given us the confidence to apply these methods in the present investigation for large-amplitude motion with elliptical velocity profile assumption. The results in the present investigation show how EIM or SAM can also be effectively used for large-amplitude motion of the Newtonian circular squeeze film, by using elliptical velocity profile assumption in the squeeze films.

Acknowledgment

The authors sincerely thank the referees for their very valuable comments and useful suggestions. The authors also wish to thank Prof. K. T. Ramesh, Associate Editor, for his encouraging remarks.

References

[1] Lu, Y., and Rogers, R. J., 1992, ‘‘A Nonlinear Model for Short Length, Cylindrical Squeeze Films With Large Planar Motions,’’ ASME J. Tribol., **114**, pp. 192–198.
[2] Lu, Y., and Rogers, R. J., 1994, ‘‘Normal Instantaneous Squeeze Film Force for a Finite Length Cylinder,’’ ASME J. Tribol., **116**, pp. 588–596.
[3] Esmonde, H., Fitzpatrick, J. A., Rice, H. J., and Axisa, F., 1992, ‘‘Modelling and Identification of Nonlinear Squeeze Film Dynamics,’’ J. Fluids Struct., **6**, pp. 223–248.
[4] Esmonde, H., 1989, ‘‘Spectral Analysis of Non-Linear Squeeze Film Dynamics,’’ Ph.D. thesis, Dublin University.
[5] Gross, W. A., Matsch, L. A., Castelli, V., Eshel, A., Vohr, J. H., and Wildmann, M., 1980, *Fluid Film Lubrication*, John Wiley and Sons, New York.
[6] Wang, C. Y., 1976, ‘‘The Squeezing of a Fluid Between Two Plates,’’ ASME J. Appl. Mech., **98**, pp. 579–582.
[7] Tichy, J. A., and Winer, R. J., 1970, ‘‘Inertial Considerations in Parallel Circular Squeeze Film Bearings,’’ ASME J. Lubr. Technol., **92**, pp. 588–592.
[8] Elkouh, A. F., 1976, ‘‘Fluid Inertia Effects in Non-Newtonian Squeeze Films,’’ ASME J. Lubr. Technol., **98**, pp. 409–411.
[9] Kuzma, D. C., 1967, ‘‘Fluid Inertia Effects in Squeeze Films,’’ Appl. Sci. Res. **18**, pp. 15–20.
[10] Han, Y., and Rogers, R. J., 1996, ‘‘Squeeze Film Force Modeling for Large Amplitude Motion Using an Elliptical Velocity Profile,’’ ASME J. Tribol., **118**, pp. 687–691.
[11] Elkouh, A. F., 1967, ‘‘Inertia Effect in Laminar Radial Flow Between Parallel Plates,’’ Int. J. Mech. Sci., **9**, pp. 253–255.
[12] Turns, S. R., 1983, ‘‘Annular Squeeze Films With Inertial Effects,’’ ASME J. Lubr. Technol., **105**, pp. 381–383.
[13] Gupta, R. S., and Kapur, V. K., 1980, ‘‘The Simultaneous Effect of Thermal and Inertia in Circular Squeeze Films,’’ ASME J. Lubr. Technol., **102**, pp. 501–504.
[14] Grimm, R. J., 1976, ‘‘Squeezing Flows of Newtonian Liquid Films—An Analysis Including Fluid Inertia,’’ Appl. Sci. Res., **32**, pp. 149–166.

Multiple Equilibria of a Hydrodynamically Coupled Flexible Disk Rotating Inside a Thin Housing

G. M. Warner and A. A. Renshaw
Department of Mechanical Engineering, Columbia
University, M/C 4703, New York, NY 10027

Experimental results are reported and a simple model proposed to explain a phenomenon in which the equilibrium deflection of a flexible disk rotating inside a narrow housing undergoes an abrupt jump when the rotation speed is varied slightly. Discontinuous jumps are observed in a small fraction (25%) of Zip disks rotating between 3000 rpm and 4500 rpm. For those disks exhibiting jumps, the jumps are repeatable for both increases and decreases in rotation speed during a test; no hysteresis is observed. A disk that initially exhibits the jump phenomenon may fail to exhibit jumps several days or weeks later and vice versa. Numerical results for a rotating membrane hydrodynamically coupled to the surrounding flow show that the number of possible equilibria is a sensitive function of the radial flows above and below the disk. In particular, a small change in radial flow from a radially inward flow to a radially outward flow can abruptly change the number of possible equilibria from two to one. The characteristics of this transition are compatible with the experimental observations. [DOI: 10.1115/1.1526121]

1 Introduction

The behavior of flexible rotating disks spinning within an enclosure is important to the design of removable computer memory disks such as I-Omega Zip disks and floppy disks. Unlike hard disk drives, flexible memory disks have often operated at speeds above the first critical speed of the disk spinning in vacuum, [1–3]. High-speed rotation decreases data acquisition times, but disks rotating near or above critical speed are particularly susceptible to small transverse vibrations which can degrade magnetic recording accuracy, [4,5]. Even steady-state deflections of a supercritical rotating disk can include small wavelength, large-amplitude harmonics which may be undesirable in magnetic recording, [2,6].

High-speed rotation of flexible computer memory disks is achievable because of hydrodynamic coupling between the disk and the surrounding air, which significantly increases the critical speed of the system over that of a disk spinning in a vacuum, [3]. Steady equilibrium behavior of a flexible disk spinning close to a rigid wall was first investigated by Pelech and Shapiro [7]. They obtained excellent agreement between experimental measurements and a model based on classical hydrodynamic lubrication theory modified to include centrifugal pressure gradients. More recently, a number of investigators (including the authors) have either extended or proposed alternative models of the coupled disk/fluid system in order to estimate the range of stable operation for these systems, [3,8–10]. To the authors' knowledge, none of these stability predictions have been experimentally verified. In addition, many of these investigations have analyzed disks with hydrodynamic coupling on only one side of the disk. Such designs have not been used commercially since the late 1970s.

The purpose of this brief note is to describe an instability phenomenon in an I-Omega Zip disk and present a very simple, possible analytical explanation. We begin by describing experimental results documenting abrupt changes in the transverse displacement of the outer periphery of the disk as the rotation speed is varied. These sudden displacement variations or jumps are not observed in all disks, but for those disks exhibiting the phenomenon, the jump is repeatable as the rotation speed is increased above or decreased below the critical transition speed.

We then introduce a simple mathematical model of the aerodynamically coupled disk in order to explain the jump phenomenon. In this model, we make two fundamental assumptions: (1), the disk deflection is axisymmetric; and (2), the bending stiffness of the disk is negligible in comparison to the stiffness derived from the in-plane stresses in the disk. In practice, neither of these assumptions is true. Zip disks have a number of intrinsic asymmetries: the enclosure is asymmetric due to a slot accommodating the read/write suspension, the polymeric disk is nonisotropic [7], and its mounting can produce noticeable runout. In addition, previous

---

Contributed by the Applied Mechanics Division of THE AMERICAN SOCIETY OF MECHANICAL ENGINEERS for publication in the ASME JOURNAL OF APPLIED MECHANICS. Manuscript received by the ASME Applied Mechanics Division, December 16, 2001; final revision, July 26, 2002. Associate Editor: O. O'Reilly.

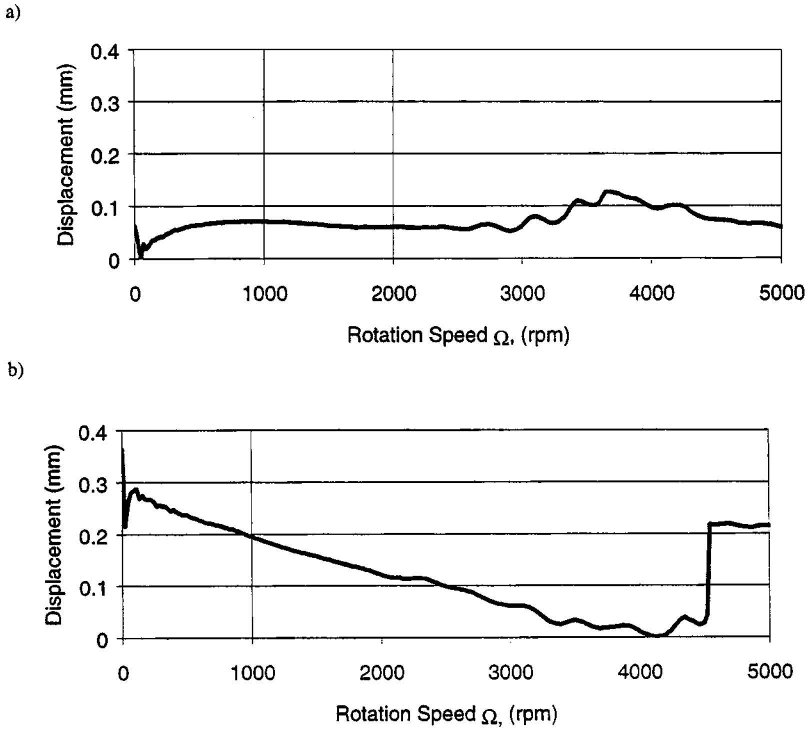

Fig. 1 Displacement versus rotation speed for two disks. (*a*): A typical Zip disk response without the jump phenomenon; (*b*): the jump phenomenon at approximately 4500 rpm.

research suggests that bending stiffness in very flexible rotating disks may be important, [2,6]. Despite these limitations, the simplified model has the numerical advantage that the search for equilibria can be performed using an ordinary differential equation shooting technique involving only one unknown parameter. As a consequence, the results obtained are definitive, robust, and free from numerical artifacts. This would not be true for a more faithful, but complicated model. For example, inclusion of the bending stiffness would lead to three unknown parameters in the shooting method; equilibria could be found, but determining that *all* equilibria had been found would be difficult.

The results indicate that the number of equilibrium states of an enclosed, flexible disk is controlled by small changes in the direction of radial flows above and below the disk. When either the upper or lower flow rate changes direction, as might be expected in an enclosed housing such as a Zip disk, an abrupt transition from one to two equilibria can occur. This equilibrium transition has many features that are compatible with experimental observations, although more definitive experimental evidence is required to validate the model. The explanation of the phenomenon offered by this simple model suggests that controlling the radial flow in floppy and Zip disks may be an important design objective.

Table 1 Jump magnitude and corresponding rotation speed for disks displaying the jump phenomenon for both horizontal and vertical orientations. All entries are the averages of multiple runs.

Horizontal Orientation			Vertical Orientation		
Disk #	Jump (mm)	Ω_{jump} (rpm)	Disk #	Jump (mm)	Ω_{jump} (rpm)
1	0.08	4325	5	0.08	4650
2	0.02	3470	2	0.09	4080
3	0.12	4318	3	0.04	3714
4	0.05	4369	6	0.10	3929
Average:	0.0675	4120	Average:	0.0775	4093

2 Experimental Results

We begin by describing a series of experiments performed on I-Omega Zip disks in order to determine the steady-state equilibrium of the disk as a function of rotation speed. The magnetic clamp and bearing of a Zip disk drive was removed and attached to a rigid frame. A DC motor was also attached to the frame and connected to the Zip disk clamp/bearing by a belt drive. Computer control of the DC motor allowed variable Zip disk rotation from 0 to 5000 rpm. Zip disk drives normally operate at approximately 2800 rpm.

The sliding dust cover of a Zip disk was removed to permanently expose approximately one square cm of the periphery of the magnetic polymer disk. This was the only modification made to the Zip disk. The Zip disk was mounted on the clamp/bearing in the same manner as in a Zip disk drive. A Philtec Photonic displacement sensor with a sensitivity of 0.610×10^{-3} m/V was positioned immediately above the magnetic polymer disk in order to measure the transverse position of the disk. The probe measures an average displacement of the disk over an area of approximately 5.0 square mm. For each experiment, only the relative displacement of the outer edge of the disk from its initial position was measured. Since the initial position of the stationary disk was uncontrolled and nonrepeatable, no attempt was made to measure or control absolute position of the disk.

In each experiment, the disk was rotated at 238 distinct, equally spaced speeds between 0 to 5000 rpm. At each fixed speed, 500 data points were acquired at 1000 Hz and averaged. The rotation speeds were either increased from 0 to 5000 rpm, or decreased from 5000 to 0 rpm.

Figure 1 shows two representative plots of the relative displacement of the disk as a function of rotation speed. In Fig. 1(*a*), the displacement of the periphery of the disk varies continuously throughout the experiment. The disk begins to ascend slightly after 3000 rpm reaching a peak at approximately 3700 rpm before declining steadily. In, Fig. 1(*b*), however, the disk abruptly jumps approximately 0.2 mm at 4500 rpm. Before and after this jump, the curve varies in a continuous manner.

An abrupt jump occurred in 4 disks out of 11 tested in a horizontal position and 4 disks out of 11 tested in a vertical position. Two disks demonstrated this behavior in both the horizontal and vertical position. The jump was repeatable during a particular test for both increasing and decreasing speed.

No significant vibration was detected when the frequency response of the disk position was calculated except for disk runout which only occurred for low speeds (<500 rpm). Above 500 rpm, the disk position was steady both before and after the jump. The spatial distribution of the disk was not possible to determine without partially removing the Zip disk cover. Since the air flow depends significantly on the integrity of the cover, the spatial distribution of the disk was not measured.

Table 1 lists the jumps magnitude and rotation speed for the eight disks exhibiting the phenomenon. In both the horizontal and vertical orientations, the jumps occur above the normal operation speed of a Zip disk (2800 rpm); for the horizontal orientation, the average rotation speed at which the jump occurs is 4120 rpm; for the vertical orientation, the average rotation speed of the jump is 4093 rpm. This suggests that gravity loading of the disk influences the phenomenon only modestly, if at all.

While the jump phenomena was repeatable for a particular test as the disk was spun up and spun down, it was not necessarily repeatable between tests conducted on different days. Some disks would exhibit the behavior over the course of consecutive days and consecutive tests, while others would vary from day to day. Over the course of testing even the most reliable of disks would vary, alternately displaying the jump behavior and not displaying the behavior.

3 Modeling

We now develop a simple model to explain the jump phenomenon. A thin, axisymmetric annular disk of outer radius R_o, density ρ_D, and Poisson's ratio ν spins about its axis of symmetry with constant angular velocity Ω while enclosed within an axisymmetric housing, as shown in Fig. 2. The disk is clamped at inner radius R_i, its thickness is Δ, and its transverse deflection is W. The in-plane radial stress is σ_r^*. The upper and lower clearances between the undeflected disk and the housing walls are C_u and C_L, and air leakage through the housing is measured by the volumetric radial upper and lower flows Q_U and Q_L. The air pressure in the clearances is P_U and P_L. The surrounding air is of density ρ_F and viscosity μ. When present, gravity g acts downward. R measures radial position.

Dimensionless variables are defined by

$$r=R/R_o \quad w=W/(C_L+C_U) \quad \sigma_r=\sigma_r^*/\rho_D\Omega^2R_o^2. \tag{1}$$

The component of the pressure fields generated by centripetal acceleration produces equal and opposite pressures on the upper and lower surfaces of the disk. We take advantage of this and define the dimensionless pressures p_L and p_U by

$$P=\frac{3}{20}\rho_F\Omega^2R_o^2(r^2-1)+\rho_D\Delta(C_L+C_U)\Omega^2 p \tag{2}$$

where, for brevity, the subscripts L and U have been omitted.

We assume the disk/air equilibria are axisymmetric and neglect the bending stiffness of the disk. Transverse equilibrium of a spinning disk written in the stationary frame of reference requires, [1],

$$\frac{1}{r}(r\sigma_r w_{,r})_{,r}+p_L-p_U-\Gamma=0 \tag{3}$$

where a comma indicates differentiation. Pelech and Shapiro's model for the axisymmetric pressure distributions reduce to, [7],

$$p_{L,r}=-\frac{6q_L}{\pi r(c_L+w)^3} \tag{4}$$

$$P_{U,r}=-\frac{6q_U}{\pi r(c_U-w)^3}. \tag{5}$$

Boundary conditions for the coupled ordinary differential Eqs. (3)–(5) are

$$w(\kappa)=p_L(1)=p_U(1)=0 \quad \lim_{r\to 1}\sigma_r w_{,r}=0. \tag{6}$$

The six dimensionless parameters in the model are the clamping ratio

$$\kappa=R_i/R_o, \tag{7}$$

gravity

$$\Gamma=g/(C_L+C_U)\Omega^2, \tag{8}$$

fractional clearances

$$c_L=C_L/(C_L+C_U) \quad c_U=C_U/(C_L+C_U), \tag{9}$$

and radial flows

$$q_L=\mu Q_L/\rho_D\Delta\Omega^2(C_L+C_U)^4 \quad q_U=\mu Q_U/\rho_D\Delta\Omega^2(C_L+C_U)^4. \tag{10}$$

The radial stresses are given by the standard generalized plane stress solution with vanishing in-plane radial displacement at $r=\kappa$ and vanishing traction at $r=1$, [11]:

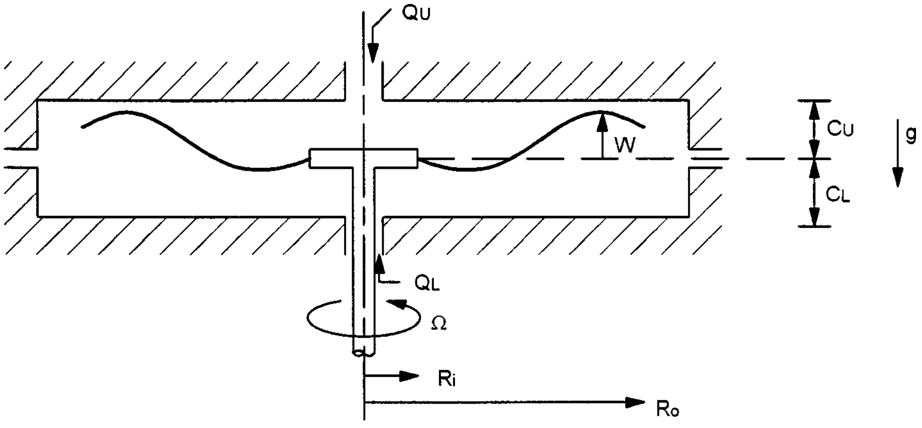

Fig. 2 Schematic of the rotating disk enclosed in a housing

$$\sigma_r=\frac{\kappa^2(1-\nu)(3+\nu-\kappa^2-\nu\kappa^2)}{8(1+\nu+\kappa^2-\nu\kappa^2)r^2}+\frac{(1+\nu)(3+\nu+\kappa^4-\nu\kappa^4)}{8(1+\nu+\kappa^2-\nu\kappa^2)}-\frac{(3+\nu)r^2}{8}. \qquad (11)$$

For an I-Omega Zip disk: $R_i=12.5$ mm; $R_o=43$ mm; $C_L=C_U=0.5$ mm; $\Delta=0.05$ mm; $\rho_d=1300$ kg/m^3; $\Omega=2800$ rpm; $\rho_f=1.2$ kg/m^3; and $m=2.0\times 10^{-5}$ kg/s/m. This give $\kappa=0.291$ and $\Gamma=0.114$. q_L and q_U are unknown. We can estimate the order of magnitude for q_L and q_U by examining the experimental studies of Pelech and Shapiro [7] in which radial flow was measured for a disk rotating close to a rigid wall. In their experiments, Γ range from 0.2 to 0.7 while q_L varies from 0.02 to 20. We suspect that these values of q_L are higher than those for the Zip disk geometry since there is no housing in Pelech and Shapiro's experiment to restrict flow. In addition, in Pelech and Shapiro's experiments only one side of the rotating disk is pressurized so that both components of the total pressure P in (2) contribute to the disk deflection. In the experiments of Pelech and Shapiro [7] as well as for the Zip disk, the nominal centrifugal pressure, $\rho_F\Omega^2R_o^2$, is approximately 10^3 times greater than the nominal Reynolds pressure, $\rho_D\Delta(C_L+C_U)\Omega^2$. Such a large pressure difference would be expected to strongly influence the order of magnitude of q_L. From these considerations, we estimate q_L and q_U to range from 10^{-3} to 10^{-1}.

4 Numerical Solution

As described in [7], the coupled ordinary differential Eqs. (3)–(5) can be solved using a shooting scheme. If one guesses a value of $w(1)$, Eqs. (3)–(5) can be integrated as an initial value problem from $r=1$ to $r=\kappa$. The error in the guess of $w(1)$ is given by $w(\kappa)$, which must vanish in order to satisfy the boundary conditions (6). A root finding technique can be used to determine values of $w(1)$ corresponding to solutions. The root finding is made easier by the fact that $-c_L<w(1)<c_U$. However, the root finding is not entirely straightforward in that for values of $w(1)$ close to either $-c_L$ or c_U, it can be impossible to integrate the differential equations to $r=\kappa$. When the disk deflection w comes sufficiently close to either $-c_L$ or c_U at some interior location $\kappa<r<1$, the right-hand side of either (4) or (5) can become large enough that it causes the integration stepsize to be reduced until it becomes numerically zero and the integration fails. This integration failure frequently occurs for values of $w(1)$ which are quite close to solution values. Consequently, the root finding scheme should approach roots from an interior value of $w(1)$ and must be able to correctly handle failed numerical integration.

The only other special feature of the shooting scheme is evaluating the derivatives at $r=1$, which is a regular singular point of (3) since $\sigma_r(1)=0$, [12]. Substitution of $r=1$ into (3) gives

$$w,_r(1)=\Gamma/\sigma_r,_r|_{r=1}. \qquad (12)$$

Differentiation of (3) with respect to r followed by substitution of $r=1$ gives

$$w,_{rr}(1)=[-p_L,_r+p_U,_r-(r\sigma_r,_r),_r w,_r/r]/2\sigma_r,_r|_{r=1}. \qquad (13)$$

Equations (12) and (13) should be used to evaluate the derivatives of w at $r=1$; everywhere else, Eq. (3) should be used.

5 Results

Figure 3 shows a contour plot of the number of equilibria as functions of q_L and q_U for the Zip disk geometry given in Table 2: $\kappa=0.291$, $\nu=0.3$, $\Gamma=0.114$, and $c_L=c_U=0.5$.

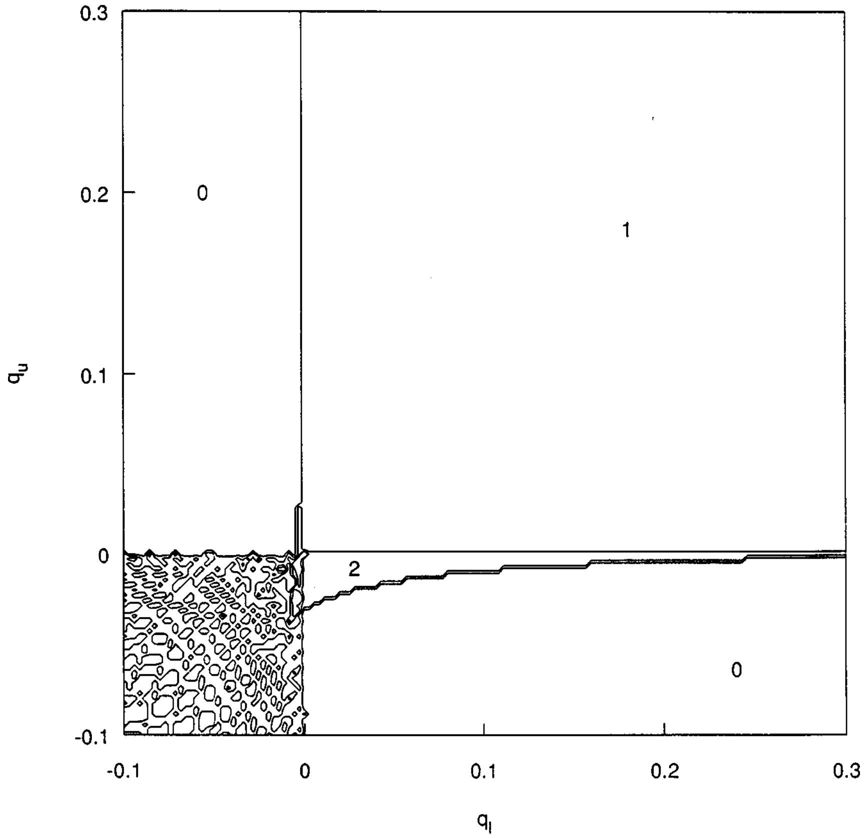

Fig. 3 Contour plot of the number of equilibria as functions of q_L and q_U. $\kappa=0.291$; $\nu=0.3$; $\Gamma=0.114$; $c_L=c_U=0.5$. The number of equilibria in each region is superimposed on the plot except for the lower left quadrant.

Table 2 Data for an I-Omega Zip disk

R_i (mm)	12.5
R_o (mm)	43
C_L (mm)	0.5
C_U (mm)	0.5
Δ (mm)	0.05
ρ_d (kg/m^3)	1300
Ω (rpm)	2800
ρ_f (kg/m^3)	1.2
μ (kg/s/m)	2.00E-05
κ	0.291
Γ	0.114

A more detailed understanding of Fig. 3 is obtained by examining the error plots of $w(\kappa)$ versus $w(1)$ given in Fig. 4 where we let $q_U = -q_L$. This corresponds to a slice through the contour plot in Fig. 3 with a slope of -1.

In Fig. 4, for the most negative values of q_L, the error curve is concave up and entirely above the $w(\kappa)=0$ axis. These curves have no equilibrium solutions. As q_L increases, (at $q_L=0$ in both figures) the curve loses its upward concavity for large negative values of $w(1)$ and intersects the $w(\kappa)=0$ axis once. As q_L is further increased, the curve becomes concave down for large positive values of $w(1)$, showing two equilibria, and then moves entirely downwards so that there are no equilibria. The plots are slightly asymmetric about the $q_L = q_U$ axis due to $\Gamma \neq 0$.

From these results, we postulate that the jumps in Zip disk displacement described in Section 2 correspond to a change from a configuration with two equilibria to a configuration with only one equilibrium. These transitions are shown in Fig. 3 by the contour at $q_L > 0$ and $q_U = 0$ and, over a smaller range, by the contour $q_L = 0$ and $q_U > 0$. In these transitions from two equilibria to one equilibrium, one equilibrium changes continuously while the other vanishes. If the disk were in the continuously varying equilibrium, no sudden displacement change would be observed. If the disk were in the other equilibrium, an abrupt displacement change would occur.

The structure of this equilibrium change is consistent with experimental observations. Since the jump requires the disk to assume one particular equilibrium of the two allowable, any changes in the disk that predispose its deflection to one or the other equilibrium would affect whether or not a jump is observed. This possibly explains why the jump phenomenon is repeatable on any given day, but not necessarily over several days: overnight storage could lead to creep in both the disk and the surrounding gauze of the disk that could alter the preferred equilibrium state. In addition, thermal stresses may play a role.

We can estimate the maximum possible jump size by computing $(\tilde{w}(1)+c_L)$ where $\tilde{w}(1)$ is the value of $w(1)$ for the continuously varying equilibrium. The maximum jump size varies between 0.50 and 0.76 over the range $0 \leqslant q_L \leqslant 0.2$ and $0 \leqslant \Gamma \leqslant 0.2$. In most cases, the continuously varying equilibrium is close to the center of the housing. The results indicate that the magnitude of the observed jumps should not vary significantly when the orientation of the disk is rotated from a horizontal to vertical position, i.e., changing Γ from 0 to 0.114. This is borne out by the data in Table 1.

6 Discussion

Although the proposed model is simple, it appears to describe the experimentally observed phenomenon. This contrasts with prior research that has often proposed and analyzed more compli-

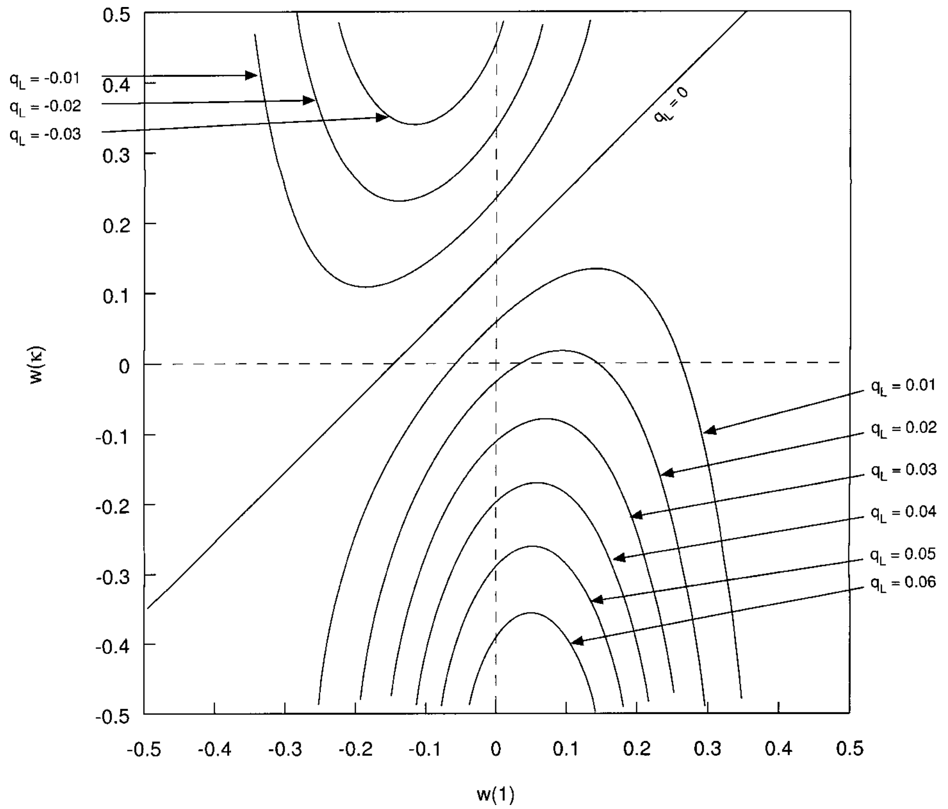

Fig. 4 $w(1)$ **versus** $w(\kappa)$ **for different** q_L **assuming** $q_U = -q_L$**. Roots indicate equilibrium solutions.** $\kappa = 0.291$; $\nu = 0.3$; $\Gamma = 0.114$; $c_L = c_U = 0.5$.

cated experimental results or analytical models without mutual corroboration. Such research makes it difficult to distinguishing primary and secondary physical effects.

Of course, the experimental results and analytical modeling performed here are preliminary rather than definitive. A number of assumptions have been made analytically that may not be adequate: the disk deflection is assumed to be axisymmetric, steady, and linear; geometric imperfections of the disk, potential thermal stresses, and bending stiffness have been neglected; hydrodynamic lubrication theory has been used even though the clearance is relatively large (although it is about the same as Pelech and Shapiro [7]). More complicated analysis of the system may lead to a different explanation of the observed phenomenon.

That being said, the present results suggest that the jump phenomenon of the disk can be avoided by precise control of the total radial flows surrounding the disk. Whether or not such control is practical or desirable remains an open question. Presently, Zip disk enclosures almost fully enclose the flow, which keeps the total radial flow small and makes small changes in radial flow direction possible and perhaps even likely. A less restrictive flow design may eliminate the jump phenomenon but may also draw more particles and debris into the enclosure.

7 Conclusion

1 Experimental results are presented showing a discontinuous jump phenomenon in I-Omega Zip disks. The jump was recorded on the transverse displacement of the disk at its outer periphery as the disk rotation speed varied. The jump behavior was not demonstrated by each disk tested, nor was it necessarily repeatable over several days.

2 A simple model was developed to explain this behavior. The model takes into account the hydrodynamic coupling between the thin flexible disk and the air circulating within the Zip disk housing. The model makes the simplifying assumptions of axisymmetry and negligible bending stiffness, which permit robust solution of the nonlinear system equations.

3 Results show that the number of disk equilibrium states is greatly affected by small changes in the air flow inside the Zip casing. The authors postulate that the jump phenomenon can be attributed to these changes in the number of equilibria caused by small changes in the radial flow above and below the disk.

References

[1] Iwan, W. D., and Moeller, T. L., 1976, "The Stability of a Spinning Elastic Disk With a Transverse Load System," ASME J. Appl. Mech., **43**, pp. 485–490.

[2] Benson, R. C., and Bogy, D. B., 1978, "Deflection of a Very Flexible Spinning Disk Due to a Stationary Transverse Load," ASME J. Appl. Mech., **45**, pp. 636–642.

[3] Renshaw, A. A., 1998, "Critical Speed for Floppy Disks," ASME J. Appl. Mech., **65**, pp. 116–120.

[4] D'Angelo, C., III,, and Mote, C. D., Jr., 1993, "Aerodynamically Excited Vibration and Flutter of a Thin Disk Rotating at Supercritical Speed," J. Sound Vib., **168**(1), pp. 15–30.

[5] McAllister, J. S., 1996, "The Effect of Platter Resonances on Track Misregistration in Disk Drives," Sound Vib., **30**(1), pp. 24–28.

[6] Benson, R. C., 1983, "Observations on the Steady-State Solution of an Extremely Flexible Spinning Disk With a Transverse Load," ASME J. Appl. Mech., **50**, pp. 525–530.

[7] Pelech, I., and Shapiro, A. H., 1964, "Flexible Disk Rotating on a Gas Film Next to a Wall," ASME J. Appl. Mech., **31**, pp. 577–584.

[8] Hosaka, H., and Crandall, S., 1992, "Self-Excited Vibrations of a Flexible Disk Rotating on an Air Film Above a Flat Surface," Acta Mech., **3**, pp. 115–127.

[9] Chonan, S., Jiang, Z. W., and Shyu, Y. J., 1992, "Stability Analysis of a 2″ Floppy Disk Drive System and the Optimum Design of the Disk Stabilizer," ASME J. Vibr. Acoust., **114**, pp. 283–286.

[10] Huang, F. Y., and Mote, C. D., Jr., 1995, "On the Instability Mechanisms of a Disk Rotating Close to a Rigid Surface," ASME J. Appl. Mech., **62**, pp. 764–771.

[11] Sokolnikoff, I. S., 1983, *Mathematical Theory of Elasticity*, R. E. Krieger and Co., Malabar, FL.

[12] Bender, C. M., and Orszag, S. A., 1978. *Advanced Mathematical Methods for Scientists and Engineers*, Springer-Verlag, New York.

Finite Element Analysis of Brittle Cracking due to Single Grit Rotating Scratch

G. Subhash[1]

W. Zhang[2]

Department of Mechanical Engineering–Engineering
Mechanics, Michigan Technological University,
Houghton, MI 49931

Finite element analysis of single grit rotating scratch on brittle materials was conducted using an "elastic-plastic-cracking" (EPC) model. The brittle material removal mechanism was modeled based on a critical crack-opening displacement criterion. It was found that the tangential and normal force profiles as well as the damage morphology observed in scratch experiments were fully captured by the EPC model. The results revealed that the induced damage zone size increases linearly with a brittleness parameter $(EY/\sigma_f^2)^{1/3}$ *as well as the maximum depth of cut.* [DOI: 10.1115/1.1526119]

1 Introduction

Grinding with diamond wheels is the most common process for finishing high-strength ceramic components. A summary of experimental investigations and empirical modeling of grinding process during the last two decades were reviewed by Li and Liao [1]. More fundamental studies that relate strength of a finished ceramic component to the grinding-induced damage continue to be reported (e.g., [2,3]).

Fundamental studies that capture the interaction between grinding medium and the workpiece were mainly conducted using Vickers indentations [4–6], and single-grit scratching models [1,7]. Results of the scratch experiments on brittle materials revealed distinct material removal patterns for different materials [8,9]. It was observed that in Homalite-100 the material removal occurs in periodic bursts with burst size increasing with instantaneous depth of cut, and accordingly, the force profiles reflected periodic oscillations. In the case of Pyrex glass, the material removal occurs in random bursts at irregular intervals and accordingly, the force profiles reflected irregular force oscillations [9].

In this paper, finite element analysis of the above single-grit scratching experiments was carried out using an "elastic-plastic-cracking" (EPC) model recently presented by the authors [10,11]. The numerical results are discussed and compared to the experimental observations on the above model brittle materials.

2 Model Descriptions

In the EPC model [10], the ceramic behavior is represented by tensile cracking and compressive yielding. A material point is assumed to fail in tension, and will be deleted from the finite element model, if the effective crack-opening displacement u_d exceeds a critical value u_c, which is assumed to be 90% of overall crack-opening displacement u_0, where $u_0 = 5\ \mu$m. The model has been successfully implemented into the commercial finite element

---

[1] To whom correspondence should be addressed. e-mail: subhash@mtu.edu

[2] Currently at Graduate Aeronautical Laboratories, California Institute of Technology, M/C 105-50, Pasadena, CA 99125.

Contributed by the Applied Mechanics Division of THE AMERICAN SOCIETY OF MECHANICAL ENGINEERS for publication in the JOURNAL OF APPLIED MECHANICS. Manuscript received by the ASME Applied Mechanics Division, Feb. 1, 2001, final revision, July 26, 2002. Associate Editor: B. M. Moran.

Table 1 Material properties of Pyrex glass

Density ρ (g/cm^3)	Young's Modulus E (GPa)	Poisson's Ratio ν	Yield Stress Y (GPa)	Hardening Modulus E_p (GPa)	Fracture Stress σ_f (GPa)
2.2	70	0.24	3	0.7	0.2

package ABAQUS (Version 5.8) through the user subroutine VUMAT. The details of the formulation can be obtained elsewhere [10,11].

The finite element model is motivated by the experimental set up of Loukus [8] and Subhash et al. [9]. The specimen ($3\times3\times1.5$ mm^3) is constrained in horizontal and vertical directions similar to the experiments, [11]. The conical indenter with an apex angle of 90 deg is pivoted at a radius 20 mm. The tangential force F_t and the normal force F_n are recorded on the side and bottom surfaces, respectively. Due to the symmetry of the problem, only half of the specimen was modeled as 22640 eight-node solid elements with a minimum element size of 10 microns. The indenter was modeled as a rigid surface and subjected to a constant angular velocity, which resulted in a 2.2-mm length scratch with a maximum depth of cut of 30 μm. The friction coefficient between the specimen and the indenter was assumed to be 0.3. The typical run time varied from 50 to 400 hours depending on material properties and scratching speed on a Sun Ultra 80 workstation with one 450 MHz processor.

3 Results and Discussions

The basic material properties are listed in Table 1. By varying systematically the material properties (i.e., Young's modulus E, yield strength Y, and tensile fracture strength σ_f) and the scratching speed, the relationships between damage zone size, material removal volume, material properties and loading conditions were investigated.

3.1 Influence of Scratch Speed. Figure 1 provides the induced damage and the evolved force profiles due to a scratch at 31 m/s. It shows that the effective crack-opening displacement on the top surface (Fig. 1(*a*)), which represents the lateral damage zone, is more irregular compared to that beneath the surface (Fig. 1(*b*)), which is the median damage zone. The resulting tangential and normal force profiles (Fig. 1(*c*)) oscillate severely during the scratch process. These oscillations are due to the instantaneous stress release as a result of crack opening or the lack of contact between the indenter and the specimen when elements were deleted due to excessive damage as per the critical crack-opening displacement criterion discussed before.

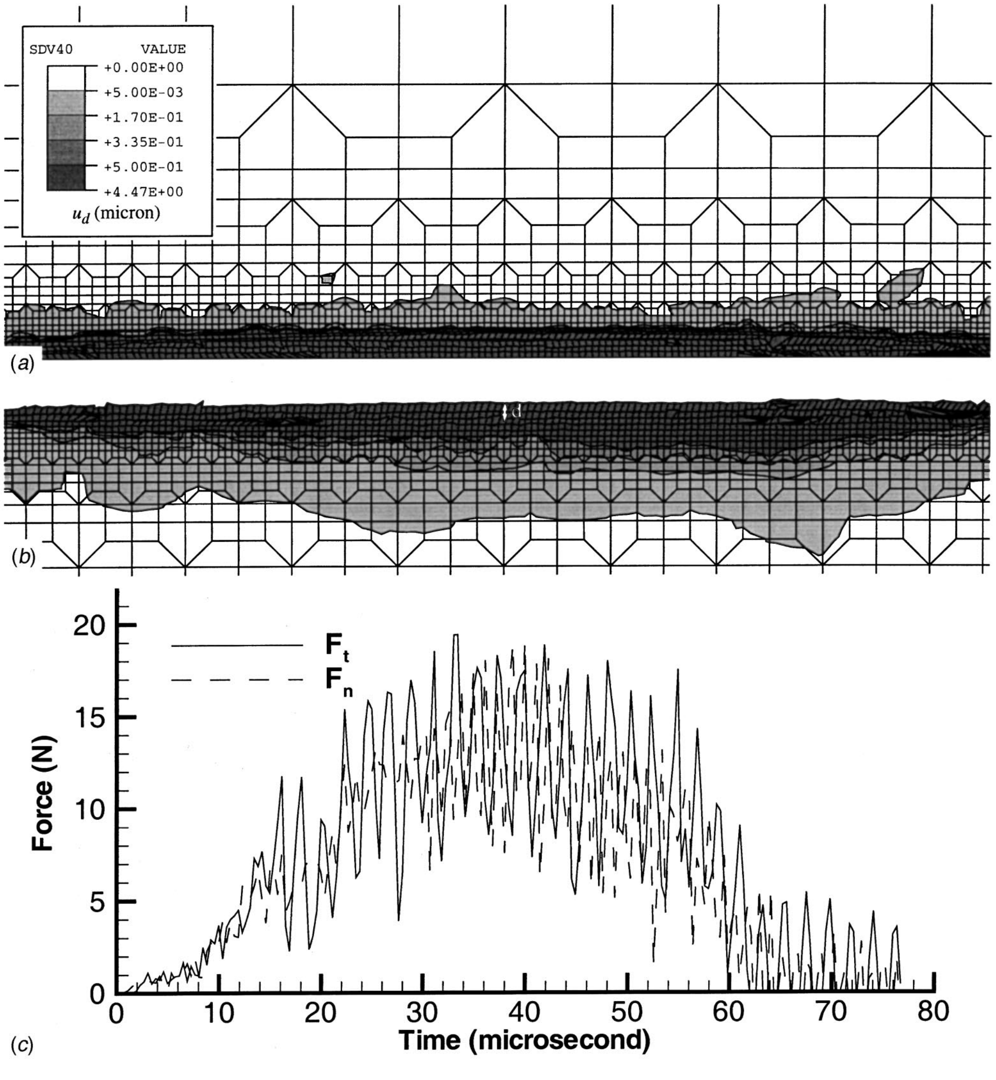

Fig. 1 Contours of evolved damage zone u_d due to a scratch at velocity 31 m/s and a duration of 76.7 μs. (a) Top view, (b) side view, and (c) the resulting tangential and normal force profiles.

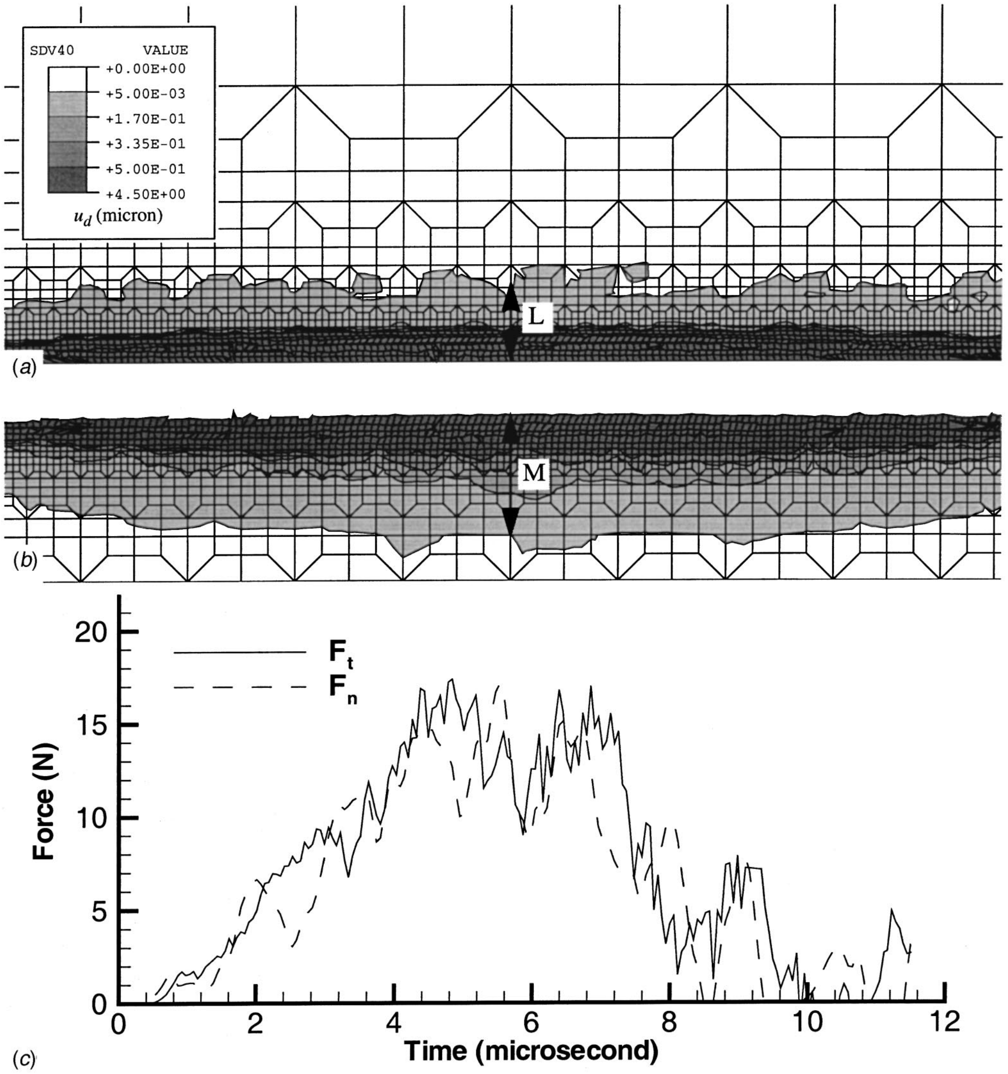

Fig. 2 Contours of evolved damage zone u_d as a result of a scratch at velocity 209 m/s and a duration of 11.5 μs. (a) Top view, (b) side view, and (c) the resulting tangential and normal force profiles. Here, *L* and *M* denotes lateral damage size and median damage size, respectively.

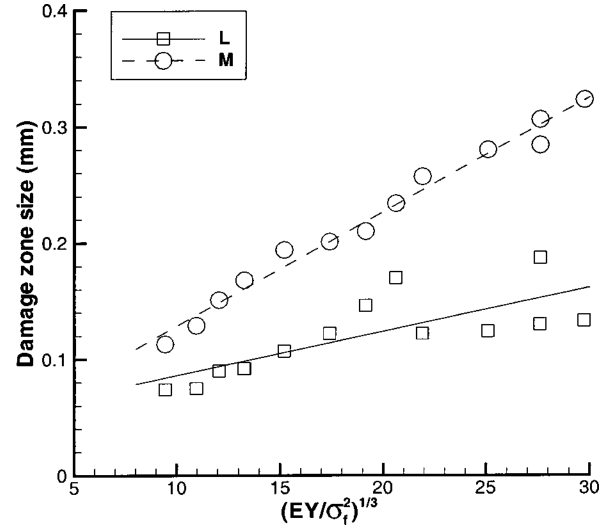

Fig. 3 Plot of induced damage zone size as a function of the brittleness parameter $(EY/\sigma_f^2)^{1/3}$ indicating that damage zone size increases linearly with brittleness parameter (depth of cut is 30 microns)

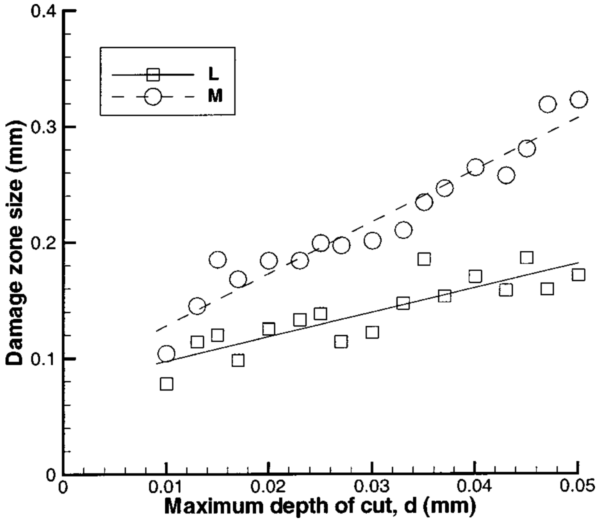

Fig. 4 The relationship between the induced damage zone size and the maximum depth of cut revealing that the scratching induced damage zone size is proportional to the imposed maximum depth of cut

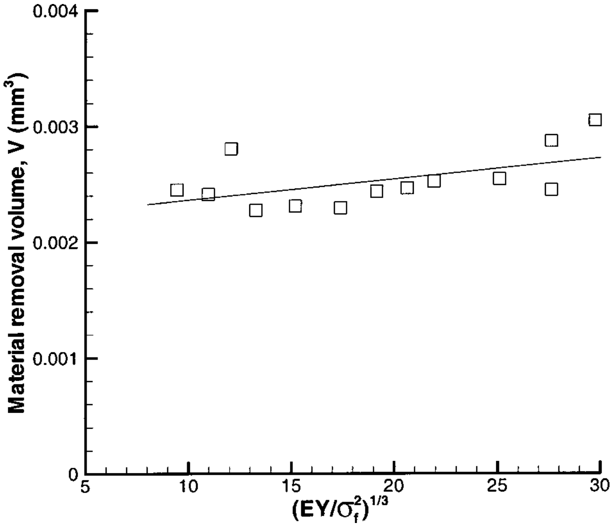

Fig. 5 The relationship between total material removal volume during scratch and the brittleness parameter revealing that brittleness parameter has marginal effect on the material removal

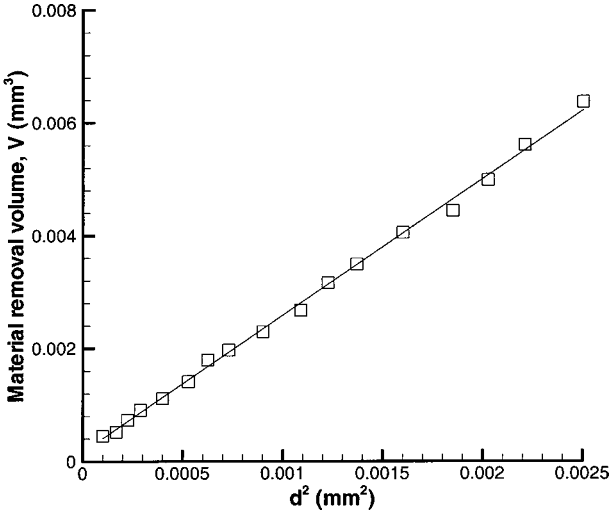

Fig. 6 The plot of total removed volume of material versus the squared maximum depth of cut suggesting material removal strongly depends on the maximum depth of cut

In Fig. 2, the scratching speed was increased to 209 m/s while other parameters were kept constant as those in Fig. 1. It is seen that the lateral damage zone size seems to increase (from Fig. 1(*a*) to Fig. 2(*a*)). However, the median damage size appears to be less sensitive to the scratch speed (from Fig. 1(*b*) to Fig. 2(*b*)). It is interesting to see that the force profiles oscillate much less frequently in Fig. 2(*c*) than in Fig. 1(*c*). This perhaps means less frequent but larger material fragment removal at higher scratch velocities. The force profiles in Fig. 1(*c*) are similar to those of Homalite, while the force profiles in Fig. 2(*c*) are more like those of Pyrex glass due to high speed scratching [9]. It should be noted that in our model the rate dependence of constitutive model was not considered. Therefore, the differences between Figs. 1 and 2 are completely due to the inertial effect.

3.2 Damage Zone Size. While keeping the maximum depth of cut a constant at 30 microns, it is shown in Fig. 3 that the induced damage zone size increases almost linearly with a nondimensional brittleness parameter $(EY/\sigma_f^2)^{1/3}$. This result is consistent with the indentation induced cracking simulation results reported earlier [10]. Figure 4 reveals that the damage zone sizes also increase linearly with the maximum depth of cut. This result is also in agreement with the experimental observations of Loukus [8].

3.3 Material Removal Volume. Since the depth of cut in our rotating scratch process is not a constant, the material removal per unit length is not an appropriate measure of material removal rate. Thus, the material removal volume per scratch is used to study the relationships between material removal, material properties, and processing parameters. The material removal volume is simply the sum of the volumes of all the finite elements that were removed as per the criterion discussed before. Figures 5 and 6 reveal that the volume of material removal increases marginally with brittleness parameter, but dramatically with the square of the maximum depth of cut, respectively. This implies that the dominant variable that affects material removal rate in an actual grinding process is depth of cut, which is consistent with the experimental reports presented elsewhere [1,12].

Although the EPC model is capable of capturing the fundamental deformation mechanisms during single-grit scratching of brittle materials, it cannot measure a single crack size or identify a specific crack direction [10]. However, the comparisons presented here are partly based on the force profiles, the general trends of the damage zone sizes and the volume of material removed.

4 Conclusions

1 The EPC model is capable of capturing the salient features of the tangential and normal force profiles as well as the damage morphology during the scratching process.

2 The damage zone size appears to increase linearly with a nondimensional brittleness parameter $(EY/\sigma_f^2)^{1/3}$ as well as the maximum depth of cut.

3 The material removal volume is affected more dramatically by the maximum depth of cut rather than by the material properties.

Acknowledgments

The authors acknowledge the financial support by the U.S. NSF under Grant No. DMI-9610454. This work was partially supported by NCSA and utilized the SGI/CRAY Origin 2000 supercomputer at UIUC.

References

[1] Li, K., and Liao, T. W., 1996, "Surface/Subsurface Damage and the Fracture Strength of Ground Ceramics," J. Mater. Process. Technol., **57**, pp. 207–220.

[2] Hessert, R., Eigenmann, B., Vöhringer, O., and Löhe, D., 1997, "Fracture Mechanical Evaluation of the Effects of Grinding Residual Stresses on Bending Strength of Ceramics," Mater. Sci. Eng., **A234-23**, pp. 1126–1129.

[3] Lee, S. K., Tandon, R., Readey, M. J., and Lawn, B. R., 2000, "Scratch Damage in Zirconia Ceramics," J. Am. Ceram. Soc., **83**(6), pp. 1428–1432.

[4] Lawn, B. R., Evans, A. G., and Marshall, D. B., 1980, "Elastic/Plastic Indentation Damage in Ceramics: The Median/Radial Crack System," J. Am. Ceram. Soc., **63**, pp. 574–581.

[5] Chiang, S. S., Marshall, D. B., and Evans, A. G., 1982, "The Response of Solids to Elastic/Plastic Indentation. I. Stresses and Residual Stresses," J. Appl. Phys., **53**(1), pp. 298–311.

[6] Malkin, S., and Hwang, T. W., 1996, "Grinding Mechanisms for Ceramics," CIRP Ann., **45**(2), pp. 569–580.

[7] Ahn, Y., Farris, T. N., Chandrasekar, S., 1998, "Sliding Microindentation Fracture of Brittle Materials: Role of Elastic Stress Fields," Mech. Mater., **29**, pp. 143–152.

[8] Loukas, J. E., 2000, "Investigation of Material Removal Mechanisms during Single Grit Scratching on Brittle Materials," Ph.D. dissertation, Michigan Technological University, Houghton, MI.

[9] Subhash, G., Loukus, J. E., and Pandit, S. M., 2002, "Application of Data Dependent Systems Approach for Evaluation of Fracture Modes During a Single-Grit Scratching," Mech. Mater., **34**(1), pp. 25–42.

[10] Zhang, W., and Subhash, G., 2001, "An Elastic-Plastic-Cracking Model for Finite Element Analysis of Indentation Cracking in Brittle Materials," Int. J. Solids Struct., **38**(34–35), pp. 5893–5913.

[11] Zhang, W., 2001, ‘‘Finite Element Analysis of Induced Damage Due to Indentation and Scratching on Brittle Materials,’’ Ph.D. dissertation, Michigan Technological University, Houghton, MI.

[12] Warnecke, G., and Rosenberger, U., 1995, ‘‘Basics of Process Parameter Selections in Grinding of Advanced Ceramics,’’ CIRP Ann., **44**(1), pp. 283–286.

An Alternative Method of Solving Multilayer Bending Problems

C. H. Hsueh
Metals and Ceramics Division, Oak Ridge National Laboratory, Oak Ridge, TN 37831-6068

S. Lee
Department of Materials Science and Engineering, National Tsing Hua University, Hsinchu, Taiwan

T. J. Chuang
Ceramics Division, National Institute of Standards and Technology, Gaithersburg, MD 20899-8521

Stress distributions in multilayers subjected to both residual stresses and external bending are analyzed to derive closed-form analytical solutions. There are always three unknowns to be solved and three equilibrium conditions to be satisfied in the present analysis. In contrast, the numbers of unknowns and conditions increase with the number of layers in the system in existing analyses. [DOI: 10.1115/1.1526123]

1 Introduction

Residual stresses and bending in a film/substrate system were documented about a century ago, [1]. In 1865, Rosse tried to make flat bimetallic mirrors for a Newtonian telescope by coating glass with silver via a chemical process and then electroplating with copper. However, upon deposition, the copper film detached from the glass and the planar glass became curved owing to the contraction of the copper film. Advances in technology have resulted in extensive applications of film/substrate and multilayer systems as microelectronic, optical, and structural components, [2]; however, the issues of residual stresses and bending remain. Considerable efforts have been devoted to analyzing these issues, [3–11], and the analyses are generally based on classical beam-bending theory, [12–14]. The ‘‘neutral axis’’ has been defined in bending theory as the line in the cross section of a beam where the normal stress is zero. When the beam is subjected to external bending only, the normal strain in the cross section is proportional to the distance from the neutral axis and inversely proportional to the radius of curvature. However, when external bending and axial loading are combined, the neutral axis may be anywhere within the cross section, at its edge, or outside it, [13,14]. In this case, the strain is not proportional to the distance from the neutral axis.

The most widely adopted equation to predict residual stresses in films is the one derived by Stoney [3], in which a film much thinner than the substrate was considered. A general solution for bending of bilayers due to residual stresses was first derived by Timoshenko [4]. The analysis was based on classical bending theory and started by assuming the individual force and bending moment in each layer. The bending moment was related to the curvature of the layer, and both layers were assumed to have the same curvature. The solution was obtained by balancing the forces and moments in the system and satisfying the strain continuity condition at the interface between the two layers. In this bilayer case, there were three unknowns to be solved and three conditions to be satisfied. Timoshenko's approach has been adopted by many others to analyze residual stresses in multilayers, [5–10]. However, for multilayers, the numbers of both the unknowns and continuity conditions at interfaces increase with the number of layers in the system, [5–10].

It should be noted that the definition of the neutral axis cannot be used in solving the bending problem of bilayers (and multilayers) when residual stresses are involved. Instead, the neutral axis can only be obtained by finding the location with zero normal stress after solving the stress distribution in the system. In analyzing residual stresses in bilayers, Hsueh and Evans found that if the neutral axis were defined as the line in the cross section of the bilayer where the bending strain component is zero, the definition could be readily used to solve the bending problem, [15]. The same finding was subsequently reported by Townsend et al. [16].

As a complement to Hsueh and Evans's analysis, the present study examines the physical significance of Hsueh and Evans' neutral axis and the extent to which it is also useful in solving the bending problem if multilayers are subjected to both residual stresses and external bending. First, redefining Hsueh and Evans' neutral axis as the ‘‘bending axis’’ to avoid confusion, the general solution for multilayers subjected to residual stresses and external bending is derived. Then, the solution is reduced to that for bilayers and compared to existing solutions. The physical significance of the bending axis is also examined. Finally, a comparison between the bending axis and the neutral axis is made by considering a bilayer subjected to both residual stresses and external bending.

2 Analyses

An elastic multilayer strip is shown in Fig. 1(*a*), where *n* layers of films with individual thicknesses, t_i, are bonded sequentially to a substrate with a thickness, t_s, at high temperatures. The subscript, *i*, denotes the layer number for the film and ranges from 1 to *n* with layer 1 being the layer immediately adjacent to the substrate. The coordinate system is defined such that the interface between the substrate and layer 1 of the film is located at $z=0$, the substrate free surface is located at $z=-t_s$, the free surface of film layers is located at $z=h_n$, and the interface between layers *i* and $i+1$ is located at $z=h_i$. With this definition, the relation between h_i and t_i is described by

$$h_i=\sum_{j=1}^{i} t_j \quad (i=1 \text{ to } n). \tag{1}$$

The coefficients of thermal expansion of the substrate and films are α_s and α_i, respectively. The system is cooled to room temperature and is subsequently subjected to applied bending. The following analytic logic is used to determine the stress field in the system. First, the system experiences an unconstrained differential shrinkage due to the cooling temperature, ΔT, such that thermal strains, $\alpha_s\,\Delta T$ and $\alpha_i\,\Delta T$, exist in the substrate and film layers, respectively (Fig. 1(*b*)). Second, uniform tensile and compressive stresses are imposed on the individual layers to achieve displacement compatibility such that the strain in the multilayer is a constant, *c*, and the total force on the system remains zero (Fig. 1(*c*)). Third, bending occurs to balance the bending moment induced bythe asymmetric stresses in the system (Fig. 1(*d*)). Fourth, the curvature of the system described in Fig. 1(*d*) is modified by an applied bending moment, *M* (Fig. 1(*e*)).

Contributed by the Applied Mechanics Division of THE AMERICAN SOCIETY OF MECHANICAL ENGINEERS for publication in the JOURNAL OF APPLIED MECHANICS. Manuscript received by the ASME Applied Mechanics Division, Mar. 17, 2002; final revision , July 26, 2002. Associate Editor: D. A. Kouris.

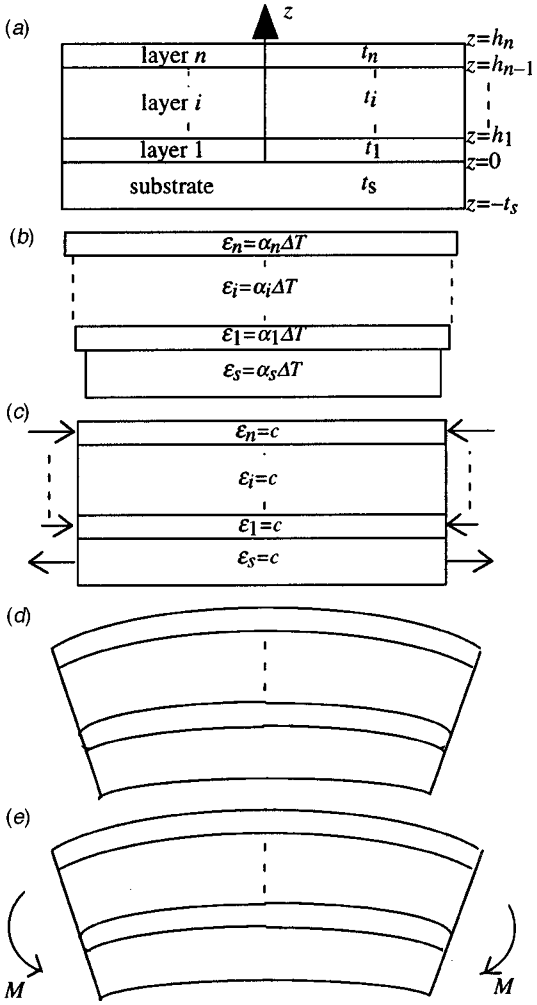

Fig. 1 Schematics showing bending of a multilayer strip due to residual stresses and external bending: (a) stress-free condition, (b) unconstrained strains due to temperature change ΔT, (c) constrained strain to maintain displacement compatibility, (d) bending induced by asymmetric stresses, and (e) external bending

Based on the logic described in Fig. 1, the strain in the multilayer, ε, can be decomposed into a uniform component and a bending component. While the uniform component, c, is dictated by the logic in Fig. 1(c), the bending component results from the logic described by Figs. 1(d) and (e). With the present definition of the bending axis, the bending strain component becomes proportional to the distance from the bending axis and inversely proportional to the radius of curvature. Therefore, the total strain in the multilayer (Fig. 1(e)) can be formulated as

$$\varepsilon=c+\frac{z-t_b}{r}\quad(\text{for } -t_s\leqslant z\leqslant h_n),\tag{2}$$

where r is the radius of curvature and t_b dictates the location of the bending axis. The advantage of using Eq. (2) to describe the strain in the system is that the strain continuity conditions at the interfaces between layers are automatically satisfied.

The normal stresses in the substrate and films, σ_s and σ_i, are related to strains by

$$\sigma_s=E_s(\varepsilon-\alpha_s\Delta T)\quad(\text{for } -t_s\leqslant z\leqslant 0),\tag{3a}$$

$$\sigma_i=E_i(\varepsilon-\alpha_i\Delta T)\quad(\text{for } i=1 \text{ to } n),\tag{3b}$$

where E_s and E_i are Young's moduli of the substrate and layer i of films, respectively. In the case of biaxial stresses (i.e., a planar instead of a strip geometry), Young's modulus in Eq. (3) should be replaced by the biaxial modulus, $E/(1-\nu)$, where ν is Poisson's ratio. The strain/stress distributions in the multilayer (i.e., Eqs. (2) and (3)) are contingent upon solutions of the three parameters, c, t_b, and r, which can be determined from the following three equilibrium conditions. First, the resultant force due to the uniform strain component (i.e., the total force in Fig. 1(c)) is zero. Second, the resultant force due to the bending strain component is zero. Third, the sum of bending moments is in equilibrium with the applied moment. With the above three equilibrium conditions, the solutions are

$$c=\frac{(E_st_s\alpha_s+\Sigma_{i=1}^{n}E_it_i\alpha_i)\Delta T}{E_st_s+\Sigma_{i=1}^{n}E_it_i},\tag{4a}$$

$$t_b=\frac{-E_st_s^2+\Sigma_{i=1}^{n}E_it_i(2h_{i-1}+t_i)}{2(E_st_s+\Sigma_{i=1}^{n}E_it_i)},\tag{4b}$$

$$\frac{1}{r}=\frac{3\left[E_s(c-\alpha_s\Delta T)t_s^2-\sum_{i=1}^{n}E_it_i(c-\alpha_i\Delta T)(2h_{i-1}+t_i)\right]+6M}{E_st_s^2(2t_s+3t_b)+\sum_{i=1}^{n}E_it_i[6h_{i-1}^2+6h_{i-1}t_i+2t_i^2-3t_b(2h_{i-1}+t_i)]}\tag{4c}$$

where M is the applied moment per unit width of the strip. When $i=1$, h_{i-1} (i.e., h_0) is defined as zero in Eqs. (4b) and (4c). Based on Eq. (4b), the position of the bending axis remains unchanged whether the multilayer is subjected to residual stresses, external bending, or both.

3 Results

A special case of one layer of film on a substrate (i.e., $n=1$) is considered to compare with existing solutions. In this case, the subscript 1 for the film is replaced by the subscript f. When the film is much thinner than the substrate (i.e., $t_f\ll t_s$), Eqs. (4a–c)

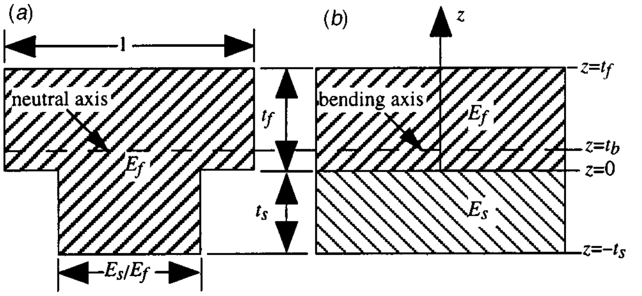

Fig. 2 Schematics showing (a) equivalent cross section of the bilayer to account for different Young's moduli between the two layers when the bilayer is subjected to only external bending and (b) the bending axis in the cross section of the bilayer is located at the same position as the neutral axis in the equivalent cross section

can be simplified, and it can be derived from Eq. (4*b*) that the bending axis is always located at the centerline of the substrate (i.e., $t_b=-t_s/2$). Furthermore, when the bilayer is subjected to residual stresses only (i.e., $M=0$), the stresses in the system become

$$\sigma_f=E_f(\alpha_s-\alpha_f)\Delta T=-\frac{E_s t_s^2}{6t_f r} \quad (\text{for } 0\leq z\leq t_f), \tag{5a}$$

$$\sigma_s=\frac{2E_f t_f(3z+2t_s)(\alpha_f-\alpha_s)\Delta T}{t_s^2} \quad (\text{for } -t_s\leq z\leq 0). \tag{5b}$$

Equation (5*a*) is the same as the well-known Stoney's equation, [3]. Also, from Eq. (5*b*), $\sigma_s=0$ at $z=-2t_s/3$, which defines the location of the neutral axis. Conversely, in the presence of external bending only (i.e., $\Delta T=0$), the stresses become

$$\sigma_f=\frac{6E_f M}{E_s t_s^2}=\frac{E_f t_s}{2r} \quad (\text{for } 0\leq z\leq t_f), \tag{6a}$$

$$\sigma_s=\frac{6(2z+t_s)M}{t_s^3} \quad (\text{for } -t_s\leq z\leq 0). \tag{6b}$$

In this case, the neutral axis is located at $z=-t_s/2$. Therefore, depending upon whether the film/substrate system is subjected to residual stresses or external bending, the neutral axis is located at a depth 2/3 or 1/2 of the substrate thickness under the interface. However, this fact has not commonly been recognized, and the assumption that the neutral axis is located at the centerline of the substrate has been made erroneously when the system is subjected to residual stresses.

It can be shown that the solution for bilayer strips subjected to residual stresses given by Timoshenko [4] is the same as the present general solution with $n=1$ and $M=0$. Bilayer strips subjected to external bending only have also been analyzed by Timoshenko, in which bending of a strip of homogeneous material with an equivalent cross section, as shown in Fig. 2(*a*) (where $E_s<E_f$ is assumed), was considered to take into account the difference between Young's moduli of the two layers, [4]. In this case, the neutral axis passes through the centroid of the equivalent cross section. It can be derived that the neutral axis in Fig. 2(*a*) is located at the same position as the bending axis defined in the present study (see Fig. 2(*b*)). It can also be derived that when a beam with a cross section shown in Fig. 2(*a*) is subjected to an applied moment, *M*, the curvature of the beam is the same as that described by Eq. (4*c*) with $n=1$ and $\Delta T=0$.

To illustrate how the combined residual stresses and external bending influence the location of the neutral axis, the GaAs film/Si substrate bilayer system, which has significant applications in semiconductors, is considered as an example. In this case, Young's moduli are $E_f=85$ GPa and $E_s=130$ GPa. The thickness ratio $t_f/t_s=0.2$ is assumed to elucidate the essential trends. By using Eqs. (2), (3), and (4) with $n=1$, the normalized position of the neutral axis is shown in Fig. 3 as a function of normalized applied moment, $M/E_s t_s^2(\alpha_f-\alpha_s)\Delta T$. The position of the bending axis given by Eq. (4*b*) with $n=1$ is also shown. The bending axis is fixed, but the neutral axis shifts with the normalized applied moment. It can be seen in Fig. 3 that when $-0.1\leq ZM/E_s t_s^2(\alpha_f-\alpha_s)\Delta T\leq -0.05$, there is no neutral axis in the bilayer. When $0.11\leq M/E_s t_s^2(\alpha_f-\alpha_s)\Delta T\leq 0.19$, a neutral axis also appears in the film which, in turn, results in dual neutral axes in the system.

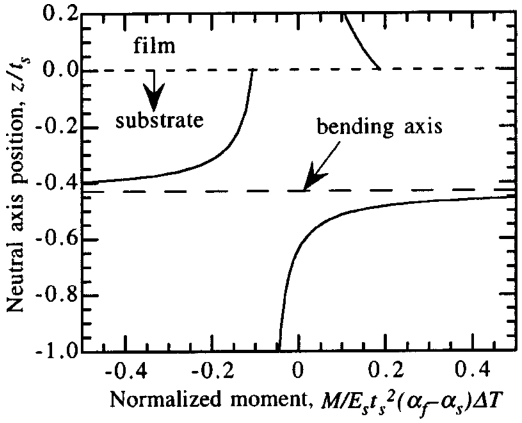

Fig. 3 Normalized position of neutral axis as a function of normalized applied bending moment, $M/E_s t_s^2(\alpha_f-\alpha_s)\Delta T$, for GaAs/Si bilayer systems with $t_f/t_s=0.2$

4 Conclusions

The neutral axis defined in classical bending theory cannot be used to analyze the bending problem of bilayer strips subjected to residual stresses. Instead, the neutral axis can only be obtained after the stress distribution in the system is solved. The neutral axis shifts with the combined residual stresses and external bending, and there can be zero, one, or two neutral axes in the bilayer (Fig. 3). The bending axis as we have defined it overcomes this limitation. It can be utilized to readily solve the bending problem presented by not only bilayers but also multilayers. The location of the bending axis remains unchanged whether the system is subjected to residual stresses, external bending, or both. The bending axis has the physical meaning of passing through the centroid of the equivalent cross section of the system (Fig. 2). Also, for a multilayer system, there are always three unknowns and three equilibrium conditions to be solved by adopting the bending axis in the analysis. However, the numbers of unknowns and conditions increase with number of layers in the existing analyses, [5–10].

Acknowledgments

The authors thank Dr. P. F. Becher, Dr. E. R. Fuller, Jr., Dr. B. R. Lawn, Prof. G. M. Pharr, and Dr. E. Lara-Curzio for reviewing the manuscript. This work was sponsored by the Division of Materials Sciences, U.S. Department of Energy, under contract DE-AC05-00OR22725 with UT-Battelle.

References

[1] Rosse, 1908, "Bimetallic Mirrors made by Electro-Deposition," Nature (London), **78**(2025), pp. 366–367.
[2] Hu, S. M., 1991, "Stress-Related Problems in Silicon Technology," J. Appl. Phys., **70**(6), pp. R53–R80.
[3] Stoney, G. G., 1909, "The Tension of Metallic Films Deposited by Electrolysis," Proc. Phys. Soc. London, **82**, pp. 172–175.

[4] Timoshenko, S., 1925, ‘‘Analysis of Bi-Metal Thermostats,’’ J. Opt. Soc. Am., **11**, pp. 233–255.
[5] Saul, R. H., 1969, ‘‘Effect of a GaAs$_x$P$_{1-x}$ Transition Zone on the Perfection of GaP Crystals Grown by Deposition onto GaAs Substrates,’’ J. Appl. Phys., **40**(8), pp. 3273–3279.
[6] Olsen, G. H., and Ettenberg, M., 1977, ‘‘Calculated Stresses in Multilayered Heteroepitaxial Structures,’’ J. Appl. Phys., **48**(6), pp. 2543–2547.
[7] Feng, Z. C., and Liu, H. D., 1983, ‘‘Generalized Formula for Curvature Radius and Layer Stresses Caused by Thermal Strain in Semiconductor Multilayer Structures,’’ J. Appl. Phys., **54**(1), pp. 83–85.
[8] Iancu, O. T., Munz, D., Eigenman, B., Scholtes, B., and Macherauch, E., 1990, ‘‘Residual Stress State of Braze Ceramic/Metal Compounds, Determined by Analytical Methods and X-Ray Residual Stress Measurements,’’ J. Am. Ceram. Soc., **73**(5), pp. 1144–1149.
[9] Jou, J. H., and Hsu, L., 1992, ‘‘Bending-Beam Measurement of Solvent Diffusions in Polyimides: Theoretical and Experimental,’’ J. Appl. Polym. Sci., **44**, pp. 191–198.
[10] Liu, H. C., and Murarka, S. P., 1992, ‘‘Elastic and Viscoelastic Analysis of Stress in Thin Films,’’ J. Appl. Phys., **72**(8), pp. 3458–3463.
[11] Chuang, T. J., and Lee, S., 2000, ‘‘Elastic Flexure of Bilayered Beams Subjected to Strain Differentials,’’ J. Mater. Res., **15**(12), pp. 2780–2788.
[12] Timoshenko, S., 1955, *Strength of Materials, Part I: Elementary Theory and Problems*, D. Van Norstrand Company, New York.
[13] Hearn, E. J., 1977, *Mechanics of Materials*, Pergamon Press, Oxford, UK.
[14] Beer, F. P., and Johnston, E. R. Jr., 1981, *Mechanics of Materials*, McGraw-Hill, New York.
[15] Hsueh, C. H., and Evans, A. G., 1985, ‘‘Residual Stresses in Metal/Ceramic Bonded Strips,’’ J. Am. Ceram. Soc., **68**(5), pp. 241–248.
[16] Townsend, P. H., Barnett, D. M., and Brunner, T. A., 1987, ‘‘Elastic Relationships in Layered Composite Media With Approximation for the case of Thin Films on a Thick Substrate,’’ J. Appl. Phys., **62**(11), pp. 4438–4444.

On the Quest for the Best Timoshenko Shear Coefficient

M. B. Rubin
Faculty of Mechanical Engineering, Technion–Israel
Institute of Technology, 32000 Haifa, Israel
e-mail: mbrubin@tx.technion.ac.il

Classical Timoshenko beam theory includes a shear correction factor κ which is often used to match natural vibrational frequencies of the beam. In this note, a number of static and dynamic examples are considered which provide a theoretical basis for specifying $\kappa = 1$. Within the context of Cosserat theory, natural frequencies of the beam can be matched by appropriate specification of the director inertia coefficients with $\kappa = 1$.
[DOI: 10.1115/1.1526122]

Introduction

For two-dimensional deformation of a Timoshenko beam, the kinematics are characterized by the lateral displacement u and the rotation δ of the beam's cross section

$$u = u(x_3, t), \tag{1a}$$

$$\delta = \delta(x_3, t), \tag{1b}$$

where x_3 denotes the axial coordinate and t denotes time. In this theory the shear force V is specified by the constitutive equation

$$V = \kappa \mu^* A(u_{,3} + \delta), \tag{2}$$

where μ^* is the shear modulus, A is the area of the beam's cross section, and throughout the text a comma is used to denote partial differentiation with respect to the rectangular Cartesian coordinates x_i $(i = 1,2,3)$. Moreover, the Timoshenko shear coefficient κ in (2) is introduced as a modification of the shear modulus to account for the fact that the shear strain is not necessarily uniform over the beam's cross section.

The history of determining the value of κ in Timoshenko beam theory is as old as the theory itself, [1,2]. This coefficient was initially studied within the context of transverse vibrations of beams, [1,2], and its value seems to be problem-dependent, [3]. The review by Kaneko [3] and the recent discussions by Hutchinson [4,5] and Stephen [6] consider much of the literature and ideas related to the determination of the shear coefficient.

The solution of a particular initial, boundary value problem in three-dimensional linear elasticity provides values for the displacement field $\mathbf{u}^*(x_i, t)$ and the stress field $\mathbf{T}^*(x_i, t)$. Within the context of the linear theory of a Cosserat beam, [7–11], the beam kinematics u and δ generalize to

$$\mathbf{u} = \mathbf{u}(x_3, t), \quad \boldsymbol{\delta}_\alpha = \boldsymbol{\delta}_\alpha(x_3, t), \tag{3}$$

and the three-dimensional displacement $\mathbf{u}^*$ is approximated by

$$\mathbf{u}^* = \mathbf{u}^*(x_i, t) = \mathbf{u}(x_3, t) + x_\alpha \boldsymbol{\delta}_\alpha(x_3, t). \tag{4}$$

Here, and throughout the text, the usual summation convention is employed over repeated indices, with Latin letters having the range $(i = 1,2,3)$ and Greek letters having the range $(\alpha = 1,2)$. Also, a superposed $(^*)$ is used to denote variables that are related to the exact three-dimensional theory. In this beam theory, $\mathbf{u}$ is the displacement vector of material points on the beam's reference line and $\boldsymbol{\delta}_\alpha$ are the rotations and extensions of line elements which in the reference configuration were oriented in two orthogonal directions in the beam's normal cross section.

In order to analyze the accuracy of a solution in beam theory it is necessary to specify formulas for calculating the values

$$\overline{\mathbf{u}} = \overline{\mathbf{u}}(x_3, t), \quad \overline{\boldsymbol{\delta}}_\alpha = \overline{\boldsymbol{\delta}}_\alpha(x_3, t), \tag{5}$$

in terms of the $\mathbf{u}^*$, which are considered to be exact values corresponding to $\mathbf{u}$ and $\boldsymbol{\delta}_\alpha$, respectively. These values are referred to as the ‘‘exact beam kinematics.’’

The quest for the best Timoshenko shear coefficient has focused mainly on determining a value for κ that predicts the best natural frequencies of the beam. The objective of this note is to emphasize the following points.

(P1) The constitutive equations for the beam are considered to yield the ‘‘best’’ solution if the predicted beam kinematics (3) closely approximate the exact values (5) for both static and dynamic responses.

(P2) The beam kinematics (4) are exact for all homogeneous deformations. Thus, if $\kappa \neq 1$, then the resulting beam theory will not correctly predict the static problem of simple shear.

(P3) The resultant force and moment are uniquely defined in terms of integrals of the three-dimensional traction vector $\mathbf{t}^*$ acting on the cross section of the beam (see (11*a*,*b*) below). In contrast, the exact beam kinematics (5) are not uniquely defined in terms of $\mathbf{u}^*$ for deformation fields which are nonlinear functions of the cross-sectional coordinates x_α. Consequently, the value of κ that yields the ‘‘best’’ solution depends explicitly on the functional forms proposed for (5). This is one reason that different expressions for κ have been proposed in the literature.

(P4) The tensorial structure of the Cosserat theory reveals that a particular functional form for (5) is consistent with the usual definitions of average strain and average stress in effective stress theory when $\kappa = 1$.

(P5) The director inertia coefficients in the Cosserat theory are measures of the distribution of inertia in vibrational modes and can be used to match natural frequencies of beams.

(P6) The standard Timoshenko theory predicts the correct result that short wavelength waves travel at the shear wave speed c_s only when $\kappa = 1$.

The remaining sections of this note justify these points.

Contributed by the Applied Mechanics Division of THE AMERICAN SOCIETY OF MECHANICAL ENGINEERS for publication in the ASME JOURNAL OF APPLIED MECHANICS. Manuscript received by the ASME Applied Mechanics Division, March 3, 2002; final revision, July 26, 2002. Associate Editor: O. O'Reilly.

Throughout the text, boldfaced symbols denote vectors or second-order tensors, $\mathbf{a}\cdot\mathbf{b}$ denotes the scalar product between two vectors $\mathbf{a}$ and $\mathbf{b}$, $\mathbf{A}\cdot\mathbf{B}=\mathrm{tr}(\mathbf{A}\mathbf{B}^T)$ denotes the scalar product between two second order tensors $\mathbf{A}$ and $\mathbf{B}$, and the symbol $\otimes$ denotes the tensor product which is defined so that $(\mathbf{a}\otimes\mathbf{b})\mathbf{c}=(\mathbf{b}\cdot\mathbf{c})\mathbf{a}$ and $\mathbf{c}(\mathbf{a}\otimes\mathbf{b})=(\mathbf{c}\cdot\mathbf{a})\mathbf{b}$ for arbitrary vectors $\mathbf{a}$, $\mathbf{b}$, $\mathbf{c}$. Also, the components of these tensors are referred to fixed orthonormal base vectors $\mathbf{e}_i$ of a rectangular Cartesian coordinate system with coordinates x_i.

Linear Equations of Cosserat Beam Theory

Here, attention is confined to a uniform, homogeneous beam that in its stress-free reference configuration occupies a right-cylindrical region with a uniform cross section $\mathscr{A}$, which is bounded by the closed curve ∂C. More specifically, the area A and the second moment of area $I_{\alpha\beta}$ of the cross section are defined by

$$A=\int_{\mathcal{A}} da, \tag{6a}$$

$$I_{\alpha\beta}=\int_{\mathcal{A}} x_\alpha x_\beta da, \tag{6b}$$

where da is the element of area. Also, it is convenient to take the reference line to be the centroid of the cross section and to take the coordinate directions to be oriented in the principal directions of the cross section, so that

$$\int_{\mathcal{A}} x_\alpha da=0, \tag{7a}$$

$$I_{12}=I_{21}=0. \tag{7b}$$

Within the context of the three-dimensional linear theory of an elastic isotropic material, the strain energy Σ^*, stress tensor $\mathbf{T}^*$ and strain tensor $\mathbf{E}^*$ are given by

$$\rho_0^*\Sigma^*=\rho_0^*\Sigma^*(\mathbf{E}^*)=\mu^*\left[\left\{\frac{\nu^*}{1-2\nu^*}\right\}(\mathbf{E}^*\cdot\mathbf{I})^2+\mathbf{E}^*\cdot\mathbf{E}^*\right], \tag{8a}$$

$$\mathbf{T}^*=\rho_0^*\frac{\partial\Sigma^*}{\partial\mathbf{E}^*}=2\mu^*\left[\left\{\frac{\nu^*}{1-2\nu^*}\right\}(\mathbf{E}^*\cdot\mathbf{I})\mathbf{I}+\mathbf{E}^*\right], \tag{8b}$$

$$\mathbf{E}^*=\tfrac{1}{2}(\mathbf{u}^*_{,i}\otimes\mathbf{e}_i+\mathbf{e}_i\otimes\mathbf{u}^*_{,i}), \tag{8c}$$

where ρ_0^* is the reference mass density and ν^* is Poisson's ratio. Also, the balance of linear momentum can be written in the form

$$\rho_0^*\ddot{\mathbf{u}}^*=\rho_0^*\mathbf{b}^*+\mathbf{t}^{*i}_{,i}, \tag{9a}$$

$$\mathbf{t}^{*i}=\mathbf{T}^*\mathbf{e}_i, \tag{9b}$$

$$\mathbf{T}^*=\mathbf{t}^{*i}\otimes\mathbf{e}_i, \tag{9c}$$

where a superposed $(\cdot)$ denotes partial differentiation with respect to time t, $\mathbf{b}^*$ is the external body force per unity mass, and the symbols with superscripts are introduced for ease of comparison with more general formulas developed in [11].

Within the context of the three-dimensional approach, the balance laws of the linearized Cosserat beam theory can be developed by taking weighted averages of the three-dimensional balance of linear momentum (9a). Specifically, the Cosserat balance of linear momentum can be obtained by averaging (9a) over the cross section, and the balances of director momentum can be obtained by weighting (9a) by x_α and then averaging the result over the cross section. This approach is similar to that used by Cowper [12] and details can be found in [[11], Sec. 5.25; [13]]. In particular, the resulting Cosserat balance laws become

$$m\ddot{\mathbf{u}}=m\mathbf{b}+\mathbf{t}^3_{,3}, \tag{10a}$$

$$my^{\alpha\beta}\ddot{\boldsymbol{\delta}}_\beta=m\mathbf{b}^\alpha-\mathbf{t}^\alpha+\mathbf{m}^\alpha_{,3}, \tag{10b}$$

where the intrinsic director couples $\mathbf{t}^i$, the director couples $\mathbf{m}^\alpha$, the external assigned director couples $\mathbf{b}^i$ due to body force and surface tractions on the lateral surface of the beam, the mass m per unit length, and the constant director inertia coefficients y^α and $y^{\alpha\beta}$ have been defined by

$$\mathbf{t}^i=\int_{\mathcal{A}}\mathbf{t}^{*i}da, \tag{11a}$$

$$\mathbf{m}^\alpha=\int_{\mathcal{A}}x_\alpha\mathbf{t}^{*3}da, \tag{11b}$$

$$m\mathbf{b}=\int_{\mathcal{A}}\rho_0^*\mathbf{b}^*da+\int_{\partial C}\mathbf{t}^*ds, \tag{11c}$$

$$m\mathbf{b}^\alpha=\int_{\mathcal{A}}x_\alpha\rho_0^*\mathbf{b}^*da+\int_{\partial C}x_\alpha\mathbf{t}^*ds, \tag{11d}$$

$$m=\int_{\mathcal{A}}\rho_0^*da=\rho_0^*A, \tag{11e}$$

$$my^\alpha=\int_{\mathcal{A}}x_\alpha\rho_0^*da=0, \tag{11f}$$

$$my^{\alpha\beta}=my^{\beta\alpha}=\int_{\mathcal{A}}x_\alpha x_\beta\rho_0^*da \tag{11g}$$

with the constitutive assumption (11f) being motivated by the condition (7a). Also, integration of (9c) over the cross section yields

$$\mathbf{T}=\int_{\mathcal{A}}\mathbf{T}^*da, \tag{12a}$$

$$\mathbf{T}=\mathbf{t}^i\otimes\mathbf{e}_i. \tag{12b}$$

The homogeneous strain $\mathbf{E}$ and the inhomogeneous strains $\boldsymbol{\beta}_\alpha$ in the Cosserat theory are defined by

$$\mathbf{E}=\tfrac{1}{2}(\boldsymbol{\delta}_i\otimes\mathbf{e}_i+\mathbf{e}\otimes\boldsymbol{\delta}_i)=E_{ij}(\mathbf{e}_i\otimes\mathbf{e}_j), \tag{13a}$$

$$\boldsymbol{\beta}_\alpha=\boldsymbol{\delta}_{\alpha,3}, \tag{13b}$$

$$\boldsymbol{\delta}_3=\boldsymbol{\delta}_3(x_3,t)=\mathbf{u}_{,3}. \tag{13c}$$

Moreover, for an elastic beam the strain energy Σ, and the constitutive equations for $\mathbf{T}$ and $\mathbf{m}^\alpha$ are given by

$$\Sigma=\Sigma(\mathbf{E},\boldsymbol{\beta}_\alpha),\quad \mathbf{T}=m\frac{\partial\Sigma}{\partial\mathbf{E}},\quad \mathbf{m}^\alpha=m\frac{\partial\Sigma}{\partial\boldsymbol{\beta}_\alpha}. \tag{14}$$

It was shown in [10] that restrictions can be placed on the strain energy which ensure that the Cosserat theory will predict solutions that are consistent with exact three-dimensional solutions for all homogeneous deformations. These restrictions are satisfied when Σ is specified in the form

$$\Sigma=\Sigma^*(\mathbf{E})+\Psi(\boldsymbol{\beta}_\alpha), \tag{15}$$

where Σ^* is three-dimensional strain energy function (8a) and Ψ represents the strain energy of inhomogeneous deformations which is a quadratic function of its argument. For the simplest theory Ψ is taken in the form

$$m\Psi=\tfrac{1}{2}E^*[I_{11}(\kappa_{13})^2+I_{22}(\kappa_{23})^2]+\tfrac{1}{2}\mu^*[J\beta^2], \tag{16}$$

where $E^*=2(1+\nu^*)\mu^*$ is Young's modulus, J is a constant, and the strains $\kappa_{\alpha i}$ and β have been defined by

$$\kappa_{\alpha i}=\boldsymbol{\beta}_{\alpha}\cdot\mathbf{e}_i\,,\quad \beta=\tfrac{1}{2}(\kappa_{12}-\kappa_{21}). \tag{17}$$

It then follows from (14)–(17) that the constitutive equations become

$$\mathbf{T}=2A\mu^*\left[\left\{\frac{\nu^*}{1-2\nu^*}\right\}(\mathbf{E}\cdot\mathbf{I})\mathbf{I}+\mathbf{E}\right], \tag{18a}$$

$$\mathbf{t}^i=\mathbf{T}\mathbf{e}_i\,, \tag{18b}$$

$$\mathbf{t}^1=2A\mu^*\left[\left\{\frac{1}{1-2\nu^*}\right\}\{(1-\nu^*)E_{11}+\nu^*E_{22}+\nu^*E_{33}\}\mathbf{e}_1 + E_{12}\mathbf{e}_2+E_{13}\mathbf{e}_3\right], \tag{18c}$$

$$\mathbf{t}^2=2A\mu^*\left[E_{12}\mathbf{e}_1+\left\{\frac{1}{1-2\nu^*}\right\}\{\nu^*E_{11}+(1-\nu^*)E_{22}+\nu^*E_{33}\}\mathbf{e}_2 + E_{23}\mathbf{e}_3\right], \tag{18d}$$

$$\mathbf{t}^3=2A\mu^*\left[E_{13}\mathbf{e}_1+E_{23}\mathbf{e}_2+\left\{\frac{1}{1-2\nu^*}\right\}\{\nu^*E_{11}+\nu^*E_{22} + (1-\nu^*)E_{33}\}\mathbf{e}_3\right], \tag{18e}$$

$$\mathbf{m}^1=\tfrac{1}{2}\mu^*J\beta\mathbf{e}_2+E^*I_{11}\kappa_{13}\mathbf{e}_3\,, \tag{18f}$$

$$\mathbf{m}^2=-\tfrac{1}{2}\mu^*J\beta\mathbf{e}_1+E^*I_{22}\kappa_{23}\mathbf{e}_3\,. \tag{18g}$$

In order to interpret the meaning of these quantities it is noted that, with respect to an arbitrary cross section with unit outward normal $\mathbf{e}_3$, the resultant force $\mathbf{n}$ and the resultant moment $\mathbf{m}$ (about the centroid of the cross section) are given by

$$\mathbf{n}=\mathbf{t}^3,\quad \mathbf{m}=\mathbf{e}_{\alpha}\times\mathbf{m}^{\alpha}=m_i\mathbf{e}_i\,,$$
$$m_1=E^*I_{22}\kappa_{23}\,,\quad m_2=-E^*I_{11}\kappa_{13}\,,\quad m_3=\mu^*J\beta. \tag{19}$$

Consequently, E^*I_{11} and E^*I_{22} are the bending rigidities associated with the bending strains κ_{13} and κ_{23}, respectively, and μ^*J is the torsional rigidity associated with the twist per unit length β. Furthermore, the value of J can be specified to be equal to the exact value for any given cross section even though warping is not included in this model.

For the simple case of bending in the $\mathbf{e}_1-\mathbf{e}_3$ plane, in the absence of body force and tractions on the lateral surface of the beam ($\mathbf{b}=0$ and $\mathbf{b}^{\alpha}=0$), the kinematic variables can be expressed in the forms

$$\mathbf{u}=u(x_3,t)\mathbf{e}_1\,,\quad \boldsymbol{\delta}_1=\delta(x_3,t)\mathbf{e}_3\,,\quad \boldsymbol{\delta}_2=0,\quad \kappa_{13}=\delta_{,3}\,,$$
$$2E_{13}=\delta+u_{,3}\,, \tag{20}$$

and the kinetic quantities become

$$\mathbf{t}^1=V(x_3,t)\mathbf{e}_3\,,\quad \mathbf{t}^2=0,\quad \mathbf{t}^3=V\mathbf{e}_1\,,\quad \mathbf{m}^1=-M(x_3,t)\mathbf{e}_3\,,$$
$$\mathbf{m}^2=0, \tag{21}$$

where the shear force V and the moment M are given by the constitutive equations

$$V=2A\mu^*E_{13}=A\mu^*(\delta+u_{,3}), \tag{22a}$$

$$M=-E^*I_{11}\kappa_{13}=-E^*I_{11}\delta_{,3}\,. \tag{22b}$$

Then, the equations of motion (10) reduce to

$$m\ddot{u}=V_{,3}\,, \tag{23a}$$

$$my^{11}\ddot{\delta}=-V-M_{,3}\,. \tag{23b}$$

Discussion

Returning to the points (P1)–(P6) made in the introduction it is obvious that (P1) is merely a statement of how to assess the accuracy of a solution in beam theory. The validity of point (P2) is deduced by the constitutive Eq. (22a) which results from the restriction on the Cosserat strain energy function that ensures consistency with exact solutions for all homogeneous deformations.

With regard to point (P3) it is noted that expressions for the exact beam kinematics (5) are either specified explicitly, [10,12], or are made tacitly when an assumed displacement field is substituted into a variational principle like that used in [4], or when different specifications are made for the strain energy function of the beam in terms of the three-dimensional strain energy function, [14].

In the discussion of effective properties of inhomogeneous materials it is common to define the average strain $\overline{\mathbf{E}}$ and average stress $\overline{\mathbf{T}}$ in terms of integrals of the exact quantities $\mathbf{E}^*$ and $\mathbf{T}^*$ over the volume of a representative volume element. Here, these average quantities are defined in terms of integrals over the cross-section of the beam

$$\overline{\mathbf{E}}=\frac{1}{A}\int_{\mathcal{A}}\mathbf{E}^*da, \tag{24a}$$

$$\overline{\mathbf{T}}=\frac{1}{A}\int_{\mathcal{A}}\mathbf{T}^*da. \tag{24b}$$

Moreover, with reference to a rectangular cross section, Rubin [10] has considered three specifications for $\overline{\mathbf{u}}$ and $\overline{\boldsymbol{\delta}}_{\alpha}$, the third of which can be generalized to the form

$$\overline{\mathbf{u}}=\frac{1}{A}\int_{\mathcal{A}}\mathbf{u}^*da, \tag{25a}$$

$$\overline{\boldsymbol{\delta}}_{\alpha}=\frac{1}{A}\int_{\mathcal{A}}\mathbf{u}^*_{,\alpha}da, \tag{25b}$$

$$\overline{\boldsymbol{\delta}}_3=\overline{\mathbf{u}}_{,3}\,, \tag{25c}$$

so that the exact result $\overline{\mathbf{E}}$ in (24a) and is given by

$$\overline{\mathbf{E}}=\tfrac{1}{2}(\overline{\boldsymbol{\delta}}_i\otimes\mathbf{e}_i+\mathbf{e}_i\otimes\overline{\boldsymbol{\delta}}_i). \tag{26}$$

Also, the result (12a) shows that $\mathbf{T}$ is related to the average stress $\overline{\mathbf{T}}$ by the formula

$$\mathbf{T}=A\overline{\mathbf{T}}. \tag{27}$$

Consequently, the specifications (25) with $(\mathbf{u}=\overline{\mathbf{u}},\boldsymbol{\delta}_{\alpha}=\overline{\boldsymbol{\delta}}_{\alpha})$ are consistent with these definitions of average stress and strain provided that the functional dependence of $\mathbf{T}$ on $\mathbf{E}$, and of $\overline{\mathbf{T}}$ on $\overline{\mathbf{E}}$ is the same as that of $\mathbf{T}^*$ on $\mathbf{E}^*$ for general anisotropic linear elastic materials. This means that for the special case of isotropic materials, the shear coefficient κ must be unity, which validates point (P4).

To explain point (P5) it is recalled that within the context of the Cosserat theory, the director inertia coefficients $y^{\alpha\beta}$ require constitutive equations and they are not necessarily determined by the expression (11g), which in view of (7b) and (11e) yields the common assumption that

$$my^{\alpha\beta}=\rho_0^*I_{\alpha\beta}\,, \tag{28a}$$

$$m=\rho_0^*A. \tag{28b}$$

Moreover, the research in [10,11,13,15] suggests that the director inertia coefficients $y^{\alpha\beta}$ model not only the distribution of mass in the cross section but they model the distribution of inertia in a particular vibrational mode. Specifically, for the case of a rectangular cross section with height H in the $\mathbf{e}_1$-direction and depth W in the $\mathbf{e}_2$-direction, the work in [15] for free vibrations of a parallelepiped, and the work in [11, Sec. 5.17] for forced shearing vibrations through the thickness of the beam, suggests that the director inertia coefficients be specified by

$$y^{11}=\frac{H^2}{\pi^2},\quad y^{22}=\frac{W^2}{\pi^2},\quad y^{12}=y^{21}=0,\tag{29}$$

instead of the values obtained by exact integration of (11f). In this regard, it should be mentioned that the values of $y^{\alpha\beta}$ for different cross-sectional shapes need to be determined by matching vibrational frequencies.

Finally, to justify point (P6) consider wave propagation in an infinite beam which is characterized by

$$u=B_1\sin[k(x_3-ct)],\tag{30a}$$

$$\delta=B_2k\cos[k(x_3-ct)],\tag{30b}$$

where B_1 and B_2 are the amplitudes, k is the wave number and c is the wave speed. Then, using the Timoshenko constitutive Eq. (2), and with the help of (22b) and (28b), the equations of motion (23) can be reduced to the forms

$$(\kappa-C^2)B_1+\kappa B_2=0,\tag{31a}$$

$$\kappa B_1+[\kappa-YK^2C^2-2(1+\nu^*)K^2]B_2=0,\tag{31b}$$

where the shear wave speed c_s and the nondimensional quantities $\{C, Y, K\}$ have been defined by

$$c_s=\sqrt{\frac{\mu^*}{\rho_0^*}},\quad C=\frac{c}{c_s},\quad Y=\frac{Ay^{11}}{I_{11}},\quad K=k\sqrt{\frac{I_{11}}{A}}.\tag{32}$$

The Eqs. (31) have a nontrivial solution when the normalized wave speed C is given by

$$C^2=\frac{a_1-\sqrt{a_1^2-4a_0a_2}}{2a_2},\quad a_0=2(1+\nu^*)\kappa K^2,$$

$$a_1=\kappa+[\kappa Y+2(1+\nu^*)K^2],\quad a_2=YK^2.\tag{33}$$

Thus, in the limit of short wavelengths [$K\to\infty$, with $\kappa Y<2(1+\nu^*)$] the solution of (31) yields

$$c\to c_s\sqrt{\kappa},\tag{34a}$$

$$\delta\to 0.\tag{34b}$$

In this limit, the transverse wave (30a) is essentially insensitive to the free lateral surface of the beam so the wave should travel at the shear wave speed c_s in an infinite media with $\kappa=1$. In view of the solution (34b), this result is independent of the director inertia coefficient. Consequently, this restriction on κ is independent of the Cosserat theory and can be obtained by considering the limit of short wavelengths in the original Timoshenko formulation, [1].

Acknowledgment

This research was partially supported by the fund for the promotion of research at the Technion. Also, the author would like to acknowledge helpful discussions with Prof. S. R. Bodner.

References

[1] Timoshenko, S. P., 1921, "On the Corrections for Shear of the Differential Equation for Transverse Vibrations of Prismatic Bars," Philos. Mag., **41**, pp. 744–746.
[2] Timoshenko, S. P., 1922, "On the Transverse Vibrations of Bars of Uniform Cross Section," Philos. Mag., **43**, pp. 125–131.
[3] Kaneko, T., 1975, "On Timoshenko's Correction for Shear in Vibrating Beams," J. Phys. D, **8**, pp. 1927–1936.
[4] Hutchinson, J. R., 2001, "Shear Coefficients for Timoshenko Beam Theory," ASME J. Appl. Mech., **68**, pp. 87–92.
[5] Hutchinson, J. R., 2001, closure to "On Shear Coefficients for Timoshenko Beam Theory," ASME J. Appl. Mech., **68**, pp. 960–961.
[6] Stephen, N. G., 2001, discussion of "Shear Coefficients for Timoshenko Beam Theory," ASME J. Appl. Mech., **68**, pp. 959–960.
[7] Green, A. E., Naghdi, P. M., and Wenner, M. L., 1974, "On the Theory of Rods—I. Derivation From the Three-Dimensional Equations," Proc. R. Soc. London, Ser. A, **337**, pp. 451–483.
[8] Green, A. E., Naghdi, P. M., and Wenner, M. L., 1974, "On the Theory of Rods—II. Developments by Direct Approach," Proc. R. Soc. London, Ser. A, **337**, pp. 451–483.
[9] Naghdi, P. M., and Rubin, M. B., 1984, "Constrained Theories of Rods," J. Elast., **14**, pp. 343–361.
[10] Rubin, M. B., 1996, "Restrictions on Nonlinear Constitutive Equations for Elastic Rods," J. Elast., **44**, pp. 9–36.
[11] Rubin, M. B., 2000, *Cosserat Theories: Shells, Rods and Points* (Solid Mechanics and its Applications), **79**, Kluwer, The Netherlands.
[12] Cowper, G. R., 1966, "The Shear Coefficient in Timoshenko's Beam Theory," ASME J. Appl. Mech., **33**, pp. 335–340.
[13] Rubin, M. B., 2001, "A Simple Derivation of Cosserat Theories of Shells, Rods and Points," *Advances in the Mechanics of Plates and Shells* (The Avinoam Libai Anniversary Volume, Solid Mechanics and Its Applications), **88**, Kluwer, Dordrecht, pp. 277–294.
[14] O'Reilly, O. M., 1998, "On Constitutive Relations for Elastic Rods," Int. J. Solids Struct., **35**, pp. 1009–1024.
[15] Rubin, M. B., 1986, "Free Vibration of a Rectangular Parallelepiped Using the Theory of a Cosserat Point," ASME J. Appl. Mech., **53**, pp. 45–50.

Dr. Daniel C. Drucker
1918–2001
Graduate Research Professor Emeritus
University of Florida

Dr. Daniel C. Drucker, 83, died Sept. 1, 2001 of leukemia in Gainesville, FL. Few people have served the engineering profession with such dedication and distinction as did Dan Drucker. He was known as a brilliant scientist, a leader in engineering education, and an eloquent spokesman for the engineering profession. Dan was a past president of the American Society of Mechanical Engineers (ASME), the American Society for Engineering Education (ASEE), the American Academy of Mechanics (AAM), and the Society for Experimental Stress Analysis (SESA) (now known as the Society for Experimental Mechanics, SEM). He also served as president of the International Union of Theoretical and Applied Mechanics (IUTAM), being only the second American ever to serve in that office. Dan was one of the most honored persons in the field of applied mechanics.

Dan was known throughout the world for contributions to the theory of plasticity and its application to analysis and design in metal structures. He introduced the concept of material stability, now known as ''Drucker's Stability Postulate,'' which provided a unified approach for the derivation of stress-strain relations for plastic behavior of metals. His theorems led directly to limit design; a technique to predict the load carrying capacity of engineering structures. Dan also made lasting contributions to the field of photoelasticity. His 1940 paper on three-dimensional photoelasticity has become a classic and ''Drucker's Oblique Incidence Method'' is widely used in university and industrial photoelastic laboratories.

ASME established the Daniel C. Drucker Medal in 1997 to honor him for his contributions to applied mechanics in research, education, and leadership. The medal is bestowed on individuals in recognition of sustained, outstanding contributions to applied mechanics and mechanical engineering through research, teaching, and/or service to the community. Dan was the first recipient of the award, which was presented at an 80th birthday luncheon honoring him during the Thirteenth U.S. National Congress of Applied Mechanics in Gainesville, FL, in June 1998. ASME also honored Dan with the Timoshenko Medal, the Thurston Lectureship, the ASME Medal, and Honorary Membership. For 12 years he was the Editor of the *Journal of Applied Mechanics*.

Dan was a highly esteemed member of SESA/SEM and received that Society's two highest honors, the Murray Lecturership and Honorary Membership; he also received SESA's M. M. Frocht Award. ASEE conferred upon Dan the Lamme Medal, the Distinguished Educator Award of the Mechanics Division; he was a Founding Fellow of ASEE, and was elected to its Hall of Fame. ASCE presented to him the von Karman Medal. The University of Liege gave Dan the Gustav Trasenter Medal and Columbia University conferred upon him the Egleston and Illig Medals. From the Society of Engineering Sciences he received the first William Prager Medal; the Founder Engineering Societies gave him the John Fritz Medal. Dan had honorary doctorates from Lehigh, the Technion, Brown, Northwestern, and the University of Illinois at Urbana-Champaign. After Dan's death, his daughter found among his mementos a ''Medal for Getting the Most Medals'' which someone had jokingly presented to him.

In 1988 Dan received the National Medal of Science. He was a member of the National Academy of Engineering and of the American Academy of Arts and Sciences, and was a Foreign Member of the Polish Academy of Science. He was listed in national and international editions of *Who's Who*.

He had a reputation as an incisive thinker, and his advice was eagerly sought and generously given at the university, state and national levels. An articulate speaker who consistently gave stimulating and informative talks, Dan was frequently invited to give keynote or other major addresses at engineering meetings. A list of such participation is too long to be given here, but recent examples include: the National Academy of Sciences Committee on Human Rights, the National Research Council Engineering Research Board, the National Science Board and the chairmanship of the National Academy of Engineering Committee on Membership Policy.

Dan Drucker was born in New York City and started his engineering career as a student at Columbia University. His ambition at that time was to design bridges. While still an undergraduate at Columbia he met a young instructor named Raymond D. Mindlin (later a SESA Founding Member, President, and Honorary Member), who told Dan that ''he *would* pursue a Ph.D. degree and he *would* write a thesis on photoelasticity.'' Dan complied, and received his doctorate in 1940. It was during his student days that Dan met a young lady named Ann Bodin. They eloped and were married in 1939, living as a loving and devoted couple for more than 61 years. Dan and Ann, who predeceased him, had a son, Dr. David Drucker now of Utica, NY, and a daughter, Mrs. Mady Drucker Upham now of Rockport, MA; and four grandchildren.

Dan taught at Cornell University from 1940 to 1943 before joining the Armour Research Foundation. After serving in the U.S. Army Air Corps, he went back to the Illinois Institute of Technology for a short time before joining the faculty of Brown University in 1947. During his tenure at Brown he did much of his pioneering work on plasticity. Dan joined the University of Illinois at Urbana-Champaign in 1968 as Dean of Engineering. During his more than 15 years there, the UIUC College of Engineering was consistently ranked among the best five in the nation. Although known for its insistence upon technical excellence, his college was also recognized for its total commitment to equal opportunity for all. He left Illinois in 1984 to become a graduate research professor at the University of Florida, from which he retired in 1994.

I met Dan during my first SESA meeting in 1949. At that time I had just started working toward a Ph.D. at the University of Illinois and intended to write a thesis on three-dimensional photoelasticity. Tom Dolan, who was my advisor, also attended the meeting and made sure that I met the important SESA members. When he saw Ray Mindlin and Dan Drucker standing across the room, he said to me, ‘‘Come over here, I want you to meet these two. They think things through pretty well before they speak, and are usually right.’’ That was my introduction to Dan Drucker, and Tom was right. After that I started to see Dan regularly at meetings and he always greeted me with a big smile and a handshake. He had just written the chapter on three-dimensional photoelasticity in the *Handbook of Experimental Stress Analysis*, so I often talked with him about my proposed thesis. He was easy to talk with and always very helpful. In a sense he was a mentor for me while he was still at Brown University. That happy relationship continued while we both worked through the various SESA offices, and while he was a very busy dean at the University of Illinois. He always made time to talk with me about technical subjects or SESA business.

When Dan came to Florida he immediately joined our department’s ‘‘lunch bunch’’ which met every school day at noon. At various times that included Knox Millsaps, Larry Malvern, Ray Bisplinghoff, Hans von Ohain, Chia-Shun (Gus) Yih, plus Dan Drucker and me. What a wonderful group of colleagues. Now all of those special friends have passed away except for me, but I feel truly blessed to have been among them.

Up until the last month of his life, Dan and I still tried to have lunch three days a week. Those were happy occasions, even though we both realized that the inevitable was sneaking up on him. We didn’t dwell on that and found lots of things to laugh about. In all of the thousands of hours we spent together, I never heard him utter a single swear word. He had a great sense of humor, but he never told a joke and he never spread gossip. I have never met a more honest man or pure person. Dan Drucker was the kind of person that we all try to be.

Of course, the Drucker family received letters of condolence from all over the world. Mady was kind enough to give me copies of most of those letters. The common thread that went through all of those letters was that Dan was highly respected as an engineering leader, but that he was also greatly admired as a human being. Everyone mentioned that his kindness and help had influenced their careers and their lives. What an impact he made and what a legacy he left!

Charles E. Taylor